

The Characterisation of Uranium Materials for Materials Provenancing in Nuclear Forensics

by

Tim Ditcham

*Thesis
Submitted to Flinders University
for the degree of*

Doctor of Philosophy

College of Science and Engineering

18th November 2019

Declaration

I certify that this thesis does not incorporate without acknowledgement any material previously submitted for a degree or diploma in any university; and, to the best of my knowledge and belief it does not contain any material previously published or written by another person except where due reference is made in the text.

Tim G. Ditcham

.....

Signed

.....

Dated

Acknowledgements

Firstly, I wish to acknowledge and thank my supervisors Rachel Popelka-Filcoff, Paul Kirkbride, Claire Lenehan, Andrew Wotherspoon and Tegan Bull for all their support, guidance and their enthusiasm through this journey. Throughout all the highs and lows, you've stuck with me and I am extremely grateful for that.

Throughout this PhD, I've had the good fortune of visiting a number of research institutions and working alongside some wonderful people who were always welcoming and always willing to help me out or offer assistance/advice. From ANSTO, I wish to thank Liz Keegan, Grant Griffiths, Ned Blagojevic, Emma Young, Elaine Loi, Kaitlyn Toole, Attila Stopic, John Bennett and Mellodee Anvia. From MURR, I wish to thank John Brown, John Brockman, Dave Robertson, Jim Guthrie and Virginie Renson. From Flinders University, I wish to thank Jason Young, Daniel Jardine, Jonathan Campbell, David Vincent, Ashley Slattery, Cameron Shearer, Alan Pring, Sean Graney, Jing Zhao and the Analytical Research Group.

I would also like to acknowledge Heathgate Resources Pty Ptd, Energy Resources of Australia Ltd, and BHP Billiton Ltd. and the South Australian Museum for the provision of UOC and uranium ore samples analysed in this thesis. I also wish to acknowledge the financial support provided to me over the course of my PhD from the following organisations/funding bodies; AINSE, Australasian Radiation Protection Society, the United Uranium Scholarship, American Nuclear Society. I also wish to acknowledge Flinders University for providing myself with a Flinders University Research Scholarship to support me for the duration of my studies.

Lastly, I would like to thank my friends and family for all of their support. To my office mates, Tiffany, Caroline and Sam, thank you for your friendship and being such wonderful sounding boards over the years! To Grant and Maryanne, I consider myself incredibly fortunate to have you both as my parents. I cannot thank you enough for your unwavering support and for always being there for me especially during the times when it has been incredibly tough going.

Table of Contents

DECLARATION	2
ACKNOWLEDGEMENTS	3
TABLE OF CONTENTS	5
TABLE OF FIGURES	11
THESIS SUMMARY	22
CHAPTER 1. INTRODUCTION	1
1.1. URANIUM	1
1.1.1. Isotopes of Uranium	1
1.1.2. Applications of Uranium	4
1.1.2.1. <i>Use in Nuclear Energy</i>	4
1.1.2.2. <i>Use in Nuclear Weapons</i>	5
1.1.2.3. <i>Other Uses of Uranium</i>	5
1.2. URANIUM DEPOSITS	7
1.2.1. Formation of Uranium Deposits	7
1.2.2. Categorisation of Uranium Deposits	8
1.2.2.1. Confidence Classification of Uranium Deposits	9
1.2.2.2. Economic Classifications of Uranium Deposits	10
1.2.2.3. Geological Classifications of Uranium Deposits	10
1.3. MINING OF URANIUM ORE DEPOSITS AND PRODUCTION OF URANIUM ORE CONCENTRATES	13
1.3.1. Mining of Uranium Ore Deposits	14
1.3.1.1. <i>Open-pit Mining</i>	14
1.3.1.2. <i>Underground Mining</i>	15
1.3.1.3. <i>In-situ Mining</i>	15
1.3.2. Production of UOC	16
1.3.2.1. <i>Milling of Uranium Ore</i>	16
1.3.2.2. <i>Leaching of Uranium from Uranium Ore</i>	17
1.3.2.3. <i>Separation and Extraction of Uranium</i>	18
1.3.2.4. <i>Precipitation of Uranium and the Drying and Calcination of Uranium Ore Concentrates</i>	20
1.4. AUSTRALIA AND URANIUM	21
1.4.1. Australia's Uranium Resources	21
1.4.2. Active Australian Uranium Mines	23
1.4.2.1. Olympic Dam, South Australia	23
1.4.2.2. Beverley, South Australia	24
1.4.2.3. Ranger, Northern Territory	25
1.4.2.4. Four Mile, South Australia	26
1.4.3. Closed Australian Uranium Mines	26

1.4.3.1 <i>Honeymoon, South Australia</i>	26
1.4.3.2 <i>Rum Jungle, Northern Territory</i>	26
1.4.3.3 <i>Mary Kathleen, Queensland</i>	27
1.4.3.4 <i>Narbarlek, Northern Territory</i>	27
1.4.3.5 <i>South Alligator, Northern Territory</i>	28
1.4.3.6 <i>Radium Hill, South Australia</i>	28
1.5 NUCLEAR FORENSIC SCIENCE	29
1.5.1 History of Nuclear Forensic Science	29
1.5.2 Nuclear forensics in the Australian context	29
1.5.3 Research focuses in nuclear forensics.....	30
1.5.4 Source Attribution of Uranium Ore Concentrate	31
1.5.4.1 Uranium Isotopic Analysis	31
1.5.4.2 Anion analysis.....	33
1.5.4.3 Trace and Rare Earth Elemental (REE) Analysis	34
1.5.4.4 Isotopic Analysis of Lead, Strontium and Oxygen Impurities in UOC.....	37
1.5.4.5 Analysis of Uranium Speciation within UOC	41
1.6 RESEARCH AIMS	41
CHAPTER 2. ANALYTICAL TECHNIQUES	43
2.1. INDUCTIVELY-COUPLED PLASMA MASS SPECTROMETRY	43
2.1.1 Sample Introduction.....	43
2.1.2 Plasma Ionisation	44
2.1.3 Mass Spectrometer Interface.....	44
2.1.4 Ion Focusing.....	45
2.1.5 Mass Analysers	45
2.1.6 Ion Detection System.....	47
2.1.2 MC-ICP-MS AND SF-ICP-MS	48
2.2 NEUTRON ACTIVATION ANALYSIS AND DELAYED NEUTRON ACTIVATION ANALYSIS	50
2.2.1 Principles of Neutron Activation Analysis and Delayed Neutron Activation Analysis	50
2.2.1.1 k_0 -NAA and relative comparator methods.....	53
2.2.2 NAA in Source Attribution	56
2.5 THERMOGRAVIMETRIC ANALYSIS.....	57
2.5.1 Principles of Thermogravimetric Analysis	57
2.5.2 Application of Thermogravimetric Analysis in Nuclear Forensics and Nuclear Chemistry	58
2.6 SCANNING ELECTRON MICROSCOPY (SEM)/ENERGY-DISPERSIVE X-RAY SPECTROSCOPY (SEM/EDX)	
.....	60
2.6.1 SEM & SEM/EDX Principles.....	60
2.6.1.1 Electron-electron interactions	60
2.6.1.1 Electron-X-ray Interactions	62
2.6.3 Detection of X-rays	64
2.6.4 Detection of Secondary and Backscattered Electrons.....	65

2.6.5 Quantitative Elemental Analysis by SEM/EDX	66
2.6.2 Scanning Electron Microscopy and Scanning Electron Microscopy/Energy-Dispersive X-ray Spectroscopy in Nuclear Forensics	67
2.7 RAMAN SPECTROSCOPY	71
2.7.1 Principles of Raman Spectroscopy	71
2.8 X-RAY FLUORESCENCE SPECTROSCOPY (XRF)	72
2.9 NIR SPECTROSCOPY	74
CHAPTER 3. URANIUM ORE CONCENTRATE AND URANIUM ORE SAMPLES	76
3.1 INTRODUCTION.....	76
3.2 AUSTRALIAN UOC AND URANIUM ORE SAMPLES.....	76
3.3 NORTH AMERICAN URANIUM ORE SAMPLES	77
3.3.1 Big Indian Wash District, Utah.....	77
3.3.2 Calyx No. 8 Mine, Utah	79
3.3.3 Ike-Nixon Shaft, Utah	81
3.3.4 Happy Jack Mine, Utah.....	81
3.3.5 Mi Vida Mine, Utah	81
3.3.6 Green Dragon Mine, Utah.....	81
3.3.7 Uravan Mineral Belt, Colorado/Utah.....	82
3.3.8 Midnite Mine, Washington	83
3.3.9 Ferguson Lode Claim, South Dakota.....	83
3.3.10 Ruggle's Mine, New Hampshire.....	84
3.3.11 Cardiff, Ontario.....	84
CHAPTER 4. THERMAL, VIBRATIONAL AND MORPHOLOGICAL ANALYSIS OF AUSTRALIAN UOCS.....	85
4.1 INTRODUCTION	85
4.2.1 Analysis of UOCs using NIR and Raman spectroscopy.....	85
4.1.2 Thermal Analyses of UOCs and uranium oxides.....	87
4.1.3 Morphological analysis of UOCs.....	89
4.1.4 Justification	91
4.2 METHODS.....	92
4.3 RESULTS.....	95
4.3.1 Thermogravimetric analysis of Australian UOCs.....	95
4.3.1.1 Beverley UOCs	95
4.3.1.2 Ranger UOCs	101
4.3.1.3 Olympic Dam UOCs.....	103
4.3.2 Differential scanning calorimetry	105
4.3.3 NIR spectroscopy	110

4.3.4 μ Raman spectroscopy	113
4.3.4.1 Beverley UOCs	113
4.3.4.2 Ranger UOCs	117
4.3.4.3 Olympic Dam UOCs.....	121
4.3.5 X-ray diffraction	125
4.3.5 Comparison of TGA traces between the Australian UOCs	128
4.3.5 Analysis of UOC morphology and the impact of temperature by SEM	130
4.3.5.1 Beverley UOCs	130
4.3.5.2 Ranger UOCs	133
4.3.5.3 Olympic Dam UOCs.....	134
4.3.6 Impact of temperature on the distinct morphologies observed within the Australian UOC samples.....	138
4.7 CONCLUSIONS.....	142
4.8 FUTURE WORK.....	144
4.8.1 High Temperature XRD analysis of the Australian UOCs	144
4.8.2 Inclusion of more UOC samples	144
4.8.3 Objective morphological analysis of UOCs.....	145
CHAPTER 5. ISOTOPE ANALYSIS OF UOCS AND URANIUM ORES	146
5.1 INTRODUCTION	146
5.1.1 Isotopes of uranium.....	146
5.1.2 Variations in uranium isotopes within natural uranium.....	146
5.1.3 Impact of UOC production processes on uranium isotope ratios within uranium ores	148
5.1.4 Application of uranium isotope analysis within nuclear forensics	150
5.1.5 Justification	152
5.2 METHODS.....	152
5.2.1 Sample Preparation for MC-ICP-MS analysis.....	152
5.2.2 Analysis of Uranium Isotope Ratios of Australian UOC and Uranium Ore Samples by MC-ICP-MS	154
5.2.3 Uranium Isotope Ratio Calculations and Corrections.....	156
5.2.4 Determination of Uncertainty in MC-ICP-MS Measurement of Uranium Isotope Ratios.....	157
5.2.5 Statistical methods to evaluate variance in isotopic ratios.....	159
5.2.5.1 E_n -Scores.....	159
5.3 RESULTS.....	160
5.3.1 Performance of MC-ICP-MS for the measurement of $^{235}\text{U}/^{238}\text{U}$ and $^{234}\text{U}/^{238}\text{U}$ isotope ratios.....	160
5.3.1.1 Expanded uncertainty.....	160
5.3.1.2 Standard deviation	168
5.3.2 Comparison with other studies analysing U isotope ratios	169
5.3.3 Comparisons between all Australian UOC and uranium ore samples and complimentary samples previously analysed within the literature	171

5.6 CONCLUSIONS.....	171
5.7 FUTURE WORK	172
CHAPTER 6. ELEMENTAL ANALYSIS OF AUSTRALIAN AND INTERNATIONAL URANIUM ORES	174
6.1 INTRODUCTION	174
6.1.1 Rare Earth Elements.....	174
6.1.2 Trace Elements.....	176
6.1.2 Elemental Analysis Techniques in Nuclear Forensics.....	179
6.1.3 Justification	184
6.2 METHODS.....	185
6.2.1 Preparation of Australian and international uranium ore samples for analysis	185
6.2.2 Quantification of uranium content within international uranium ore samples using SEM/EDX, pXRF and DNAA.....	188
6.2.2.1 SEM/EDX.....	188
6.2.2.2 Portable XRF	191
6.2.2.3 DNAA.....	193
6.2.3 Quantification of the trace and rare earth elemental content of Australian and international uranium ore samples using k_0 -NAA.....	195
6.3 RESULTS.....	198
6.3.1 Quantification of uranium content within international uranium ore samples by SEM/EDX, pXRF and DNAA	198
6.3.2 Comparison between U analyses between k_0 -NAA and DNAA within OREAS Standards.....	202
6.3.3 Analysis of OREAS certified reference materials with k_0 -NAA	204
6.3.3.1 Analysis of OREAS 100a CRM by k_0 -NAA	204
6.3.3.2 Analysis of OREAS 106 CRM by k_0 -NAA	207
6.3.3.3 Analysis of OREAS 120 CRM by k_0 -NAA	209
6.3.3.4 Analysis of OREAS 124 CRM by k_0 -NAA	211
6.3.4 Impact of k_0 -NAA interferences in chondrite-normalised REE patterns of uranium certified reference materials	213
6.3.5 Chondrite-normalised rare earth elemental patterns of Australian and international uranium ore samples.....	217
6.3.5.1 Olympic Dam.....	217
6.3.5.2 Beverley and Four Mile	218
6.3.5.3 Ranger.....	219
6.3.5.4 Mary Kathleen	221
6.3.5.7 Happy Jack Mine, Mi Vida Mine, Big Indian Wash District, Green Dragon Mine, Calyx No 8 Mine.....	223
6.3.5.8 Ferguson Lode Claim.....	227
6.3.5.9 Uravan Mineral Belt	228
6.3.5.10 Midnite Mine	229
6.3.6 Trace Elements of the Australian and North American Uranium Ore Samples	230

6.3.6.1 Thorium.....	230
6.3.6.2 Major Trace Elements.....	233
6.3.6.3 Minor trace elements.....	238
6.3.7 Comparison between the REE and trace elemental composition of the uranium ores and UOCs from the same Australian mine	240
6.3 CONCLUSIONS	248
6.4 FUTURE WORK.....	251
6.4.1 Reanalysis of Australian and North American uranium ore samples by ICP-MS.....	251
6.4.2 HPLC Separation or Online HPLC-ICP-MS method for the analysis of REEs within UOCs	251
6.4.3 CRM development	252
CHAPTER 7. CONCLUSIONS	259
APPENDIX A COMPARISON OF URANIUM ISOTOPE RATIOS MEASURED WITHIN AUSTRALIAN UOCS AND URANIUM ORES WITH LITERATURE RATIOS	263
8.1 Analysis of several Australian UOCs and uranium ore samples by MC-ICP-MS	263
8.1.1 Beverley UOC and uranium ore samples.....	263
8.1.2 Ranger UOC and uranium ore samples	264
8.1.3 Olympic Dam UOC and uranium ore samples	265
8.1.4 Mary Kathleen ore sample.....	266
8.1.5 Comparison between all Australian UOC and uranium ore samples	267
8.2 Comparison with other UOC and uranium ore samples reported in the literature	271
REFERENCES	278

Table of Figures

Figure 1. Radium series decay chain ($4n+2$) [9].....	2
Figure 2 Actinium series decay chain ($2n+3$) [12]	3
Figure 3. Nuclear share of electricity generation (as of 31 st December 2018)[17]	5
Figure 4. Comparison and approximate correlation in major resource classification systems between countries and organisations [18]. Note: 1) United Nations Framework Classification (UNFC) correlation with NEA/IAEA and national classification systems is still under consideration. ..	10
Figure 5. Rössing open-pit uranium mine, Namibia [41]	15
Figure 6. Schematic of Beverley ISL uranium mine, Australia [43]	16
Figure 7. Diagram of the various zones of a conventional thickener: (a) clear solution zone, (b) free settling zone, (c) transition zone, (d) compression zone [49]	19
Figure 8. Global distribution of identified uranium deposits (<USD 130/kgU) as of 1 st January 2017 [58].....	22
Figure 9. Uranium deposits and current, former and prospective uranium mines in Australia [37].	23
Figure 10. Simplified geological plan of the Olympic Dam hematite-breccia complex deposit [67]	24
Figure 11. Illicit trafficking cases recorded by the IAEA on the ITDB as of the 31 st of December 2018 [94].....	29
Figure 12. Anion ratios in different uranium ore concentrate samples [112].....	33
Figure 13. Chondrite-normalised REE pattern of uranium oxide from six different categories of uranium deposits [115]	37
Figure 14. Measured $^{87}\text{Sr}/^{86}\text{Sr}$ isotope ratios of UOC samples from different mines (presented at the 95% confidence level) [116].....	39
Figure 15. Comparison of typical FTIR spectra of various UOC compounds [113].....	41
Figure 16. Schematic Diagram of Quadrupole-ICP-MS instrument [129].....	43
Figure 17. Mechanism of conversion of a droplet to a positive ion in the ICP [130].....	44
Figure 18. Quadrupole separation of ions with different m/z ratios [125].....	46
Figure 19. Schematic diagram of a reverse ‘Nier-Johnson’ SF-ICP-MS [130].....	47
Figure 20. Schematic diagram of channel electron multiplier [135]	48
Figure 21 Diagram of MC-ICP-MS detector array [138]	50
Figure 22 Reaction scheme following neutron capture during NAA [141].....	51
Figure 23 Typical neutron spectrum from a nuclear fission reactor [29]	52
Figure 24 ^{235}U thermal fission yield versus atomic number [142]	55

Figure 25 Interactions of incident electrons with sample: a) secondary electrons, b) backscattered electrons c) Auger electrons or X-ray fluorescence (XRF) [157].....	61
Figure 26 Degree of penetration by electrons according to atomic number and incident electron energy [157].....	62
Figure 27 Relative probabilities of X-ray fluorescence and Auger emission as a function to atomic number (Z) for k-electron excitation [157].....	63
Figure 28 Rayleigh, Stokes and Anti-Stokes scattering.....	71
Figure 30 Location of uranium mines/deposits within North America.....	77
Figure 31 Location of the Big Indian Wash District within the continental United States [180].....	78
Figure 32 Location of uranium occurrences and mines within the Big Indian Wash District, Utah [180].....	78
Figure 33 Location of the Calyx No 8 Mine (Shaft Number 8) within the Temple Mountain District of Utah [183].....	80
Figure 34 Index map of south-western Colorado and south-eastern Utah outlining the boundary of the Uravan Mineral Belt by Chenoweth (1981) [191], which was modified from Butler and Fischer (1978) [192].....	82
Figure 35 Presentation of TGA intermediates and product from Beverley UOC 3 in preparation for analysis by μ Raman spectroscopy.....	94
Figure 36 Diagram of sample mount for NIR analysis of UOC samples.....	95
Figure 37 Colour changes in the Beverley UOC 1 upon heating to different temperatures during TGA.....	96
Figure 38 TGA plot of the three Beverley UOCs analysed in an air atmosphere.....	96
Figure 39 TGA plot of the three Beverley UOC samples analysed in a nitrogen atmosphere.....	97
Figure 40 XRD patterns obtained from intermediates and products from the thermal decomposition of synthetic uranyl peroxide/studtite samples by Sato (1976) [223] (top) and Guo <i>et al.</i> (2016) (bottom) [221].....	100
Figure 41 Colour of the Beverley UOC 1 upon heating to different temperatures during TGA.....	101
Figure 42 TGA plot of the three Ranger UOCs analysed in an air atmosphere.....	102
Figure 43 TGA plot of the three Ranger UOCs analysed in a nitrogen atmosphere.....	103
Figure 44 Colour of the Beverley UOC 1 upon heating to different temperatures during TGA.....	103
Figure 45 TGA plot of the two Olympic Dam UOCs analysed in a nitrogen atmosphere.....	104
Figure 46 TGA plots of the three Olympic Dam UOCs analysed in a nitrogen atmosphere.....	105
Figure 47 DSC plot of Beverley, Ranger and Olympic Dam UOCs analysed by TGA in a nitrogen atmosphere.....	106

Figure 48 DSC plot of Beverley, Ranger and Olympic Dam UOCs analysed by TGA in an air atmosphere.....	107
Figure 49 First derivative of the DSC data obtained from the Beverley UOCs in an air atmosphere	108
Figure 50 First derivative of the DSC data obtained from the Ranger UOCs in an air atmosphere.	109
Figure 51 First derivative of the DSC data obtained from the Olympic Dam UOCs in an air atmosphere.....	109
Figure 52 NIR reflectance spectra of frosted and clear quartz, and soda-lime glass backed by Spectralon white reference standard	111
Figure 53 Effect of mass analysed on the NIR analysis of a Beverley UOC	112
Figure 54 NIR spectra of UOCs from Ranger and Olympic Dam (~10 mg).....	113
Figure 55 Raman spectra of the three Beverley UOCs.....	114
Figure 56 Raman spectra of the Beverley TGA intermediates obtained at 280 °C in both air and nitrogen atmospheres	115
Figure 57 Raman spectra of the Beverley TGA intermediates obtained at 500 °C in both air and nitrogen atmospheres	116
Figure 58 Raman spectra of the Beverley TGA products obtained at 1000 °C in both air and nitrogen atmospheres.....	117
Figure 61 Raman spectra of the Ranger TGA intermediates obtained at 500 °C in both air and nitrogen atmospheres	120
Figure 62 Raman spectra of the Ranger TGA intermediates obtained at 1000 °C in both air and nitrogen atmospheres	121
Figure 64 Raman spectra of the Olympic Dam TGA intermediates obtained at 200 °C in both air and nitrogen atmospheres	123
Figure 65 Raman spectra of the Olympic TGA intermediates obtained at 500 °C in both air and nitrogen atmospheres	124
Figure 66 Raman spectra of the Olympic Dam TGA intermediates obtained at 1000 °C in both air and nitrogen atmospheres	125
Figure 67 X-ray diffraction patterns of Beverley UOC 1, the two intermediates obtained at 280 °C and 500 °C, and the TGA product obtained via TGA in an air atmosphere at 1000 °C.....	126
Figure 68 X-ray diffraction patterns of Ranger UOC 2, the two intermediates obtained at 280 °C and 500 °C, and the TGA product obtained via TGA in an air atmosphere at 1000 °C.....	127
Figure 69 X-ray diffraction patterns of Olympic Dam UOC 1, the two intermediates obtained at 280 °C and 500 °C, and the TGA product obtained via TGA in a air atmosphere at 1000 °C.....	128

Figure 70 Analysis of Australian UOC samples by TGA in an air atmosphere	129
Figure 71 Expanded graph of the 50-250 °C region of the TGA plot of the Australian UOCs analysed in an air atmosphere	130
Figure 72 SEM images of the Beverley UOCs at various magnifications: a) Beverley UOC 1 at 500x, b) Beverley UOC 1 at 500x, c) Beverley UOC 2 at 500x and d) Beverley UOC 3 at 1000x.....	131
Figure 73 SEM images of Beverley UOCs at various magnifications; a) Beverley UOC 1 at 30,000x, b) Beverley UOC 1 at 100,000x, c) Beverley UOC 2 at 30,000x, d) Beverley UOC 2 at 100,000x, e) Beverley UOC at 30,000x and f) Beverley UOC 3 at 100,000x	132
Figure 74 SEM images of the three Ranger UOCs at various magnifications; a) Ranger UOC 1 at 1000x, b) Ranger UOC 2 at 500x, c) Ranger UOC 2 at 1000x and d) Ranger UOC 3 at 500x	133
Figure 75 SEM images of the three Ranger UOCs at various magnifications; a) Ranger UOC 1 at 30,000x, b) Ranger UOC 1 at 100,000x, c) Ranger UOC 2 at 30,000x, d) Ranger UOC 2 at 100,000x, e) Ranger UOC 3 at 30,000x and f) Ranger UOC 3 at 100,000x	135
Figure 76 SEM images of the three Ranger UOCs at 100,000x magnification; a) Ranger UOC 1, b) Ranger UOC 1, c) Ranger UOC 2 and d) Ranger UOC 3	136
Figure 77 SEM images of the two Olympic Dam UOCs at various magnifications; a) Olympic Dam UOC 1 at 1000x, b) Olympic Dam UOC 1 at 1000x, c) Olympic Dam UOC 2 at 500x and d) Olympic Dam UOC 2 at 1000x	137
Figure 78 SEM images of the two Olympic Dam UOCs at various magnifications; a) Olympic Dam UOC 1 at 30,000x, b) Olympic Dam UOC 1 at 100,000x, c) Olympic Dam UOC 2 at 30,000x and d) Olympic Dam UOC 2 at 100,000x	138
Figure 79 SEM images of the Beverley UOC 1 TGA samples analysed in a nitrogen atmosphere and collected at various temperatures; a) r.t., b) 280 °C, c) 500 °C and d) 1000 °C.....	140
Figure 80 SEM images of the Ranger UOC 1 TGA samples analysed in a nitrogen atmosphere and collected at various temperatures; a) at r.t., b) 200 °C, c) 500 °C and d) 1000°C.....	141
Figure 81 SEM images of the Olympic Dam UOC 2 TGA samples analysed in a nitrogen atmosphere and collected at various temperatures; a) at r.t., b) 200 °C, c) 500 °C and d) 1000°C	142
Figure 82 ²³⁵ U/ ²³⁸ U isotope ratios of the eight uranium samples obtained from a South African uranium mine. Error bars = expanded uncertainty (k=2). (Note - The position of the samples indicates the location of the sample within the production process going from left to right i.e. the Ore total dissolution sample is the starting material and U ₃ O ₈ sample is the final product.)	149

Figure 84 $^{234}\text{U}/^{238}\text{U}$ isotope ratios of the eight uranium samples obtained from a South African uranium mine. Error bars = expanded uncertainty (k=2) (Note - The position of the samples indicates the location of the sample within the production process going from left to right i.e. the Ore total dissolution sample is the starting material and U_3O_8 sample is the final product.) 150

Figure 84 Comparison between replicate analyses (green) of $^{235}\text{U}/^{238}\text{U}$ isotope ratio of 100 ng/g non-certified natural uranium U_3O_8 standard during the analysis of UOC and uranium ore samples in this study and the measurement of same standard by Brown *et al.* (2014) (blue) against the consensus value for the $^{235}\text{U}/^{238}\text{U}$ isotope ratio of natural uranium (orange) used by Brown *et al.* (2014) (error bars = expanded uncertainty (k=2)) [256]. 162

Figure 85 Comparison between replicate analyses (green) of $^{235}\text{U}/^{238}\text{U}$ isotope ratio of four 100 ng/g non-certified natural uranium U_3O_8 standard during analysis of UOC and uranium ore samples in this study and the measurement of same standard by Brown *et al.* (2014) (blue) against the consensus value for the $^{235}\text{U}/^{238}\text{U}$ isotope ratio of natural uranium (orange) used by Brown *et al.* (2014) (error bars=expanded uncertainty (k=2)) [256]. 162

Figure 86 Comparison between certified (blue) and measured (orange) values of U630 CRM analysed by Brown *et al.* (2014) [256]. Error bars represent expanded uncertainty (k=2). 163

Figure 87 Comparison between replicate analyses (green) of $^{234}\text{U}/^{238}\text{U}$ isotope ratio of non-certified natural uranium U_3O_8 standard during analysis of UOC and uranium ore samples and measurement of same standard by Brown *et al.* (2014) (blue) against the consensus value for the $^{235}\text{U}/^{238}\text{U}$ isotope ratio of natural uranium (orange) used by Brown *et al.* (2014) (error bars = expanded uncertainty (k=2)) [256]. 164

Figure 88 Comparison between replicate analyses (green) of $^{235}\text{U}/^{238}\text{U}$ isotope ratio of 100 ng/g non-certified natural uranium U_3O_8 standard during the analysis of UOC and uranium ore samples in this study and the consensus value for the $^{235}\text{U}/^{238}\text{U}$ isotope ratio of natural uranium (orange) (error bars = standard deviation) [256]. 168

Figure 89 Comparison between replicate analyses (green) of $^{234}\text{U}/^{238}\text{U}$ isotope ratio of 100 ng/g non-certified natural uranium U_3O_8 standard during the analysis of UOC and uranium ore samples in this study and the consensus value for the $^{234}\text{U}/^{238}\text{U}$ isotope ratio of natural uranium (orange) (error bars = standard deviation) [256] 169

Figure 90 Comparison of several $^{238}\text{U}/^{235}\text{U}$ isotope measurements of two standards with natural uranium isotopic abundance: a non-certified natural uranium standard by this study and Brown *et al.* (2014), and the isotopically certified CRM 129 analysed by Arizona State University,

LLNL as part of a study published by Brennecka <i>et al.</i> (2010)[7] and a second study by Uvarova <i>et al.</i> (2014) [258]. Error bars = expanded uncertainty ($k=2$).....	171
Figure 91 Comparison between the Ore total/cleared leachate and In-house leach/cleared leachate ratios for the REEs normalised to uranium analysed by Varga <i>et al.</i> (2017)	179
Figure 92 Distribution of SEM/EDX measurements across Ruggles Mine uranium ore sample.....	191
Figure 93 Schematic diagrams of the sample cup and Mylar film used for the pXRF analysis of the international uranium ore samples	192
Figure 94 Quantification of U content within the North American uranium ore samples using SEM/EDX, pXRF and DNAA.....	200
Figure 96 Semi-quantitative measurements of U concentration (% wt) at various spots within the Ike-Nixon Shaft samples by SEM/EDX	201
Figure 97 DNAA measurements of the uranium concentration (wt%) within the international uranium ore samples	202
Figure 98 Quantification of U content within Ike-Nixon Shaft U Ore sample using DNAA, corrected DNAA, ICP-MS and Gamma Counting	202
Figure 100 [U] measured by DNAA vs short and long irradiation k_0 -NAA within International Uranium Ore samples, with the exception of the Ike-Nixon Shaft sample	204
Figure 101 Comparison of chondrite-normalised REE patterns of Fusion and 4-Acid certified values in OREAS 100a versus concentrations measured by k_0 -NAA. (Chondrite values from Anders & Grevasse 1989)	215
Figure 102 Comparison of chondrite-normalised REE patterns of Fusion certified values in OREAS 106 versus REE concentrations measured by k_0 -NAA. (Chondrite values from Anders & Grevasse 1989).....	215
Figure 103 Comparison of chondrite-normalised REE patterns of Fusion and 4-Acid certified values in OREAS 120 versus concentrations measured by k_0 -NAA. (Chondrite values from Anders & Grevasse 1989).....	216
Figure 104 Comparison of chondrite-normalised REE patterns of Fusion and 4-Acid certified values in OREAS 124 versus concentrations measured by k_0 -NAA. (Chondrite values from Anders & Grevasse 1989).....	217
Figure 105 Chondrite-normalised REE patterns for Olympic Dam A&B U ores obtained through INAA, and comparison patterns of UOCs (Keegan 2008) and U ores (Ciobanu et al. 2013) also from Olympic Dam from literature. Normalised using chondrite data from Anders & Grevasse (1989).....	218

Figure 106 Chondrite-normalised REE patterns for Beverley and Four Mile U ores obtained through INAA, and comparison patterns of a UOC (Keegan 2008) and U ores (Wülser et al. 2011) also from Beverley from literature. Normalised using chondrite data from Anders & Grevasse (1989).....	219
Figure 107 Chondrite-normalised REE patterns for Ranger uranium ores obtained through k_0 -NAA, and comparison patterns of a UOC (Keegan 2008) and uranium ores (Fisher <i>et al.</i> 2013) also from Ranger from literature. Normalised using chondrite data from Anders & Grevasse (1989).	220
Figure 108 Chondrite-normalised REE patterns for Mary Kathleen uranium ores obtained through k_0 -NAA, and comparison patterns of a UOC (Keegan 2008) and uranium ores (Maas <i>et al.</i> (1987)). Normalised using chondrite data from Anders & Grevasse (1989).....	221
Figure 109 Chondrite-normalised REE patterns for Cardiff uranium ores obtained through k_0 -NAA, and comparison patterns of uranium ores from Faraday (Fryer & Taylor (1987) and Fission mines (Satterly (1957])). Normalised using chondrite data from Anders & Grevasse (1989) ..	222
Figure 110 Chondrite-normalised REE patterns for Ruggles mine uranium ore obtained through k_0 -NAA, and comparison patterns uranium ores (Balboni <i>et al.</i> 2016) also from Ruggles mine from literature. Normalised using chondrite data from Anders & Grevasse (1989).	223
Figure 111 Chondrite-normalised REE patterns for Big Indian Wash District, Calyx No 8, Green Dragon, Happy Jack Mi Vida uranium ores obtained through k_0 -NAA. Normalised using chondrite data from Anders & Grevasse (1989).....	224
Figure 112 Chondrite-normalised REE patterns for the Happy Jack uranium ore obtained through k_0 -NAA, and comparison patterns of uranium ores (Balboni <i>et al.</i> 2016) also from Happy Jack from literature. Normalised using chondrite data from Anders & Grevasse (1989).	226
Figure 113 Chondrite-normalised REE patterns for the Ferguson Lode Claim uranium ore obtained through k_0 -NAA. Normalised using chondrite data from Anders & Grevasse (1989).....	227
Figure 114 Chondrite-normalised REE patterns for the Uravan Mineral Belt uranium ore obtained through k_0 -NAA. Normalised using chondrite data from Anders & Grevasse (1989).....	228
Figure 115 Chondrite-normalised REE patterns for the Midnite Mine uranium ore obtained through k_0 -NAA. Normalised using chondrite data from Anders & Grevasse (1989).....	229
Figure 116 Concentration of thorium ($\mu\text{g/g}$) in the Australian and North American uranium ore samples measured by k_0 -NAA	230
Figure 117 Concentration of sodium ($\mu\text{g/g}$) in the Australian and North American uranium ore samples measured by k_0 -NAA	233

Figure 118 Concentration of magnesium ($\mu\text{g/g}$) in the Australian and North American uranium ore samples measured by k_0 -NAA	234
Figure 119 Concentration of aluminium ($\mu\text{g/g}$) in the Australian and North American uranium ore samples measured by k_0 -NAA	234
Figure 120 Concentration of potassium ($\mu\text{g/g}$) in the Australian and North American uranium ore samples measured by k_0 -NAA	235
Figure 121 Concentration of calcium ($\mu\text{g/g}$) in the Australian and North American uranium ore samples measured by k_0 -NAA	236
Figure 122 Concentration of manganese ($\mu\text{g/g}$) in the Australian and North American uranium ore samples measured by k_0 -NAA	237
Figure 123 Concentration of iron ($\mu\text{g/g}$) in the Australian and North American uranium ore samples measured by k_0 -NAA	237
Figure 124 Concentration of arsenic ($\mu\text{g/g}$) in the Australian and North American uranium ore samples measured by k_0 -NAA	238
Figure 125 Concentration of tungsten ($\mu\text{g/g}$) in the Australian and North American uranium ore samples measured by k_0 -NAA	239
Figure 126 Concentration of vanadium ($\mu\text{g/g}$) in the Australian and North American uranium ore samples measured by k_0 -NAA	240
Figure 127 Chromatogram of the elution of individual REEs through the HDEHP/ α -HIBA HPLC system [316].....	252
Figure 128 Histogram of CRMs available and uranium ores analysed in this study binned according to their uranium concentration (%).....	253
Figure 129 Histogram of CRMs and uranium ores analysed in this study with uranium concentrations less than 1% binned according to their uranium concentration (%).....	254
Figure 130 Number of certified REEs and concentration of lanthanum [La] within the seventeen CRMs with at least one certified REE	255
Figure 131 Histogram of lanthanum concentrations (ppm) of commercially available CRMs and uranium ores analysed in this study	256
Figure 132 Histogram of the number of certified trace elements amongst the survey of commercially available CRMs.....	257
Figure 133 Replicate analyses of the $^{235}\text{U}/^{238}\text{U}$ isotope ratios of Beverley UOCs 1-3 and Beverley Ore analysed by MC-ICP-MS (error bars = expanded uncertainty ($k=2$)).....	263
Figure 134 Replicate analyses of the $^{234}\text{U}/^{238}\text{U}$ isotope ratios of Beverley UOCs 1-3 and Beverley Ore analysed by MC-ICP-MS (error bars = expanded uncertainty ($k=2$)).....	264

Figure 135 Replicate analyses of the $^{235}\text{U}/^{238}\text{U}$ isotope ratios of Ranger UOC 1-3 and Ranger Ore analysed by MC-ICP-MS (error bars = expanded uncertainty (k=2)).....	265
Figure 136 Replicate analyses of the $^{234}\text{U}/^{238}\text{U}$ isotope ratios of Ranger UOCs 1-3 and Ranger Ore analysed by MC-ICP-MS (error bars = expanded uncertainty (k=2)).....	265
Figure 137 Replicate analyses of the $^{235}\text{U}/^{238}\text{U}$ isotope ratios of Olympic Dam UOCs 1&2 and Olympic Dam Ore analysed by MC-ICP-MS (error bars = expanded uncertainty (k=2))	266
Figure 139 Replicate analyses of the $^{234}\text{U}/^{238}\text{U}$ isotope ratios of Olympic Dam UOCs 1&2 and Olympic Dam Ore analysed by MC-ICP-MS (error bars = expanded uncertainty (k=2))	266
Figure 139 Comparison between the $^{235}\text{U}/^{238}\text{U}$ isotope ratio of a Mary Kathleen uranium ore samples analysed by MC-ICP-MS (error bars = 1σ) and a literature value of a UOC from Mary Kathleen analysed by Keegan <i>et al.</i> (2014) [103].	267
Figure 140 Average $^{235}\text{U}/^{238}\text{U}$ isotope ratios of Beverley, Ranger, Olympic Dam and Mary Kathleen UOC and uranium ore samples analysed by MC-ICP-MS (error bars = expanded uncertainty (k=2)).	268
Figure 141 Average $^{234}\text{U}/^{238}\text{U}$ isotope ratios of Beverley, Ranger, Olympic Dam and Mary Kathleen UOC and uranium ore samples analysed by MC-ICP-MS (error bars=expanded uncertainty (k=2)).	268
Figure 142 Average $^{234}\text{U}/^{238}\text{U}$ vs $^{235}\text{U}/^{238}\text{U}$ comparison between Beverley, Ranger, Olympic Dam and Mary Kathleen UOC and uranium ore samples (error bars = expanded uncertainty (k=2))	269
Figure 143 Average $^{235}\text{U}/^{238}\text{U}$ isotope ratios of Beverley, Ranger, and Olympic Dam and Mary Kathleen UOC and uranium ore samples analysed by MC-ICP-MS (error bars = standard deviation).	270
Figure 144 Average $^{234}\text{U}/^{238}\text{U}$ isotope ratios of Beverley, Ranger, and Olympic Dam and Mary Kathleen UOC and uranium ore samples analysed by MC-ICP-MS (error bars = standard deviation).	270
Figure 145 Average $^{234}\text{U}/^{238}\text{U}$ vs $^{235}\text{U}/^{238}\text{U}$ comparison between Beverley, Ranger, Olympic Dam and Mary Kathleen UOC and uranium ore samples (error bars = standard deviation).	271
Figure 146 Comparison of measured $^{235}\text{U}/^{238}\text{U}$ isotope ratios from uranium ore and UOCs samples originating from Beverley and a UOC sample from Beverley previously analysed by Keegan <i>et al.</i> (2008) [39]. Error bars = Expanded uncertainty (k=2).....	273
Figure 147 Comparison of measured $^{234}\text{U}/^{238}\text{U}$ isotope ratios from uranium ore and UOCs samples originating from Beverley and a UOC sample from Beverley previously analysed by Keegan <i>et al.</i> (2008) [39]. Error bars = Expanded uncertainty (k=2).....	273

Figure 148 Comparison of measured $^{235}\text{U}/^{238}\text{U}$ isotope ratios from uranium ore and UOCs samples originating from Ranger and a UOC and uranium ore sample from Ranger previously analysed by Keegan *et al.* (2008) and Richter *et al.* (1999), respectively. Error bars = Expanded uncertainty (k=2).....275

Figure 149 Comparison of measured $^{234}\text{U}/^{238}\text{U}$ isotope ratios from uranium ore and UOCs samples originating from Ranger and a UOC and uranium ore sample from Ranger previously analysed by Keegan *et al.* (2008) and Richter *et al.* (1999), respectively. Error bars = Expanded uncertainty (k=2).....275

Figure 150 Comparison of measured $^{235}\text{U}/^{238}\text{U}$ isotope ratios from uranium ore and UOCs samples originating from Olympic Dam and a UOC and uranium ore sample from Olympic Dam previously analysed by Keegan *et al.* (2008) and Richter *et al.* (1999), respectively. Error bars = Expanded uncertainty (k=2)276

Figure 151 Comparison of measured $^{234}\text{U}/^{238}\text{U}$ isotope ratios from uranium ore and UOCs samples originating from Olympic Dam and a UOC and uranium ore sample from Olympic Dam previously analysed by Keegan *et al.* (2008) and Richter *et al.* (1999), respectively. Error bars = Expanded uncertainty (k=2)276

Thesis Summary

The trafficking of nuclear and radioactive materials is of significant concern to national and international security, with more than 2000 incidents involving radioactive and nuclear materials outside of regulatory control reported to the International Atomic Energy Agency since 1995 [1]. In response to these incidents, the discipline of nuclear forensics was created to develop the capability to ascertain answers to critically important questions, such as the material's origin, its original intended use and its age. While these seizures encompass a wide variety of different nuclear or radioactive materials, uranium ore concentrates (UOCs) in particular are of significant interest to the international nuclear forensics community. UOCs contain greater than 65% uranium and are a commodity exported internationally for their future fabrication into nuclear fuel, which makes them vulnerable to proliferation. Developing the capabilities of nuclear forensics is also aligned within Australia's national interest, as Australia is the world's third largest uranium exporter and possesses the world's largest uranium deposit at Olympic Dam, South Australia.

This thesis describes efforts to further develop the capabilities of materials provenancing within nuclear forensics through the investigation and evaluation of new analytical techniques that may compliment or surpass the current techniques used for the analysis of chemical and elemental composition of UOCs and uranium ores. In Chapter 4, the efficacy of thermogravimetric analysis (TGA) for distinguishing between UOCs of different provenances was investigated through the analysis of eight UOCs from three different Australian uranium mines. In both air and nitrogen atmospheres, the TGA patterns from uranyl peroxide UOCs from Beverley could readily be differentiated from the U_3O_8 UOCs from Ranger and Olympic Dam. The UOCs from Ranger and Olympic Dam could also be differentiated from one another based upon their moisture content. Further research is required to determine how consistent the moisture content is within various UOC sample types, as well as identify some unknown intermediates that formed at various temperatures during TGA. Scanning electron microscopy (SEM) imaging also revealed that UOCs from each of the three mines had unique morphologies that were resistant to temperatures up to 800 °C, when they underwent mild sintering.

In Chapter 5, eight UOCs and four uranium ore samples from four Australian uranium mines were analysed by multi-collector inductively-coupled plasma mass spectrometry (MC-ICP-MS) to investigate whether the $^{235}U/^{238}U$ and $^{234}U/^{238}U$ isotope ratios from a particular location exhibited any significant intra-mine variability. During the data analysis process, it became apparent that the

MC-ICP-MS was not performing properly likely due to poor calibration/set-up of the instrument by the operators, and no further opportunity was available to reanalyze the samples.

In Chapter 6, the efficacy of k_0 -neutron activation analysis (k_0 -NAA) towards the analysis of the trace and rare earth element (REE) composition of uranium ores was investigated. As the chondrite normalised REE pattern of the mined ore deposit has been found to be preserved through the UOC production process [2], REEs are of particular interest to nuclear forensics provide as they potential link back to the UOCs origin. Fifteen of the sixteen uranium ore samples from Australia and North America and four uranium ore certified reference materials (CRMs) were analysed by k_0 -NAA, as pre-screening by delayed neutron activation analysis (DNAA) found that one of the samples, the Ike-Nixon Shaft sample, contained a uranium concentration that would be unsafe to analyse with k_0 -NAA. Analysis of the CRMs and the uranium ore samples revealed that many of the REEs were significantly impacted by the presence of uranium fission products and other interferences formed during neutron irradiation. Where comparisons could be made, the chondrite-normalised REE patterns between the Australian uranium ores measured by k_0 -NAA and literature values from UOCs from the same locations were found to be in good agreement, with the exception of Mary Kathleen. As many of the REEs were subject to interferences at moderate uranium concentrations, it is apparent k_0 -NAA is not currently a suitable elemental analysis technique for nuclear forensics applications, requiring further development.

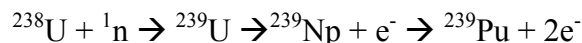
Chapter 1. Introduction

1.1. Uranium

Uranium is a naturally occurring actinide-series element with an atomic number of 92, first discovered by Martin Heinrich Klaproth in 1789 through the analysis of a sample of pitchblende (UO₂) [3, 4]. Uranium is widely distributed in Earth's terrestrial and aquatic environments, present at an average concentration of 2.8 parts per million (ppm) in the crust and 0.003 ppm and 0.002 ppm for seawater and groundwater, respectively [5]. Uranium is not found, however, in its pure elemental form in the terrestrial environment, but incorporated with other elements forming minerals, with over 250 different species of uranium minerals known to exist [6]. While uranium minerals can have oxidation states of U(IV) (5f³, 6d¹, 7s²), U(V) (5f¹) and U(VI) (5f⁰) [6], uranium may also exist in a fourth oxidation state as U(III) (5f³).

1.1.1. Isotopes of Uranium

Uranium has no stable isotopes, and therefore they all undergo radioactive decay. Natural uranium is typically comprised of three different isotopes: ²³⁸U, ²³⁵U and ²³⁴U. ²³⁸U is the most abundant isotope of uranium, constituting 99.28% of natural uranium, and has a half-life of 4.468 billion (10⁹) years [7]. While ²³⁸U is not a fissile material, it is considered to be 'fertile' as it can undergo a neutron capture reaction to form the fissile ²³⁹Pu [8];



²³⁸U is a member of the radium series decay chain (4n+2) (Figure 1), sometimes referred to as the uranium series, and undergoes alpha (α) decay to produce the daughter nuclide ²³⁴Th. Each isotope within the uranium series decay chain has a mass number (A) = 4n+2, where n is an appropriate integer, and is designated as such accordingly. This decay chain produces the ²³⁴U isotope as an intermediate, before terminating with ²⁰⁶Pb isotope.

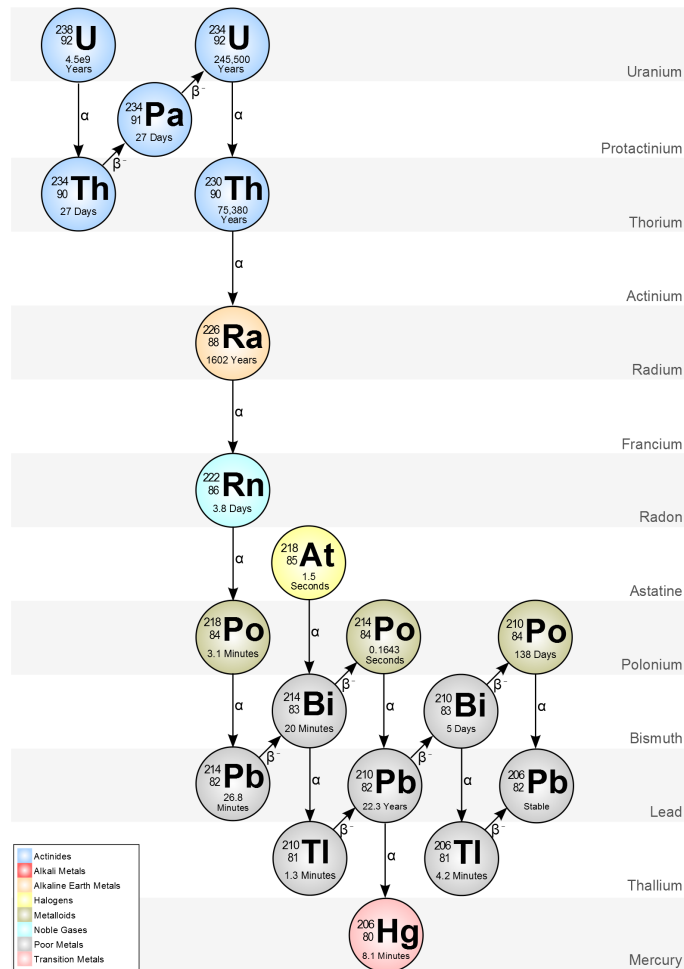


Figure 1. Radium series decay chain (4n+2) [9]

^{235}U is the second-most abundant isotope, present at $\sim 0.72\%$ in naturally-occurring uranium, and has a half-life of 0.7038 billion years [10]. This isotope is a member of the actinium decay chain (4n+3), and undergoes α decay forming ^{231}Th , with the chain terminating with the ^{207}Pb isotope. ^{235}U is the only isotope of the primordial nuclides that is considered ‘fissile’, as it has the ability to sustain a chain reaction of nuclear fission with slow neutrons to produce vast amounts of energy [11]. As ^{235}U is the most important isotope of uranium, samples of uranium are often categorised with respect to the amount of ^{235}U present into four different groupings: less than 0.72% = depleted uranium (DU), 0.72% = natural uranium, greater than 0.72% but less than 20% = low enriched uranium (LEU) and greater than 20% = high enriched uranium (HEU).

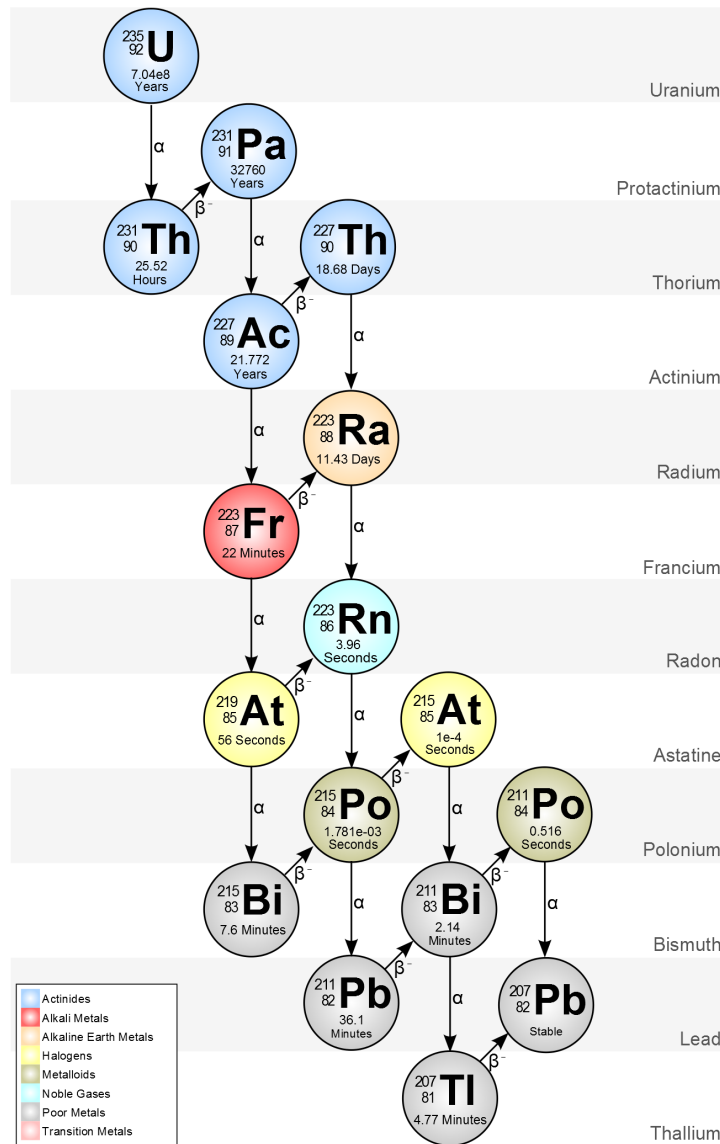


Figure 2 Actinium series decay chain (2n+3) [12]

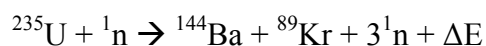
^{234}U is the least abundant of the naturally occurring isotopes of uranium, as it is only present at an abundance of 0.0056% and has a relatively short half-life of 0.235 million (10^6) years. It is a member of the uranium series decay chain, and is formed through the decay of the ^{238}U isotope. The ^{236}U isotope of uranium, with a half-life of 23.7 million years, is a naturally occurring isotope of uranium produced through thermal neutron capture of the ^{235}U isotope within an ore body, albeit at ultra-trace concentrations ($^{236}\text{U}:\text{}^{238}\text{U}$ of $\sim 10^{-10}$) [13, 14]. The thermal neutrons captured by the ^{235}U isotope are produced either by spontaneous fission of neighbouring ^{238}U atoms in the ore body or the emission of a neutron following the absorption of an alpha (α) particle by a light element (i.e. fluorine, sodium or magnesium) within the uranium ore body [15]. Within nuclear fuel where ^{236}U is

similarly produced through thermal neutron capture, ^{236}U : ^{238}U ratios of between 0.1-0.5% may be experienced as the thermal neutron capture cross-section of ^{236}U is approximately one fifth of the fission cross-section [14].

1.1.2. Applications of Uranium

1.1.2.1. Use in Nuclear Energy

One of uranium's primary uses today is as the fuel for nuclear energy generation. Similar to other energy generation, nuclear reactors use heat energy to produce steam that power turbines. The heat energy used to generate steam is produced through nuclear fission of the ^{235}U isotope. Fission of the ^{235}U nucleus is induced through the absorption of neutrons, producing energy, fission products and other neutrons that are able to induce fission in other ^{235}U nuclei, creating a chain reaction:



80% of the energy generated through nuclear fission of a ^{235}U nucleus is in the form of kinetic energy, but this is converted into heat energy through the interaction of the fission products with the core material [16]. Thermal energy may also be produced through the interaction of neutrons and gamma rays, produced through fission, with the core materials. In total, a single fission event liberates an average of 200 MeV of energy, with the energy produced through complete fission of a single pound (0.454 kg) of uranium equivalent to the complete combustion of 6000 barrels of oil, or 1000 tonnes of high-quality coal [16].

Nuclear energy is used by a number of countries in varying capacities to meet their current energy demands. Thirty countries around the world are currently using nuclear energy to achieve their current energy demands with a total of 451 reactors in operation as of the 31st of December 2018, with a further 55 reactors under construction, including 9 in 4 countries (Bangladesh, Belarus, Turkey and UAE) which do not currently possess any operating reactors [17]. Australia does not use nuclear energy as a source of energy however, and only operates a single reactor for research, commercial and radiopharmaceutical production purposes. For some countries, i.e. France and Slovakia, nuclear energy is the major source of energy whereas other countries use nuclear energy to supplement their other means of energy production or have only recently begun using nuclear energy as a source of energy (Figure 3).

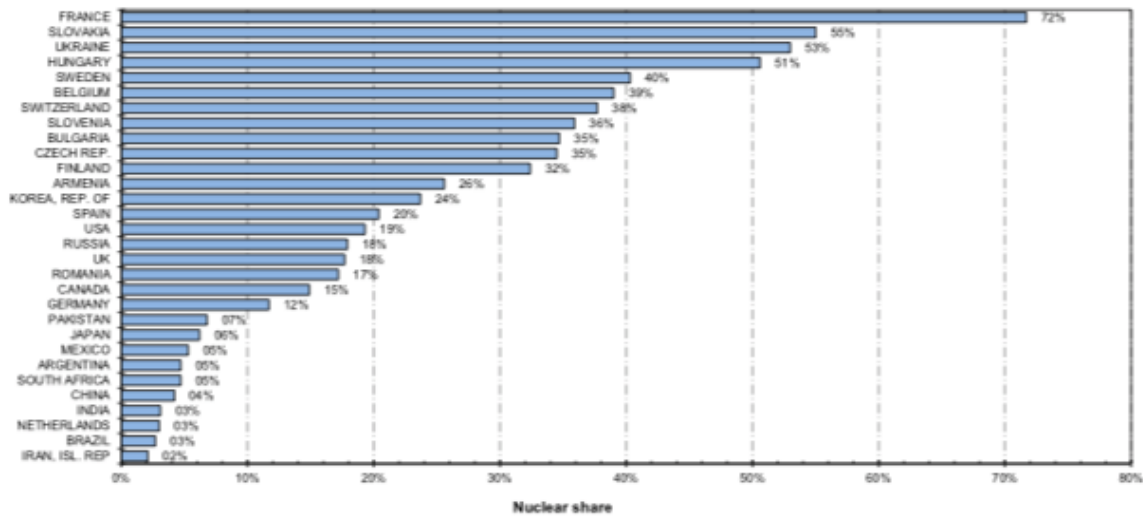


Figure 3. Nuclear share of electricity generation (as of 31st December 2018)[17]

Since the Fukushima Daiichi incident in 2011, a number of countries, including Germany, Italy and Switzerland, have changed their position on nuclear energy and are now either accelerating their phase-out of nuclear reactors or have halted any further development of new or replacement reactors [18]. Other countries, including Sweden, Czech Republic, Finland, France and Hungary, have remained committed maintaining nuclear energy as a means to achieve their current and estimated energy demands [18].

1.1.2.2. Use in Nuclear Weapons

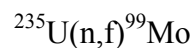
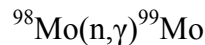
Uranium is also used in nuclear weapons, with a uranium-based nuclear device the first ever nuclear weapon used in war. On the 6th of August 1945, the ‘Little Boy’ device was detonated over Hiroshima, Japan during World War II, exploding with a yield equivalent of 12.5 kilo tonnes of trinitrotoluene [19, 20]. Currently, there are an estimated 17,300 nuclear weapons in existence between 9 countries (Russia, United States, France, China, United Kingdom, Israel, Pakistan, India and North Korea), however the accuracy of this estimate is uncertain, due to the variability of information regarding each country’s nuclear inventory [21]. The ²³⁵U abundance in weapons-grade uranium is considered to be approximately 90%, however a grade >20% can theoretically be used to create a nuclear device [22].

1.1.2.3. Other Uses of Uranium

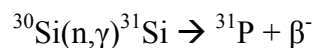
Nuclear reactors may also be used for non-energy purposes, such as the production of radiopharmaceuticals, doping of silicon for the production of semiconductors, and to facilitate a variety of research platforms that utilise neutrons (research reactor). Radiopharmaceuticals are primarily used to perform medical diagnoses (95%), with the remaining used for therapeutic

purposes [23]. Radiopharmaceuticals have two components; the radionuclide, and the pharmaceutical to which it is bound to transport it within the body to the target organ. The radionuclide used is selected based upon a number of factors; its half-life (a short half-life is preferred), its mode of decay (α , β and Auger electron preferred) and emission energy (30-300 keV), target uptake rate, mode of excretion and availability [23].

The radionuclides used in nuclear medicine can be produced in either a nuclear reactor or a cyclotron. The production of radionuclides in a nuclear reactor use three different types of nuclear reactions; (n, γ), (n,p) and (n,f) [23]. ^{177}Lu , a radiopharmaceutical used for endo-radiotherapy, is produced via the neutron capture reaction $^{176}\text{Lu}(n,\gamma)^{177}\text{Lu}$ [24]. In a related form of radiotherapy, boron neutron capture therapy administers non-radioactive ^{10}B for the treatment of head and neck cancers and undergoes a (n,p) reaction via exposure of a patient to a neutron beam to form ^7Li and an α -particle (^4He), which destroys the tumour cells [25]. ^{99}Mo , which undergoes β^- decay to form metastable $^{99\text{m}}\text{Tc}$, which is used as a tracer for a range of diagnostic examinations, can be produced through two different nuclear reactions [23];



Another application of uranium and nuclear reactors is neutron transmutation doping (NTD) of silicon, which utilises neutrons from a reactor to convert silicon to phosphorus within the irradiated sample, through the following reaction [26];



By introducing impurities, such as phosphorus, into the silicon material, it improves the electrical properties of the material, making them suitable for high power electrical devices [26]. NTD is particularly suited to be performed at research reactors, including the OPAL reactor at the Australian Nuclear Science and Technology Organisation (ANSTO), in particular, due to their high neutron flux densities [26].

Research reactors also support a large variety of research infrastructure that utilise the interaction of neutrons with matter for a host of different types of analyses [27]. For instance, the diffraction of

neutrons within a beam by a sample (neutron powder diffraction) can provide information on the atomic and magnetic structures of materials [28], whereas the irradiation of a sample with neutrons can form radioactive nuclides that emit characteristic γ -rays, allowing elemental composition of the sample to be quantified (neutron activation analysis) [29].

Uranium also has a number of other applications not related to the fissile nature of the ^{235}U isotope. Uranium was once incorporated within glass as it produces a fluorescent green color when exposed to an ultraviolet light source or to a ceramic to obtain a yellow glaze [30]. DU is also used in a number of different applications, both civilian and military, due to its high density (19.1 g/cm^3) [31]. DU metals have been used in the military in three major conflicts: the Gulf War (1991), in Bosnia-Herzegovina (1995) and in Kosovo (1999) as kinetic energy penetrators, a type of ammunition, and as tank armor. Uranium was chosen for these applications over tungsten, which has a similar density (19.3g/cm^3) as uranium can be produced at a lower cost, is more readily available and is pyrophoric [31]. Civilian uses of DU include as a cladding material of nuclear reactors, keels for yachts and counterweights for rudders.

1.2. Uranium Deposits

1.2.1. Formation of Uranium Deposits

The formation of uranium deposits is a complex series of processes that occurs over billions of years. Substantial concentration of uranium is required (uranium is present at an average concentration of 2.83 ppm in the Earth's crust), to form the large deposits mined today. The mineralisation of uranium has been suggested to have occurred in four main stages, which were influenced by various stages in the development of the Earth [32].

The first stage in the formation of uranium deposits occurred approximately 4.5 to 3.5 billion years ago (Ga) and involved the initial concentration of uranium from the trace levels it was present at within the Earth's crust. Low-density silicon melt-phases were found to concentrate uranium within the crust by factors of greater than 100, along with the activity of magmatic hydrothermal fluids [32]. Uraninite may have been one of the first uranium minerals to precipitate out when the uranium-bearing hydrothermal fluid mixed with cool, pH-neutral meteoric water [32]. Oxidation of U^{4+} to the soluble U^{6+} can also result in mineralisation, as the hexavalent uranium can reach the Earth's surface and precipitate through evaporation processes, or be reduced back to U^{4+} in a redox environment, before forming uraninite [32].

The second stage occurred approximately 3.5 and 2.2 Ga ago, and saw the formation of uranium-enriched granites that were capable of crystallising uraninite [32]. Following the weathering and erosion of these enriched granites in an anoxic environment, the concentration of the newly-formed uraninite grains in continental basins, such as the Witwatersrand, South Africa and Blind River, Canada, enabled the development of quartz-pebble conglomerates [6]. During this stage, the uraninite also began to undergo auto-oxidation through radioactive decay to produce lead progeny, forming other uranium minerals, including uranium oxide-hydroxides [6].

The third stage occurred following the Great Oxidation Event 2.2 Ga ago, resulting in the widespread oxidation of tetravalent uranium to the hexavalent oxidation state. During this period, over 200 different uranium minerals, in a variety of environments, were formed due to the formation of uranyl-bearing aqueous solutions, the oxidising weathering of reduced uranium minerals and the uranium leaching of low-grade deposits [6]. It was during this stage in the formation of uranium minerals that the 14 natural fission reactors at Oklo and Bangombé, Gabon became critical. Due to the unique geological conditions of the uranium deposits and the high grade, isotopically enriched ore ($^{235}\text{U} = 3.7\%$), these natural fission reactors reached criticality approximately 1.7 billion years ago and underwent chain fission reactions on and off for hundreds of thousands of years [33].

The fourth stage in the formation of uranium mineralisation extends from 0.4 Ga to the present, and coincides with the development of plant life. During this stage, uraninite and coffinite were precipitated at reduction fronts in organic-rich continental sediments from cool, oxygenated uranium-rich near-surface waters, forming sandstone deposits [6]. During this stage, microbial organisms also influenced the formation of uranium minerals through the oxidation and reduction of uraninite and soluble uranyl species, respectively [6].

1.2.2. Categorisation of Uranium Deposits

Uranium deposits can be categorised in 3 different ways: the confidence in the size and abundance of uranium in the deposit, their geological setting and the amount of investment required to extract the uranium ore. Uranium ore deposits are not recorded by the International Atomic Energy Agency's (IAEA) uranium deposit database 'UDEPO' unless they are expected to contain a minimum of 500 tonnes of uranium and an average uranium grade of 0.03% [34]. Exceptions have, however, been made to include small deposits that are located near other proposed or operating production areas [34].

1.2.2.1. Confidence Classification of Uranium Deposits

The confidence in the estimate of the size, grade and configuration is but one measure used to describe a uranium deposit. The category where there is the most confidence in the deposit is ‘reasonably assured resources’ and refers to known mineral deposits of defined size, grade and configuration such that the quantities that could be recovered within a given production cost with currently proven mining and processing technologies [18]. This degree of confidence is awarded to a deposit based upon specific data, knowledge and measurements of the deposits, from which estimations of the size and grade can be specified. The second-most confident estimate is ‘inferred resources’, and refers to the uranium deposit that is inferred to exist based on direct geological evidence, in extensions of well-explored deposits, or in deposits in which geological continuity has been established, but measurements of the deposits have considered it to be inadequate to be categorised reasonably assured resources [18, 34]. Reasonably assured resources and inferred resources can be combined to form the ‘identified resources’ super-category.

Prognosticated resources refer to deposits of uranium where the evidence of their existence is determined through indirect methods, and are believed to occur in well-defined geological trends or areas of mineralisation with known deposits [34]. The confidence associated with these deposits is less than those considered to be inferred or reasonably assured resources. Speculative resources refers to deposits thought to exist based upon indirect evidence and geological extrapolations in deposits discoverable with existing exploration techniques[34]. The prognosticated resources and speculative resources categories can be combined to form the undiscovered category [34].

There is not, however, a unified global classification system for the confidence in a uranium deposit, despite efforts by the IAEA to improve the consistency of national reporting of uranium resource inventories [35]. Different countries have their own systems, resulting in overlapping definitions of uranium deposits, which may impact global assessments of uranium deposits (Figure 4).

Image removed due to copyright restriction.
Available online on page 462 of *Uranium
2011: Resources, Production and Demand*:

https://www.oecd-nea.org/jcms/pl_14760

Figure 4. Comparison and approximate correlation in major resource classification systems between countries and organisations [18]. Note: 1) United Nations Framework Classification (UNFC) correlation with NEA/IAEA and national classification systems is still under consideration.

1.2.2.2. Economic Classifications of Uranium Deposits

Deposits may also be categorised by the investment required to extract the uranium resources from the ground. These costs include the mining and processing of the ore to extract the uranium, waste and environmental management strategies, exploration and development of other deposits, and taxes and royalties where applicable [18]. The four different economic categories used to classify deposits are: <USD 40/kgU, <USD 80/kgU, <USD 130/kgU and <USD 260/kgU. Due to changing production costs and fluctuating uranium markets, the categorisation of a particular deposit is updated regularly to provide an accurate insight into the resources and the size of the investment required to extract the ore.

1.2.2.3. Geological Classifications of Uranium Deposits

Uranium resources may also be categorised by their respective geological settings and technical characteristics. There are 13 different geological categories acknowledged by the IAEA, however individual mining companies may have their own categorisation schemes, resulting in different numbers of individual categories for uranium ore deposits.

Sandstone deposits are the largest source of uranium in the world, constituting 27.9% of the world's uranium resources [34]. Sandstone uranium deposits are found in medium to coarse-grained loosely compacted soil that are deposited in a continental fluvial or marginal marine sedimentary environment [18]. These deposits are precipitated from groundwater at low temperatures (<80°C)

in a reducing environment, due to presence of reducing agents including carbonaceous materials, sulphites, hydrocarbons, ferro-magnesium minerals (as chlorite) and microbial activity. The major uranium minerals found in sandstone deposits are pitchblende (U_3O_8) coffinite ($U(SiO_4)_{1-x}OH_{4x}$) and carnotite ($K_2O \cdot 2UO_3 \cdot V_2O_5 \cdot 3H_2O$). Major sandstone deposits are known to have been formed between the Palaeozoic (541 – 252.2 myr) and Tertiary (65 – 1.806 myr) geological periods, however smaller deposits formed by algae in the Precambrian period (4600 – 541 myr) have also been discovered [34]. Sandstone deposits are comprised of four different sub-types (roll-front, tabular, basal channel and tectonic/lithologic deposits) of varying grades of uranium content, ranging from 0.05% – 3% [34].

Unconformity-related deposits are major pods, veins and/or disseminations of uraninite (UO_{2+x}) associated with unconformities between Archean-Paleoproterozoic metamorphosed basement rocks from overlying Paleo-Mesoproterozoic sandstones unites in marginal or intercratonic basins [32]. Unconformity-related deposits constitutes 11.9% of the world's uranium reserves [18], with the major uranium minerals associated with these deposits being uraninite and pitchblende (U_3O_8), which precipitate from formational brines at temperatures between 150 - 250°C [36]. Unconformity-related deposits also contain varied amounts of nickel, cobalt, arsenic and lead, as well as trace amount of other elements including gold, platinum and copper. The uranium content in this deposit type varies greatly, from 5 - 15% above the unconformity, to 0.3 – 2% below [34].

Hematite breccia complex deposits are formed in hematite (Fe_2O_3)-magnetite (Fe_3O_4) rich breccias and constitute 16.5% of the world's uranium reserves [18]. Along with uranium, these deposits also contain a number of other elements including iron oxide-copper-gold (IOCG), silver and rare earth elements (REE). Hematite breccia complex deposits are formed by a number of different processes, including hydraulic fracturing, faulting, chemical corrosion and gravity collapse associated with near-surface eruptive events [36]. These deposits were formed between 2570 – 1000 myr through the mixing of groundwater with magmatic brines [32]. The major uranium mineral present in hematite breccia complex deposits are pitchblende, along with coffinite and brannerite ($(U, Ca, Fe, Th, Y)_3Ti_5O_{16}$) [32].

Quartz-pebble conglomerates deposits are found in conglomerates formed 3070 - 2200 million years (myr) that overlie granitic and metamorphic basements [37]. Quartz-pebble conglomerate deposits comprise 5.5% of the world's uranium reserves, and are among the world's lowest grade uranium deposit mined, with average grades mined for uranium may be as high as 0.015% [37]. The major

minerals associated with quartz-pebble conglomerates include detrital uraninite, uranothorianite ((Th, U)O₂), monazite ((Ce, La, Pr, Nd, Th, Y)PO₄) and xenotime (YPO₄) and uranothorite ((Th, U)SiO₄), and brannerite, which was formed by hydrothermal fluids [32]. Other elements associated with this deposit include gold, REE and other detrital metallic oxides and sulphide minerals, including pyrite [34].

Vein deposits occur when uranium minerals develop in voids, including cracks, veins, fissures pore spaces, breccias and stockworks, a complex systems of veins. These deposits consist mostly of gangue materials, including quartz and carbonates, as well as uraninite, coffinite and pitchblende. Vein deposits are formed from hot (200-350°C) hydrothermal-magmatic fluids filling these voids, and are therefore highly variable in thickness and extension [32]. These deposits only constitute 5.9% of the world's uranium resources, and having varying grades of U₃O₈, from 0.1% - 2.4% [37].

Intrusive deposits are associated with a number of high-temperature magmatic systems, including alaskite, granite and pegmatite [32]. These deposits constitute 5.3% of the world's uranium resources and are typically low grade, with uranium present at 20 – 500 parts per million (ppm) [18, 34]. The main uranium minerals associated with intrusive uranium deposits are uraninite, thorianite and uranothorite [32] and are formed under high temperatures.

Volcanic and caldera-related deposits occur with mafic and felsic volcanic caldera complexes associated with continental extensional settings [38]. These deposits were formed between the Proterozoic (2500 – 542 myr) and Tertiary (65 – 1.806 myr) geological periods in uranium-rich felsic magmas that were subsequently enriched by hydrothermal fluids [4]. The major uranium mineral found in volcanic and caldera-related deposits are pitchblende, however, other minerals associated with molybdenum (molybdenite (MoS₂)), sulphides, fluorides, REEs, lead, tin and tungsten are also found [32, 37]. 3.9% of the world's uranium resources are volcanic and caldera-related deposits, but are typically characterised as low grade, with low uranium content in the range of 0.02% to 0.2% U₃O₈ [37].

Metasomatite deposits are found in structurally deformed rocks that were affected by sodium metasomatism [37], a process of alteration that increases the soda (Na₂O) content and reduces the amount of silica (SiO₂). These deposits contain primarily uranium and thorium minerals including uraninite, uranothorite, and brannerite and constitute 12.3% of the world's uranium reserves [18].

The grade in metasomatite deposits are typically low, usually less than 0.2%, however, deposits have been known to contain up to 3% U_3O_8 [37].

Surficial deposits are near surface uranium concentrations found in sediments and soils, and are considered young, as they formed during the Tertiary (65 – 1.806 myr) and Recent geological periods [37]. These deposits form in low temperature ground water in arid environments to produce calcretes (calcium and magnesium carbonates), or under cool wet conditions in peat bogs or in limestone caves [4]. The main uranium mineral ore mined in surficial deposits is carnotite, and the grade of surficial deposits vary between 0.06% and 0.2% [4].

Collapse breccia pipe deposits are unique to Arizona, US and form circular, vertical pipes [32]. The main uranium mineral found in this deposit is uraninite and the uranium grade on average is 0.5% [4]. They have similar properties to both sandstone and unconformity-related uranium systems.

Phosphorite deposits are formed from the upwelling of nutrient-rich marine waters onto a continental shelf with restricted circulation. While phosphorite deposits are large, the uranium content in these deposits ranges from 0.01 to 0.015%, and is extracted as a by-product of phosphate production [18].

There is also a number of minor uranium deposits found throughout the world. Metamorphic deposits are formed as the direct result of metamorphic processes and are of low grade (0.001 – 0.15% U_3O_8) [37]. Limestone deposits comprised of uraninite form in intra-formational folds and fractures [18]. Uranium coal deposits are associated with lignite/coal and in the clay and sandstone surrounding the lignite [18]. The grade of uranium in these coal deposits are quite low, with concentrations below 50 ppm [18]. A number of rock types, including rare metal pegmatites, granites and blackshale contain low levels of uranium (<50 ppm), and aren't likely to be mined to recover uranium in the foreseeable future [18].

1.3 Mining of Uranium Ore Deposits and Production of Uranium Ore Concentrates

In order to be used as nuclear fuel or for nuclear weapons, uranium has to be first recovered from the environment through mining and processed. Through a number of processing stages in the production of uranium ore concentrates (UOCs), the concentration of uranium is increased from amounts as low as 0.06% in the ore to greater than 65%, which becomes purer towards the end of processing. The removal of impurities is important, as a number of different elements have detrimental effects to latter processing stages or during its use within a nuclear reactor, should they

persist in the product. Elements including boron, cadmium, samarium, gadolinium, europium and dysprosium reduce the performance of the nuclear fuel as they are strong neutron absorbers, while molybdenum, vanadium and chromium can form volatile fluorides that can be problematic in latter stages of processing [39]. Depending on the ore deposit, a number of different mining and processing strategies may be considered to efficiently extract as much uranium from the deposit as possible.

1.3.1. Mining of Uranium Ore Deposits

The first step in the nuclear fuel cycle is the extraction of the raw uranium ore from the earth. The mining method used to extract the ore, or the uranium solution, is determined by the shape, depth and grade of the uranium deposit. Environmental, geographical, personnel and financial factors as well as the regulations of the country the uranium deposit is located within can influence which mining technique is used for a particular mine [40].

1.3.1.1. *Open-pit Mining*

Open-pit mining has historically been one of the principle methods for the mining of uranium. It is widely used today with 23% of the world's uranium mines being an open-pit mine [18]. This mining technique is used when the ore-body is close to the surface, and the earth overlying the ore deposit, called the overburden, is removed (Figure 5). Open-pit mining boasts the highest uranium recovery factor (80%) of all the different mining methods [18] and is generally considered to be a more efficient method to extract uranium than underground mining [40].

Image removed due to copyright restriction.

Available online from: <https://www.mining-technology.com/projects/rossingsouth-uranium/>

Figure 5. Rössing open-pit uranium mine, Namibia [41]

1.3.1.2. *Underground Mining*

Underground mining is another conventional mining technique used to extract and recover uranium from the ore deposit. This method is typically used when the ore deposit is found much deeper into the earth, and is the most common method for the mining of uranium, with 32% of the world's uranium mines operating as an underground mine [18]. With underground mining, only 75% of the uranium mined is recovered, and therefore not as efficient as open-pit mining [18, 40], however this method doesn't produce nearly as much overburden, which needs to be removed and stored.

1.3.1.3. *In-situ Mining*

In-situ leaching is a different mining method to open-pit and underground mining, as it doesn't require raw uranium ore to be physically mined and removed. *In-situ* leaching instead utilises acidic or basic chemical solutions to oxidise, complex and mobilise the uranium within the ore body. The pregnant solution is then pumped to the surface, where the uranium is extracted through the use of ion-exchange (IX) columns [42] (Figure 6). A requirement for *in-situ* leaching is that the uranium ore deposit is porous; otherwise the leaching fluid is unable to reach the entire deposit, or return to the surface.

Another consideration for *in-situ* leaching is that the uranium deposit is confined within an impermeable material; to prevent the loss of the leaching solution to the surroundings. Monitoring wells are also placed around the leaching and extracting wells at various depths to detect the loss of the leaching solution. It is therefore typically reserved for sandstone-related deposits, due to the porosity of this type of deposit. 39% of the world's uranium mines currently employ *in-situ* leaching

as the means to extract uranium from an ore deposit, and achieve recovery factors of 75% and 70% for acidic and basic leaching solutions, respectively [18].

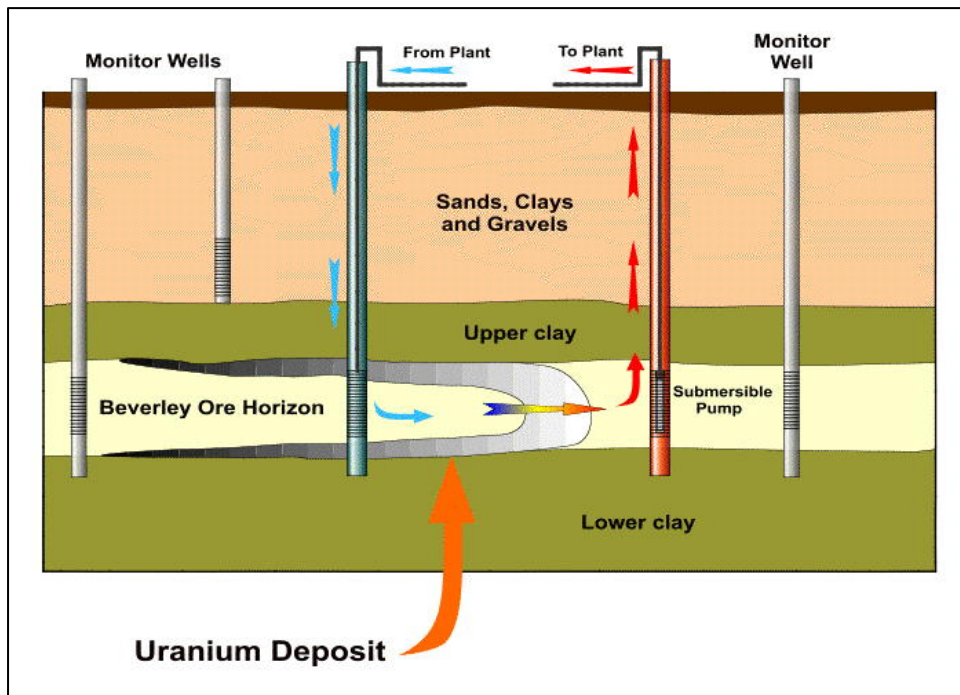


Figure 6. Schematic of Beverley ISL uranium mine, Australia [43]

1.3.2. Production of UOC

The next step is the production of a UOC, the first major intermediate in the nuclear fuel cycle. Through chemical and physical processing of the uranium ore, the uranium content is increased and impurities present in the original ore deposit are removed, purifying the material. UOCs are characterised as having a uranium content of $>65\%$, and a uranium isotopic composition the same as natural uranium [44].

1.3.2.1. Milling of Uranium Ore

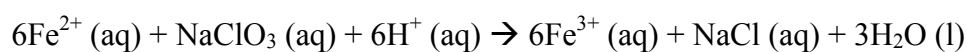
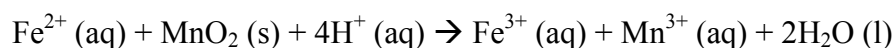
The first step in the processing of uranium ore is milling, which reduces the size of the material through physical processes. This ensures that the uranium contained within the mined ore is susceptible to chemical leaching in latter stages. This step in the processing of uranium ore is also the most energy demanding, accounting for approximately half of the energy used throughout the whole production of UOCs [45]. While originally crushing and both rod and ball milling were used to reduce the size of the uranium ore, it has been phased out in favour of grinding, which reduces both the cost and energy, as well as minimising the generation of dust and release of radon gas [42].

Ore sorting techniques such as radiometric ore sorting, magnetic sorting, gravimetric sorting flotation and grain size classification may be utilised to increase the quality, in terms of uranium content, of the mined uranium ore introduced to the leaching stage of processing and thereby reduce the co-extraction of gangue material by selectively removing ore suspected of containing little-to-no uranium [40]. Of great importance to low-grade ores, such processes have been known to significantly increase the uranium content of the, mainly, davidite ((U, Ca, Fe, Th, Y)₃Ti₅O₁₆) - containing ore that was mined at Radium Hill from 0.6% to 3%, through the exclusion of ore consisting of low, or little, amounts of uranium [46].

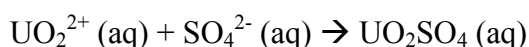
1.3.2.2. *Leaching of Uranium from Uranium Ore*

Leaching is the next step in the process, and is used to extract the uranium content from the other constituents in the mined ore. Acidic or alkaline leaching solutions can be used, and the selection of either regime is dependent on the properties of the ore. Acidic leaching has an advantage over alkaline leaching as it can digest gangue minerals in the ore to leach the uranium, while alkaline cannot, requiring better milling to expose the uranium minerals [42]. Alkaline leaching may also be used as an alternative to acidic leaching, particularly when the uranium contains limestone or other alkaline components that would require excessive quantities of acidic leaching solution to be used [47]. Another advantage of alkaline processing is that a relatively pure uranium precipitate, sodium diuranate (Na₂U₂O₇), can be obtained from the leaching process [48].

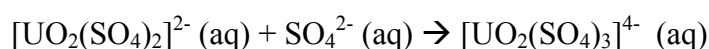
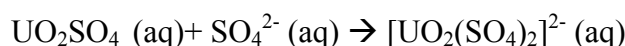
A requirement for either leaching method used is that the uranium must be in the hexavalent state (U^{VI}) otherwise the recovery of uranium will be diminished as the tetravalent uranium (U^{IV}) is less soluble. For acidic leaching, ferric iron (Fe^{III}) is used to oxidise the U^{IV} to U^{VI}, as shown in Reaction 1, and can be regenerated from ferrous iron (Fe^{II}) using a number of different oxidisers including manganese dioxide (MnO₂) and sodium chlorate (NaClO₃) [42];



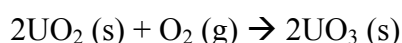
Sulphuric acid is typically used in acidic leaching, due to its low cost and availability [42], and forms a uranyl sulphate species with UO_2^{2+} :



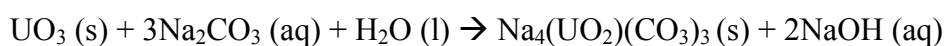
Further reaction with sulphuric acid can also produce two other uranyl species that are negatively charged:



Oxygen is used in alkaline leaching to oxidise the U^{IV} to U^{VI} , before forming a uranyl carbonate species;



The formation of UO_3 is followed by the subsequent reaction with bicarbonate, and then sodium diuranate is precipitated with sodium hydroxide;



1.3.2.3. Separation and Extraction of Uranium

A physical separation is the next step in the processing, in order to remove any solids remaining from the leaching process from the leachate solution containing the uranium. Both conventional and high-rate thickeners can be used to separate the uranium-bearing solution from the slurry, by allow any remaining solids to deposit at the bottom of the vessel (Figure 7(d)). Polyacrylamide flocculants are also used to assist in the solid-liquid separation of the leachate through the agglomeration of particles [49].

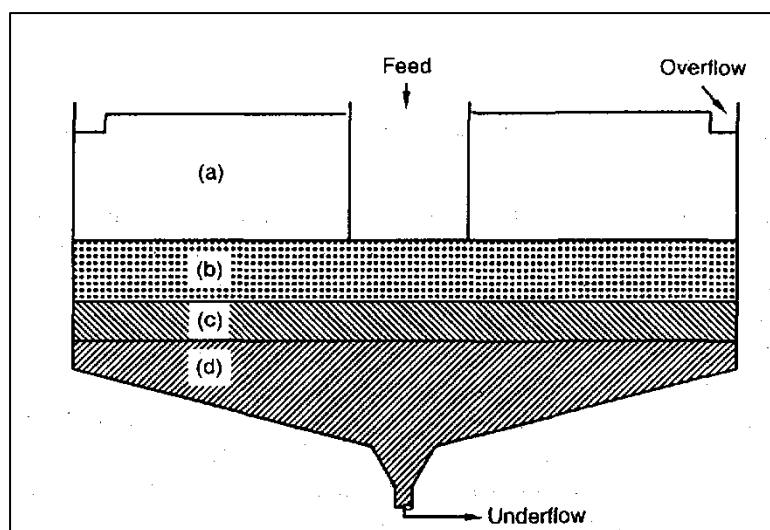
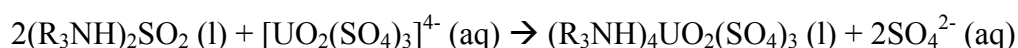
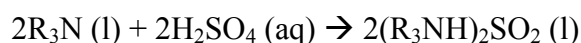


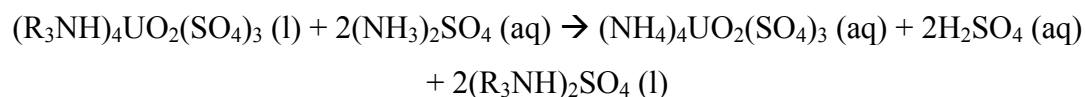
Figure 7. Diagram of the various zones of a conventional thickener: (a) clear solution zone, (b) free settling zone, (c) transition zone, (d) compression zone [49]

The uranium solution is collected in the overflow at (a) whereas the underflow, containing 20-60% solids [49], undergoes a counter-current wash to minimise the loss of any dissolved uranium. This process may be repeated numerous times until 98% recovery is obtained, as 90% of the production costs have been incurred prior to this stage and any loss would therefore be at high cost. The uranium solutions are then filtered to remove any suspended solids, as they can be problematic in later extraction stages.

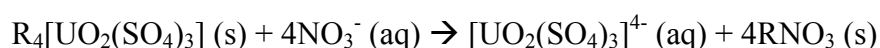
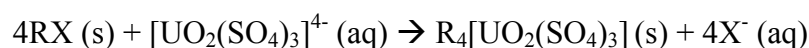
To isolate and concentrate the uranium in solution, either solvent extraction or ion-exchange techniques can be used. Solvent extraction utilises long-chain aliphatic primary, secondary and tertiary amines to extract the uranium species from the solution. The amines used are selective for uranium in the presence of other metal impurities that have persisted through the processing chain [49]. These aliphatic amine solvents are first conditioned with an acid, typically sulphuric acid, to convert them into a salt, before the extraction of the uranium;



Removal of the uranium compound from the loaded aliphatic amine is achieved through the use of a stripping agent. Ammonium sulfate is a common stripping agent, eluting the uranium species into an aqueous phase;

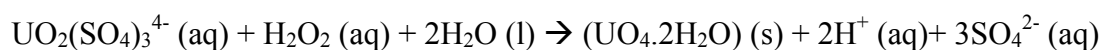


Ion exchange extraction of uranium is commonly accomplished through the use of a polystyrene-divinyl benzene polymer-coated bead. The uranyl species displaces the counter-anion on the ion exchange resin and is eluted later with a nitrate solution;

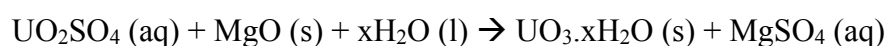


1.3.2.4. *Precipitation of Uranium and the Drying and Calcination of Uranium Ore Concentrates*

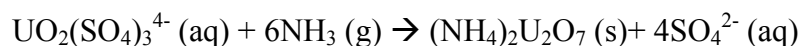
The final stage in the production of uranium ore concentrates is the recovery of uranium through precipitation, followed by solid-liquid separation and drying. A precipitate, sodium diuranate, has already been recovered before this stage through alkaline leaching (Equation 10), therefore the following methods are with respect to acidic leaching. Hydrogen peroxide (H₂O₂), magnesium oxide (MgO) and ammonia (NH₃) may all be used to precipitate the uranium out of solution, however, the use of hydrogen peroxide is advantageous over the other precipitating agents as its use prevents the co-precipitation of impurities including vanadium and molybdenum, producing a purer product [42, 49]. Precipitation using hydrogen peroxide yields uranium peroxide (UO₄.xH₂O);



Uranium trioxide can be produced through the use of magnesium oxide:



Ammonium diuranate ((NH₄)₂U₂O₇) is produced through the addition of gaseous ammonia, or ammonium hydroxide, however the appropriate amount must be added to prevent the formation of basic uranyl sulphate ((UO₂)SO₄(OH)₂·4H₂O) [49];



A combination of conditions including high sulfate concentration, increased temperature, slow neutralisation rate, low pH and long retention time favour the production of basic uranyl sulphate over ammonium diuranate [49]. Through the experience of the Soc Bessines and l'Escarprière plants owned by Société Industrielle Des Minerais De L'ouest, a continuous excess of ammonia and a low concentration of uranium will favour the precipitation of ADU, therefore limiting the formation of basic uranyl sulphate [50].

The uranium precipitates are then washed with dilute ammonium sulphate or process water to remove any residual amounts of soluble impurities and then dried at temperatures between 150-250 °C. Products may also be calcined to completely remove water and ammonia at temperatures between 400-700 °C in an effort to increase the purity of the precipitate [42, 49].

1.4 Australia and Uranium

1.4.1 Australia's Uranium Resources

Australia holds a significant position in the world's uranium industry due to our vast resources. Australia contains 29% of the world's total identified resources of uranium (Figure 8), and was the third largest producer of uranium behind Kazakhstan and Canada in 2017-2018, producing 7,343 tonnes of UOCs which equates to 9.6% of the world's uranium requirements [51]. In 2014, North America (but mainly the US) was the largest market for Australian uranium (39.9%), followed by Europe (34.4%) and Asia (26.6%) [52]. All of the countries to which Australia's uranium is exported to are required to enter into a nuclear cooperation agreement with Australia; to ensure that the uranium is solely used for peaceful purposes [53]. In addition to the nuclear cooperation agreement with Australia, these countries also all have safeguard agreements with the IAEA as well as an Additional Protocol, which grants the IAEA authority to inspect all aspects of a State's nuclear fuel cycle and access to information concerning the State's nuclear program [54]. Interestingly,

Australia signed a civilian nuclear supply treaty with India in 2014 and has since begun exporting uranium, despite India not being a signatory to the nuclear non-proliferation treaty [55-57].

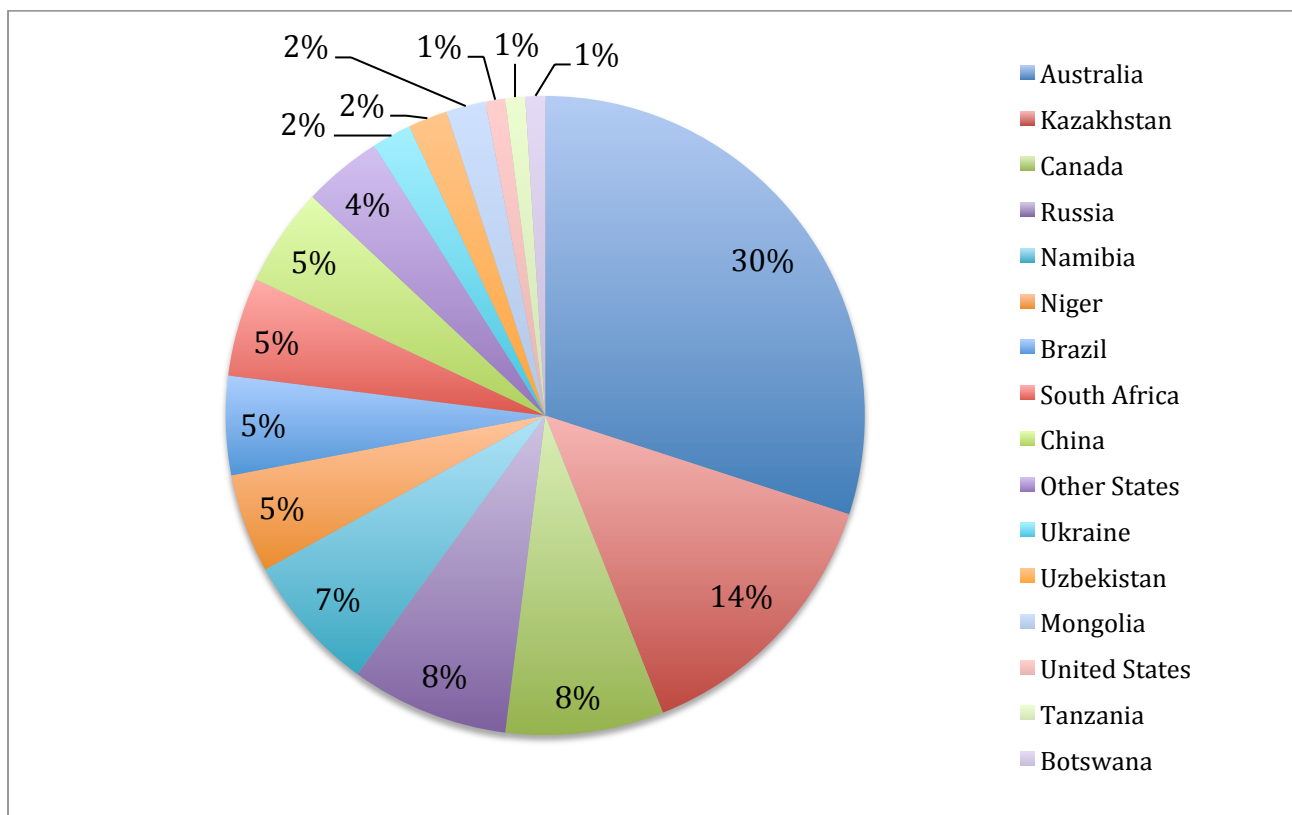


Figure 8. Global distribution of identified uranium deposits (<USD 130/kgU) as of 1st January 2017 [58].

The exportation of uranium provides considerable revenue for Australia, as in 2016-17, 7081 tonnes of uranium was exported at a value of \$596 million [59]. Production in Australia is expected to increase into 2019-20, due to the return of normal production at Olympic Dam following upgrades, however in outlook, the export value is expected to remain similar to previous years due to weak uranium prices [60].

The first uranium mine in Australia to enter production was Rum Jungle (NT) in 1954, followed by Radium Hill (SA) also in 1954, Mary Kathleen (QLD) in 1958 and the two South Alligator mines in 1959, in what is considered the ‘first phase’ of uranium production in Australia [37] (Figure 9). As these mines ceased production, a ‘second phase’ began in 1976 through the revival of Mary Kathleen and the commencement of mining at Nabarlek (NT) in 1979, Ranger (NT) in 1981 and Olympic Dam (SA) in 1988 [37]. Since then, Mary Kathleen and Nabarlek have ceased production while the

Beverley (SA) uranium mine began in 2000. More recently, a number of new uranium mines have been proposed and planned, including Honeymoon (SA) and Yeelirrie (WA) [18].

Image removed due to copyright restriction.

Available online on page 5 of *Australia's Uranium: resources, geology and development of deposits*

http://www.ga.gov.au/webtemp/image_cache/GA9508.pdf

Figure 9. Uranium deposits and current, former and prospective uranium mines in Australia [37].

1.4.2 Active Australian Uranium Mines

1.4.2.1 Olympic Dam, South Australia

Olympic Dam is located 650 kilometres north of Adelaide, South Australia, and is the world's largest single deposit of uranium, accounting for 65% of Australia's uranium resources [37] (Figure 5). Owned by BHP Billiton, the Olympic Dam deposit is the only hematite breccia complex deposit that features significant uranium resources [37]. Copper, uranium, silver and gold are the only elements recovered from the deposit, despite REE elements, such as cerium (0.3%) and lanthanum (0.2%) being present [34]. U-Pb age-dating of rocks within the breccia complex indicate that it formed approximately 1590 Ma ago [61]. The formation of the Olympic Dam deposit is not currently well understood, with the origin of the deposit-forming hydrothermal fluids and metals still unknown [62], however, a number of authors have agreed that multiple fluids were involved [63, 64].

The main section of the hematite breccia complex deposit covers approximately 3 x 3.5 km and is located 300 metres beneath sedimentary rock, and utilises underground mining as the means of extracting ore (Figure 10). The total uranium resources of Olympic Dam amount to 996,000 tonnes

of U_3O_8 with an average uranium (U_3O_8) concentration of 0.3kg/t [65]. While 0.3kg/t is a considerably low concentration of uranium for mining, it is still economically viable as the uranium is recovered as a by-product of the recovery of copper; therefore the production costs are shared. Uranium recoveries up to 80% are obtained when tailings, produced through the flotation of copper sulphates, are collected and subjected to an acidic leach [42]. Olympic Dam uses two solvent extraction processes to recover the uranium, before it is precipitated with ammonia (Equation 18) and then dried and calcined to produce uranium oxide. In 2018, Olympic Dam produced 3,364 t of uranium oxide, which is a decrease on both 2017 and 2016, where 3,661 t and 4363 t were produced, respectively [66].

Image removed due to copyright restriction.

Figure 10. Simplified geological plan of the Olympic Dam hematite-breccia complex deposit [67]

1.4.2.2 *Beverley, South Australia*

Beverley is a sandstone-related uranium deposit 550 km north of Adelaide. The deposit exists 125 metres underground, within permeable sands that are restricted within the highly saline Beverley aquifer [68] (Figure 6). The major uranium minerals associated with the Beverley deposit are coffinite with minor amounts of uraninite, however the upper section of the mineralisation of Beverley has a different mineralogy, with carnotite as the predominant uranium mineral [69]. The lower section of the deposit underwent mineralisation in alkaline conditions (pH 6.3 to 8.4), log fO_2 from -50 to -70 at 25°C and in a reductive bacterial environment, while the upper section mineralised in oxidative (fO_2 between 0 and -25), acidic (pH between 3.9 and 4.5) conditions at 25°C [69]. U-Pb age dating of coffinite and carnotite indicate that mineralisation of the Beverley deposit occurred

between 6.7 and 3.4 Ma [69]. Rare-earth elements, nickel, cobalt, copper, zinc, lead, vanadium, arsenic and molybdenum are associated with coffinite nodules in the Beverley deposit [69].

Uranium is extracted from the ore through a closed-system *in-situ* leaching process, using a moderately acidic, oxidising ($\text{H}_2\text{SO}_4\text{-O}_2$) leaching solution to form a uranyl sulfate species ($\text{UO}_2(\text{SO}_4)_2^{2-}$) and other uranium complexes as field trials demonstrated that acidic leaching was faster and a more efficient extraction than alkaline leaching [37]. Uranium is recovered from the pregnant leaching solution using anion IX resins. The uranyl species are eluted from the IX resins in two stages; first, the main elution with 1.5 bed-volume of 1M sodium chloride solution, and second, the conversion with 1.5 bed-volume with 0.1M H_2SO_4 solution [70]. Hydrogen peroxide is used to precipitate the uranium, forming uranyl peroxide, before undergoing thickening, washing, dewatering and drying processes to produce the final product. The total resources estimated for Beverley is 7.7 Mt at 0.27% U_3O_8 and 2.2 Mt at 0.18% U_3O_8 for Beverley North [71].

1.4.2.3 Ranger, Northern Territory

Ranger is a uranium mine located 230 km east of Darwin, Northern Territory, and is comprised of multiple unconformity-related deposits; two ore bodies, No. 1 and No. 3, and six anomalies. U-Pb age dating of Ranger ore bodies indicate that the average age of the deposit is 1737 ± 20 Ma [72, 73], and was formed through the interaction of a weakly acidic, but highly oxidised saline solution with a reduced, less saline solution [73]. The major uranium mineral mined at Ranger is uraninite, with minor amounts of brannerite and pitchblende [37].

Uranium was first mined at the No. 1 body through open-pit mining in 1980, and ceased in 1994, after exhausting the uranium ore resources. 55,000 tonnes of U_3O_8 was produced during this period, with an average grade of 0.333% U_3O_8 [37]. Mining then began at the No. 3 ore body in 1997, where it produced 80.251 tonnes of U_3O_8 at an average grade of 0.24% U_3O_8 [37], until it was mined out in 2012 [74]. Since 2012 where mining of Pit 3 ceased, Ranger have been producing uranium oxide from stockpiled ore, where it produced 1,999 t of uranium oxide in 2018 and forecasted to produce between 1,400 and 1,800 t of uranium oxide in 2019 [75]. Energy Resources of Australia Ltd., the owners of Ranger, are currently investigating the potential of developing the Ranger 3 Deeps deposit as an underground mine, as it contains 34,000 tonnes of U_3O_8 at an average grade of 0.34% U_3O_8 [74].

In the first stage of processing at Ranger, the raw uranium ore is first crushed to a size less than 19 millimetres and forms a slurry after mixing with water. Uranium from the ore is extracted with a sulphuric acid-pyrolusite (MnO_2) leaching solution [76]. The dissolved uranium is then washed with a counter-current decantation (CCD), before passing through a clarifier and a series of sand filters, to remove any small particulates. Kerosene and an amine are used during solvent extraction (SX), before the uranium is precipitated out as ammonium diuranate, following the addition of ammonia. The final stage is calcination, producing uranium oxide, through heating the ammonium diuranate precipitate at approximately 800°C .

1.4.2.4 *Four Mile, South Australia*

Four Mile is a sandstone-hosted uranium deposit located 500 km north of Adelaide, nearby the Beverley uranium deposit. Discovered in 2005, the mine is comprised of two deposits: Four Mile East and Four Mile West. Four Mile East commenced operation in December 2012 and is inferred to contain 13,000 tonnes of U_3O_8 with a grade of 0.31% U_3O_8 , while Four Mile West commenced operation in June 2013 and contains 19,000 tonnes of U_3O_8 with a grade of 0.34% U_3O_8 [77]. Uranium from the two sandstone-hosted deposits is extracted via *in-situ* leaching, and is processed using the facilities at Beverley [77].

1.4.3 Closed Australian Uranium Mines

1.4.3.1 *Honeymoon, South Australia*

Honeymoon is a sandstone-hosted uranium deposit located 75 km northwest of Broken Hill. The estimated total resources for the Honeymoon and East Kalkaroo, located 2.5 km from Honeymoon, are 7,900 tonnes of U_3O_8 [78]. Pilot production began in September 2011 with the ore, located 110 m underground, extracted through *in-situ* leaching and producing 303 tonnes of uranium [77] [79]. The processing plant was placed into ‘care and maintenance’ over the summer of 2013/14 due to declining uranium prices [79], however the feasibility of restarting the operation at Honeymoon is currently being explored [80].

1.4.3.2 *Rum Jungle, Northern Territory*

The Rum Jungle uranium mine was comprised of 4 unconformity-related uranium deposits located 90 km south of Darwin. Over 1,526,000 tonnes of uranium ore was extracted through open-pit mining during its operation, with U_3O_8 grade ranging between 0.21 and 0.43% [37]. Two of the deposits were poly-metallic, with copper ore also recovered. While the exact genesis of the uranium mineralisation in the four deposits is not well understood [81], age dating of the proximal Kylie deposit indicates that it was formed 1627 ± 45 Ma [82].

During its operation, three different processing strategies were used at Rum Jungle [83]. While all processing strategies featured a sulphuric acid leach [84], during the first period of operation (1954-1962) ion exchange with 0.9 M sodium chloride and 0.09 M sulphuric acid was used to elute the dissolved uranium before precipitating with magnesia. During the second period (1962-1966), solvent extraction, with a 1 M sodium chloride strip, was introduced while retaining the uranium precipitation stage using magnesia. The final period (1966-1971) introduced the precipitation of dissolved uranium with sodium hydroxide, which then underwent calcification at 800°C.

1.4.3.3 *Mary Kathleen, Queensland*

The Mary Kathleen uranium deposit is Australia's only metamorphic uranium deposit and is located approximately 100 km east of Mount Isa. Concentration of uranium, and rare-earth elements in the Mary Kathleen deposit and surrounding areas occurred between 1780 and 1760 Ma, within the skarn and ore body, while age-dating of uraninite, the primary uranium mineral mined, indicates uranium mineralisation occurred 200-250 Ma later [37].

Open-pit mining of Mary Kathleen occurred in two periods; between 1958 and 1963, and 1976 and 1982. During the first phase, 8,882 tonnes of U_3O_8 was mined, whereas 1,200 tonnes of U_3O_8 was extracted when Mary Kathleen was reopened. During both phases, an acidic leach with sulphuric acid was used to digest the uranium ore [84]. The first period utilised ion exchange, with sodium chloride and dilute sulphuric acid used to elute the dissolved uranium, and precipitate with magnesia [83]. The second period used solvent extraction, with 5% Alamine 336 (tri-n-octylamine), 3% alcohol and 92% diluent. After stripping with aqueous ammonium sulphate, the uranium was precipitated using ammonia, before it was calcined at 700°C.

1.4.3.4 *Nabarlek, Northern Territory*

Nabarlek was an unconformity-related uranium deposit located approximately 270 km east of Darwin, discovered through airborne radiometric surveying. Sm-Nd age-dating for the mineralisation of the Nabarlek deposit indicates that it occurred 1600-1650 Ma, purportedly through the mixing of hot, oxidising meteoric water with the reducing metasediments of the Paleoproterozoic basement [85]. Uraninite is the primary uranium mineral present at Nabarlek, with minor amounts of coffinite, pitchblende and possible brannerite also identified [86].

During its operation between 1979 and 1988, 10,858 tonnes of U_3O_8 was produced. Sulphuric acid was used in the acidic leaching, with manganese dioxide used as an oxidant initially until Caro's acid

(a mixture of sulphuric acid and hydrogen peroxide) was introduced [87]. A mixed solvent (4% Alamine 336, 2.4% iso-decanol and 93.6% kerosene) was used to extract the dissolved uranium, before it was stripped using aqueous ammonium sulphate [83]. Ammonia was used to precipitate out the dissolved uranium, before it was calcified at 500°C.

1.4.3.5 *South Alligator, Northern Territory*

South Alligator is an unconformity-related deposit located 320 km east of Darwin. Similar to Rum Jungle, the South Alligator mine is comprised of multiple deposits spread through the South Alligator River system. Multiple mechanisms for the formation of the South Alligator uranium deposits have been proposed [37], with alternative ideas on the type of uranium-bearing fluid (groundwater versus meteoric) and the identity of the reducing agent that caused the uranium to precipitate out of the fluid [88-90]. Pitchblende and uraninite were the major uranium minerals mined at the South Alligator, while minor amounts of secondary uranium minerals, including as phosphuranylite ($\text{KCa}(\text{H}_3\text{O})_3(\text{UO}_2)_7(\text{PO}_4)_4\text{O}_4 \cdot 8(\text{H}_2\text{O})$), metatorbernite ($\text{Cu}(\text{UO}_2)_2(\text{PO}_4)_2 \cdot 8(\text{H}_2\text{O})$) and autunite ($\text{Ca}(\text{UO}_2)_2(\text{PO}_4)_2 \cdot 10-12(\text{H}_2\text{O})$) [37]. Gold, platinum and palladium are also present in these deposits at sufficient quantities to enable their extraction and recovery.

Eight hundred and seventy four tonnes of U_3O_8 was, in total extracted, from 14 different deposits in the South Alligator Valley during its operation between 1959 and 1962, with the U_3O_8 grade ranging from 0.13 to 0.82% [37]. Uranium was leached from the mined uranium ore using sulphuric acid, before it was separated by solvent extraction. Sodium chloride was used to strip the uranium from the organic phase, before it was precipitated out using magnesia [83].

1.4.3.6 *Radium Hill, South Australia*

Radium Hill is an intrusive deposit located 340 km north of Adelaide in the Olary Uranium Field. Initially mined for radium between 1906 and 1931, uranium mining commenced in 1954 and produced 152,000 tonnes of 'sorted' uranium ore that was transported to Port Pirie for processing. After a sulphuric acid leach, the dissolved uranium was purified using ion exchange, before being stripped with sodium chloride and dilute sulphuric acid [83]. The purified uranium solution was then precipitated with two different agents; lime to remove any residual impurities, followed by magnesia to precipitate out the uranium.

1.5 Nuclear Forensic Science

1.5.1 History of Nuclear Forensic Science

After the dissolution of the Soviet Union, instances of the illicit trafficking of nuclear materials were first reported in Switzerland and Italy [91]. As of the 31st of December 2016, the IAEA Incidents and Trafficking Database (ITDB), developed in 1995 to record and analyse incidents of illegal trafficking of nuclear and other radioactive material, recorded 3068 confirmed incidents, including 'unauthorised possession and related criminal activities', 'theft or loss' and 'other unauthorised activities or events' [1]. While nuclear materials represent only a small percentage of the total materials reported (

Figure 11), the potential impact of this material is concerning. The type and quantity of recovered nuclear material is varied, ranging from seizures of 17 kg of HEU [92], to four uranium dioxide (UO₂) fuel pellets for nuclear reactors [93]. It has been suggested that, similar to drug trafficking, the quantity of nuclear material seized only represents only a small fraction of the amount of material available on the black market [92].

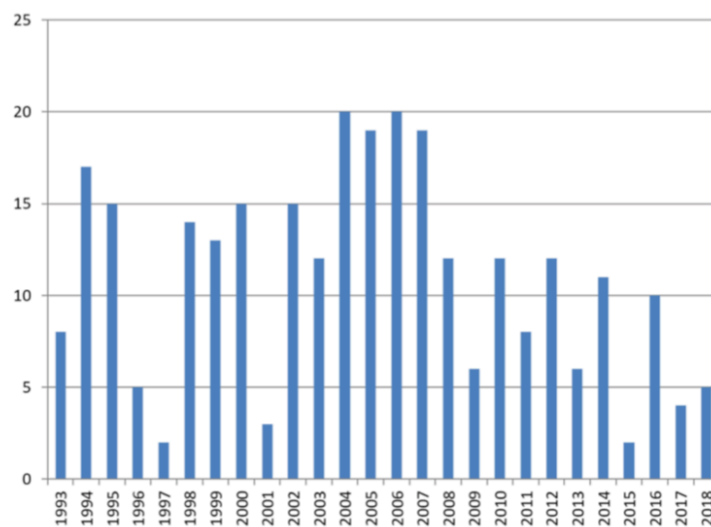


Figure 11. Illicit trafficking cases recorded by the IAEA on the ITDB as of the 31st of December 2018 [94]

1.5.2 Nuclear forensics in the Australian context

Since the 1970s, Australia has experienced several instances of uranium materials falling outside of regulatory control. Between April 1977 and July 1978, 2,200 kg of UOC (often referred to as 'yellowcake'), with a then-current value of \$132,000, was stolen from Mary Kathleen Uranium Ltd

[95, 96]. Allegedly stolen in small quantities, the yellowcake was later found within six drums located at a warehouse in Sydney [97, 98]. In April 2007, 10 jars containing 3 kg of uranium were located within the Olympic Dam residential village in outback South Australia [99]. Originally been sent to the Honeywell conversion facility in the US [99], the uranium samples were lost somewhere on the return route to Olympic Dam, be it the Roxby Downs airport, in transit to Olympic Dam or at Olympic Dam itself, the uranium was stolen; the location at which it was stolen is still not known and is under investigation by police [100]. In April 2009 during a raid of a clandestine drug laboratory, Victorian police seized two different samples of uranium material, containing 42.9 g and 48.6 g respectively [101, 102]. The samples were analysed by researchers at the Australian Nuclear Science and Technology Organisation (ANSTO) in Lucas Heights, NSW and Lawrence Livermore National Laboratory (LLNL) in the US. Both samples were found to be unrelated to one another; the first sample NSR-F-270409-1 was found to contain depleted uranium in a form similar to $K_2(UO_2)_3O_4 \cdot 4H_2O$ with a purity of ~71% U by weight, whereas the second sample NSR-F-270409-2 also contained depleted uranium principally in the chemical form of $UO_3 \cdot 2H_2O$ but of higher purity (~80% U by weight) [101]. As the presence of ^{232}U and ^{236}U in both samples is indicative of exposure to a neutron flux and at levels consistent with plutonium production, this indicates both samples have separately undergone reprocessing and therefore are not from Australia as Australia has never had the capability to reprocess uranium [101]. In May 2009, a state policing agency seized a jar labeled ‘Gamma Source’ containing 41.95 g of a green granular powder during a raid on a clandestine drug laboratory [103]. Through analysis by researchers at ANSTO and LLNL, it was determined the powder was a natural UOC, and likely originated from the Mary Kathleen uranium mine whilst the mine was in its second period of production [103].

1.5.3 Research focuses in nuclear forensics

The developing discipline of nuclear forensics is ‘examination of nuclear or other radioactive material, or evidence that is contaminated with radionuclides, in the context of legal proceedings under international or national law related to nuclear security’ [104]. Created in response to the confirmed incidents of illegal trafficking of nuclear material, nuclear forensics is used to determine the origins of the nuclear material and its intended use [104]. This ability of nuclear forensics to identify the source of the material is based on the analysis of endogenous (related to the ore deposit) and exogenous (related to the processing of the material to its current form) characteristics. While materials throughout the nuclear fuel cycle may differ in their uranium isotopic composition, this may provide information on their intended use.

Uranium materials each undergo radioactive decay and feature in-growth of their daughter products, providing additional information regarding the age of the material (i.e. the duration of time since last purification). Known as a ‘chronometer’, this relationship between the parent and daughter nuclides can be used to determine the age of a material based on the assumption that during the chemical separation processes, any in-grown daughter nuclide is removed. The other assumption on which chronometry calculations are based is that the in-growth of the daughter nuclide present in the material has resulted solely from its in-growth during the period of time between processing and the interception of the material, and it is thereby proportional to the amount of the parent nuclide and length of time since purification [105]. These chronometers have varying degrees of value as tools for use in nuclear forensics, due to the dependence on the half-lives of both parent and daughter nuclides, with the $^{214}\text{Bi}/^{234}\text{U}$, $^{231}\text{Pa}/^{235}\text{U}$ and $^{230}\text{Th}/^{234}\text{U}$ relationships the most promising whereas the $^{229}\text{Th}/^{233}\text{U}$ and $^{228}\text{Th}/^{233}\text{U}$ have limited applications [106, 107].

The morphological features of UOC powders can also reveal important information regarding the processing stages within the production. The particle size and microstructure of the UOC powder are influenced by a number of different factors, including the conditions under which the UOC powder is precipitated in and the morphological properties of the starting material, as well as the conditions of the calcination the a UOC powder underwent [106, 108]. The analysis of morphological features can also be applied in the analysis of UO_2 pellets, where the physical dimensions of the pellets themselves may indicate where the pellets were manufactured [109].

1.5.4 Source Attribution of Uranium Ore Concentrate

The identification of the provenance of an illegally trafficked nuclear material is based on the analysis of signatures that demonstrate enough variability that they can be used to differentiate between materials of different origins. While these characteristics may be endogenous or exogenous, they may be present in differing concentrations due to the successive purification stages involved in the formation of UOCs.

1.5.4.1 Uranium Isotopic Analysis

While it was long held that the $^{235}\text{U}/^{238}\text{U}$ isotope ratio remained constant, variations in this ratio of approximately 1.3% have been observed [10]. Analysis of uranium ore samples revealed that low-temperature redox changes ($\text{U}^{\text{VI}}\text{O}_2^{2+} \rightarrow \text{U}^{\text{IV}}\text{O}_2^{2+}$) are the major influence on isotopic fractionation between the ^{235}U and ^{238}U isotopes [7]. The results also suggest that the isotopes of uranium

fractionate according to the ‘nuclear volume effect’, similar to other heavy elements, and results in the heavier isotope being concentrated in the reduced species during redox reactions [7].

Larger variations have been observed in the $^{234}\text{U}/^{238}\text{U}$ isotopic ratio, due to the increased mobility of ^{234}U with respect to the other uranium isotopes, caused by the α -recoil damage to the crystal structure [110]. Aqueous weathering of these damaged crystal sites enables preferential leaching of ^{234}U , resulting in ^{234}U -depleted deposits, with respect to the other uranium isotopes, if they have been in an aqueous environment for an extended period of time.

Analysis of the $^{235}\text{U}/^{238}\text{U}$ isotopic ratio by Keegan *et al.* (2008) revealed that a UOC sample from each of the operating Australian uranium mines (Olympic Dam, Beverley and Ranger) were not significantly different and had a good agreement with the IUPAC value for natural uranium [39]. These three mines did, however, differ in their $^{234}\text{U}/^{238}\text{U}$ isotopic ratio, enabling them to be distinguished from one another. All three mines were also found to contain differing amounts of depletion in the ^{234}U isotope due to prolonged leaching, which is dependent on their respective geological condition, structure and permeability [39].

A study by Srncik *et al.* (2011) assessed the applicability of using the $^{236}\text{U}/^{238}\text{U}$ isotope by analysing uranium ore and UOC samples of known locations with accelerator mass spectrometry (AMS) [13]. ^{236}U is produced through the thermal neutron capture by ^{235}U . The abundance of ^{236}U is quite varied between mines, as the main source of thermal neutrons in the ore deposit originates from the spontaneous fission of ^{238}U or through the release of a neutron (α, n) by lighter elements [13]. Other elements, such as gadolinium and dysprosium, and water within the deposit are neutron absorbers may interfere with the formation of ^{236}U [111]. A comparison of the $^{236}\text{U}/^{238}\text{U}$ isotope ratios obtained from the uranium ore samples revealed that there is an inter-mine variability, however the samples were found to be heterogeneous, with the exception of the Ranger samples [13]. Uranium ore and UOC samples originating from the same mine were compared and only the Ranger samples showed good agreement. This observation suggests the heterogeneity of the uranium deposits, and is also complicated with the fact that uranium mills may process ores from other deposits as well as their own. UOCs may be preferable for provenancing as they results from a blending of the uranium ore and thus, the $^{236}\text{U}/^{238}\text{U}$ isotope composition is averaged.

1.5.4.2 Anion analysis

Throughout the processing of UOC, anions, in the form of mineral acids or salt solutions, are introduced to leach uranium from the ore deposits itself, as in the case of *in-situ* leaching, or from ore extracted from the deposits. Anionic solutions may also be used in latter stages to precipitate the uranium out of solution, forming UOC. Due to the diversity of uranium deposits, the steps used are tailored to efficiently extract as much uranium as possible, and therefore may be indicative of an individual uranium mine.

Badaut *et al.* (2009) first demonstrated the applicability of using the anionic content to differentiate between UOC samples from 8 different uranium mines around the world, as differences in patterns and concentrations between all of the mines in the study were observed through ion chromatography (IC) (Figure 12) [112]. In the uranium mines where multiple samples were obtained on different dates, variations were observed in their respective anionic patterns, however these variations were found to be smaller than the variations observed between different mines. It has been suggested that the intra-mine variability observed may be indicative of a change in processing method at those particular mines, resulting in the discrepancy observed between the different samples obtained on different dates [105]. While concluding that the anionic content could be used for source attribution purposes, it was suggested that this information be used in conjunction with other analyses due the ambiguity observed, in part due to the intra-mine variability [112].

Image removed due to copyright restriction.

Available online from:

<https://doi.org/10.1007/s10967-008-7404-3>

Figure 12. Anion ratios in different uranium ore concentrate samples [112]

Another study further investigated the applicability of the use of anionic content for the differentiation of UOC samples from different uranium mines [84]. This research expanded on the sample set of the first (24 different mines) and attributed the presence of particular anions to particular stages in the production of UOC to account for all the different sources of anions

throughout the processing. Fluoride (F^-) was thought to be the only anion present that originated from the uranium deposit itself, as the other anions present could be attributed to their various processing stages. It was also found, through a comparison between the IC analysis and the inductively-coupled plasma mass spectrometry (ICP-MS) analysis performed in another section of this study, that only a small percentage of the phosphate (PO_4^{3-}) was water soluble, and therefore detectable by IC.

Analysis of UOC samples from 70 different mines with Fourier-transform infrared spectroscopy (FTIR) also identified a number of different anion impurities that are indicative of specific processes in the production of UOC, during the identification of different UOC compounds [113]. Sulphates (1120cm^{-1}), nitrates (1384cm^{-1}) and carbonates (1330cm^{-1} , 1500cm^{-1} and 1050cm^{-1}) were the most common anions detected using FTIR, and their concentration in the UOC samples varied, as it was dependent on the precipitation conditions and the effectiveness of the washing stages.

1.5.4.3 Trace and Rare Earth Elemental (REE) Analysis

Trace elements are considered to be indicative of both the raw uranium ore as well as from the processing, where they may have been introduced either intentionally or accidentally [105]. These elements may have been present in higher concentrations originally, but as they progressed further down the processing path, the uranium material becomes more refined, resulting in them being present at only trace concentrations. As a subset of trace elements, the REE composition may be of greater use as their composition in UOC samples is reflective of the uranium deposit itself.

Svedkauskite-LeGore *et al.* (2008) [114] identified 66 elemental impurities present at various concentrations within 45 UOC and uranium ore samples from 30 different uranium mines and analysed them by cluster analysis, to determine which samples have similar elemental patterns and therefore could be considered to be from the same source. Within both the yellowcake and uranium ore data sets, a number of samples from different geographical locations (for example Cluff, Canada and Mounana, Gabon) were placed in the same cluster thereby demonstrating that despite the geographical separation between these uranium mines, these samples within the clusters have similar elemental compositions. It was then suggested that due to the grouping of samples from mines of vastly different geographical locations, additional criteria is required to identify the source of uranium ore or UOC material.

A second study analysed 24 UOC samples from different uranium mines for 65 different elements using ICP-MS, and through canonical analysis of principle coordinates (CAP) tested whether the samples could be grouped according to their deposit category [84]. Each deposit category (phosphorite, quartz-pebble conglomerate and, to a lesser extent, unconformity-related) were found to contain characteristic elements that could be used to differentiate between deposits. CAP was also used to determine whether samples originating from certain geographical locations could be differentiated from one another based upon their elemental composition; however this resulted in limited success. Two geographical areas were tested for Australian samples (Northern Territory and South Australia) but the results were unable to be validated, whereas three different regional areas in Canada were found to be distinct (Elliot Creek, Bancroft and Northern Saskatchewan), but the results were inconclusive as this may be a reflection on the deposit category, as all three locations have different geologies [84].

The REE content of UOCs is considered to be one of the most powerful tools in source attribution studies, due to the direct dependence between the abundance of REE and the geological conditions associated with the formation of uranium oxides [115]. In the analysis of uranium oxide samples from 18 different uranium occurrences representing 6 different major uranium deposit categories, Mercadier *et al.* [115] demonstrated that each different deposit type had a characteristic chondrite-normalised REE pattern, reflecting the variability in the mineralising processes and geological settings involved in the formation of each category of deposit, such as the salinity of fluids, REE source and temperature of the deposits (Figure 13).

Keegan *et al.* (2008) determined that, in combination with trace element data, for UOC samples from three different Australian uranium mines (Olympic Dam, Beverley and Ranger) the REE concentrations were significantly different and the REEs were major contributors to the variability observed between the mine samples [39]. While it was found that the REE pattern may be a key characteristic of UOCs that could be used to identify the source of the material, Keegan *et al.* (2008) recommended that a broader study be conducted to determine whether REE, in conjunction with other characteristics, could be used for source attribution studies [39].

In order to evaluate the effect of the processing stages involved in the production of UOCs, Varga *et al.* (2010) compared the literature values of the REE pattern of raw uranium ore to experimental data obtained from sector field ICP-MS (SF-ICP-MS) for the UOC from the same uranium mines [2]. The comparison revealed that the REE pattern remained unaltered by the processing stages, enabling

the REE composition of the UOC samples to be directly linked to the uranium ore deposit. The REE patterns were also analysed by cluster analysis, to determine how similar they were for UOC samples obtained from different mines. The cluster analysis revealed that while a number of uranium deposit categories featured similar REE patterns and were clustered together, a number of samples were mis-grouped. This has been attributed to the small number of variables used in the analysis, the loss of information during the normalisation against chondrite data and the variation in the lighter REE. On the basis of this miss-grouping, Varga *et al.* (2010) suggested that the REE pattern is not the ultimate tool for source attribution studies, but it can, however, be used in conjunction with other characteristics of UOC [2].

Image removed due to copyright restriction.

Available online (figure 3) from:

<https://doi.org/10.1111/j.1365-3121.2011.01008.x>

Figure 13. Chondrite-normalised REE pattern of uranium oxide from six different categories of uranium deposits [115]

1.5.4.4 Isotopic Analysis of Lead, Strontium and Oxygen Impurities in UOC

In addition to the analysis of trace impurities, the isotopic composition of a number of elements may also be beneficial for source attribution purposes, as they are presumed to reflect that of the ore and provide information on the ore deposit, as well as the processing [32, 116].

Lead isotope analysis has previously been investigated for use in source attribution studies of UOCs and uranium ore as three of the four isotopes are of radiogenic origin, while ^{204}Pb is of primordial origin [114, 116, 117]. ^{206}Pb is the final nuclide of the uranium series decay chain ($4n+2$) that begins with ^{238}U , ^{207}Pb is the final nuclide of the actinium series decay chain ($4n+3$) that begins with ^{235}U , and ^{208}Pb is the final nuclide of the thorium decay series ($4n$) that begins with ^{232}Th . As these isotopes are produced through the decay of uranium and thorium isotopes, their composition is reflective of the age and composition of the uranium deposit. This results in lead isotopic compositions that differ from natural lead ($^{204}\text{Pb} = 1.4\%$, $^{206}\text{Pb} = 24.1\%$, $^{207}\text{Pb} = 22.1\%$ and $^{208}\text{Pb} = 52.1\%$) [118], as the in-growth of the radiogenic isotopes is continuously increasing, and may be

characteristic of a particular uranium mine. While the use of lead isotopic abundance ratios have been suggested as a UOC characteristic applicable for source attribution purposes, its use has been cautioned with the proviso that relatively high intra-mine variabilities are observed and contamination with lead featuring natural isotopic abundances should be taken into account when drawing conclusions [114, 116, 117].

The analysis of 9 different UOC and uranium ore samples by Svedkauskite *et al.* [117] revealed that the lead isotopic abundance ratios varied significantly, with only two mines (Rössing, Namibia and Beverley, Australia) featuring similar $^{207}\text{Pb}/^{206}\text{Pb}$ ratios, suggesting that the age of the deposit or the processing technologies used are similar. Four samples were analysed from Beverley and two distinct pairs were identified, displaying a significant difference in the $^{207}\text{Pb}/^{206}\text{Pb}$ and $^{208}\text{Pb}/^{206}\text{Pb}$ lead abundance ratios between the pairs. A second study by Svedkauskite *et al.* [117] analysed the lead isotopic abundance ratios of 35 uranium ore and 10 UOC samples, and was used to distinguish between ambiguous results obtained through cluster analysis, demonstrating how a combinatorial approach to source attribution studies can be effective in reducing the uncertainty in the identification of the origin of the material.

A similar study was performed by Varga *et al.* (2009), who used the ratios between the three radiogenic lead isotopes (^{206}Pb , ^{207}Pb and ^{208}Pb) against the primordial lead isotope (^{204}Pb) to assess their applicability in source attribution studies [116]. The results obtained agreed with what was observed with Svedkauskite *et al.* (2008), that the variability in lead isotopic abundance ratios enabled different sources to be differentiated, however the intra-mine variability of a number of different mine samples was high and could potentially lead to false conclusions [114]. Varga *et al.* (2009) attributed this intra-mine variability to two factors: that lead isotopic abundance ratios within the uranium deposits are heterogeneous, and that the radiogenic lead was continuously removed during the many stages of processing and was isotopically diluted through the contamination of lead with a natural isotopic abundance [116]. A number of UOC samples featured lead isotope ratios that were indistinguishable to natural lead, which was proposed to occur by three different reasons; the UOC was highly purified (removal of all lead and contaminated with natural lead), the uranium deposit was recently formed (where the radiogenic isotopes had not in-grown due to large uranium and thorium half-lives) and the uranium and thorium content is low in the deposit (and therefore the amount of radiogenic lead is reflective of that). Varga *et al.* (2009) concluded that, in agreement with other studies [114, 117], lead isotope abundance ratios have only limited use for source attribution

purposes, while suggesting that their application is more appropriate to compare known samples or to verify that the uranium material originates from a known location or production batch.

Varga *et al.* (2009) also investigated the applicability of using strontium isotope ratio measurements for source attribution purpose [116]. The $^{87}\text{Sr}/^{86}\text{Sr}$ ratio was analysed as their strontium isotopic abundance is presumed to reflect the geology of the uranium ore deposit, as well as the age and category as ^{87}Sr is a radiogenic and produced through the decay of ^{87}Rb ($t_{1/2} = 4.8 \times 10^{10}$ a) [116]. Analysis of UOC samples demonstrated that samples from different sources could be distinguished (Figure 14), and the intra-mine variability observed in Beverley and Rabbit Lake samples were reduced when compared to the lead isotopic abundance ratio results. These results suggested that the strontium isotopic composition is less affected by the processing of the uranium ore, and that within the ore deposit there is less variability [116]. In summary, Varga *et al.* [116] concluded that despite the smaller inter-mine variability in the strontium isotopic composition, it offered a greater degree of confidence in source attribution than lead isotopic composition analysis.

Image removed due to copyright restriction.

Available online (figure 3) from:
<https://pubs.acs.org/doi/abs/10.1021/ac901100e#>

Figure 14. Measured $^{87}\text{Sr}/^{86}\text{Sr}$ isotope ratios of UOC samples from different mines (presented at the 95% confidence level) [116]

The oxygen isotopic composition of UOC has also been suggested as another signature that could be used to differentiate between UOCs originating from different mines. Three major factors that may work together or separately, influence the $^{18}\text{O}/^{16}\text{O}$ isotopic ratio of uranium deposit; the fluid involved in the formation of the uranium deposit, the temperature under which the deposits forms, and the type of uranium mineral formed [32]. Other minor factors that may also influence the $^{18}\text{O}/^{16}\text{O}$ isotopic ratio include water/rock ratios, diffusion or isotopic exchange between late fluids and uranium minerals following precipitation and alteration of uranium minerals [32]. Variations in the $^{18}\text{O}/^{16}\text{O}$ isotopic ratios are expressed as $\delta^{18}\text{O}$, which is the relative variation compared to the standard mean ocean water (SMOW) value ($^{18}\text{O}/^{16}\text{O} = 2.005 \times 10^{-3}$) [119]. The oxygen isotopic composition of UOC may not be truly reflective of the uranium ore deposit it was extracted from, as UO_2^{2+} in solution may undergo oxygen isotopic exchange with water during the processing stages in UOC production [120, 121].

Pajo *et al.* (2001) analysed a series of natural and standard uranium oxides and uranium dioxide pellets from different geographical locations to determine the effectiveness of the $^{18}\text{O}/^{16}\text{O}$ isotopic ratio in source attribution studies [122]. Small, but significant differences were observed in the $^{18}\text{O}/^{16}\text{O}$ isotopic ratios of the uranium oxide materials, enabling samples from different geographical locations to be differentiated from one another. More distinct differences were observed in the UO_2 pellets from different geographical locations, which was reflective of the water and acids used in the production of the pellets from uranium hexafluoride (UF_6). A correlation between the $^{18}\text{O}/^{16}\text{O}$ isotopic ratios and the local minimum rainfall precipitation $\delta^{18}\text{O}$ values was observed for all but one sample, and was attributed to the different chemical composition of this sample (magnesium diuranate (MgU_2O_7)).

Fayek *et al.* (2011) suggested that $\delta^{18}\text{O}$ and REE (La/Yb) ratios could be applied in combination to better differentiate between uranium ore deposits in different geographical locations, as it is expected that overlaps in trace element compositions may occur [32]. Using $\delta^{18}\text{O}$ and REE (La/Yb) ratios, clear differences were observed between uranium ore originating from Canada, Australia and the natural fission reactors of Okla, Gabon, with Fayek *et al.* (2011) concluding that the combination of these different characteristics of uranium ore may be used to differentiate between samples that were previously indistinguishable [32].

1.5.4.5 Analysis of Uranium Speciation within UOC

Varga *et al.* (2011) investigated the applicability of FTIR in identifying the chemical speciation and chemical impurities (discussed in 1.5.4.2) within UOC samples [113]. FTIR analysis of UOC samples was easily able to distinguish between different uranium uranium compounds through the comparison of peaks associated with different functional groups (Figure 15). Near-infrared spectroscopy (NIR) has also been used to identify uranium compounds present within UOC with similar results to Varga *et al.* (2013)[123], and requires no sample preparation and less time for analysis. Classification of UOC samples analysed with NIR by principal component analysis (PCA) featured segregation of different UOC compounds, however some compounds (UO_3 and U_3O_8 , and UO_4 and ammonium uranyl carbonates (AUC), respectively) were found to overlap [124].

Image removed due to copyright restriction.

Figure 15. Comparison of typical FTIR spectra of various UOC compounds [113]

1.6 Research Aims

The aims of this research are to investigate and evaluate new analytical methodologies and signatures for their potential to improve the current capabilities of materials provenancing within the nuclear forensics discipline. As there is currently no single signature that can confidently identify the source of an unknown UOC, further research into developing new high-confidence methodologies and signatures will be invaluable to the nuclear forensic community. A particular

focus is placed on analytical techniques that can provide results with great accuracy and precision reflecting their use at latter stages of an investigation, where the immediacy of results is less critical.

This research will focus on three different areas;

1. Investigate the novel use of TGA for the analysis of the chemical composition of Australian UOC for its efficacy towards materials provenancing. This research will also be supported by NIR and Raman spectroscopy, and XRD to help identify the changes to the UOC composition as a function of temperature. Additionally, the morphology of the UOCs will be investigated, and how the morphologies are affected by increasing temperature.
2. Investigate the intra-mine variability of the $^{234}\text{U}/^{238}\text{U}$ and $^{235}\text{U}/^{238}\text{U}$ UOCs and uranium ores from Australian mines using MC-ICP-MS, an established technique in nuclear forensics
3. Evaluate the novel use of k_0 -NAA for the analysis of the trace and rare earth elemental composition of Australian and North American uranium ore samples. XRF, SEM/EDX and DNAA were also used to measure the uranium content within the uranium ore samples in advance of the k_0 -NAA analysis.

The analytical techniques proposed for this research are detailed in Chapter 2.

Chapter 2. Analytical Techniques

2.1. Inductively-Coupled Plasma Mass Spectrometry

Inductively-coupled plasma mass spectrometry (ICP-MS) is a widely used analytical technique due to its capacity for multi-elemental analysis, high sensitivity, high precision and high throughput [125, 126] (Figure 16). Quadrupole ICP-MS is frequently used in a wide range of applications, including environmental, medical, biological and geological studies [125]. It does, however, suffer from a number of interferences that can influence the reliability in the measurement of elements with the same mass-to-charge ratio. Some strategies, such as analyte extraction [127], and use of collision cells [128], can be implemented to reduce their influence. Alternatively, increasing the mass resolution of the instrument can also reduce their influence, leading to the development of high mass resolution ICP-MS instruments such as sector-field ICP-MS [126].

Image removed due to copyright restriction.

Figure 16. Schematic Diagram of Quadrupole-ICP-MS instrument [129].

2.1.1 Sample Introduction

Typically, nebulisation is commonly used in ICP-MS to introduce the sample (in solution) to the plasma. A peristaltic pump is used to feed the solution into nebuliser, where it is forced into an aerosol with a gas, commonly argon. The aerosol then enters a spray chamber, which has two primary functions [130]; selectively remove droplets based on their size, and smooth out pulses from the peristaltic pump during nebulisation. Larger droplets ($>10\ \mu\text{m}$ diameter) are separated by gravity

as they travel the length of the central tube within the spray chamber, as the plasma is less efficient in dissociating larger droplets. Fine droplets, representing only 1-2% of the sample, are introduced to the plasma via a sample injector.

Other strategies may be used to introduce the sample to the plasma, due to the potential to introduce contaminants and difficulty in digesting samples into solutions. Laser ablation (LA) of solid samples reduces sample preparation steps, analysis times and spectral interferences when compared to solution ICP-MS [131]. Fractional ablation, modification of the elemental composition at the bottom of craters, and transport efficiencies of the aerosol and the semi-quantitative nature of the analysis are some of the disadvantages associated with LA sample introduction to ICP-MS [131-133]. Alternatively, ICP-MS may be used on-line following chromatographic separation with high performance liquid chromatography (HPLC), IC or flow injection analysis [130].

2.1.2 Plasma Ionisation

The aerosol consisting of small droplets, by way of the sample injector, is introduced to the plasma torch. As the aerosol passes through the various stages within the plasma, it is desolvated, vaporised, atomised and ionised, where finally it exists as both ground state atoms and ions [130] (Figure 17). The plasma is formed within the torch when argon gas is subjected to radiofrequency alternative-current oscillations, forming an electromagnetic field. Electrons within the argon gas are stripped with a high-voltage spark, and then accelerated in the magnetic field, which can result in a chain reaction as they strip off more electrons from other argon atoms. The combination of argon atoms, argon ions and electrons formed within the chain reaction form an ICP discharge. The energy required to strip the electrons from the argon atom (i.e. first ionisation potential) is 15.8 eV.

Image removed due to copyright restriction.

Figure 17. Mechanism of conversion of a droplet to a positive ion in the ICP [130]

2.1.3 Mass Spectrometer Interface

The interface of an ICP-MS separates the ICP from the mass spectrometer, and its role is to transport the ions efficiently and consistently between the different pressures of the two regions, 760 torr and 10^{-6} torr, respectively. Within the interface are two metallic cones with small orifices operating at 1-2 torr. The ions pass through the first cone, referred to as the sampler cone, which has an orifice with

an internal diameter of 0.8-1.2 mm. The second cone, the skimmer cone, has a smaller orifice (0.45-0.8 mm) but is much sharper in shape. The cones are typically comprised of nickel, but platinum and other materials may be used to prevent corrosion and degradation.

2.1.4 Ion Focusing

Before the ions are separated according to mass/charge ratio, they must first be focused. This is a crucial section in the detection of analytes, as the efficiency of ion formation within the plasma is very low. Interfering species including neutral species, particulates and photons can also influence the detection of analytes, as they can contribute the background signal. There are three common strategies employed to focus the ion beam; a grounded metal stop after the skimmer cone, a chicane design, and a hollow ion mirror [130]. The placement of the grounded metal stop after the skimmer cone focuses the beam through the electrostatic repulsion of the positively-charged ions, and has the added benefit of blocking neutral species, photons and particulates from passing into the mass analyser, which can increase the noise of the background. A chicane design uses multiple electrostatic lens components to redirect positively-charged ions towards the off-axis mass analyser, while the interfering species are removed from the ion beam. The third, and most recent, ion focusing technique is the use of an ion mirror. The positively-charged ions are reflected 90° towards the mass analyser, while the interfering species remain on their original trajectory and pass through the ‘hollow’ mirror.

2.1.5 Mass Analysers

The function of mass analysers is to separate out ions according to their mass-to-charge ratio (m/z). The quadrupole ICP-MS (Q-ICP-MS) is the most commonly used and is available in a number of different applications. A quadrupole consists of four cylindrical or hyperbolic rods that have a direct current (DC) and time-dependent alternative current (AC) applied to the opposite pairs of rods (Figure 18). For each ion with a given m/z , there is a specific AC/DC ratio that will allow that ion to pass through the quadrupole with a stable trajectory and contact the detector (Figure 19). Ions that feature a stable trajectory through a quadrupole mass analyser can be described by the Mathieu Equation (Equation 1), which relates the motion of an ion to the size of the quadrupole (r_0), the amplitude of the radio frequency voltage (V), the radial frequency (Ω) and the mass/charge ratio [134]:

$$q_z = \frac{4eV}{mr_0^2\Omega^2} \quad \text{Equation 1}$$

For all other ions with different m/z , their trajectory is unstable and will be ejected from the quadrupole, enabling only the ions with the correct m/z to be detected. During analysis, the AC/DC ratio is scanned sequentially to allow all identified ions formed in the ICP to be detected.

Image removed due to copyright restriction.

Figure 18. Quadrupole separation of ions with different m/z ratios [125]

Ions of different m/z ratios can also be separated out by their different behaviour under an applied magnetic field. Sector field mass analysers utilise an electromagnet and an electrostatic analyser (ESA), in addition to entrance and exits slits, to selectively separate out ions of different m/z (Figure 20). Ions from the plasma are accelerated towards the magnetic field of the electromagnet through the entrance slit. Ions of different m/z ratios are separated from one another based upon the following equation, where B is the magnetic field, U_a is the potential difference of the electric field and r_m is the radius of the circle the ions move on due to the Lorenz force of the magnetic field [126] (Equation 2);

$$m/z = \frac{B^2 r_m^2}{2U_a} \quad \text{Equation 2}$$

The ESA further focusses the ions onto the exit slit, towards the detector system. As the radius r of the curvature of ions within in electric field is proportional to their kinetic energy, ions with different kinetic energies can be separated, where E is the electrostatic force (Equation 3):

$$r = \frac{mv^2}{E} \quad \text{Equation 3}$$

The ESA is commonly positioned after the electromagnet (the reverse ‘Nier-Johnston geometry’) to improve the mass sensitivity and reduce the background noise, as the influx of ions are first reduced according to their mass that is followed by an analysis of their energy (Figure 19). The alternative arrangement, with the electromagnet positioned before the ESA can also be used [126].

Image removed due to copyright restriction.

Figure 19. Schematic diagram of a reverse ‘Nier-Johnson’ SF-ICP-MS [130]

2.1.6 Ion Detection System

Detection systems quantify the ions that pass through the mass analyser. Conversion of the ions into electrical pulses use a number of different detection systems, each with their advantages and disadvantages. For detection of ions at low levels, an electron multiplier is used, whereas a Faraday cup may be used for higher concentrations.

Two different types of electron multipliers may be used; a channel electron multiplier or a discrete dynode electron multiplier. The channel electron multiplier features an open cone structure coated with a semi-conductor, and generates electrons when an ion strikes the surface (Figure 20). Due to the applied negative bias, the electrons are swept towards the end of the multiplier, and by doing so collide with the surface producing more electrons. This results in a cascade effect, where millions of electrons are detected from the initial interaction of one ion. These electrons are detected by a preamplifier as a discrete pulse, and are counted by other electrical circuitry if the pulse is greater than a given threshold.

Image removed due to copyright restriction.

Figure 20. Schematic diagram of channel electron multiplier [135]

Similar to a channel electron multiplier, discrete dynode electron multipliers utilise a different technology to multiply the electrons. Positioned off-axis to minimise background noise, the ions travel on a curved trajectory and strike the first dynode, forming secondary electrons. In a similar fashion to channel electron multipliers, a cascade of secondary electrons is formed at each successive dynode, forming a pulse. Compared to channel electron multipliers, the discrete dynode electron multiplier is 50-100% more sensitive [130].

Faraday cups are not used widely in Q-ICP-MS as they are not suited to low ion count rates, but is more prevalent in SF-ICP-MS or multi-collector ICP-MS (MC-ICP-MS) systems. On impact with the Faraday cup, the charge of the ion is transferred to the metal, producing a current that is directly proportional to the number of ions collided.

2.1.2 MC-ICP-MS and SF-ICP-MS

Q-ICP-MS is commonly used as an elemental analysis technique due to its multi-element analysis capabilities, fast analysis and low detection limits. While it is routinely used in a number of different applications, this technique has a number of limitations, most notably the variety of spectroscopic interferences it is prone to. Isobaric, polyatomic, oxides and doubly-charged ions are all problematic for Q-ICP-MS, but a number of strategies have been developed to reduce the influence on these interferences on the analysis [125].

Compared to Q-ICP-MS, SF-ICP-MS is less affected by the presence of these interferences due to its higher resolution, and can resolve between the overlapping ions due to their slight differences in mass [125]. A compromise, however, for the higher resolution is lower abundance sensitivity of the SF-ICP-MS when compared to Q-ICP-MS, due to the reduction in the slit width, thus reducing the amount of ions entering the mass analyser and detector systems [126]. SF-ICP-MS does however feature a lower background signal and has a better counting efficiency than Q-ICP-MS [136], in

addition to a greater sensitivity for two reasons; Ion transmission for Q-ICP-MS is mass dependent, which can result in losses of the heavier ions analysed, and the lack of a central stop that is used to halt the transmission of photons to reduce the background noise, which can result in losses [126].

Rather than having a single detector, MC-ICP-MS instruments have an array of faraday cups and ion detectors to measure multiple ions simultaneously (Figure 21). This negates the need to cycle through different m/z ratios to detect multiple ions of different masses and prevents fluctuations in the production and transmission of the ions from ultimately impacting on the measured ion currents, thereby reducing the uncertainty in the measurement [137]. MC-ICP-MS also feature 'flat-top peaks', where the width of the slit in front of the detector beam is wider than the width of the ion beam. This prevents any movement of the ion beam from impacting on its detection, improving the precision of the measurement.

Image removed due to copyright restriction.

Figure 21 Diagram of MC-ICP-MS detector array [138]

2.2 Neutron Activation Analysis and Delayed Neutron Activation Analysis

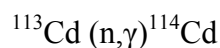
2.2.1 Principles of Neutron Activation Analysis and Delayed Neutron Activation Analysis

In neutron activation analysis (NAA) experiments, a sample placed is bombarded with neutrons from a neutron source, such as a nuclear reactor. Inelastic collisions between an incident neutron and a nucleus within the sample lead to the formation of a compound nucleus in an excited state (Figure 22). With a very short half-life ($t_{1/2} = 10^{-9}$ - 10^{-12} s), the compound nucleus emits a γ -ray, which is referred to as a prompt γ -ray, equal to the difference in energy between the excited levels of the excited nucleus [139]. Following the emission of the γ -ray by the compound nucleus, the product of the reaction is a nucleus with the same atomic number but with an atomic weight increased by one unit. This product is nearly always radioactive, requiring it to undergo radioactive decay to return to a stable form. It is the measurement of the energy E and intensity I of the γ -rays emitted from the radioactive nucleus, as well as the half-life of the nuclide $t_{1/2}$, that provides the basis for NAA [140].

Image removed due to copyright restriction.

Figure 22 Reaction scheme following neutron capture during NAA [141]

The neutrons within most nuclear reactors are formed through the thermal neutron-induced fission of ^{235}U , which releases, on average, 2.2 neutrons with kinetic energies between 0-15 MeV and an average of 2.5 MeV [29]. Three different classes of neutrons are produced in a reactor, and are classed according to their respective kinetic energies; thermal, epithermal and fast (Figure 23) [29]. Fast neutrons are the primary fission neutrons that are unmoderated by the reactor environment, resulting in them having the highest energy. Epithermal neutrons have undergone some deceleration through collision with the low atomic number moderating materials (i.e. water) within the reactor, however the amount of deceleration can vary, resulting in a continuum with regards to neutron energy. This continuum generally follows a $1/E$ slope beginning at the cadmium cutoff energy of 0.5 eV and finishing at 10 keV [29]. Neutrons with energies less than 0.5 eV are absorbed by a thin cadmium foil;



Finally, thermal neutrons are in thermal equilibrium with the moderator atoms. According to the Maxwell-Boltzmann distribution, a thermal neutron at 20 °C has a probable velocity of 2200 m/s and a corresponding kinetic energy of 0.025 eV [142]. Thermal neutrons are typically involved in NAA as they typically have larger cross-sections for (n,γ) reactions, whereas fast neutrons typically have smaller cross-sections [29, 139]. Fast neutrons also favour a variety of other reactions, such as (n,p)

and (n,α) reactions, which interfere with determination of certain elements with NAA [29]. Therefore it is ideal to perform NAA in reactors characterised with high thermal/epithermal flux ratios.

The number of atoms (N) of a particular element, and from this its concentration, can be determined using the following equation (Equation 4);

$$N = \frac{A}{\sigma\phi(1-e^{-\lambda t_a})e^{-\lambda t_w}} \quad \text{Equation 4}$$

where A is the activity of the activation product, σ is the thermal neutron capture cross-section of the target nuclide, φ is the thermal neutron fluence rate, λ is the decay constant of the activation product, t_a is the activation time and t_w is the time interval between the end of activation and the commencement of counting. The neutron cross-section (σ) is a measure of the probability that a reaction will take place between a target atom and a neutron, and varies according to element type, reaction type and neutron energies. (n,γ) and (n,f) reactions have the highest cross-section for thermal neutrons (~0.1-100 b) whereas other interfering reactions ((n,p), (n,a), (n,n'), (n,2n)) can occur two-to-three orders of magnitude less [143].

Image removed due to copyright restriction.

Figure 23 Typical neutron spectrum from a nuclear fission reactor [29]

As each element has a different half-life, a different analytical approach is needed for elements that have a short half-life (i.e. ^{28}Al $t_{1/2} = 2.241$ min or ^{52}V $t_{1/2} = 3.743$ min) than those that have a longer half-life (^{60}Co $t_{1/2} = 5.27$ y). Therefore, elements with shorter half-lives typically undergo a separate irradiation and measurement procedure than those that have longer half-lives.

2.2.1.1 k_0 -NAA and relative comparator methods

For the quantification of elements present within a given sample, the relative comparator standardisation method was historically the predominant method used. The concentration of an element can be determined using Equation A if the induced activity is measured and the neutron flux and reaction cross-section known; however this is rarely used as the neutron flux and reaction cross-section vary according to the neutron energy [144]. To determine the concentration of an element within a sample, two different methods can be used: relative comparator method or k_0 .

The relative comparator method determines the concentration of an element within a sample through a comparison of its decay with a matrix and geometry-matched standard with known concentrations analysed under identical irradiation conditions. The comparator method uses the following equation for the determination of an element's concentration within the sample (Equation 5);

$$\frac{A_{sam}}{A_{std}} = \frac{m_{sam} (e^{-\lambda T_d})_{sam}}{m_{std} (e^{-\lambda T_d})_{std}} \quad \text{Equation 5}$$

where A_{sam} and A_{std} is the activity of the sample and standard, respectively, m_{sam} and m_{std} is the mass of the sample and standard, respectively, and T_d is the decay time [29]. As all of the time-dependent factors (irradiation time, decay time and counting time), Equation X can be simplified to the following (Equation 6);

$$c_{sam} = c_{std} \frac{W_{std} A_{sam}}{W_{sam} A_{std}} \quad \text{Equation 6}$$

where c_{sam} and c_{std} is the concentration of the target element in the sample and standard respectively, and W_{sam} and W_{std} is the weight of the sample and standard, respectively. The major disadvantage of the relative comparator method is the requirement of matrix and geometry-matched standards certified for the target elements for the relative comparator method may be prohibitive if such standards cannot be sourced or analysed in identical irradiation conditions.

k_0 -NAA is a newer method for the quantification of elements analysed by NAA, which overcomes some of the limitations of the relative comparator method. This method does not require a matrix-matched multi-elemental standard and instead allows quantification of all detectable elements using a single-element standard, typically an Al – 0.1% Au wire, which is already used as a neutron cross-section and gamma-intensity standard [145]. Rather than a matrix-matched multi-elemental standard, k_0 -NAA uses an experimentally determined value, k_0 , for each radionuclide compared to a single-element monitor [29]. This method does however require more extensive gamma detector and neutron spectrum calibration [146]. The concentration of a particular element (ρ) is determined using the following k_0 -NAA equation (Equation 7) [147];

$$\rho = \frac{A_{sp}}{A^*_{sp}} \frac{k_0^*}{k_0} \left(\frac{f + Q_0^*(\alpha)}{f + Q_0(\alpha)} \right) \frac{\varepsilon^*}{\varepsilon} \quad \text{Equation 7}$$

Where A_{sp} and A^*_{sp} is the specific activity of the sample and ^{198}Au comparator (formed via $^{197}\text{Au}(n,\gamma)^{198}\text{Au}$ reaction) respectively, f is the thermal/epithermal neutron flux ratio at the irradiation position within the reactor, Q_0 and Q_0^* is the ratio of the resonance integral (the effective neutron capture cross-section in the epithermal region) to the thermal neutron cross-section of the sample and ^{198}Au comparator respectively [146]. α is the deviation of epithermal flux from the ideal 1/E relationship with the reactor, ε and ε^* are the efficiencies of the detector at each gamma energy of the sample element or ^{198}Au comparator respectively. The k_0 factor is derived from the following equation (Equation 8);

$$k_0 = \frac{M^* \cdot \theta \cdot I_\gamma \cdot \sigma_0}{M \cdot \theta^* \cdot I_\gamma^* \cdot \sigma_0^*} \quad \text{Equation 8}$$

where M and M^* are the molar masses of the element and ^{198}Au comparator respectively, θ and θ^* are the isotopic abundances of the sample or ^{198}Au comparator respectively, I_γ and I_γ^* are the gamma abundances of the sample and the 411.8 keV peak of ^{198}Au respectively, and σ_0 and σ_0^* are the (n, γ) cross-section of the sample and ^{198}Au comparator at 2200 ms^{-1} respectively [147]. k_0 factors are not usually calculated from this equation but have been experimentally determined [147].

Within this study, nuclear fission as a mode of relaxation for a compound nucleus poses a considerable complication due to the relatively high concentration of uranium with the samples, with respect to the majority of samples analysed by NAA. ^{235}U can undergo nuclear fission following the

capture of a thermal neutron, where an unstable compound nucleus ($^{236}\text{U}^*$) is formed. While the nucleus may emit the excess energy through β^- decay, the nucleus splits into two fragments of different size (Figure 7). Approximately 80 different products are created through the fission of ^{235}U [142], which can complicate the measurement of target elements within that mass range. The REEs, namely lanthanum, cerium, samarium and neodymium, are particularly affected by the presence of ^{235}U fission products, requiring corrections through the use of interference factors [148, 149].

Image removed due to copyright restriction.

Figure 24 ^{235}U thermal fission yield versus atomic number [142]

Following the fission of ^{235}U and other fissile nuclides through neutron capture, the majority of fission products undergo β^- decay to attain a stable form. A small percentage of neutron-rich nuclides (e.g. ^{235}U) remain in an excited state undergo a delayed β^- emission 1 to 60 s after undergoing fission. During their decay, they also emit neutrons, referred to as ‘delayed neutrons’, which can be measured and used to calculate the concentration of fissile nuclides within the sample, in a technique known as delayed neutron activation analysis (DNAA). As the number of neutrons emitted and measured is proportional to the number of fissile nuclides present within the sample, the concentration ($[^{235}\text{U}]$) of the particular nuclide (or the element assuming a natural abundance is present) can be calculated using a comparative method (Equation 9);

$$[^{235}_{92}\text{U}] \text{ in sample} = [^{235}_{92}\text{U}] \text{ in standard} \cdot \frac{\# \text{ of counts in sample}}{\# \text{ of counts in standard}} \quad \text{Equation 9}$$

2.2.2 NAA in Source Attribution

The use of NAA is advantageous in source attribution studies due to the multi-elemental nature of the technique, the sensitivity and selectivity. Almost all elements are detectable using NAA, with the exception of elements including lithium, beryllium, boron, carbon, nitrogen, oxygen, silicon, phosphorus, sulfur, tin, thallium and lead, as their nuclides do not emit γ -rays, their reaction half-lives are too short (<1 s) or extremely long (<100 yr) for measurement, or their reaction cross section is too small [144]. NAA, unlike techniques such as ICP-MS, is largely free from matrix effects and other interferences due to the nature of the interaction between the irradiated neutron and an atom, as nuclear reactions and radioactive decay are unaffected by the sample composition. NAA can provide accurate results due to the almost negligible absorption of γ -rays and neutrons by matter, resulting in small corrections, and requires little sample preparation, typically only requiring the sample to be packaged within an appropriate container. Packaging of solids also reduces the potential for contamination, as digestion of the sample for other elemental techniques (ICP-MS) may introduce contaminants, the loss of analyte through incomplete dissolution and/or poor recoveries, volatilisation and co-precipitation, and difficulty associated with the digestion of some solids [144]. While the detection limits of NAA are dependent on the element (as the induced activity is partly a function of the neutron cross section of the target atom and the half-life of the radionuclide produced) [144], elemental impurities present within uranium samples at concentrations as low as 250 ppb have been detected [150].

The major disadvantage of NAA towards the analysis of UOCs and other uranium materials for source attribution purposes is the fission spectral interferences originating from the matrix element. The spectral interferences occur by two means; firstly, the uranium fission progeny are identical to the activated nuclides of interest, or the fission nuclide emit γ -rays of similar energy to the activated nuclides of interest, and the peaks cannot be separated [149]. A radiochemical NAA (RNAA) separation procedure has been developed to extract uranium post-irradiation, enabling 26 elements to be detected, with detection limits between 10^{-5} - 10^{-9} % mass [151]. Despite the development of a RNAA method, only uranium ore samples, with uranium concentrations below 2%, will be analysed with NAA.

2.5 Thermogravimetric Analysis

2.5.1 Principles of Thermogravimetric Analysis

Thermogravimetric analysis (TGA) is a destructive technique that measures the change in mass of a sample as a function of temperature (Figure 1). This platform can be extremely versatile, with the ability to investigate multiple different physical and chemical properties of the sample in question as the mass of the sample changes due to the temperature or the surrounding atmosphere [152]. In addition to TGA, this platform can allow for the differential scanning calorimetry (DSC) measurement simultaneously, as well as evolved gas analysis by coupling a mass spectrometer or infrared spectrometer to the exhaust of the TGA instrument [152]. The ability to alter the type of gas also enables the investigation of how a sample may behave at elevated temperatures, from an inert (nitrogen), oxidative (air or oxygen) or reductive (carbon monoxide) environment.

Most modern TGA instruments feature a compensation thermobalance, which ensures the sample occupies [153]the same position within the furnace throughout the operation of the instrument [152]. During analysis, the balance itself is protected from damage from any corrosive gases that may form within the sample by an inert gas (often nitrogen) [152]. For each measurement, a buoyancy correction is made to correct for the changes in density of gases as a function of temperature, through the use of a blank measurement [152]. The relationship between density (ρ) and temperature (K) of a gas is expressed in the following equation (Equation 10);

$$\rho = \rho_0 \frac{T_0}{T} \quad \text{Equation 10}$$

where ρ_0 is the density of the gas at the reference temperature, T_0 , of 25 °C (298 K) and T is the temperature in K [152].

Undertaking DSC measurements simultaneous to the TGA analysis can provide important, and often complimentary, information on the physico-chemical transitions occurring within the sample due to changes in temperature. DSC is used to measure heat flow within the sample as a function of temperature, and can identify endothermic and exothermic transitions that occur during heating [153]. When performed simultaneously with TGA, the first derivative is often used to pair transitions where mass is lost from a sample with changes to the heat flow within the sample, however the second derivative curve can often reveal more information, such as multiple processes

occurring at similar temperatures, and easier to interpret [153]. One major advantage to DSC is that it can reveal transitions that don't cause a change in mass, such as crystallisation, melting and glass transition [153]. DSC is closely related to differential thermal analysis (DTA); the difference between the two analytical techniques is that DTA is measured as a microvolt signal whereas DSC is converted to a heatflow equivalent [153].

2.5.2 Application of Thermogravimetric Analysis in Nuclear Forensics and Nuclear Chemistry

There have been several studies investigating the thermal decomposition of UOCs and uranium oxides using TGA or similar heating strategies, largely for the characterisation of UOCs and uranium oxides at temperature. Eloirdi *et al.* (2014) investigated the thermal decomposition of ADU using TGA, DTA and *in-situ* high temperature X-ray diffraction (XRD) between 30 – 1000 °C [154]. Through the heating of ADU to 1000 °C, Eloirdi *et al.* (2014) identified five instances where the UOC decomposed, corresponding in a loss of weight (TGA) and the occurrence of an endothermic or exothermic peak with DTA, as well as the formation or loss of diffraction peaks via XRD for the intermediates formed [154]. In concert with high-temperature XRD, Eloirdi *et al.* (2014) identified TGA/DTA as a potential tool to aid nuclear forensics investigations, as the composition of the UOC material may provide insight into the processing used to produce a suspect UOC [154].

The majority of studies involving the use of thermal analysis techniques for UOCs and uranium oxides is towards the thermal decomposition pathways that may occur concerning the fabrication of nuclear fuel. The impact of ammonium and nitrate impurities, originating from the precipitation process, on the composition of ammonium uranates (AU) was investigated by Yahia *et al.* (1996) using TGA and DTA [155]. Washed and unwashed AUs, synthesized from uranyl nitrates with different ammonia products and at different pHs, were analysed by TGA and DTA from room temperature to 400, 500 and 800 °C. The washed and unwashed AU products, as well as the products of the TGA/DTA analysis were subsequently analysed by XRD. Both the washed and unwashed AU samples were found to feature a non-stoichiometric composition, which is previously been found to vary according to how the AU was prepared. According to the results of Yahia *et al.* (1996), the unwashed AU precipitated at a pH of 6 formed β -UO₃ after heating to 500 °C, which subsequently formed U₃O₈ after heating further to 800 °C [155]. This is in contrast to the washed AU sample, which formed amorphous (A)-UO₃ after heating to 500 °C, and U₃O₈ after heating to 800 °C [155]. Furthermore, hydrated A-UO₃ that had been immersed in 100% ammonium nitrate solution and heated to 500 °C formed β -UO₃, which when heated further to 800 °C formed the orthorhombic (O) and hexagonal (H) polymorphs of U₃O₈ [155]. In contrast, hydrated A-UO₃ that

had been immersed in 100% ammonium nitrate solution and then washed and filtered also produced β - UO_3 after heating to 500 °C, but only formed the O- U_3O_8 polymorph after heating further to 800 °C [155].

Two different ammonium uranyl nitrate compounds (AUN) ($(\text{NH}_4)_2\text{UO}_2(\text{NO}_3)_4 \cdot 2\text{H}_2\text{O}$ and $\text{NH}_4\text{UO}_2(\text{NO}_3)_3$) were analysed by Kim *et al.* (2012) using TGA/DTA to investigate the pathway in which AUN thermally decomposes during the conversion to uranium oxides for the manufacturing of nuclear fuel [156]. The thermal decomposition was performed under three different atmospheres (nitrogen, air and hydrogen) and each different product, as well as the starting AUN samples, were also analysed via XRD. Under a nitrogen and air atmospheres, the hydrated AUN sample $(\text{NH}_4)_2\text{UO}_2(\text{NO}_3)_4 \cdot 2\text{H}_2\text{O}$ underwent two dehydrations at ~ 50 °C, to form $(\text{NH}_4)_2\text{UO}_2(\text{NO}_3)_4$, which decomposed to $\text{NH}_4\text{UO}_2(\text{NO}_3)_3$ following the loss of NH_4NO_3 between 168 and 240 °C [156]. Between 268 and 307 °C, a second exothermic decomposition of NH_4NO_3 was observed before A- UO_3 was formed during an exothermic reaction at ~ 400 °C. At 480 °C, the A- UO_3 phase recrystallized to form γ - UO_3 , which subsequently formed U_3O_8 at 800 °C. In a hydrogen atmosphere, the decomposition of $(\text{NH}_4)_2\text{UO}_2(\text{NO}_3)_4 \cdot 2\text{H}_2\text{O}$ was similar to the reactions under an air and nitrogen atmospheres until 440 °C where a large exothermic reaction was observed in the DTA results. A- UO_3 was found to decompose to instead form γ - UO_3 that decomposed further to form α - U_3O_8 at 490 °C, which subsequently decomposed to UO_2 at 600 °C [156]. For the other AUC analysed ($\text{NH}_4\text{UO}_2(\text{NO}_3)_3$), the decomposition involved fewer intermediaries, with the air and nitrogen atmospheres featuring the sample decomposition pathway.

2.6 Scanning Electron Microscopy (SEM)/Energy-Dispersive X-ray Spectroscopy (SEM/EDX)

2.6.1 SEM & SEM/EDX Principles

SEM is a technique that utilises the interaction of a focused beam of electrons with the surface of the sample to produce a two-dimensional image, whereas SEM/EDX measures the characteristic X-rays emitted by elements within the sample through said interaction.

Older SEM instruments generated their electrons through thermionic emission, where the tungsten or lanthanum hexaboride (LaB_6) filament is heated through the application of a current to 2700 or 1400-2000 K, respectively, leading to the emission of electrons into the vacuum [157]. New SEM instruments utilise a field emission gun (FEG), where electrons are emitted when a high electric field is applied to an extremely sharp tungsten tip in an ultra-high vacuum ($\sim 10^{-8}$ Pa) at room temperature (hence the process also called ‘cold field emission’) [157]. Despite requiring greater electric fields and vacuums when compared to both thermionic emission from tungsten and lanthanum hexaboride filaments, the major advantages to FEG as the source of electrons is the longer lifetime of the filament ($\sim 10^4$ hrs versus $\sim 10^2$ - 10^3 hrs), the reduced spread in the energy of the emitted electrons (0.3 eV versus 1.0-1.5 eV) and better spatial resolution due to its greater brightness ($\sim 10^{12}$ $\text{Am}^{-2}\text{sr}^{-1}$ versus $\sim 10^9$ - 10^{10} $\text{Am}^{-2}\text{sr}^{-1}$) [157].

Electrons emitted from the cathode are then accelerated through an anode by the application of a potential difference, where the electron energy is ultimately equal to the magnitude of the accelerating voltage (potential difference) [157]. The accelerated electrons then pass through a series of magnetic condensers that focus and collimate the electron beam, as well as control the spot size of the beam. A stigmator and an aperture are also present to correct astigmatism within the condensers and control the illumination of the sample by the electron beam, respectively. Following a final objective lens, the electron beam interacts with the sample.

2.6.1.1 Electron-electron interactions

Upon penetrating the surface of the sample being analysed, the electrons within the beam can undergo both elastic and inelastic scattering. Only a small proportion of electrons are elastically backscattered ($\theta > 90^\circ$), where they may undergo both a single collision or several before they can exit the sample and be measured by a photomultiplier (PMT) detector typically located below the

objective lens as a backscattered electron (BSE) signal (Figure 25b). As these BSEs lose a small amount of energy during the scattering event, most BSEs measured have energies close to the energy of the incident electrons within the beam. The amount of scattering an electron may undergo is also somewhat proportional to the atomic number of elements within the sample; the backscattering coefficient η does increase with atomic number, and is almost linear with low-Z elements [157]. This enables BSE to be used to investigate variations with the chemical composition of elements within a sample, as high Z elements appear brighter in the resultant BSE image when contrasted against low Z elements.

Image removed due to copyright restriction.

Figure 25 Interactions of incident electrons with sample: a) secondary electrons, b) backscattered electrons c) Auger electrons or X-ray fluorescence (XRF) [157]

Conversely, electrons that undergo inelastic scattering within the sample can reveal different information about the sample. Following a succession of scattering incidents, these electrons are arrested within the sample and absorbed at a variable depth within the sample, dependent on the elements present within the sample (due to differences in density and η) and the energy of the incident electrons (Figure 1). As each electron is arrested, they impart their kinetic energy into the atomic electrons that caused the scattering due to the conservation of energy. For valence electrons, this energy is sufficient to overcome the weak, electrostatic attraction between the electron and the nucleus, enabling the expulsion of the free electron from the atom (now referred as a 'secondary electron') (Figure 2a). As most secondary electrons have a kinetic energy of < 100 eV, they typically come to rest through successive inelastic collisions and travelling a very small distance (1-2 nm) [157]. However, those secondary electrons near the surface (< 2 nm) can escape the sample, where they can enter the vacuum of the SEM chamber and be detected. As the secondary electrons

that escape essentially from the surface of the sample, they can provide topographical information about the structure of the surface.

Image removed due to copyright restriction.

Figure 26 Degree of penetration by electrons according to atomic number and incident electron energy [157]

2.6.1.1 Electron-X-ray Interactions

A second type of interaction occurs between the incident electrons with the electrons within the shells of an atom in the sample. If an incident electron collides with and ejects an inner-shell electron, it causes a vacancy, which can be resolved through one of two modes of relaxation; the emission of a photoelectron (Auger effect) or an X-ray photon (X-ray fluorescence). For elements with an atomic number less than 30, the Auger effect is the predominant mode of relaxation (Figure 27), where the excited electron returns to its original ground state by donating its energy to an outer-shell electron, which is subsequently emitted from the atom (also referred to as an “Auger electron”) [157].

Image removed due to copyright restriction.

Figure 27 Relative probabilities of X-ray fluorescence and Auger emission as a function to atomic number (Z) for k-electron excitation [157]

Elements with an atomic number greater than 30 (Figure 4), primarily relax through the production of an X-ray photon. The vacancy within an inner-shell is filled by the relaxation of an outer-shell electron. As the outer shell electron is greater in energy, it emits an X-ray with an energy equal to the difference between the two shells. This X-ray, which is characteristic for any particular element, is emitted from the sample and measured by a detector. Different transitions (i.e. the relaxation of an electron from a particular shell into a vacancy within another shell) result in different X-ray energies, and become more complicated with higher Z elements as the number of atomic electrons and the complexity of the shell structure increases [158].

In thick, solid samples, the intensity (I) of the X-ray produced through the interaction of an electron beam with the samples can be expressed through the following equation (Equation 11) [158, 159];

$$I \approx i_p [(E_0 - E_c)/E_0]^n \approx i_p [U - 1]^n \quad \text{Equation 11}$$

where i_p is the beam current, E_0 is the incident beam energy, E_c is the ionization energy, n is a constant that is dependent on a particular element Z and electron shell. U represents the ‘overvoltage’ between the incident electron with energy E and E_0 (Equation 12) [158];

$$U = E/E_0 \quad \text{Equation 12}$$

In addition to the characteristic X-rays emitted from elements within the sample, a continuum of X-rays of different energies is also present. This continuum, known as the bremsstrahlung, is caused by the deceleration of electrons within the Coulombic fields of an atom, resulting in an X-ray being emitted proportional in energy to the degree of deceleration. As each electron within the beam can undergo different degrees of deceleration, a continuum consisting of varying X-ray energies is observed within the resultant spectrum. The maximum energy of a bremsstrahlung X-ray is equal to accelerating voltage E_0 where an electron decelerates and undergoes a complete arrestment.

The intensity of the bremsstrahlung I_b at a given energy E_v can be described by the following equation (Equation 13) [158, 160];

$$I_b \approx i_p Z [(E_0 - E_v)/E_v] \quad \text{Equation 13}$$

As the intensity of bremsstrahlung is proportional to atomic number Z , therefore elements such as uranium and lead will have a more prominent bremsstrahlung than sodium or iron.

2.6.3 Detection of X-rays

The two different types of detectors used for the measurement of X-rays are differentiated from one another based upon how they distinguish between X-rays of different energies. Wavelength-dispersive X-ray detectors (WDX) separate X-rays of different energies according to their wavelength, as X-rays of different energies E have different wavelengths λ , as described by Planck's Law (Equation 14);

$$E = \frac{hc}{\lambda} \quad \text{Equation 14}$$

where h is the Planck constant and c is the speed of light in a vacuum. A WDS detector uses an analysing crystal to diffract incident X-rays of a particular wavelength towards a detector, following the Bragg equation (Equation 15);

$$n\lambda = 2d\sin\theta_i \quad \text{Equation 15}$$

where n is the order of the reflection and θ_i is the angle between the incident X-ray and the atomic planes of spacing d in the crystal [157]. To measure each desired wavelength of X-ray radiated from

the sample, the geometry between the sample, the analysing crystal and the detector has to change. While the sample remains in the same location, the analysing crystal and detector are moved along the arc of a circle accordingly for the measurement of each different wavelength of X-ray [157].

The second type of detectors, energy-dispersive X-ray detectors (EDX), differentiates between X-rays according to their energy. X-rays interacting with the EDX detector, which consist of a semiconductor material like a single crystal of silicon or germanium, undergo photoelectric absorption where the energy of the X-ray photon is absorbed by bound inner-shell electrons with the material. The electron, which absorbs the X-ray photon's energy, is ejected from the shell with the original energy of the X-ray photon minus the shell ionization energy before undergoing inelastic scattering within the semiconductor material [158]. This results in a bound valence electron from the outer shell being promoted to the conduction band of the semiconductor, which leaves a positively-charged electron-hole within the valence band [158]. With the application of a voltage, a charge is produced as the electrons and holes migrate to opposite electrodes within the detector. The charge generated is proportional to the energy of the incident X-ray, as shown in the following equation (Equation 16);

$$N = hf/\Delta E \quad \text{Equation 16}$$

where N is the number of electron-hole pairs caused by the incident X-ray, hf is the energy of incident X-ray and ΔE is the energy required for create the electron-hole pair and is dependent on the semiconductor crystal (i.e. 3.6 eV is required to create one electron-hole pair in silicon) [158]. For instance, 3.6 eV is the energy required to create one electron-hole pair in silicon [158]. The charge produced by the semiconductor diode is then passed through a series of electronic circuitry to first amplify the charge using a field-effect preamplifier, before the charge is converted into a signal by pulse-processing unit and finally counted by a multichannel analyser [157].

2.6.4 Detection of Secondary and Backscattered Electrons

The Everhart-Thornley detector is most commonly used for the detection of secondary electrons in a SEM instrument. Secondary electrons emitted from the sample are attracted to the detector due to a wire mesh with a positive potential between -50-+300 V applied [157, 158]. Those electrons are then further accelerated within the wire mesh by a considerably greater (>10 kV) positive potential applied towards a scintillator with thin metal coating [158]. The second acceleration aids in the scintillation of the secondary electrons, where the impact of the electrons causes the emission of

light. The light caused by the scintillation of the secondary electrons is then guided to a photomultiplier tube, where it is converted into an electrical signal.

As backscattered electrons that interact with the sample are emitted with more than half of their original incident energy, passive detectors such a scintillation and semiconductor detectors are commonly used and are typically mounted around the path of the incident electron beam and above the sample stage [157, 158]. To prevent the detection of secondary electrons by the scintillator detector, a negative potential is applied.

2.6.5 Quantitative Elemental Analysis by SEM/EDX

For the quantification for a given element Z by SEM/EDX, the k-ratio is first calculated using the measured X-ray intensities from an unknown (I_{unk}) and standard (I_{std}) (Equation 17) [158];

$$k = I_{unk}/I_{std} \quad \text{Equation 17}$$

The SEM measurements to obtain both I_{unk} and I_{std} must be performed under similar experimental conditions (for instance, the same electron beam energy, the same flux of electrons, the sample thickness and coating material to prevent charging) [158]. With SEM/EDX, multiple X-ray spectral lines are used in to calculate the k-ratio, whereas wavelength-dispersive spectrometers, an alternative detection system to EDX, would only measure a single X-ray spectral line [158]. For each element measured, multiple k-ratios may be encountered as the element may have more than one spectral line (i.e. 17.48 keV for K_{α} and 2.29 keV L_{α} spectral lines for molybdenum), however the k-ratio that is thought to give the most accurate measurement is typically used [158]. From the k-ratio, an approximation of the mass fraction of a given element Z can be estimated using Castaing's first approximation (Equation 18) [158, 161];

$$C_{Z,unk} \sim k_Z C_{Z,std} = \frac{I_{unk}}{I_{std} C_{Z/std}} \quad \text{Equation 18}$$

where $C_{Z,unk}$ and $C_{Z,std}$ are the mass fraction of element Z in the unknown and standard respectively, and k_Z is the k-ratio measured for element Z [158]. The contribution provided by bremsstrahlung to the intensity of the measured X-ray spectral lines of element Z can be accounted for by interpolating two adjacent peaks and subtracting that value from the overall intensity of an X-ray spectral line of element Z [158].

Matrix correction procedures, such as ZAF and $\phi(\rho z)$, are then applied to correct for differences between the standard sample and the unknown sample with respect to their composition, which can impact on the results of the measurement. The ZAF matrix-correction accounts for three factors; the mean atomic number, Z , X-ray absorption, A , and secondary fluorescence, F [158]. The terms that comprise ZAF can be included to calculate k_z , through the following equation (Equation 19) [158];

$$k_z = \frac{ZAF(C_{unk};P)C_{unk}}{ZAF(C_{std};P)C_{std}} \quad \text{Equation 19}$$

where $ZAF(C_{unk};P)$ and $ZAF(C_{std};P)$ are the matrix corrections associated within the measurement of the composition (C) and the analysis parameters of the SEM (P) for the unknown (unk) and standard (std), respectively [158]. To solve for C_{unk} , Equation 40 can be rearranged as follows (Equation 20);

$$C_{unk} = k_z C_{std} \frac{ZAF(C_{std};P)}{ZAF(C_{unk};P)} \quad \text{Equation 20}$$

Through an iterative approach, the composition of the unknown sample is estimated using Castaing's first approximation (Equation 39), calculate a revised C_{unk} (Equation 41), update the composition estimate from C_{unk} and then evaluate whether the computed k-ratios are similar to the measured k-ratios [158].

Standardless quantitation is performed through the use of a library of standards previously analysed using a range of defined conditions, in place of a standard [158]. The elements that are not certified within the library reference sample used in the standardless quantitation are supplied through interpolation, as well as calculations concerning X-ray generation and propagation [158]. Similarly, if the electron beam energy used differs from the defined conditions used to generate the reference library, corrections can be calculated to adjust the intensities of the X-ray emission spectra [158].

2.6.2 Scanning Electron Microscopy and Scanning Electron Microscopy/Energy-Dispersive X-ray Spectroscopy in Nuclear Forensics

The characterisation of morphology of uranium-containing materials, often as a function of temperature, is one of the frequent uses of SEM in the nuclear forensics discipline. There has been considerable interest in understanding what properties, including morphology, of uranium compounds are affected during calcination, and the relationship between precursor material and calcination product. Examination of the morphology of uranium oxides formed through the

calcination of ADU at a variety of temperatures (450, 550, 650 and 750 °C) revealed that the original morphology was mostly persistent, with some minor deviations [162]. Pores formed due to the release of gaseous ammonia and water were found in the ADU samples calcined at 550 °C or higher at 50,000x magnification, and sintering of particles occurs at 650 °C or higher. The formation of pores and subsequent sintering observed using SEM was in agreement with measurements taken using the Brunauer-Emmett-Teller technique using N₂ gas, finding an initial increase in surface area at 550 °C and decrease at 650 and 750 °C within the respective calcination products [162]. UO₂, α-U₃O₈ and α-UO₃, produced through the calcination of synthesized UO₂(O₂).xH₂O, were similarly found to feature identical morphologies to their precursor [163].

SEM has also been used to examine how the precipitation of uranium compounds is impacted by changes in the chemical environment (pH, ionic strength etc). Changes to the particles size and degree of agglomeration were identified in part by SEM during a study that investigated how precipitation of uranyl peroxide (UO₄) was affected by pH, ionic strength, and concentrations of uranyl nitrate (UO₂(NO₃)₂) and hydrogen peroxide (H₂O₂) [164]. The effect of the use of gaseous and aqueous ammonia, as well as using silica as seed crystals for the synthesis of ADU particles on the morphology and formation of agglomerates of ADU particles produced, was examined using SEM by Manna *et al.* [165]. ADU, precipitated in the presence of excess ammonium nitrate, were observed by SEM to form larger, more uniform agglomerates comprised of platelets, when compared to ADU produced in the absence of ammonium nitrate [166]. The presence of ammonium ions is thought to accelerate the nucleation and growth of ADU crystals, leading to the generation of larger and more uniform agglomerates [166]. The three different uranium precipitates formed by Singh *et al.* (2017) through the recovery of uranium from alkaline media using three different phosphate-based reagents were found to feature different porosities which affected their ability to filter the aqueous media [167].

The impact of vanadium, zirconium, calcium and magnesium impurities introduced during precipitation on the morphology of α-U₃O₈ was investigated by Hanson *et al.* (2019), which found vanadium as the only impurity that had an appreciable impact [168]. Powder diffraction of the doped and control α-U₃O₈ samples identified patterns consistent with α-U₃O₈ with the exception of the vanadium-doped washed and unwashed samples, which featured additional peaks attributable to an analogue of uranyl pyrovanadate ((UO₂)₂V₂O₇) [168]. SEM-EDS analysis identified that the calcium and magnesium doped samples had morphologies consistent with the control samples and with other U₃O₈ samples in the literature, but the unwashed calcium and magnesium doped samples consisting

of smaller features and less agglomeration [168]. The zirconium doped samples were found to have the smallest features whilst the vanadium doped samples were found to feature two different sub-morphologies; one sub-morphology consistent with other α - U_3O_8 samples and a second feature that SEM/EDX analysis revealed featured concentrated amounts of vanadium present, which was consistent with the powder diffraction data that indicated an additional phase of $(\text{UO}_2)_2\text{V}_2\text{O}_7$ present [168].

Images obtained via SEM of UOCs have also been analysed by image analysis techniques, which apply statistical treatments to quantitatively identify differences between various samples. Using morphological analysis of materials software, Olsen *et al.* (2017) were able to identify differences in the micro-particle size distributions and circularity of α - U_3O_8 particles produced through calcination of UO_4 at different temperatures (600, 650, 700, 750 and 800 °C) in images obtained by temperature [169]. Following the application of the Kolmogorov-Smirnov two sample test, Olsen *et al.* (2017) were able to differentiate between five types of α - U_3O_8 with a confidence interval of 99.00% where ≥ 750 particles are present based upon their respective micro-particle size distribution [169]. In a different study, Fongaro *et al.* (2016) used the Angle Measurement Technique algorithm to obtain quantitative information regarding the surface topography and texture from SEM images obtained from different 26 UOC samples [170]. Paired with principle component analysis (PCA) on the entire dataset and partial least squares discriminant analysis (PLS-DA) of a selection of samples, the total explained variance was $>90\%$ for PCA and each sample from the subset had its own classification for PLS-DA [170].

Several studies have specifically employed the ‘Morphological Analysis for Materials’ (MAMA) software developed by Los Alamos National Laboratory to quantitatively analyse the morphology of UOCs imaged by SEM. The study investigating the impact of vanadium, zirconium, calcium and magnesium impurities morphology of washed and unwashed α - U_3O_8 samples also used MAMA and machine learning classification to determine whether the different doped samples could be statistically differentiated from one another [168]. When analysed by MAMA, over 6000 discrete particles were classified by different attributes, including pixel area, circularity and ellipse aspect ratio, with pixel area being found to be the most distinguishing attribute. With 95% confidence, it was found that all unwashed samples were distinguishable from the unwashed controls, and all washed samples were distinguishable from their corresponding unwashed samples [168]. Washed calcium doped samples were not distinguishable from the washed control samples, whereas the washed calcium and magnesium doped samples were [168]. The machine learning classification

approach was found to be more successful, as it was able to distinguish between all samples with an overall accuracy of 83.84% [168]. A second study investigating the potential changes to the morphology in response to different temperatures (100 – 400 °C), aging times (2 – 48 h) and oxygen partial pressures (~0.0 – 21.3 kPa) that may be experienced during the storage of UO₂ and U₃O₈ materials [171]. The products of these experiments were imaged using SEM, before their morphologies were analysed using the MAMA software. Qualitatively, it was found that U₃O₈ remained unchanged throughout the experiments, whereas the circularity of the UO₂ particles decreased in the aged samples [171]. Using the Kolmogorov-Smirnov two sample test in concert with the quantitative data obtained using MAMA, statistically significant changes with respect to particle area and circularity were observed within the aged UO₂ samples [171].

SEM has also been found to be amenable to the incorporation of other micro-analytical techniques, providing chemical or elemental information that can compliment the morphological information. Several studies have developed SEM systems that incorporate micro-Raman spectroscopy for the analysis of uranium particles obtained from swipe or soil samples, allowing the SEM instrument to image the particles as well as train the laser beam for micro-Raman analysis. The SEM-micro-Raman system developed by Pointurier & Marie (2007) was able to obtain Raman spectra from a variety of different UOC speciations (UO₂, U₃O₈, UO₃, UO₄.4H₂O) found in particles between 3-10 µm in size, which is typically larger than particles typically collected within swipe samples [172]. For particles more reminiscent of those collected during swipe samples (< 3 µm), measurement by micro-Raman is made extremely difficult, but not impossible, due to several factors [172]; the particle may simply be too small to obtain any signal, the laser beam may be larger (>1 µm) than the particle, making both alignment and detection of signal difficult and the laser power may lead to the thermal degradation of the particle.

Other studies have demonstrated the ability to detect uranium hexafluoride (UF₆) particles less than 1 µm in size, using a system that incorporates SEM, micro-Raman spectroscopy and SEM/EDX [173]. Another application of SEM has been as part of the sample preparation process for secondary ion mass spectrometry [174]. Using specialty equipment, suspect particles from a simulated swipe sample were manipulated onto a carbon planchet using the imaging capabilities of a SEM instrument, in preparation for uranium isotope analysis using secondary ion mass spectrometry (SIMS) [174].

2.7 Raman Spectroscopy

2.7.1 Principles of Raman Spectroscopy

Raman spectroscopy is a non-destructive analytical technique based upon the inelastic scattering of incident radiation through their interaction with molecules within the analyte in question. Radiation in the form of a monochromatic laser is scattered by the sample in two modes; inelastic scattering (Raman scattering) and elastic scattering (Rayleigh scattering). As the majority of the incident radiation undergoes Rayleigh scattering (~ 1 in 10^3), only a very small proportion undergoes Raman scattering (~ 1 in 10^7), where either the energy of the scattered light is less than the energy of the incident light (Stokes scattering) or greater than the incident light (anti-Stokes scattering) [175] (Figure 28).

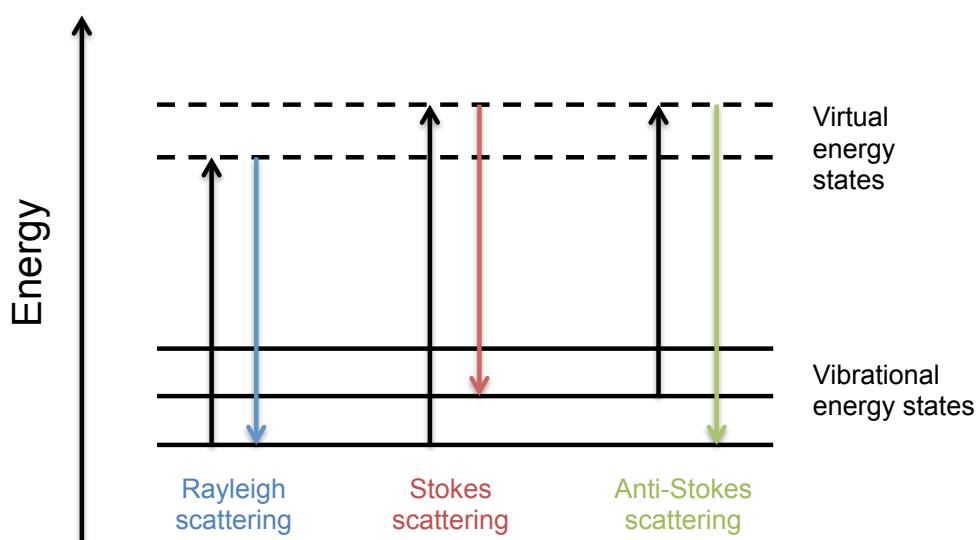


Figure 28 Rayleigh, Stokes and Anti-Stokes scattering

The amount of Stokes scattering relative to anti-Stokes scattering is dependent upon the absolute temperature of the sample and the difference in energy between the ground and excited vibrational states; however, at ambient temperature Stokes scattering is the favoured mode, and therefore more intense, as the majority of molecules exist in the ground state [176]. In order for a vibration to be considered 'Raman-active', the polarizability of the molecule must change [175], however a change in dipole moment is not needed making Raman spectroscopy complimentary to IR spectroscopy. The intensity of a Raman band (I_r) is also dependent on the intensity of the incident radiation (I_o) and several other factors, as shown in Equation 21;

$$I_r \propto v^4 I_o N \left(\frac{\partial \alpha}{\partial Q} \right)^2 \quad \text{Equation 21}$$

where v is the frequency of the incident radiation, N is the number of scattering molecules in a given state, α is the polarizability of the molecules and Q vibrational amplitude [176]. While the frequency of the incident radiation, and thus the wavelength of incident radiation, is shown in Equation 1 to impact the intensity of the Raman bands, the Raman shift (the change in frequency in relation to the incident radiation frequency) is independent of the wavelength of the incident radiation.

Raman spectrometers use a laser as their source of radiation, where a variety of different wavelengths can be used. Shorter wavelength lasers provide a more intense Raman spectra as seen in Equation 1, however it makes them more susceptible to fluorescence. Following irradiation of the sample, the Raman scattered light is filtered to remove Rayleigh-scattered light before it passes through a monochromator, which separates out each wavelength of light before they are detected.

The spectra obtained from Raman spectroscopy can have either Raman shift or wavenumber (cm^{-1}) on its X-axis and intensity (counts) on the Y axis. Wavenumber is inversely proportional to wavelength (nm), as seen through the following equation (Equation 22);

$$\text{wavenumbers } (\text{cm}^{-1}) = \frac{10^7}{\text{wavelength } (\lambda) \text{ (nm)}} \quad \text{Equation 22}$$

The Raman shift ($\bar{\nu}$), which is the difference in energy between the starting and final vibrational levels, can be calculated from the respective wavelengths (cm) of the incident laser and the Raman scattered photons coming off the sample, using the following equation (Equation 23);

$$\bar{\nu} = \frac{1}{\lambda_{\text{incident}}} - \frac{1}{\lambda_{\text{scattered}}} \quad \text{Equation 23}$$

2.8 X-ray Fluorescence Spectroscopy (XRF)

The underlying principles of XRF are largely similar to the underlying principles of SEM/EDX, except the mode of excitation for the inner-shell electron within atoms that make up the sample. Where SEM/EDX uses electrons to excite an inner-shell electron from normal state, XRF instead uses an X-ray, which are produced within the instrument by an X-ray tube. As the energy differences between different electron shells of an atom are independent of the incident mode of

excitation (i.e. X-ray or electron), the energy of the emitted X-ray for a particular element within the sample analysed remains the same when comparing between XRF and SEM/EDX.

While the incident X-ray used to excite the inner-shell electron can originate from natural and artificial radioactive isotopes, it more likely generated by an X-ray tube [177]. While these sources have several advantages (e.g. low cost, compact, require no power and are consistent in their radiation emissions), the major disadvantage is their potential for radiation exposure as it does not cease by design and requires significant engineering controls and instruction to safely use [177].

Within a X-ray tube, two distinct types of X-rays (bremsstrahlung and characteristic X-rays) are generated when electrons emitted from a cathode are accelerated towards and strike the target anode [177]. Depending on the acceleration energy selected, the composition of the X-ray produced will change. For instance, the L_{α} and L_{β} spectral lines of rhodium, a common target material for XRF, have an energy of 2.69 and 2.83 keV, respectively whilst the K_{α} and K_{β} lines have an energy of 20.21 keV and 22.73 keV. If the accelerating voltage was selected to be 10 kV, only the L_{α} and L_{β} spectral lines of rhodium would be produced, in addition to the bremsstrahlung. However if 25 kV were instead selected, the K_{α} , K_{β} , L_{α} and L_{β} , spectral lines of rhodium, again in addition to the bremsstrahlung, would all be produced to irradiate the sample.

When the X-rays generated by the X-ray tube interact with the sample, a number of different processes can occur. The X-rays may undergo Rayleigh scattering, where the X-rays are elastically scattered by the sample, or Compton scattering, where the X-rays are inelastically scattered by the sample. If a rhodium K_{α} X-ray undergoes Rayleigh scattering by a sample and is subsequently detected, it will appear in the spectrum at an energy of 20.21 keV, whereas if the X-ray had instead undergone Compton scattering, it would have lost a portion of its energy to an electron within the sample, and appear at an energy less than 20.21 keV if detected.

The most important interaction between an X-ray and the sample is the photoelectric effect, where an inner-shell electron absorbs an incident X-ray if the energy of the X-ray is greater than its binding energy. The electron is ejected from the electron orbital, leaving a vacancy within the inner-shell. The resolution of the inner-shell vacancy is identical to SEM/EDX; an outer-shell relaxes into the vacancy losing the difference in energy between the two shells as an X-ray (fluorescence), or through the Auger effect, where the energy equal to the difference between the shells is transferred to another electron, which is subsequently ejected from the atom.

The detection of X-rays is also identical to SEM/EDX, where either EDS or WDS detectors may be employed (See Section 2.6.3).

2.9 NIR Spectroscopy

The near-infrared (NIR) is a region of the electromagnetic spectrum that describes light with a wavelength between 780-2500 nm. NIR radiation may also be described with regards to wavenumbers, which is inversely proportional to wavelength, where NIR occupies the range of 12,820 – 4000 cm^{-1} [178].

The absorption of IR radiation generally by molecules within a sample is caused by the vibration of individual atoms through bonds within the molecule, where the energy E of this ‘harmonic oscillator’ system between the two atoms is defined by the following (Equation 24) [179];

$$E = \frac{h}{2\pi} \sqrt{\frac{k}{\mu}} \quad \text{Equation 24}$$

where h is Planck’s constant, k is the force constant of the bond between the two atoms. μ is the reduced mass of the system, and is defined by the following equation (Equation 25);

$$\mu = \frac{m_1 m_2}{m_1 + m_2} \quad \text{Equation 25}$$

where m_1 and m_2 are the masses of the atoms in the bond. This system has a discrete set of energy levels, according to quantum mechanics, requiring the incident IR radiation to match the energy difference between the ground level ($v=0$) and the first excitation level ($v=1$), in order for the vibration to occur [178]. The energy of the discrete energy levels of a particular vibration is defined by the following equation (Equation 26) [179];

$$E_v = (v + 1/2)h\nu \quad \text{Equation 26}$$

where v is the vibrational quantum number for the vibration, E_v is the energy of the v th quantum level of that particular vibration, and ν is the fundamental frequency of the vibration (equal to $1/2\pi$ or $\sqrt{k/\mu}$). Before a particular vibration is ‘IR active’, a second requirement must be met. In addition to

matching the energy difference between the two energy levels, only vibrations that cause a change in the dipole moment of a molecule will lead to the absorption of the incident IR radiation [178]. Therefore, vibrations that do not change the dipole moment of a molecule, such as symmetrical stretches, will not absorb IR radiation.

With NIR radiation, the main vibrations experienced by a NIR-active molecule are not fundamental vibrations, as is the case in Mid-IR spectroscopy, but rather overtones and combination bands. Overtones occur when the vibrational quantum number increase by more than one, while combination bands occur when multiple vibrations from a single photon increase their vibrational quantum number by more than one, due to mechanical and electrical anharmonicity.

Chapter 3. Uranium Ore Concentrate and Uranium Ore Samples

3.1 Introduction

Eight UOC samples and sixteen uranium ore samples from Australia and North America have been analysed in one or more chapters in this thesis. The Australian UOC and uranium ore samples were acquired through ANSTO, whereas the international uranium ore samples were acquired from the South Australian Museum.

3.2 Australian UOC and uranium ore samples

The locations of the mines where the Australian UOC and uranium ore samples analysed within this thesis originated from can be found in **Error! Reference source not found..** Information for the five Australian mines (Olympic Dam, Beverley, Ranger, Four Mile and Mary Kathleen) where the UOC and uranium ore samples originated from can be found in Sections 1.4.2 (Active Australian Mines) and 1.4.3 (Closed Australian Mines).



Figure 29 Location of active uranium mines in Australia

3.3 North American Uranium Ore Samples

The locations of the North American mines/deposits where uranium ore samples analysed in this study originated from can be found in Figure 30. Figure 30 Location of uranium mines/deposits within North

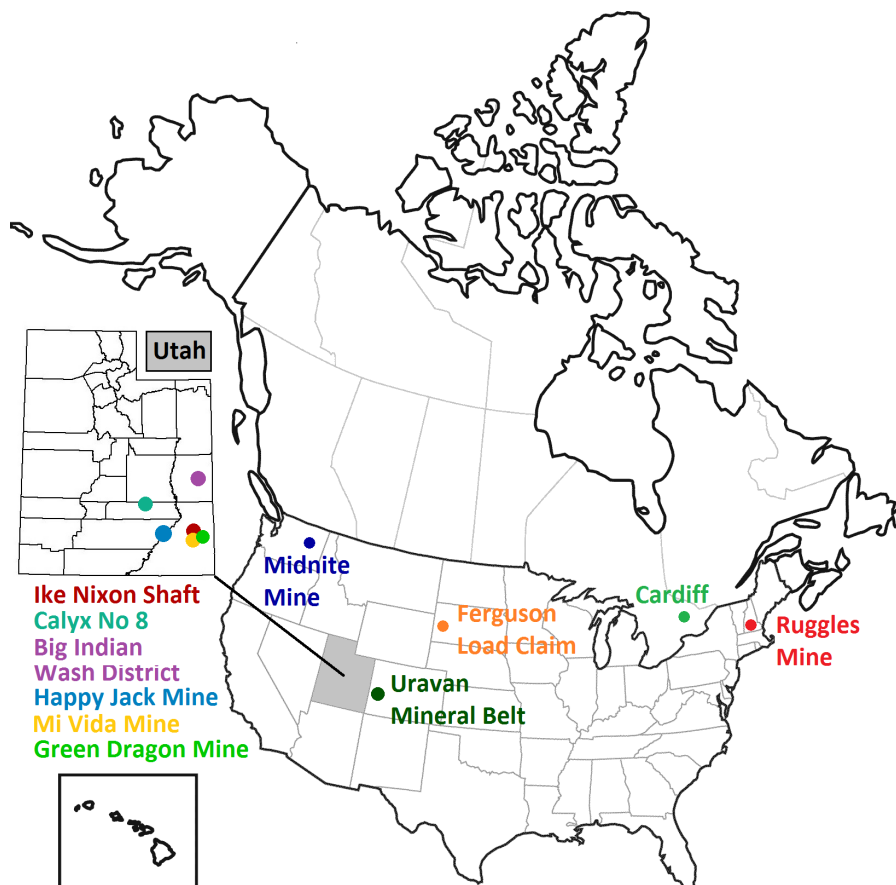


Figure 30 Location of uranium mines/deposits within North America

3.3.1 Big Indian Wash District, Utah

The Big Indian Wash District, otherwise known as the Lisbon Valley uranium district, is a region in southeastern Utah (Figure 31) that encompasses several uranium occurrences and mines (Figure 32) [180]. The northern section of the district (which includes Ike-Nixon Shaft and Mi Vida Mine) features several irregular-shaped sandstone-hosted deposits along the narrow belt, which is 1 km wide and 10 km long, with an average grade of 0.39% U_3O_8 [180]. The principle uranium mineral within the Big Indian Wash District is uraninite, but features significant amounts of vanadium in the central and southeastern parts of the belt [181]. The amount of V_2O_5 relative to U_3O_8 decreases significantly from the southeastern end with ratios of 2.36:1, 3.34:1, 1.84:1 and 1.81:1 to the north western end with ratios of 0.05:1, 0.09:1 and 0.07:1 [182].

Image removed due to copyright restriction.

Figure 31 Location of the Big Indian Wash District within the continental United States [180]

Image removed due to copyright restriction.

Figure 32 Location of uranium occurrences and mines within the Big Indian Wash District, Utah [180]

3.3.2 Calyx No. 8 Mine, Utah

The Calyx No. 8 Mine is located within the Temple Mountain District of Emery County, Utah, and is one of thirteen shafts located on the eastern side of the Calyx Bench, a topographical bench (Figure 33) [183]. Calyx No. 8 Mine was the largest producer in the Temple Mountain District between 1948 and 1956, producing 42,000 tonnes of ore containing 228-320 pounds of U_3O_8 and 753,800 pounds of V_2O_5 [183]. The uranium deposit is sandstone-hosted, and of multiple ore bodies with both roll-like and tabular shapes; the larger ore bodies of Calyx No. 8 have produced up to 6,000-10,000 tonnes of ore [183]. The ores in the entire Temple Mountain District are typically unoxidised, with uraninite being the primary uranium mineral present, however some deposits may be oxidised and feature carnotite or tyayamunite [183].

Image removed due to copyright restriction.

Figure 33 Location of the Calyx No 8 Mine (Shaft Number 8) within the Temple Mountain District of Utah [183]

3.3.3 Ike-Nixon Shaft, Utah

The Ike-Nixon shaft is a sandstone-hosted uranium deposit located within the San Juan County, Utah [184]. Limited information is currently available about Ike-Nixon Shaft, except that the deposit was previously mined underground for uranium (as uraninite) and vanadium [185].

3.3.4 Happy Jack Mine, Utah

Happy Jack Mine is located within the White Canyon Area, San Juan County, Utah and features a sandstone-hosted uranium deposit that is the largest deposit within the area [186]. The uranium minerals are present in ‘bedded deposits’, where they replace carbonaceous material debris or larger wooden fragments within the sandstone [186]. Therefore, the bedded deposits can vary considerably in size, from less than one inch to three feet thick for the uranium formed in debris, whereas the larger deposits can be as large as 3.5 feet long and 3 inches in diameter [186]. The primary uranium mineral encountered at Happy Jack Mine is uraninite, however sooty pitchblende (UO_2) is often co-located with uraninite, along with betazippeite ($(\text{UO}_2)_2(\text{SO}_4)(\text{OH})_2 \cdot 4\text{H}_2\text{O}$), johannite ($\text{Cu}[\text{UO}_2(\text{OH})\text{SO}_4]_2 \cdot 8\text{H}_2\text{O}$) and uranopilite ($(\text{UO}_2)_6\text{SO}_4(\text{OH})_6\text{O}_2 \cdot 14\text{H}_2\text{O}$) [186]. Several other sulfide minerals are also present within the sandstone beds, including covellite (CuS), bornite (Cu_5FeS_4), chalcopyrite (CuFeS_2) and pyrite (FeS_2) [186].

3.3.5 Mi Vida Mine, Utah

The Mi Vida uranium mine is a sandstone-hosted deposit and is located 39 miles southeast of Moab, San Juan County, Utah [187]. Uranium and vanadium minerals, as well as vanadium clay, comprise 22% of the average mineral composition of 39 sections collected from Mi Vida Mine [187]. The two primary uranium minerals identified within the Mi Vida Mine are uraninite and coffinite, with uraninite being the major uranium mineral present and located commonly in carbonaceous material as a replacement for wood within the sandstone, forming black pods two inches in diameter and several feet long [187]. Coffinite is encountered less frequently within the mine, but also as a replacement for wood [187]. The primary vanadium mineral found at Mi Vida Mine is montroseite ($(\text{V},\text{Fe})\text{O}(\text{OH})$), with corvusite ($\text{V}_2\text{O}_6 \cdot 6\text{V}_2\text{O}_8 \cdot n\text{H}_2\text{O}$), pascoite ($\text{Ca}_2\text{V}_6\text{O}_{17} \cdot \text{H}_2\text{O}$), metayuyamunite ($\text{Ca}(\text{UO}_2)_2(\text{VO}_4)_2 \cdot 5\text{-}7\text{H}_2\text{O}$), lenoblite ($\text{V}_2\text{O}_4 \cdot 2\text{H}_2\text{O}$) and uranium clay also present [187].

3.3.6 Green Dragon Mine, Utah

The Green Dragon Mine is a sandstone-hosted deposit located in Grand County, Utah that features ores of chalcocite (Cu_2S_2), malachite ($\text{Cu}_2\text{CO}_3(\text{OH})_2$) and uraninite [188]. Any other information, such as past production or the size of the deposit, about Green Dragon Mine is unavailable.

3.3.7 Uravan Mineral Belt, Colorado/Utah

Unlike many of the other deposits/mines that are represented by UOC and/or uranium ore samples in this thesis, the Uravan Mineral Belt is not a discrete deposit or group of deposits, but rather a region where a series of sandstone-host carnotite ($K_2(UO_2)_2(VO_4)_2 \cdot 3H_2O$) deposits are found with closer spacing, are larger in size and at higher grade than the surrounding area [189]. As such, the bounds of the Uravan Mineral Belt is difficult to define, with some authors indicating the belt is located in both Utah and Colorado [190], whereas other authors indicate the belt solely exists in Colorado as there is insufficient evidence the belt clearly extending into Utah (Figure 34) [189, 191].

Image removed due to copyright restriction.

Figure 34 Index map of south-western Colorado and south-eastern Utah outlining the boundary of the Uravan Mineral Belt by Chenoweth (1981) [191], which was modified from Butler and Fischer (1978) [192]

The carnotite deposits that comprise the Uravan Mineral Belt often run perpendicular to the general direction of the deposit in clusters, where the individual deposits are between one to several thousand feet wide and typically at least several thousand feet long [189]. The average thickness of the ore deposits is between two to four feet [189, 191], however thicker deposits up to 29 feet have also been

mined [191]. In the northern section of the Uravan Mineral Belt, the bounds of the belt itself are more recognizable than the southern section, where the deposits are more sparse and scattered [189]. The carnotite deposits that comprise the Uravan Mineral Belt are found in oxidised ore bodies, along with tyuyamunite ($\text{Ca}(\text{UO}_2)_2\text{V}_2\text{O}_8 \cdot 5-8\text{H}_2\text{O}$) and metatyuyamunite ($\text{Ca}(\text{UO}_2)_2(\text{VO}_4)_2 \cdot 3-5\text{H}_2\text{O}$), whereas in unoxidised bodies, the principle uranium minerals are uraninite and coffinite ($\text{U}(\text{SiO}_4)_{1-x}(\text{OH})_{4x}$) [191]. The Uravan Mineral Belt also has a high vanadium content, which can be between three to ten times greater in concentration than uranium, resulting in several different vanadium minerals being present, including montroseite ($\text{V}(\text{III}),\text{Fe}(\text{III})\text{O}(\text{OH})$), corvusite, hewettite ($\text{CaV}_6\text{O}_{16} \cdot 9\text{H}_2\text{O}$), meta-hewettite ($\text{CaV}_6\text{O}_{16} \cdot 9\text{H}_2\text{O} \cdot 3\text{H}_2\text{O}$), pascoite ($\text{Ca}_3\text{V}_{10}\text{O}_{28} \cdot 17\text{H}_2\text{O}$) [191].

3.3.8 Midnite Mine, Washington

Located 65 km northeast of Spokane, Washington within the Spokane Indian Reservation in Stevens County [193], Midnite Mine was a vein-type deposit mined initially between 1955 and 1965, before resuming in 1969 until November 1981 [194]. The mine was operated by the Dawn Mining Company, which is jointly owned by the Newmont Mining Corporation and Midnite Mines Incorporated. The mined uranium ore was not processed on site, but instead transported to the nearby Dawn Mining Company mill for processing [194].

The Midnite Mine consists of multiple ore bodies, which can range in size up to several hundred feet in length and thirty feet in width [195]. The primary uranium minerals found at Midnite mine are autunite ($\text{Ca}(\text{UO}_2)_2(\text{PO}_4)_2 \cdot 10-12\text{H}_2\text{O}$) and uranophane ($\text{Ca}(\text{UO}_2)_2 \cdot 2\text{H}_2\text{O}$), however uraninite (UO_2) was found at depths of 150 feet with pyrite (FeS_2) [195]. Other uranium minerals also identified at Midnite Mine include gummite (amorphous mixture of several secondary uranium minerals [196]), torbenite ($\text{Cu}(\text{UO}_2)_2(\text{PO}_4)_2 \cdot 12\text{H}_2\text{O}$), liebigite ($\text{Ca}_2\text{UO}_2(\text{CO}_3)_3 \cdot 11\text{H}_2\text{O}$) and phosphuranylite ($(\text{H}_3\text{O})_3\text{KCa}(\text{UO}_2)_7(\text{PO}_4)_4 \cdot 8\text{H}_2\text{O}$) [195]. The grade of uranium was found to be between 0.48-0.86% U_3O_8 and was estimated to contain 700,000 tonnes of ore reserves in 1956 [195].

3.3.9 Ferguson Lode Claim, South Dakota

Ferguson Lode Claim is a small feldspar ($(\text{K},\text{Na},\text{Ca})\text{AlSi}_3\text{O}_8$) deposit located four miles east-southeast of Keystone, South Dakota [197]. A pegmatite deposit, the Ferguson Lode Claim was principally mined for beryl ($\text{Be}_3\text{Al}_2(\text{SiO}_3)_6$) [198]. Uranium is present only as a gangue material in the form of uraninite, uranophane meta-autunite and phosphuranylite [197, 199].

3.3.10 Ruggle's Mine, New Hampshire

Ruggle's Mine is a former uranium mine located in Grafton County, New Hampshire, which was first mined in 1803 for mica $((K,Na,Ca)_2(Al,Mg,Fe)_{4-6}(Si,Al)_8O_{20}(OH,F)_2)$ [200], rather than any uranium mineral. The Ruggles ore body is a granitic pegmatite that was estimated to have formed 304 million years ago [201], and is 500 m long, 100 m wide at its maximum and a thickness of 50 m [202]. The primary uranium mineral found at Ruggle's Mine is uraninite, however several secondary uranium minerals, including β -uranophane $(Ca(UO_2)_2[SiO_3(OH)]_2 \cdot 5H_2O)$, phosphuranylite $(KCa(H_3O)_3(UO_2)_7(PO_4)_4O_4 \cdot 8H_2O)$ and soddyite $(UO_2)SiO_4 \cdot 2H_2O)$, are also present [202].

3.3.11 Cardiff, Ontario

The Cardiff Mine is a former uranium mine located in the Haliburton-Bancroft region of southern Ontario, Canada, which is comprised of a calcite-fluorite-apatite vein deposit [203]. This type of deposit is somewhat unique to the Cardiff Mine, as other uranium mines within the Bancroft region are either pegmatite or metasomatic deposits [203]. First set up to prospect fluorospar (CaF_2) in 1943, the Cardiff Mine owned by Cardiff Uranium Mines, begun exploration for uranium between 1953-1955 [204].

Uranium was mined from several calcite-fluorite-uraninite veins that were over 100 feet in length and an average width of ~4 feet [203]. The primary uranium mineral identified within the vein was uraninite, which could be found as cubes between 5 mm to 2.5 cm in size [204], with the average grade of uranium found to be 0.095 % U_3O_8 [203]. An interesting feature of the uraninite sourced from the Bancroft region is the relatively high concentration of thorium present, with the uraninite containing between 8-40 % of thorite (ThO_2) [203].

Chapter 4. Thermal, Vibrational and Morphological Analysis of Australian UOCs

4.1 Introduction

Compositional information of an unknown UOC can be highly valuable to a nuclear forensic investigation as it can reduce the number of potential sources as there are several different types of UOCs produced worldwide, as well as providing intelligence on how a seized UOC sample may have been processed [205, 206]. While the thermal analysis of uranium oxides and UOCs is well established within the literature, there are few studies that have sought to investigate whether the thermal decomposition of UOC samples could be used in a nuclear forensics context.

4.2.1 Analysis of UOCs using NIR and Raman spectroscopy

Analysis of the chemical composition of UOCs for nuclear forensics has largely been performed by spectroscopic methods, such as NIR [123, 206], Raman spectroscopy [172, 207-209] and XRD, or multiple techniques used. Eight UOC samples of different compositions were analysed by Klunder *et al.* (2013) using UV-Vis/NIR spectroscopy which were found to contain unique bands corresponding to their different speciations and how the UOCs samples were produced [206].

NIR analysis of laboratory-derived and real UOC samples of different compositions was performed by Plaue *et al.* (2012), to investigate how the chemical composition was affected by changes in temperature (heated in air for 12 hrs at 85, 150, 400, 600 and 750 °C) [123]. Again, each type of UOC was found to feature characteristic bands attributable to their different compositions, which were found to change according to temperature. UOC samples, such as AUC, uranyl peroxide ($\text{UO}_4 \cdot 2\text{H}_2\text{O}$) and AU, that were synthesized using volatile precursor compounds (ammonium carbonate, hydrogen peroxide and ammonium hydroxide, respectively) were found to thermally decompose through a variety of intermediate products to U_3O_8 [123]. The NIR bands attributable to the three different precursor compounds were found to extinguish between 400 and 750 °C, as they were volatilized off. The two UOCs precipitated out using magnesia and sodium hydroxide where unable to be positively identified by NIR or XRD, however they formed uranium oxides that incorporated the precursor compounds (MgUO_4 , MgU_3O_8 and $\text{Na}_2\text{U}_{2.5}\text{O}_{8.5}$, U_3O_8 , respectively) [123]. In a comparison between four real-world $\text{UO}_4 \cdot 2\text{H}_2\text{O}$ samples and two laboratory-synthesized $\text{UO}_4 \cdot 2\text{H}_2\text{O}$ samples that were previously heated to 85 and 150 °C, all six samples were considered to be in relatively good agreement, however some variability still observable [123]. Similar results were observed in the six real and two laboratory-derived U_3O_8 samples, with the differences

observed in both $\text{UO}_4 \cdot 2\text{H}_2\text{O}$ and U_3O_8 samples attributed to differences in the processing methods used, source materials used and the presence of contaminants [123].

The variability of real-world UOC samples was also explored by Raman spectroscopy, where impurities originating from precursor material were identified in several real UOC samples [207]. In addition of various several Raman bands characteristic of five different types of UOCs, several Raman bands were identified from either the precipitation process or another stage of the UOC production process [207]. For instance, the most prominent Raman peak of anhydrous calcium sulphate (1015 cm^{-1}) was observed in a UOC sample originating from Blind River, Canada [207]. Lime is used in the UOC production process to remove iron, sulphates and hydroxides, where the sulphates are precipitated out as calcium sulphate [207]. Several other chemicals were identified within a number of real world UOC samples, including sodium chlorate, sodium nitrate, dolomite (calcium magnesium carbonate) and gypsum (calcium sulfate dehydrate), which were all attributed to different processes used in the production of UOCs [207]. Therefore, the presence of such compounds, as identified by Raman spectroscopy, may provide valuable information concerning the process history of an unknown UOC [207].

Raman spectroscopy has been used extensively to identify the different composition of uranium oxides, uranium minerals and UOCs [208-211], and may be coupled with other techniques such as SEM/EDX for the analysis of small uranium particles [172, 173, 212, 213]. Raman spectroscopy and Fourier transform infrared spectroscopy (FT-IR), in concert with multivariate analysis techniques such as Fisher discriminant analysis (FDA), principle component analysis (PCA) and partial least squares discriminant analysis (PLS-DA), could be used to rapidly determine the chemical speciation of an unknown UOC [210]. Eighty-nine real UOC samples and six laboratory-synthesized UOC samples, representing nine different uranium compounds (seven UOCs, as well as UO_2 and UF_4), were analysed by Raman and FT-IR spectroscopy and their resultant spectra was analysed using the three different multivariate analyses [210]. When analysed by PCA, three principle components were found to explain 74.50% of the total variance and when plotted in two and three-dimensional plots, samples of the same uranium compound (ADU, U_3O_8 , UF_4 , AUC, UO_4 and possibly SDU) were largely found to group together [210]. Two large clusters consisting of ADU and uranyl hydroxide (UH) ($\text{UO}_2(\text{OH})_2$) were observed, however some overlap was evident [210]. The overlap between the ADU and UH clusters was attributed to the presence of multiple uranium compounds in within each real-world sample, whose presence was based upon the assumption that purity with respect to uranium, not composition, was critical to UOC producers and that various reagents may

cause uranium to precipitate out prior to the precipitation stage in the UOC production process [210]. When analysed by PLS-DA, four UOC samples (AUC, U_3O_8 , UO_3 and UO_4) were considered well classified, with R^2 values greater than 0.8 (0.9, 0.8, 1.0 and 0.9, respectively) [210]. ADU and UH samples were again difficult to distinguish from one another with overlapping clusters in the PLS-DA score plot and the greatest values for classification errors and root mean square error in calibration and root mean square error cross validation parameters [210]. The final statistical analysis approach, a supervised visualization of Raman spectra using FDA, was able to distinguish between six different UOC types (UO_3 , UF_4 , UO_4 , ADU, U_3O_8 and UO_2), however the ADU, U_3O_8 and UO_2 samples are clustered closer together than the other three types [210]. Due to the supervised nature of PLS-DA, this approach is not appropriate for the classification of unknown UOC samples as the identity of the UOC compound is needed to perform the treatment [210].

4.1.2 Thermal Analyses of UOCs and uranium oxides

Thermal analysis techniques are frequently used to investigate the chemical and physical properties of UOCs and uranium oxides, however this is largely focused towards the conversion of UOCs and uranium oxides to the fabrication of nuclear fuel. Understanding the underpinning chemical principles involves in these processes, where thermal treatment is often a major consideration, improves the production of nuclear fuel and provides greater versatility in the processes available [156, 214]. The decomposition of anhydrous and hydrated ammonium uranyl nitrate ($NH_4UO_2(NO_3)_3$ and $(NH_4)_2UO_2(NO_3)_4 \cdot 2H_2O$, respectively) were analysed using thermogravimetric analysis (TGA)/differential thermal analysis (DTA) and XRD in nitrogen, air and hydrogen atmospheres [156]. In both air and nitrogen atmospheres, both $(NH_4UO_2(NO_3)_3)$ and $(NH_4)_2UO_2(NO_3)_4 \cdot 2H_2O$ were found to go through a number of intermediates due to dehydration, denitrification and recrystallization processes, to eventually form U_3O_8 [156]. In an hydrogen atmosphere, both $(NH_4UO_2(NO_3)_3)$ and $(NH_4)_2UO_2(NO_3)_4 \cdot 2H_2O$ went through an additional decomposition process, to form UO_2 from U_3O_8 [156]. For both $NH_4UO_2(NO_3)_3$ and $(NH_4)_2UO_2(NO_3)_4 \cdot 2H_2O$, their decomposition pathways were found to differ however, the change in atmosphere did not affect the intermediates and final product (both U_3O_8) formed [156].

TGA and DTA, in concert with FTIR and XRD, has also been used to characterise the chemical impurities that may be present within a real magnesium diuranate ($MgU_2O_7 \cdot 2H_2O$) sample [214]. Unlike other studies where FTIR, NIR or Raman spectroscopy was used to analyse the intermediate(s) and final product, FT-IR was used to measure the evolved gases such as water, sulfur

dioxide and carbon dioxide *in-situ*, to correspond with decomposition processes occurring during the TGA/DTA analysis [214]. The simultaneous TG-DTA-FTIR measurements were performed in an air environment between room temperature and 1000 °C and a heating rate of 10 °C/min [214]. Four decomposition processes were observed across the measured temperature range of 70 – 1175 °C, which correlated with XRD and FTIR data. Following the loss of moisture and crystalline water from 70 – 300 °C, a second decomposition resulting the evolution of water was attributed to the decomposition of the impurity magnesium hydroxide (Mg(OH)₂) to magnesium oxide (MgO) at 330 – 475 °C [214]. A two-step decomposition process has then been observed between 1025-1100 °C, where the two following reactions are occurring, hence the presence of the three different uranyl compounds in the XRD patterns [214];



In addition to the evolution of water, sulfur dioxide and carbon dioxide were also produced through the decomposition of the magnesium diuranate sample, however the exact composition of the impurities that give rise to those gasses is not currently known [214].

The impact of impurities, arising from the precursor materials, on the thermal decomposition pathway during the calcination of AU was also investigated using TGA/DTA and XRD [155]. Unwashed and washed AU, as well as washed UO₃ and UO₃ samples spiked with 10% ammonium nitrate solution, were analysed from room temperature to various temperatures between 400 – 800 °C in an nitrogen atmosphere, with two different heating rates of 2 °C/min and 10 °C/min [155]. The unwashed AU sample was found to have lost 29.99% of its weight across the temperature range, whereas the washed sample lost 16.91%, which was attributed to the greater amount of impurities present within the unwashed sample, as well as crystalline water [155]. Following incomplete denitration at ~300 °C, a second decomposition occurs at ~440 °C, removing any residual ammonia, to form UO₃, which decomposes further at 600-645 °C to form U₃O₈ [155]. The unwashed AU sample, which was found to be non-stoichiometric in its composition reflecting its mode of preparation, was found to form β-UO₃ after heating to 500 °C, whereas the washed AU sample formed A-UO₃ instead [155]. The rate of temperature increase was also found to have an effect, as the unwashed AU samples heated at a rate of 2 °C/min formed poorly crystallised β-UO₃, whereas the same sample heated at a rate of 10 °C/min formed a more well-defined XRD pattern for β-UO₃

[155]. The presence of ammonium nitrate was also found to influence which polymorph(s) of U_3O_8 were formed following the heating of A- UO_3 , which first formed β - UO_3 for both washed and unwashed A- UO_3 after heating to 500 °C [155]. Heating both β - UO_3 samples further to 800 °C, again irrespective of the heating rate, produces two different products; the unwashed A- UO_3 sample forms both polymorphs of U_3O_8 (orthorhombic (O) and hexagonal (H)) whereas the washed A- UO_3 forms just U_3O_8 (O) [155].

The decomposition of laboratory-synthesized ammonium diuranate ($(NH_4)_2UO_2O_7$) during its calcination has similarly been investigated by TGA/DTA and high-temperature XRD [154]. Following two stages of dehydration at 100 and 200 °C, the sample then undergoes denitration to form A- UO_3 [154]. A- UO_3 then recrystallizes to form β - UO_3 at 600 °C, which then decomposes between 600-700 °C [154].

4.1.3 Morphological analysis of UOCs

The morphology of UOCs has also been an area of focus for nuclear forensics, as like the chemical speciation, it can also provide information on how the UOC samples were produced or stored. As such, the morphological analysis of seized UOC and uranium oxide samples has been invaluable for real cases reported in the literature [101, 103].

The effect of calcination on the morphology, along with other physical properties, of laboratory-synthesized ADU was investigated using SEM [108]. The morphology of the original ADU, predominantly long platelets, was retained despite the calcination of the UOC sample at 750 °C for 2 hours [108]. One difference observed in the morphology was the development of pores in the UOCs upon heating to 550 °C as gaseous ammonia and water vapour were released during calcination, leading to an increase in surface area [108]. However, the sample (at this stage having decomposed to UO_3) begins to sinter above 650 °C, resulting in a reduction in its surface area. These changes in surface area, and similarly as well with porosity, agree with Brunauer-Emmett-Teller (BET) method measurements performed using nitrogen gas (

Table 1) [108].

Table 1 Changes to the surface area and porosity of ADU as a function of temperature, as measured by Manna *et al.* (2012) [108]

Temp (°C)	Surface Area (m ² /g)	Porosity (cm ² /g)
450	22.5	0.07
550	35.39	0.17
650	12.15	0.04
750	7.24	0.03

Another factor that can impact the morphology of laboratory-synthesized ADU is the means at which the precipitating agent is added. A comparison by Manna *et al.* (2012) between gaseous ammonia and liquid ammonia, used to precipitate ADU from a uranyl nitrate solution, shows that several properties, including their respective morphologies, are different [165]. ADU produced using aqueous ammonia has a significantly higher moisture content (60-70%) and overall greater density than ADU produced from gaseous ammonia (5-10%) [165]. The morphology of the ADU produced through aqueous ammonia was found to be less defined as the particles appeared to be fused or cemented together, whereas ADU produced from gaseous ammonia was more defined, with large rods commonplace throughout the sample [165].

Examining the morphological features of UOCs and other radioactive and nuclear materials can provide insight into the production process of a seized sample, as illustrated above, and be used as a signature to compare an unknown sample to a reference set [215]. In 2009, police, conducting a series of drug raids in Victoria, Australia, encountered two containers containing uranium materials within a working drug laboratory [101]. In addition to several other types of analyses on the two samples, their morphologies were also examined using SEM. The morphology and agglomeration behavior of the NSR-F-270409-1 sample was found to be consistent with uranium oxides that were produced through a caustic precipitation process [101]. A comparison between NSR-F-270409-1 and an in-house standard (produced through the precipitation of uranyl ions with potassium hydroxide) found the two samples having a similar morphology, however this morphology was not found to be unique as other samples produced using a different method in the literature also shared this morphology [101]. The second sample, NSR-F-270409-2, was found to have a morphology

dissimilar to any reference standard LLNL had, however from the examination it was thought the sample was more likely produced via a solution-based precipitation than a gas phase process [101]. NSR-F-270409-2 also showed evidence of heat exposure due to the faceted structure of its grains [101].

SEM images of an unknown radioactive sample seized by an Australian state policing agency during a clandestine drug laboratory raid were used to compare its morphology against a UOC sample from Mary Kathleen, which was identified as a potential source from other preliminary analyses performed [103]. The seized sample was characterised as consisting of a mostly single, homogeneous phase, with irregular to sub-euhedral particles (0.5 -1 μm in diameter) and larger agglomerates (~10-100 μm) made up of the smaller particles [103]. In a direct comparison at low magnification (5000x) using secondary electron imaging where the seized sample and the UOC sample from Mary Kathleen were prepared through surface transfer, both samples were found to feature larger agglomerates made up of smaller particles [103]. The major difference observed between the two samples, was however the UOC sample from Mary Kathleen featured larger agglomerates that formed a rounder shape [103]. Further analysis (2500x magnification) was performed by disaggregating both samples through ultra-sonication with solvent and backscatter imaging, finding the UOC sample from Mary Kathleen consisting of larger particles in general [103]. The microstructures between the seized sample and the UOC sample from Mary Kathleen were found to be dissimilar at higher magnification (50000x), where the Mary Kathleen sample featured 'rougher, more textured morphologies' than the seized sample [103]. Despite the difference observed in the morphologies at the micro-scale, on the weight of other evidence and statistical analysis it was 'strongly suggested' the seized sample originated from Mary Kathleen during its second production period [103].

4.1.4 Justification

TGA and other related thermal analysis techniques have been heavily used to investigate how physical properties and chemical composition of a UOC or uranium oxide sample changes as a function of temperature; however this, so far, has been largely been conducted from a materials science/nuclear fuel perspective [154, 155]. As the final product, the fuel pellet, has to pass stringent quality controls in order for it to be used in a reactor, a greater understanding of the series of chemical and metallurgical processes involved can produce a better product.

For nuclear forensics, however, there has been little attention paid towards the use of thermal analysis techniques for the analysis of a UOC sample, and whether the chemical information can be used for the materials provenancing. So far, no study has analysed real UOC samples using TGA, despite it being identified as a ‘potential tool for nuclear forensics investigations’ [216], as the chemical composition of an unknown UOC may provide information on the samples processing history [216].

Therefore, the potential use of TGA to characterise the chemical composition of UOCs for nuclear forensics applications will be evaluated in this chapter. The TGA analysis of eight UOCs from 3 Australian mines (Beverley, Ranger and Olympic Dam) currently in operation will form the basis of this evaluation. NIR spectroscopy, Raman spectroscopy and XRD, in addition to TGA, will also be used to analyse the eight UOC samples, as well as intermediate samples collected throughout the temperature program, in order to identify the different uranium compounds formed and decomposed.

In parallel to the analysis of chemical composition of the UOCs by NIR spectroscopy, Raman spectroscopy and XRD, SEM will also examine the morphologies of the UOCs, and to observe any changes as a function of temperature. Identifying characteristic morphologies for each Australian mine, and assessing their consistency across the eight UOC sub-samples, will be invaluable for a nuclear forensic investigation.

4.2 Methods

Preliminary TGA results were first obtained by heating ~10-15 mg of each of the eight Australian UOCs from 50 to 1400 °C at a heating rate of 20 °C/min in air and nitrogen atmospheres, with a gas flow rate of 20 mL/min. It was found that in an air atmosphere that the final mass loss event across all of the samples occurred within the Beverley samples at ~680 °C, whereas all the samples in the nitrogen atmosphere experienced a similar mass loss at ~1300 °C. Therefore an optimised TGA method featuring a lower temperature range from 50-1000 °C was developed.

Approximately 10 mg of each of the eight Australian UOCs were loaded into porcelain pans and inserted into a PerkinElmer Simultaneous Thermal Analyser 8000 (Waltham, MA) for TGA (Table 2). The UOCs were heated from 50 to 1000 °C at a heating rate of 10 °C/min in air and nitrogen atmospheres, with a gas flow rate of 20 mL/min. Each UOC sample was analysed in triplicate, and the TGA products were stored in plastic vials for further analysis. Between analyses, the sample pans were cleaned by leaving them in 7.8 M nitric acid overnight to digest any affixed UOC

material, before rinsed twice with reverse osmosis (RO) water and dried for 2-3 hours at 150 °C within an oven. Pans that still contained UOC materials were then cleaned in 10 M nitric acid, with any pans that still had UOC material within were removed from further analysis.

Table 2 Masses (mg) of Australian UOCs analysed by TGA in triplicate in air and nitrogen atmospheres

Sample	Atmosphere	Mass #1 (mg)	Mass #2 (mg)	Mass #3 (mg)
Beverley 1	N ₂	13.306	7.360	9.896
	Air	9.420	9.347	9.717
Beverley 2	N ₂	11.000	11.700	10.804
	Air	9.221	8.537	11.134
Beverley 3	N ₂	11.382	10.316	10.049
	Air	10.875	9.326	8.556
Ranger 1	N ₂	12.145	9.859	10.827
	Air	7.791	9.765	9.018
Ranger 2	N ₂	14.494	10.026	11.071
	Air	10.351	10.260	8.554
Ranger 3	N ₂	8.861	15.240	11.071
	Air	10.991	11.934	9.623
Olympic Dam 1	N ₂	9.285	11.343	11.197
	Air	9.982	10.818	12.634
Olympic Dam 2	N ₂	10.031	10.439	10.018
	Air	11.041	10.059	9.561

In addition to the TGA products, intermediate samples were also obtained from the PerkinElmer Simultaneous Thermal Analyser 8000 following the analysis and interpretation of the TGA profile obtained from each sample. Intermediates were collected at temperatures which followed major decompositions within each sample; for Beverley samples, intermediates were collected at 280 and 500 °C, whereas for Ranger and Olympic Dam, they were collected at 200 and 500 °C. A background subtraction was performed using the TGA profile of an empty pan to correct for a negative slope observed in the untreated data. Differential scanning calorimetry (DSC) measurements were recorded simultaneously with the TGA measurements.

The original UOCs, TGA intermediates and final products were independently analysed by micro-Raman (μ Raman) spectroscopy using a Horiba XploRA ONE microscope (Edison, NJ). The instrument was calibrated using the 520.5 cm^{-1} band of a Si wafer. Raman spectra was recorded using a 638 nm laser at a power of 10% optical density, with a spectral range from $50 - 1400\text{ cm}^{-1}$. 532 and 785 nm laser wavelengths were also investigated, however they resulted in fluorescence and laser-induced sample heating. The spot size of the laser was $100\ \mu\text{m}$ with a 10x objective lens. Approximately 10 mg of each sample analysed was mounted on a soda-lime glass slide with double-sided adhesive tape (Figure 35). Three replicate measurements were taken from each sample, and all samples were analysed for 400 s, except the Beverley UOCs, which were measured for only 200 s due to the high counts.



Figure 35 Presentation of TGA intermediates and product from Beverley UOC 3 in preparation for analysis by μ Raman spectroscopy

The speciation of the original UOC samples and TGA intermediates and final products was initially investigated using near-infrared spectroscopy (NIR). NIR reflectance measurements were recorded using an ASD Inc. FieldSpec 4 High Resolution Spectroradiometer (Boulder, CO) between 350-2500 nm, with a spectral resolution of 3 nm at 700 nm and 8 nm at 1400 and 2000 nm. A fibre optic bundle with a takeoff angle of 20° is used to transmit light from the sample to the ASD's detectors, with a 50 W halogen lamp illuminating the sample. A number of different substrates were investigated to present the samples to the fibre optic bundle, as there was insufficient material to completely cover the analysed surface area. These substrates include glass, quartz and frosted quartz microscope slides, where the initial optimisation of the instrument was performed on the Spectralon® white reference standard, followed by the white reference measurement of the microscope slide on top of the Spectralon® standard. A weigh paper/microscope slide apparatus was used to prevent the contamination of the Spectralon® standard with uranium materials (Figure 36) for the duration of the NIR analysis.

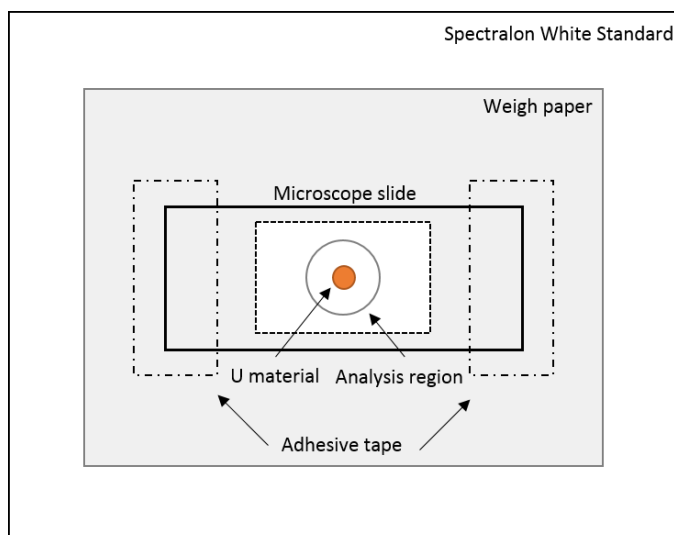


Figure 36 Diagram of sample mount for NIR analysis of UOC samples

XRD analysis was performed using a Bruker D8 X-ray diffractometer (Billerica, MA) with a Cu X-ray tube (1.5418 Å) (40 kV, 40 mA) and a diffraction angle range of $10^\circ > 2\theta > 150^\circ$. Samples were adhered onto double-sided carbon tape and mounted on Si single crystals in preparation for XRD analysis. Due to the small amount of material available (0.8-1.4 mg), each sample were analysed for 60 hrs. Due to time constraints, this only allowed three UOCs and their associated intermediates and TGA products to be analysed; Beverley UOC 1 in an air atmosphere, Ranger UOC 2 in an air atmosphere and Olympic Dam UOC 1 in a nitrogen atmosphere.

Scanning electron microscopy was performed using an FEI Inspect 50 SEM (Hillsboro, OR), with an acceleration voltage of 15 keV. Approximately 1 mg of each sample were adhered to aluminium SEM stubs with double-sided carbon tape and coated with 10 nm of Pt, to prevent the accumulation of charge.

4.3 Results

4.3.1 Thermogravimetric analysis of Australian UOCs

4.3.1.1 Beverley UOCs

Following TGA of the Australian UOC, an immediate observation was the change in colour of the UOC samples from Beverley. The Beverley UOCs changed from a golden yellow colour to an increasingly darker orange colour at 280 °C and 500 °C, respectively, to finally a black colour at 1000 °C (Figure 37).

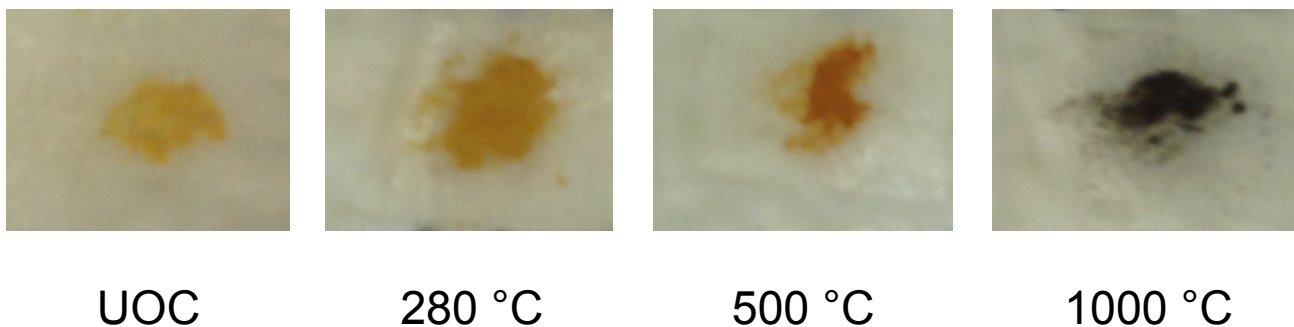


Figure 37 Colour changes in the Beverley UOC 1 upon heating to different temperatures during TGA

Within the UOC samples from Beverley analysed by TGA in an air atmosphere (Figure 38), the first mass loss is observed at ~100 °C, particularly within the Beverley 3 UOC sample. The largest mass loss (9.36%) seen within the Beverley UOC samples occurred at ~220 °C. Two minor mass losses (0.73% and 0.3%, respectively) were observed at 485 °C and 600 °C, before a final mass loss (0.93%) at ~680 °C. A similar TGA profile is obtained when the UOC samples from Beverley are analysed in a nitrogen atmosphere (Figure 39).

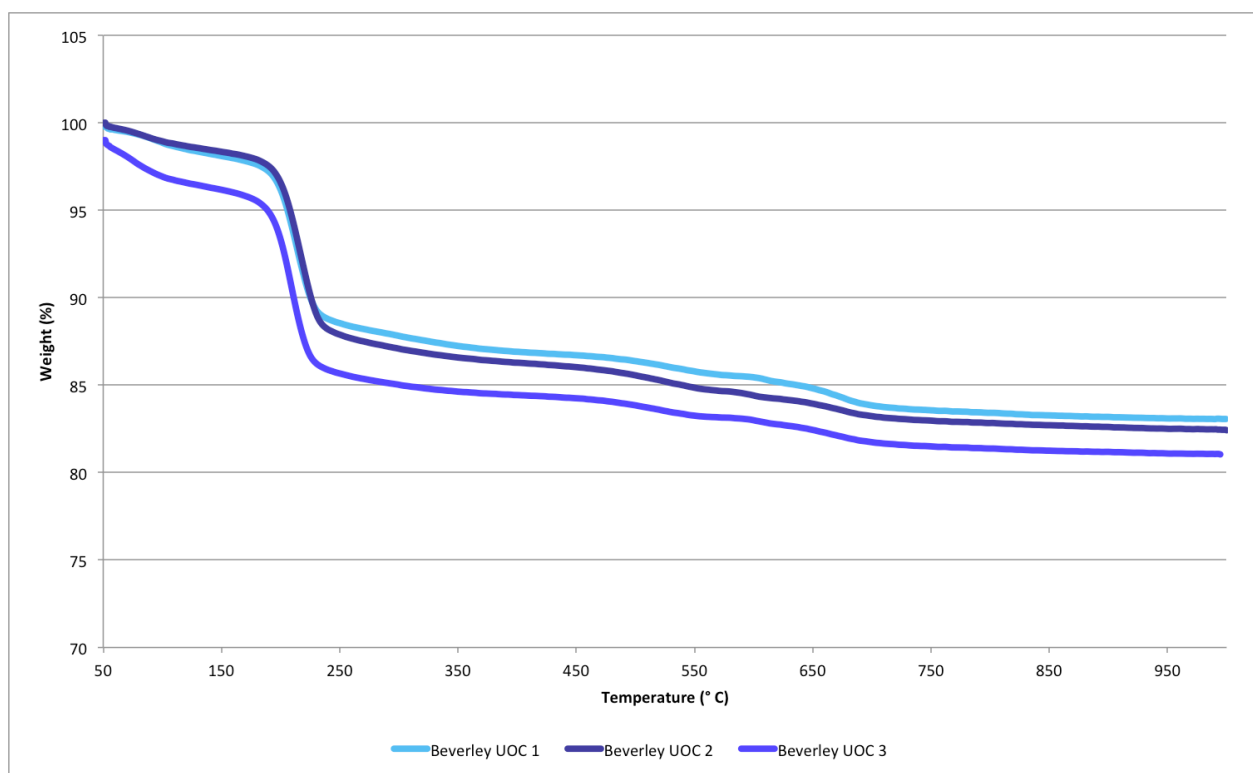


Figure 38 TGA plot of the three Beverley UOCs analysed in an air atmosphere

The mass loss at ~100 °C is likely attributable to the loss of water and varies within the three Beverley UOC samples as the Beverley 3 sample undergoes a mass loss of 3.3%, whereas Beverley UOCs 1 & 2 samples have a mass loss of 1.2%. While past XRD analysis of UOC sourced from

Beverley has identified trace amounts of tetra-hydrated UO_4 ($\text{UO}_4 \cdot 4\text{H}_2\text{O}$) [217], a second dehydration process at $\sim 130^\circ\text{C}$ attributable to the conversion of $\text{UO}_4 \cdot 4\text{H}_2\text{O}$ to di-hydrated UO_4 ($\text{UO}_4 \cdot 2\text{H}_2\text{O}$) was not observed within the TGA plot [218].

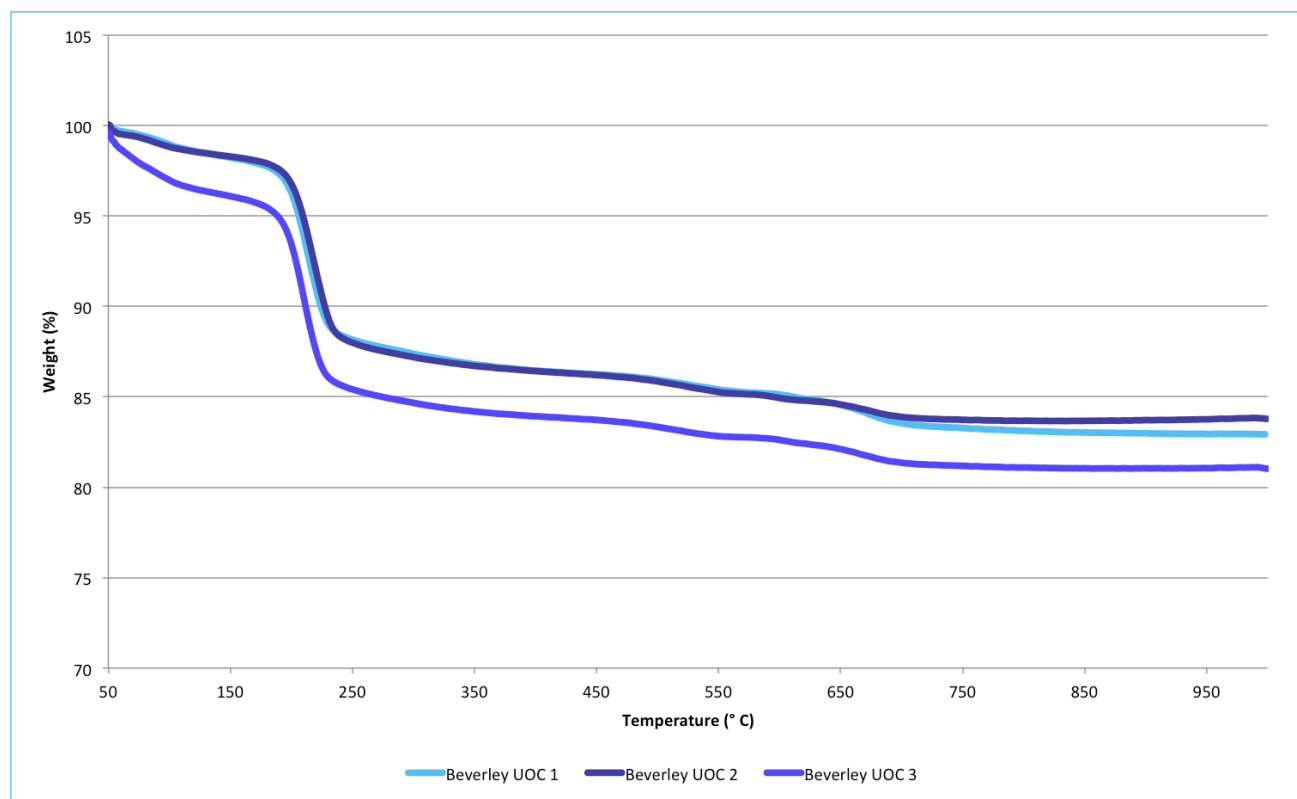
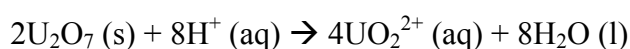


Figure 39 TGA plot of the three Beverley UOC samples analysed in a nitrogen atmosphere

A number of different studies have previously investigated the thermal decomposition of uranyl peroxide or studtite ($(\text{UO}_2)_2\text{O}_2 \cdot (\text{H}_2\text{O})_2 \cdot 2\text{H}_2\text{O}$), the tetra-hydrated, mineralised form chemically identical to the synthetic uranyl peroxide [219], as a disagreement still exists within the literature concerning the identity of the intermediate(s) formed during the decomposition of uranyl peroxide to U_3O_8 . Using XRD and IR in conjunction with TGA and differential thermal analysis, Sato (1976) concluded that upon heating both $\text{UO}_4 \cdot 2\text{H}_2\text{O}$ and $\text{UO}_4 \cdot 4\text{H}_2\text{O}$ synthesized samples (which converted to $\text{UO}_4 \cdot 2\text{H}_2\text{O}$ after heating beyond $\sim 130^\circ\text{C}$) beyond 220°C in an air atmosphere, it decomposed to an amorphous UO_x ($3 \leq x \leq 3.5$) phase [218]. At 485°C , the amorphous UO_x ($3 \leq x \leq 3.5$) phase recrystallized to form α -uranyl trioxide ($\alpha\text{-UO}_3$), before undergoing a final decomposition to form U_3O_8 at $\sim 580^\circ\text{C}$. The thermal decomposition pathway suggested by Sato (1976), through the formation of an amorphous UO_x ($3 \leq x \leq 3.5$) phase at 220°C , disagreed with the conclusions drawn previously by Boggs & El-Chehabi (1957), who suggested $\text{UO}_4 \cdot 2\text{H}_2\text{O}$ formed another uranyl peroxide U_2O_7 at 195°C through the following decomposition [220]:



Boggs & El-Chehabi (1957) asserted the U_2O_7 oxide had formed due to presence of an IR band at 1428.57 cm^{-1} , alongside other 'usual absorptions' below 1000 cm^{-1} , which was not present within the IR spectra obtained from UO_3 and $\text{UO}_4 \cdot 2\text{H}_2\text{O}$ [220]. Good agreement (94%) was also reportedly found between the theoretical and experimental measurement of the released oxygen when U_2O_7 was treated with dilute sulphuric acid, with the remaining 8% of oxygen thought to be captured by water [220]:



Sato (1976) also utilised IR to characterise the intermediates that were collected at various temperatures during the thermal decomposition of both the di- and tetra-hydrated uranyl peroxides, but was unable to identify the IR band at 1400 cm^{-1} attributed to U_2O_7 within the intermediate collected at $200 \text{ }^\circ\text{C}$ during the study [218]. Interestingly, this intermediate collected at $200 \text{ }^\circ\text{C}$ by Sato (1976) was found to not feature any patterns when analysed by X-ray diffraction, suggesting the uranium compound present was amorphous [218].

Recently, a number of studies have found evidence to support the earlier U_2O_7 intermediate decomposition pathway suggested by Boggs & El-Chehabi (1957). Guo *et al.* (2016) identified an amorphous U_2O_7 (A- U_2O_7) phase forming after heating at studtite ($\text{UO}_4 \cdot 4\text{H}_2\text{O}$) samples in an inert atmosphere beyond $200 \text{ }^\circ\text{C}$, before decomposing at $500 \text{ }^\circ\text{C}$ to form amorphous UO_3 [221]; a revision of the decomposition previously reported where a hydrated, amorphous UO_3 phase (A- $\text{UO}_3 \cdot n\text{H}_2\text{O}$) was thought to form [222]. Where previously Guo *et al.* (2014) had identified A- $\text{UO}_3 \cdot n\text{H}_2\text{O}$ as the compound that formed with evolved gas analysis, finding an agreement (0.35% difference) through a comparison between the measured and theoretical mass loss of O_2 gas generated [222], the revised U_2O_7 decomposition pathway also investigated the intermediate samples with IR spectroscopy, identifying two IR bands at 901 and 740 cm^{-1} [221]. Interestingly, Guo *et al.* (2016) attributed both peaks to the stretching vibrations of uranyl within amorphous uranium oxides citing Sato (1976), who observed two peaks at 905 and 720 cm^{-1} due to the stretching U-O vibration in UO_x [221]. The only IR band at 740 cm^{-1} reported by Sato (1976) was obtained in the uranyl peroxide samples heated to $600 \text{ }^\circ\text{C}$, and was attributed to U_3O_8 [218]. Despite this, due to the amorphous nature of the intermediate formed, made the identification difficult, the presence of these two IR bands, the TGA

profile itself and ‘charge neutrality’ Guo *et al.* (2016) concluded that that an amorphous U₂O₇ phase had been formed [221], and consistent with Boggs & El-Chehabi (1957) and another study undertaken by Odoh *et al.* (2016) [220, 223]. Evolved gas analysis (EGA) of oxygen and water vapour and DSC were also used by Guo *et al.* (2016) all measured a single peak at ~200 °C, however the decomposition of metastudtite/di-hydrated uranyl peroxide to U₂O₇ also features the dehydration of water, and could not delineate between the two events [221].

The study undertaken by Odoh *et al.* (2016) also analysed synthetic studtite samples with TGA and XRD, finding the amorphous material formed a compound with a composition between UO₄ and UO₃, consistent with Boggs & El-Chehabi (1957) [223]. Odoh *et al.* (2016) also undertook neutron scattering measurements to investigate the position of oxygen atoms within a dry A-U₂O₇ sample, finding that there was some local order within the sample, but not to the extent XRD would be able to identify any structure [223]. Pair-distribution functions calculated from the neutron scattering data were also used to determine peroxide and uranyl ions were present within the dry A-U₂O₇ sample, through the identification of bond lengths consistent with peroxide O-O and uranyl U(VI)-O bonds [223].

Upon heating the studtite samples beyond 500 °C, both Guo *et al.* (2016) and Odoh *et al.* (2016) suggest that an A-UO₃ phase forms through the decomposition of U₂O₇ [221, 223]. A-UO₃ as the intermediate that forms at 500 °C disagrees with Sato (1976), who suggests α -UO₃ is instead formed from the recrystallization of A-UO₃ at 220 °C, based upon XRD patterns and IR spectra taken from the intermediate sample collected at 500 °C [218], which differs from the XRD pattern obtained by Guo *et al.* (2016) [221] (Figure 40). The Guo *et al.* (2016) XRD pattern of the intermediate collected at 535 °C largely feature an amorphous pattern, however a trace diffraction pattern is observable but was not explored further by the authors (Figure 40).

Images removed due to copyright restriction.

Figure 40 XRD patterns obtained from intermediates and products from the thermal decomposition of synthetic uranyl peroxide/studtite samples by Sato (1976) [223] (top) and Guo *et al.* (2016) (bottom) [221]

Further heating to 535 °C is said to form non-stoichiometric α -UO_{2.9}, according to Guo *et al.* (2016) and Odoh *et al.* (2016) [221, 223], whereas Sato (1976) indicated that the α -UO₃ persists until ~580 °C, before it decomposes to U₃O₈ [218]. Both studies utilised XRD to identify the two intermediates

suggested, however both agree that U_3O_8 is the final product formed, albeit at different temperatures, with Sato (1976) at ~ 580 °C and Guo *et al.* (2016) at ~ 610 - 660 °C [221, 223].

4.3.1.2 Ranger UOCs

Unlike the Beverley UOCs, the Ranger UOCs did not undergo any visible colour change during TGA, remaining black throughout (Figure 41).

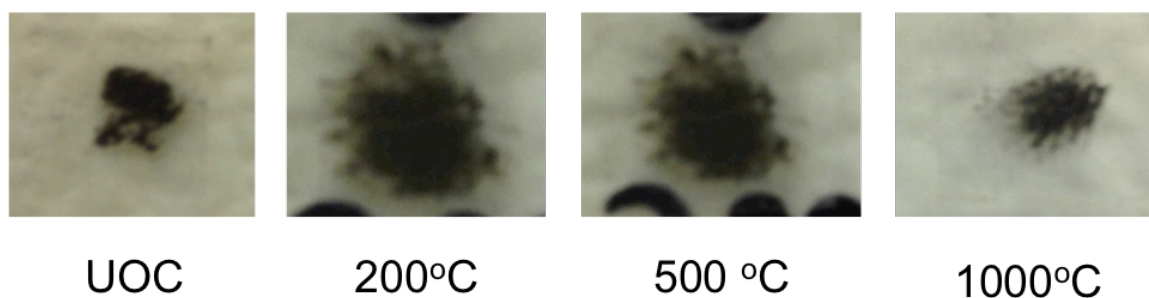


Figure 41 Colour of the Beverley UOC 1 upon heating to different temperatures during TGA

Ranger UOCs 1 and 3 appear to undergo two weight loss events in both air (Figure 42) and nitrogen (Figure 43) atmospheres between 60 - 100 °C and 220 - 390 °C, whilst the Ranger UOC 2 appears to undergo an additional weight loss event, with weight losses occurring at 60 - 110 °C, 220 - 440 °C and 600 - 710 °C.

The first weight loss between 60 - 100 °C is likely due to the loss of water and varies between the three Ranger UOCs. Ranger UOC 2 contained the greatest amount of water of the three UOCs, with weight losses of 1.86% and 1.97% in an air and nitrogen atmospheres, respectively, whilst Ranger UOC 3 featured the least with weight losses of 1.06% and 1.16% in an air and nitrogen atmospheres, respectively. The slight differences in the moisture content likely reflect the small sample sizes used in the analysis (Table 2) and the lack of homogenization of the samples as they were analysed as received.

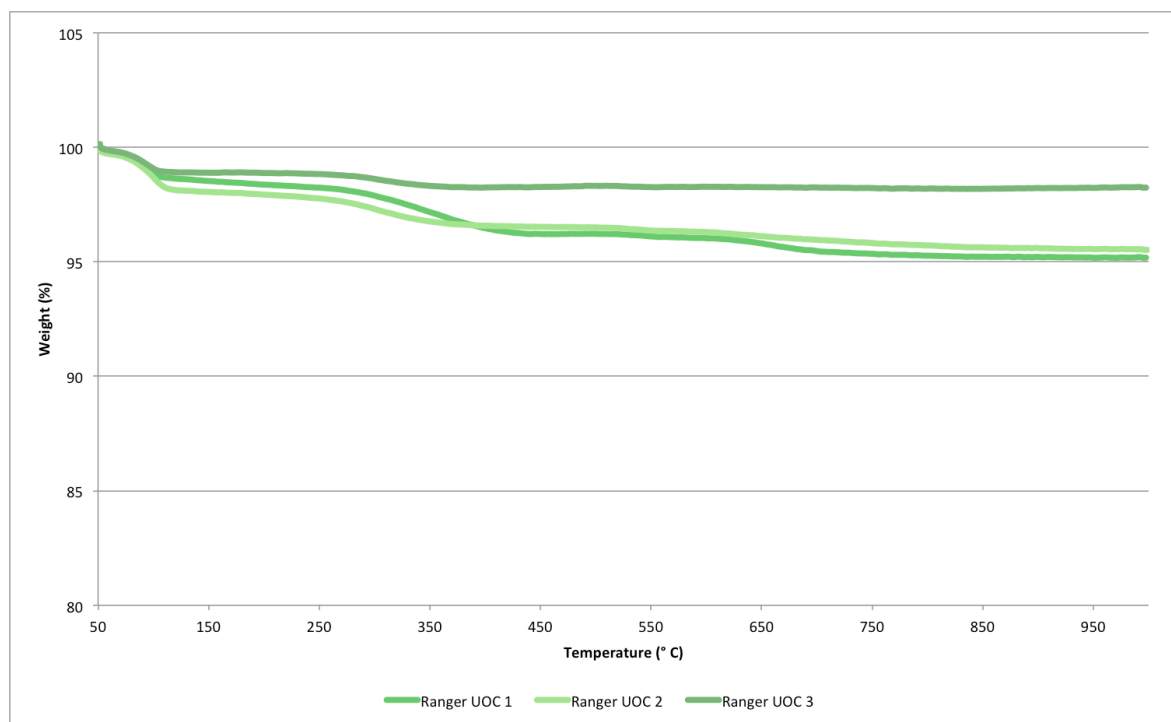


Figure 42 TGA plot of the three Ranger UOCs analysed in an air atmosphere

These two later weight loss events between 250-360 °C and at 600-700 °C for all three Ranger UOC samples is not attributable U_3O_8 , but from other minor phases present within the Ranger, as U_3O_8 is thermally stable at normal pressures in air and nitrogen atmospheres until the temperature exceeds at least 800 °C, where $U_8O_{21\pm z}$ compound is formed [216, 224]. Previous analyses of UOCs from Ranger have identified the minor presence of $UO_3 \cdot 2H_2O$ [217], which may be as a result of the process Ranger uses to precipitate the uranium as ADU using ammonia, as the presence of nitrate and ammonium ions within ADU during calcination can lead to the formation of a β - UO_3 phase, in lieu of an amorphous UO_3 (A- UO_3) phase [155]. Furthermore, calcination of ADU at temperatures ≤ 650 °C leads to the formation of both β - UO_3 and α - U_3O_8 , whereas calcining 750 °C leads to a single phase of α - U_3O_8 [108] Additionally, U_3O_8 is a stable compound and does not revert back to UO_3 at atmospheric pressures [225].

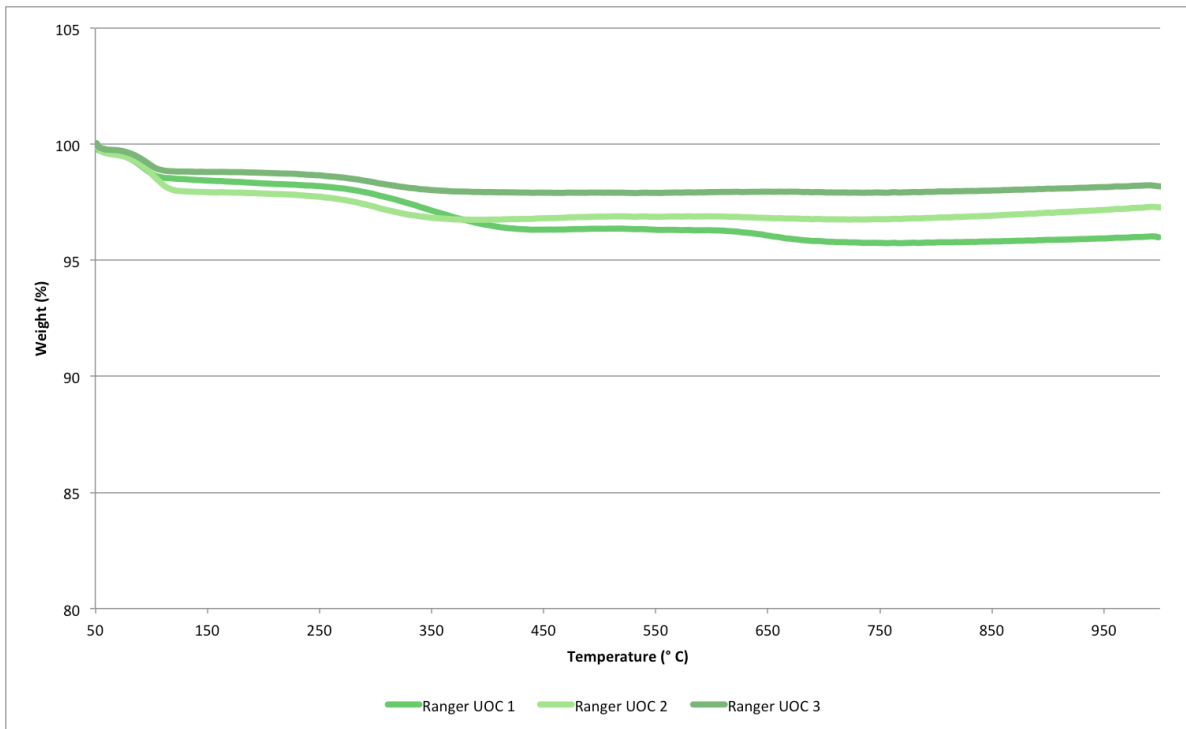


Figure 43 TGA plot of the three Ranger UOCs analysed in a nitrogen atmosphere

4.3.1.3 Olympic Dam UOCs

Similar to the Ranger UOCs, no visible colour change occurred within the Olympic Dam UOC analysed by TGA, as they remained a dark olive/black colour (Figure 44).

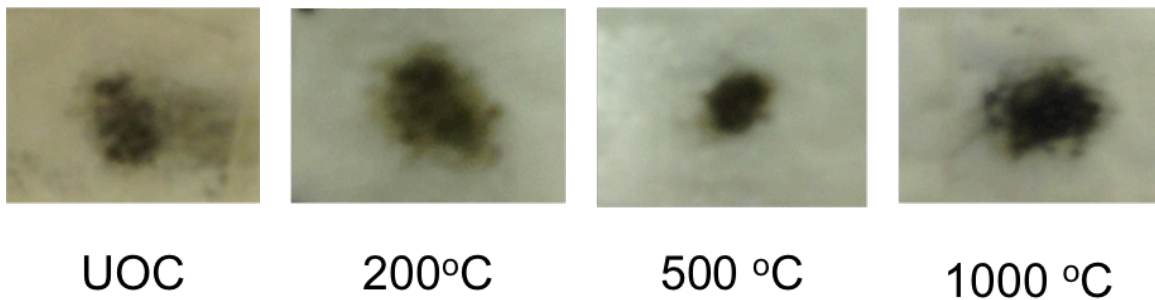


Figure 44 Colour of the Beverley UOC 1 upon heating to different temperatures during TGA

Unlike the UOCs from Ranger, the Olympic Dam UOCs do not contain any water as evidenced by the lack of a mass loss event below ~110 °C, with the first mass loss event observed in both air (Figure 45) and nitrogen (Figure 46) atmosphere occurs between 250-360 °C, followed by a second mass loss event at 600-700 °C. This is similar to what was previously observed in the Ranger UOC 2 sample. The latter stages in the UOC production process at Olympic Dam is similar to Ranger,

where the uranium is also precipitated out as ADU, and the samples are subsequently calcined to produce U_3O_8 for export [37]. The similarity between the UOC production process, as well as the similar weight loss events within the TGA plots suggests the same minor phase may be present, however further analysis with μ Raman spectroscopy and XRD is required. It is difficult to attribute the differences observed in moisture between the Ranger and Olympic Dam UOCs due the lack of limited detailed information concerning how the UOCs were calcined (i.e. temperature and duration), or if any additional steps, such as drying prior to calcination, are taken at either location.

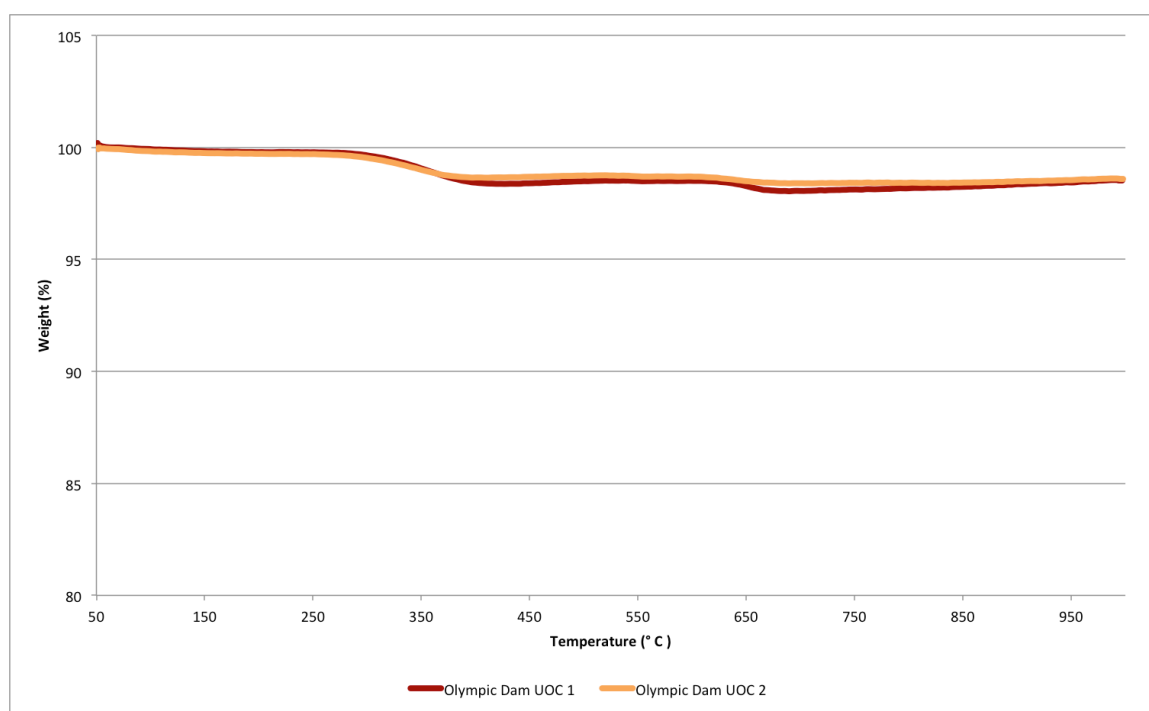


Figure 45 TGA plot of the two Olympic Dam UOCs analysed in a nitrogen atmosphere

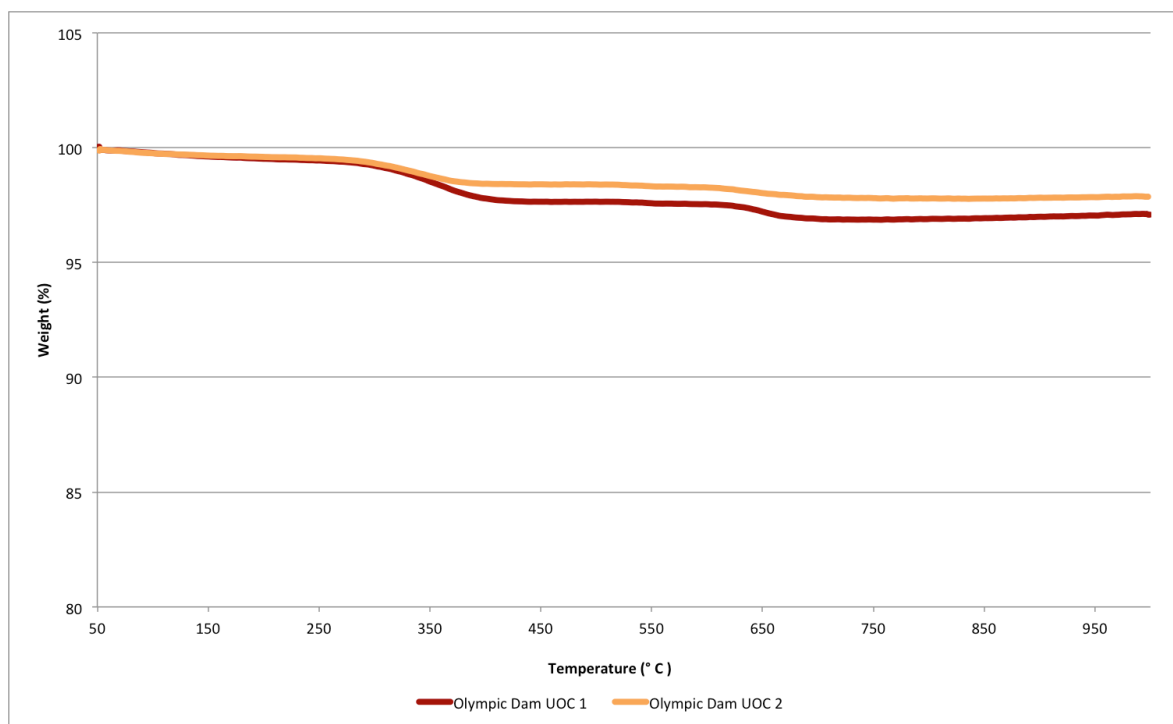


Figure 46 TGA plots of the three Olympic Dam UOCs analysed in a nitrogen atmosphere

4.3.2 Differential scanning calorimetry

In conjunction with the TGA results, DSC measurements were also simultaneously obtained during the heating of the eight UOCs in both nitrogen (Figure 47) and air (Figure 48) atmospheres. While they exhibited large intra-mine variability and feature a severe curvature in the baseline, the presence of a number of peaks corresponding to decomposition events was still somewhat informative and helped confirm the identity of some of the compound formed.

Within the Beverly and Ranger UOC samples analysed within a nitrogen atmosphere, a positive peak, indicating an endothermic process has occurred, at 100 °C indicates the dehydration of both samples (Figure 47). At 220 °C, the all three Beverly samples exhibits a large endothermic peak due to decomposition of $\text{UO}_4 \cdot 2\text{H}_2\text{O}$, which is consistent with both Sato (1976) and Guo *et al.* (2016) [218, 221]. Interestingly, the suggested exothermic crystallization of A-UO_3 to $\alpha\text{-UO}_3$ by Sato (1976) is not observed within the DSC plot at ~ 485 °C [218]. A small exothermic peak appears to occur at 550 °C within the Beverly UOC 2, however with the curved baseline it is difficult to conclusively state this with complete confidence. The presence of an exothermic peak at 550 °C within the Beverly UOCs would lend support to the decomposition pathway suggested by Guo *et al.* (2016), where a similar peak was observed as the A-UO_3 decomposed to $\alpha\text{-UO}_{2.9}$ [221]. This peak is difficult to observe within Beverly UOCs 1 and 3, due to the irregular baseline.

An endothermic peak is observed at 610 °C within Beverley UOC 2, however it is difficult to conclusively differentiate this peak again from the irregular background. This would again support the decomposition pathway suggested by Guo *et al.* (2016), where it was thought α -UO_{2.9} decomposed to U₃O₈ [221]. A small additional endothermic peak is identified at 670 °C, however again it is difficult to say with any confidence that this is not an irregularity within the baseline. Neither Sato (1976) or Guo *et al.* (2016) observed any composition change at this temperature, however the loss of oxygen during the decomposition of α -UO_{2.9} to U₃O₈ was measured between the range of 610-660 °C [221].

Within the Ranger UOCs, only one peak was observed between 90-100 °C which was attributable to the loss of water whereas the Olympic Dam UOCs featured no peaks that could be conclusively distinguished from the curved baseline. Within the Olympic Dam UOC trace, a very broad peak with a maxima at 350 °C corresponding to the mass loss at 220-390 °C within the TGA may exist however it is difficult to again conclusively state with any certainty due to the irregularity of the baseline.

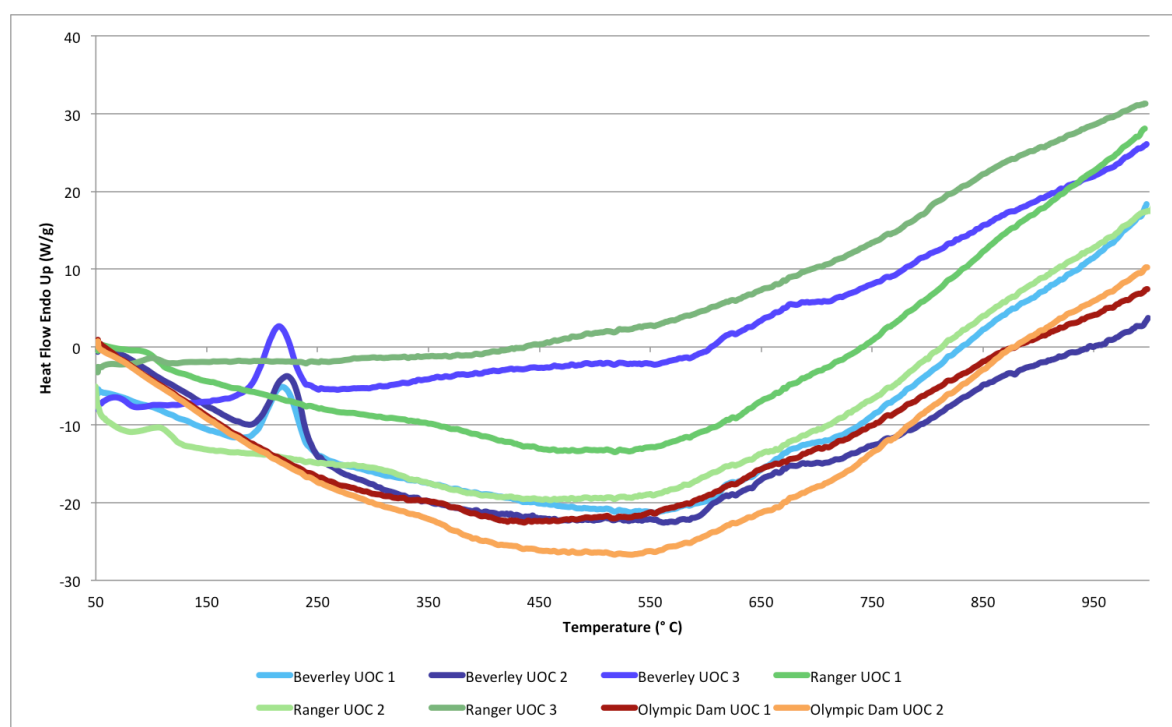


Figure 47 DSC plot of Beverley, Ranger and Olympic Dam UOCs analysed by TGA in a nitrogen atmosphere

In the DSC plot where the eight UOCs are analysed in an air atmosphere, the curvature of the baseline is less severe however no additional peaks are identified (Figure 48). The broad peak previously identified with the Olympic Dam UOCs with a maxima at 350 °C is present in the Olympic Dam UOC 1 sample and possibly also within the Ranger UOC 1 sample, however it is less defined within the Olympic Dam UOC 2.

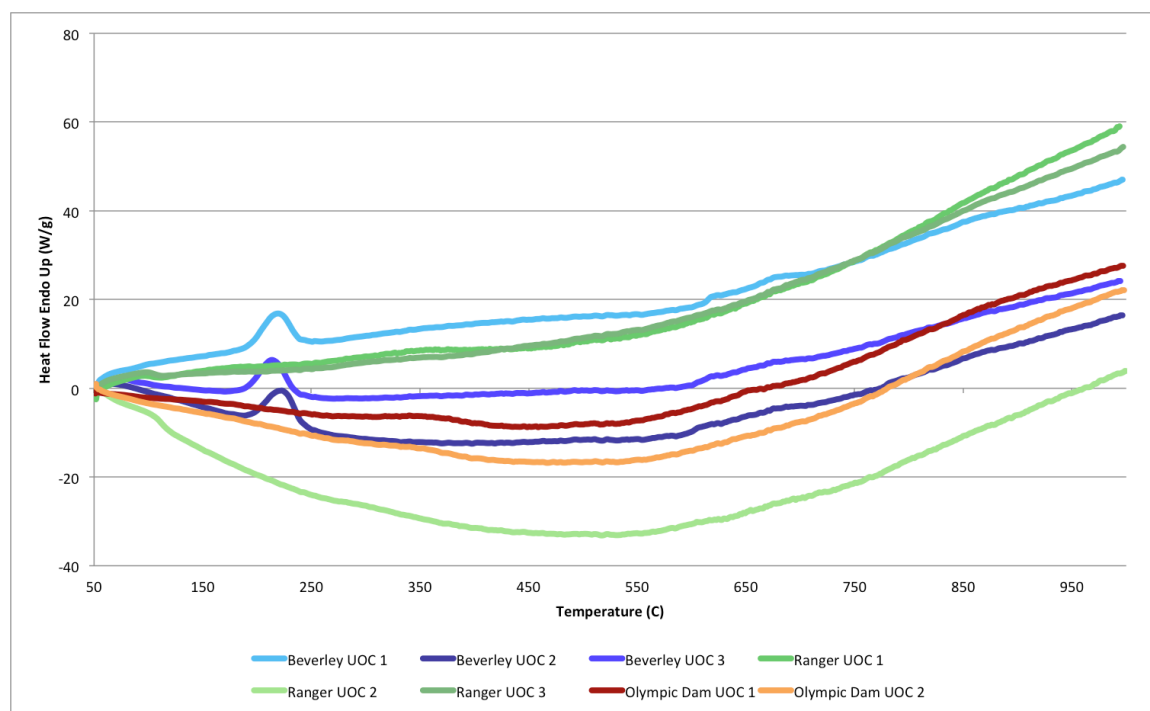


Figure 48 DSC plot of Beverley, Ranger and Olympic Dam UOCs analysed by TGA in an air atmosphere

Taking the first derivative of the DSC data failed to identify any further peaks within any of the UOC samples analysed, in part due to large background arising from the sloping background of the original data. Within the Beverley UOC samples, only the large peak previously identified within the original DSC data at ~220 °C could be confidently distinguished from the background (Figure 49). A small peak may be present at ~600 °C, however this is difficult to distinguish from the background with any degree of confidence. Similarly, the small peak that was possibly thought to exist at ~670 °C within the original Beverley DSC data (Figure 48) is also difficult to confidently distinguish from the irregular background (Figure 49).

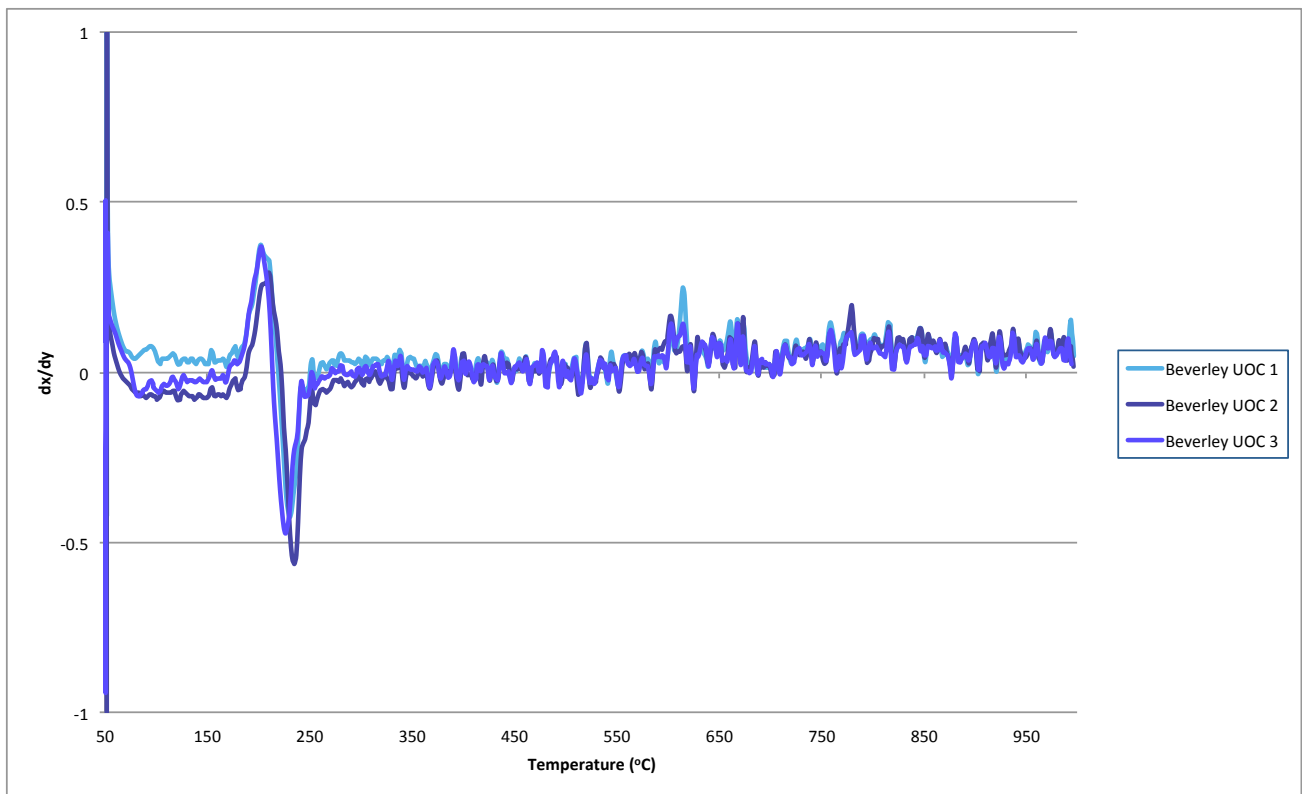


Figure 49 First derivative of the DSC data obtained from the Beverley UOCs in an air atmosphere

Within the Ranger UOC plot of the first derivative of the original Ranger data, only a single peak at ~ 100 °C attributable to the dehydration of the UOC samples can be observed (Figure 50). A similar peak at ~ 100 °C may be observed within the Olympic Dam plot (Figure 51), however the smaller magnitude of the peak makes it more difficult to confidently distinguish it from the background.

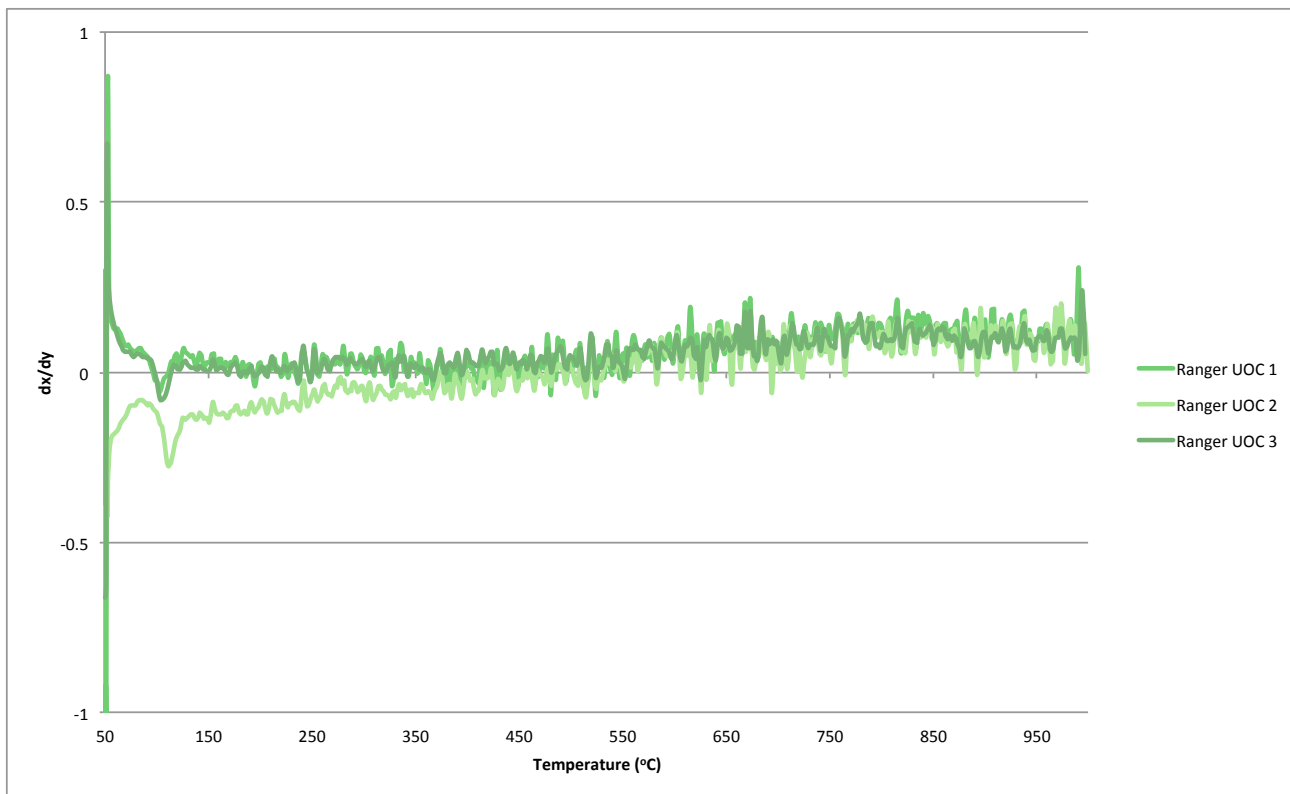


Figure 50 First derivative of the DSC data obtained from the Ranger UOCs in an air atmosphere

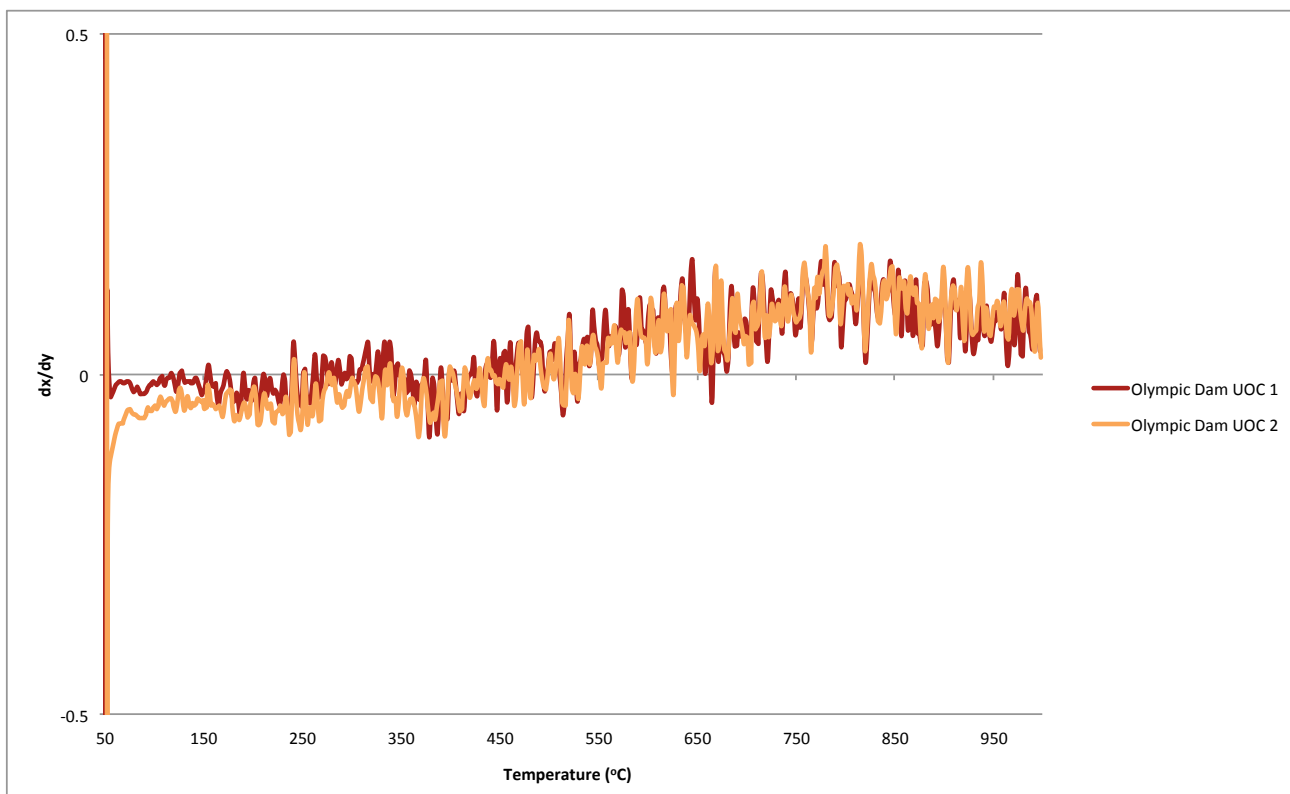


Figure 51 First derivative of the DSC data obtained from the Olympic Dam UOCs in an air atmosphere

4.3.3 NIR spectroscopy

To confirm the identity of the different phases formed during the calcination and identify the unknown phases, NIR and Raman spectroscopy were both examined. For NIR, direct analysis was unfeasible (as previously performed by Klunder *et al.* (2013) with similar instrumentation [206]), due to limited amounts of material (~10 mg) and a 20° take-off angle of the fibre-optic bundle of the FieldSpec NIR spectroradiometer, as the area surrounding the sample and within voids in the sample would also be analysed. As this may result in the measurement of the substrate through voids and a measurement area greater than the UOC sample, the identification of substrates which have minimal absorption between 350-2500 nm was required as directly analysing UOC samples on the Spectralon white reference standard was unfeasible due to contamination concerns.

A variety of different substrates were investigated to identify which set of experimental conditions maximised the measurable reflectance of the UOC samples when backed by Spectralon white reference standard (Figure 52). Reflectance spectra were obtained following optimisation and white reference measurements directly with the Spectralon standard. All three substrates had an absorption band at ~2215 nm, which is attributable to M-OH absorption in glass/quartz (SiO₂) while the clear and frosted quartz slide spectra also featured an additional band at ~1380 nm, due to the Si-OH first overtones [226, 227]. The soda-lime spectra also contained a large absorbance from 650 – 1693 nm, with a peak maxima at 1073 nm, which made it particularly unsuitable for the application. As the clear quartz slide ultimately featured the least amount of absorbance across the wavelength range of the NIR spectra obtained, it was selected for use in future experiments.

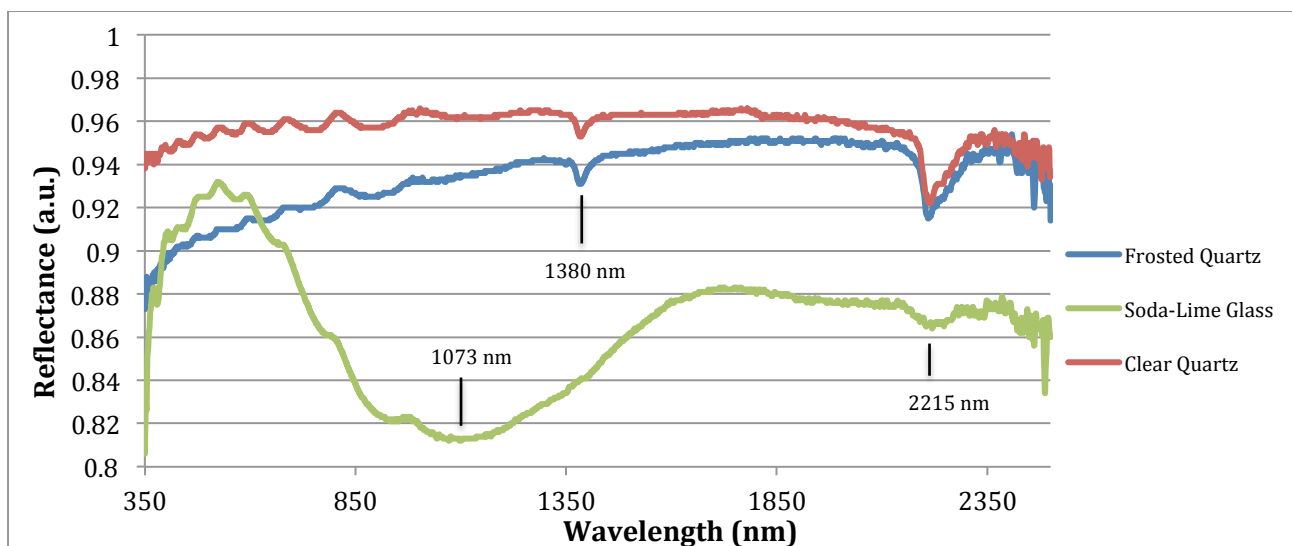


Figure 52 NIR reflectance spectra of frosted and clear quartz, and soda-lime glass backed by Spectralon white reference standard

Given the constraint concerning the amount of sample available, the effect of sample mass on the resultant spectra was also investigated. With increasing mass of the Beverley UOC analysed, it was hypothesized that the surface coverage of the UOC would also increase, resulting in a greater area analysed and producing a more intense NIR bands characteristic of UO_4 . While the characteristic NIR bands for UO_4 were observed at 1461 and 1962 nm for OH overtone and combination bands, respectively, as well as a small shoulder peak at 2111 nm similar to spectra reported by Klunder *et al.* (2013) [206], the overlaid spectra demonstrates the general linear relationship between the amount of sample analysed and the intensity of the absorbance (Figure 53). There are some departures from this relationship, as the spectrum collected from the Beverley UOC sample containing 2.1 mg is more intense through the entire collection range than the 4.9 mg sample analysed. Additionally, at the OH overtone band at 1461 nm, the 2.1 mg sample was of similar intensity and almost indistinguishable from samples with greater amounts (6.4, 8.0 and 10.3 mg) of the Beverley UOC. A likely cause for this peculiarity is that, despite the increase in the mass analysed, the surface coverage (i.e. the area analysed by the FieldSpec 4) did not increase, highlighting the variability in sample preparation and its potential effect on the analysis of small samples (<10 mg).

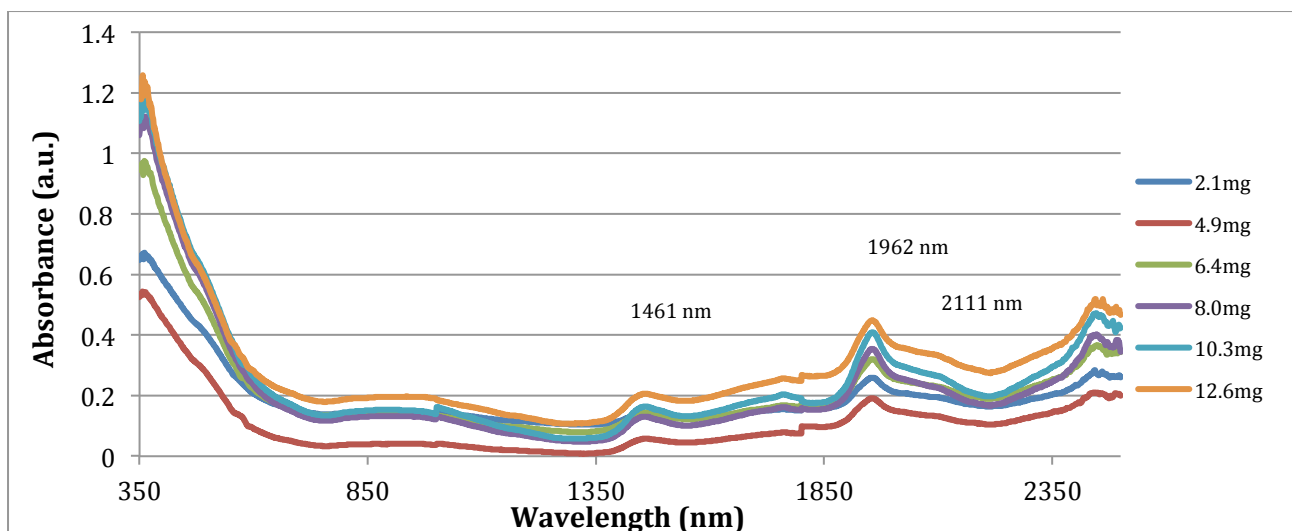


Figure 53 Effect of mass analysed on the NIR analysis of a Beverley UOC

UOCs from Ranger and Olympic Dam were also analysed to determine whether NIR was an appropriate technique to investigate changes in the speciation of UOCs analysed by TGA (Figure 54). All five UOCs featured a number of peaks attributable to U_3O_8 , the principle compound in UOCs from Ranger and Olympic Dam, or UO_3 , which is a minor phase present at varying amounts within UOCs from both mines [217]. Two large peaks at 1491 nm and 1551 nm identified within the NIR spectra coincide with both U_3O_8 and UO_3 , which both have two prominent peaks at similar wavelengths (1509 nm and 1560 nm, and 1490 and 1557 nm, respectively) making it difficult to ascertain the presence of UO_3 from the background of U_3O_8 [206]. Within all five UOC samples, a small peak may be observed at varying intensities at 1916 nm which is not attributable to either U_3O_8 or UO_3 , however a peak at 1934 nm was observed within a $UO_3 \cdot H_2O$ sample due to the combination stretching of OH within the water molecule [123].

As the minor amounts of UO_3 within the Ranger and Olympic Dam UOC samples is likely to be the phase that decomposes during TGA, NIR is unlikely to detect changes to the overall composition of the sample across the two intermediates collected and the TGA project. Therefore, NIR was not pursued further as a means to characterise the speciation changes to the Beverley, Ranger and Olympic Dam UOC throughout TGA analysis.

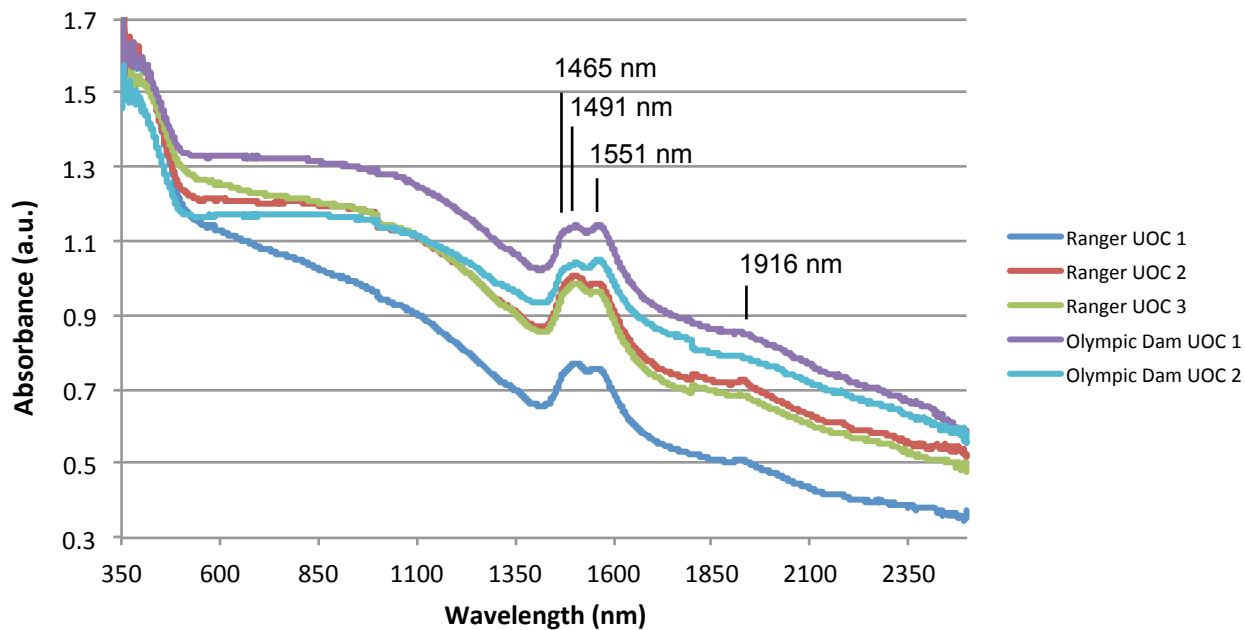


Figure 54 NIR spectra of UOCs from Ranger and Olympic Dam (~10 mg)

4.3.4 μ Raman spectroscopy

4.3.4.1 Beverley UOCs

The Raman spectra of the three Beverley UOCs analysed in the nitrogen atmosphere was found to feature the symmetrical $\nu(\text{U-O})$ and the symmetric $\nu(\text{O-O})$ stretching vibrations characteristic of UO_4 at 829 and 867 cm^{-1} [207, 222] (Figure 55).

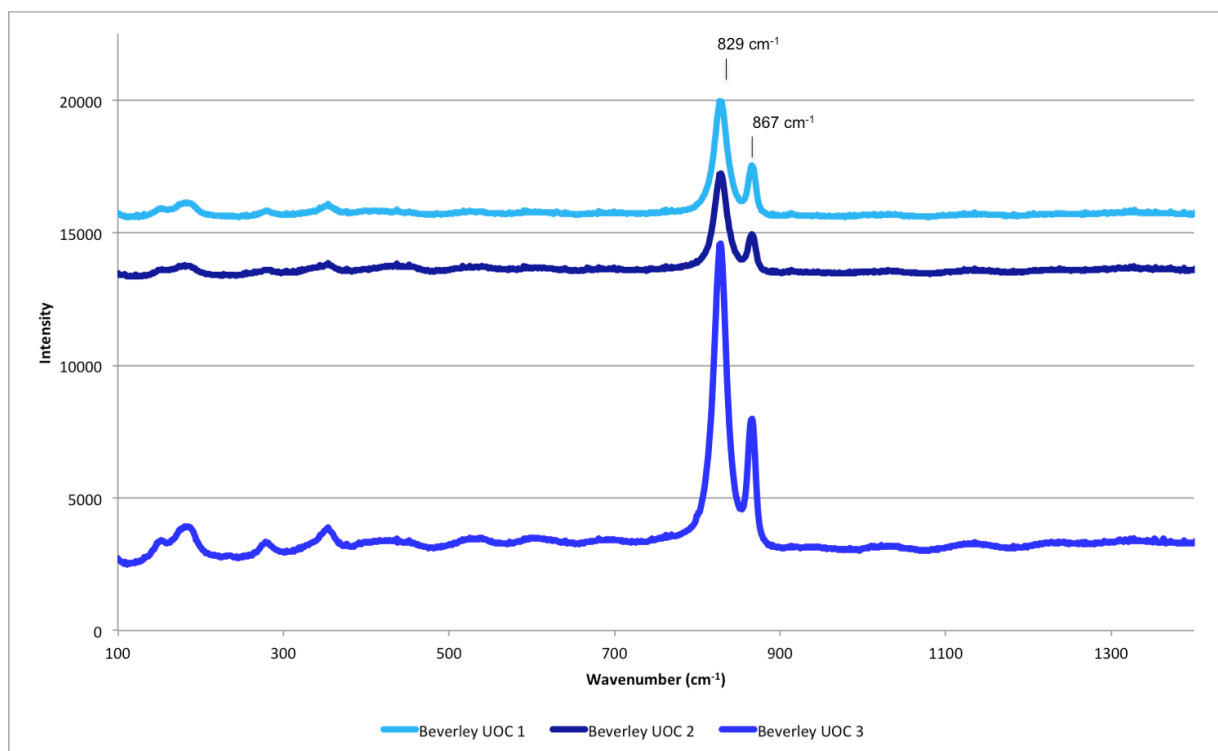


Figure 55 Raman spectra of the three Beverley UOCs

Upon heating the Beverley UOC to 280 °C, the two Raman bands attributable to UO_4 become extinct while three new peaks were observed at 711, 762 and 843 cm^{-1} (Figure 57). The 843 cm^{-1} band is of similar wavenumber to the U-O stretching Raman bands characteristic of UO_3 (845 cm^{-1}), however two other bands at 185 and ~ 350 cm^{-1} attributable to UO_3 , are not observed [172]. In spectra reported in the literature, the 845 cm^{-1} band is considerably more intense than the other two [172]. Their association with UO_3 is also less concrete when compared to the 843 cm^{-1} Raman band, as the 185 and ~ 350 cm^{-1} bands may also be associated U_3O_8 , resulting in the authors conceding that their relationship is not well understood [172]. The band at 762 cm^{-1} is also similar in wavenumber to the U-O-U-O stretching vibration reported for $\gamma\text{-UO}_3$ [209], however reported synthesis procedures for $\gamma\text{-UO}_3$ involve heating $\text{NH}_4\text{UO}_2(\text{NO}_3)\cdot 2\text{H}_2\text{O}$ or $\text{UO}_2(\text{NO}_3)_2\cdot 6\text{H}_2\text{O}$ to 400-600 °C, and $\gamma\text{-UO}_3$ has two other reported peaks of 339 and 484 cm^{-1} [228, 229]. The other Raman bands at 711 cm^{-1} was unable to be attributed to any stoichiometric or non-stoichiometric uranium oxide samples reported in the literature [172, 207, 208, 211], and U_2O_7 , the oxide suggest by Guo *et al.* (2016) and Odoh *et al.* (2016) to have formed at 200 °C, has not been analysed by Raman spectroscopy and reported within the literature [221, 223].

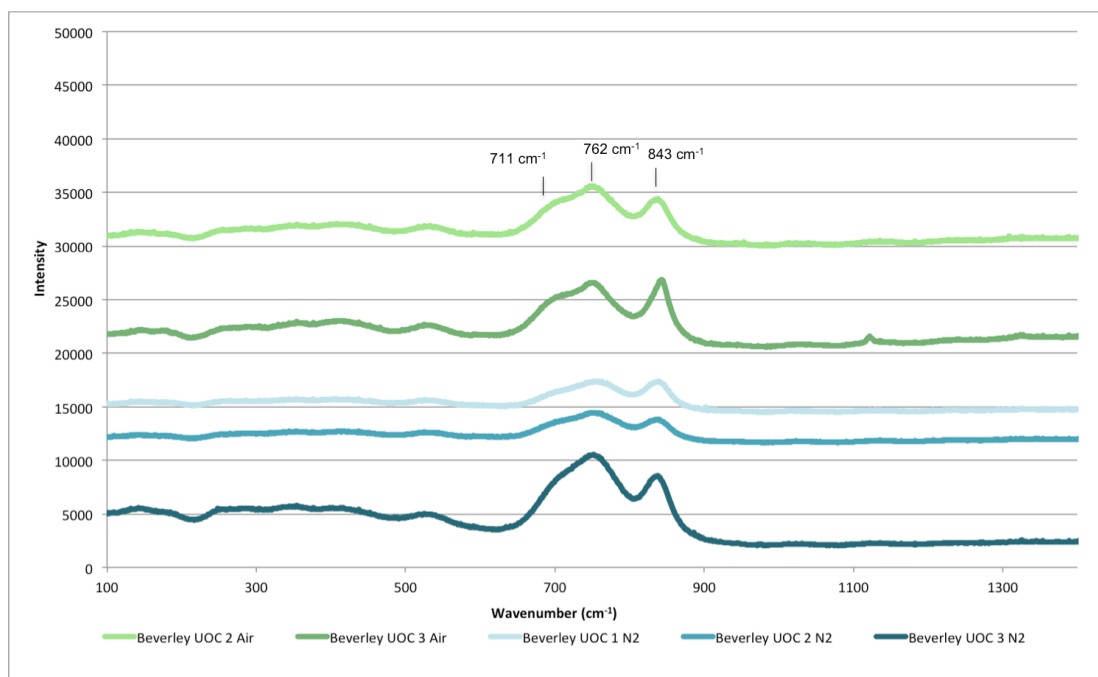


Figure 56 Raman spectra of the Beverley TGA intermediates obtained at 280 °C in both air and nitrogen atmospheres

Heating the Beverley samples further to 500 °C, the three same major Raman bands are observed (708, 769 and 848 cm^{-1}), however their intensities relative to one another have changed (Figure 57). The unidentified Raman band at 708 cm^{-1} is now the most intense band in the spectra, whereas the two other bands are now present as shoulder peaks. The presence of the 848 cm^{-1} band still suggests UO_3 is present, and the increase in the band at 708 cm^{-1} , and the absence of any new peak within the Raman spectra, suggest that the UO_3 degrades into this unknown uranium compound previously identified as forming before 280 °C.

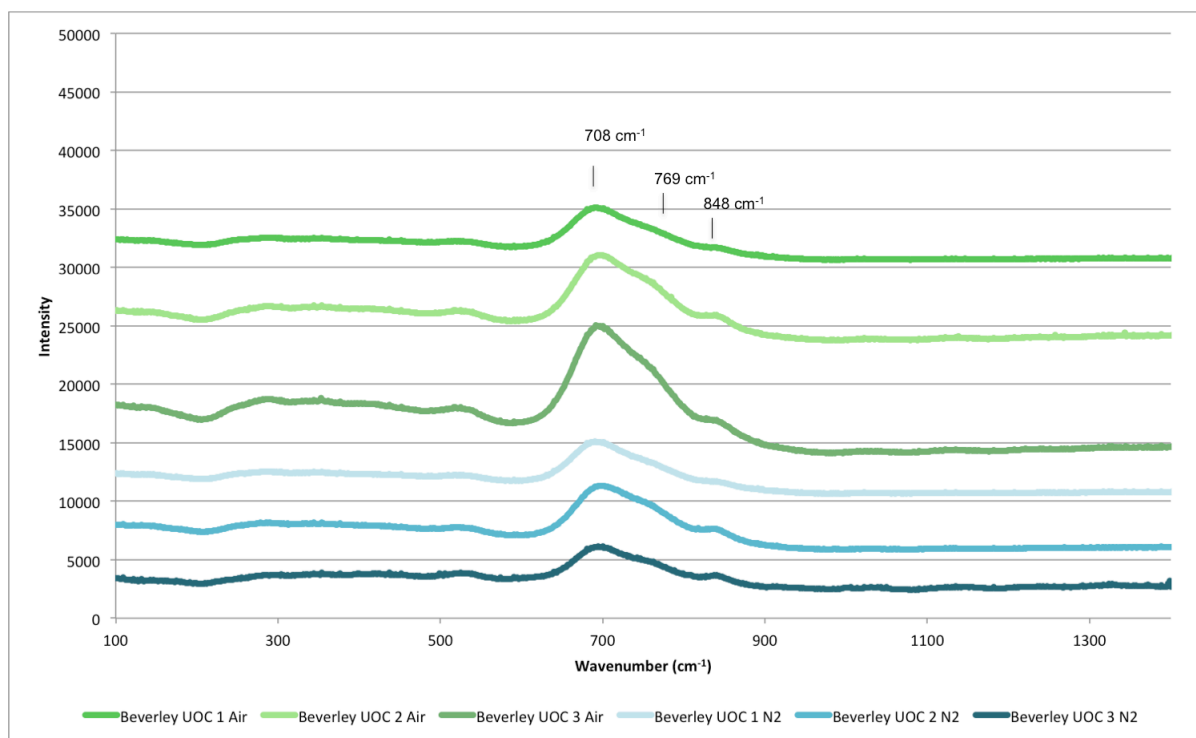


Figure 57 Raman spectra of the Beverley TGA intermediates obtained at 500 °C in both air and nitrogen atmospheres

Heating the sample further to 1000 °C leads to the removal of the Raman bands attributable to UO_3 and the unidentified uranium compound, while several bands characteristic of U_3O_8 are present (Figure 58). The Raman bands at 415 and $\sim 475 \text{ cm}^{-1}$ are the A_{1g} and E_g U-O stretching vibrations [211], while the U-O stretching vibration band present at 815 cm^{-1} is also characteristic of U_3O_8 [208, 209]. The formation of U_3O_8 is consistent with both proposed thermal decomposition pathways by Sato (1976), and Guo et al. (2016) and Odoh et al. (2016) [221].

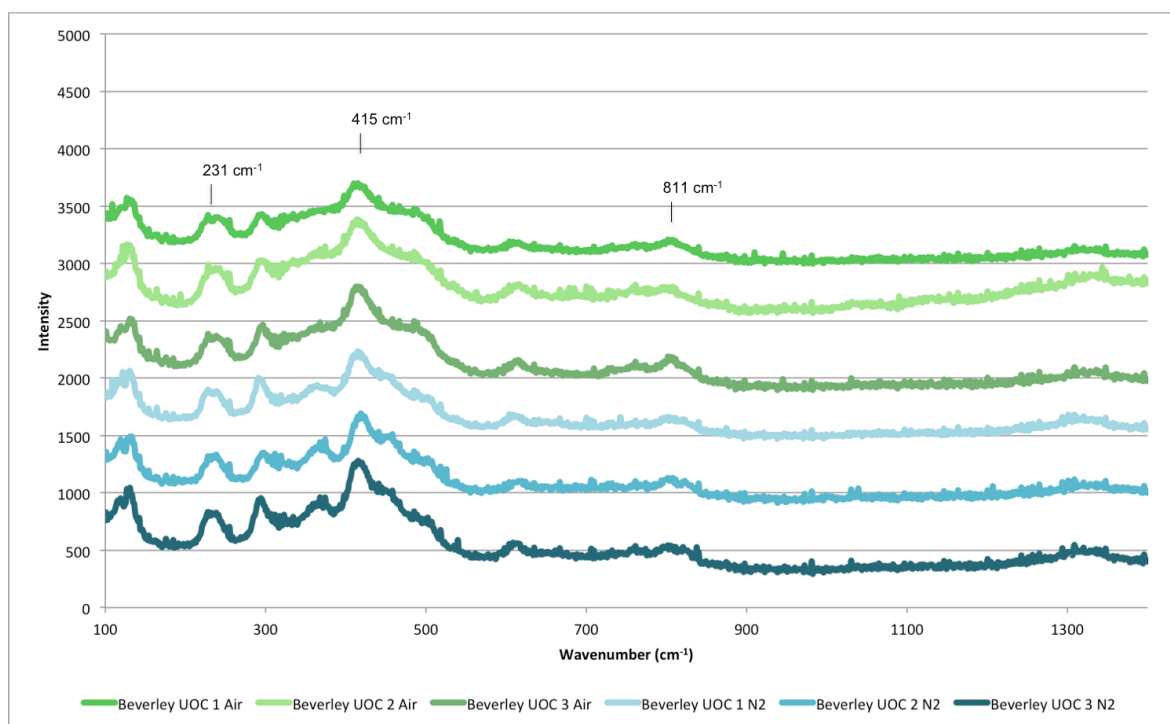


Figure 58 Raman spectra of the Beverley TGA products obtained at 1000 °C in both air and nitrogen atmospheres

4.3.4.2 Ranger UOCs

Within the Ranger UOC samples 1 and 3, Raman bands attributable to U_3O_8 (235, 420 and 811 cm^{-1}) and UO_3 (840 cm^{-1}) are present (Figure 59). Within Ranger UOC 2 however, only the three peaks attributable to U_3O_8 (235, 420 and 811 cm^{-1}) are observed with the single peak attributable to UO_3 is absent. However, the UO_3 band is present in the Raman spectra obtained from heating the Ranger UOCs to 200 °C in both air and nitrogen atmospheres (Figure 57).

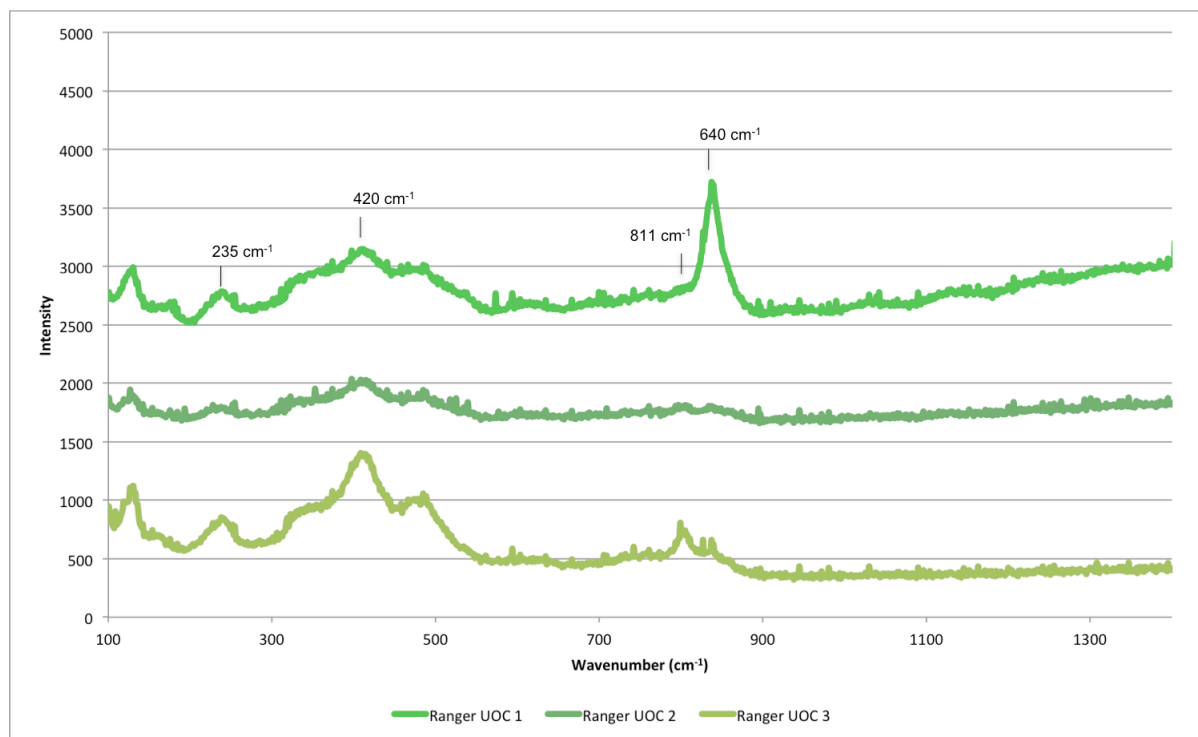


Figure 59 Raman spectra of the three Ranger UOCs

When heated to 200 °C, no change observed in spectra obtained from the three Ranger UOCs in both air and nitrogen atmospheres, with the Raman band attributable to U_3O_8 (420 and 811 cm^{-1}) and UO_3 (840 cm^{-1}) present (Figure 60). The wavenumber of one U_3O_8 band has shifted from 231 cm^{-1} to 253 cm^{-1} as seen within the original Ranger UOC (Figure 59), however the cause and significance of this is not known.

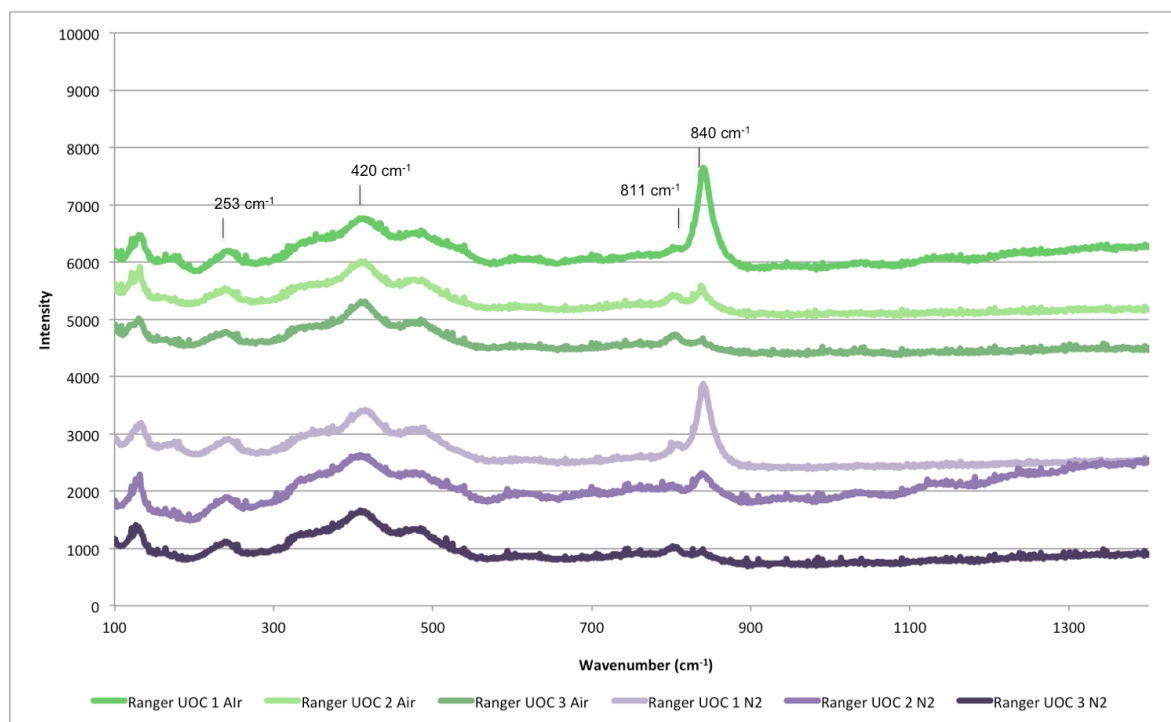


Figure 60 Raman spectra of the Ranger TGA intermediates obtained at 200 °C in both air and nitrogen atmospheres

Heating the Ranger samples to 500 °C in both atmospheres also leads to the evolution of an unknown intermediate with a broad Raman band at 680 cm^{-1} within the Ranger 1 sample, in addition to several bands attributable to U_3O_8 (254, 419 and 811 cm^{-1}) being present in all three TGA intermediates (Figure 61). The formation of this unknown intermediate coincides with the loss of UO_3 , as evidenced by the loss of the 840 cm^{-1} band, suggesting they are linked. However, a similar broad band at 680 cm^{-1} is not observed in the spectra of Ranger UOCs 2 and 3, which previously featured the UO_3 band at 840 cm^{-1} in the spectra.

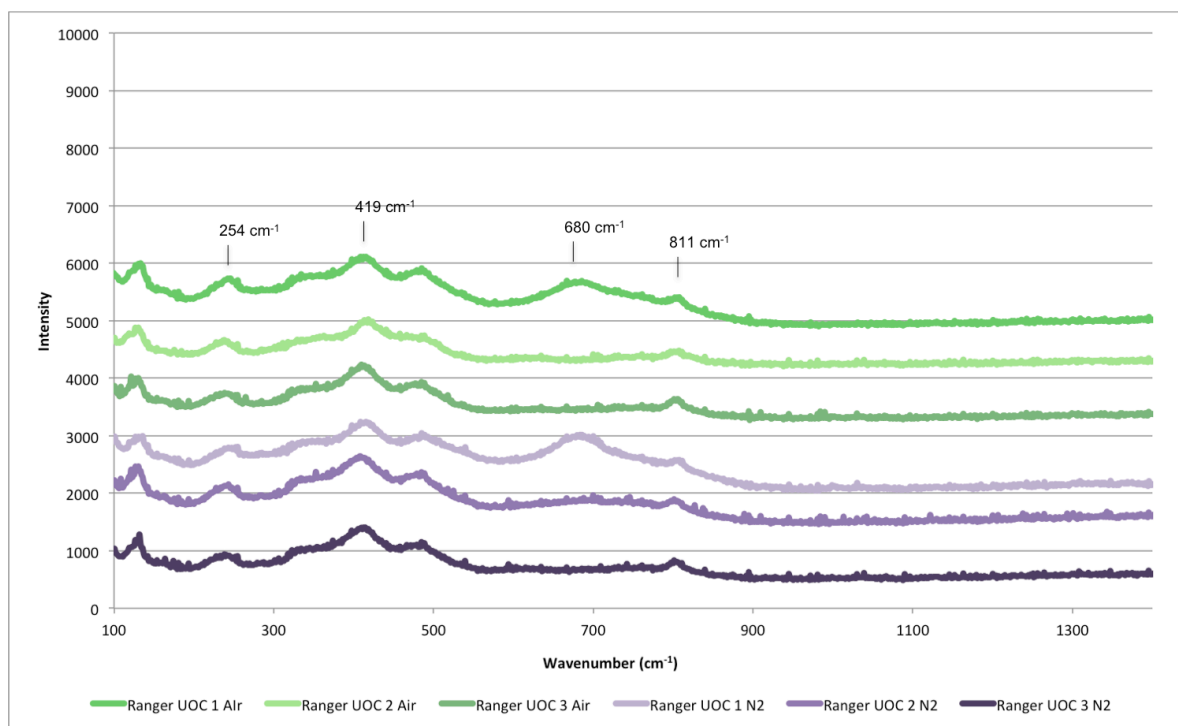


Figure 61 Raman spectra of the Ranger TGA intermediates obtained at 500 °C in both air and nitrogen atmospheres

Upon heating the Ranger UOC samples further to 1000 °C, several peaks attributable to U₃O₈, are present (251, 423 and 812 cm⁻¹) (Figure 62). The unknown intermediate that was previously identified at 680 cm⁻¹ in the spectra obtained after heating the Ranger samples to 500 °C is no longer present, which strongly suggesting that it decomposed to form U₃O₈.

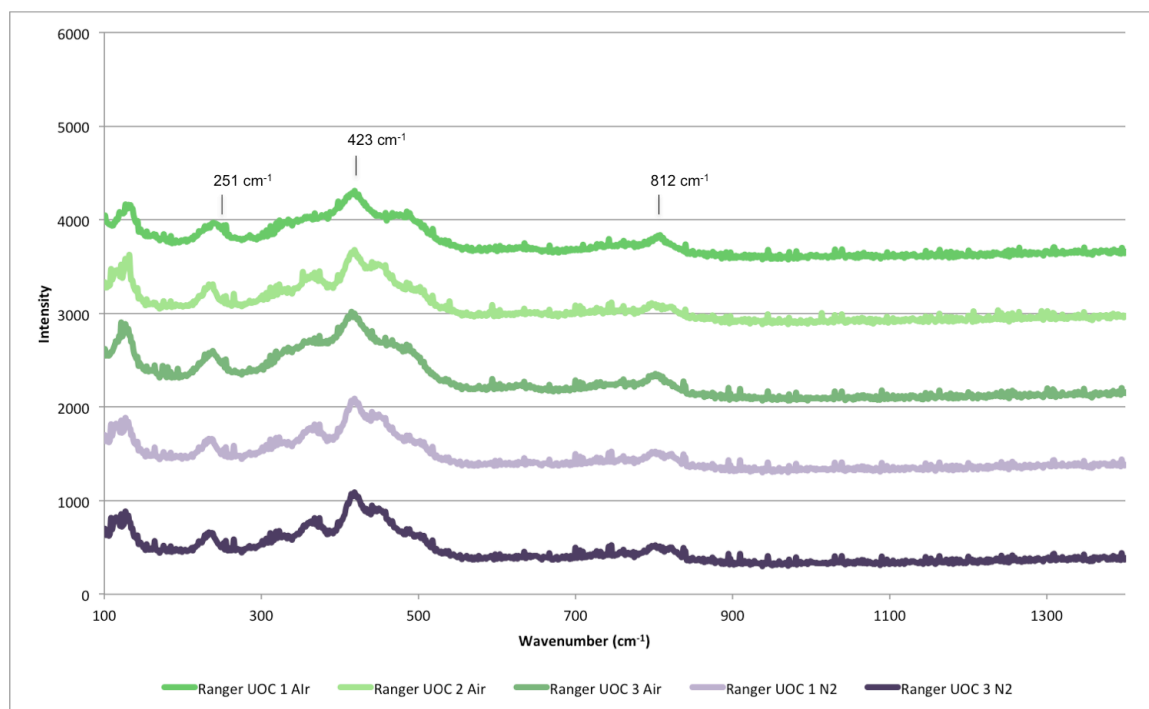


Figure 62 Raman spectra of the Ranger TGA intermediates obtained at 1000 °C in both air and nitrogen atmospheres

4.3.4.3 Olympic Dam UOCs

The two Olympic Dam UOCs feature Raman bands characteristic of both U_3O_8 (241, 423 cm^{-1}) and UO_3 (843 cm^{-1}), with Olympic Dam UOC 1 featuring a larger UO_3 band (Figure 63).

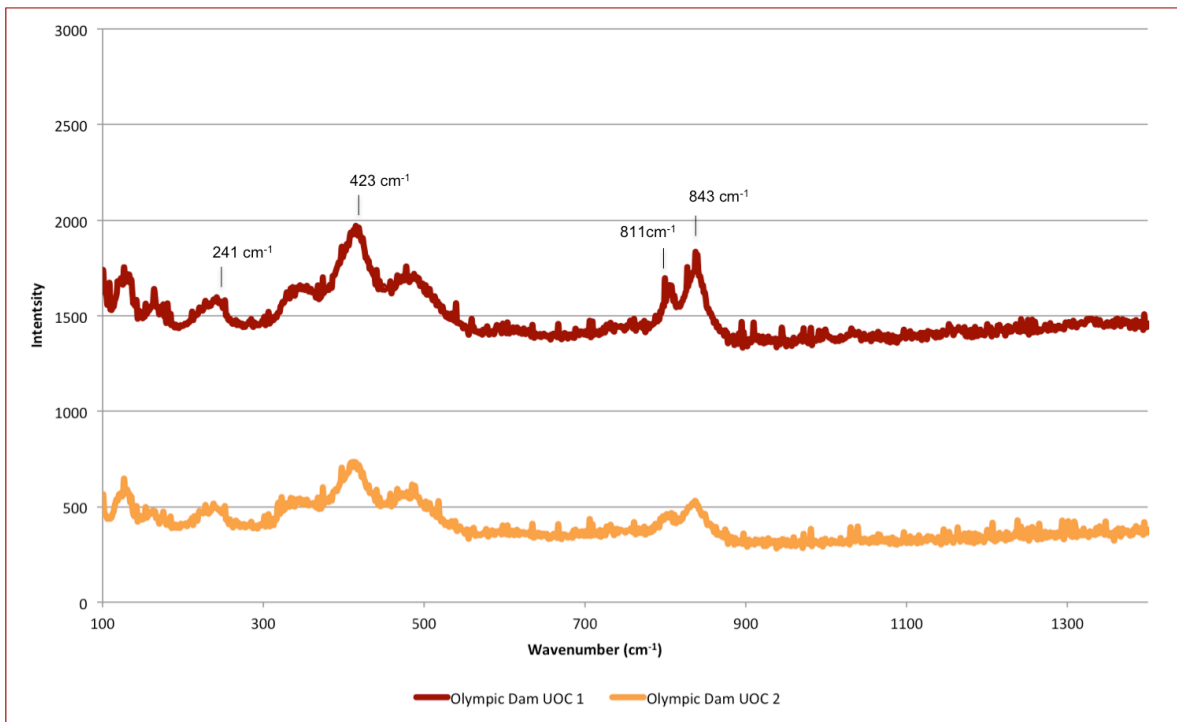


Figure 63 Raman spectra of the two Olympic Dam UOCs

Upon heating the Olympic Dam UOC samples to 200°C in air and nitrogen atmospheres, no change is observed in the Raman spectra with peaks attributable to both U_3O_8 (245, 423 and 810 cm^{-1}) and UO_3 (840 cm^{-1}) present (

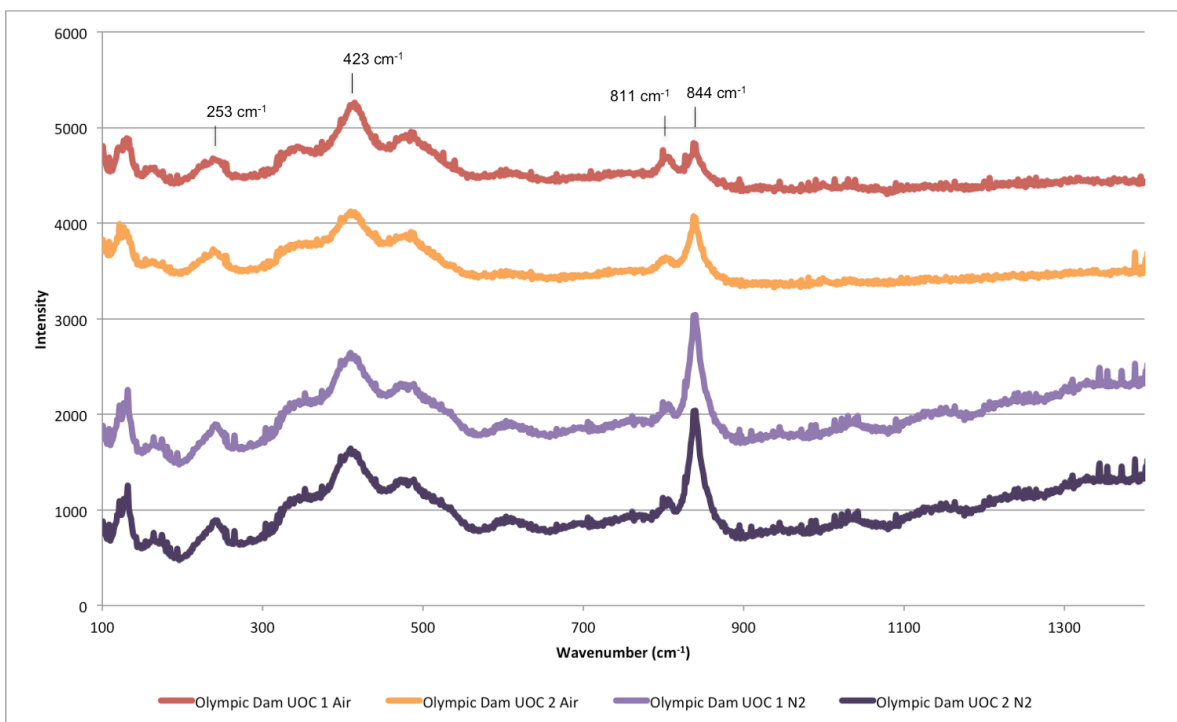


Figure 64).

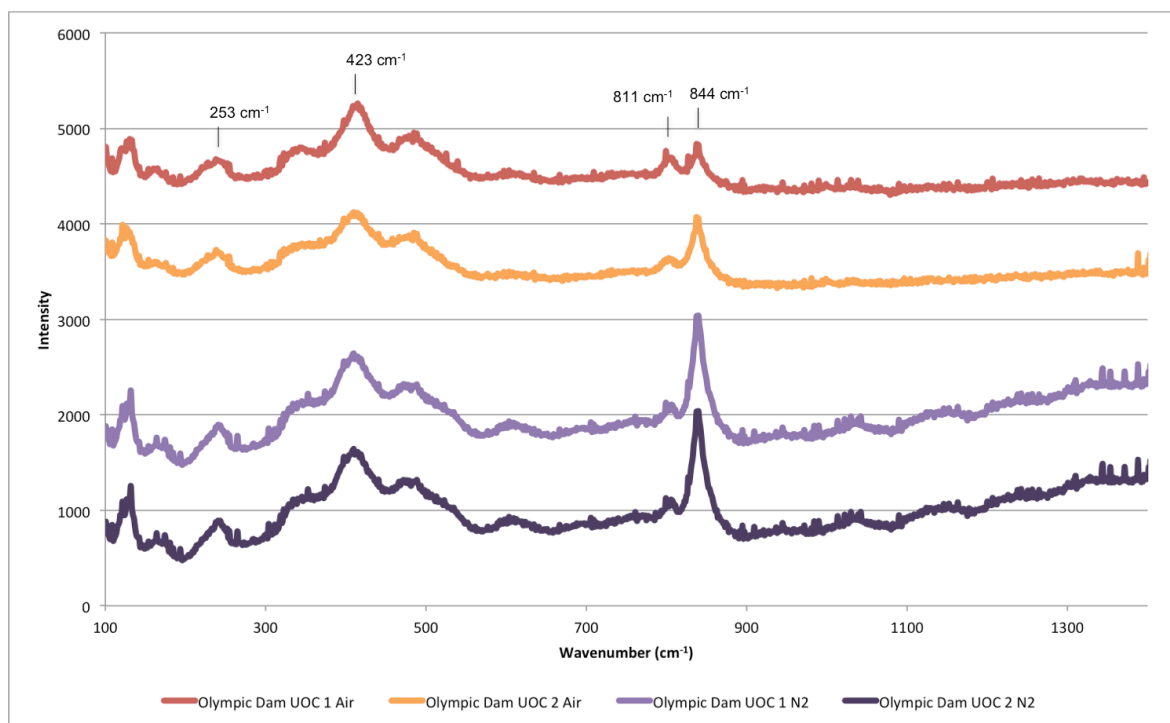


Figure 64 Raman spectra of the Olympic Dam TGA intermediates obtained at 200 °C in both air and nitrogen atmospheres

Heating the Olympic Dam samples to 500 °C results in the formation of a broad band at 681 cm⁻¹, along with the U₃O₈ bands at 245, 419 and 810 cm⁻¹, similar to the Ranger UOC 1 sample (Figure 65). This peak, and consequently this unknown intermediate, is consistently observed within both Olympic Dam samples, whereas it is only observed in the Ranger UOC 1 sample when heated to 500 °C.

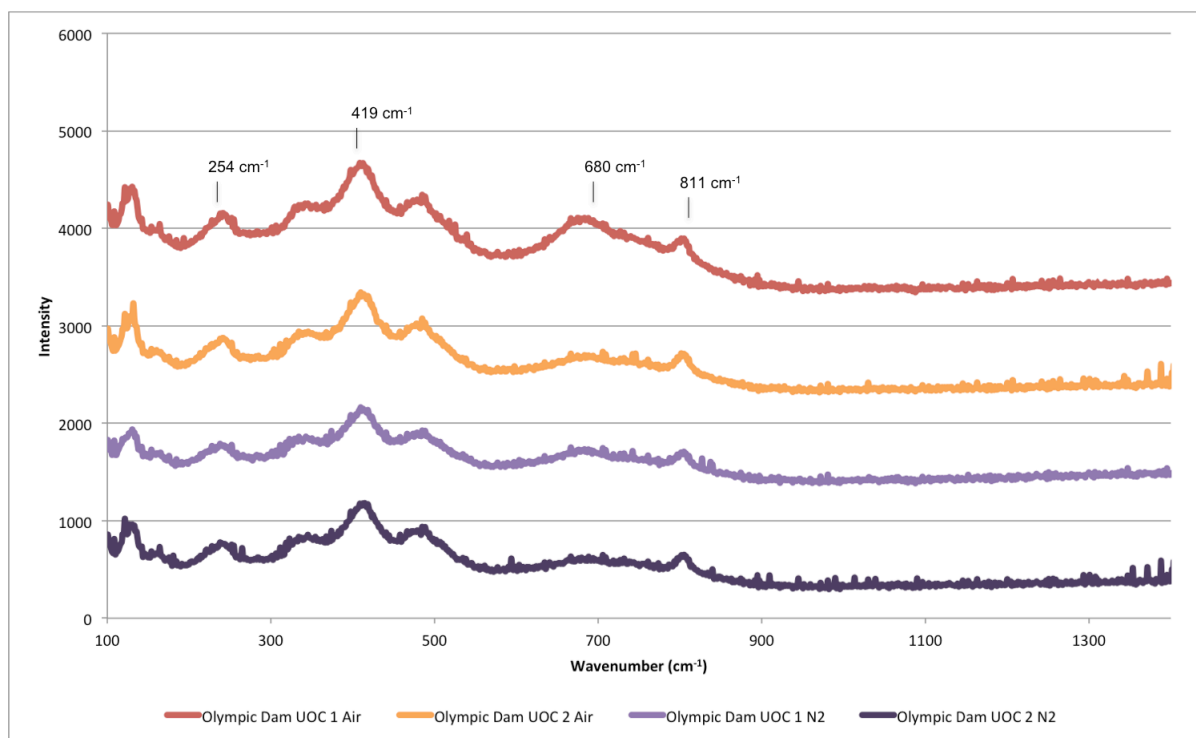


Figure 65 Raman spectra of the Olympic TGA intermediates obtained at 500 °C in both air and nitrogen atmospheres

Upon heating to 1000 °C, only bands attributable to U₃O₈ (251, 423 and 812 cm⁻¹) are observed in the Raman spectra (Figure 66). The unknown intermediate, which formed after heating the Olympic Dam UOCs beyond 200 °C, is no longer present within the spectra, which again suggests it thermally decomposes to U₃O₈ at between 600-700°C.

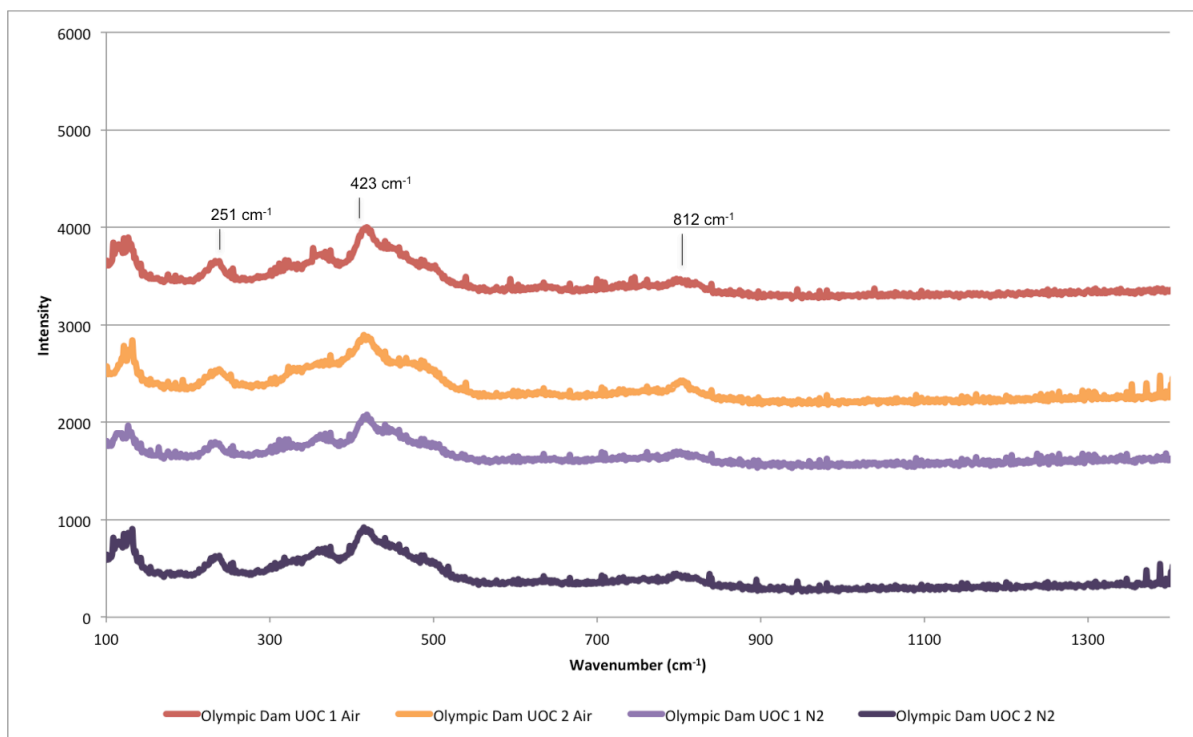


Figure 66 Raman spectra of the Olympic Dam TGA intermediates obtained at 1000 °C in both air and nitrogen atmospheres

4.3.5 X-ray diffraction

XRD was performed on one of each of the Beverley, Ranger and Olympic Dam UOCs and their respective intermediates and TGA products collected at various temperatures. With the Beverley UOC 1 sample, an amorphous phase is formed when heated to 280 °C in an air atmosphere (Figure 67). Both suggested thermal decomposition pathways of uranyl peroxide suggest an amorphous phase, with Sato (1976) suggesting amorphous- UO_3 is formed whilst Guo *et al.* (2016) and Odoh *et al.* (2016) both suggesting amorphous- U_2O_7 is instead formed [218, 221, 223]. The pattern of the Beverley intermediate collected at 500 °C featured a $\text{UO}_3 \cdot \text{H}_2\text{O}$ phase (reference number 00-0530877), which disagrees with Guo *et al.* (2016) and Odoh *et al.* (2016) who suggest an amorphous UO_3 is instead formed at 500 °C [221, 223]. Sato (1976) suggested thermal decomposition pathway however identified $\alpha\text{-UO}_3$ as the uranium compound that would be present, following the recrystallization of amorphous- UO_3 to $\alpha\text{-UO}_3$ at 485 °C [218]. Heating the Beverley UOC sample further to 1000 °C produces U_3O_8 (reference number 01-089-4906), which is the final product both thermal decomposition pathways agree forms, and is positively identified by Raman spectroscopy (Figure 58).

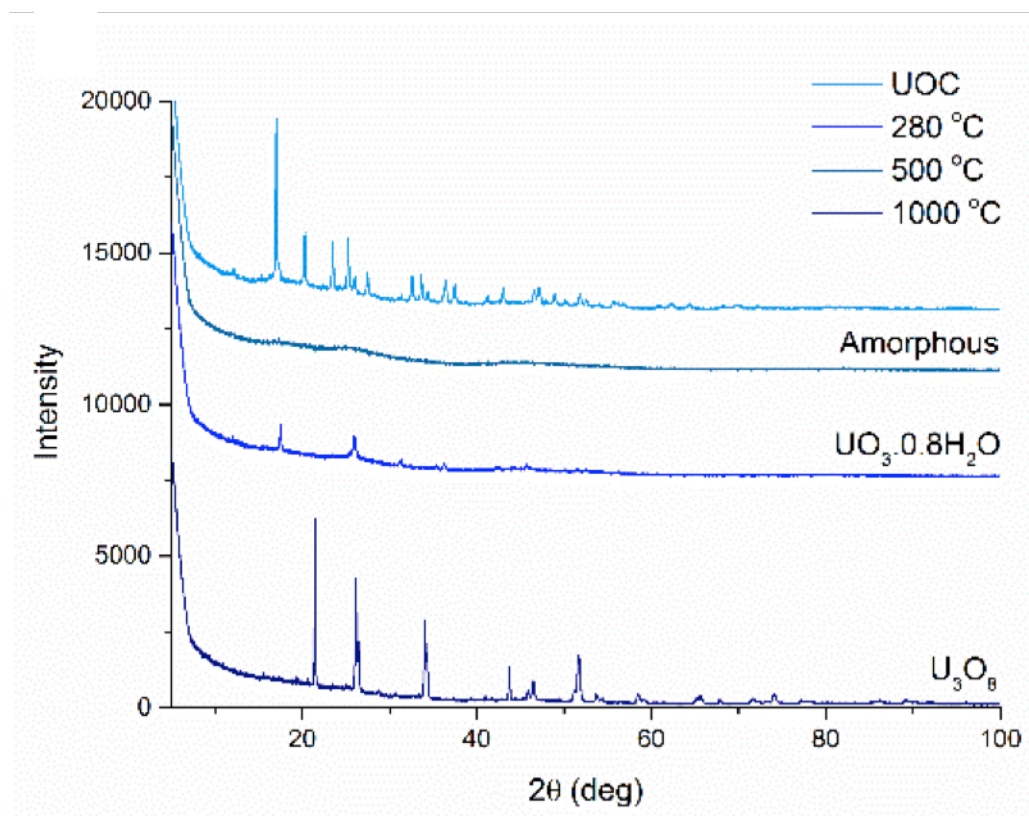


Figure 67 X-ray diffraction patterns of Beverley UOC 1, the two intermediates obtained at 280 °C and 500 °C, and the TGA product obtained via TGA in an air atmosphere at 1000 °C

XRD identified the phases of U_3O_8 and $UO_3 \cdot H_2O$ within the Ranger TGA intermediate collected at 200 °C (reference numbers 00-047-1493 and 00-012-0043, respectively), however heating further to 500 °C leaves a pattern consisting of only U_3O_8 (reference number 01-074-2101) (Figure 68). The Ranger UOC 2, was not found to feature new band appearing at 680 cm^{-1} within Raman spectra collected at 500 °C following the decomposition of UO_3 (Figure 61). No further change is observed in the XRD pattern when the Ranger UOC 2 sample was heated further to 1000 °C.

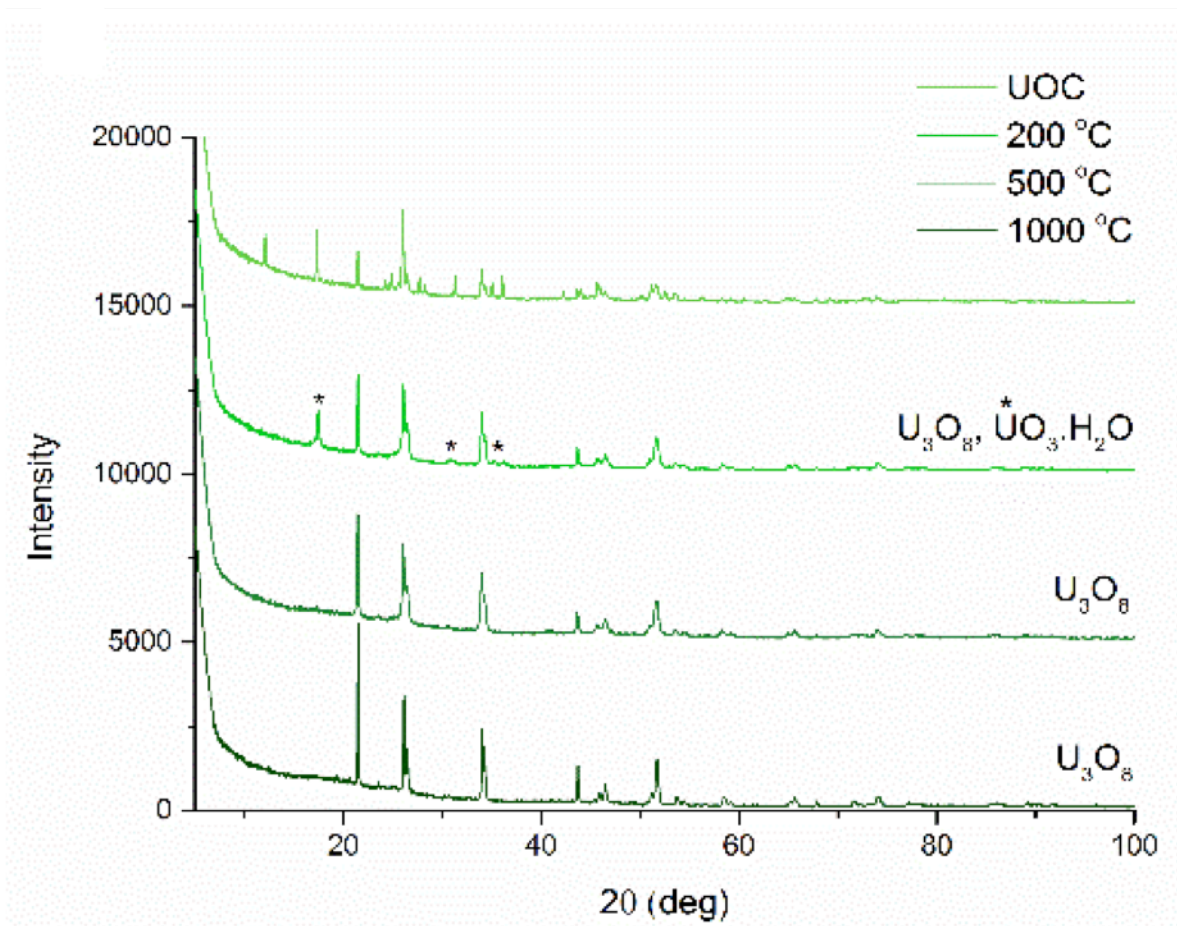


Figure 68 X-ray diffraction patterns of Ranger UOC 2, the two intermediates obtained at 280 °C and 500 °C, and the TGA product obtained via TGA in an air atmosphere at 1000 °C

The XRD patterns of the Olympic Dam UOC 2 sample show no change in the composition upon heating to 200 °C, with $\text{UO}_3 \cdot 0.8\text{H}_2\text{O}$ and U_3O_8 observed (reference numbers 00-0530877 and 01-074-2101, respectively) (Figure 68). Upon heating further to 500 °C, only a single phase of U_3O_8 is observed (reference number 00-47-1493). In the Raman spectra obtained from the Olympic Dam UOCs, a new Raman band appeared at 680 cm^{-1} within Raman spectra collected at 500 °C following the decomposition of UO_3 (Figure 65), as identified by a band at 840 cm^{-1} within both the original UOC (Figure 63), and the TGA intermediate collected at 200 °C (

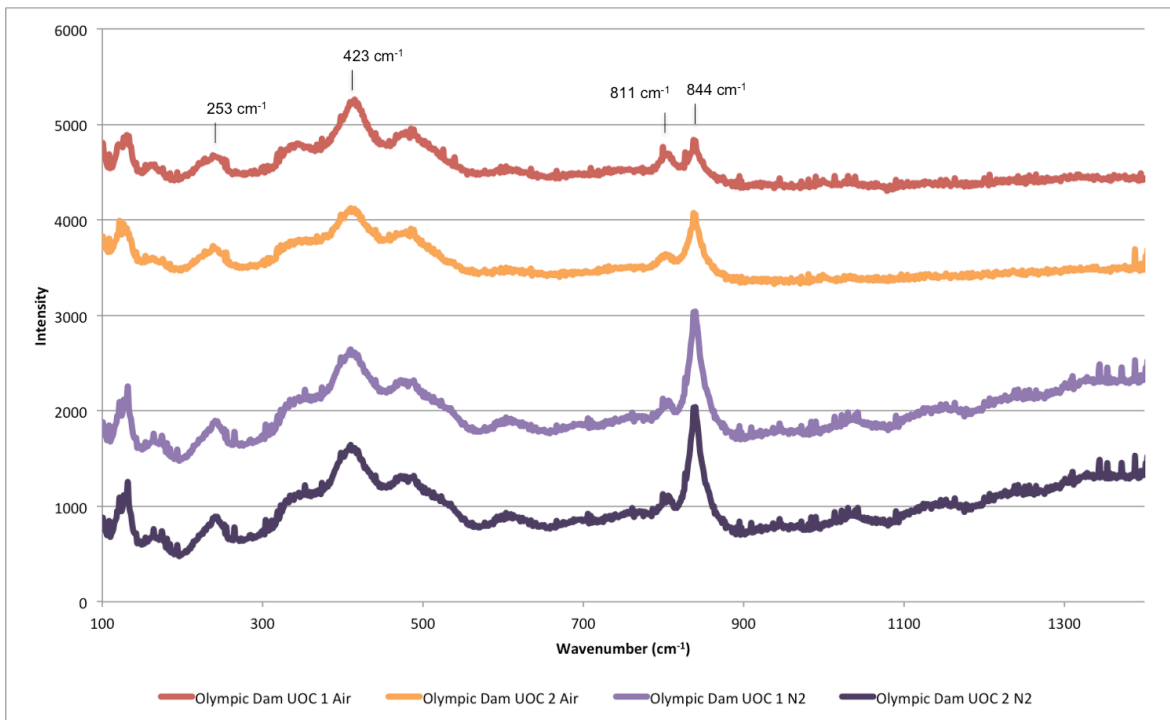


Figure 64). It is not known why these two datasets are in disagreement, and requires further research identify the reason(s) behind this discrepancy. In the final XRD pattern obtained from heating the Olympic Dam UOC 2 sample to 1000 °C within an air atmosphere, a single phase of U_3O_8 is observed (reference number 00-47-1493).

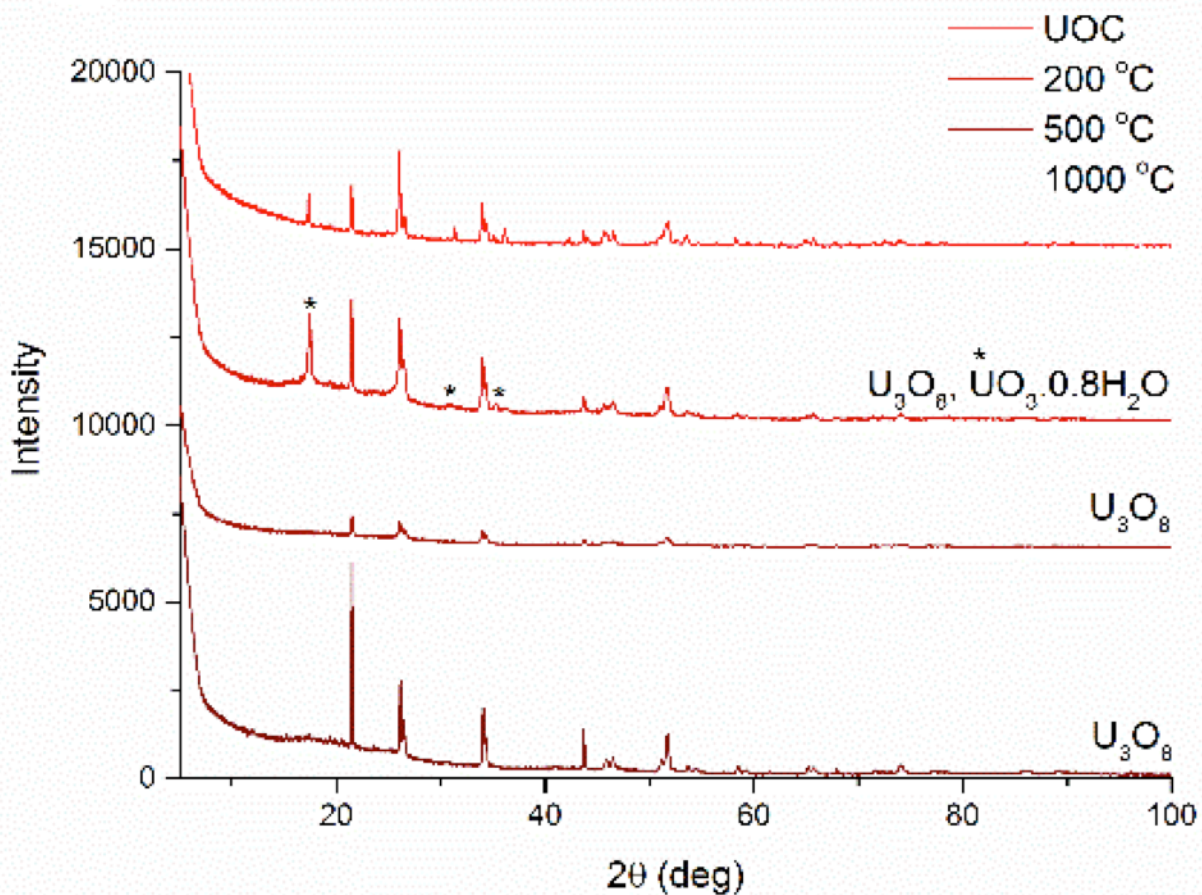


Figure 69 X-ray diffraction patterns of Olympic Dam UOC 1, the two intermediates obtained at 280 °C and 500 °C, and the TGA product obtained via TGA in a air atmosphere at 1000 °C

4.3.5 Comparison of TGA traces between the Australian UOCs

In a comparison between the TGA traces of the eight Australian UOCs, the three Beverley UOCs were found to be the most distinct group of UOCs analysed (Figure 70) with the U_3O_8 samples from Ranger and Olympic Dam featuring more similar traces. The capability of TGA to differentiate between UOCs from different sources is primarily based upon differences in the major speciation of the UOC samples, however the difference in water content also contributes as it allows Ranger and Olympic Dam UOCs to be differentiated from another (Figure 71). The major speciation and moisture of a UOC reflects the latter stages of the UOC production process, where the uranium is precipitated out (using one of a variety of different precipitation agents available), before it is dried and potentially undergo calcination.

The TGA traces permit a differentiation between UOCs of different speciations (i.e. UO_4 vs U_3O_8), the ability for TGA, as with other techniques such as Raman spectroscopy, XRD and NIR, to

differentiate between UOCs of the same speciation will largely depend on the UOCs themselves. The UOCs from Ranger and Beverley exhibited a large degree of intra-mine variability compared to the UOCs from Olympic Dam, which makes identifying a feature, features or the entire TGA trace characteristic for those two mines significantly more difficult than for the Olympic Dam UOCs. The consistency of the minor speciations and moisture of a UOC is critically important for differentiating between UOCs of the same speciation as seen between the Ranger and Olympic Dam UOCs, and is dependent on the consistency of the UOC production process. Small changes in the production process could have significant impacts on the TGA traces; for example, the amount of $\text{UO}_4 \cdot 2\text{H}_2\text{O}$ and $\text{UO}_4 \cdot 4\text{H}_2\text{O}$ formed through the addition of hydrogen peroxide is dependent upon the precipitation temperature: at $<50\text{ }^\circ\text{C}$, the $\text{UO}_4 \cdot 4\text{H}_2\text{O}$ compound is made whereas at $>70\text{ }^\circ\text{C}$, the $\text{UO}_4 \cdot 2\text{H}_2\text{O}$ compound is produced [230]. A small increase in temperature (or decrease, depending on what compound is the desired product) during the precipitation could cause enough of the alternative compound to form and could significantly impact the resultant TGA trace. Understanding the variability in the composition of UOC from a particular will be crucial in further evaluating the capability of TGA for the differentiation of UOCs from different sources.

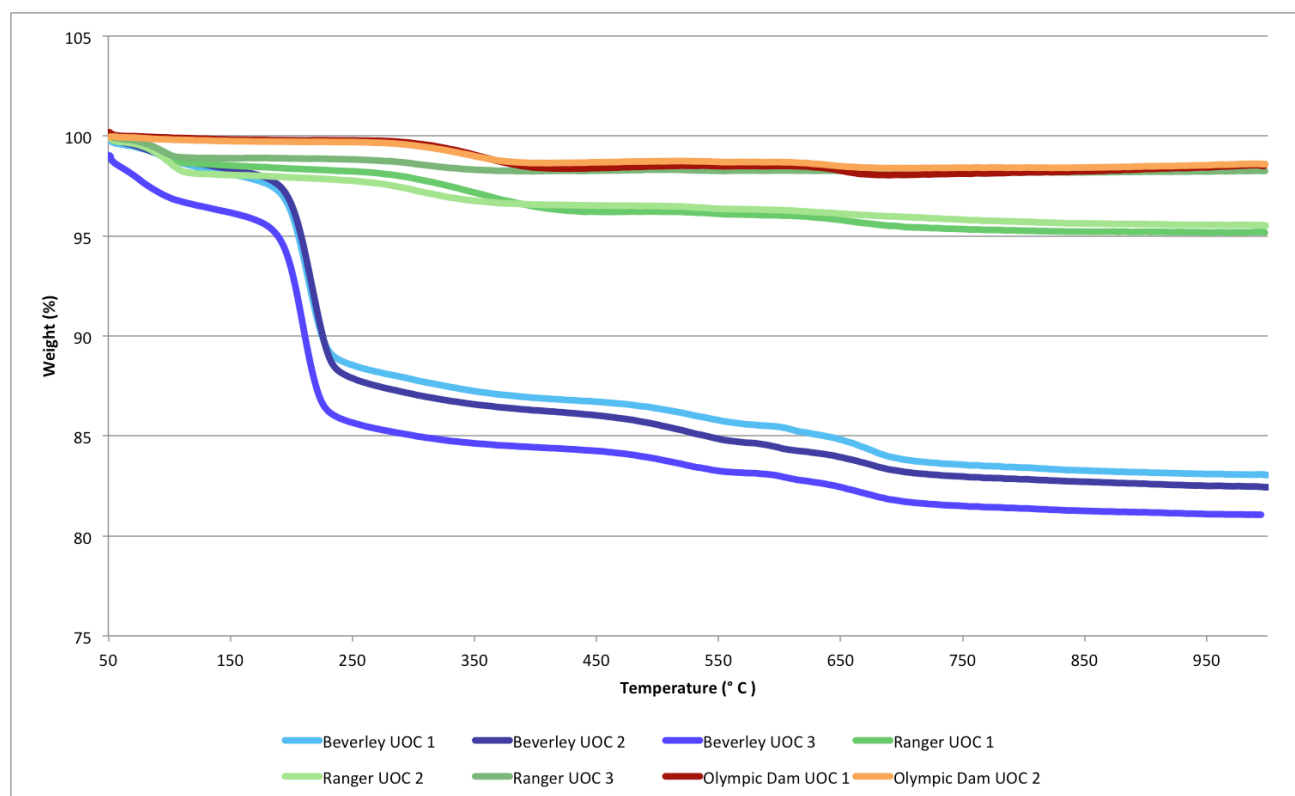


Figure 70 Analysis of Australian UOC samples by TGA in an air atmosphere

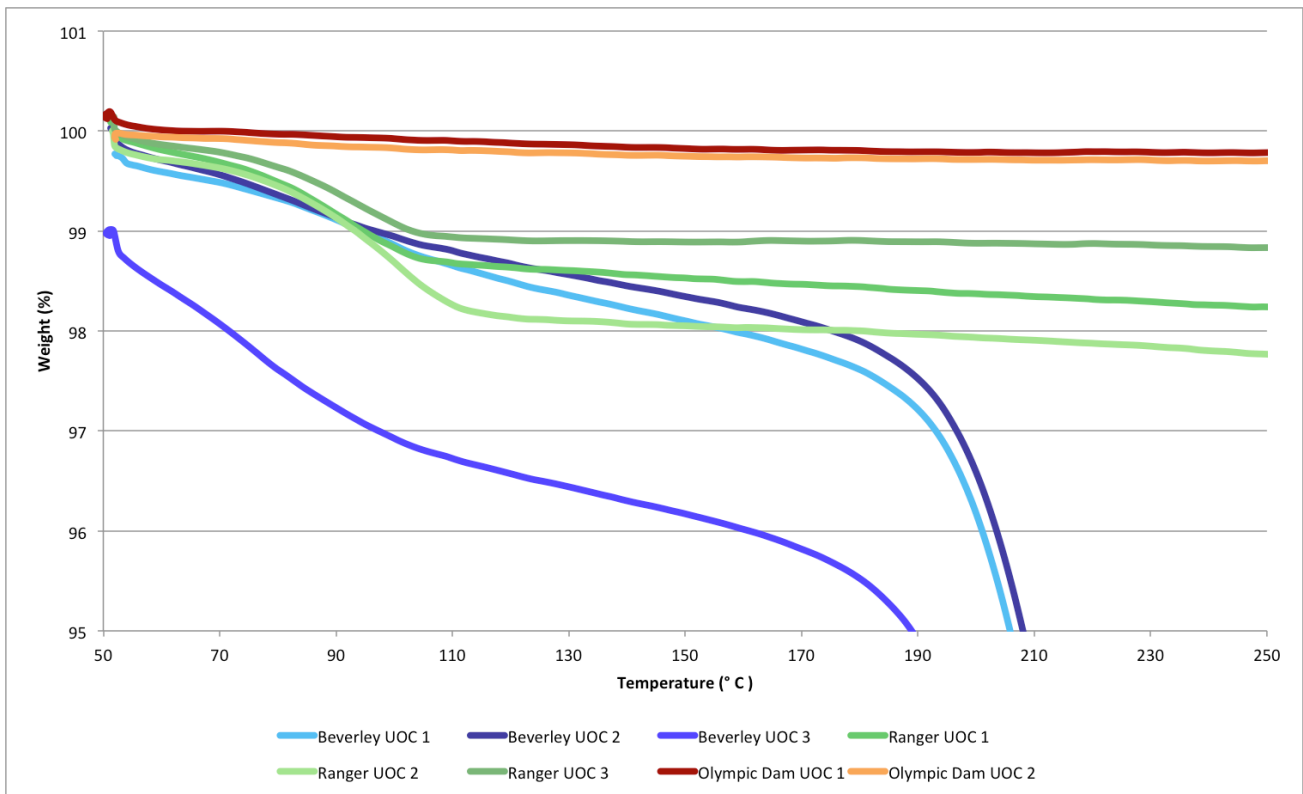


Figure 71 Expanded graph of the 50-250 °C region of the TGA plot of the Australian UOCs analysed in an air atmosphere

4.3.5 Analysis of UOC morphology and the impact of temperature by SEM

As the morphology of UOCs is a valuable parameter to compare and/or distinguish between different sources, as it reflects of the latter metallurgical processes used during the production of UOCs, the Beverley, Ranger and Olympic Dam samples were analysed by SEM. This would not only allow for the identification of distinctive morphological features within UOCs from each mine, but also assess the potential impact that high temperatures experienced through analysis by TGA might have on these morphologies.

4.3.5.1 Beverley UOCs

At low magnifications ($\leq 1000\times$), the three UOCs from Beverley were found to primarily consist of small irregular agglomerates, with larger agglomerates interspersed throughout (Figure 72). At higher magnifications ($\geq 30,000\times$), the distinctive morphology, when compared to the UOCs from Ranger and Olympic Dam, become evident. All three UOCs from Beverley appear to consist primarily of thin rectangular platelets, however some intra-mine variability is observed (Figure 73). Compared to Beverley UOCs 1 and 3, the platelets within Beverley 2 UOC sample appear be thinner and elongated, as well as feature more equiaxed platelets.

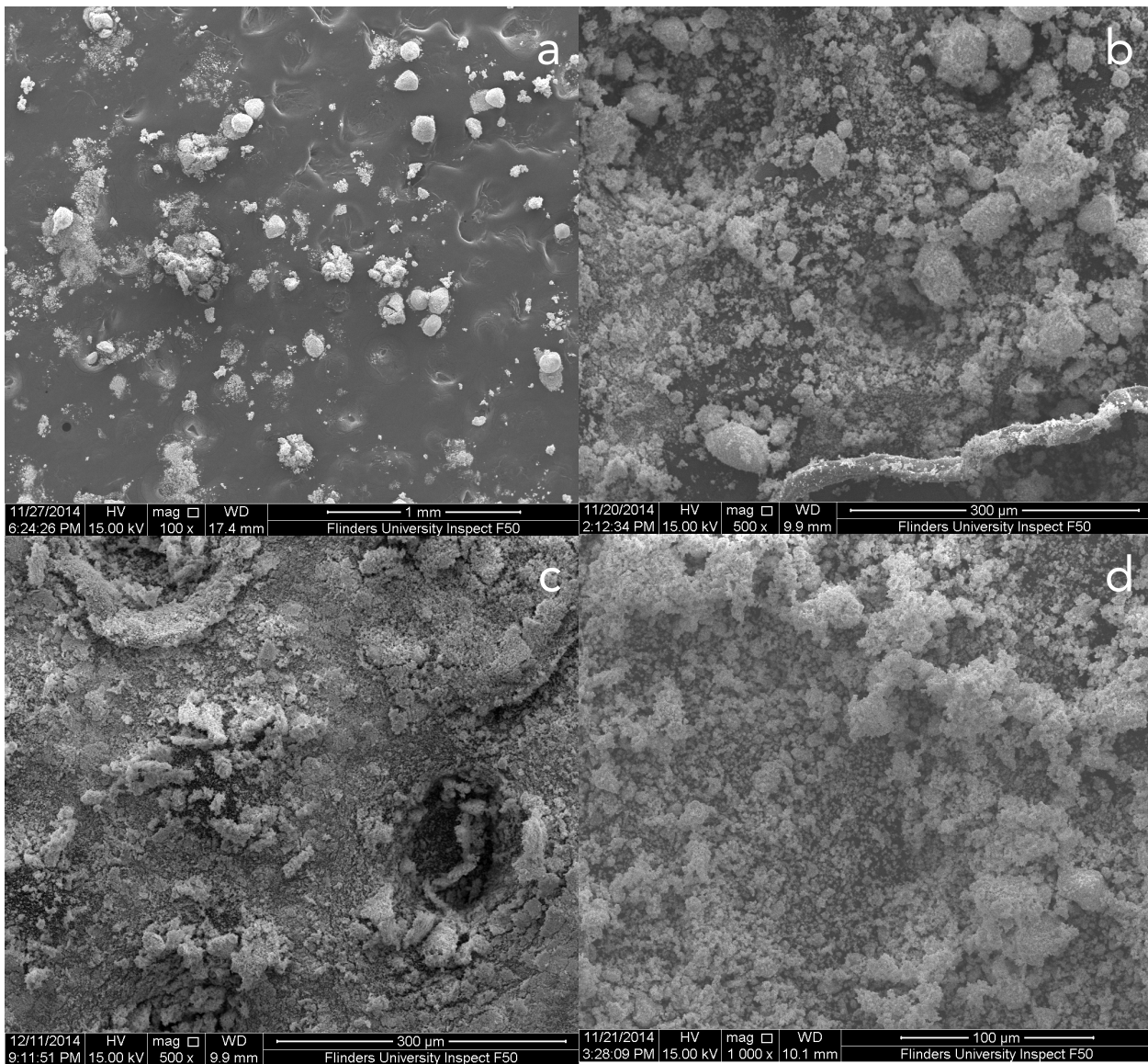


Figure 72 SEM images of the Beverley UOCs at various magnifications: a) Beverley UOC 1 at 500x, b) Beverley UOC 1 at 500x, c) Beverley UOC 2 at 500x and d) Beverley UOC 3 at 1000x

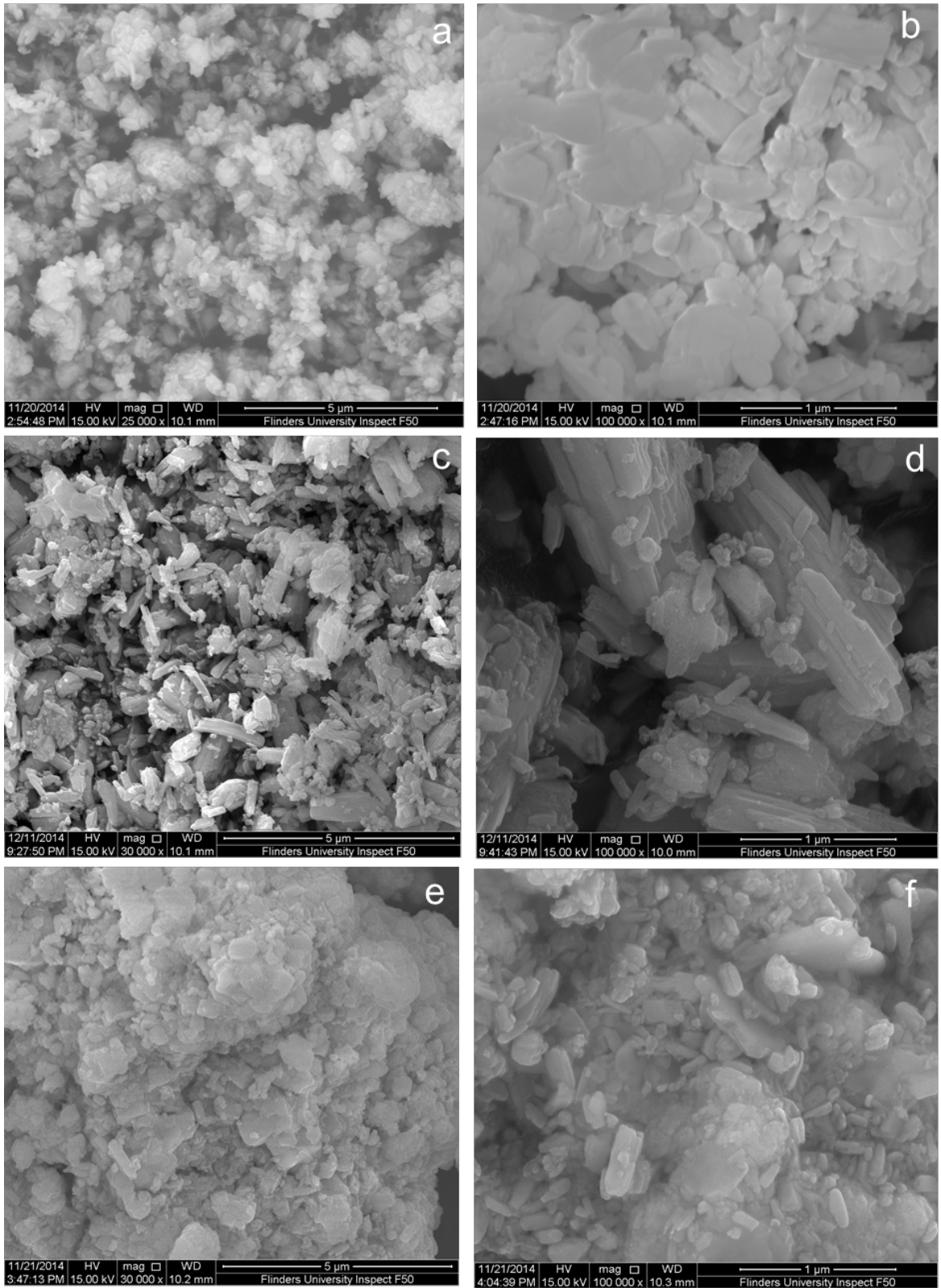


Figure 73 SEM images of Beverley UOCs at various magnifications; a) Beverley UOC 1 at 30,000x, b) Beverley UOC 1 at 100,000x, c) Beverley UOC 2 at 30,000x, d) Beverley UOC 2 at 100,000x, e) Beverley UOC at 30,000x and f) Beverley UOC 3 at 100,000x

4.3.5.2 Ranger UOCs

The three Ranger UOCs were found to be similar to the Beverley UOCs at low magnification ($\leq 100x$), as they were also found to primarily consist of smaller irregular agglomerates with larger structures also present (Figure 74). The only observable difference was the Beverley UOCs appeared to feature the larger agglomerates at a greater frequency than the Ranger UOCs.

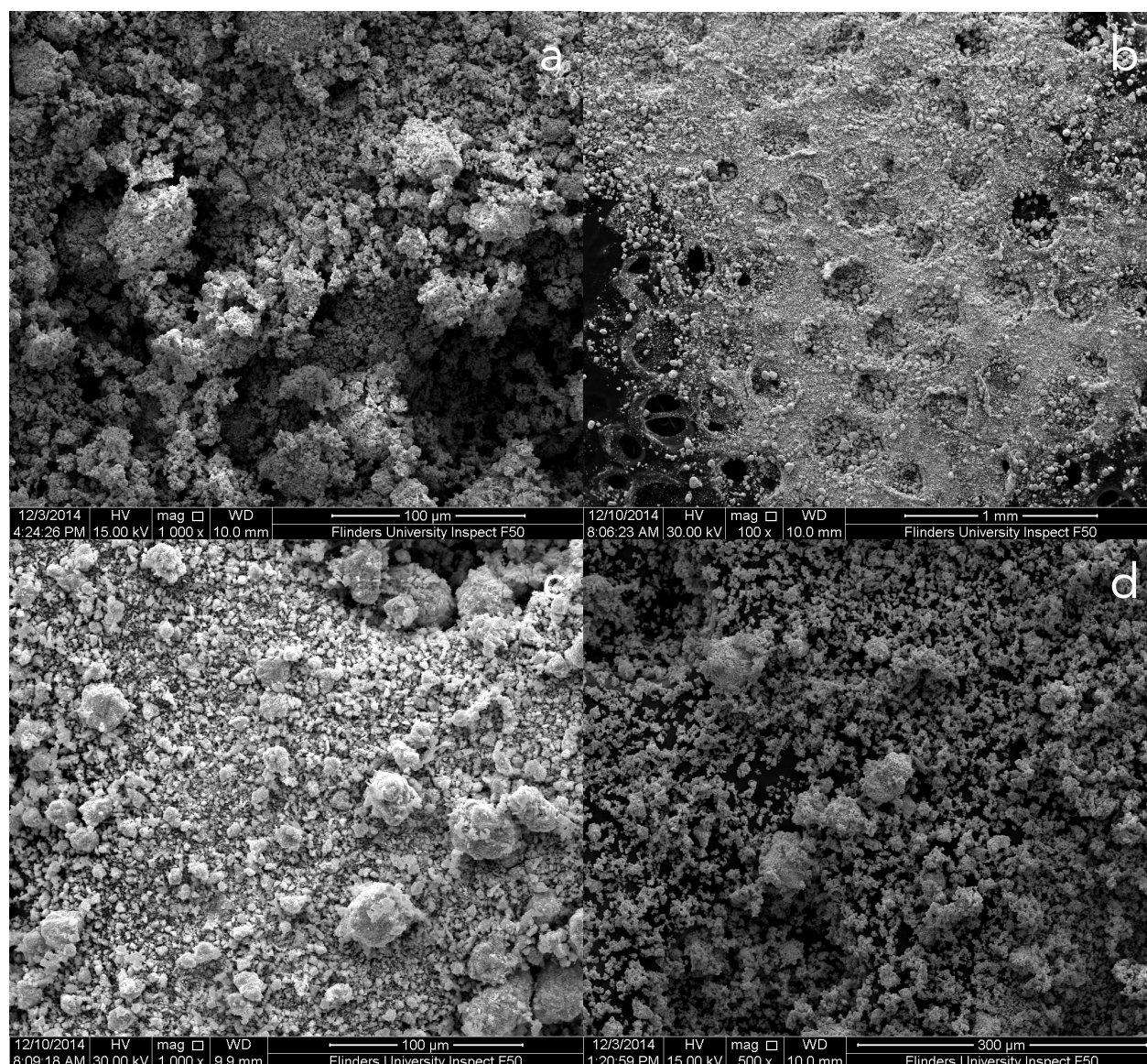


Figure 74 SEM images of the three Ranger UOCs at various magnifications; a) Ranger UOC 1 at 1000x, b) Ranger UOC 2 at 500x, c) Ranger UOC 2 at 1000x and d) Ranger UOC 3 at 500x

Of the three different UOCs analysed in this study, the three UOCs from Ranger were found to be the most complex, with four different morphological features observed; rod-like structures, large smooth-faced structures, globular structures and quasi-cuboidal structures (Figure 75). The globular structures were found to have slightly different morphology in Ranger UOC 1, when compared to

Ranger UOCs 2 and 3, where they had a more jagged appearance and the ends terminating into points (Figure 76).

4.3.5.3 Olympic Dam UOCs

At a low magnification ($\leq 1000\times$), the two Olympic Dam UOCs had the most unique structures of the Australian UOCs analysed, as they predominantly feature smooth spherical agglomerates which varied in size between ~ 5 to $55\ \mu\text{m}$ (Figure 77). At higher magnifications ($30,000\times$ and $100,000\times$ magnification), Olympic Dam UOCs were found to consistently feature predominantly small, globular structures with a number of rod-like structures also present, with no intra-mine variability observed (Figure 78).

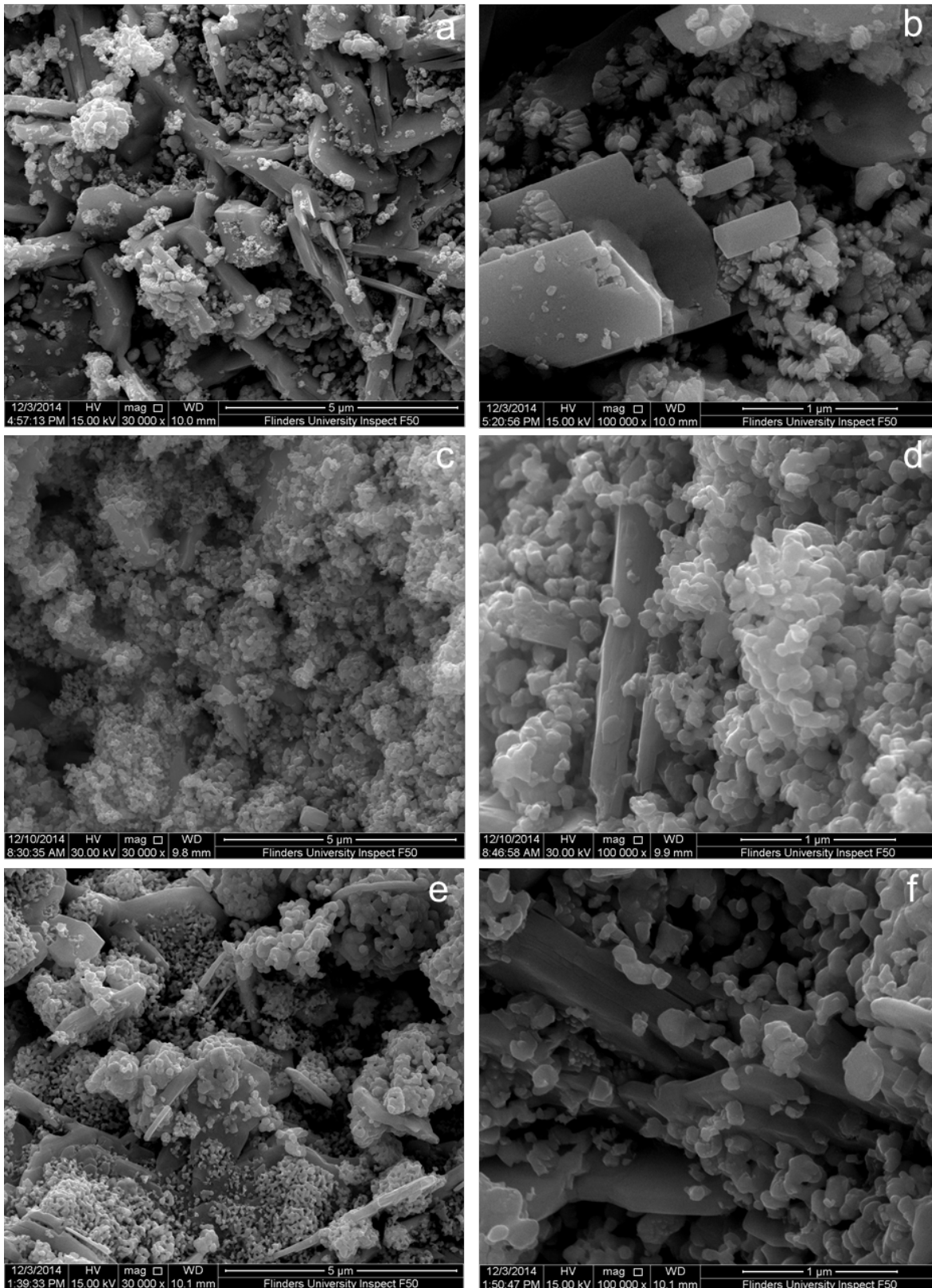


Figure 75 SEM images of the three Ranger UOCs at various magnifications; a) Ranger UOC 1 at 30,000x, b) Ranger UOC 1 at 100,000x, c) Ranger UOC 2 at 30,000x, d) Ranger UOC 2 at 100,000x, e) Ranger UOC 3 at 30,000x and f) Ranger UOC 3 at 100,000x

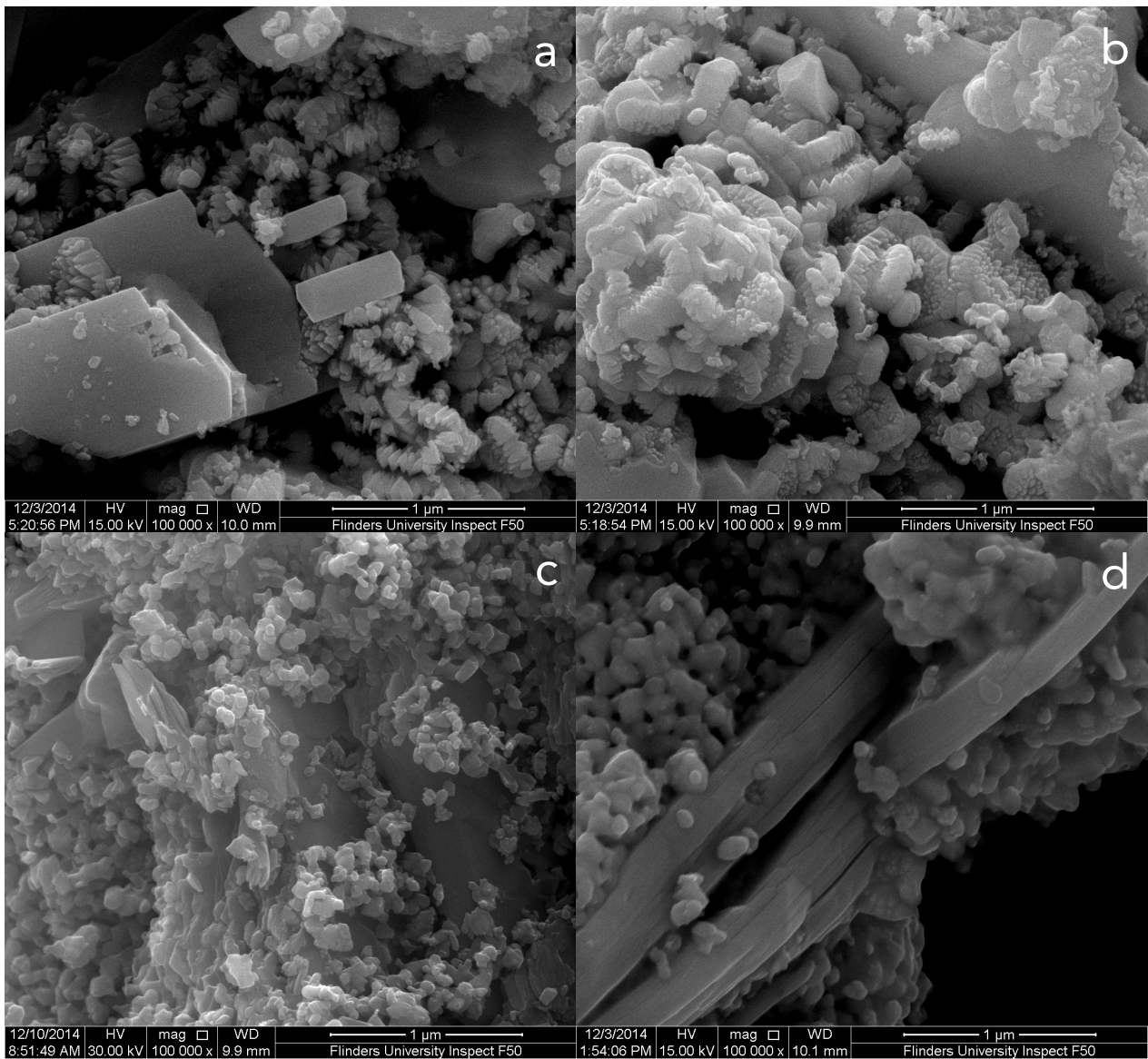


Figure 76 SEM images of the three Ranger UOCs at 100,000x magnification; a) Ranger UOC 1, b) Ranger UOC 1, c) Ranger UOC 2 and d) Ranger UOC 3

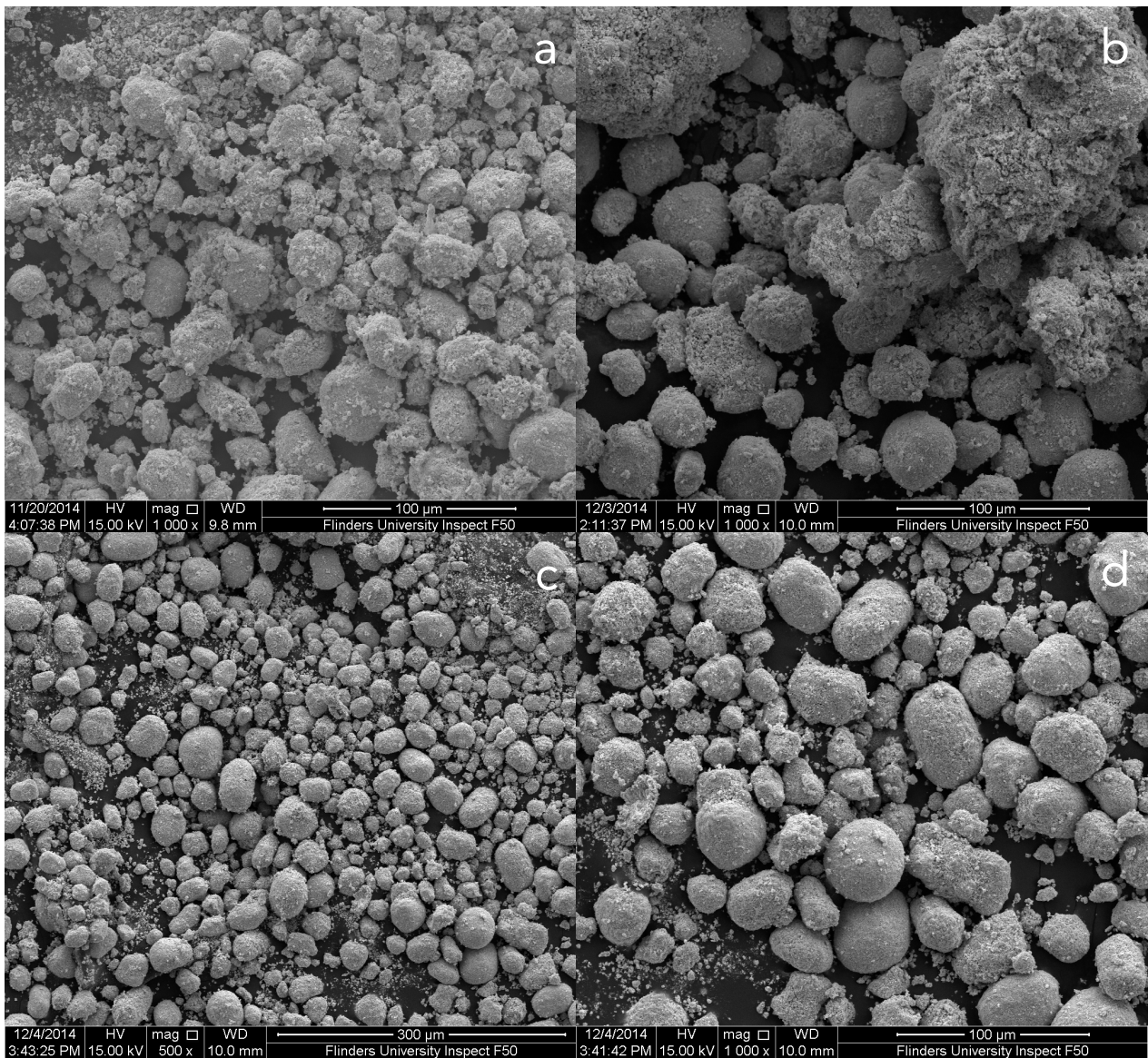


Figure 77 SEM images of the two Olympic Dam UOCs at various magnifications; a) Olympic Dam UOC 1 at 1000x, b) Olympic Dam UOC 1 at 1000x, c) Olympic Dam UOC 2 at 500x and d) Olympic Dam UOC 2 at 1000x

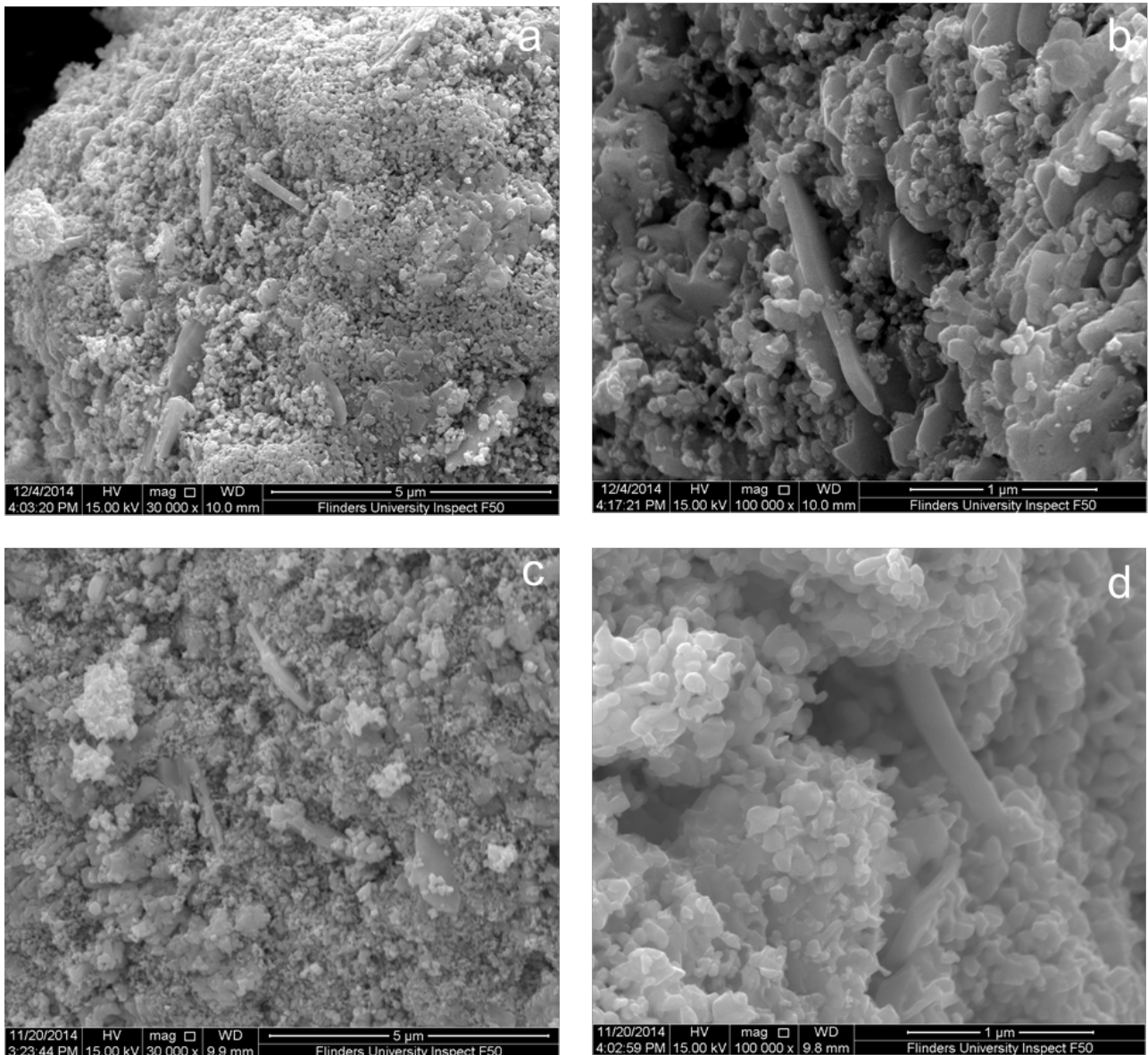


Figure 78 SEM images of the two Olympic Dam UOCs at various magnifications; a) Olympic Dam UOC 1 at 30,000x, b) Olympic Dam UOC 1 at 100,000x, c) Olympic Dam UOC 2 at 30,000x and d) Olympic Dam UOC 2 at 100,000x

4.3.6 Impact of temperature on the distinct morphologies observed within the Australian UOC samples

By comparing the original UOCs, the intermediates collected at various temperatures according to the TGA trace and the final TGA product, the impact of temperature on the distinct morphological features identified within the three groups of UOC was investigated. The intermediate samples collected at 200/280 °C and 500 °C in both air and nitrogen atmospheres for the three UOC samples were found to be unaffected by increased temperature, preserving their distinct morphological features of Beverley (Figure 79), Ranger (Figure 80) and Olympic Dam (Figure 81) UOCs. Upon

heating further to 1000 °C, all three UOCs were found to have underwent mild sintering, as the individual particles began to fuse together to form larger agglomerates. Interestingly, the sintering had not occurred to such a degree where the distinct morphologies identified within the three UOC groups were unable to be identified however. The sintering of U_3O_8 (as each Australian UOC analysed by TGA has previously been identified as having decomposed to solely U_3O_8) likely occurred between 800-1000 °C, where the thermal analysis of ADU, AUC and UO_4 heated from room temperature to 800 °C did not cause any observable sintering [231]. The reduction of surface area through sintering of the three UOC samples at high temperatures is consistent with another study, where ADU was calcined to form orthorhombic $\alpha-U_3O_8$ [108].

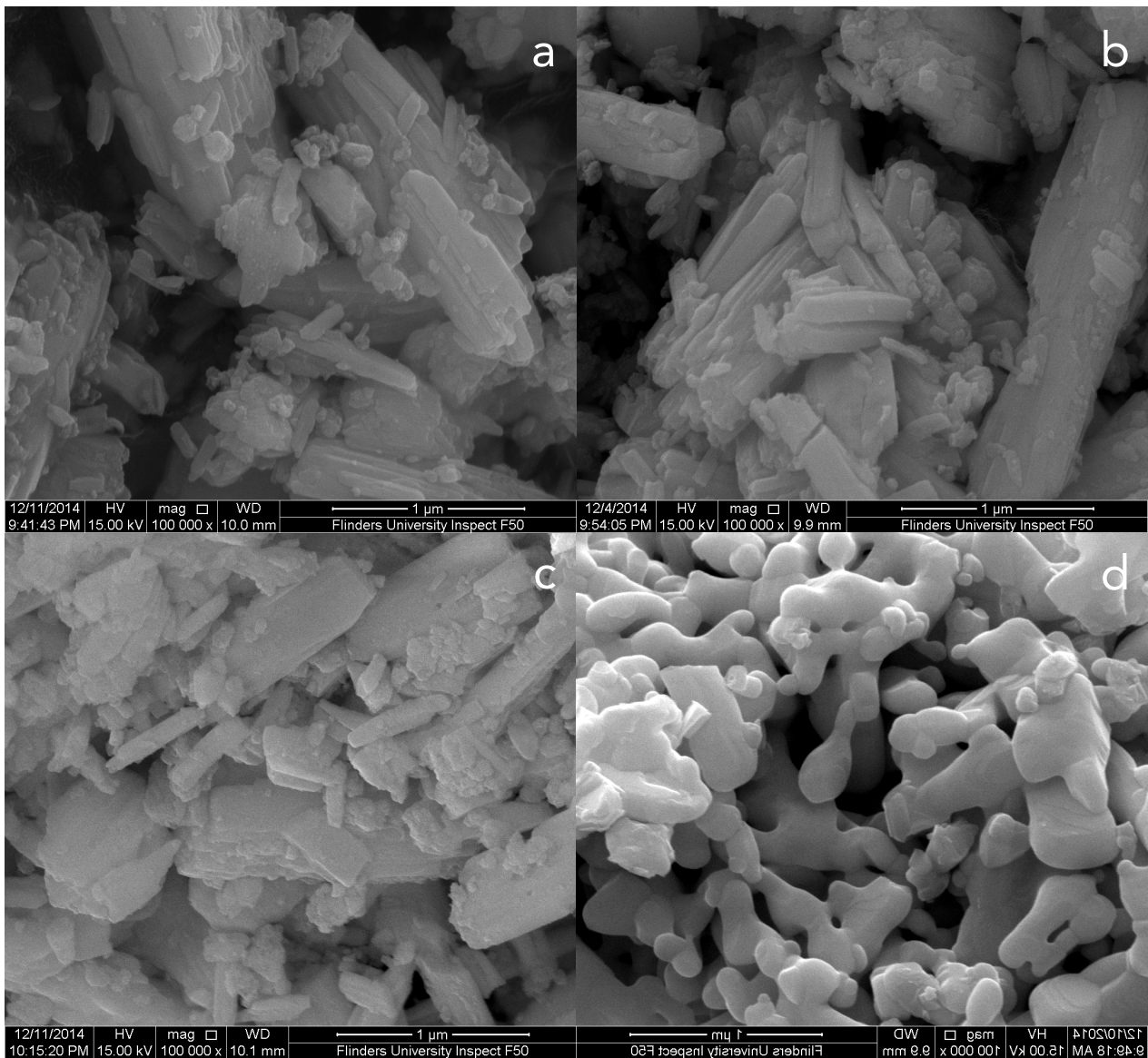


Figure 79 SEM images of the Beverley UOC 1 TGA samples analysed in a nitrogen atmosphere and collected at various temperatures; a) r.t., b) 280 °C, c) 500 °C and d) 1000 °C

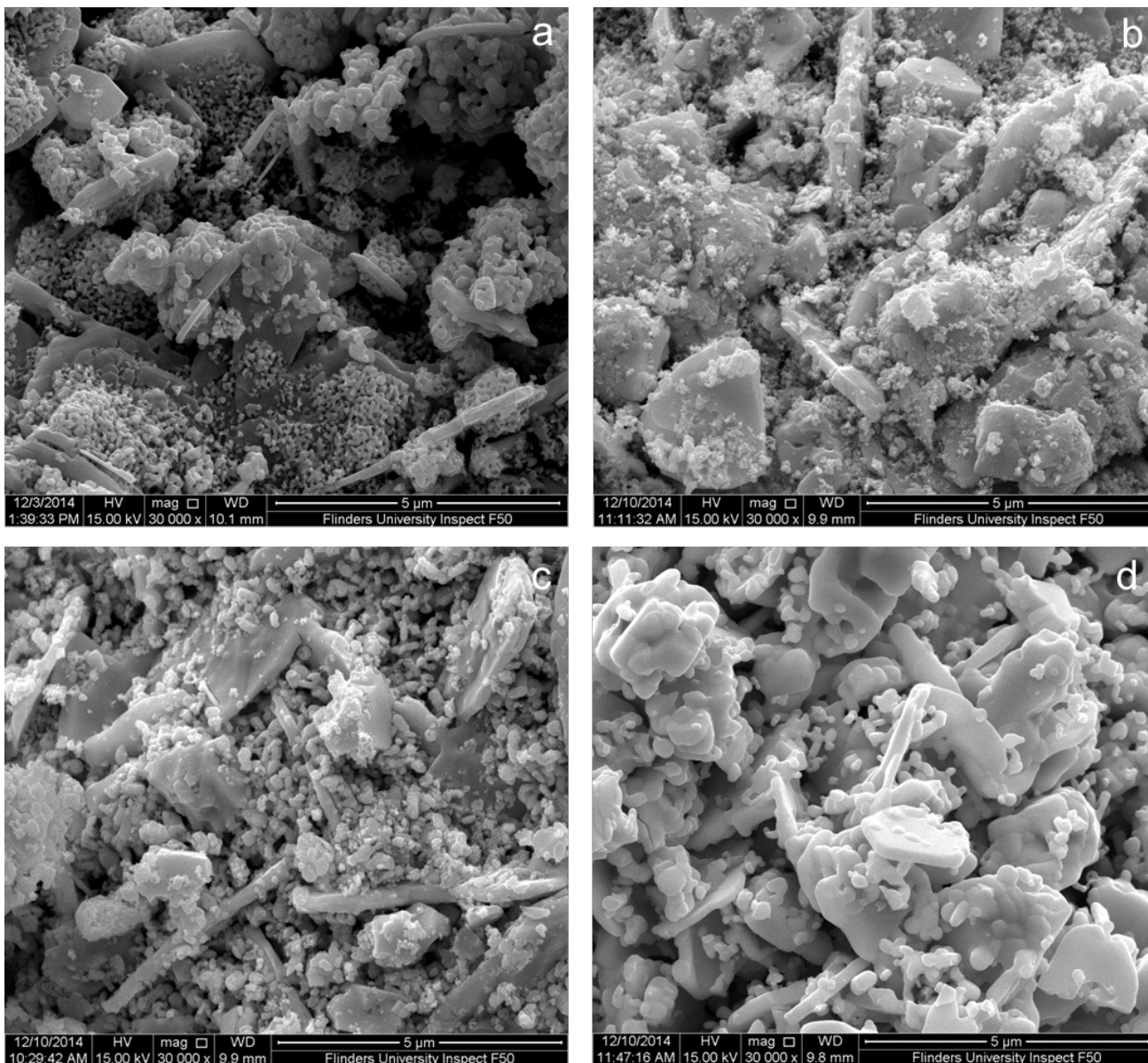


Figure 80 SEM images of the Ranger UOC 1 TGA samples analysed in a nitrogen atmosphere and collected at various temperatures; a) at r.t., b) 200 °C, c) 500 °C and d) 1000°C

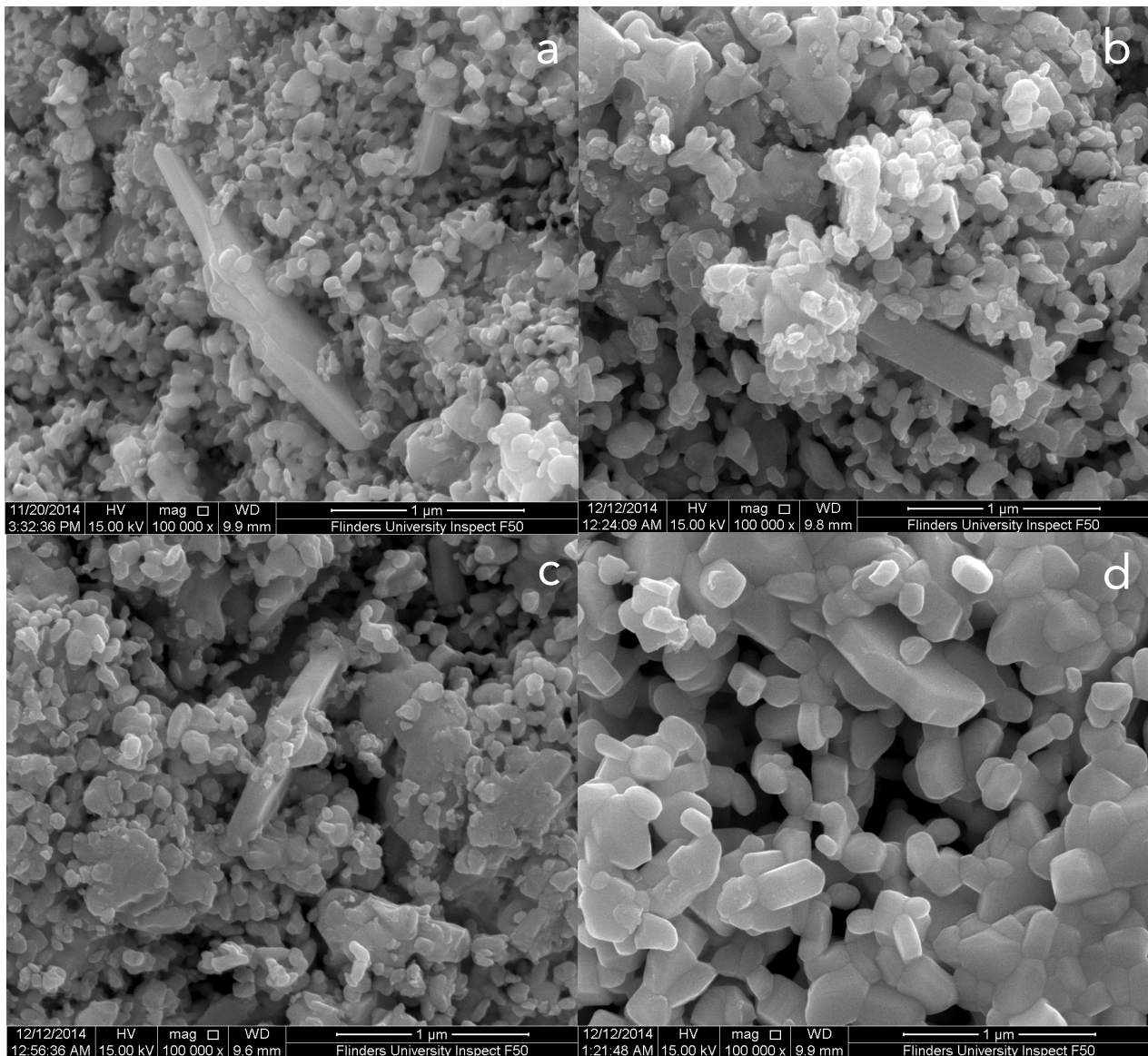


Figure 81 SEM images of the Olympic Dam UOC 2 TGA samples analysed in a nitrogen atmosphere and collected at various temperatures; a) at r.t., b) 200 °C, c) 500 °C and d) 1000 °C

4.7 Conclusions

Eight UOC samples from three operating Australian mines were analysed using TGA in nitrogen and air atmospheres. Based upon the TGA profiles in both atmospheres, the uranyl peroxide samples from Beverley could readily be differentiated from the U_3O_8 samples from Ranger and Olympic Dam (Figure 70). The major point of difference between the Ranger and Olympic Dam UOCs based on TGA alone in this study was their moisture content. The variability of moisture content is currently not known and requires further analysis, however the Ranger UOCs themselves exhibit a considerable amount of intra-sample variability already. At this stage, TGA appears to be able to readily differentiate between UOCs of different major speciations, however its ability to consistently differentiate UOCs of the same major composition is largely dependent on the samples themselves.

Attempts to utilise NIR spectroscopy for the characterisation of the Australian UOCs were made difficult by the design of the instrument and the limited amount of each UOC anticipated being available for analysis. Mounting the sample on a selection of transparent substrates was investigated in order to prevent contamination of the Spectralon standard used as a backing, and found that clear quartz slides had the least absorbance measured (Figure 52). The relationship between mass analysed and absorbance was found to be linear with some exceptions, for instance where the increase in mass did not result in an increase in surface area. The analysis of five UOCs from Ranger and Olympic Dam were used to assess the applicability of NIR for the identification of the speciation in the original UOC samples and the intermediates and final products formed during TGA analysis (Figure 54). While the spectra from Ranger and Olympic Dam both feature multiple peaks characteristic of U_3O_8 , the absence of peaks attributable to UO_3 , a minor phase previously observed in UOC samples from these two mines, indicated the sensitivity of NIR in this study was insufficient to measure changes in the composition of UOC samples across the temperature analysed.

Raman spectroscopy, and to a lesser extent XRD, were invaluable in identifying the different uranium compounds formed within the intermediate samples and TGA products obtained at various temperatures. Some confusion lingers over the identity of several intermediates formed from all three samples, as several uranium compounds identified by Raman spectroscopy or XRD do not agree with the two different thermal decomposition pathways for the uranyl peroxide samples from Beverley suggested by Satio (1976), Guo *et al.* (2016) and Odoh *et al.* (2016) [218, 221, 223]. Further research will hopefully provide clarity on which decomposition pathway, or another alternative, best describes the different uranium compounds formed during the heating of uranyl peroxide samples up to 1000 °C as the results obtained by this study does not strongly endorse either one so far. Further research is also required to elucidate the identity of the intermediate uranium compounds and its parent that formed within Ranger UOC 1 and the two Olympic Dam UOCs when heated to 500 °C and identified by a broad Raman band at 680 cm^{-1} (Figure 61 and Figure 65).

The three Australian UOCs were each found to feature distinct morphologies when analysed by SEM. The Beverley UOCs were found to consist of thin rectangular platelets (Figure 73) whilst Ranger UOCs were found to be the most complex with four different morphologies identified (rod-like structures, large smooth-faced structures, globular structures and quasi-cuboidal structures) (Figure 75). Olympic Dam UOCs on the macro-scale were the most unique, forming large round agglomerates, and were identified with having a morphology of small, globular structures with a

number of rod-like structures (Figure 73). These morphologies were found to be immune from the impact of temperature until the temperature exceeded 500 °C, where the UOC samples collected at 1000 °C demonstrated mild signs of sintering.

4.8 Future Work

4.8.1 High Temperature XRD analysis of the Australian UOCs

In-situ high temperature experiments are currently being conducted on the UOC samples from Beverley, Ranger and Olympic Dam at the Australian Synchrotron on the powder diffraction beamline to replicate the TGA measurements performed in this study. These measurements will hopefully help contribute to the resolution of a number of discrepancies observed between the different thermal decomposition pathways proposed and the Raman and XRD results obtained by this study. The significantly higher intensity of the X-rays produced by the synchrotron and high signal-to-noise ratio of the powder diffractometer will allow small quantities of any intermediates formed during the heating program to be identified, and exceeds the capabilities of the μ Raman and XRD instruments used in this study.

4.8.2 Inclusion of more UOC samples

Access to more UOCs from the three Australian mines, as well more UOCs from other mines, will be invaluable in further assessing the applicability of TGA for materials provenancing in nuclear forensics. While the UOCs from the three different Australian mines could be differentiated from one another, understanding the consistency of their compositions present within each sample will be important. This is especially important for the moisture content, as this was the major point of differentiation between the Ranger and Olympic Dam UOCs. With little understood concerning the consistency of the moisture content and the impact of production, environmental and storage factors, a more comprehensive understanding of the variability within UOC samples from a particular location will be critical for establishing the efficacy of TGA for the analysis of UOCs. Expanding the study to include a more diverse range of UOCs from either real UOC samples or laboratory-derived samples will also aid in determining the effectiveness of TGA.

Access to more UOC samples will have a similar effect on our understanding of UOC morphologies, to further investigate how consistent the distinct morphologies identified within the Australian UOCs are and whether there is sufficient inter-mine variability between other UOCs to still enable UOCs from different sources to be distinguished from one another in an investigation.

4.8.3 Objective morphological analysis of UOCs

Further research could explore the application of MAMA and other image analysis software to quantitatively analyse the morphologies of the Australian UOCs, which has been used previously for similar applications [168, 169, 171]. Analysis of the images obtained from SEM analysis could reveal more detailed information, including circularity, particle size distribution and pixel area, about how the distinct morphologies of the three Australian UOCs are impacted by increasing temperature.

Chapter 5. Isotope Analysis of UOCs and Uranium Ores

5.1 Introduction

Measurement of uranium isotope ratios, namely $^{234}\text{U}/^{238}\text{U}$ and $^{235}\text{U}/^{238}\text{U}$, has been a staple within the suite of signatures identified within nuclear forensics for the investigation of UOCs and uranium ores. The analysis of these particular uranium isotope ratios within these uranium materials can reveal anthropogenic or natural alterations to uranium-containing samples [7, 232], which can provide valuable information for nuclear forensics regarding their origin and treatment.

5.1.1 Isotopes of uranium

Uranium has two long-lived and one short-lived natural isotope; ^{238}U ($t_{1/2} \approx 700$ Ma), ^{235}U ($t_{1/2} \approx 4.5$ Ga) and ^{234}U ($t_{1/2} \approx 245,000$ y), respectively. ^{238}U is the parent nuclide of the “4n+2” decay series (otherwise referred as the “uranium series”), which decays eventually to ^{206}Pb through several intermediaries, including ^{234}U (Figure 1). ^{235}U is the parent nuclide of the “4n+3” decay series (otherwise referred to as the “actinium series”), which eventually decays to ^{207}Pb (Figure 2). Typically, uranium isotope ratios are reported relative to ^{238}U (i.e. $^{234}\text{U}/^{238}\text{U}$ and $^{235}\text{U}/^{238}\text{U}$), however there are exceptions where the isotope ratio is reported relative to the lightest isotope (i.e. $^{238}\text{U}/^{235}\text{U}$ or $^{235}\text{U}/^{234}\text{U}$) [7].

5.1.2 Variations in uranium isotopes within natural uranium

Variations within the $^{234}\text{U}/^{238}\text{U}$ isotope ratio has long been recognised within groundwater and ocean systems, where ^{234}U is preferentially leached from crystal lattices of uranium-bearing minerals due to α -recoil damage caused by the emission of α particles during the decay of ^{238}U , and the subsequent β -decay of daughter intermediaries ^{234}Th and ^{234}Pa [110, 233]. Furthermore, if the particle size of the uranium-bearing sample is sufficiently small ($<$ particle size of sand), the ^{234}U atom may be emitted into the surrounding medium [234]. This phenomenon results in ocean and ground waters having ratios far exceeding the secular equilibrium of $^{234}\text{U}/^{238}\text{U}$ (Equation 27); however, the complimentary depletion of ^{234}U is considered significant only when the particle size of the uranium-bearing mineral is small enough or is at the interface with the fluid, but is still measurable by mass spectrometry [234].

$$\frac{A_{234\text{U}}}{A_{238\text{U}}} = \frac{\lambda_{238\text{U}}}{\lambda_{234\text{U}}} = 5.489 \times 10^{-5} \quad \text{Equation 27}$$

While the $^{235}\text{U}/^{238}\text{U}$ ratio was once thought to be constant throughout the Solar System, several studies have identified that the ratio can vary within terrestrial samples [7, 10, 235]. Typically, most elements undergo the mass-dependent fractionation process, however this process is not amenable for uranium, due to the small difference in masses between the uranium isotopes [236]. Uranium has been found to fractionate according to the ‘nuclear volume effect’, ‘where a nucleus with an odd number of neutrons (^{235}U), will behave in a chemical exchange reaction as though it has a smaller atomic mass, leading to a concentration of the heavier isotope (^{238}U) into the chemical species with the smallest electron density’ [237]. The magnitude of the fractionation of uranium isotopes due to nuclear volume effects is not proportional to the differences in isotopic mass [238, 239], unlike mass-dependent fractionation where the magnitude scales inversely with isotopic mass [240]. Furthermore, the magnitude of fractionation through nuclear volume effects would be most pronounced in uranium than other elements as the effects are most felt at the bottom of the periodic table [237, 240-244], whereas mass-dependent fractionation decreases as the atomic number or mass number increases [245]. Also, nuclear volume fractionation has been found to be sensitive to temperature (scaling as T^{-1}) [246], indicating fractionation may occur at relatively high temperatures [240].

Another factor that promotes the fractionation of uranium isotopes, leading to variations in the $^{235}\text{U}/^{238}\text{U}$ isotope ratio, is the reduction/oxidation (redox) and temperature conditions of the deposit [7, 10]. In a comparison between UOCs sourced from low-temperature redox uranium deposits, high temperature redox uranium deposits and non-redox sensitive uranium deposits, only low-temperature redox uranium deposits were found to exhibit variations in their $^{238}\text{U}/^{235}\text{U}$ ratios [7]. This was attributed to the low-temperature transition from the highly soluble $\text{U}^{\text{VI}}\text{O}_2^{2+}$ species to the nearly insoluble $\text{U}^{\text{IV}}\text{O}_2$ species [7]. Another study investigating the fractionation of $^{238}\text{U}/^{235}\text{U}$ across a number of different natural samples (including basalts, granites, ferromanganese crusts, black shales and seawater), found the black shale samples, which occur in the most anoxic/euxinic environmental conditions of the samples analysed, with a +0.84% swing in the $\Delta^{238}\text{U}$ value relative to seawater [10]. In ferromanganese crust samples, representing the most oxic environments of the samples analysed, a -0.13% to 0.21% swing in the $\delta^{238}\text{U}$ value, relative to seawater, was observed [10]. These results are consistent with theoretical calculations that indicate the fractionation of uranium isotopes occurs via volume-dependent effects [10], rather than mass-dependent or kinetic fractionation during microbial reduction [247].

5.1.3 Impact of UOC production processes on uranium isotope ratios within uranium ores

For nuclear forensics, the measurement of $^{234}\text{U}/^{238}\text{U}$ and $^{235}\text{U}/^{238}\text{U}$ uranium isotope ratios can provide valuable information concerning the type of deposit the uranium was produced from, as it is thought the production of UOCs does not impact the uranium isotopic ratios of the original uranium ore [7]. Sequential leaching experiments on uraninite, zircon and euxenite using three different concentrations of nitric acid (0.1 N, 0.7 N, and 1.4 N) observed no variation in the $\delta^{235}\text{U}$ value [248], and as the production of UOC involves the digestion of ore material with an efficiency of 90-95% [249], the isotope ratios of the original is more than likely conserved into the UOC [7]. A comparison between uranium ores analysed by Richter *et al.* (1999) and UOCs analysed by Brennecka *et al.* (2010) from Straz Pod Ralskem mine in the Czech Republic and Rössing mine in Namibia found their respective $^{238}\text{U}/^{235}\text{U}$ isotope ratios for each mine were in agreement within error [7, 232]. The $^{235}\text{U}/^{234}\text{U}$ isotope ratios for the uranium ore and UOC samples from Rössing were also in agreement within error, however the samples from Straz Pod Ralskem did not, which was attributed to sample heterogeneity as the most likely cause [7, 232]. This is despite low $^{235}\text{U}/^{234}\text{U}$ isotope ratios relative to the other uranium ore UOC samples analysed by Richter *et al.* (1999) Brennecka *et al.* (2010), which was attributed to contamination with plutonium as ^{238}Pu decays to ^{234}U ($t_{1/2} = 87.7$ yrs) and high concentrations ($\sim 3.5 \times 10^{-6}$) of ^{236}U (formed through neutron capture by ^{235}U) being detected in the uranium ore sample [7].

A study by Varga *et al.* (2017) investigated whether the UOC production process had any affect on several signatures used in nuclear forensics research, including $^{234}\text{U}/^{238}\text{U}$, $^{235}\text{U}/^{238}\text{U}$ and $^{236}\text{U}/^{238}\text{U}$ isotope ratios, through the analysis of eight uranium samples collected at various stages at an operating South African uranium mine [250]. While the $^{236}\text{U}/^{238}\text{U}$ isotope ratios were found to be below the limits of detection by the NuPlasma MC-ICP-MS, the $^{235}\text{U}/^{238}\text{U}$ isotope ratios of all eight uranium samples were found to feature no impact by the UOC production process and consistent with a $^{235}\text{U}/^{238}\text{U}$ isotope ratio of natural uranium (Figure 82).

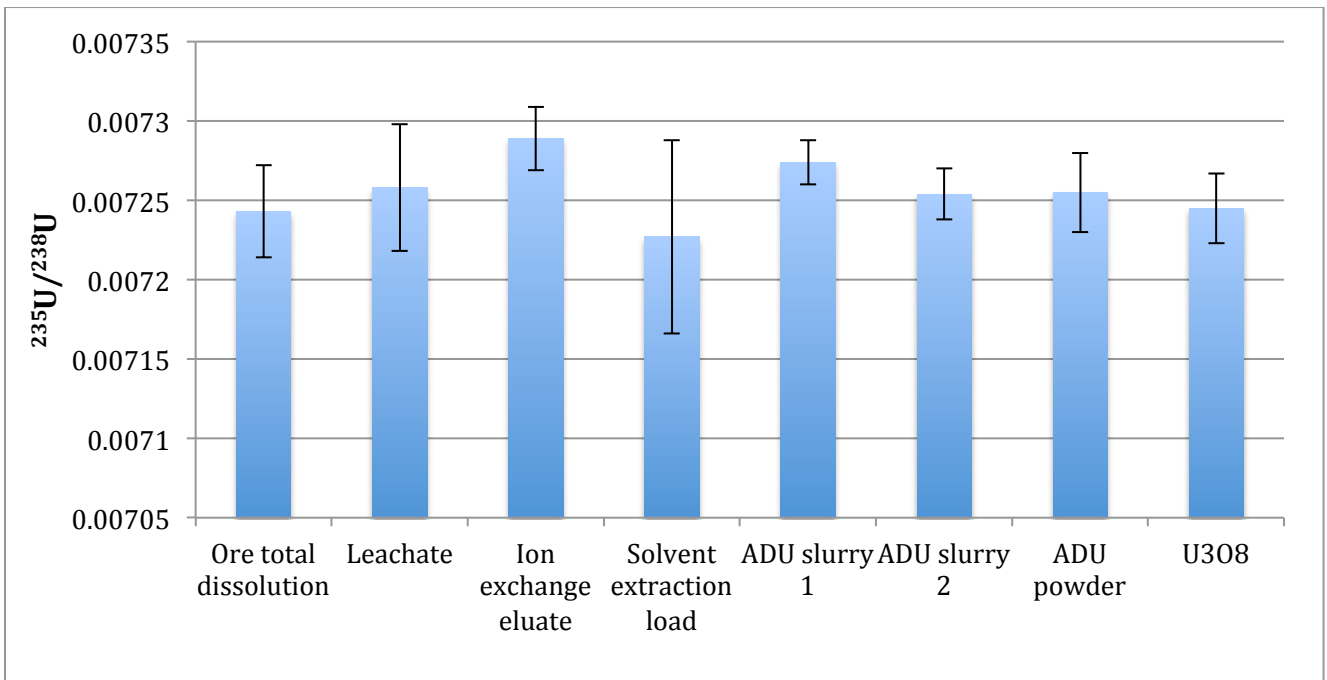


Figure 82 $^{235}\text{U}/^{238}\text{U}$ isotope ratios of the eight uranium samples obtained from a South African uranium mine. Error bars = expanded uncertainty ($k=2$). (Note - The position of the samples indicates the location of the sample within the production process going from left to right i.e. the Ore total dissolution sample is the starting material and U_3O_8 sample is the final product.)

With the $^{234}\text{U}/^{238}\text{U}$ isotope ratios, it was observed that the $^{234}\text{U}/^{238}\text{U}$ isotope ratio decreased as the uranium material passed through successive stages of the UOC production process (Figure 83) [250]. This, however, was not deemed to be significant by the authors due to the overlapping of error bars representing the expanded uncertainty and consistent with other quartz-pebble conglomerates samples [7].

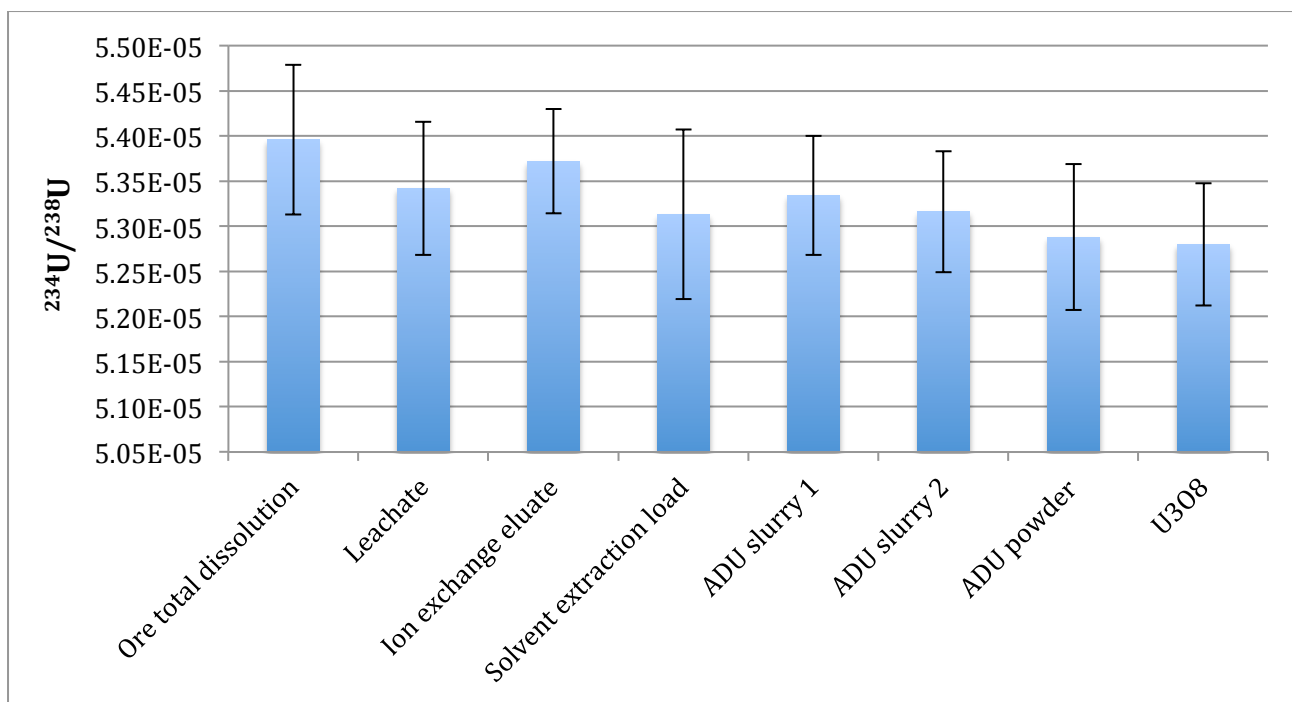


Figure 83 $^{234}\text{U}/^{238}\text{U}$ isotope ratios of the eight uranium samples obtained from a South African uranium mine. Error bars = expanded uncertainty ($k=2$) (Note - The position of the samples indicates the location of the sample within the production process going from left to right i.e. the Ore total dissolution sample is the starting material and U_3O_8 sample is the final product.)

5.1.4 Application of uranium isotope analysis within nuclear forensics

A study by Brenneka *et al.* (2010) analysed forty known UOCs by MC-ICP-MS to investigate how the geological conditions of the uranium ore deposit influenced their respective $^{238}\text{U}/^{235}\text{U}$ and $^{234}\text{U}/^{235}\text{U}$ isotope ratios [7]. The original uranium deposits where the forty UOC samples were produced from consisted of three different geological environments during the genesis of the deposit; low-temperature redox, high-temperature redox and non-redox sensitive. UOC samples classified as belonging to the low-temperature redox group (137.887 ± 0.072 (2SD)) were found to feature enriched $^{238}\text{U}/^{235}\text{U}$ isotope ratios, when compared to the high-temperature redox and non-redox sensitive samples (137.833 ± 0.034 (2SD)), which were indistinguishable from one another [7]. These observations are consistent with fractionation through the nuclear volume effect, where the heavier isotope ^{238}U is enriched in the reduced phase [7]. The high temperature redox and non-redox sensitive UOC samples were found to have $^{235}\text{U}/^{234}\text{U}$ isotopes consistent with secular equilibrium (~ 132), whereas the low-temperature redox varied greatly, with values both lesser and greater than secular equilibrium observed [7]. The variations observed in the $^{235}\text{U}/^{234}\text{U}$ low temperature redox UOC samples are due to the type of deposits that form in this environment; roll front deposits that

form beneath the water table, allowing ^{234}U to leach out due to alpha-recoil damage of the crystal lattice [7].

Multiple authors have performed analyses of the $^{235}\text{U}/^{238}\text{U}$ and $^{234}\text{U}/^{238}\text{U}$ isotope ratios of UOC and uranium samples, to investigate whether variation exists between samples of different provenances to enable differentiation. Richter *et al.* (1999) investigated six different uranium ore samples for their uranium isotope ratios using UF_6 -gas inlet isotope mass spectrometry ($^{235}\text{U}/^{238}\text{U}$) and thermal ionization mass spectroscopy ($^{235}\text{U}/^{238}\text{U}$ and $^{234}\text{U}/^{238}\text{U}$). Four of the six samples (Comuf Mounana, Gabon, Straz Pod Ralskem, Czech Republic, Cogema Lodeve, France and CETAMA Amethyste, France) were found to feature unique uranium isotopic compositions when comparing across all three isotopic ratios [232]. The uranium ore samples from CAMECA Rabbit Lake Op., Canada and Rössing Uranium Mine, Namibia were, however, unable to be distinguished from one another [232].

TIMS analysis of $^{235}\text{U}/^{238}\text{U}$ and $^{234}\text{U}/^{238}\text{U}$ UOCs from Ranger, Olympic Dam and Beverley was also performed by Keegan *et al.* (2008), finding that the three different UOC samples featured no significant difference in their $^{235}\text{U}/^{238}\text{U}$ isotope ratios [39]. Their $^{234}\text{U}/^{238}\text{U}$ isotope ratios, however, enabled all three UOC samples to be differentiated from one another and all less than secular equilibrium, indicating ^{234}U had leached from each of the deposits over time since their genesis [39].

Uranium isotope ratios have also contributed in real cases of seized UOC and uranium materials, where they have helped identify the provenance of these materials. Following a police raid in Victoria, Australia in April 2009 where two containers of uranium material were seized, the samples were analysed by high-resolution gamma-ray spectrometry, MC-ICP-MS and AMS for their uranium isotopic composition [101]. Measurement of the $^{235}\text{U}/^{238}\text{U}$ isotope ratios indicated that both samples consisted of depleted uranium ($<0.72\%$ ^{235}U), with differing degrees of depletion (NSR-F-270409-01 = $\sim 0.44\%$ and NSR-F-270409-02 = $\sim 0.42\%$ ^{235}U) [101]. Furthermore, both samples were found to contain differing but measurable amounts of ^{236}U (NSR-F-270409-01 = 2.312×10^{-5} and NSR-F-270409-02 = 7.711×10^{-5} $^{236}\text{U}/^{238}\text{U}$), which signifies some previous exposure to prior reactor irradiation (neutron capture by ^{235}U) [101]. From these measured uranium isotopes ratios, it is evident the two samples are from two separate materials, and are tailings from an enrichment program that has recycled reprocessed uranium that has previously been irradiated [101]. This is significant as Australia has never had the capability to reprocess uranium, therefore indicating these seized uranium samples have originated from overseas [101].

A second seizure of an unknown radioactive material by a state policing agency in Australia in 2009 also utilised uranium isotope ratios for the identification and provenance of the sample [103]. As preliminary REE analysis of the seized sample found a chondrite-normalised REE pattern matching closely to a reference UOC sample from Mary Kathleen, the uranium isotopic composition was also compared to this reference sample [103]. MC-ICP-MS analysis of the seized and Mary Kathleen reference samples identified both samples having $^{234}\text{U}/^{238}\text{U}$ and $^{235}\text{U}/^{238}\text{U}$ consistent with each other and of a natural uranium composition (i.e. no depletion or enrichment of ^{235}U) [103]. This information, in coordination with other chemical and elemental properties, strongly suggested the seized sample originated from Mary Kathleen during its second period of operation [103].

5.1.5 Justification

Given the value of the uranium isotope ratios, particularly the $^{234}\text{U}/^{238}\text{U}$ isotope ratio, to a nuclear forensics practitioner for the provenancing of an unknown UOC or uranium ore sample, this research seeks to investigate the degree of intra-mine variability throughout each uranium mine. Understanding the intra-mine variability of the $^{235}\text{U}/^{238}\text{U}$ and $^{234}\text{U}/^{238}\text{U}$ isotope ratios, through the comparison of multiple samples from the same uranium mine, will provide additional confidence in the capability of using these uranium isotope ratios for the provenancing of an unknown UOC or uranium ore sample.

In this chapter, eight UOC and five uranium ore samples from four former and operating Australian uranium mines (Beverley, Ranger, Olympic Dam and Mary Kathleen) were analysed by MC-ICP-MS for their $^{235}\text{U}/^{238}\text{U}$ and $^{234}\text{U}/^{238}\text{U}$ isotope ratios in collaboration with the University of Missouri. In addition to the UOC and uranium ore samples analysed in this study, comparisons with other UOC and uranium ores from the same Australian uranium mines previously analysed and reported in the literature will be made to provide further data on the intra-mine variability of the $^{235}\text{U}/^{238}\text{U}$ and $^{234}\text{U}/^{238}\text{U}$ isotope ratios.

5.2 Methods

5.2.1 Sample Preparation for MC-ICP-MS analysis

Approximately 50 mg of each of the Australian UOCs were digested in duplicate using 3 mL of 10 M nitric acid (Fisher Scientific, USA) in Teflon beakers whilst heated to 90 °C for 3 hours to dryness (Table 3). 10 mL of 2% nitric acid solution was used to reconstitute the sample and transfer to a 50 mL vessel.

During the digestion of the Beverley 88 (#1) sample, a yellow crystalline solid was found to form when the nitric acid had evaporated. The addition of 3 mL of 10 M nitric acid was repeated three times to ensure the UOC had been digested fully in each sample, however the crystalline solid was found to reform each time following evaporation of the acid. More concentrated 1.5 mL aliquots of 11.86 M and 12.58 M of nitric acid were added sequentially to ensure complete digestion however the solid still formed. As the crystalline solid was soluble in all of the acid solutions trialed until they had evaporated off, 10 mL of 2% nitric acid solution was added. The crystalline solid was soluble in the 2% nitric acid solution.

Table 3 Masses for Australian UOCs digested for uranium isotopic analysis by MC-ICP-MS

Sample	1st Digest Mass (mg)	2nd Digest Mass (mg)
Beverley UOC #1	51.4	50.7
Beverley UOC #2	49.6	51.4
Beverley UOC #3	50.4	52.0
Ranger UOC #1	49.9	50.0
Ranger UOC #2	46.7	58.4
Ranger UOC #3	49.2	49.8
Olympic Dam UOC #1	49.6	51.3
Olympic Dam UOC #2	44.1	58.7

The Australian uranium ore samples were found to be far more difficult to digest, requiring two attempts and several further additions of increasing higher concentrations of acids, and use of multiple acids. The first attempt to digest the uranium ore samples sought to use the same method used for the digestion of the UOC samples: approximately 50 mg of each uranium ore sample (Table 4) was digested with 3 mL of 10 M nitric acid in Teflon beakers at 90 °C. This was found to be insufficient to completely digest all of the ore samples, as the 3 mL of nitric acid would evaporate before the samples had completely digested. Further attempts were made to digest the sample using increasing greater concentrations of acid and the inclusion of a second acid (see below), however these attempts were similarly unsuccessful as the acid solution would evaporate before the samples could be completely digested;

1. 3 mL of 10 M nitric acid (Fisher Scientific, USA) and 1 mL of neat (12 M) hydrochloric acid (Fisher Scientific, USA)

2. 2 mL of neat (15.5 M) nitric acid and 2 mL of neat hydrochloric acid
3. 2.948 mL of neat nitric acid and 0.052 mL of 0.1 M of hydrofluoric acid (Fisher Scientific, USA)
4. 2.48 mL of neat nitric acid and 0.52 mL of 1 M hydrofluoric acid
5. 2 mL of neat nitric acid and 1 mL of neat (29.3 M) hydrofluoric acid

A different digestion method was then used, as the previous approach using increasingly more concentrated acids failed to completely digest the uranium ore samples.

Table 4 Masses of Australian uranium ore samples digested for uranium isotopic analysis by MC-ICP-MS

Sample	1 st Attempt Mass (mg)	2 nd Attempt Mass (mg)
Beverley Ore	58.9	34.9
Olympic Dam Ore	46.1	51.0
Mary Kathleen Ore	51.8	40.8
Ranger Ore	50.8	50.0

The second procedure utilised 2 mL of neat nitric acid and 1 mL of neat hydrochloric acid to digest the uranium ore samples in sealed perfluoroalkoxyalkane (PFA) tubes at 120 °C in an aluminium hot block. After 4 hours, the ore samples had failed to completely digest, however the acid solution containing the digested material was collected for dilution in preparation for isotopic analysis by MC-ICP-MS. The UOC samples were diluted by 1/40,000 while the uranium ore samples were diluted by 1/100, according to their different concentrations of uranium. During their analysis, the Ranger uranium ore and the Olympic Dam UOC 1 #2 samples had to be further diluted by 1/10 to continue counting ²³⁵U on the ion counter (IC), as their previous concentration was too high.

5.2.2 Analysis of Uranium Isotope Ratios of Australian UOC and Uranium Ore Samples by MC-ICP-MS

The uranium isotope analysis of the Australian UOC and uranium ore samples were analysed by researchers at the University of Missouri Research Reactor (MIRR) with a Nu Instruments Ltd NuPlasma II MC-ICP-MS (Wrexham, UK) equipped with a PerkinElmer SC-2 DX autosampler sample introduction system (Waltham, US) and Nu Instruments Ltd. DSN-100 desolvating nebuliser. Both the spray chamber and nebuliser were fitted with borosilicate glass and operated in auto-

aspirating mode. A Peltier chiller attached to the spray chamber was operated at 7 °C. The MC-ICP-MS instrument was optimised for signal and peak shape before use. The operating conditions for the NuPlasma II MC-ICP-MS are outlined below (Table 5).

Table 5 NuPlasma II MC-ICP-MS and DSN-100 desolvating nebuliser operating conditions for U isotope analysis

Plasma Power	1300	W
Cooling Gas Flow Rate	13.0	L/min
Auxiliary Gas Flow Rate	1.2	L/min
Cones	Nickel	
Solution Uptake Rate	~110	µL/min
Spray Chamber Temperature	105	°C
Membrane Temperature	108	°C
Hot Gas Flow Rate	0.37	L/min
Membrane Gas Flow Rate	2.3	L/min
Nebulizer Pressure	29.4	PSI
Mass Resolution	300	m/Δm
Number of Spectra Acquired	25	
Magnet Delay	2	Sec
Scan Type	Static Multi-collection	
Cup Configurations	²³⁸ U:L1 ²³⁵ U: L4 ²³⁴ U:IC0	L=Faraday collector IC= Ion counter

The faraday gain calibration and signal optimisation were performed daily, while the ion counter gain and mass bias corrections were performed using a 100 ng/g solution of the enriched U010 certified reference material (CRM) (New Brunswick Laboratory, USA) analysed every six samples. The mass bias correction was made using the exponential method described by Albarède *et al.* [251]. A 3% nitric acid wash solution bracketed each solution analysed, and used for background signal subtractions. Every six samples, a 100 ppb natural uranium U₃O₈ solution from High Purity Standards (Charleston, USA), which was not isotopically certified, was analysed as a quality control check.

The ^{235}U and ^{238}U ion beams were analysed with Faraday cup detectors, whilst the ^{234}U ion beam was measured using an ion counter detector. Twenty-five measurements were made in total for each sample, in five blocks of five measurements.

5.2.3 Uranium Isotope Ratio Calculations and Corrections

The uranium isotope ratios reported in this chapter are calculated and corrected using an approach laid out by Williams (2010) [252]. For the $^{235}\text{U}/^{238}\text{U}$ isotope ratio, which measured both isotopes on the same type of detector (faraday cups), the ratio ($R_{A/B}$) is calculated via the following equation (Equation 28);

$$R_{A/B} = \left(\frac{S_A - B_A}{S_B - B_B} \right) \cdot K_{A/B} \quad \text{Equation 28}$$

where S_A is the measured counts of the A isotope in the sample, B_A is the measured counts of the A isotope in the blank, S_B is the measured counts of the B isotope in the sample, B_B is the measured counts of the B isotope in the blank and $K_{A/B}$ is the mass bias correction factor. $K_{A/B}$ is calculated via to the following equation (Equation 29);

$$K_{A/B} = \left(\frac{M_A}{M_B} \right)^\beta \quad \text{Equation 29}$$

where M_A is the mass of isotope A, M_B is the mass of isotope B and β is calculated from the following equation (Equation 30);

$$\beta = \left(\frac{\ln \left(\frac{\text{Std}_A / \text{Std}_B}{\text{Obs}_A / \text{Obs}_B} \right)}{\ln (M_A / M_B)} \right) = \left(\frac{\ln \left(\frac{\text{Std}_A / \text{Std}_B}{\left(\frac{R_A - B_A}{R_B - B_B} \right)} \right)}{\ln (M_A / M_B)} \right) \quad \text{Equation 30}$$

where Std_A is the certified atomic ratio of the A isotope in the U010 CRM (New Brunswick Laboratory, USA), Std_B is the certified atomic ratio of the B isotope in the U010 CRM, R_A is the measured counts of the A isotope in the U010 CRM and R_B is the measured counts of the B isotope in the U010 CRM.

For the $^{234}\text{U}/^{238}\text{U}$ isotope ratio, which was measured on two different detectors (^{234}U isotope measured using an ion counter and ^{238}U measured using a Faraday cup), an additional correction (IC_{CORR}) is required in the calculation of $R_{A/B}$ (Equation 31);

$$R_{A/B} = \left(\frac{S_{A-B_A}}{S_{B-B_B}} \right) \cdot K_{A/B} \cdot IC_{CORR} \quad \text{Equation 31}$$

where IC_{CORR} is calculated via (Equation 32);

$$IC_{CORR} = \left(\frac{True_{A/B}}{K_{A/B}} \right) \quad \text{Equation 32}$$

Where $True_{A/B}$ is the ratio of the certified atomic percentages of the A and B isotopes within the U010 CRM.

5.2.4 Determination of Uncertainty in MC-ICP-MS Measurement of Uranium Isotope Ratios

The uncertainties associated to the measured $^{235}\text{U}/^{238}\text{U}$ and $^{234}\text{U}/^{238}\text{U}$ isotope ratios have been calculated using two different methods. The first set of uncertainties is the standard deviation (σ) of the 25 replicate measurements of the $^{235}\text{U}/^{238}\text{U}$ and $^{234}\text{U}/^{238}\text{U}$ isotope ratios for each Australian UOC and uranium ore sample (Equation 33);

$$\sigma = \sqrt{\frac{1}{N-1} \sum_{i=1}^N (x_i - \bar{x})^2} \quad \text{Equation 33}$$

where N is number of measurements, (x_1, x_2, \dots, x_N) are the measured ratios values of the individual measurements and \bar{x} is the mean value of the replicate measurements.

The second method used to represent the uncertainty associated with the $^{235}\text{U}/^{238}\text{U}$ and $^{234}\text{U}/^{238}\text{U}$ isotope ratios is the expanded uncertainty, and was calculated using the Kragten spreadsheet approach [253]. The Kragten approach is based on the general equation for error propagation (Equation 34), and has been used for the estimation of combined total uncertainty ($u_c(y)$) for a variety of applications, including strontium isotope ratios by MC-ICP-MS [254], neutron flux parameters and element mass fractions for k_0 -NAA [255];

$$u_c(y) = \sqrt{\left[\frac{\partial Y}{\partial x_1} u(x_1)\right]^2 + \left[\frac{\partial Y}{\partial x_2} u(x_2)\right]^2 + \dots + \left[\frac{\partial Y}{\partial x_n} u(x_n)\right]^2} \quad \text{Equation 34}$$

To calculate the combined total uncertainty, the partial differential ($\partial Y/\partial X_1$) for each component of the function is approximated as follows (Equation 35);

$$u(y, x_1) = \frac{\partial Y}{\partial x_1} u(x_1) \approx \frac{\Delta Y}{\Delta x_1} u(x_1) \quad \text{Equation 35}$$

ΔY is calculated by through the following equation (Equation 36);

$$\Delta Y = F(x_1 + \Delta x_1, + \dots, x_n) - F(x_1, + \dots, x_n) \quad \text{(Equation 36)}$$

The standard uncertainty for X_1 ($u(y, x_1)$) is determined through the following equation (Equation 37);

$$u(y, x_1) = \frac{F(x_1 + \Delta x_1, + \dots, x_n) - F(x_1, + \dots, x_n)}{\Delta x_1} \cdot u(x_1) \quad \text{(Equation 37)}$$

If $\Delta x_1 = u(x_1)$;

$$\therefore u(y, x_1) = F(x_1 + u(x_1), + \dots, x_n) - F(x_1, + \dots, x_n) \quad \text{(Equation 38)}$$

For each component used in the isotope ratio, the Δx_n is calculated and subtracted from the original function (Equation 38). Each component is then squared, and then summed together before the square root is taken to calculate the combined standard uncertainty. The expanded uncertainty is the product of the combined standard uncertainty and the coverage factor. The coverage factor used in this study is 2 ($k=2$), in order for the expanded uncertainty to have a level of confidence of approximately 95%. Another advantage to using the Kragten spreadsheet approach is that it can identify the magnitude of the contribution each component (i.e. $\left[\frac{\partial Y}{\partial x_1} (x_1)\right]^2$ in Equation 34) provided to the overall uncertainty budget in a measured isotopic ratio.

5.2.5 Statistical methods to evaluate variance in isotopic ratios

5.2.5.1 E_n-Scores

E_n-scores were used to compare the uranium isotope results, which takes into account the uncertainty associated with the measurement. If the E_n score was <1, the experiment result was found to be in agreement with the reference value. E_n scores (E_n) are calculated through the following equation (Equation 39);

$$E_n = \frac{\chi - X}{\sqrt{U_\chi^2 + U_X^2}} \quad \text{Equation 39}$$

Where χ is the experiment result, X is the reference value, U_χ is the expanded uncertainty of the participant result and U_X is the expanded uncertainty of the reference value. As there was no single reference value for each deposit, multiple E_n scores will be calculated to compare each UOC and ore sample from each deposit, to see if there was agreement across all of the samples from a particular deposit.

5.2.5.2 One-way Analysis of Variance (ANOVA)

One-way ANOVAs were also used to compare isotopic ratios between standards and reference values to determine whether the mean values of the measurements were equal. The F-value is calculated through the following series of equations (Equations 40-46);

$$SS_{\text{Between}} = \sum n_j (\bar{x}_j - \bar{x})^2 \quad \text{Equation 40}$$

$$SS_{\text{within}} = \sum (x_i - \bar{x}_j)^2 \quad \text{Equation 41}$$

where n_j is the sample size per group, \bar{x}_j is the group mean and \bar{x} is the overall mean. The degrees of freedom between the groups (df_{between}) and within the groups (df_{within}) are calculated using the following equations;

$$df_{\text{between}} = m - 1 \quad \text{Equation 42}$$

$$df_{\text{within}} = n - m \quad \text{Equation 43}$$

where m is equal to the number of groups.

where x_i is an individual data point.

$$MS_{within} = \frac{SS_{within}}{dt_{within}} \quad \text{Equation 44}$$

$$MS_{between} = \frac{SS_{between}}{dt_{between}} \quad \text{Equation 45}$$

$$F = \frac{MS_{between}}{MS_{within}} \quad \text{Equation 46}$$

5.3 Results

5.3.1 Performance of MC-ICP-MS for the measurement of $^{235}\text{U}/^{238}\text{U}$ and $^{234}\text{U}/^{238}\text{U}$ isotope ratios

During the MC-ICP-MS analysis run, four 100 ng/g non-certified natural uranium U_3O_8 standard solutions were interspersed throughout the UOC and uranium ore samples as a quality control check. Due to the lack of a certified $^{235}\text{U}/^{238}\text{U}$ or $^{234}\text{U}/^{238}\text{U}$ value within the U_3O_8 standard solutions, determining the accuracy in the analysis of the $^{235}\text{U}/^{238}\text{U}$ isotope ratios cannot be determined with any precision or certainty (i.e. if the isotope ratio is or is not truly higher than the supposed natural uranium used as the standard). However, the $^{235}\text{U}/^{238}\text{U}$ and $^{234}\text{U}/^{238}\text{U}$ values of the four solutions run as part of this study can be compared to a previous study by Brown *et al.* [256], which used the same MC-ICP-MS instrument and natural uranium non-isotope certified standard (henceforth referred to as the “natural uranium standard”). The performance of MC-ICP-MS instrument for the measurement of the $^{235}\text{U}/^{238}\text{U}$ and $^{234}\text{U}/^{238}\text{U}$ isotope ratios were evaluated using two different means of representing the uncertainty in the measurements; expanded uncertainty and standard deviation.

5.3.1.1 Expanded uncertainty

Reasonable agreement is found amongst the four replicate analyses of the natural uranium standard in this study and the measurement reported within Brown *et al.* (2014) [256], against the consensus value considered for the natural uranium standard (7.257×10^{-3}) for the $^{235}\text{U}/^{238}\text{U}$ ratio (Figure 84). A single-factor analysis of variance (ANOVA) test between the four replicate analyses and result reported by Brown *et al.* (2014) of the natural uranium standard however, reported a p-value of 0.0078, which is less than the alpha value of 0.05, indicative of a significant difference between the mean values from this study and Brown *et al.* (2014). This finding suggests the reproducibility in the

measurement of the $^{235}\text{U}/^{238}\text{U}$ is poor, given the same natural uranium standard were analysed by the same MC-ICP-MS between this study and Brown *et al.* (2014) [256].

Unlike the $^{235}\text{U}/^{238}\text{U}$, a good agreement appears to be found between the replicate analyses of this study and Brown *et al.* (2014) for the $^{234}\text{U}/^{238}\text{U}$ isotope ratio (Figure 87), however a single-factor ANOVA test reported a p-value of 0.061, greater than the alpha value of 0.05, indicating that there is not a significant difference between the means of the two groups.

The difference in the magnitude of the error bars, reflecting their expanded uncertainties with a coverage factor of $k=2$, between this study and Brown *et al.* (2014) [256], may be due to the difference in concentration that the natural uranium standard was analysed at, as well as reflecting the performance of the MC-ICP-MS instrument. In this study, the concentration of the natural uranium standard was 100 ppb whereas for Brown *et al.* (2014), the natural uranium standard was analysed at a concentration of 20 ppb [256]. An expanded graph of the measured $^{235}\text{U}/^{238}\text{U}$ ratios in this study and Brown *et al.* (2014) of the natural uranium standard is shown below (Figure 85).

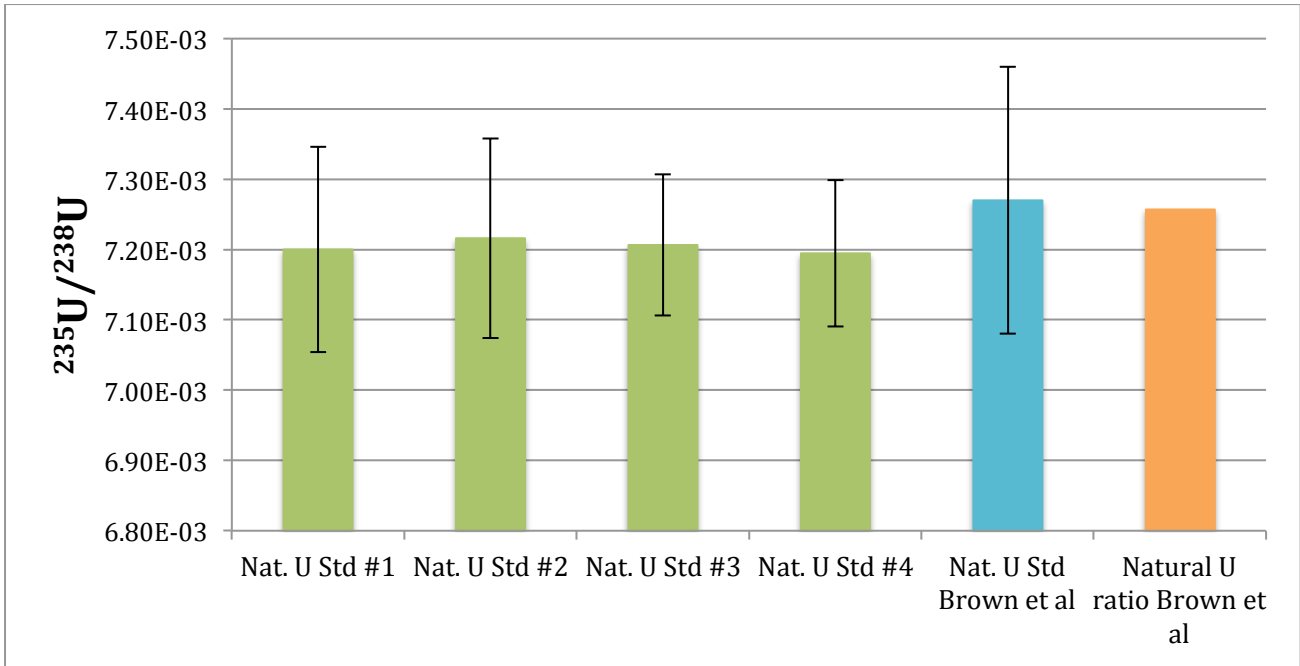


Figure 84 Comparison between replicate analyses (green) of $^{235}\text{U}/^{238}\text{U}$ isotope ratio of 100 ng/g non-certified natural uranium U_3O_8 standard during the analysis of UOC and uranium ore samples in this study and the measurement of same standard by Brown *et al.* (2014) (blue) against the consensus value for the $^{235}\text{U}/^{238}\text{U}$ isotope ratio of natural uranium (orange) used by Brown *et al.* (2014) (error bars = expanded uncertainty ($k=2$)) [256].

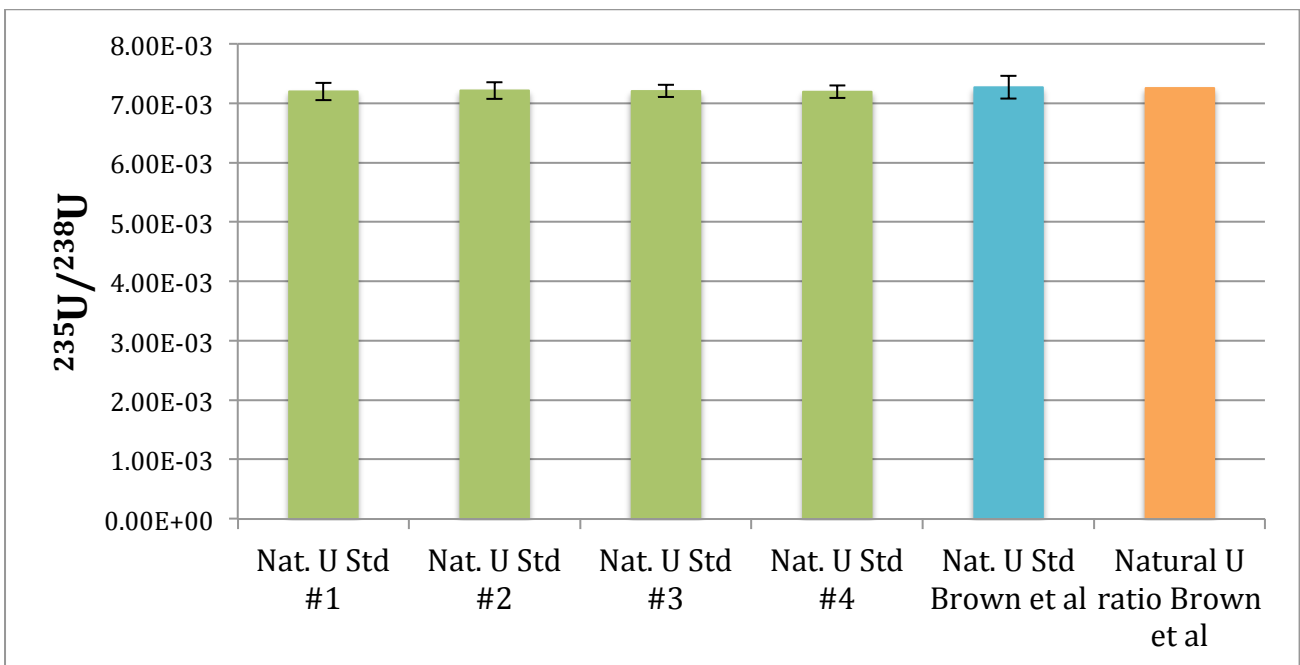


Figure 85 Comparison between replicate analyses (green) of $^{235}\text{U}/^{238}\text{U}$ isotope ratio of four 100 ng/g non-certified natural uranium U_3O_8 standard during analysis of UOC and uranium ore samples in this study and the measurement of same standard by Brown *et al.* (2014) (blue) against the consensus value

for the $^{235}\text{U}/^{238}\text{U}$ isotope ratio of natural uranium (orange) used by Brown *et al.* (2014) (error bars=expanded uncertainty (k=2)) [256].

In addition to the non-certified natural uranium U_3O_8 standard solution, Brown *et al.* (2014) also analysed a second standard as part of their study, which was isotopically certified for $^{235}\text{U}/^{238}\text{U}$ and $^{234}\text{U}/^{238}\text{U}$ ratios (Figure 86). Good agreement was found between the certified and measured values of the $^{235}\text{U}/^{238}\text{U}$ isotope ratio within the U630 CRM. Given the results between the analyses of the non-certified natural U_3O_8 standard solution between our study and Brown *et al.* (2014), along with this agreement using the same instrument, these results suggest the analysis of the $^{235}\text{U}/^{238}\text{U}$ is accurate. Doubt, however, still remains in the precision in the measurement of the $^{235}\text{U}/^{238}\text{U}$ given the large uncertainty, which dwarfs the natural variation within the $^{235}\text{U}/^{238}\text{U}$ isotope ratio exhibited within UOCs [7].

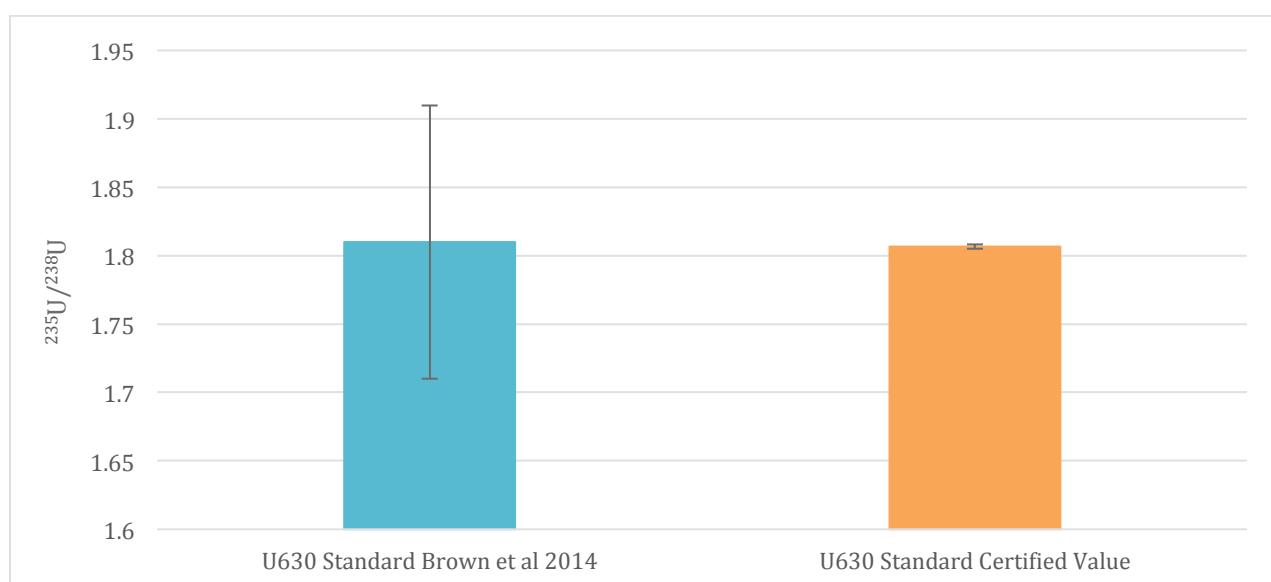


Figure 86 Comparison between certified (blue) and measured (orange) values of U630 CRM analysed by Brown *et al.* (2014) [256]. Error bars represent expanded uncertainty (k=2).

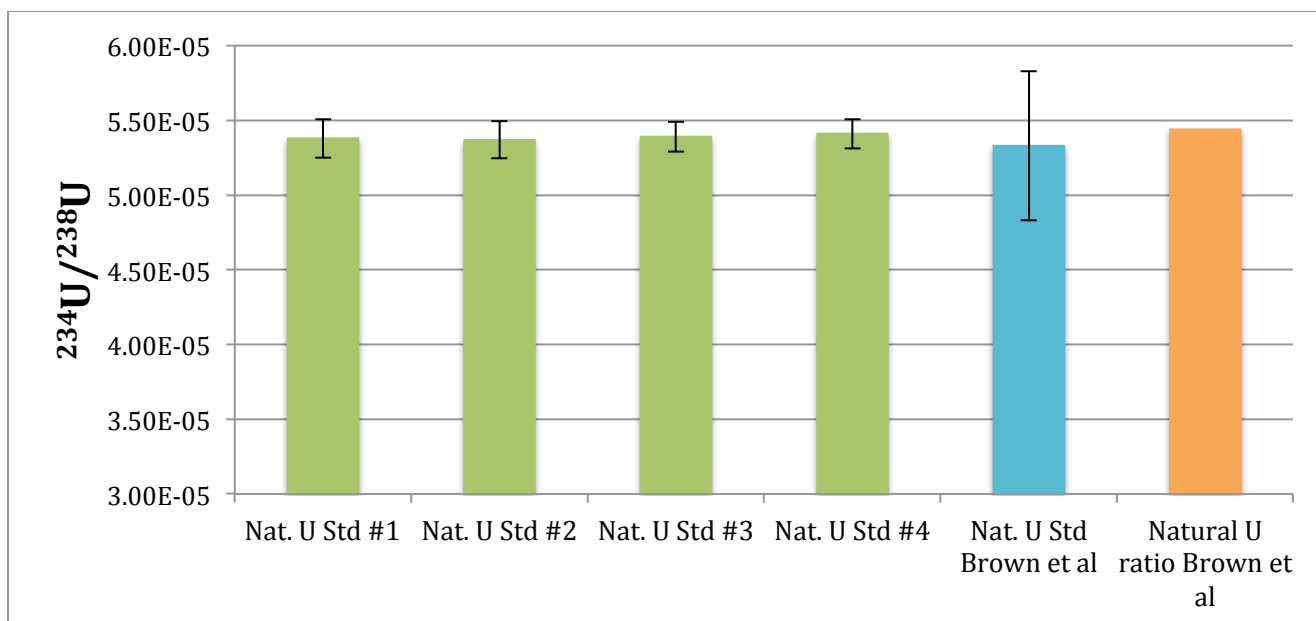


Figure 87 Comparison between replicate analyses (green) of $^{234}\text{U}/^{238}\text{U}$ isotope ratio of non-certified natural uranium U_3O_8 standard during analysis of UOC and uranium ore samples and measurement of same standard by Brown *et al.* (2014) (blue) against the consensus value for the $^{235}\text{U}/^{238}\text{U}$ isotope ratio of natural uranium (orange) used by Brown *et al.* (2014) (error bars = expanded uncertainty (k=2)) [256].

The use of an expanded uncertainty approach however, for the representation of uncertainty associated with the measurement of $^{235}\text{U}/^{238}\text{U}$ and $^{234}\text{U}/^{238}\text{U}$ isotope ratios has been cautioned by our collaborators at MURR due to the high relative uncertainties associated with the certified atomic abundances of ^{234}U , ^{235}U and ^{238}U within the U010 CRM used to calculate β in Equation 3. In their experience, the uncertainty associated with the atom ratios of each uranium isotope significantly contributes to the overall expanded uncertainty when the counts are high, which is extremely pertinent in this instance as the samples and standards analysed in this study are at a higher concentration (100 ppb) than the previous study (20 ppb) by Brown *et al.* (2014) [256].

The contribution of each component used to calculate the $^{235}\text{U}/^{238}\text{U}$ and $^{234}\text{U}/^{238}\text{U}$ isotope ratios towards the expanded uncertainty can be determined however, using the Kragten spreadsheet approach. For the $^{235}\text{U}/^{238}\text{U}$ isotope ratios measured in the four natural uranium standards, the largest contributors by percentage towards the expanded uncertainty were the uncertainties associated with the average counts of the ^{235}U and ^{238}U isotopes at both 49.18% (Table 6). In contrast, the contribution to the overall expanded uncertainty associated with the average counts of the ^{235}U and ^{238}U during the measurement of the U010 CRM for the calculation of β in Equation 3 is 1.47% and 0% (Table 6).

The combined overall contribution to the expanded uncertainty by the measurement of ^{234}U and ^{238}U for the $^{234}\text{U}/^{238}\text{U}$ isotope ratios of the natural uranium standards (79.31%) decreases when compared to the ^{235}U and ^{238}U for the $^{235}\text{U}/^{238}\text{U}$ isotope ratios (98.36%) (Table 7). Furthermore, the contribution by the average counts of both isotopes is not equivalent (as observed previously in the $^{235}\text{U}/^{238}\text{U}$ isotope ratio), but a greater contribution by the uncertainty associated with the average counts of the ^{234}U isotope (61.11%) is observed than the ^{238}U isotope (18.20%) (Table 7). Similarly to the $^{235}\text{U}/^{238}\text{U}$ isotope ratio, the contribution of the uncertainty associated with the average counts of the ^{234}U and ^{238}U during the measurement of the U010 CRM for the calculation of β in Equation 3 is 2.33% for both isotopes, which is significantly less than the contributions by the average counting of ^{234}U (61.11%) and ^{238}U (18.20%) in the natural uranium standards (Table 7).

Given the past experiences of our collaborators at MURR, where they have found that high uranium concentrations lead to large expanded uncertainties due to the relative uncertainty of the certified atom percentage of ^{234}U , ^{235}U and ^{238}U in the U010 CRM, it would be expected that the average counts of ^{234}U , ^{235}U and ^{238}U would be the largest contributor to the expanded uncertainties of the measured $^{235}\text{U}/^{238}\text{U}$ and $^{234}\text{U}/^{238}\text{U}$ isotope ratios of the natural uranium standards as they were analysed at a concentration five times greater than in previous studies [256]. Instead, the contribution from the measurement of ^{234}U , ^{235}U and ^{238}U isotopes in the U010 CRM is almost negligible (combined 1.47% for the $^{235}\text{U}/^{238}\text{U}$ ratio and 4.66% for $^{234}\text{U}/^{238}\text{U}$ ratio) when compared to the contribution from the measurement of the isotopes of the natural uranium standards (Table 6 and Table 7). This may suggest that the instrument was improperly calibrated and therefore renders all subsequent results questionable.

The contributions by the measurement of the uranium isotopes towards the overall expanded uncertainty in the analysis of the natural uranium standards differs between the $^{235}\text{U}/^{238}\text{U}$ and $^{234}\text{U}/^{238}\text{U}$ isotope ratios. For the $^{235}\text{U}/^{238}\text{U}$ isotope ratio, the counting of the ^{235}U and ^{238}U isotopes were found to equally contribute 49.18% each to the overall expanded uncertainty of the $^{235}\text{U}/^{238}\text{U}$ isotope ratio (Table 6). In contrast, for the $^{234}\text{U}/^{238}\text{U}$ isotope ratios, the counts of the ^{234}U isotope contributed 61.11% whilst the ^{238}U only contributed 18.20% (Table 7). This is despite the orders of magnitude difference in the atomic abundances between the three uranium isotopes ($^{238}\text{U} = 99.2748\text{-}99.2739\%$, $^{235}\text{U} = 0.7207\text{-}0.7201\%$, $^{234}\text{U} = 0.0054\text{-}0.0051\%$ [232]) and relative standard deviations (RSDs) of $\leq 1.03\%$ for both the raw and blank-subtracted counts of the 25 replicate measurements of the three uranium isotopes across the four natural uranium standards analysed.

The major difference between the $^{235}\text{U}/^{238}\text{U}$ and $^{234}\text{U}/^{238}\text{U}$ isotope ratios appears to be the detection systems used for the measurement of the uranium isotopes. The measurement of the ^{235}U and ^{238}U isotopes was performed using faraday cups, and despite the atomic abundance of the ^{238}U isotope being two orders of magnitude greater than the ^{235}U isotope, they both equally contribute 49.18% each towards the expanded uncertainty of the measured $^{235}\text{U}/^{238}\text{U}$ ratios of the four natural uranium standards. For the $^{234}\text{U}/^{238}\text{U}$ isotope ratio, the different contributions of the ^{234}U and ^{238}U isotopes towards the expanded uncertainty of the measured $^{234}\text{U}/^{238}\text{U}$ ratios of the four natural uranium standards is likely due to the different detection systems used, as the ^{234}U isotope is measured instead on an ion counter. Despite the ^{234}U isotope being present at an abundance four orders of magnitude less than the ^{238}U isotope, the RSDs of the raw and blank-subtracted counts of the ^{234}U isotope would be expected to be greater than 1.03% if there was any issue concerning the sampling or detection limits of the ion counter. This would then suggest that there was an issue with the calibration or equalization of the faraday cups and ion counters of the MC-ICP-MS instrument during the analysis of these samples.

With no opportunity to investigate this phenomenon further or reanalyze the samples following the recalibration of the instrument and/or equalization of the detector array, there is little confidence in the accuracy and precision of the results obtained from the Australian UOC and uranium ore samples also analysed in this run. The samples were left for later analysis by our collaborators at MURR, as multiple successive instrumental failures were experienced during a research trip to MURR and therefore afforded no opportunity to undertake the reanalysis of the samples with the MC-ICP-MS in working order.

Table 6 Percentage (%) contributions of calculation components towards the expanded uncertainties of the $^{235}\text{U}/^{238}\text{U}$ isotope ratios measured in the four natural uranium standards calculated using the Kragten method

	Nat. U Std	Nat. U Std	Nat. U Std	Nat. U Std	Average
Average Measured ^{235}U in Sample (S_A)	48.79%	49.02%	49.56%	49.37%	49.18%
Average Measured ^{238}U in Sample (S_B)	50.09%	49.87%	48.25%	48.52%	49.18%
Average Measured ^{235}U in Blank (B_A)	0.16%	0.09%	0.16%	0.23%	0.16%
Average Measured ^{238}U in Blank (B_B)	0.00%	0.00%	0.00%	0.00%	0.00%
Atomic Mass of ^{235}U (M_A)	0.00%	0.00%	0.00%	0.00%	0.00%
Atomic Mass of ^{238}U (M_B)	0.00%	0.00%	0.00%	0.00%	0.00%
Standard ^{235}U Abundance in U010 CRM (Std_A)	0.00%	0.00%	0.00%	0.00%	0.00%
Standard ^{238}U Abundance in U010 CRM (Std_B)	0.00%	0.00%	0.00%	0.00%	0.00%
Average Measured ^{235}U in U010 CRM (R_A)	0.95%	1.01%	2.03%	1.88%	1.47%
Average Measured ^{238}U in U010 CRM (R_B)	0.00%	0.00%	0.00%	0.00%	0.00%

Table 7 Percentage (%) contributions of calculation components towards the expanded uncertainties of the $^{234}\text{U}/^{238}\text{U}$ isotope ratios measured in the four natural uranium standards calculated using the Kragten method

	Nat. U Std	Nat. U Std	Nat. U Std	Nat. U Std	Average
Average Measured ^{234}U in Sample (S_A)	62.13%	61.55%	61.47%	59.30%	61.11%
Average Measured ^{238}U in Sample (S_B)	22.13%	21.96%	13.21%	15.51%	18.20%
Average Measured ^{234}U in Blank (B_A)	1.78%	1.86%	2.86%	2.84%	2.33%
Average Measured ^{238}U in Blank (B_B)	1.78%	1.86%	2.86%	2.84%	2.33%
Atomic Mass of ^{234}U (M_A)	1.78%	1.86%	2.86%	2.84%	2.33%
Atomic Mass of ^{238}U (M_B)	1.87%	1.96%	3.01%	3.00%	2.46%
Standard ^{234}U Abundance in U010 CRM (Std_A)	1.44%	1.51%	2.31%	2.29%	1.89%
Standard ^{238}U Abundance in U010 CRM (Std_B)	1.78%	1.86%	2.86%	2.84%	2.33%
Average Measured ^{234}U in U010 CRM (R_A)	1.78%	1.86%	2.86%	2.84%	2.33%
Average Measured ^{238}U in U010 CRM (R_B)	1.78%	1.86%	2.86%	2.84%	2.33%
$^{234}\text{U}/^{238}\text{U}$ ratio in CRM ($\text{True}_{A/B}$)	1.78%	1.86%	2.86%	2.84%	2.33%

5.3.1.2 Standard deviation

Standard deviation was suggested by our collaborators at MURR as an alternative means of representing the uncertainty of the measured isotope ratios of the natural uranium standards, in order to attempt to extract some usable data. However, a significant difference was observed between the measured $^{235}\text{U}/^{238}\text{U}$ isotope ratios of the interspersed natural uranium standards and the natural $^{235}\text{U}/^{238}\text{U}$ ratio used by Brown *et al.* (2014) as a reference value (Figure 88) [256]. Compared to the reference value, the measured $^{235}\text{U}/^{238}\text{U}$ isotope ratios of the four natural uranium standards are significantly less. This result indicates the use of standard deviation to represent the uncertainty associated with the measurement of the $^{235}\text{U}/^{238}\text{U}$ ratios within the Australian UOC and uranium ore samples is no better than previous attempt to represent the uncertainty as expanded uncertainty and does not alleviate the issues previously identified. These results likely reflect the calibration issues that have been discussed in the previous section.

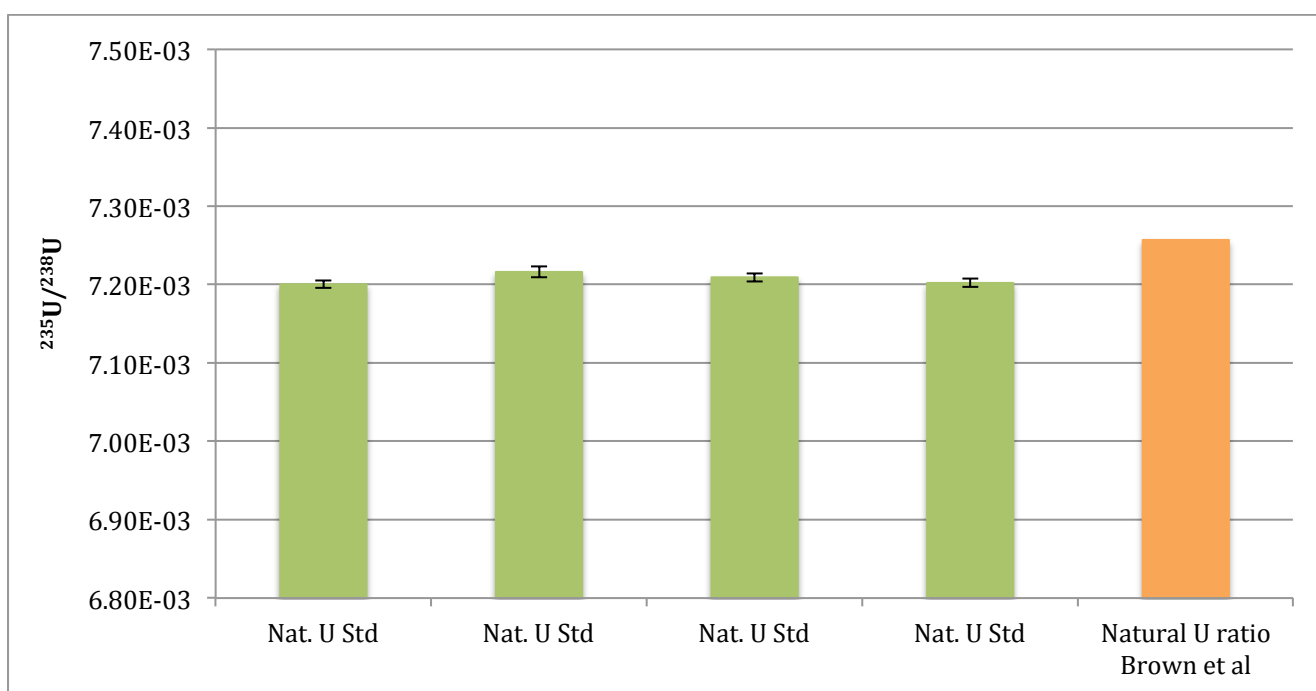


Figure 88 Comparison between replicate analyses (green) of $^{235}\text{U}/^{238}\text{U}$ isotope ratio of 100 ng/g non-certified natural uranium U_3O_8 standard during the analysis of UOC and uranium ore samples in this study and the consensus value for the $^{235}\text{U}/^{238}\text{U}$ isotope ratio of natural uranium (orange) (error bars = standard deviation) [256].

Similarly, the measured $^{234}\text{U}/^{238}\text{U}$ ratios of the interspersed natural uranium standards were also found to significantly differ from the reference value previously used by Brown *et al.* (2014) to assess the performance of the measurement (Figure 89) [256].

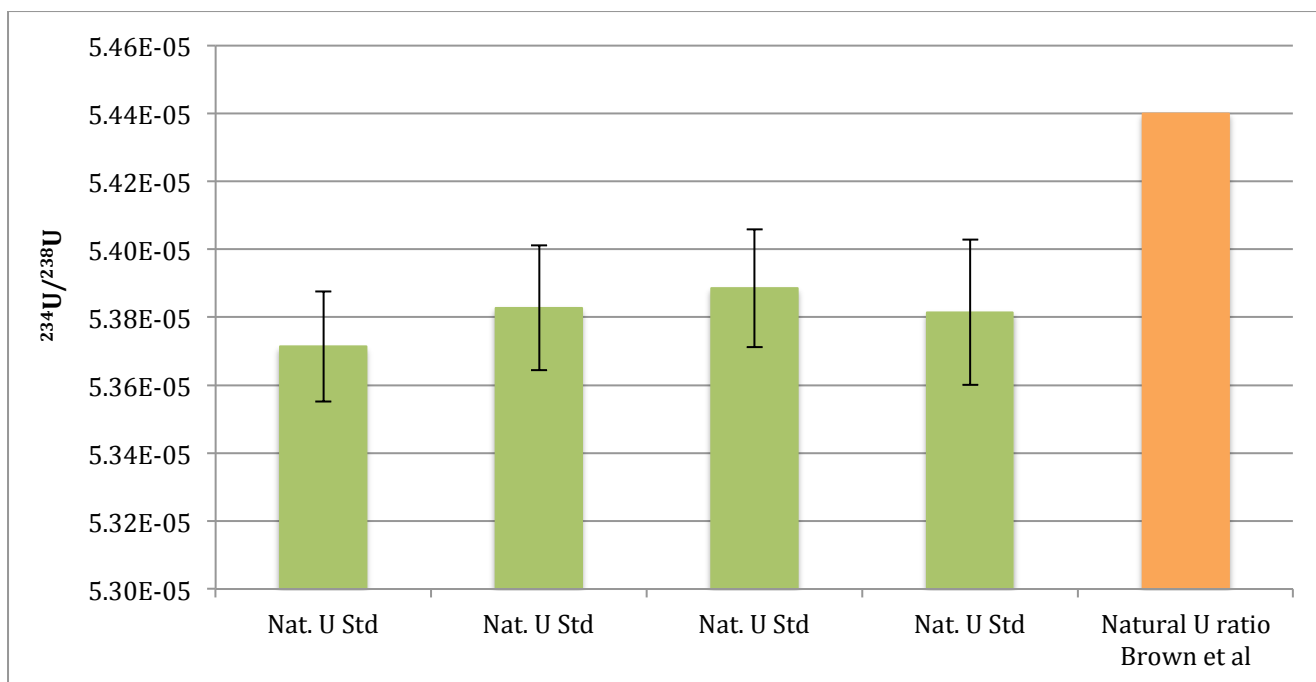


Figure 89 Comparison between replicate analyses (green) of $^{234}\text{U}/^{238}\text{U}$ isotope ratio of 100 ng/g non-certified natural uranium U_3O_8 standard during the analysis of UOC and uranium ore samples in this study and the consensus value for the $^{234}\text{U}/^{238}\text{U}$ isotope ratio of natural uranium (orange) (error bars = standard deviation) [256]

As both uncertainty approaches (where the uncertainty is represented as expanded uncertainty and standard deviation) feature significant issues concerning the calibration and performance of the MC-ICP-MS instrument, attempting to interpret the data from the Australian UOC and uranium ore samples also analysed during this run appears to be ill-advised. As the same issues undoubtedly feature within the Australian UOC and uranium ore samples despite the uncertainty represented as either expanded uncertainty or standard deviation, reanalysis of the samples on a recalibrated instrument is required at a minimum as the current method is not fit-for-purpose and requires revision. (See future work section)

5.3.2 Comparison with other studies analysing U isotope ratios

Within the literature, several other studies have utilised a variety of different approaches for the analysis of isotopic ratios within uranium materials. While our approach analysed the uranium isotopes directly, several other studies have utilised a ^{233}U - ^{236}U double-spike to correct for instrumental isotopic fractionation [7, 10, 235, 257-259]. Relative to thermal ionisation mass spectrometry (TIMS), which was previously the standard approach for measuring uranium isotope ratios [232], MC-ICP-MS experiences significant mass bias effects during isotopic analysis [251]. While the exponential law used for the mass bias correction can account for most of the mass bias

[251], the ^{233}U - ^{236}U double-spike approach has been used by several authors to further correct and account for mass bias, leading to greater precision in the analysis of uranium isotope ratios.

Furthermore, the ^{233}U - ^{236}U double-spike is often used to check for isotopic fractionation during chemical purification, with several authors utilising ion exchange chromatography to pre-concentrate and/or remove any potential interferences prior to analysis by MC-ICP-MS [7, 10, 235, 256, 258, 259]. The presence of both lead and platinum can lead to the formation of multiple polyatomic species with and within the plasma (i.e. $^{195}\text{Pt}^{40}\text{Ar}$ and $^{207}\text{Pb}^{14}\text{N}^{14}\text{N}$ for ^{235}U), which have the same mass of the three uranium isotopes (^{234}U , ^{235}U , ^{238}U) measured in this study, resulting in the distortion of the peak shapes and ultimately impact the accurate measurement of uranium isotope ratios [260, 261]. Mitroshkov *et al.* (2015) [262] and Pollington *et al.* (2016) [260] have both concluded that a desolvating nebuliser can limit the production of oxide and hydride polyatomic interferences, their studies disagree with regards to whether argide polyatomic species (MAr^+) are similarly affected, and therefore require further examination. This, however, is outside the scope of this study and will require further research to be undertaken.

With our study, both the ^{233}U - ^{236}U double-spike (to further account correct for instrumental mass bias) and extraction chromatography (to clean up the samples to remove any polyatomic interfering-forming species within the samples) were unable to be implemented due to several reasons outside of our control. It is therefore for the combination of these phenomena our replicate measurements of the non-certified natural uranium U_3O_8 standard solution deviate from both the natural uranium $^{235}\text{U}/^{238}\text{U}$ ratio Brown *et al.* (2014) compared his analyses to [256]. In studies where both measures were applied [7, 258], greater accuracy and precision is achieved as demonstrated in the analysis of CRM 129 than our study (Figure 90), which will be an important consideration in the evaluation of our data moving forward.

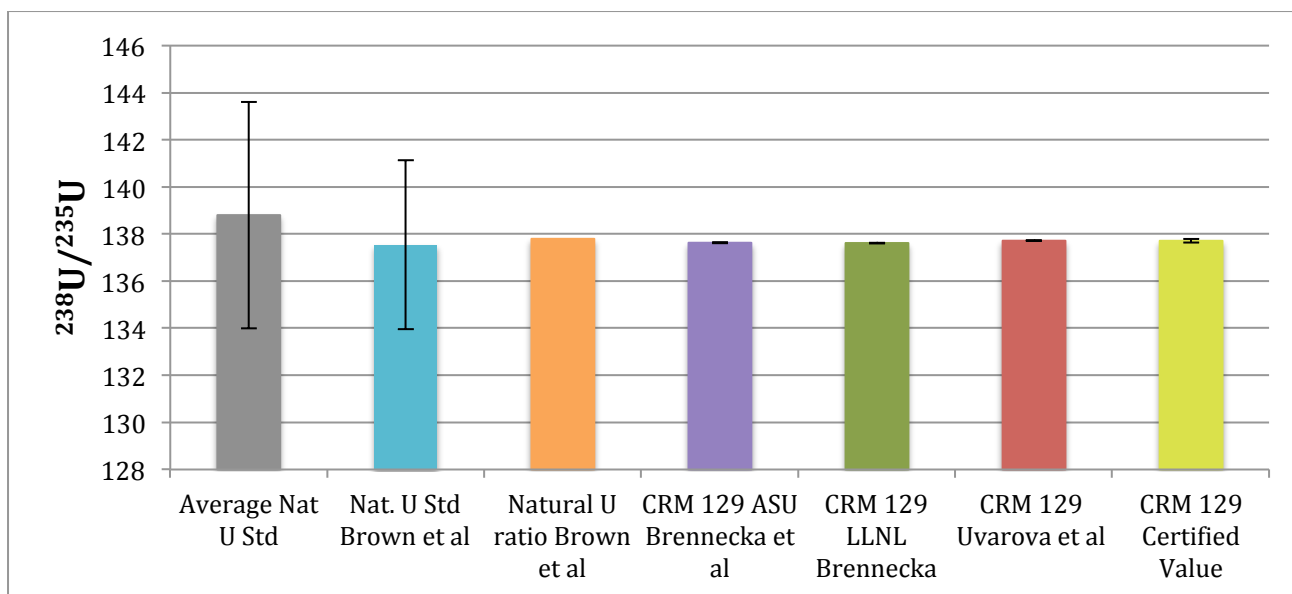


Figure 90 Comparison of several $^{238}\text{U}/^{235}\text{U}$ isotope measurements of two standards with natural uranium isotopic abundance: a non-certified natural uranium standard by this study and Brown *et al.* (2014), and the isotopically certified CRM 129 analysed by Arizona State University, LLNL as part of a study published by Brennecka *et al.* (2010)[7] and a second study by Uvarova *et al.* (2014) [258]. Error bars = expanded uncertainty (k=2).

5.3.3 Comparisons between all Australian UOC and uranium ore samples and complimentary samples previously analysed within the literature

An analysis and discussion on the comparison between the Australian UOC and uranium samples for their $^{235}\text{U}/^{238}\text{U}$ and $^{234}\text{U}/^{238}\text{U}$ isotope ratios can be found within Appendix A, as well as a comparison with literature values of samples from the same mines previously analysed.

5.6 Conclusions

Analysis of the $^{235}\text{U}/^{238}\text{U}$ and $^{234}\text{U}/^{238}\text{U}$ isotope ratios of four natural uranium standards by MC-ICP-MS found mixed results with the previous study performed by Brown *et al.* (2014) [256]. While the $^{234}\text{U}/^{238}\text{U}$ ratio was found to significantly agree with the previous analysis by Brown *et al.* (2014) through single-factor ANOVA, the $^{235}\text{U}/^{238}\text{U}$ results were found to feature to a significant difference with a p-value (0.0078) less than the alpha value (0.05).

Further analysis of the expanded uncertainty budget identified the disproportionate contribution by the counting of the ^{234}U , ^{235}U and ^{238}U for their respective uranium isotope ratios for the four natural uranium standards. For the $^{235}\text{U}/^{238}\text{U}$ ratio, the uncertainty associated with the counting of ^{235}U and ^{238}U isotopes contributed 49.18% each, therefore contributing to 98.36% overall to the expanded uncertainty. The contribution associated with the counting of ^{234}U and ^{238}U contributed 61.11% and

18.20% to the expanded uncertainty of the measured $^{235}\text{U}/^{238}\text{U}$ isotope ratios of the four natural uranium standards. These contributions towards the expanded uncertainty of both isotope ratios far exceeded the contribution by the uncertainty (1.47% and 0% for ^{235}U and ^{238}U respectively) in the certified atomic abundances of the ^{234}U , ^{235}U and ^{238}U in U010 CRM, which was thought to disproportionately contribute to the overall expanded uncertainty when the counts are relatively high and was cautioned to us by our collaborators at MURR.

Given the large uncertainties associated with both the $^{235}\text{U}/^{238}\text{U}$ and $^{234}\text{U}/^{238}\text{U}$ isotope ratios for the Australian UOC and uranium ore samples as well as the ambiguity surrounding the accuracy and precision of the MC-ICP-MS instrument during the analysis, there is little that can be said concerning the variability of $^{235}\text{U}/^{238}\text{U}$ and $^{234}\text{U}/^{238}\text{U}$ isotope ratios within a particular source. This therefore requires further research, as well as the development of better methods, in order to investigate this area of research further.

5.7 Future work

As the current MC-ICP-MS approach was found to lack sufficient precision to measure the $^{235}\text{U}/^{238}\text{U}$ and $^{234}\text{U}/^{238}\text{U}$ isotope ratios, it would be worthwhile to investigate developing a method that used a $^{233}\text{U}/^{236}\text{U}$ double-spike approach, as these methods are markedly superior in the measurement of $^{235}\text{U}/^{238}\text{U}$ isotope ratio than the method used in this study (Figure 90). Previous studies have shown that these methods have considerably smaller uncertainties associated with the measurement of the 3 uranium isotopes in question and has become the norm for the analysis of $^{235}\text{U}/^{238}\text{U}$ and $^{234}\text{U}/^{238}\text{U}$ isotope ratios within UOCs and uranium ores for nuclear forensics [7, 257, 258]. Given that the differences in the $^{238}\text{U}/^{235}\text{U}$ and $^{234}\text{U}/^{235}\text{U}$ according to the formation conditions of the deposit (temperature and oxidising conditions during their genesis) are small (Table 8), a far more sensitive analytical approach is required to better facilitate an investigation into the variability of the $^{235}\text{U}/^{238}\text{U}$ and $^{234}\text{U}/^{238}\text{U}$ isotope ratios into Australian UOCs and uranium ores.

Table 8 Approximate $^{238}\text{U}/^{235}\text{U}$ ratios from three different deposit types of UOCs analysed by Brennecka *et al.* (2010)

Deposit Type	Mean $^{238}\text{U}/^{235}\text{U}$	2 Standard Deviations
Low Temperature Redox	~ 137.88	~ 0.02
High Temperature Redox	~137.83	~ 0.01
Non-Redox	~137.83	~ 0.015

Associated within this, to provide a better objective, robust measure to evaluate the accuracy and precision of the MC-ICP-MS approach used for the measurement of the $^{235}\text{U}/^{238}\text{U}$ and $^{234}\text{U}/^{238}\text{U}$, I would use a CRM in place of the natural uranium standard. For instance, CRM-129A (Uranium Oxide U_3O_8) and CRM-145 (Uranyl (Normal) Nitrate Assay and Isotopic Solution) from New Brunswick Laboratory has been used in several studies for this purpose [7, 235, 258]. Uranium CRMs that are slightly enriched isotopically in $^{235}\text{U}/^{238}\text{U}$, such as NBL U020 CRM (Uranium (Enriched) Isotope U_3O_8 2%) have also been used to calibrate MC-ICP-MS instruments for uranium isotope analysis [263].

For the measurement of uranium ores in particular, the use of extraction chromatography resins for the cleanup and pre-concentration of uranium isotopes should also be investigated. Several other studies analysing ore samples for their $^{238}\text{U}/^{235}\text{U}$ isotope ratios have utilised extraction chromatography resins as part of the preparation of samples, as well as other studies analysing UOCs [7, 258].

Chapter 6. Elemental Analysis of Australian and International Uranium Ores

6.1 Introduction

The elemental composition of samples from the front end of the nuclear fuel cycle (e.g. uranium ores and UOCs) has long been an area of particular focus for nuclear forensics, given the established links between both materials and their ability to ascertain information about the geological conditions of the original uranium deposit mined [2]. The rare earth elements (REE), when normalised against chondrite REE values, provides considerable insight into the original uranium deposit as each type of deposit has been found to feature a characteristic chondrite-normalised REE pattern [115]. Furthermore, the chondrite-normalised REE pattern of the ore deposit is conserved through the chemical and metallurgical processes involved in the production of UOCs, thereby providing a direct link back to its original source [2, 250]. Along with other signatures, this information can assist investigators in determining the provenance of an unknown UOC sample [103, 264].

6.1.1 Rare Earth Elements

The preservation of the chondrite-normalised REE pattern occurs despite the decreases in the total concentration of REEs when comparing between the uranium ore and UOC from the same location [2, 250, 265], and is driven by similarities in the valence and ionic radii between uranium and the REEs. REEs, along with thorium and yttrium, readily substitute for U^{4+} within uraninite (UO_2), a primary uranium mineral, in eight-fold coordination, due to their similar sensitivities towards redox changes and ionic radii (1.16 – 0.977 Å for REEs and 1 Å for U^{4+}) [115, 266].

Several authors, often through a comparison between UOCs and uranium ores from the same source, have studied the preservation of the chondrite-normalised REE pattern. While an earlier study identified that three different Australian UOCs from three different mines feature different, and ‘characteristic’, chondrite-normalised REE patterns [39], a study by Varga *et al.* (2010) found that the whole-rock uranium ores and complimentary UOCs produced at four different mines had the identical chondrite-normalised REE patterns, with no significant alteration or fractionation observed [2]. A more recent study by Varga *et al.* (2017) examined, amongst other nuclear forensics signatures, the chondrite-normalised REE profile of uranium ore from a quartz-pebble conglomerate deposit in South Africa as it was processed through several, successive stages into U_3O_8 , through an ammonium diuranate (ADU) intermediary [250]. While there was some alteration observed between the ore and the UOC (i.e. the extent of the light rare earth (LREE = lanthanum, cerium,

praseodymium, neodymium and samarium) depletion), the chondrite-normalised REE patterns were largely conserved from the ore to the final U_3O_8 product [250]. A comparison between a UOC and uranium ore sample both from a roll front deposit from Wyoming also found their respective chondrite-normalised REE patterns to be indistinguishable from one another given their associated uncertainties [265]. Furthermore, Varga *et al.* (2010), through the analysis of 31 UOCs from different mines and a variety of uranium deposit types by ICP-MS, was able to identify a characteristic overall pattern for each type of uranium deposit [2].

The chondrite-normalised REE patterns within uranium ores, and subsequently UOCs, are considered characteristic of the type of uranium deposit mined; therefore analysis of REE composition of an unknown UOC can provide important geological information that may assist an investigation even if a reference UOC sample of a suspected source is not available. The fractionation of REEs within uraninite and other uranium oxides is thought to reflect several different geochemical factors during the genesis of the uranium deposits, namely the crystallisation temperature, crystallisation of co-genetic REE-rich phases, REE signature of the host rock, salinity of the mineralizing fluids and elemental availability [115, 265]. For instance, flat ($\Sigma LREE/\Sigma HREE \approx 1$) (Heavy rare earth elements (HREE = dysprosium, holmium, erbium, thulium, ytterbium, lutetium)) chondrite-normalised REE patterns with high total (ΣREE) REE concentration are encountered in uranium deposits (intrusive and syn-metamorphic) that formed at high temperatures (>350 °C) [115], whereas vein-type and roll-front deposits have highly fractionated chondrite-normalised REE patterns which are consistent with the host rock, and are unaffected by temperature but influenced by low salinity [115].

The incorporation of REEs within uranium oxides reflects the geological conditions the uranium deposit formed under. When the uranium deposits form at temperatures exceeding 350 °C, no fractionation occurs between the LREEs and HREEs, resulting in a flat chondrite-normalised REE pattern [115]. Furthermore, the chondrite-normalised concentration of europium, relative to the adjacent REEs samarium and gadolinium, can also describe the geochemical environment of the uranium deposit, due to the variability of europium's valence state. Unique for the REEs, europium can exist as both Eu^{2+} and Eu^{3+} , according to the oxygen fugacity of the deposit, resulting in it behaving anomalously with respect to the other REEs, hence it is often being referred to as the europium anomaly, when compared with the chondrite-normalised values of samarium and gadolinium [267]. The behavior of europium may also be examined quantitatively as a ratio (Eu_N/Eu^*); as shown in Equation 47;

$$Eu_N/Eu^* = \frac{Eu_N}{\sqrt{(Sm_N \times Gd_N)}} \quad \text{Equation 47}$$

where Eu_N is the chondrite-normalised ratio of europium within a sample, Eu^* is the theoretical value for no Eu anomaly, Sm_N is the chondrite-normalised ratio of samarium within a sample and Gd_N chondrite-normalised ratio of gadolinium within a sample [267].

6.1.2 Trace Elements

Unlike the REEs, the preservation of the trace element composition between a uranium ore and its corresponding UOC has not been established within the literature concerning nuclear forensics. While the trace elemental composition may be measured within an unknown UOC to compare against other reference UOC samples [101, 103], there has been little evidence attempting to or identifying a reliable link back to the original uranium ore/deposit. Henceforth, in research or case studies involving the comparison between uranium ores and UOCs from or thought to be from the same location, the only elements analysed and reported are the REEs (and their chondrite-normalised REE pattern), despite ICP-MS, a multi-elemental technique, being the principle technique used [268].

A study by Varga *et al.* (2017) investigated several samples obtained throughout various stages of the UOC production process at a facility in South Africa that produces U_3O_8 , via the production and subsequent calcination of ADU [250]. Through the acquisition of these ten samples, the trace and REE composition were measured by ICP-MS to better understand how each stage of the UOC production impacts the composition. Between the ore slurry and cleared leachate solution, the following elements were found to feature a ratio of <2 (a threshold indicating that the element was not highly affected); dysprosium, erbium, holmium, lutetium, nickel, palladium, sulphur, terbium, thorium, thulium, yttrium and ytterbium [250] (Figure 91). Amongst the fifty-three trace and REE measured, the majority of elements had ratios >2 , notably including cerium (11), europium (3.3), gadolinium (2.3), lanthanum (14), neodymium (7.2), praseodymium (8.8), samarium (3.3) [116, 250]. The ore total values were obtained through the digestion of the dried ore slurry using 8 M HNO_3 /0.02 M HF whereas the in-house leach was performed via the following method, to best emulate the leaching process used by the mine; 10 % H_2SO_4 , 1:1 solid:liquid ratio, 24 hour leaching duration and centrifugation and filtering using a 0.45 μm cellulose-acetate membrane [250]. Significant levels of incomplete leaching is evident when sulphuric acid is solely used, with only between 1-40% of the trace element content being leached through this process [250]. In addition to

the impact to the REEs, certain trace elements may be further impacted, such as barium, lead and strontium, which form insoluble sulphate precipitates and will be removed from the process stream [250]. A comparison between the in-house leach and the cleared leachate trace element compositions identified manganese, sodium and cadmium may be impacted through process-related contamination or by the addition of manganese oxide (II) as an oxidant, whilst niobium, zirconium and titanium are found in higher concentrations (ratios of 45, 25 and 41 in-house leachate/cleared leachate) and are located in the cleared leachate [250].

Ion exchange (IX) separation is the second stage in the production of UOC in this study, where changes to the trace composition were reflected through separation factors between the concentrations in the cleared leachate and the IX eluate. Molybdenum, niobium, thorium, titanium and zirconium were found to feature low separation factors (<10), as these elements could form sulphate complexes that remained well retained by the IX resin [250]. In addition to REEs (which had high separation factors between 88.3-104), the following elements had separation factors greater than 80; aluminium, beryllium, calcium, cadmium, caesium, gallium, potassium, lithium, magnesium, nickel, palladium, rubidium, antimony, selenium, strontium, yttrium and zinc [250].

The third stage was the stripping of uranium, as well as trace and REE impurities, from the IX resin and a second purification stage using solvent extraction (SX). Again, a separation factor was used to express changes in the trace composition between the IX eluate and the loaded SX solution [250]. Several elements were found to feature low separation factors (< 10), including; gold, bismuth, cobalt, hafnium, iridium, molybdenum, niobium, platinum, rhenium, selenium, technetium, tungsten and zinc [250]. Several platinum-group elements present, such as iridium, platinum, osmium, ruthenium, rhodium and palladium, within the South African uranium ore have been identified by the authors as potential signatures to be explored further, such as iridium and platinum which were found to have low separation factors (1.3 and 1.9, respectively) during the SX phase [250]. The authors however fail to note that palladium and ruthenium have separation factors of 120 and 'higher than 1070' respectively during the SX process, which would indicate the platinum-group elements do not in fact 'behave chemically relatively similar' as claimed by the authors [250]. Furthermore, there is a lack of data concerning the behavior of these elements in the previous two stages, as for the first stage (leaching) only palladium was reported, with a ratio between the ore versus the cleared leachate of 1.4 [250]. In the second stage, IX separation, again only one of the six identified platinum-group elements was reported with a ratio between the cleared leachate versus the IX eluate for palladium reported as a ratio of 99.6 [250].

The fourth stage examined was the precipitation of the loaded solution with ammonia to form ADU, where the separation factor between the precipitate and loaded solution was again used to examine changes in the composition [250]. In this instance, a separation factor between 0.75 and 1.25 was considered a 'quantitative precipitation' with no separation effect [250], which is a departure from the previous interpretation of separation factors in the earlier stages. Eleven elements (cadmium, hafnium, molybdenum, platinum, rubidium, antimony, scandium, technetium, thorium, tungsten and zirconium) were found to quantitatively precipitate into the ADU, with the majority of elements remaining in the aqueous phase [250]. Several elements were found to concentrate within the ADU (aluminium, barium, cerium, chromium, dysprosium, iron, gallium, gadolinium, indium, neodymium, strontium and titanium), whilst only palladium (separation factor >3), platinum (1.16) and iridium (1.29) were measurable within the ADU of the platinum-group elements [250].

In the final stage, where ADU was calcined to U_3O_8 , the majority of trace elements were found to feature separation factors of 1, indicating that there was little change in their concentration following the calcination process [250]. Of the platinum-group elements, only platinum could be measured and was found to have a ratio ~ 0.9 [250]. Ultimately, the authors concluded that the REEs and 'certain impurities', as well as other signatures (i.e. organic compounds and radiochronometry via $^{230}\text{Th}/^{234}\text{U}$) 'were relevant' for presumably the assessment of uranium material provenance of production process, but failed to identify which, if any, impurities aside from the REE could link the trace elemental composition of the ore to the UOC [250].

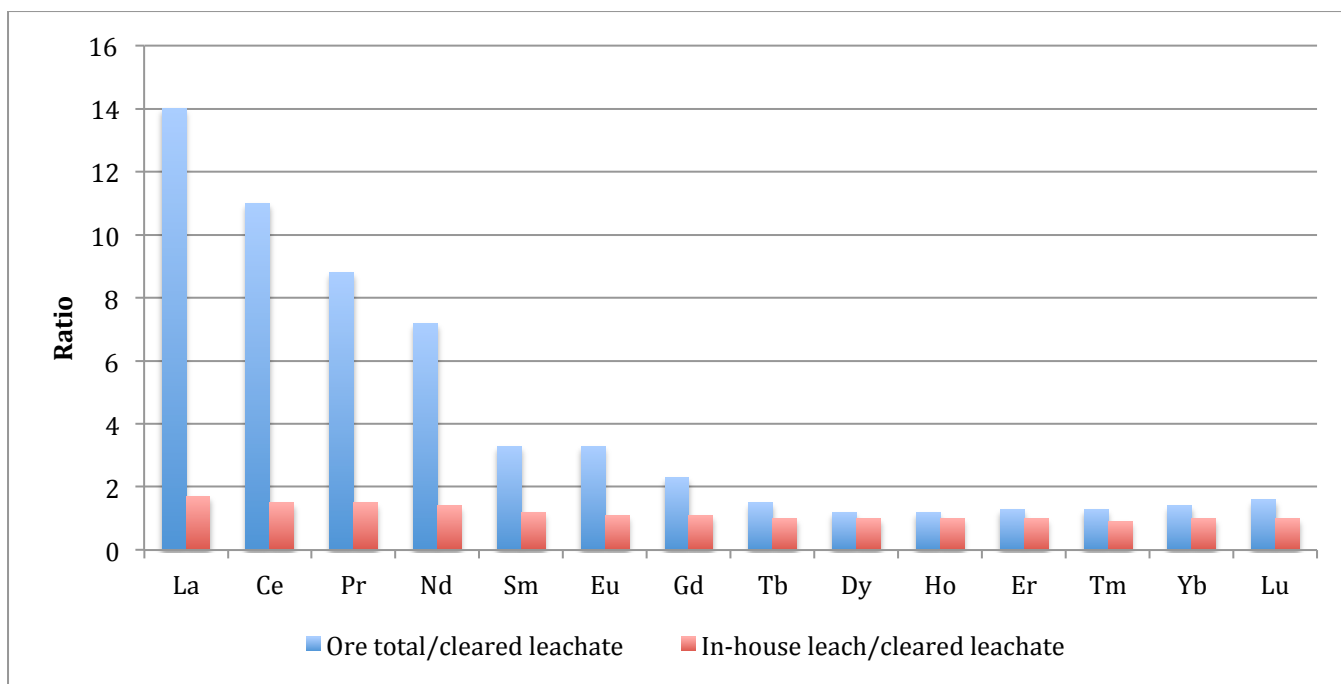


Figure 91 Comparison between the Ore total/cleared leachate and In-house leach/cleared leachate ratios for the REEs normalised to uranium analysed by Varga *et al.* (2017)

6.1.2 Elemental Analysis Techniques in Nuclear Forensics

The trace element and REE analysis of UOCs and uranium ores within nuclear forensics are typically performed using two different approaches and set of analytical techniques; point/spot analysis and bulk analysis. Point analysis typically involves laser ablation inductively coupled plasma mass spectrometry (LA-ICP-MS) [268], secondary ion mass spectrometry (SIMS) or electron probe microanalysis (EPMA) of specific regions within a sample (i.e. uraninite crystal grains from an ore deposit [269]), to measure the trace and REE composition.

Bulk analysis is predominantly performed using ICP-MS, where the entire or subset of the sample undergoes acid digestion into solution. While the digestion of uranium oxides and UOCs may be considered relatively straightforward with nitric acid (HNO₃) used in concert with a hot plate (50 – 140 °C) or microwave digestion [127], additional acids, such as hydrofluoric acid (HF) or hydrochloric acid (HCl) may be required [84, 270]. Given the complexity of ores with several mineral phases, and particularly the presence of difficult-to-digest minerals such as silicates, multiple acids are frequently used. There is, however, some reported concern that the complete digestion of ores, through the use of multiple acids, may lead to ‘overprinting’ of the chondrite-normalised REE pattern from the uranium minerals present, due to the inclusion of REE incorporated within silicates and other refractory minerals within the ore sample [271].

The digested uranium solution may then be analysed directly by ICP-MS following dilution, however they are typically put through an additional treatment to either remove the matrix element uranium or remove other trace elements that may be detrimental to the analysis of particular analytes. As the concentration of REEs are often considerably less than the concentration of uranium in both UOCs (0.1 – several 100 µg/g [2]) and uranium ores, the high concentration of uranium can have an adverse effect on the measurement of REEs by ICP-MS due to matrix effects [39, 127]. While such a discrepancy between the concentration of the analytes and the matrix element is in itself problematic, having uranium as the matrix element further complicates the analysis as the severity of space-charge effects is dependent upon the mass of the matrix element [39, 272].

A second issue concerning the direct analysis of the digested uranium solution is the presence of other elements within the digested uranium sample. The other elements can impact the analysis of particular analytes, having the same atomic mass-to-charge ratios (m/z) (isobaric interference) or form a polyatomic species within the ICP-MS instrument with the same mass [127]. While the impact of isobaric interferences can be minimised by analysing a different isotope of the target analyte (as long as the new isotope chosen doesn't have any interference issue of its own) or subtracting its contribution to the target analyte signal, this may not always be possible. Another form of interference arises from the formation of polyatomic species, where metal species (M) bond with oxides ($M^{16}O^+$), argides ($M^{40}Ar^+$) and hydroxides ($M^{16}OH^+$) species within the plasma, which have the same m/z as the target analytes. For instance, barium has several isotopes that can form oxides that have the same m/z as several REEs, as well as instances where the oxides of LREE themselves have the same m/z as particular HREEs (

Table 9) [273-277].

To overcome the issues of matrix suppression and polyatomic interferences surrounding the analysis of UOCs and uranium ores with ICP-MS, several different strategies have been reported in the literature. One common strategy used in the literature is extraction chromatography, where the digested uranium solution is passed through a chromatography column packed with a preconditioned extraction resin, which consists of beads coated with an organic compound with functional groups that have an affinity for the target analyte(s) [2, 127, 271]. As the affinity of the resin towards the matrix element uranium and the interfering elements is significantly less than the target elements, they are less strongly held by the column and can be stripped by successive washes. The analytes

can then removed from the column with a separate stripping solution. The extraction chromatography method can drastically improve the analysis of REEs within UOCs, with a method developed by Varga *et al.* (2010) using an Eichrom TRUTM extraction resin improving the detection limits two orders of magnitude (into the low pg/g range) when compared to no chemical extraction [278]. Other strategies used to separate the REEs from the uranium include precipitation, solvent extraction or the use of multiple methods in a sequence (for example, precipitation of the REEs before preconcentration using extraction chromatography) [279, 280].

Table 9 Analytes and their respective interfering species for ICP-MS analysis [273-277]

Analyte (M)	Analyte Abundance (%)	Interfering species (M ¹⁶ O ⁺ , M ¹⁶ O ¹ H ⁺)
¹⁵¹ Eu ⁺	52.18	¹³⁵ Ba ¹⁶ O ⁺
¹⁵³ Eu ⁺	47.82	¹³⁷ Ba ¹⁶ O ⁺
¹⁵² Sm ⁺	26.7	¹³⁶ Ba ¹⁶ O ⁺
¹⁵⁵ Gd ⁺	14.8	¹³⁹ La ¹⁶ O ⁺
¹⁵⁷ Gd ⁺	15.68	¹⁴¹ Pr ¹⁶ O ⁺
¹⁵⁹ Tb ⁺	100	¹⁴³ Nd ¹⁶ O ⁺
¹⁶³ Dy ⁺	24.97	¹⁴⁷ Sm ¹⁶ O ⁺
¹⁶⁶ Er ⁺	33.6	¹⁵⁰ Nd ¹⁶ O ⁺ , ¹⁵⁰ Sm ¹⁶ O ⁺
¹⁶⁷ Er ⁺	22.94	¹⁵¹ Eu ¹⁶ O ⁺
¹⁶⁹ Tm ⁺	100	¹⁵³ Eu ¹⁶ O ⁺
¹⁷² Yb ⁺	21.9	¹⁵⁶ Gd ¹⁶ O ⁺
¹⁷³ Yb ⁺	16.13	¹⁵⁷ Gd ¹⁶ O ⁺
¹⁷⁵ Lu ⁺	97.41	¹⁵⁹ Tb ¹⁶ O ⁺
¹⁶⁵ Ho ⁺	100	¹⁴⁹ Sm ¹⁶ O ⁺

While extraction chromatography or other approaches can remove either the matrix element uranium or the interfering species, they are often labour intensive [280], require the use of expensive chemicals and extraction resins [127], generate moderate quantities of radioactive waste and introduce potential opportunities for human-related biases and errors that may influence the measurement of the analytes. Therefore, while ICP-MS has been extensively used so far in the nuclear forensics discipline for the trace and REE analysis of UOCs and uranium ore samples, there is an opportunity for other bulk-analysis elemental analysis techniques to be used in conjunction with ICP-MS should their performance (accuracy, precision etc) be comparable to, or better than, ICP-MS.

Hence, in this chapter we explored the efficacy of neutron activation analysis (k_0 -NAA), a technique seldom used in this nuclear forensics discipline, which has long been recognized for its accuracy, reproducibility and precision, as well as its high selectivity and absence of several matrix and interference effects [281]. Furthermore, k_0 -NAA is suitable for a variety of different samples and a large breadth of target elements across the periodic table, with minimal sample preparation required.

k_0 -NAA has been employed for the measurement of trace elements and REE for a variety of different fields including botany [282], archaeology [283, 284], hydrology [285], metallurgy [286] and atmospheric science [287]. More importantly, NAA has been extensively used across a variety of geological samples, such as volcanic ash [288], soils [289], phosphorite ore deposits [289, 290], which most closely parallels the type of samples encountered in nuclear forensics, uranium ores and UOCs. An example of the implementation of NAA towards the analysis of a geological sample is the study performed by Gméling *et al.* (2014) where NAA and prompt gamma activation analysis (PGAA) were both used to measure the trace and REE composition of a series of volcanic rock and soil samples, as well as three geological standard reference materials (SRMs) (JBL2, GSP2 and Sco-1) [281]. For the three different SRMs, both PGAA and NAA (both employing k_0 -NAA standardisation) were used to measure the major certified elements within a relative bias of below 10%, which is equal to the measured value minus the recommended value divided by the recommended value and reported as a percentage [281]. Of the four elements (zirconium, strontium, samarium and gadolinium) to fall outside of the 10% relative bias across the Sco-1 and JB-2 SRMs, they still fell within the recommended value's uncertainty [281]. Comparing the two techniques, NAA was found to analyse a larger number of elements with lower limits of detection, when compared to PGAA, however there were instances where the complementarity of using both techniques was advantageous; silicon, boron, hydrogen and cadmium were only measurable by PGAA and the chlorine and gadolinium results were found to be more reliable with PGAA than NAA [281].

While k_0 -NAA has previously been identified as a potentially valuable technique for nuclear forensics again recognizing its ability for multi-elemental analysis with great sensitivity and selectivity [291], there has been little interest so far to consider and evaluate k_0 -NAA for nuclear forensics applications. One instance within the literature concerning NAA and nuclear forensics is the analysis of a uranium ore sample by NAA for its chondrite-normalised rare earth pattern, in order to compare with the chondrite-normalised patterns of a number of UOC and uranium ores from former and currently operating Australian uranium mines as part of an investigation of a seized UOC

sample [103]. The NAA results were reported to be agreeable to XRF and ICP-MS analysis to within 5%, when elements were above their detection limits [103].

Another study by Asim *et al.* (2017) analysed four different uranium ore CRMs (IAEA-S-8, IAEA-S-12, IAEA-S-13 and IAEA-S-17) and a lake sediment CRM (IAEA-SL-1) for their elemental composition using both k_0 -NAA and ICP-OES [292]. As the four uranium ore CRMs were only certified for their uranium concentration, k_0 -NAA was found to be the superior technique for the measurement of uranium with relative differences between -6%-14% observed from the certified uranium values, whereas relative differences of 13%-50% were obtained by ICP-OES [292].

The predominant issue in regards to the utilisation of NAA for the trace and REE composition of UOCs and uranium ores, besides the limitations concerning access to a facility capable of performing NAA, is the generation of fission-product nuclides originating from the fission of ^{235}U [29, 103]. The formation of fission-product nuclides further complicates the measurement of REEs in UOCs and uranium ores, as several of the REEs (^{140}La , ^{141}Ce , ^{143}Ce , ^{147}Nd , ^{153}Sm) themselves are directly affected [29, 293, 294]. ^{140}La is a particularly interesting case as it may be formed through three different processes; $^{139}\text{La}(n,\gamma)^{140}\text{La}$ (activation), $^{235}\text{U}(n,f)^{140}\text{La}$ (fission of ^{235}U) and $^{235}\text{U}(n,f)^{140}\text{Ba} \rightarrow ^{140}\text{La}$ (fission of ^{235}U and β^- decay of ^{140}Ba) [148, 295].

The interference on ^{140}La is a unique case, as ^{140}La can also be formed as the decay product of ^{140}Ba ($t_{1/2} = 12.75$ days), which itself a fission product of ^{235}U [294]. ^{153}Sm is also noteworthy, as it is interfered by a second process where neutron capture by ^{238}U produces ^{239}Pu , which emits X-rays of the same energy (103 keV) as the γ -rays produced through the decay of ^{153}Sm [293].

Fortunately, several of these interferences arising from the fission of ^{235}U can be corrected for through the calculation of interference factors, as well as changes to the analysing or sampling strategies. An interference factor F is a ratio of the specific activity directed by neutron capture and the specific activity originated from uranium fission and is calculated using the following equation (Equation 48) [294];

$$F = \frac{m_X}{m_U} \cdot \frac{A_U}{m_X} \quad \text{Equation 48}$$

where m_x and m_U are the masses of the analyte (X) and uranium, respectively, whereas A_U and A_X are the activities from the fission product and the activation product of the analyte X, respectively [294]. A_U and A_X can be calculated using the following equations (Equations 49 & 50) [294, 296];

$$A_U = \frac{m_U a_U N_0 f}{M_U} \cdot (\phi_{th} \sigma_{th}^U \phi_{ep} \sigma_{ep}^U) \cdot (1 - e^{-\lambda_X t_{irrad}}) \quad \text{Equation 49}$$

$$A_X = \frac{m_X a_X N_0}{M_X} \cdot (\phi_{th} \sigma_{th}^X \phi_{ep} \sigma_{ep}^X) \cdot (1 - e^{-\lambda_X t_{irrad}}) \quad \text{Equation 50}$$

where the indices X and U refer to analyte X and uranium, M is the atomic weight, a is the isotopic abundance, N_0 is Avogadro's number, f is the cumulative fission yield, σ_{th}^U and σ_{ep}^U are the fission cross-sections for thermal and epithermal neutrons, λ_X is the decay constant of the activation product of the analyte, ϕ_{th} and ϕ_{ep} are the thermal and epithermal neutron fluxes, σ_{th}^X and σ_{ep}^X are the capture cross-sections for thermal and epithermal neutron fluxes and t_{irrad} is the irradiation time [294]. Equations Y and Z can then be combined with Equation X to enable the interference factor F for a particular analyte to be calculated from experimental nuclear data of the analyte and the neutron parameters of the reactor itself (Equation 51) [294];

$$F = \frac{M_X a_U f [\sigma_{th}^U + (\phi_{ep}/\phi_{th}) \sigma_{ep}^U]}{M_U a_X [\sigma_{th}^X + (\phi_{ep}/\phi_{th}) \sigma_{ep}^X]} \quad \text{Equation 52}$$

Apart from the limitations surrounding access to a research reactor capable of performing NAA, the most prevalent issue concerning the measurement of trace and REE elements in uranium-rich samples is the generation of fission products during analysis. During irradiation, the ^{235}U present within the samples will undergo fission and split, which can produce daughter products that can impede the analysis of several REEs in particular (Figure 24).

6.1.3 Justification

To date, ICP-MS is the predominant elemental analysis technique used for the measurement of REEs and trace elements within UOCs and uranium ores for nuclear forensics [2, 39, 250]. The measurement of REE, in particular, is of high importance to nuclear forensics, as the chondrite-normalised REE pattern of a uranium ore sample remains largely unaffected by the chemical and metallurgical processes in the production of UOCs, resulting in the UOC having a similar pattern [2, 250]. Therefore, the chondrite-normalised REE pattern can provide a direct link back to the original ore deposit mined through the analysis of the UOC.

The analysis of REEs within UOCs and uranium ore concentrates can however, be complicated by the high concentration of uranium (relative to the concentration of the REEs), as well as polyatomic interferences arising from barium and LREEs [127, 273, 274]. While some of these issues can be overcome using extraction chromatography and co-precipitation methods [127], they also invite opportunities for sample contamination and human-related biases, as well as generating large quantities of radioactive waste and requiring expensive resins.

k_0 -NAA is an alternative multi-elemental analysis technique, which, so far has been seldom used for the analysis of trace and REEs within uranium ore and UOC samples. While it has been used to investigate the REE composition of a uranium ore sample in a nuclear forensics investigation and the trace elements within uranium ores for geological studies, there has been no systematic study to assess the suitability to k_0 -NAA for the analysis of uranium ore samples for nuclear forensics.

The aims of this study were to;

1. Evaluate the suitability of k_0 -NAA at the OPAL research reactor at ANSTO for the trace and rare earth elemental analysis of 4 uranium ore CRMs, and compare with ICP-MS (the industry standard)
2. Investigate links between the trace and rare earth elemental composition of uranium ores and UOCs from different sources, and differences between uranium ores from different sources/deposit types

6.2 Methods

6.2.1 Preparation of Australian and international uranium ore samples for analysis

A table of the eighteen Australian and North American uranium ore samples analysed as part of this study is provided below (Table 10). Their geographical location is provided in **Error! Reference source not found.** and **Error! Reference source not found.**, respectively.

Table 10 Australian and North American uranium ore samples analysed in this study

Name	Location
Australian Samples	
Beverley	South Australia
Ranger 1 & 2	Northern Territory
Olympic Dam 1 & 2	South Australia
Four Mile	South Australia
Mary Kathleen	Queensland
North American Samples	
Big Indian Wash District	Utah, USA
Calyx No 8	Utah, USA
Green Dragon	Utah, USA
Happy Jack	Utah, USA
Mi Vida Mine	Utah, USA
Ike-Nixon Shaft	Utah, USA
Uravan Mineral Belt	Colorado, USA
Midnite Mine	Washington, USA
Ferguson Lode Claim	South Dakota, USA
Ruggles Mine	New Hampshire, USA
Cardiff Mine	Ontario, Canada

Each North American uranium ore sample obtained from the South Australian Museum was received as a rock sample with a single or a number of smaller pieces. For some of the larger single pieces (>0.8 cm in length), a hammer with its head covered by plastic bags was needed to break them down into more manageable pieces for the agate mortar and pestle. Afterwards, all of the samples were ground into a fine powder through wet grinding in acetone. To minimize cross-contamination between each sample, the plastic bags were replaced on the head of the hammer, and the mortar and pestle cleaned with an acetone-dampened paper towel, immersed and cleaned with a Decon 90 detergent solution, and finally rinsed with acetone. Between 0.693 and 1.6 g of each North American uranium ore sample was ground and stored in glass scintillation vials within a desiccator.

The Australian uranium ore samples were received in a powdered form, with the exception of the Ranger 2 sample, which consisted of several smaller (~ 1 cm in length) rocks. This samples was wet-ground using the procedure earlier described.

Four uranium ore CRMs obtained from ORE Assay Standards (OREAS) were also included within the study (CRM 100a, 106, 120 and 124) (

Table 11), as they were the only CRMs available that had the largest number of REEs with certified and varied concentrations in a high uranium matrix. These four CRMs were selected as they were uranium ores with the greatest number of REEs certified. Each CRM has multiple certified values for each certified element, reflecting different sample preparation procedures (4-acid digestion, sodium peroxide or lithium borate fusion, powdered pressed pellets) for different analytical techniques (ICP-MS, inductively-coupled plasma optical emission spectrometry (ICP-OES), X-ray fluorescence spectroscopy (XRF)). The variety of different certified values for a suite of analytical techniques reflects the intended use of the CRMs from OREAS, where they would be used for mining quality control (QC) analyses. Already in a powdered form, these four OREAS CRMs were also stored in multiple glass scintillation vials within a desiccator until required.

Table 11 Summary of OREAS U Ore CRMs (CRMs) analysed within the study

CRM	Certified [U] ($\mu\text{g/g}$) ($\pm 1\sigma$)	Number of certified REE	Certified [La] ($\mu\text{g/g}$)	Number of certified elements	Source of CRM material
100a	135 ± 11	14	260 ± 13	15	U ore from Mt Gee uranium prospect, South Australia
106	1143 ± 34	14	54 ± 30	1	U ore from Croker Well project, South Australia. Mixed with dry rhyodacite (volcanic rock)
120	40.8 ± 1.39	14	21.1 ± 1.77	17	Uranium ore sourced from Mantra Resources Nyota Prospect, Tanzania
124	1794 ± 73.9	14	21.6 ± 1.30	32	Uranium ore sourced from Mantra Resources Nyota Prospect, Tanzania

6.2.2 Quantification of uranium content within international uranium ore samples using SEM/EDX, pXRF and DNAA

The uranium content of the international uranium ore samples needed to be known prior to their analysis by NAA in order to determine what masses of each sample could be analysed, or if any samples should be excluded due to impermissible concentrations of uranium and/or other problematic elements. Preliminary results were obtained through SEM/EDX and portable (pXRF), whereas more robust results were obtained through DNAA.

6.2.2.1 SEM/EDX

For the SEM/EDX analysis, approximately 0.5-1 mg of each uranium ore sample was affixed to double-double-sided carbon tape adhered to an aluminium stub. The Ranger 2 uranium ore was not included in this study as the sample was not in our possession at this time. Platinum (10 nm thickness) was initially used to prevent charging, however this was changed to carbon (175-250 Å) as the software that calculated the elemental composition of the sample did not allow platinum to be excluded as a function, unlike carbon (

Table 12). Henceforth, carbon was used to coat the remaining samples, as it did not impact the elemental composition of each point analysed. For the samples that were coated in platinum, platinum was not initially excluded from the list of elements identified within the sample to prevent it from being included within the elemental composition calculations, however for a select number of samples it was then manually excluded

Table 12).

Elemental analysis was performed using a FEI Phenom F50 SEM/EDX instrument (Hillsboro, OR) operating with a 20 kV accelerating voltage and a spot size of 6 at 100x magnification. Measurements were taken for 30 seconds with the exception of the Ranger 1 sample, which was instead 50 s. The lowering of the duration of each measurement location was due to high counts in excess of 20,000 counts per second. Approximately 20 locations were analysed across each sample (Figure 92), and the elemental concentrations obtained from the ZAF calculation, with the subtraction of the coating material (Pt or C) prior to the calculation. The average concentration and the standard deviation was determined from the ~20 individual measurements across a sample, however a number of analyses were omitted across all of the samples if they featured low counts or high backgrounds (

Table 12).

Table 12 Sample preparation and analysis of the Australian and North American uranium ore samples by SEM/EDX

Sample	Coating and thickness	Inclusion of Pt within ZAF calculations	No of spots analysed	No of spots excluded
Beverley	Pt (10 nm)	Yes	20	0
Ranger 1	Pt (10 nm)	Yes	22	0
Olympic Dam 1	Pt (10 nm)	Yes	23	0
Olympic Dam 2	Pt (10 nm)	Yes	20	0
Four Mile	Pt (10 nm)	No	21	0
Mary Kathleen	Pt (10 nm)	No	22	1 (Zero data reported for spot 13)
Big Indian Wash District	C (~175 Å)	N/A	21	0
Calyx No 8	Pt (10 nm)	No	22	0
Green Dragon	C (~175 Å)	N/A	20	0
Happy Jack	C (~200-250 Å)	N/A	21	0
Mi Vida Mine	C (~175 Å)	N/A	21	1 (Zero data reported for spot 2)
Ike-Nixon Shaft	C (~200-250 Å)	N/A	21	1
Uravan Mineral Belt	C (~200-250 Å)	N/A	22	0
Midnite Mine	Pt (10 nm)	No	21	0
Ferguson Lode Claim	C (~200-250 Å)	N/A	20	1 (Zero data reported for spot 15)
Ruggles Mine	Pt (10 nm)	No	21	0
Cardiff Mine	C (~200-250 Å)	N/A	22	1 (Zero data reported for spot 8)

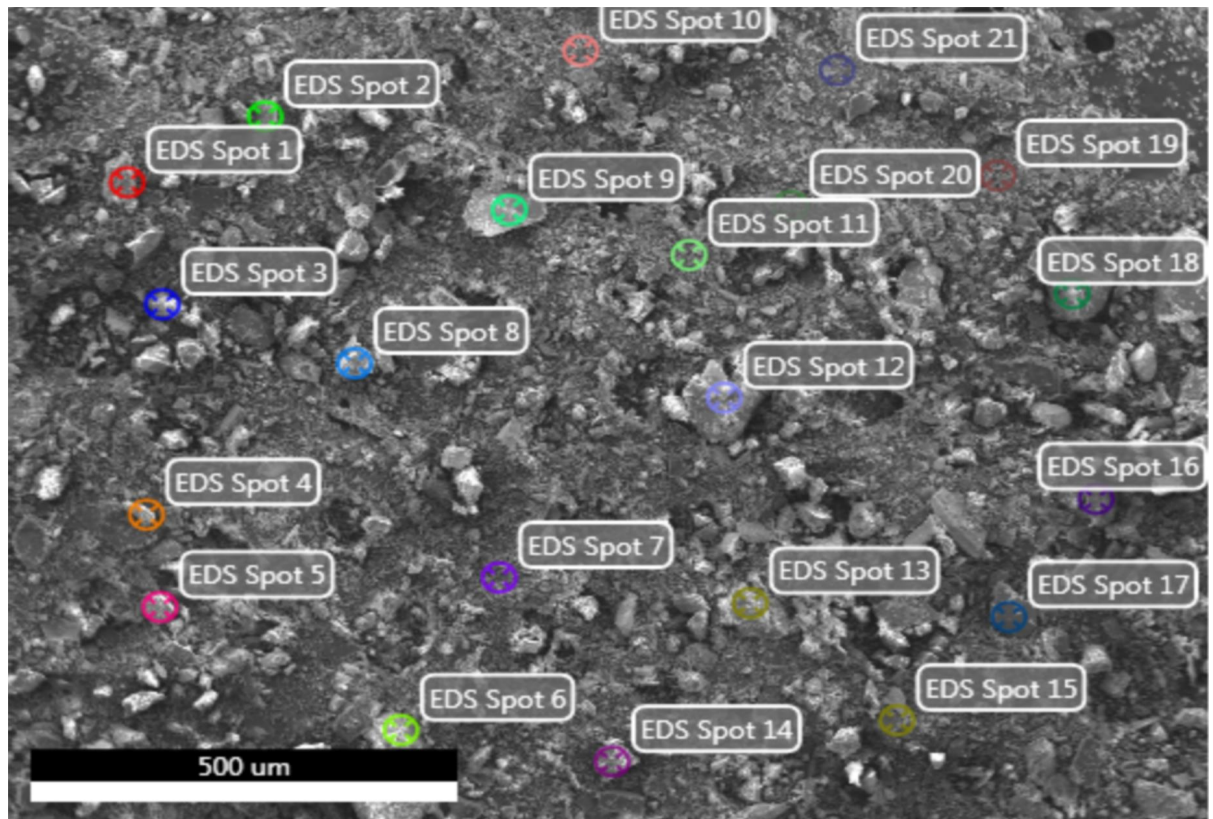


Figure 92 Distribution of SEM/EDX measurements across Ruggles Mine uranium ore sample

6.2.2.2 Portable XRF

A Bruker Tracer-III V⁺ portable X-ray fluorescence spectrometer (Billerica, MA) was also used to determine the uranium content of the North American uranium ore samples. Approximately ~ 100 mg of each uranium ore sample was loaded into polyethylene sample cups fitted with an X-ray transparent 100 μm Mylar film, which was found to be sufficient to completely cover the elliptical window (8 x 6 mm) of the pXRF device (Figure 93).

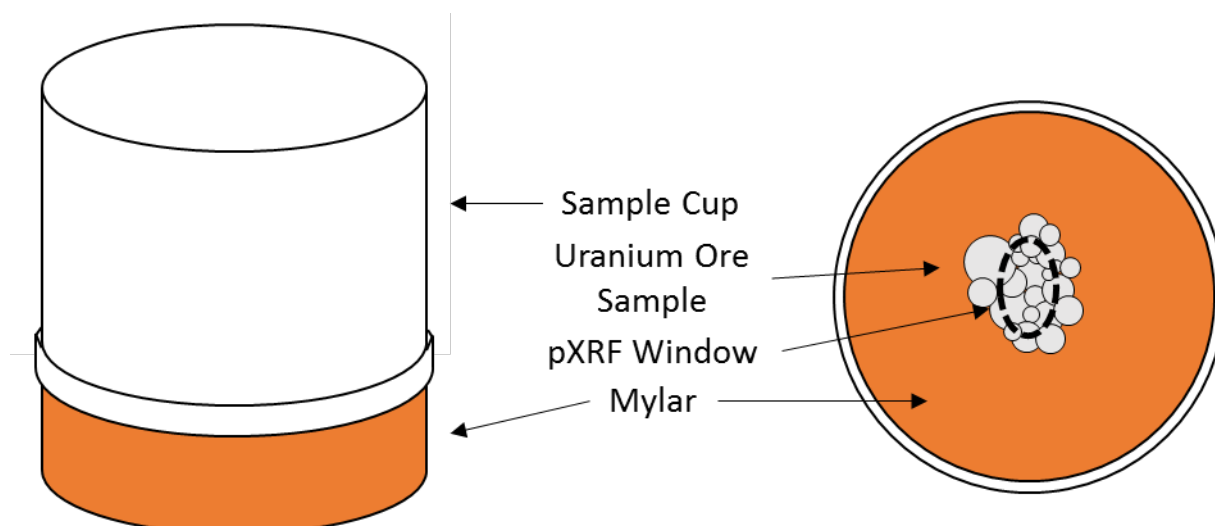


Figure 93 Schematic diagrams of the sample cup and Mylar film used for the pXRF analysis of the international uranium ore samples

Four different sets of experimental parameters were trialed to identify the particular setting that provided the greatest sensitivity, with the Cardiff uranium ore samples used in the comparison (Table 13). An increase in the accelerating voltage enables more elements and the more X-ray spectral lines of elements to be detected, as the accelerating voltage has to be equal to or greater than the absorption edge for a particular X-ray spectral line for a particular element to fluoresce. An increase in the current increases the intensity of X-rays emitted by the pXRF, as the cathode emits more electrons. Performing XRF measurements under vacuum is advantageous for two reasons; it reduces the background due to scatter caused by the interaction of X-rays with the atmosphere and reduces the absorption of low energy X-rays [297]. This has the effect of improving the detection limits and allows low atomic number elements, such as sodium, to be detected by XRF, respectively [297]. The first set of conditions (Set #1) was used for the further elemental analysis of the remaining uranium ore samples.

Table 13 Experimental conditions trialled for pXRF analysis of Cardiff uranium ore sample

	Set #1	Set #2	Set #3	Set #4
Accelerating Voltage (kV)	40	40	25	25
Current (mA)	2	2.5	2.5	2.5
Analysis Time (s)	60	60	60	60
Under Vacuum?	Yes	No	Yes	No

Quantification of the uranium content was performed using the Bruker ‘S1CalProcess’ add-in for Microsoft Excel. Using the four OREAS CRM as the reference set, a calibration set for U was developed following the ‘Empirical Calibrations’ quantification method. S1CalProcess is a propriety calibration method that uses empirical calibrations for the quantification of elemental data. This calibration was then applied to the spectra obtained from the international uranium ore samples, quantifying the amount of U present in each sample.

6.2.2.3 DNAA

Delayed neutron activation analysis (DNAA) measurements were made at the OPAL reactor at ANSTO. Between 1.6 and 6.1 mg of each international samples was loaded into a polyethylene canister and pneumatically transferred to SRT-DNAA position for a 1 minute irradiation in a thermal neutron flux of $\sim 5 \times 10^{12} \text{ cm}^{-2} \text{ s}^{-1}$ (Table 14). The neutron flux has previously been characterised as highly thermalized, with a calculated thermal/epithermal neutron ratio of >6500 . After a 10 second decay (during which the samples were also pneumatically transferred back), delayed neutron measurements were taken within an array of six BF_3 detectors (Centronic, UK) for 1 minute. The DNAA method used CRMs 104 (Pitchblende Ore – Silica Mixture Uranium Standard (0.01% U)) and 105 (Pitchblende Ore – Silica Mixture (0.001% U)) (New Brunswick Laboratory, US) to generate a two-point linear calibration, from which the uranium concentration of the international samples could be calculated.

Given the grade of uranium of Australian uranium ore samples have been previously well characterised within the literature (the maximum uranium concentration $<0.1\%$ U), these samples were not pre-analysed to determine their uranium content.

Table 14 Masses of International Uranium Ore Samples analysed by DNAA

Sample	Mass analysed by DNAA (mg)
Cardiff Mine	6.1
Happy Jack Mine	4.0
Ferguson Lode Claim	4.1
Green Dragon	2.2
Uravan Mineral Belt	2.5
Ruggles Mine	2.8
Midnite Mine	4.2
Big Indian Wash District	3.2
Mi Vida Mine	3.2
Ike-Nixon Shaft	3.8
Calyx No 8	1.6

The Ike-Nixon Shaft sample was also reanalyzed using DNAA by Dr Mellodee Anvia of ANSTO Minerals, who then applied a correction method developed to correct for the uranium self-shielding phenomenon that can lead to the underestimate of the true uranium concentration within the sample [298]. In addition to the corrected DNAA values, Dr Anvia also performed ICP-MS and gamma counting measurements to validate the accuracy of the DNAA correction in its application to the Ike-Nixon Shaft sample. The correction method utilises the following equation by Dyer *et al.* (1962) to calculate the expected delayed neutron counts [299] (Equation 53);

$$N_d = \sigma_f \phi N \sum \frac{a_i}{\lambda_i} (1 - e^{-\lambda_i t_b}) e^{-\lambda_i t_d} (1 - e^{-\lambda_i t_c}) \quad \text{Equation 53}$$

where N_d is the number of delayed neutrons emitted, σ_f is the thermal neutron cross-section of ^{235}U (cm^2), ϕ is the effective thermal neutron flux ($\text{n cm}^{-2}\text{s}^{-1}$), N is the number of atoms of ^{235}U , a_i is the absolute group yield of neutron precursors in delayed neutron group I, λ_i is the decay constant of delayed neutron group i (s^{-1}), t_b is the irradiation time (s), t_c is the counting time (s) and t_d is the delay time (s) [298]. Through a comparison with the measured neutron counts, the expected delayed neutron counts could be used to determine the detector efficiency (%), which was found to decrease linearly with the measured counts [298]. From the equation of the line generated through the

analysis of multiple standards plotting detector efficiency versus measured counts, the corrected counts can be calculated from the following equation (Equation 54) [298];

$$\text{Corrected neutron counts} = \frac{\text{Measured neutron counts}}{\text{Detector efficiency}} \quad \text{Equation 54}$$

6.2.3 Quantification of the trace and rare earth elemental content of Australian and international uranium ore samples using k_0 -NAA

In order to measure as many REE and trace elements as possible, two different irradiation and sampling protocols were employed. While the majority of REE and trace elements would be measurable by performing long irradiations, a short irradiation strategy was also employed in order to measure dysprosium, however it also enabled several trace elements (aluminium, chlorine, indium, iodine, magnesium, manganese and titanium) to be measured also. The experimental parameters used for the long and short irradiations can be found in Table 15. Each uranium ore sample and CRM from OREAS would also be measured in duplicate.

Table 15 Experimental parameters for k_0 -NAA short and long irradiations

Irradiation	Position in OPAL	Neutron Flux	Irradiation Duration	Measurement Protocol
Short	SRT-NAA	$\sim 2.2 \times 10^{13} \text{ cm}^{-2} \text{ s}^{-1}$	30 s	3 min collection less than 15 min after irradiation for Al (^{28}Al $t_{1/2} = 2.241$ min) and V (^{52}V $t_{1/2} = 3.743$ min)
				Minimum 10 minute collection within 20 minutes following irradiation
				Minimum 30 minute collection, within a few hours after irradiation. Samples with high manganese required a longer decay, for the measurement of dysprosium within the samples
Long	LE1-1A, LE1-1B, LE1-1C	$\sim 2.6 \pm 0.5 \times 10^{12} \text{ cm}^{-2} \text{ s}^{-1}$	4 hrs	Minimum 30 minute collection, four to five days after irradiation
				Minimum 4 hour collection, at a minimum of 15 days after irradiation

As all of the uranium ore samples, particularly the North American samples, were found to be highly variable with respect to their elemental composition, the samples were analysed in two batches for both long and short irradiation protocols. This approach was taken to ensure the activity of the samples post-irradiation were within permissible limits for the facility. Furthermore, the Ike-Nixon Shaft sample, with a corrected uranium concentration of 55.7 ± 1.8 wt%, was deemed to be too high in the concentration of uranium to be safely irradiated within the OPAL reactor and was excluded for the remainder of the study. The masses analysed for both long and short irradiations of all uranium ore samples, with the exception of the excluded Ike-Nixon Shaft sample, and the four OREAS CRMs are below (Table 16).

Table 16 Masses for the long and short irradiation of samples by k_0 -NAA in the OPAL reactor

Sample	Short #1 mass (mg)	Short #2 mass (mg)	Long #1 mass (mg)	Long #2 mass (mg)
Cardiff Mine	6.1	6.1	6.6	5.6
Happy Jack Mine	4.0	5.9	6.1	5.3
Ferguson Lode Claim	42.6	39.1	38.3	39.5
Green Dragon	2.2	6.2	20.0	22.7
Uravan Mineral Belt	2.5	5.3	30.0	28.3
Ruggles Mine	9.3	11.2	10.0	11.2
Midnite Mine	21.9	14.3	21.2	20.6
Big Indian Wash District	3.2	6.0	4.4	4.2
Mi Vida Mine	3.2	22.7	21.4	19.9
Calyx No 8	1.6	19.5	19.7	19.0
Beverley	41.9	15.5	38.6	40.3
Olympic Dam A	10.0	21.3	10.9	11.5
Olympic Dam B	28.9	32.6	31.6	31.8
Ranger A	40.7	7.4	40.1	39.1
Ranger B	30.3	59.9	32.5	25.9
Four Mile	31.1	33.4	29.6	29.4
Mary Kathleen	33.3	21.4	31.9	33.2
OREAS CRM 100a	50.3	53.0	52.9	56.4
OREAS CRM 106	51.0	47.0	49.8	46.2
OREAS CRM 120	50.7	48.7	50.7	49.5
OREAS CRM 124	49.5	48.0	50.5	46.3

The rare earth and trace elemental data obtained from the four OREAS U ore CRMs were reported as percentage deviation (%) from their certified values, respective of the multiple certifications due to different sample preparation methods. The rare earth elemental data from the Australian and international uranium ore samples was normalized using chondrite values reported by Anders & Grevesse (1989), while the trace element data was reported in parts per million ($\mu\text{g/g}$).

6.3 Results

6.3.1 Quantification of uranium content within international uranium ore samples by SEM/EDX, pXRF and DNAA

Three different analytical techniques were used to determine the concentration of uranium within the international samples; two preliminary approaches (SEM/EDX & pXRF) and DNAA. The first technique employed was SEM/EDX, which identified highly variable quantities within the international uranium ore samples analysis, with respect to the measured average concentration and the variance (uncertainty) (Figure 94). However, the variable mean values for each sample were accompanied by large uncertainties due to the high percentage errors in the semi-quantitative uranium concentrations measured using this ‘point analysis’ approach, particularly when the uranium concentration is found to be low (Figure 94). These results highlight the major fault in the point analysis approach, as the concentration (and its associated uncertainty) measured are entirely dependent on the spot analysed i.e. region with little concentration of uranium results in low value with high associated uncertainty whereas regions with greater concentrations result in higher values with a small associated uncertainty (Figure 94 & Figure 96). The representativeness of the SEM/EDX measurements towards the uranium concentration in the international uranium ore samples is also questionable, given the total size of the regions analysed versus the field of view (Figure 94), much less the larger amount of sample (0.5-1 mg) deposited on the SEM stubs themselves.

Despite measuring a larger area of the samples, the pXRF measurements were largely found to feature similar uranium concentrations across in the international uranium ore samples (in comparison to the results of DNAA), with possibly the Calyx No 8 sample as an exception. This aberration is likely due to limited number of reference materials certified for uranium used during the development of the empirical calibration and the limited range in uranium concentration between them. The four OREAS standards had certified uranium concentrations between the range of 40.8 ppm (OREAS 120 CRM) and 1794 ppm (OREAS 124 CRM), which is significantly less than the uranium concentrations obtained by DNAA/corrected DNAA for a number of the international uranium ore samples (Figure 2). An empirical calibration method requires the desired elements to be within the concentration range of the CRMs used to develop the calibration in order to account for matrix effects (absorption or enhancement of X-ray spectral lines within the sample), as pXRF is a matrix-dependent technique [300]. With a grossly insufficient amount of CRMs available, of which had considerably lower concentrations of uranium that were later found within the North American

uranium ore samples, there is little confidence in the ability of pXRF to accurately quantify the concentration of uranium within any of the North American samples analysed.

Of the three different analytical techniques used, DNAA was found to provide the most precise measurement of the uranium concentration within the international uranium ore samples (Figure 97). Four samples (Cardiff Mine, Happy Jack Mine, Big Indian Wash District and Ike-Nixon Shaft) were found to contain uranium concentrations in excess of 10% wt U, with the Ike-Nixon Shaft sample reporting a uranium concentration of $46.6 \pm 2.6\%$. However, the measured concentration of the Ike-Nixon Shaft sample is likely to underappreciate the uranium concentration due to the non-linearity between the counting of delayed neutrons and the masses of uranium used in the calibration in high-uranium matrices [298]. The non-linearity is thought to be due to delayed neutron counting losses arising from high dead times of the BF_3 detectors, and is encountered when the mass of ^{235}U within a sample exceeds approximately 0.05 mg [298]. The loss of linearity due to increasing dead time due to a high uranium matrix has been recognized within other studies, where a linear response was predicted to occur until the amount of uranium exceeds 200 μg using the DNAA system at the National Institute of Standards and Technology (NIST), however this was outside the scope of the study [301].

The Ike-Nixon Shaft sample was reanalyzed by Dr Mellodee Anvia of ANSTO Minerals using DNAA, who applied a correction algorithm developed to correct for this non-linearity responsive [298]. This DNAA approach found the uranium concentration in the Ike-Nixon Shaft sample to be $55.7 \pm 1.8\%$ (Figure 98). As part of her analysis, the corrected DNAA results was corroborated and found to be in good agreement with the results of ICP-MS and gamma counting (measurement of ^{239}Np (228 & 278 KeV).

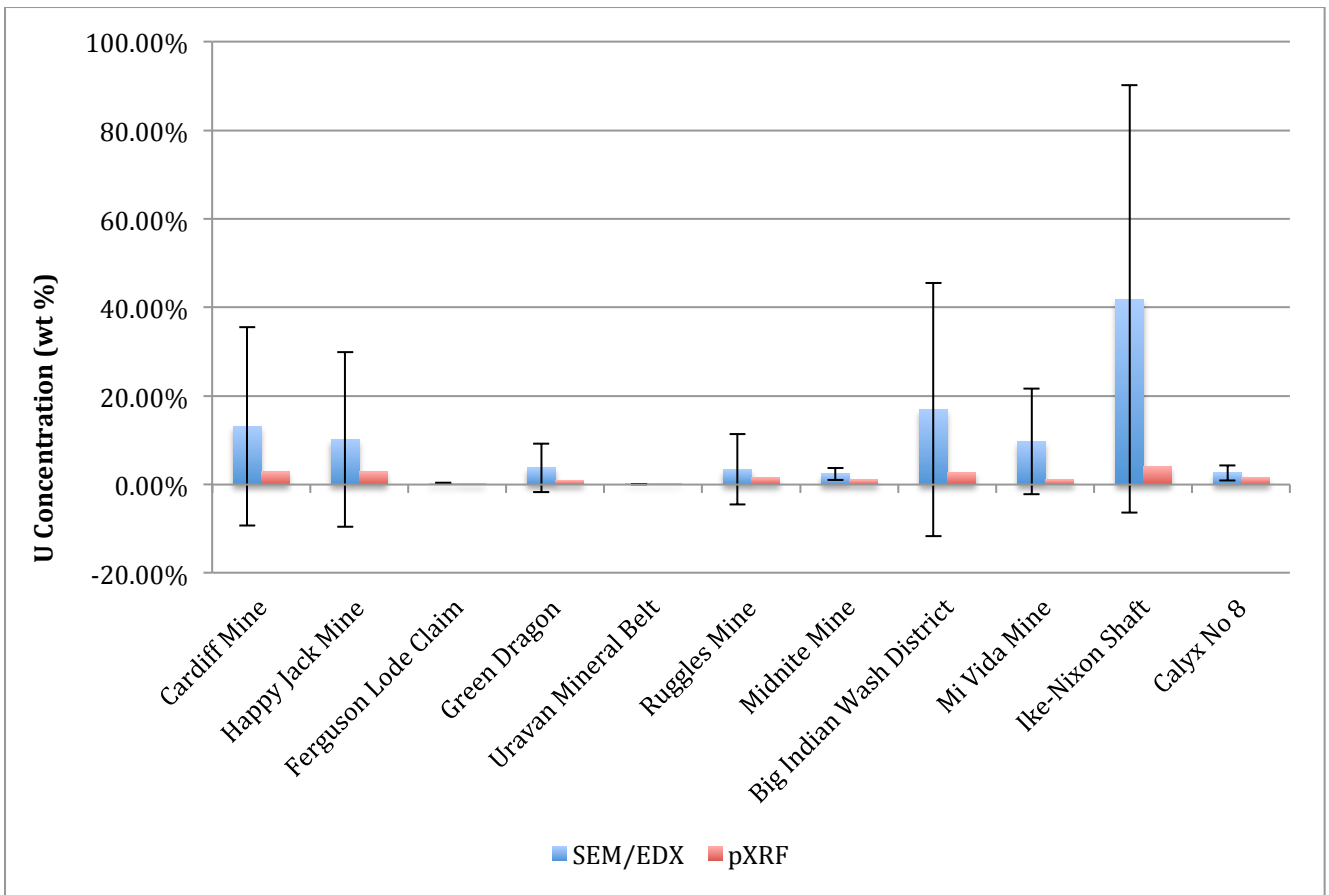


Figure 94 Quantification of U content within the North American uranium ore samples using SEM/EDX, pXRF and DNAA

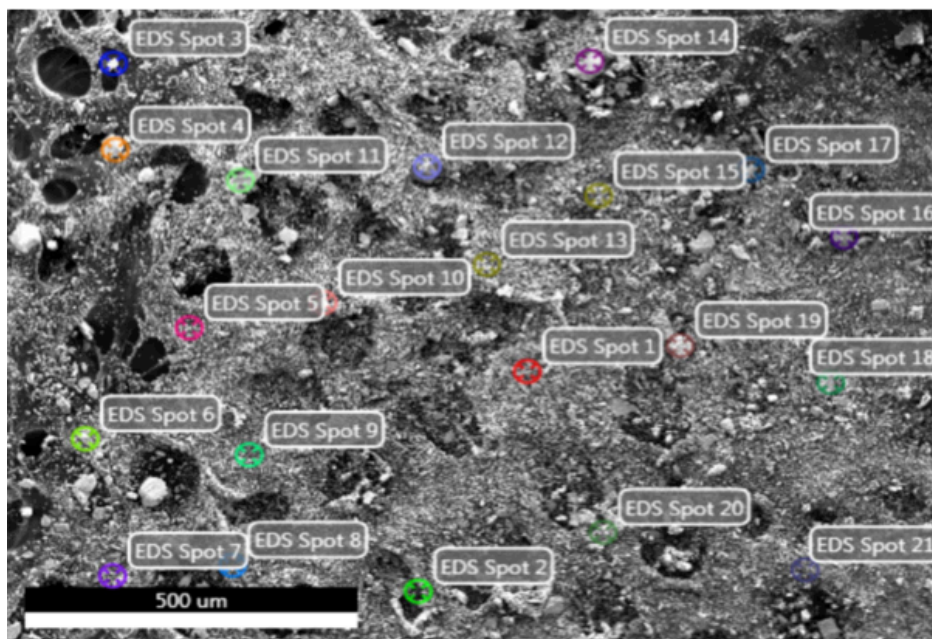


Figure 95 Analysis sites for EDX measurements within Ike-Nixon Shaft international uranium ore samples

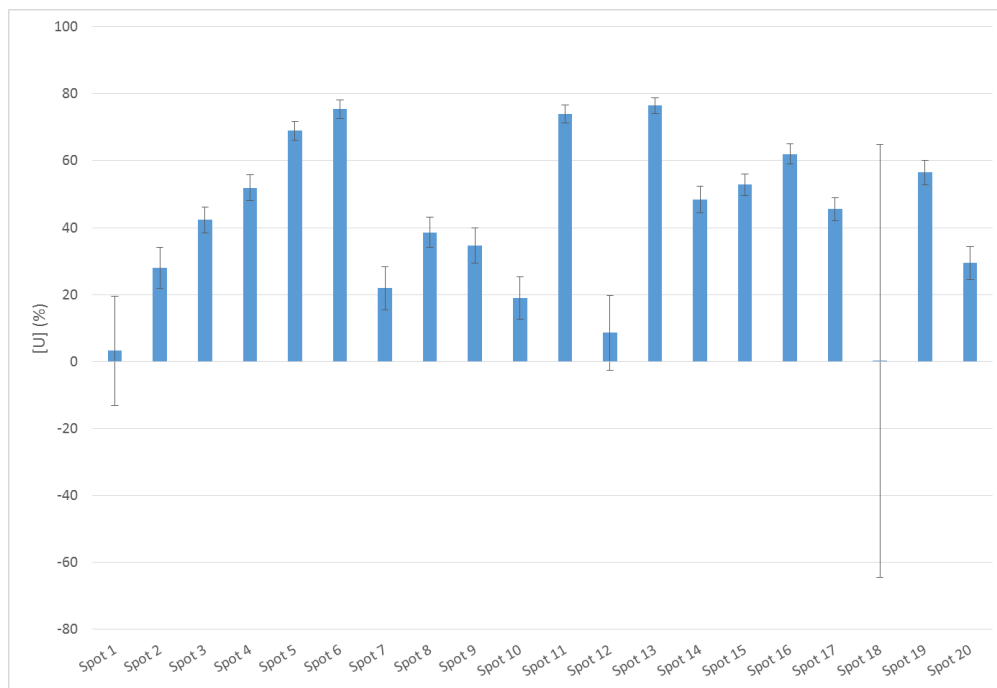


Figure 96 Semi-quantitative measurements of U concentration (% wt) at various spots within the Ike-Nixon Shaft samples by SEM/EDX

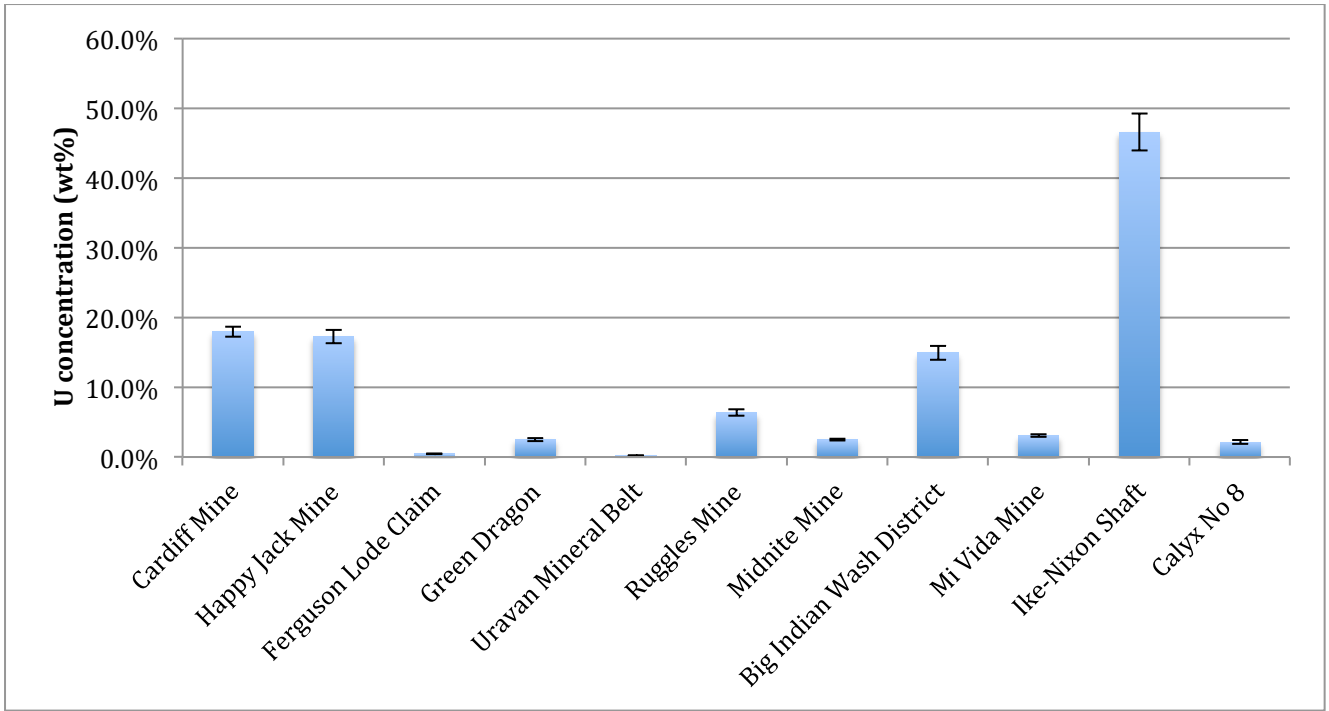


Figure 97 DNAA measurements of the uranium concentration (wt%) within the international uranium ore samples

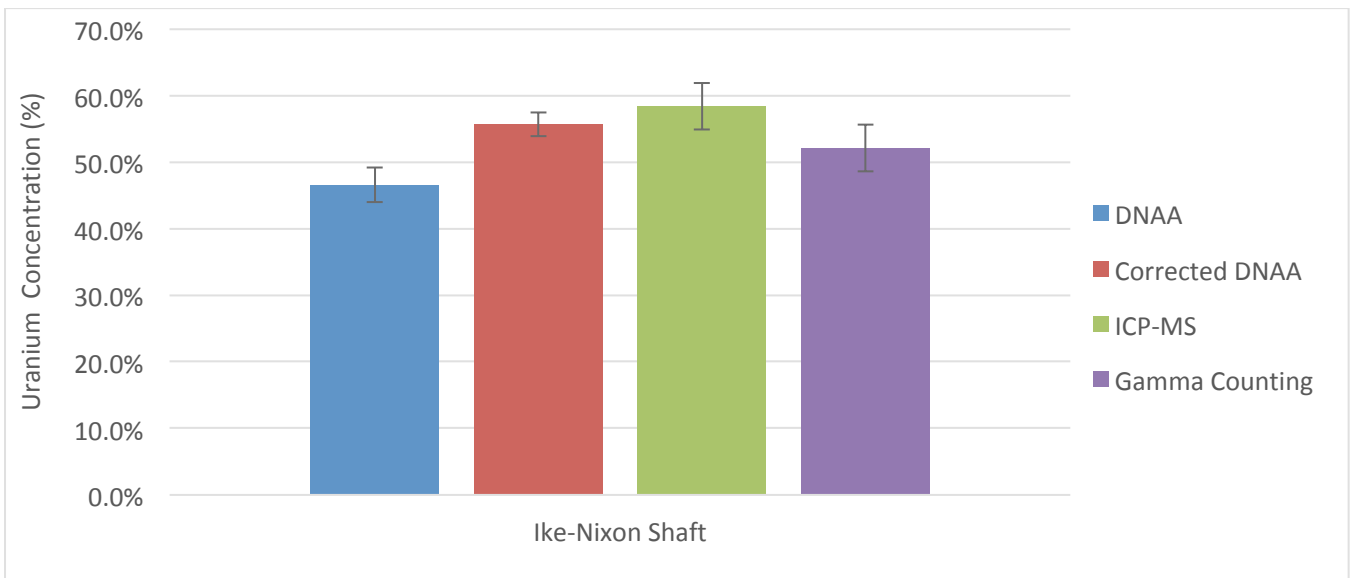


Figure 98 Quantification of U content within Ike-Nixon Shaft U Ore sample using DNAA, corrected DNAA, ICP-MS and Gamma Counting

6.3.2 Comparison between U analyses between k_0 -NAA and DNAA within OREAS Standards

In addition to DNAA, k_0 -NAA analyses, with the exception of the Ike-Nixon Shaft sample, which was excluded from further analysis, were also able to quantify the uranium concentration within the international uranium ore samples. Quantification of uranium was performed by k_0 -NAA through

the measurement of the γ -emission of ^{239}Np (106 keV) formed from the β^- decay of ^{239}U formed through neutron capture by ^{238}U [289]. In the long and short irradiation k_0 -NAA measurements of uranium within the four OREAS standards, good agreement is found between the measured and certified values (Figure 98).

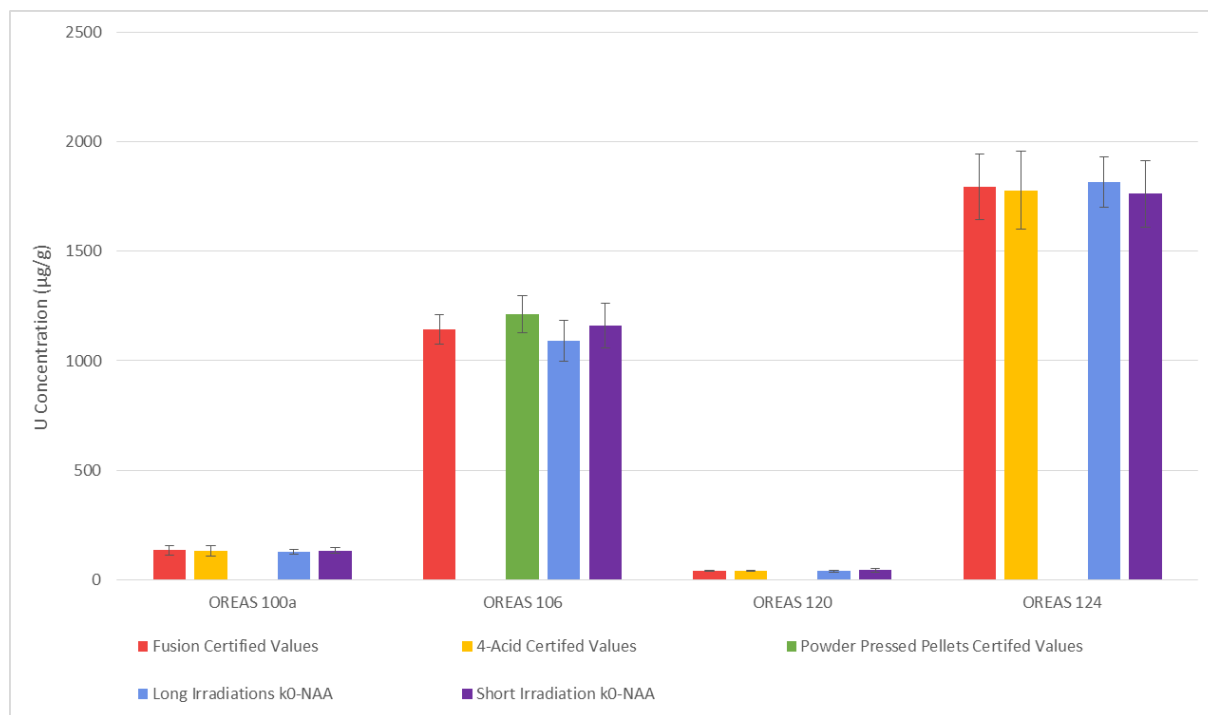


Figure 99 Comparison of long and short irradiation k_0 -NAA measurements of U within OREAS CRMs with certified values (error bars = 2σ)

A good linear agreement is also found between the two k_0 -NAA measurements and the DNAA measurements of the international uranium ore samples excluding the Ike-Nixon Shaft sample, which was not analyzed by k_0 -NAA (Figure 100).

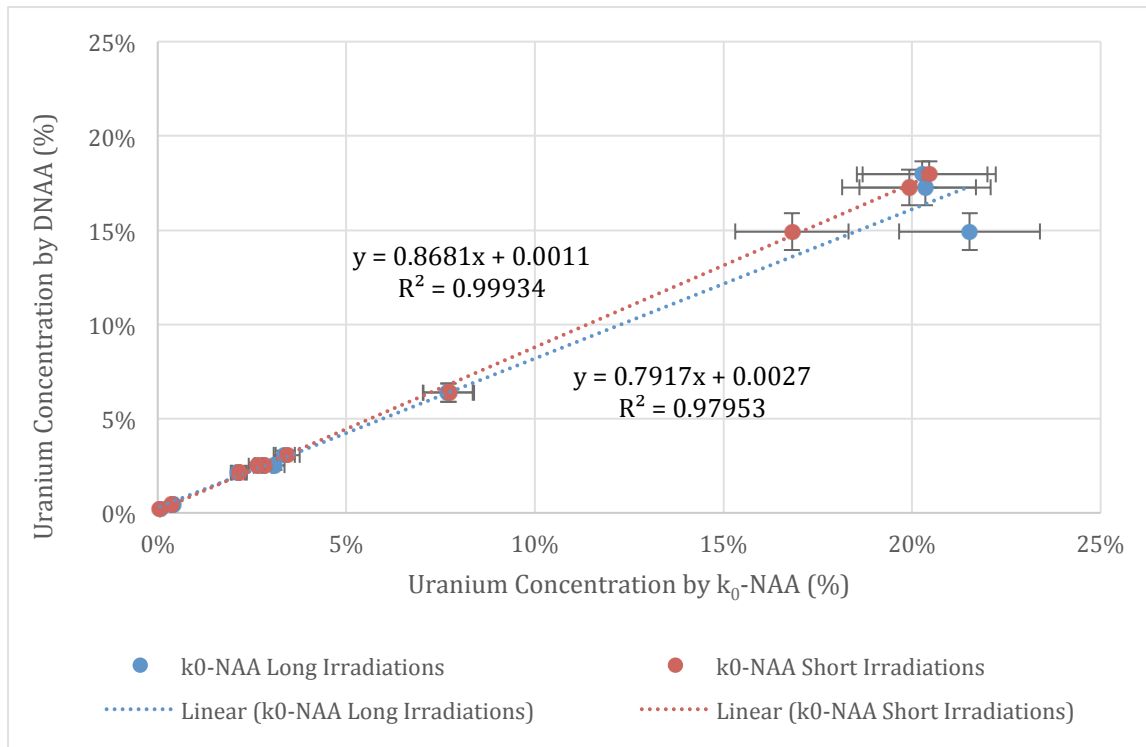


Figure 100 [U] measured by DNAA vs short and long irradiation k_0 -NAA within International Uranium Ore samples, with the exception of the Ike-Nixon Shaft sample

6.3.3 Analysis of OREAS certified reference materials with k_0 -NAA

Four OREAS CRMs (100a, 106, 120 and 124) were analysed to evaluate the accuracy of k_0 -NAA at OPAL for the analysis of trace and rare earth elements within uranium matrices. The four OREAS CRMs were chosen for this study as they collectively have certified concentrations for all the rare earth elements and a wide selection of trace elements. One caveat with their use in this study, however, is that as the OREAS CRMs are intended only to be used in the validation and quality control of XRF, ICP-OES and ICP-MS methods, and have different certified values according to which sample preparation method is used (for example, fusion methods using sodium peroxide or lithium borate vs four-acid digestion ($\text{HF-HCl-HNO}_3\text{-HClO}_4$) for ICP-OES/MS analysis). Despite their lack of absolute certified values for their selection of certified trace and rare earth elements, these OREAS reference materials were included within the study as they are the only reference materials of a similar uranium matrix with certified rare earth elements.

6.3.3.1 Analysis of OREAS 100a CRM by k_0 -NAA

In the analysis of the OREAS 100a CRM by k_0 -NAA, reasonable agreement is observed in the measurement of the trace elements with a percentage difference of $\pm 10\%$ with the exception of

copper and vanadium, which exhibit larger deviations of 21.7% and 15.6%, respectively (Table 17). High overall activity limits the measurement of copper (as often observed within geological materials), as ^{64}Cu has a weak γ -emission at 1346 keV, due to its low emission probability (0.474%) [302]. The analysis of vanadium through the measurement of the 1.434 MeV γ -emission ^{52}V , a short-lived radionuclide ($t_{1/2} = 3.74$ min), is made difficult due to Compton background interference from several radionuclides, including ^{24}Na , ^{28}Al , ^{28}Cl , ^{49}Ca and ^{56}Mn [303].

A positive bias is observed for several rare earth elements, in particular gadolinium and holmium, due to spectral interferences arising from decay products of uranium present within the matrix ($[\text{U}] = 135 \mu\text{g/g}$). Measurement of ^{166}Ho is equally difficult, with a weak γ -emission at 80.6 keV, which is consistent with other analyses of OREAS 100a performed at OPAL and other international facilities as part of an inter-laboratory comparison, where concentrations higher than the certified values were measured [304]. Accurate measurement of the weak 97.5 keV γ -emission of ^{153}Gd is made difficult by the proximal photopeaks of U $K\alpha_1$ X-ray emission of ^{233}Pa (a decay product of ^{235}U) at 98.44 keV, the γ -emission of ^{153}Sm at 97.43 keV and the γ -emission of ^{239}Np at 99.52 keV, resulting in an over appreciation of gadolinium within the OREAS 100a reference material [295, 305]. ^{153}Gd has a second photopeak at 103.18 keV, however this is similarly affected by spectral interferences from ^{153}Sm , ^{239}Np and ^{233}Pa at 103.18, 103.73 and 103.73 keV, respectively [295]. Despite the two sets of spectral overlays of ^{153}Sm , ^{239}Np and ^{233}Pa which impede the accurate measurement of ^{153}Gd , measurement of ^{153}Sm appears to be unaffected by these spectral interferences, with percentage deviations of 2.8 and 2.0 % for the fusion and 4-acid certified values, respectively.

Interestingly, the certified values for the heavy rare earth elements (HREE) demonstrate a fractionation between the 4-acid and fusion sample preparation methods, with the fusion method featuring higher certified concentrations. The HREE, in particular, have been found to be more susceptible to incomplete dissolution via the 4-acid digestion method due to insoluble mineral phases, and in a comparison study, lead to less accurate measurements in geological materials by ICP-MS, when compared to INAA [306]. It is therefore likely that the absolute concentrations of the HREE within OREAS 100a are closer to the fusion certified values than those obtained from the 4-acid method, which agrees with the k_0 -NAA data as the percentage difference (%) between the certified and measured values is less for the fusion method than the 4-acid method (Table 17). As the k_0 -NAA technique itself does not require dissolution of the samples

Table 17 Comparison between trace and rare earth elemental data from k_0 -NAA analysis of OREAS 100a CRM and Fusion and 4-Acid certified values. Concentrations in $\mu\text{g/g}$, unless stated otherwise (as percentage weight (%))

	k_0 -NAA			Fusion Certified Values			4-Acid Certified Values		
	Conc.	2σ	LOD	Conc.	Unc.	% Diff.	Conc.	Unc.	% Diff.
Mg (%)	0.88	0.09	3.45	0.839		5.3	0.81		9.1
K (%)	3.80	0.42	433.20	3.94		0.4	3.8		4.1
Ti (%)	0.22	0.05	505.60	0.239		-5.9	0.218		3.2
V (%)	40.1	5.5	2.1	36.7		9.3	34.7		15.6
Mn	550	47	0.7	537		2.6	532		3.5
Fe (%)	4.47	0.38	215.95	4.66		-4.0	4.51		-0.8
Co	16.6	1.5	0.3	18.1		-8.2	17.5		-5.0
Cu	203	125	12	169		20.2	167		21.6
Y	-	-	10360	142		-	95.5		
Mo	-	-	-	24.1		-	22.2		
La	255	23	0.5	260		-1.9	259		-1.5
Ce	463	42	2	463		0.0	467		-0.9
Pr	47.4	19.2	47.8	47.1		0.5	47.1		0.5
Nd	163	28	8	152		7.2	152		7.2
Sm	24.3	2.2	0.1	23.6		2.8	23.8		2.0
Eu	3.43	0.30	0.08	3.71		-7.5	3.7		-7.3
Gd	37.6	4.8	9.07	23.6		59.3	20.3		85.2
Tb	3.4	0.3	0.3	3.8		-11.2	3.25		3.8
Dy	24.4	2.1	0.6	23.2		5.3	18.9		29.3
Ho	9.91	1.77	2.07	4.81		106.0	3.66		170.7
Er	-	-		14.9	-		11.6		
Tm	1.99	0.65	1.13	2.31		-13.7	1.61		23.9
Yb	13.41	1.31	0.6	14.9		-10.0	11.4		17.6
Lu	2.19	0.39	0.07	2.26		-3.2	1.56		40.2
Th	49.6	4.3	0.4	51.6		-3.8	49.2		0.9
U	128	11	5	135		-5.0	130		-1.4

6.3.3.2 Analysis of OREAS 106 CRM by k_0 -NAA

For the OREAS 106 CRM, only eight of the sixteen REE were able to be measured with relatively good agreement within the certified values (Table 6). Of the four uranium ore standard analysed OREAS 106 has the second-highest uranium content (1143 $\mu\text{g/g}$), with several REE (cerium, praseodymium, gadolinium, holmium and terbium) now below the indicated detection limits, which are dependent on the composition of the sample analysed and the presence of interfering elements that contribute a high background or overall activity [290]. As ^{141}Ce is a fission product of uranium with an interference factor of 0.27, the inability to quantify ^{141}Ce within OREAS 106 (produced through the (n,γ) reaction of ^{140}Ce (isotopic abundance 88.48%), possibly suggests the over-correction of the fission product contribution of approximately 308 $\mu\text{g/g}$, in addition to the native concentration of cerium within the reference material, to below detection limits. The increase in the limits of detection for several REE, relative to the OREAS 100a CRM, is likely due to the change in composition with OREAS 106 having a higher uranium content, leading to higher concentrations of several uranium fission products. Of the eight rare earth elements that were able to be measured in OREAS 106, neodymium and dysprosium appear to be affected by interferences. ^{147}Nd is a fission product of ^{235}U with a fission yield of 2.23% [307], however the cause for the enhancement in the dysprosium concentration is not currently known.

Table 18 Comparison between trace and rare earth elemental data from k_0 -NAA analysis of OREAS 106 CRM and Fusion and Powder Pressed Pellet (PPP) certified values. Concentrations in $\mu\text{g/g}$, unless stated otherwise (as percentage weight (%)).

	k_0 -NAA			Fusion Certified Values			PPP Certified Values		
	Conc.	2σ	LOD	Conc.	Unc.	% Diff.	Conc.	Unc.	% Diff.
K (%)	1.50	0.32	0.40	1.59		-5.7	-		-
La	51.4	28.28	1.35	54		-4.8	-		-
Ce	-	-	310	137			-		-
Pr	-	-	174.6	19.7			-		-
Nd	111.3	56.5	15.2	84		32.5	-		-
Sm	18.68	4.08	0.43	20.7		-9.8	-		-
Eu	1.9255	0.18	0.16	2		-3.7	-		-
Gd	-	-	18.04	18.2			-		-
Tb	3.06	0.35	0.42	3.1		-1.1	-		-
Dy	22.82	2.81	1.45	19		20.1	-		-
Ho	-	-	5.38	3.9			-		-
Er	-	-	9702	12.2			-		-
Tm	-	-	2.24	1.88			-		-
Yb	11.91	1.15	0.86	12.1		-1.6	-		-
Lu	1.79	0.30	0.13	1.66		8.1	-		-
Th	649.1	55.11	0.67	644		0.8	689		-0.4
U	1089	93.43	13.38	1143		-4.7	1213		-3.4

6.3.3.3 Analysis of OREAS 120 CRM by k_0 -NAA

With the exception of magnesium, chromium, tantalum, cesium and hafnium, the other trace elements measurable by k_0 -NAA in OREAS 120 are found to be in good agreement with their respective certified concentrations (Table 7). The large percentage difference in the 4-acid certified value for hafnium appears to lie in the accuracy of the certified values itself, as good agreement exists between the fusion certified value and the measured concentration. Most likely due to a lower uranium concentration in OREAS 120 (40.8 $\mu\text{g/g}$), ten rare earth elements are now measurable by k_0 -NAA and in good agreement with the certified values, with the exception of holmium, dysprosium and ytterbium. Fractionation of the HREE again appears to be the cause of the high percentage difference between the measured and 4-acid certified values for dysprosium and ytterbium, as good agreement is found with the fusion certified values.

Table 19 Comparison between trace and rare earth elemental data from k_0 -NAA analysis of OREAS 120 CRM and Fusion and 4-Acid certified values. Concentrations in $\mu\text{g/g}$, unless stated otherwise (as percentage weight (%)).

	k_0 -NAA		Fusion Certified Values			4-Acid Certified Values		
	Conc.	2σ	Conc.	Unc.	% Diff.	Conc.	Unc.	% Diff.
Na (%)	0.231	197.996	0		-	0.234		-1.3
Mg (%)	0.291	131	0.24		21.3	0.231		26.0
Al (%)	4.81	4090.77	4.68		2.8	4.63		3.9
K (%)	2.63	1819	2.66		-1.0	2.59		1.7
Ca (%)	-	-	0.064		-	0.062		-
Ti (%)	0.262	560.584	0.243		7.9	0.238		10.1
Mn (%)	0.080	67.859	0.079		0.6	0.078		1.9
Fe (%)	1.54	1349.14	1.58		-2.4	1.57		-1.8
Sc	2.86	0.24	-		-	2.73		4.7
V	23.74	4.6	-		-	21.3		11.4
Co	3.99	0.60	-		-	4.22		-5.6
Ni	-	-	-		-	8.22		-
Zn	15.09	5.147	-		-	13.1		15.2
Ga	11.99	4.017	10.7		12.1	11		9.0
Nb	-	-	-		-	7.7		-
Mo	-	-	-		-	6.97		-
In	-	-	-		-	0.0014		-
Sn	-	-	-		-	0.67		-
Cs	0.60	0.30	-		-	0.74		-19.6
Ba	936.2	1034.0	973		-3.8	983		-4.8
La	19.8	2.6	21.1		-6.0	20.3		-2.3
Ce	45.0	6.0	46.3		-2.9	44.5		1.1
Pr	-	-	5.01		-	-		-
Nd	18.3	4.8	19.1		-4.2	-		-
Sm	3.8	0.52	3.74		0.8	-		-
Eu	1.03	0.103	1.03		-2.2	1.11		-9.3

Gd	-	-	3.04		-	-		-
Tb	0.44	0.11	0.44		-2.4	0.43		-0.1
Dy	2.62	0.50	2.4		9.3	2.29		14.6
Ho	1.6	0.50	0.48		228.1			-
Er	-	-			-			-
Tm	-	-	0.2		-			-
Yb	1.30	0.18	1.34		-2.9	1.03		26.3
Lu	0.23	0.04	0.21		9.7	-		-
Y	-	-	12.2		-	10.1		-
Hf	6.95	0.62	5.97		16.4	1.5		363.4
Ta	0.66	0.26	0		-	0.55		19.2
Th	5.64	0.65	5.45		3.5	5.57		1.2
Zr	298.6	118.27	255		17.1	-		-
U	38.3	3.5	40.8		-6.2	39.6		-3.3
Cr	42.6	4.7	46.9		-9.3	32.7		30.1
Rb	90.6	11.1	87		4.1	88		2.9
Sr	-	-	127		-	124		-

6.3.3.4 Analysis of OREAS 124 CRM by k_0 -NAA

In the analysis of the OREAS 124 CRM by k_0 -NAA, only seven of the fourteen rare earth elements were able to be quantified (Table 8). Two of the rare earth elements (samarium and lutetium) measured featured large percentage deviations from the fusion certified reference values due to spectral overlaps and the secondary formation of ^{177}Lu . The 208 keV photopeak for ^{177}Lu has a spectral overlap with the 198 keV photopeak of ^{169}Yb , while ^{177}Lu is also formed through the β^- decay of ^{177}Yb ($t_{1/2} = 1.9$ hr) formed through the neutron activation of ^{176}Yb [308]. While the majority of trace elements also agreed with the fusion and 4-acid certified values, gallium, strontium and hafnium as determined by k_0 -NAA differed significantly.

Table 20 Comparison between trace and rare earth elemental data from k_0 -NAA analysis of OREAS 124 CRM and Fusion and 4-Acid certified values. Concentrations in $\mu\text{g/g}$, unless stated otherwise (as percentage weight (%)).

	k_0 -NAA		Fusion Certified Values			4-Acid Certified Values		
	Conc.	2σ	Conc.	Unc.	% Diff.	Conc.	Unc.	% Diff.
Na	0.244	157.323	-		-	0.232		5.3
Mg	0.205	570.8	0.224		-8.3	0.221		-7.1
Al	4.70	4020.13	4.62		1.8	4.61		2.0
K	2.83	3380.03	2.62		8.0	2.56		10.5
Ca	-	-	0.088		-	0.089		
Sc	3.09	0.20	0		-	3.01		2.6
Ti	2411	788	0.254		-5.1	0.252		-4.3
V	26.6	5.4	23.3		14.1	23		15.5
Cr	43	7.5	51		-15.7	37.5		14.6
Mn	693.55	59.768	0.07		-0.9	0.069		0.5
Fe	15255	1023.38	1.56		-2.2	1.57		-2.8
Co	4.36	0.54	0		-	4.26		2.3
Ni	-	-	0		-	9.31		
Zn	-	-	0		-	14.3		
Ga	15.3	8.0	10.5		45.7	11.2		36.6
Rb	91.6	25.3	86		6.5	85		7.8
Sr	159.1	69.6	0		-	188		-15.4
Y			14.2		-	12.1		
Zr			260		-	49.8		
Nb			0		-	7.84		
Mo			0		-	7.36		
In			0		-	0.014		
Sn			0		-	0.71		
Sb					-	0.083		
Cs			0		-	0.78		
Ba	1125.5	282.5	1017		10.7	1046		7.6
La	21.4	10.0	21.6		-1.2	21.4		-0.2
Ce			47.6		-	48.9		

Pr			5.39		-	0		
Nd			20.8		-	0		
Sm	5.4	0.69	4.21		28.3	0		
Eu	1.22	0.14	1.15		6.4	1.23		-0.5
Gd		11.97	3.47		-	0		
Tb	0.42	0.361	0.48		-11.0	0.5		-14.5
Dy	2.93	0.55	2.82		4.0	2.71		8.2
Ho			0.58		-	0		
Er			1.6		-	0		
Tm			0.22		-	0		
Yb	1.65	0.87	1.63		1.4	0		
Lu	0.31	0.16	0.26		18.5	0		
Hf	8.02	1.12	6.22		28.9	1.56		413.8
Ta			0		-	0.56		
W			0		-	0.71		
Th	5.76	0.75	5.74		0.3	5.79		-0.5
U	1815.5	114.9	1794		1.2	1779		2.1

6.3.4 Impact of k_0 -NAA interferences in chondrite-normalised REE patterns of uranium certified reference materials

Due to several spectral interferences and fission products that arise during the analysis of rare earth elements within uranium matrices, an evaluation of their potential impact on the data obtained from the Australian and international uranium ore samples analysed by k_0 -NAA must first be made. Rare earth elements data is often reported within the literature as chondrite-normalised patterns [2, 115, 127, 269], to compare and contrast the fractionation between the individual rare earth elements, which can be reflective of many different, underlying processes. In the context of nuclear forensic science and geology, the chondrite-normalised rare earth pattern of a particular uranium ore sample reflects the geological conditions the uranium ore deposit formed under, specifically the source of the REE as well as the temperature of formation and the nature of the mineralizing fluid [2, 115]. As the current literature suggests that the REE profile remains unaltered by the UOC production process [2], due to similarities in the valences and atomic radii of REEs (1.16 to 0.977 Å) and uranium (1 Å) [309, 310], comparing the chondrite-normalised REE pattern of an unknown UOC samples to reference uranium ore samples can be invaluable means of identifying its origin. Therefore, the

accurate measurement of the rare earth elements within a uranium ore sample is imperative for a positive identification.

To evaluate the accuracy in the measurement of certified rare earth elements within the four OREAS uranium ore CRMs, their chondrite-normalised rare earth patterns were compared to the patterns of the fusion and 4-acid certified values. Within the CRMs with the lower uranium concentrations (OREAS 100a and 120), the light rare earth elements (lanthanum-europium) agree well with the fusion and 4-acid chondrite-normalised patterns where a comparison can be made, with the exception of neodymium (Figure 101 & Figure 103). Within the heavy rare earth elements (gadolinium-lutetium), holmium, in particular, deviates from the certified value patterns in varying magnitudes. For the higher uranium concentration CRMs (OREAS 106 & 124), fewer rare earth elements are measureable by k_0 -NAA, making the overall chondrite-normalised pattern difficult to compare to the patterns of other samples (Figure 102 & Figure 104). More rare earth elements (neodymium, dysprosium, samarium and lutetium) appear to be impacted by spectral overlaps or fission products, which further contributes to the difficulty in comparing patterns.

Despite these identified complications, the chondrite-normalised patterns still appear to be valuable for comparing between uranium ore samples and UOCs in this study, particularly as consecutive rare earth elements appear to be unaffected (i.e. when neighbouring REE in a sequence are able to be measured by k_0 -NAA). When evaluating chondrite-normalised patterns further in this study, special consideration will be made for elements that are impacted by spectral overlaps or fission products. While there has been no evidence for europium being affected, special consideration will be made given its anomalous nature in chondrite-normalised rare earth patterns (due to its 2+ valence) independent of the other consecutive rare earth elements.

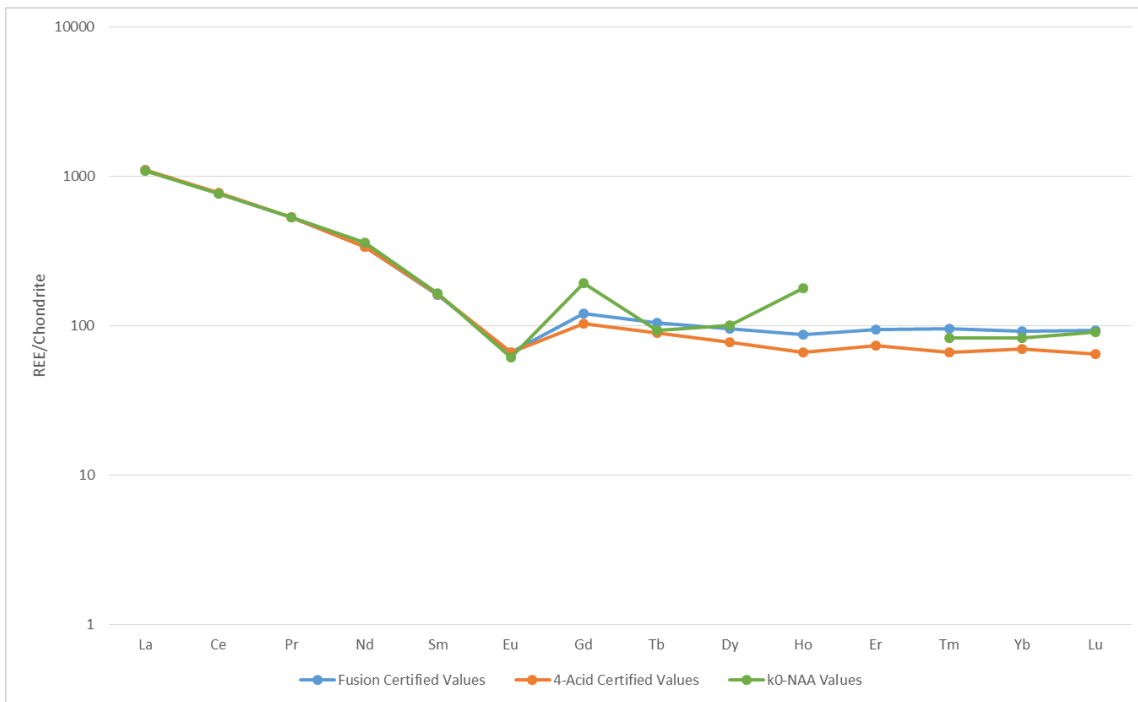


Figure 101 Comparison of chondrite-normalised REE patterns of Fusion and 4-Acid certified values in OREAS 100a versus concentrations measured by k_0 -NAA. (Chondrite values from Anders & Grevasse 1989)

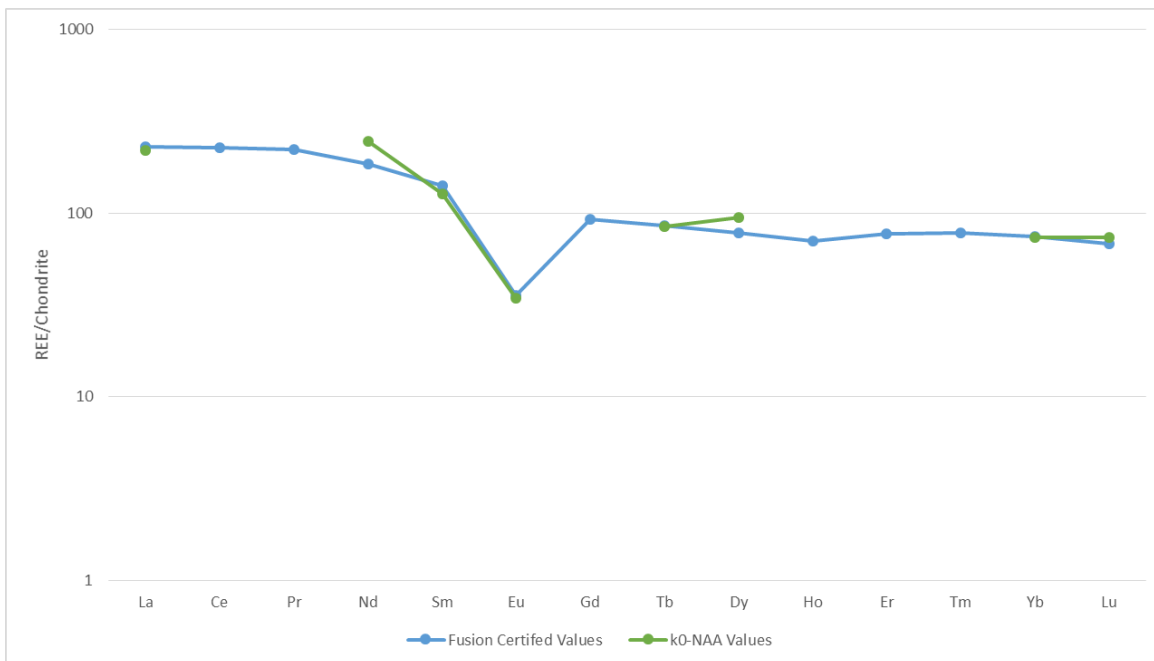


Figure 102 Comparison of chondrite-normalised REE patterns of Fusion certified values in OREAS 106 versus REE concentrations measured by k_0 -NAA. (Chondrite values from Anders & Grevasse 1989)

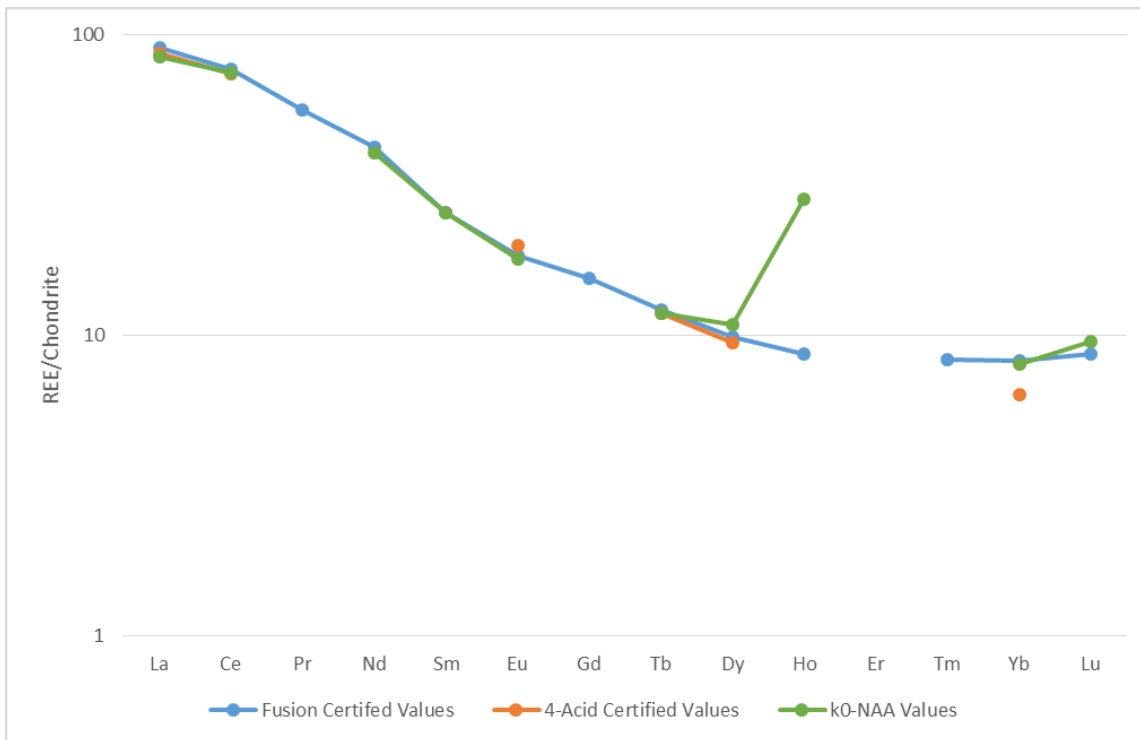


Figure 103 Comparison of chondrite-normalised REE patterns of Fusion and 4-Acid certified values in OREAS 120 versus concentrations measured by k_0 -NAA. (Chondrite values from Anders & Grevasse 1989)

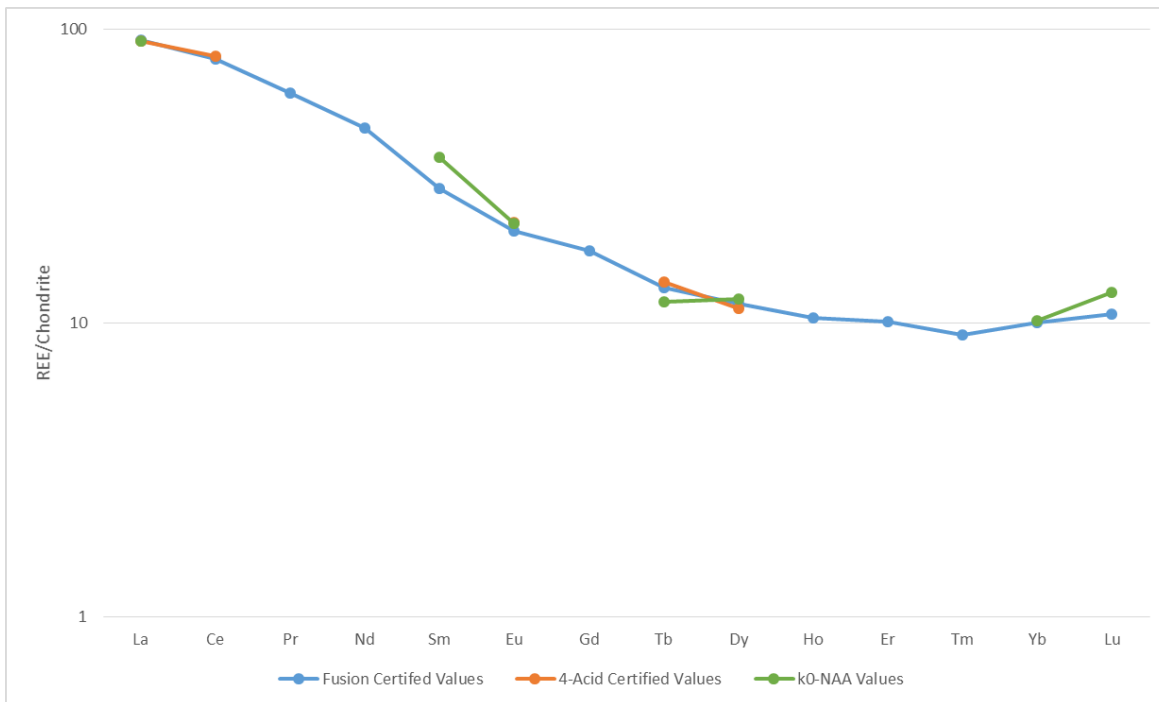


Figure 104 Comparison of chondrite-normalised REE patterns of Fusion and 4-Acid certified values in OREAS 124 versus concentrations measured by k_0 -NAA. (Chondrite values from Anders & Grevasse 1989)

6.3.5 Chondrite-normalised rare earth elemental patterns of Australian and international uranium ore samples

6.3.5.1 Olympic Dam

The two uranium ore samples from Olympic Dam were found to feature similar chondrite-normalised REE patterns, notably with enrichment in the LREEs (Figure 9). While both samples have certain artifacts as a consequence of their analysis by INAA (i.e. inability to measure all of the REE and enrichment of Ho, as seen previously in the measurement of OREAS CRMs), their chondrite-normalised REE patterns are somewhat consistent with the patterns of other Olympic Dam UOC and uranium bearing-hematite ore samples analysed within the literature [39, 311]. The hematite breccias at Olympic Dam are however found to be highly variable with respect to their chondrite-normalised REE patterns, reflecting different types of zonations that correspond to their hematite content [312]. Greater La/Lu and Dy/Lu ratios and the reversal of Eu anomalies (from negative to positive) occur as a result of an increase in the percentage of hematite within zonations the Olympic Dam deposit, while the total REE enrichment is also dependent on the proximity the centre of the deposit. Given this variation observed between the chondrite-normalised REE patterns from the Olympic Dam A&B U ore samples, the UOC sample analysed by Keegan *et al.* (2008) and the various U ore and hematite breccia samples analysed by Ciobanu *et al.* (2013) and Oreskes &

Einaudi (1990), greater consideration must be taken when comparing two UOC and/or U ore samples from Olympic Dam, or a sample suspected of coming from Olympic Dam when compared against a reference sample.

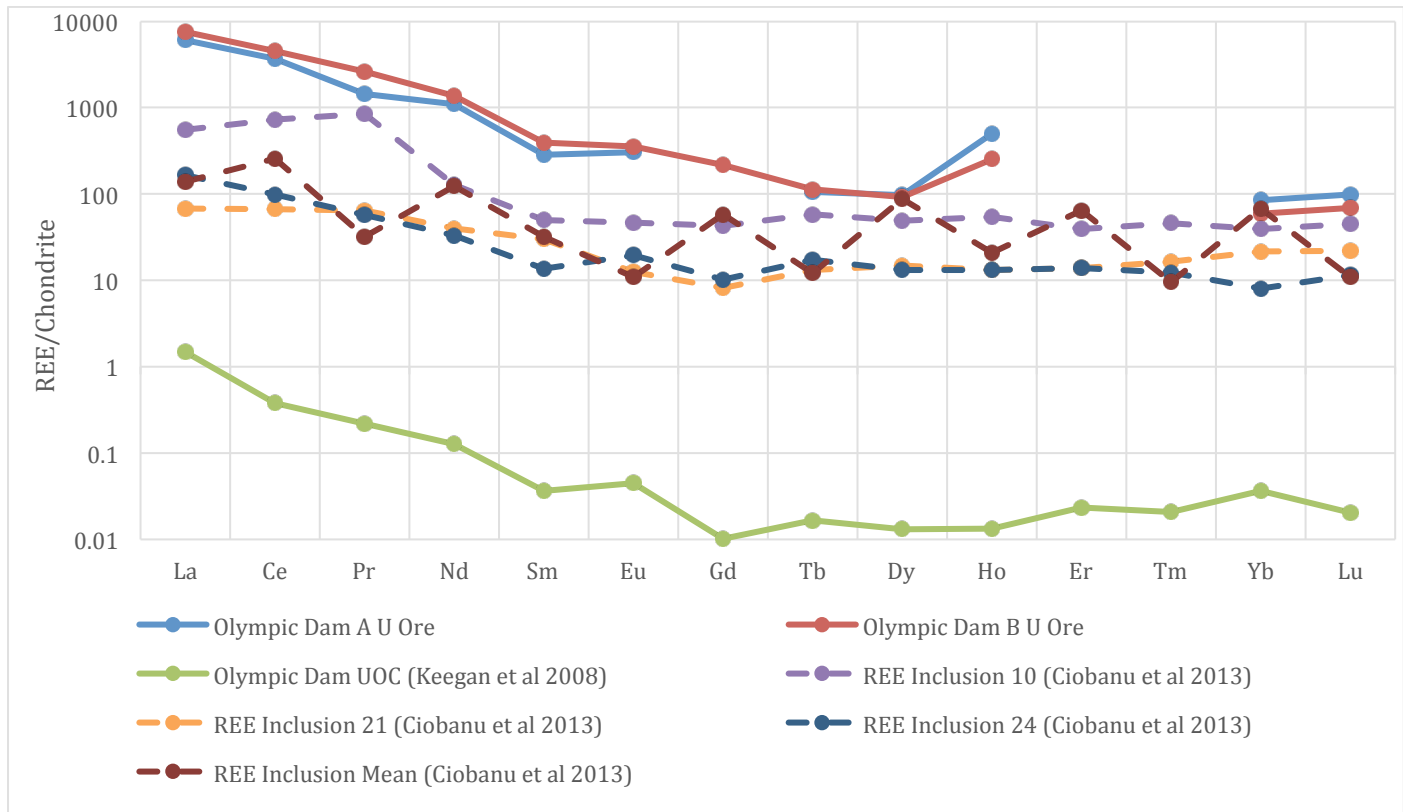


Figure 105 Chondrite-normalised REE patterns for Olympic Dam A&B U ores obtained through INAA, and comparison patterns of UOCs (Keegan 2008) and U ores (Ciobanu et al. 2013) also from Olympic Dam from literature. Normalised using chondrite data from Anders & Grevasse (1989)

6.3.5.2 Beverley and Four Mile

Several REE elements were unable to be measured on the U ores from Beverley and Four Mile, making comparisons with other UOC and U ore samples from similar sites difficult. Four Mile and Beverley U ores were compared against one another due to their close geographic proximity, the possibility of their linked origins and the use of shared facilities in the manufacturing of UOCs; ion-exchange (IX) resin beds impregnated with uranium from the Four Mile in-situ leaching site are transported to the Beverley production facility to convert the uranium into uranyl peroxide (UO₄). While more evident in the Four Mile sample, both appear to feature LREE enrichment, negative Eu anomalies and a plateau across the HREE where measurable (Figure 10). This general pattern is consistent with several core samples taken at the Beverley U deposit at a variety of depths within the Namba and Willawortina formations, with the exception of the core sample #978 taken within the

Namba formation at -135 m, which coincides with the greatest U occurrence of ~1% U₃O₈ seen across all of the core samples [69]. While the Beverley UOC pattern from Keegan *et al.* (2008) features a similar negative Eu anomaly and a flat HREE pattern as seen in the Beverley and Four Mile U ores (Figure 10), the LREEs have a markedly different pattern with the enrichment of Ce-Sm. This chondrite-normalised rare earth pattern is largely consistent with other Beverley UOCs reported in the literature [2], which feature a similar prominence from Ce to Sm and flat HREE profile.

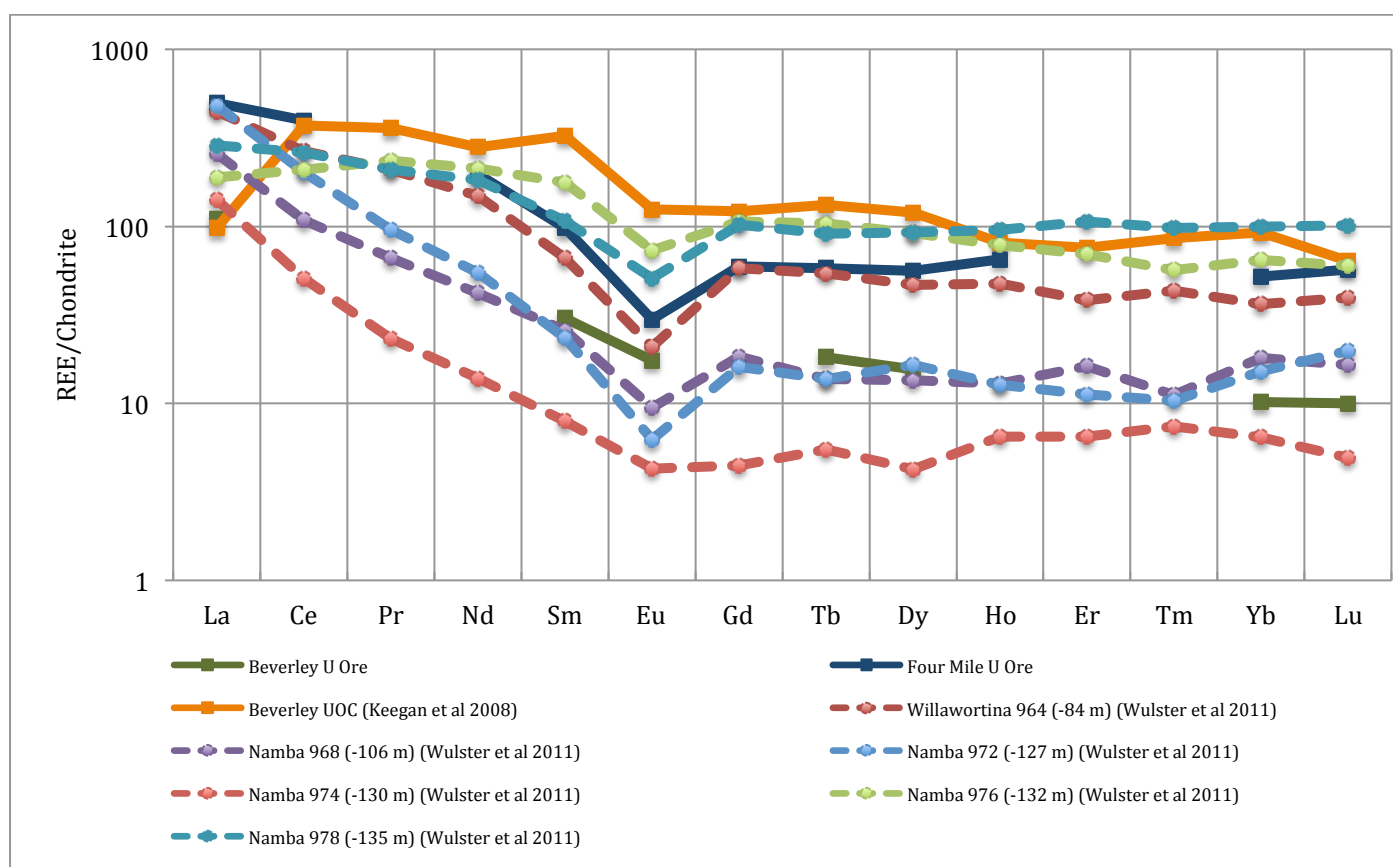


Figure 106 Chondrite-normalised REE patterns for Beverley and Four Mile U ores obtained through INAA, and comparison patterns of a UOC (Keegan 2008) and U ores (Wülser et al. 2011) also from Beverley from literature. Normalised using chondrite data from Anders & Grevasse (1989).

6.3.5.3 Ranger

Both the Ranger A&B U ore samples were found to feature several REEs not measurable by NAA, rendering the interpretation of their respective chondrite-normalised REE patterns difficult (Figure 11). The Ranger A sample appears to feature a greater total REE content than the Ranger B sample, with both patterns also suggesting they feature a negative Eu anomaly. While the overall pattern of Ranger A is difficult to characterise, the Ranger B sample appears to feature an enrichment of the

LREE and a flat HREE pattern. When compared to the chondrite-normalised REE pattern of the Ranger UOC sample analysed by Keegan (2008), the pattern of the UOC samples appears to be the mirror image of the Ranger B sample, with a depletion of the LREE and a relatively flat HREE pattern [39]. However, when plotted against the chondrite-normalised REE patterns of two U ores from Ranger analysed by Fisher *et al.* (2013), the overall pattern of Ranger B samples demonstrates some similarity to the 0.06% U Ranger ore sample [313]. This is in contrast with the pattern observed within the 0.85% U Ranger ore sample that is reminiscent of the Ranger UOC analysed by Keegan (2008), albeit with a greater total REE content. Ce and La concentrations have been found to decrease with increasing U concentration within U ores from Ranger, whereas the concentration of Dy and enriched flatter HREE profiles has been found to be highest where the highest grades of U and the strongest chlorite alterations have been observed [313]. It does stand to reason that chondrite-normalised REE pattern of the Ranger UOC analysed by Keegan (2008) would be similar to patterns of ore samples with the highest U mineralisation, given mining at these locations would be prioritized [39].

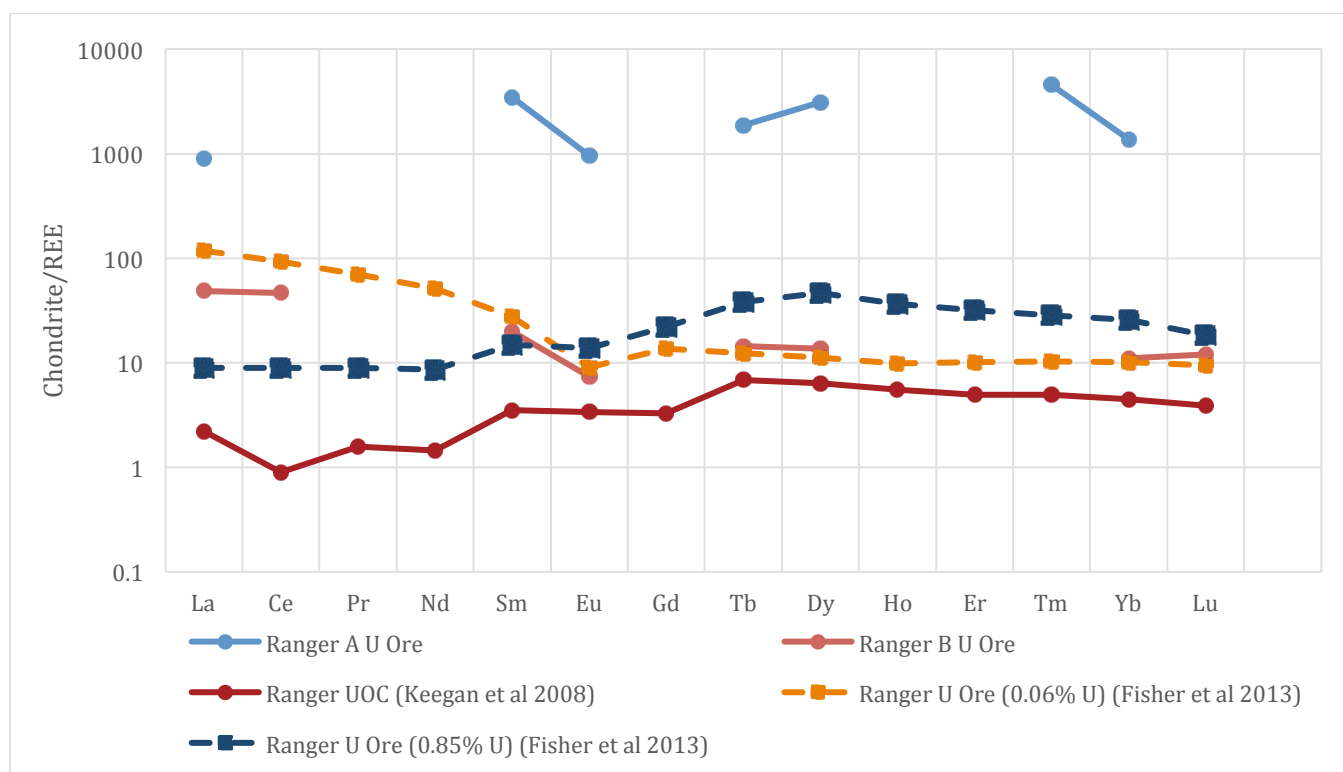


Figure 107 Chondrite-normalised REE patterns for Ranger uranium ores obtained through k_{θ} -NAA, and comparison patterns of a UOC (Keegan 2008) and uranium ores (Fisher *et al.* 2013) also from Ranger from literature. Normalised using chondrite data from Anders & Grevasse (1989).

6.3.5.4 Mary Kathleen

The U ore sample from Mary Kathleen analysed by k_0 -NAA features a distinct LREE enrichment, which continues to decrease across the HREE also, except an enrichment of Ho relative to Dy (Figure 108). When compared to the Mary Kathleen UOC analysed by Keegan *et al.* (2014), it features a similar pattern with the exception of Ho, which may likely suggest the high Ho concentration is caused by a fission product interference, as seen previously with the OREAS 100a and 120 CRMs (Figure 101 & Figure 103). Other ore (MK68) and whole rock (MK69) samples from Mary Kathleen analysed by Maas *et al.* (1987) share a similar pattern with respect to the enrichment of the LREEs, which is due to the high concentration (80-90%) of the gangue mineral allanite ((Ce,Ca,Y,La)₂(Al,Fe)₃(SiO₄)₃(OH)) [314].

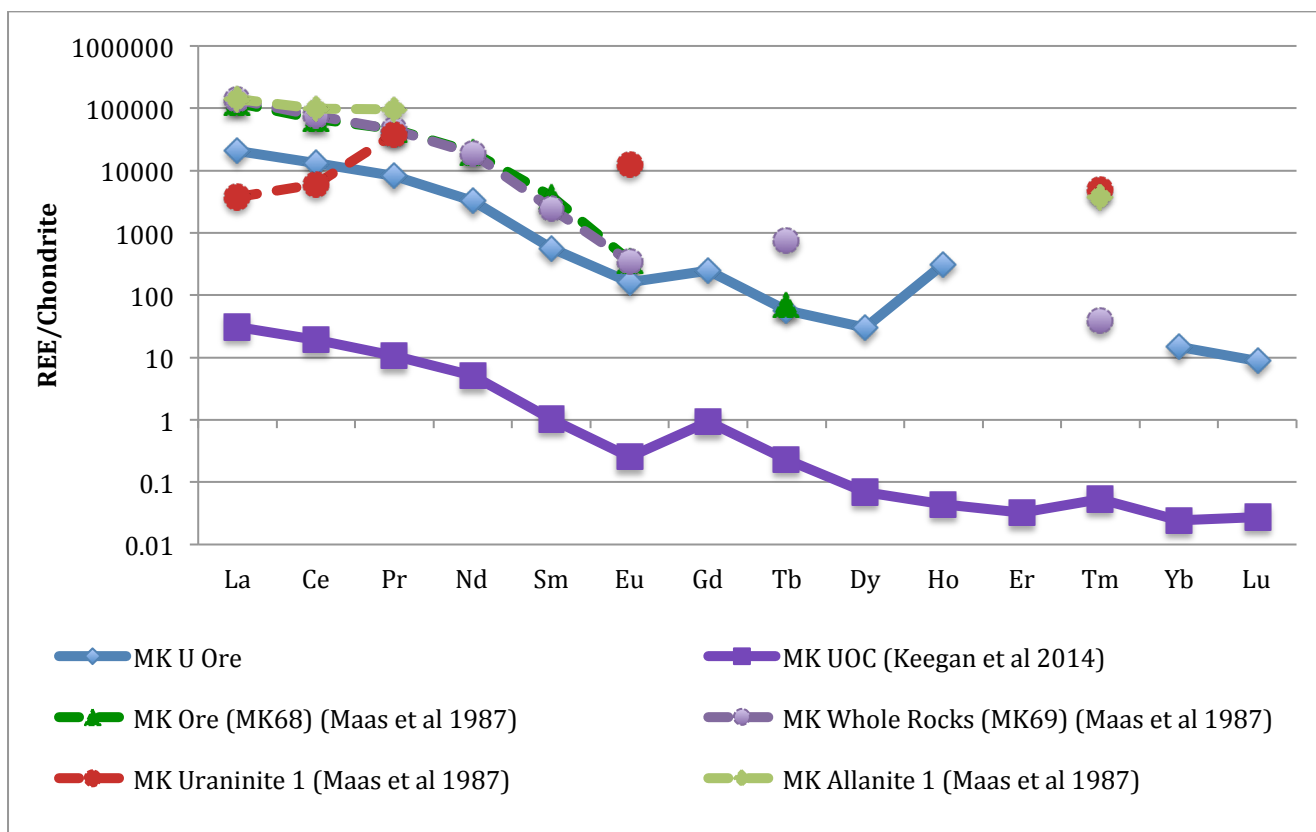


Figure 108 Chondrite-normalised REE patterns for Mary Kathleen uranium ores obtained through k_0 -NAA, and comparison patterns of a UOC (Keegan 2008) and uranium ores (Maas *et al.* (1987)). Normalised using chondrite data from Anders & Grevasse (1989)

6.3.5.5 Cardiff

Only six rare earth elements were found to be measurable within the Cardiff ore sample by k_0 -NAA (Figure 109). Due to the decrease in the chondrite-normalised REE pattern on going from samarium to europium, the Cardiff ore sample may feature a negative europium anomaly, which is also observed in the neighbouring Faraday/Madawaska and Fission deposits (Figure 109) [203, 267], however the lack of elemental data for gadolinium makes this assertion difficult to confirm. The Faraday/Madawaska deposit in the Bancroft region of Ontario was first operated between 1954-1964 as the Faraday Mine, before it was reopened in 1972 for ten years as the Madawaska Mine [203, 267]. Compared to the Faraday/Madawaska and Fission deposits, which feature similar flat terbium/dysprosium normalised values, the Cardiff ore sample instead features an increase.

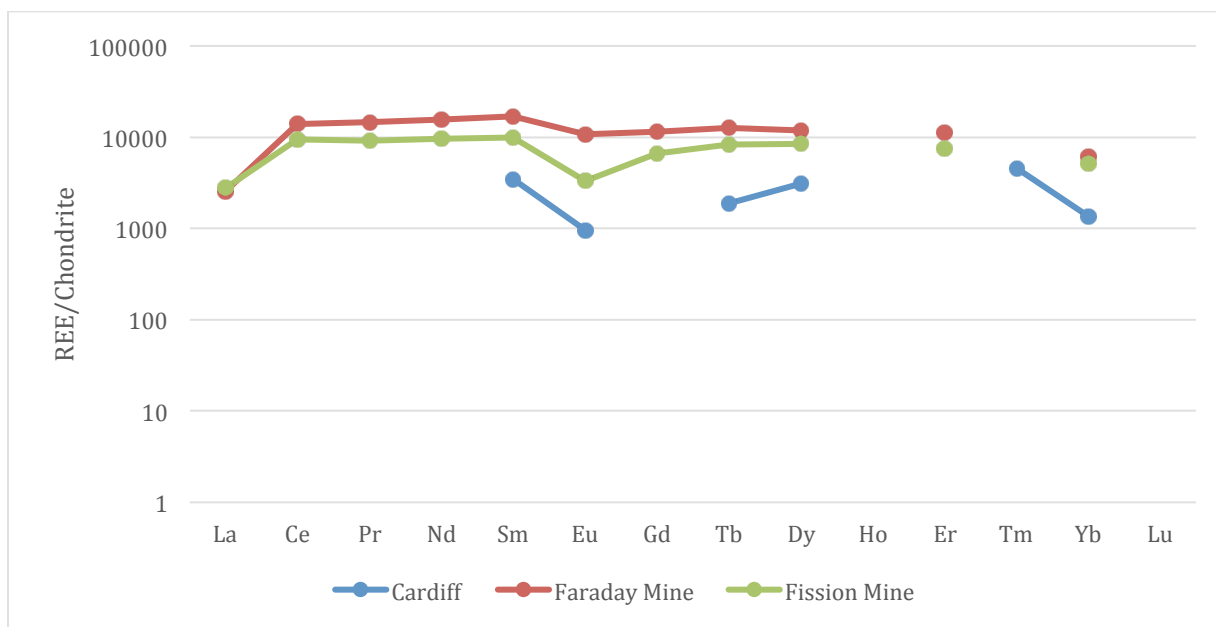


Figure 109 Chondrite-normalised REE patterns for Cardiff uranium ores obtained through k_0 -NAA, and comparison patterns of uranium ores from Faraday (Fryer & Taylor (1987) and Fission mines (Satterly (1957)). Normalised using chondrite data from Anders & Grevasse (1989)

6.3.5.6 Ruggles Mine

With only three REE measurable within the Ruggles Mine sample and none of them consecutive, little can be said concerning its chondrite-normalised REE pattern (Figure 110). When compared to the chondrite-normalised REE patterns of uraninite sourced from Ruggles Mine analysed by Balboni *et al.* (2016), the relative concentrations of the europium and dysprosium in the sample analysed in this study appear to be considerably greater and lesser, respectively.

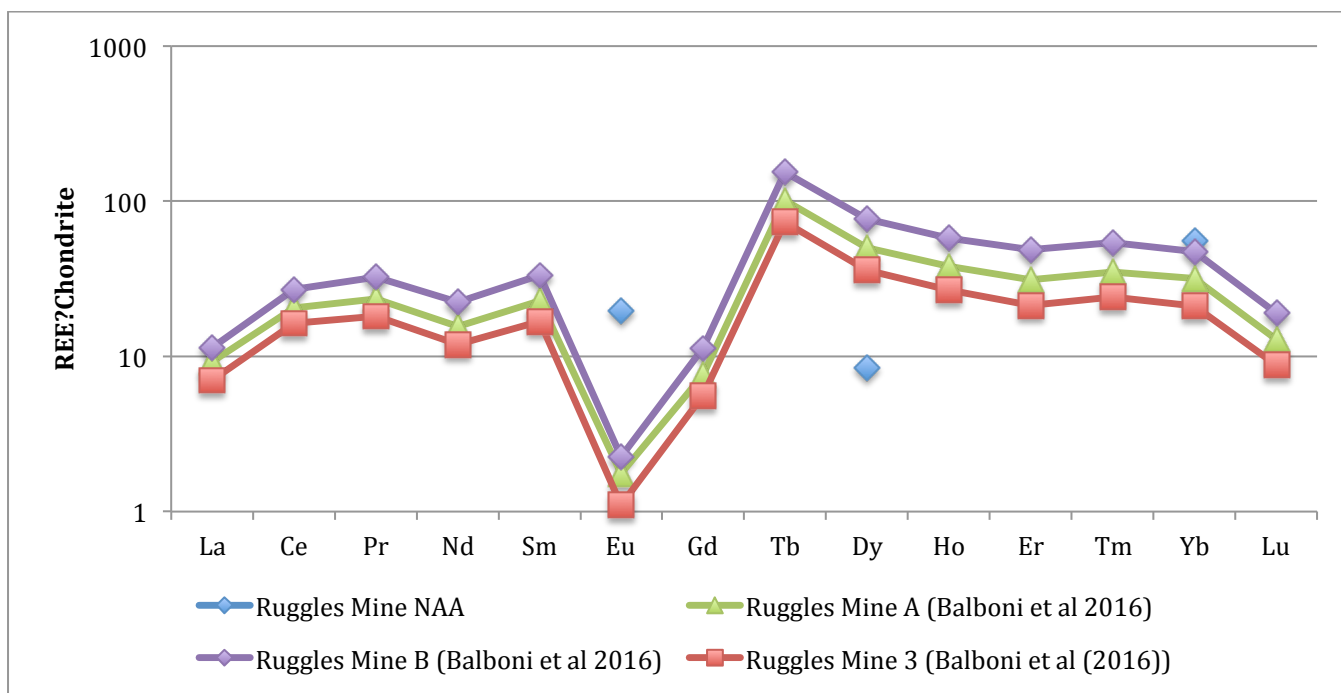


Figure 110 Chondrite-normalised REE patterns for Ruggles mine uranium ore obtained through k_0 -NAA, and comparison patterns uranium ores (Balboni *et al.* 2016) also from Ruggles mine from literature. Normalised using chondrite data from Anders & Grevasse (1989).

6.3.5.7 Happy Jack Mine, Mi Vida Mine, Big Indian Wash District, Green Dragon Mine, Calyx No 8 Mine

Again, the limited number of REE observed across the five samples located within the Big Indian Wash District of southeastern Utah make interpretation of the chondrite-normalised REE patterns impossible (Figure 111). In terms of total REE, Happy Jack Mine appears to feature the greatest concentration of REE, however it is difficult to rank the remaining due to the lack of complete data. The Happy Jack Mine also appears to have a flat chondrite-normalised REE distribution, whereas the Green Dragon Mine sample appears to feature an enriched LREE/depleted HREE pattern. The Big

Indian Wash District sample appears to increase in the LREE, as seen by the high ytterbium normalised value.

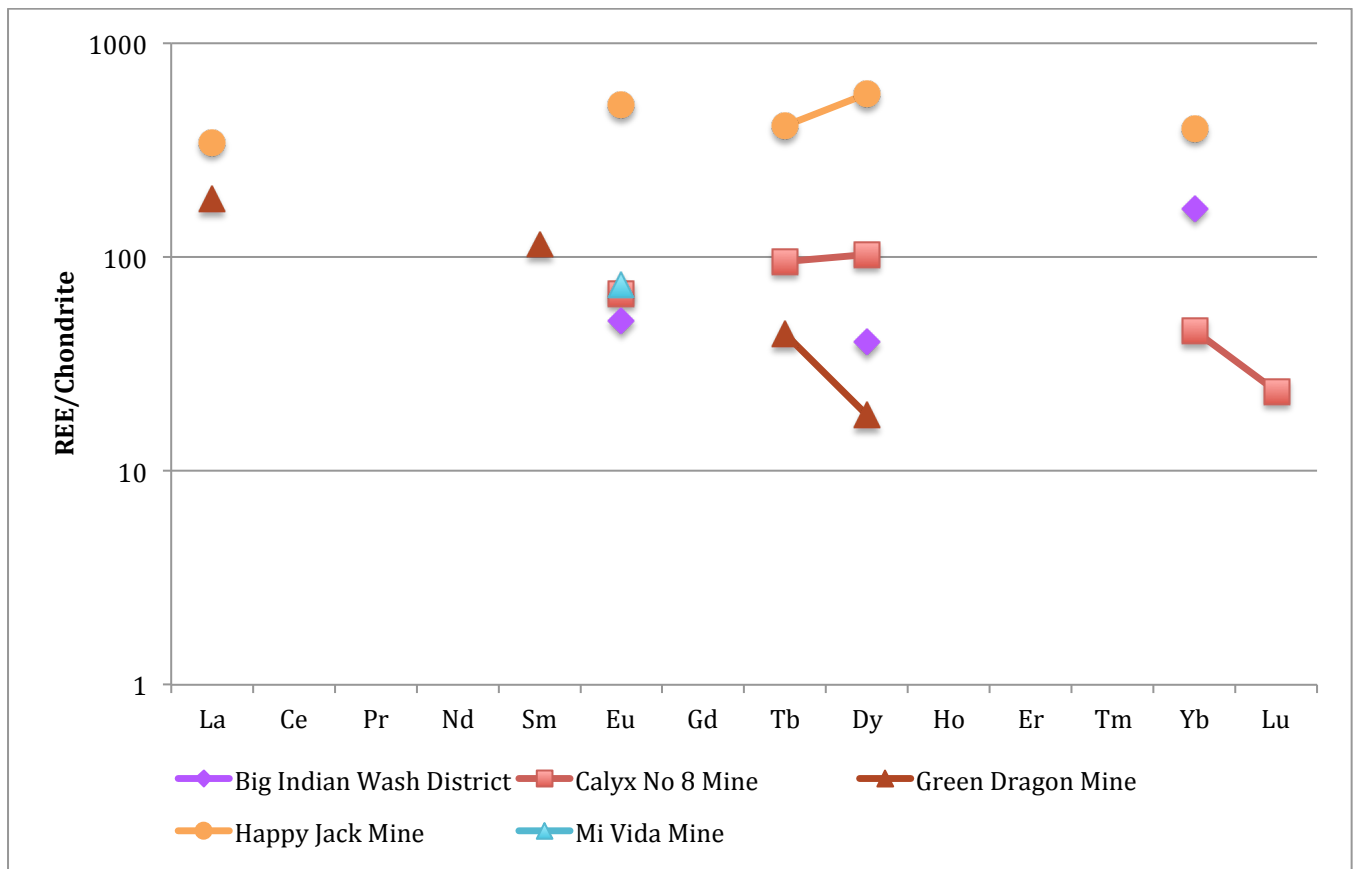


Figure 111 Chondrite-normalised REE patterns for Big Indian Wash District, Calyx No 8, Green Dragon, Happy Jack Mi Vida uranium ores obtained through k_0 -NAA. Normalised using chondrite data from Anders & Grevasse (1989).

Despite only a few REE measurable by k_0 -NAA, some differences can be observed between the Happy Jack Mine sample in this study and the chondrite-normalised REE patterns of uraninite samples also from Happy Jack Mine analysed by Balboni *et al.* (2016) (Figure 112). The most noticeable difference is seen with the relationship between the terbium and dysprosium results, where an increase was seen in the results of this study, whereas a decrease is observed in the results of Balboni *et al.* (2016). Another difference concerns the normalised values of lanthanum respective to the subsequent REEs (Figure 112); in this study the normalized value for is at similar value to the other REE, whereas in Balboni *et al.* (2016), the normalised value is a greater than a factor of 10 less than the other REEs.

One explanation for both of these differences concerns the difference between the samples; in this study, little is known about the Happy Jack sample and is analysed using a bulk analysis technique, whereas Balboni *et al.* (2016) specifically targeted uraninite crystals within their sample with LA-ICP-MS. Therefore, one possible source for the difference between the two studies is the inclusion of all of minerals with the uraninite in the analysis, whereas the gangue material is excluded due to specificity associated with LA-ICP-MS. It is however, with limited information regarding the Happy Jack Mine samples from both studies, their relationship with one another, as well as the entire deposit, impossible to identify the source of these differences with any degree of certainty, rather than attribute the differences observed solely due to the analytical approaches and techniques solely.

It should also be noted that the Happy Jack mine data from Balboni *et al.* (2016) in Figure 112 has been normalised using a different chondrite dataset, resulting in a chondrite-normalised pattern that differs from the data reported in the original study. As Balboni *et al.* (2016) did not identify the chondrite dataset used to normalise their REE data from Happy Jack mine, the original LA-ICP-MS data included within the article's Supplementary Data was normalised using the chondrite data from Anders & Grevasse (1989), which has been consistently used through this study and several other studies referred to throughout this chapter. When comparing the original normalised data in Balboni *et al.* (2016) to the data normalised using the chondrite data from Anders & Grevasse (1989), much of the chondrite-normalised REE pattern is similar, with the exception of the relative amounts of gadolinium and terbium. In the original data, the praseodymium normalised-value was the greatest of all of the REE, with the following REE decreasing very slightly. While much of this trend can be seen in the re-normalised data (Figure 112), the significant deviations in gadolinium and terbium with respect to the adjacent REEs is in stark contrast with the original dataset.

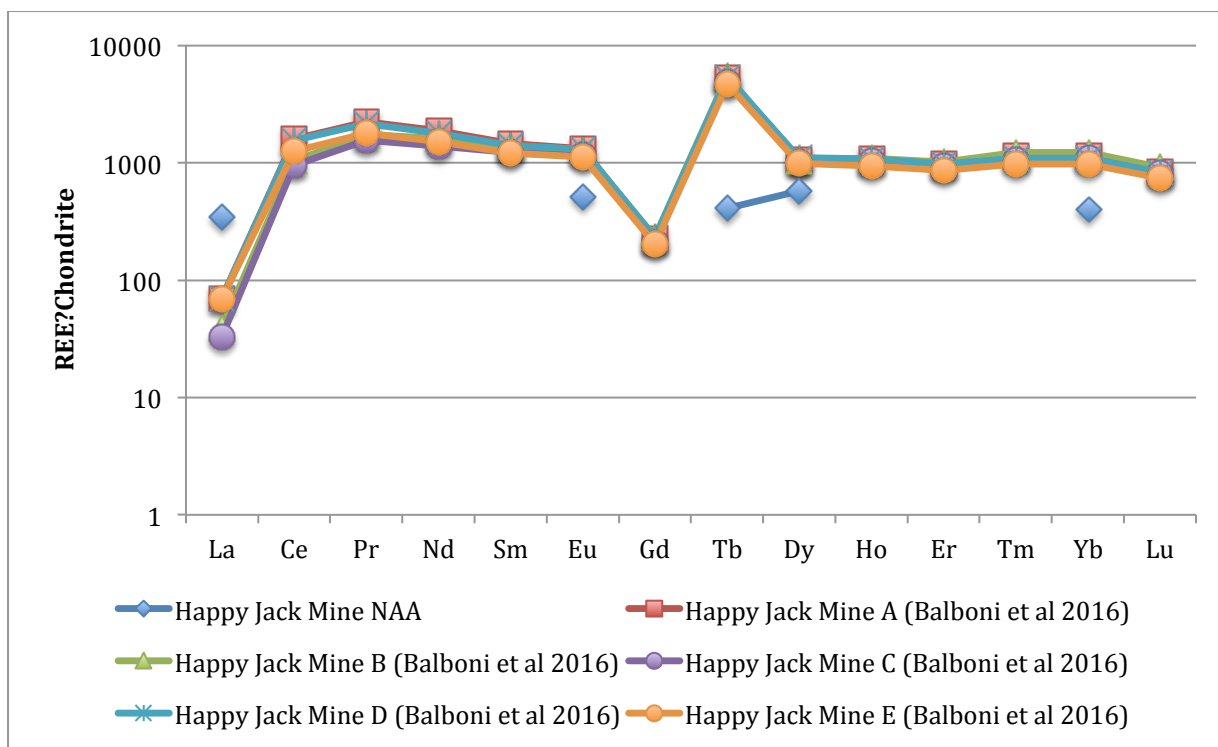


Figure 112 Chondrite-normalised REE patterns for the Happy Jack uranium ore obtained through k_0 -NAA, and comparison patterns of uranium ores (Balboni *et al.* 2016) also from Happy Jack from literature. Normalised using chondrite data from Anders & Grevasse (1989).

6.3.5.8 Ferguson Lode Claim

Limited REE information was obtained from the Ferguson Lode Claim sample, with only four REE being measured by k_0 -NAA (Figure 113). From these elements, it appears that the samples is enriched in LREE and depleted in HREE, however the lack of HREE measurable by k_0 -NAA makes this determination impossible to confirm.

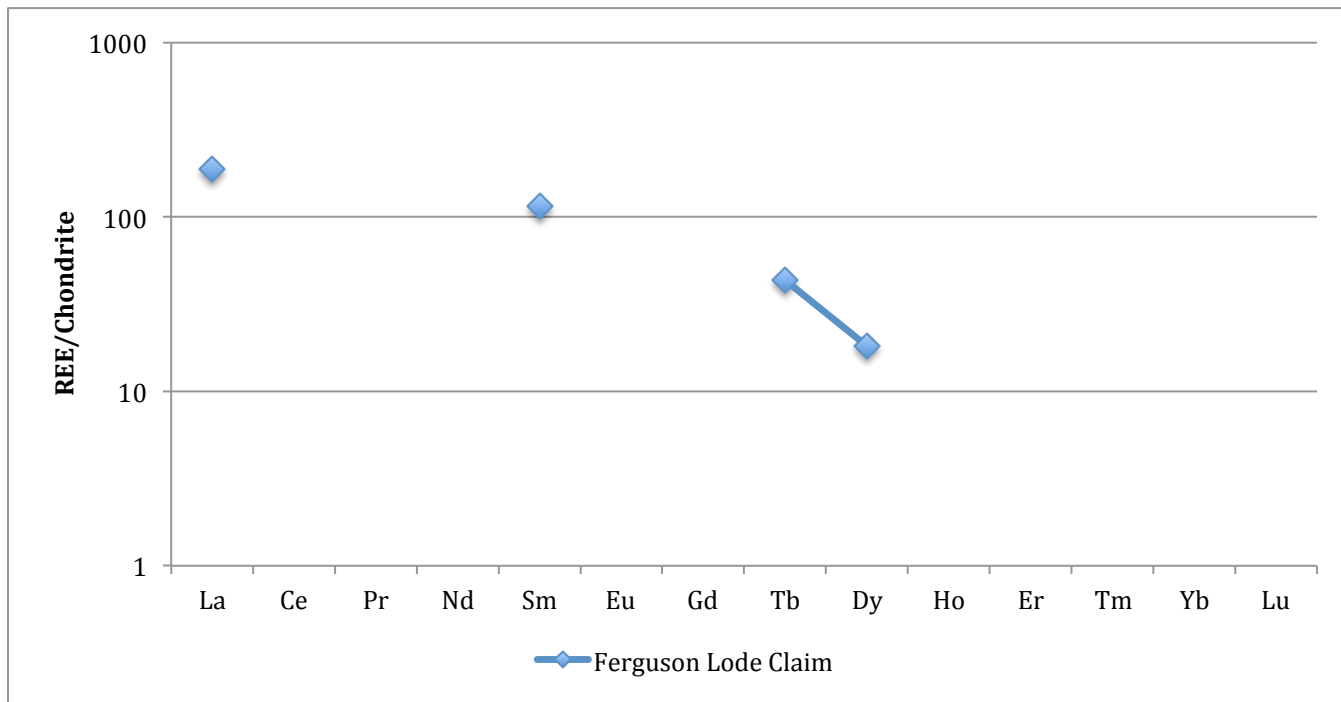


Figure 113 Chondrite-normalised REE patterns for the Ferguson Lode Claim uranium ore obtained through k_0 -NAA. Normalised using chondrite data from Anders & Grevasse (1989).

6.3.5.9 Uravan Mineral Belt

Of the nine North American ore samples analysed as part of this study, the Uravan Mineral Belt sample was found to provide the most elemental information, with eight REEs found to be measurable by k_0 -NAA (Figure 114). The ore sample appears to have a concave pattern, with a relative enrichment in the LREEs and HREEs. From the relative amounts of samarium and europium, it appears the Uravan Mineral Belt sample doesn't feature a europium anomaly, however without the measurement of gadolinium, this cannot be concluded with any degree of confidence.

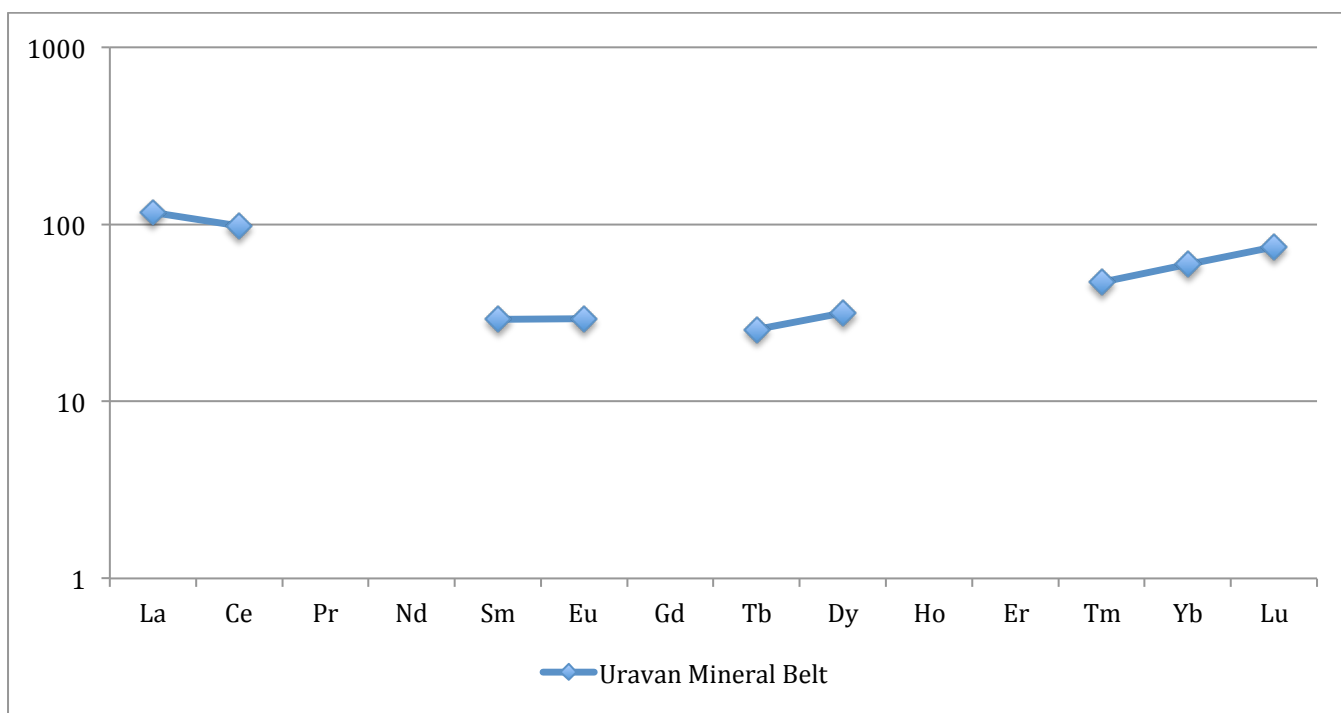


Figure 114 Chondrite-normalised REE patterns for the Uravan Mineral Belt uranium ore obtained through k_0 -NAA. Normalised using chondrite data from Anders & Grevasse (1989).

6.3.5.10 Midnite Mine

With only six of the REE measurable within the Midnite Mine sample, limited information can be obtained from its chondrite-normalised REE pattern (Figure 115). Due to the relative increase between samarium and europium and the relative decrease for terbium and dysprosium, it is likely that this Midnite Mine sample has a positive europium anomaly. From terbium onwards, the Midnite Mine pattern appears to plateau with similar normalised values for ytterbium and lutetium observed.

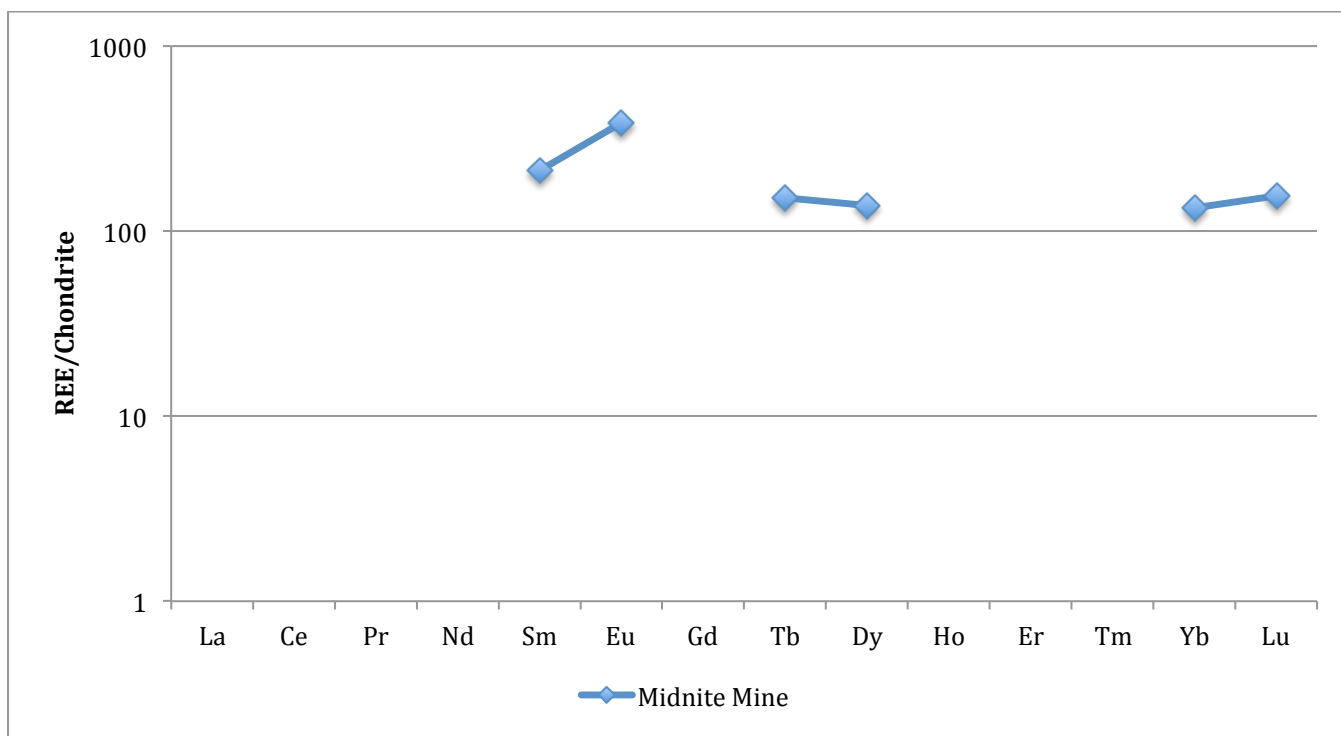


Figure 115 Chondrite-normalised REE patterns for the Midnite Mine uranium ore obtained through k_0 -NAA. Normalised using chondrite data from Anders & Grevasse (1989).

6.3.6 Trace Elements of the Australian and North American Uranium Ore Samples

6.3.6.1 Thorium

14 of the 17 Australian and North American uranium ore samples were found to contain measureable concentration of thorium (Figure 116). Of these samples, Cardiff was found to have the highest concentration of thorium (42,775 $\mu\text{g/g}$), likely due to the presence of thorium-containing minerals including thorite ($\text{ThO}_2\cdot\text{SiO}_2$) and uranothorite ($(\text{U,Th})\text{O}_2\cdot\text{SiO}_2$). Uraninite found within the Bancroft region of southern Ontario has previously been found to contain between 8 to 40% thorite [203].

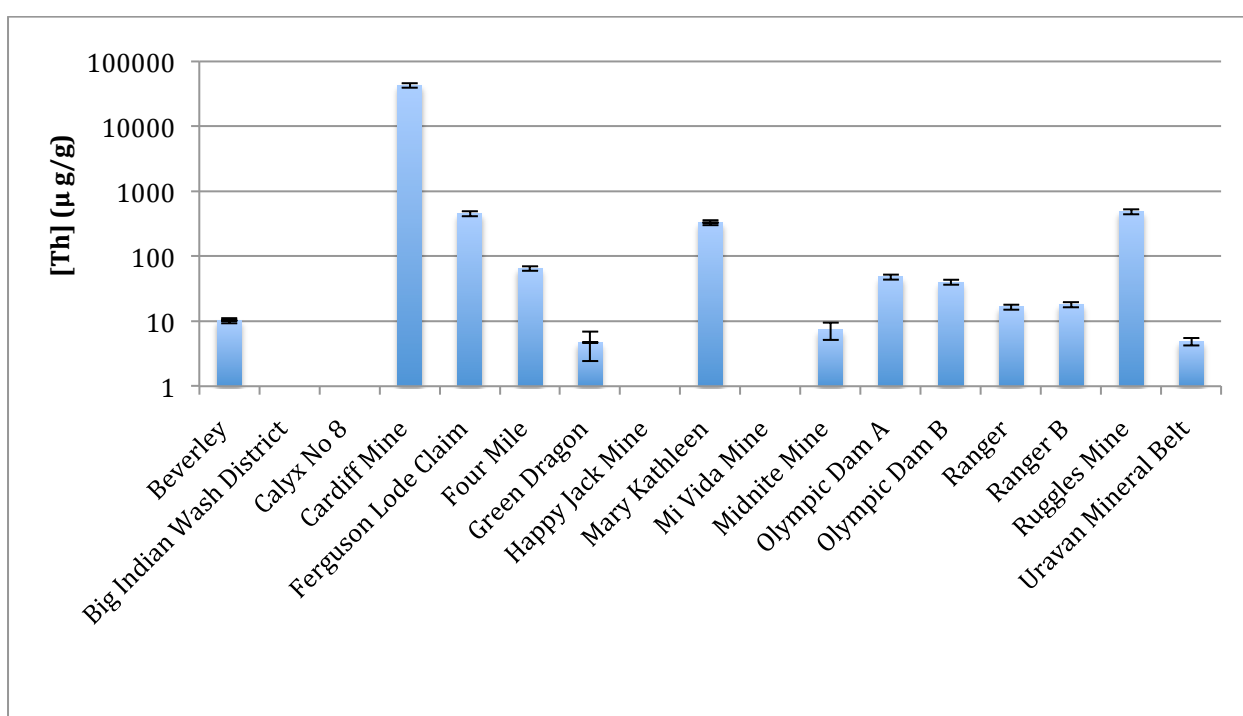


Figure 116 Concentration of thorium ($\mu\text{g/g}$) in the Australian and North American uranium ore samples measured by k_0 -NAA

Other uranium ore samples that feature appreciable concentrations of thorium include Ferguson Lode Claim (451 $\mu\text{g/g}$), Mary Kathleen (328 $\mu\text{g/g}$) and Ruggles Mine (483 $\mu\text{g/g}$). Within uraninite previously analysed from Ruggles Mine, the percentage of thorium present was to be 0.38% ($\text{ThO}_2 = 0.43\%$) [201]. At Mary Kathleen, thorium has been observed to concentrate within uraninite with concentrations previously observed between 1.49 – 7.22%, which is considerably higher than other mineral, including allanite ($(\text{Ce,Ca,Y,La})_2(\text{Al,Fe}^{3+})_3(\text{SiO}_4)_3(\text{OH})$), apatite ($\text{Ca}_5(\text{PO}_4)_3(\text{F,Cl,OH})$), titanite (CaTiSiO_5), garnet ($\text{Fe}_3\text{Al}_2\text{Si}_3\text{O}_{12}$) and clinopyroxene ($(\text{Ca,Mg,Fe,Al})_2(\text{Si,Al})_2\text{O}_6$), observed (<196 – 748 ppm) [314]. Analysed as a whole rock sample, the concentration of thorium within

MK68, a uranium-REE ore sample from Mary Kathleen, was found to be 2,890 ppm, with an U/Th ratio of 1.8 [314].

The U/Th ratio can itself be diagnostic, as it may indicate whether the uraninite was formed at high or low temperature [269]. If the U/Th ratio is $>10^3$, it is likely that the uraninite is of low-temperature ($\leq 450 \pm 50$ °C), hydrothermal origin, whereas a U/Th ratio of 10^1 - 10^2 would indicate the uraninite is of a higher temperature (>500 °C) and metamorphic or magmatic origin [269]. Further refinement can be obtained through the inclusion of total REE content as an additional parameter [269], however due to the lack of completeness in our dataset concerning the measurement of REE, only a preliminary characterisation of uraninite within the Australian and North American uranium ore samples will be performed. Of the Australian and North American samples, Green Dragon (6580) and Midnite Mine (3780) were the only samples to have U/Th ratios greater than 10^3 (Table 21).

Table 21 Thorium concentration ($\mu\text{g/g}$) and uncertainty and U/Th ratios in the Australian and North American uranium ore samples analysed by k_0 -NAA

	Th Conc. ($\mu\text{g/g}$)	Uncertainty ($\mu\text{g/g}$)	U/Th
Beverley	10.27	0.99	113
Big Indian Wash District	-	-	-
Calyx No 8	-	-	-
Cardiff	42775	3631.16	5
Ferguson Lode Claim	451.25	38.66	9
Four Mile	64.68	5.56	0
Green Dragon	4.7	2.27	6580
Happy Jack Mine	-	-	-
Mary Kathleen	328.45	27.96	3
Mi Vida Mine	-	-	-
Midnite Mine	7.37	2.21	3780
Olympic Dam A	48.08	4.39	15
Olympic Dam B	40	3.54	10
Ranger A	16.60	1.55	127
Ranger B	18.02	1.62	20
Ruggles Mine	483.65	41.5	159
Uravan Mineral Belt	4.85	0.61	130

6.3.6.2 Major Trace Elements

Ruggles Mine was found to have the greatest concentration of sodium (6.8% wt) across the Australian and North American uranium ore samples when analysed by k_0 -NAA, followed by Ferguson Lode Claim (6.3% wt) and Cardiff Mine (2.6% wt) (Figure 117). Of the Australian samples, Mary Kathleen was found to be the highest, with a concentration of 0.5% wt.

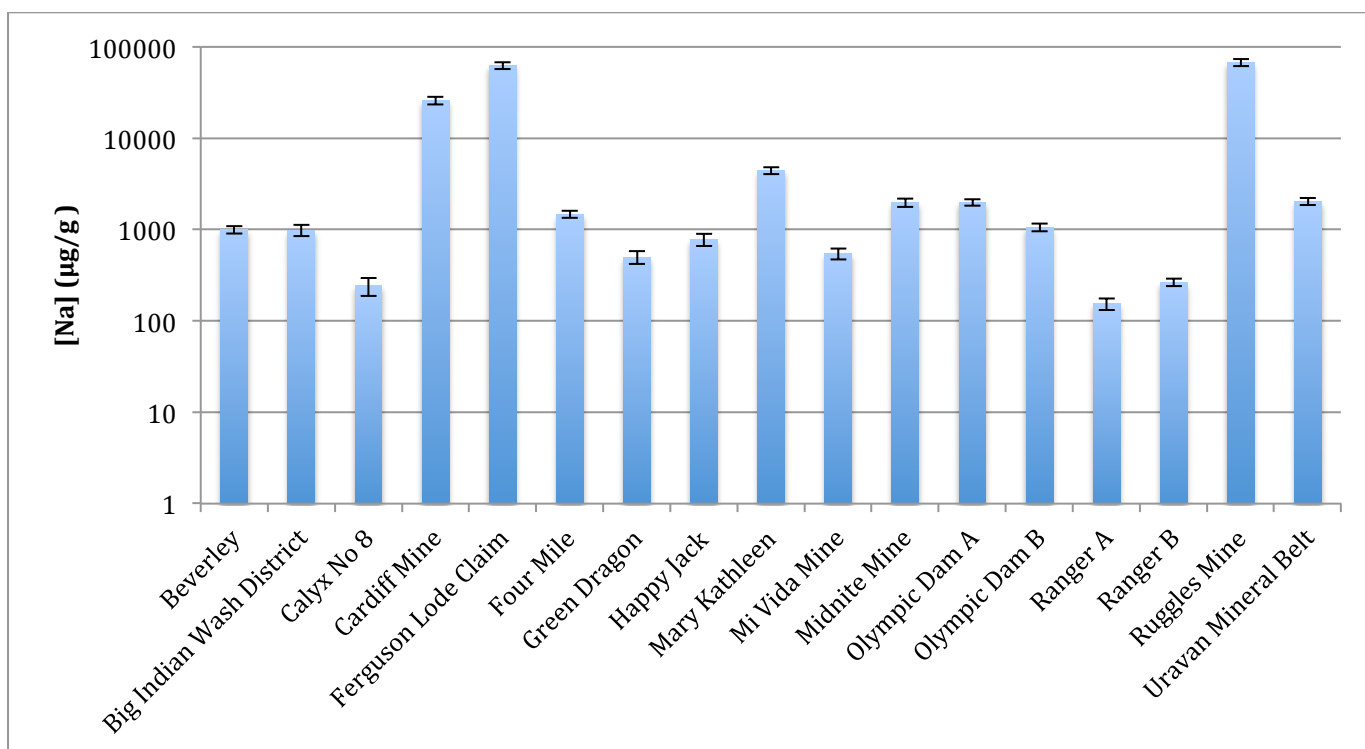


Figure 117 Concentration of sodium (µg/g) in the Australian and North American uranium ore samples measured by k_0 -NAA

With the exception of Mary Kathleen, all of the Australian ore samples were found to contain measureable quantities of magnesium, whereas none of the North American samples were found to contain reportable concentration magnesium concentrations (Figure 118). Ranger samples A (7.8% wt) and B (4.4% wt) were found to be consistent with one another, and had the greatest concentrations of magnesium. Similarly, both Olympic Dam samples were also found to be consistent with one another, with both Olympic Dam A and Olympic Dam B featuring a magnesium concentration of 0.2%.

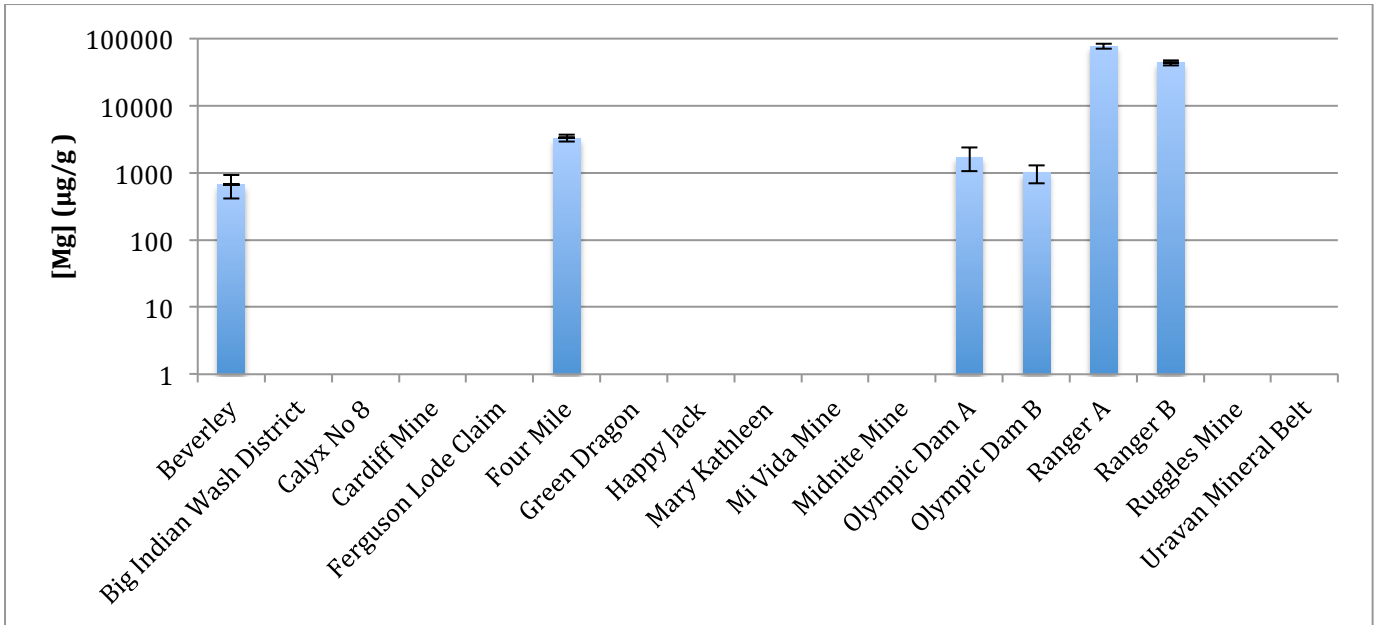


Figure 118 Concentration of magnesium ($\mu\text{g/g}$) in the Australian and North American uranium ore samples measured by k_{θ} -NAA

Ferguson Lode Claim was found to contain the greatest concentration of aluminium (12.3% wt) of all the uranium ore samples analysed, followed by Ruggles Mine (9.6% wt), Ranger B (8.4% wt) and Ranger A (6.9% wt) (Figure 119).

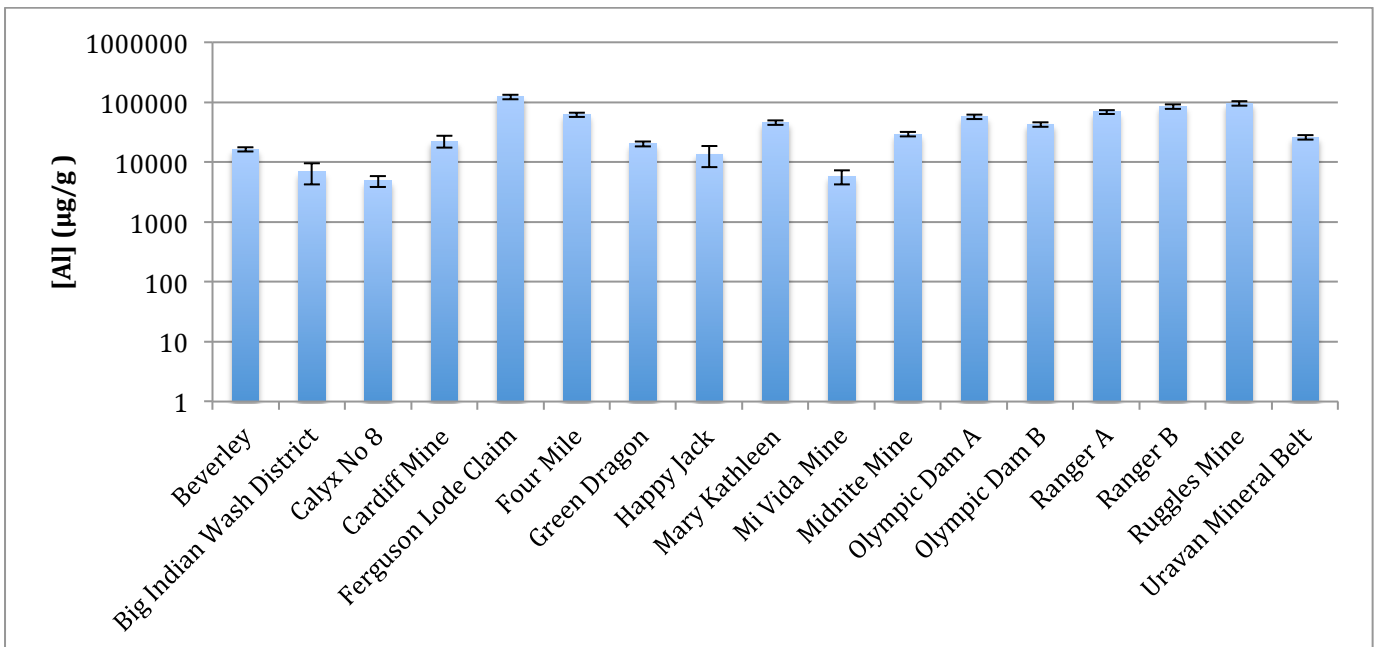


Figure 119 Concentration of aluminium ($\mu\text{g/g}$) in the Australian and North American uranium ore samples measured by k_{θ} -NAA

Olympic Dam A was found to have the highest concentration of potassium (2.2% wt), followed by Ranger B (2.2% wt), Midnite Mine (2.1% wt) and Olympic Dam B (1.9% wt) (Figure X). Whilst the Olympic Dam samples were found to have consistent concentrations of potassium, the samples from Ranger were found to differ greatly, with Ranger A having a concentration of 0.7% wt (Figure 120).

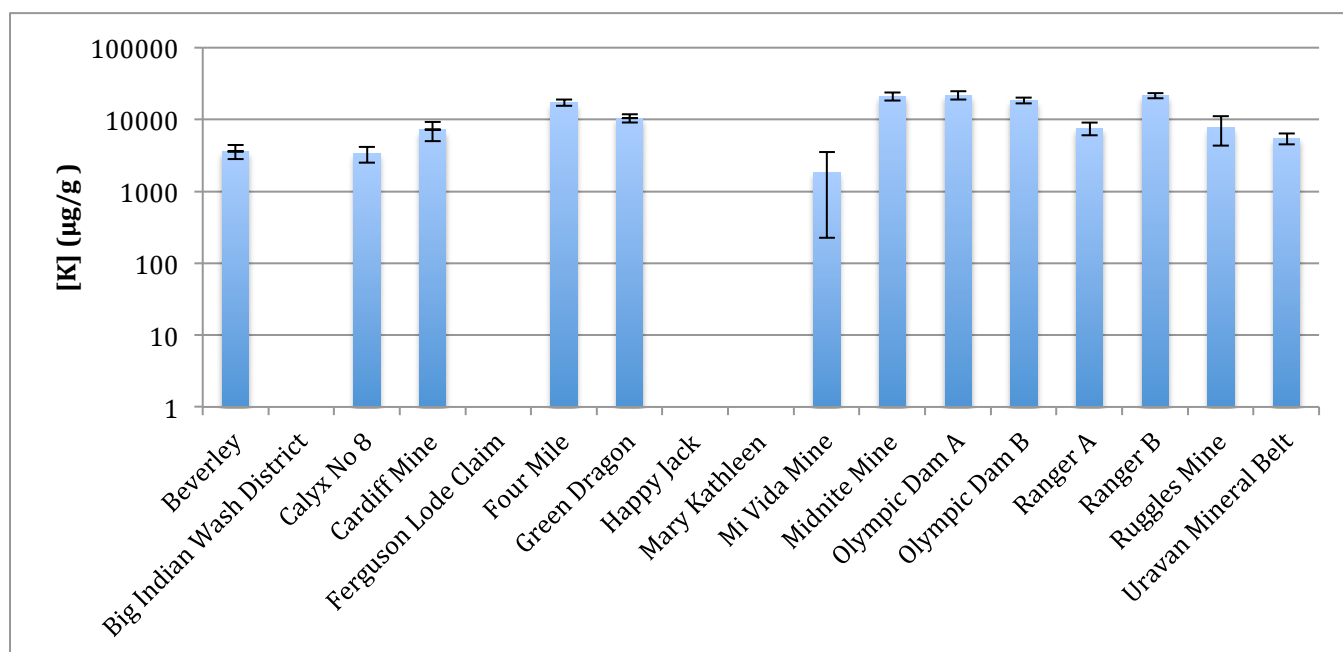


Figure 120 Concentration of potassium (µg/g) in the Australian and North American uranium ore samples measured by k_0 -NAA

Big Indian Wash District was found to have the highest concentration of calcium across the Australian and North American uranium ore samples, which was found to be 23.4% wt (Figure 121). Mi Vida Mine and Mary Kathleen were also found to have high concentrations, at 19.3 and 17.9% wt, respectively.

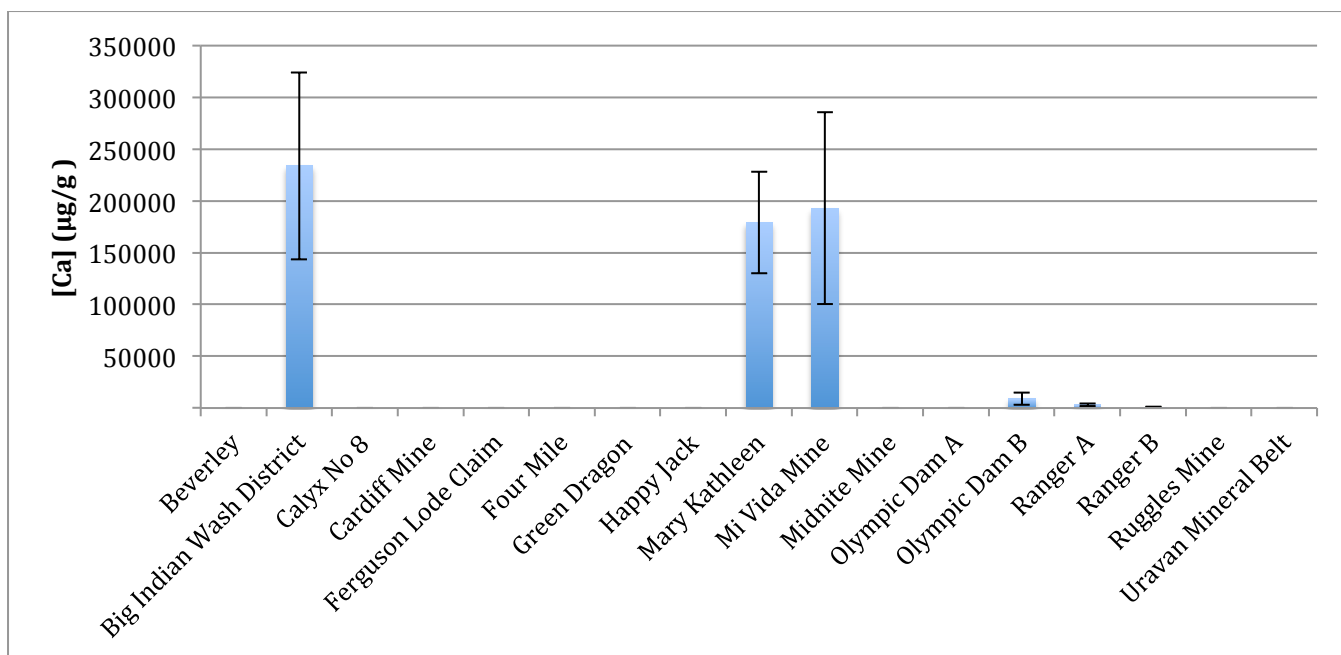


Figure 121 Concentration of calcium (µg/g) in the Australian and North American uranium ore samples measured by k_0 -NAA

The highest concentrations of manganese across the Australian and North American uranium ore samples were found in Big Indian Wash District (11280 µg/g), Mary Kathleen (4913 µg/g) and Mi Vida Mine (10855 µg/g) (Figure 122). Whilst the Olympic Dam A & B samples were found to feature manganese at different concentrations (89 and 128 µg/g, respectively), however the Ranger A & B samples were found to have the larger variation (719 & 164 µg/g, respectively).

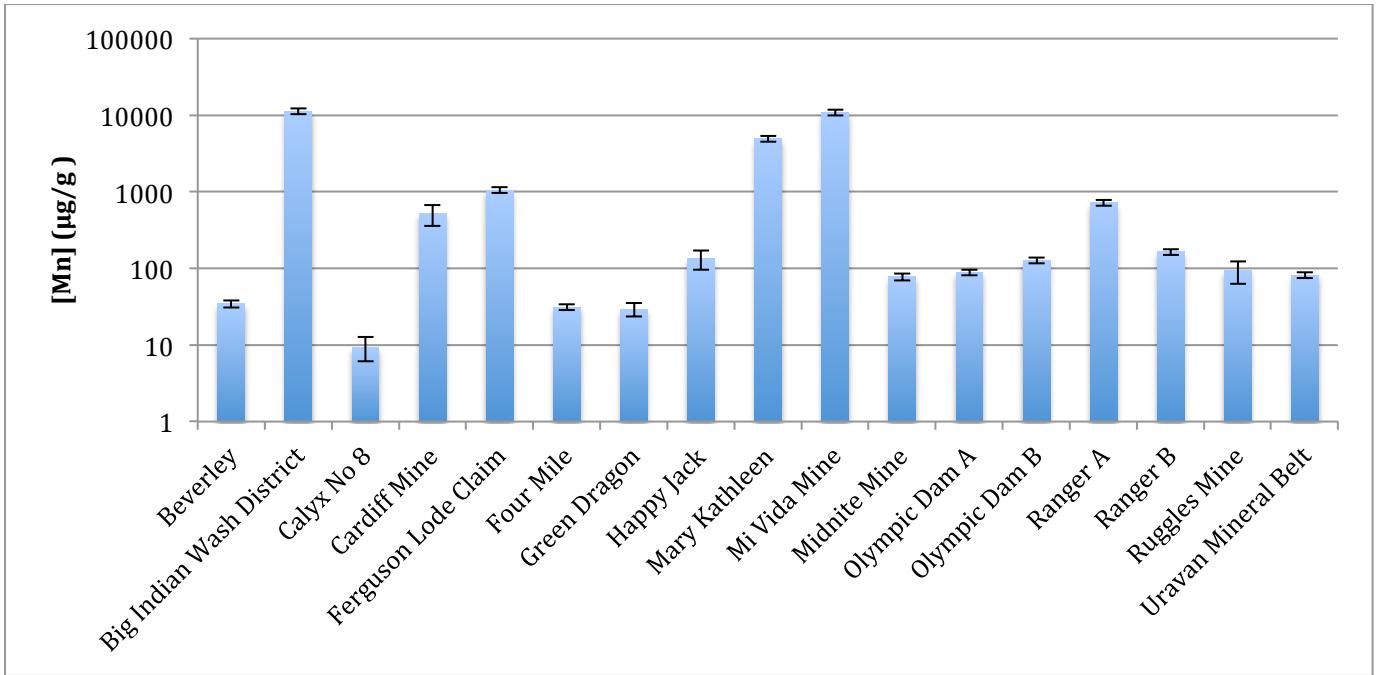


Figure 122 Concentration of manganese ($\mu\text{g/g}$) in the Australian and North American uranium ore samples measured by k_0 -NAA

The largest iron concentrations were found within the Olympic Dam A & B samples (245050 & 298800 $\mu\text{g/g}$, respectively), whilst Midnite Mine and Mary Kathleen had the third and fourth highest concentrations (134900 and 162350 $\mu\text{g/g}$, respectively) (Figure 123).

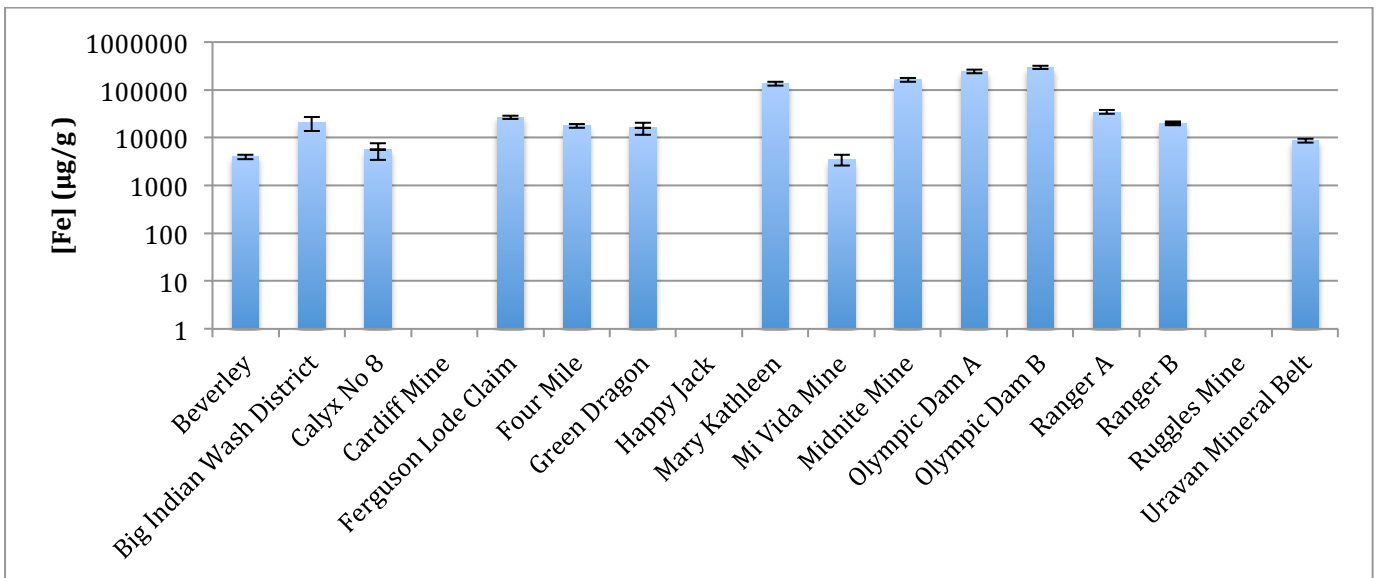


Figure 123 Concentration of iron ($\mu\text{g/g}$) in the Australian and North American uranium ore samples measured by k_0 -NAA

6.3.6.3 Minor trace elements

Elements, including arsenic, tungsten and vanadium, that were typically measured at concentrations less than 1% wt (10000 ppm) by k_0 -NAA within the Australian and North American U ore samples were classed as minor trace elements. Out of the twelve Australian and North American uranium ore samples that were found to have measureable amounts of arsenic present, Big Indian Wash District (8143.5 $\mu\text{g/g}$) was found to have the highest concentration, followed by Happy Jack Mine (5093 $\mu\text{g/g}$) Calyx No 8 (986 $\mu\text{g/g}$) (Figure 124).

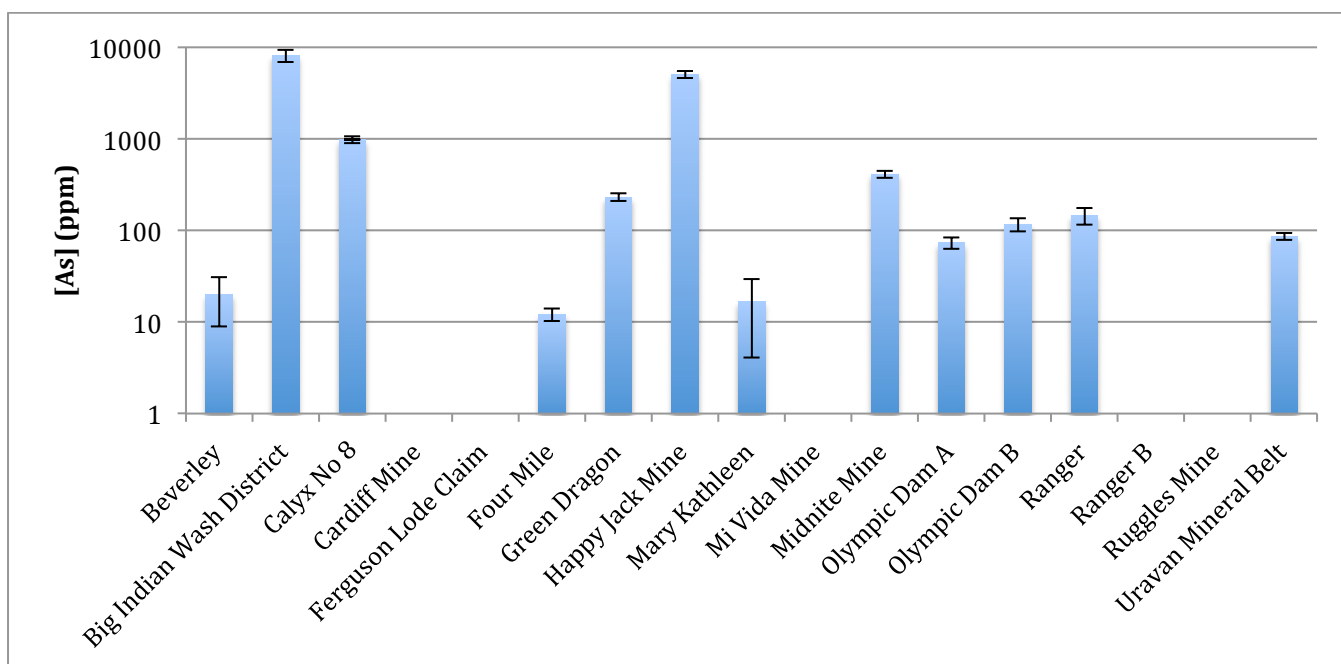


Figure 124 Concentration of arsenic ($\mu\text{g/g}$) in the Australian and North American uranium ore samples measured by k_0 -NAA

Tungsten could only be measured within six of the seventeen Australian and North American uranium ore sample by k_0 -NAA, with Olympic Dam B (80 $\mu\text{g/g}$) having the greatest concentration, followed by Olympic Dam A (65 $\mu\text{g/g}$) (Figure 125).

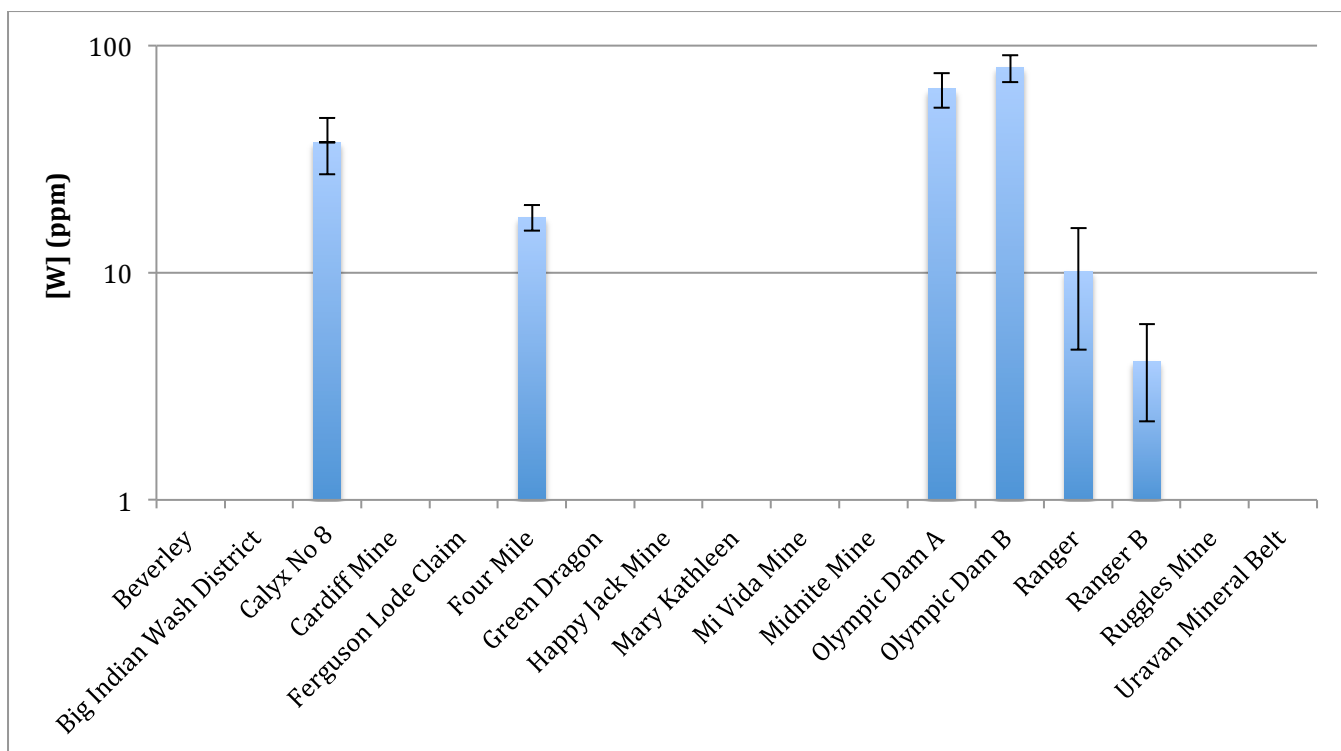


Figure 125 Concentration of tungsten ($\mu\text{g/g}$) in the Australian and North American uranium ore samples measured by k_0 -NAA

Four uranium ore samples from Calyx No 8 (38140 $\mu\text{g/g}$), Green Dragon (29995 $\mu\text{g/g}$), Mi Vida Mine (25500 $\mu\text{g/g}$) and Uravan Mineral Belt (30925 $\mu\text{g/g}$) were found to have high concentrations of vanadium (Figure 126). These uranium ore samples, located within Utah and Colorado, are within the same region as the Uravan Mineral Belt itself, which is a region that is characterised as high uranium and vanadium ores due to the presence of multiple sandstone-hosted carnotite ($\text{K}_2(\text{UO}_2)_2(\text{VO}_4)_2 \cdot 3\text{H}_2\text{O}$) ores (See Section 3.3.7) [189].

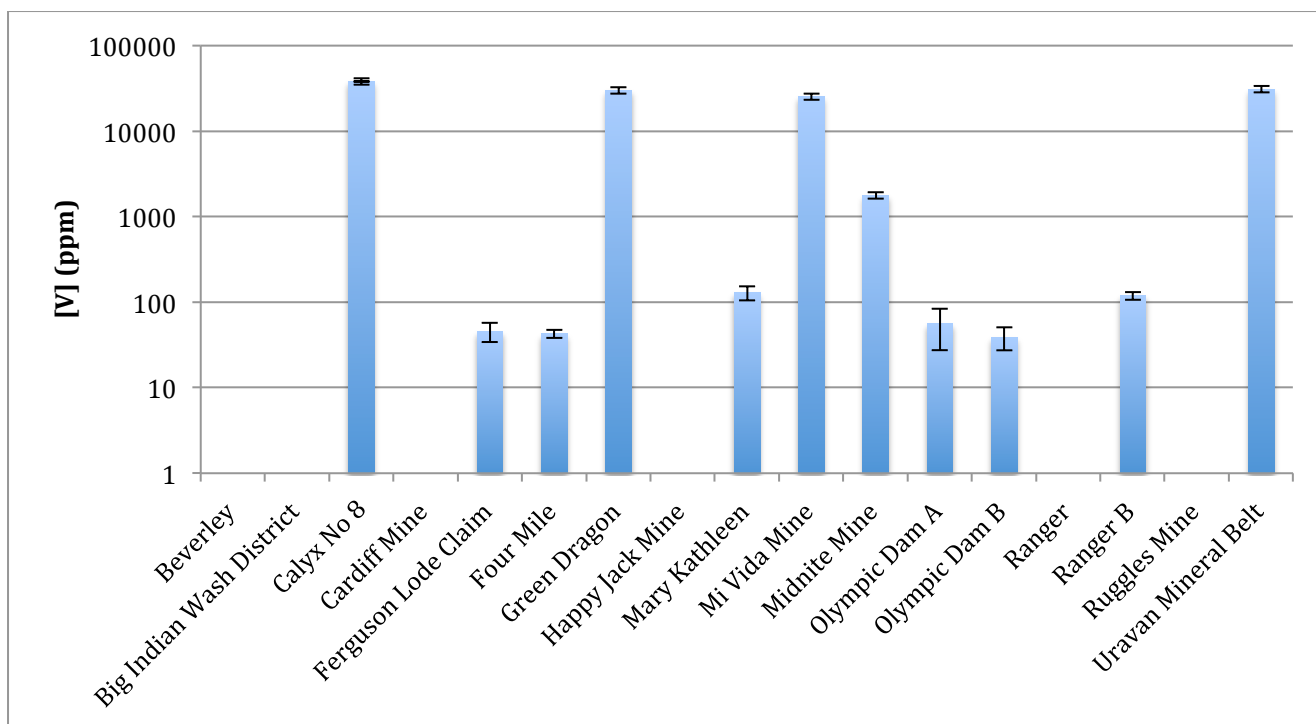


Figure 126 Concentration of vanadium ($\mu\text{g/g}$) in the Australian and North American uranium ore samples measured by k_0 -NAA

6.3.7 Comparison between the REE and trace elemental composition of the uranium ores and UOCs from the same Australian mine

In a similar fashion to Varga *et al.* (2017), where the trace and REE composition of a uranium ore, intermediates throughout the UOC production process and the resultant UOC from a South African uranium mine were compared to investigate how the original composition changed throughout the process [250], the trace and REE composition of five Australian uranium ores and their respective UOCs, which were analysed previously by Keegan *et al.* (2008) [39], were compared. Unlike the aforementioned study by Varga *et al.* (2017) however, no intermediate samples were collected and analysed in this comparison and the relationship between the uranium ores and their UOCs for each mine is not understood. In the study by Varga *et al.* (2017), the uranium ore, intermediates and final UOC samples were collected by the plant operators in relatively large quantities (>50 g) and were assumed to be as best as representative of the original uranium ore itself as it could be [250], whereas there is minimal information concerning the relationship between the uranium ore and UOC in this comparison, namely whether the UOC was produced from the sample U ore material.

Between the Beverley uranium ore sample analysed by k_0 -NAA in this study and the Beverley UOC analysed by Keegan et al. (2008), only nineteen of the thirty-eight elements could be compared (

Table 22). The major trace elements (sodium, magnesium and aluminium) and first-row transition elements (titanium, vanadium chromium, manganese and cobalt), where measurable within the Beverley uranium ore sample by k_0 -NAA, experienced a significant decrease in concentration ($>10^2$ to $10^4\%$) when compared to the UOC sample from Keegan et al. (2008) [39]. With the exception of lanthanum (962%), the six measureable REEs were found to decrease by a smaller percentage and range (75 to 134%) than the majority of the aforementioned major and first-row transition elements. Scandium and thorium were found to have the smallest percentage decrease (10 % and 5%, respectively).

The two uranium ore samples from Ranger vary considerably from one another, with Ranger B uranium ore sample consistently having a higher concentration of REEs and trace elements than the Ranger A uranium ore sample (Table 23). For some major elements (sodium, aluminium, titanium, and vanadium), the concentration in Ranger B is an order of magnitude higher than Ranger B. The compositional differences observed in the comparison between the two uranium ore samples also manifests in the percentage change values (%), with larger differences observed in the Ranger B uranium ore sample.

Compositionally, the two uranium ore samples from Olympic Dam appear to be less variable than the two uranium ore samples from Ranger (Table 24). Due to the low impurity concentration measured within the Olympic Dam UOC by Keegan *et al.* (2008) and the high concentrations of REEs measured within the A&B uranium ore samples, the Olympic Dam samples experience the largest percentage change (%) when compared to Ranger and Beverley uranium ore comparisons. With the exception of lanthanum, gadolinium and ytterbium, the other REEs measureable in both the uranium ore and UOCs as well as iron and barium experience percentage changes greater than 10^7 (Table 24).

Table 22 Elemental composition of Beverley Ore and Beverley UOC (Keegan et al. (2008)) and percentage change (%)

	Beverley Ore (This Study)	Beverley UOC (Keegan et al. 2009)	Δ (%)
	<i>Conc (μg/g U)</i>	<i>Conc (μg/g U)</i>	
Na	843523	4293	-1.95E+02
Mg	1159307	226	-5.13E+03
Al	13987987	1055	-1.33E+04
S	< dl	5231	-
Ca	< dl	741	-
Sc	2501	224	-1.02E+01
Ti	1421320	26	-5.47E+04
V	16877	60	-2.80E+02
Cr	103041	21	-4.91E+03
Mn	29395.7	5.1	-5.76E+03
Fe	3455424	31185	-1.10E+02
Co	7744.20	5.07	-1.53E+03
Ni	< dl	7.5	-
Cu	< dl	15	-
Zn	< dl	11	-
As	< dl	9.3	-
Rb	21506.3	1.6	-1.34E+04
Sr	< dl	32	-
Y	< dl	98	-
Zr	< dl	29	-
Mo	< dl	4	-
Sn	< dl	22	-
Ba	< dl	7	-
La	22156	23	-9.62E+02
Ce	< dl	223	-
Pr	< dl	32	-
Nd	< dl	127	-
Sm	3650	48	-7.50E+01
Eu	883	7	-1.25E+02
Gd	< dl	24	-

Tb	571.1	4.8	-1.18E+02
Dy	3208	29	-1.10E+02
Ho	< dl	4.5	-
Er	< dl	12	-
Tm	< dl	2.08	-
Yb	1424	15	-9.40E+01
Lu	209.28	1.55	-1.34E+02
Pb	< dl	2.8	-
Th	8856	1399	-5.33E+00

Table 23 Elemental composition of Ranger Ores A&B and Ranger UOC (Keegan et al. (2008)) and their respective percentage changes (%)

	Ranger A Ore (This Study)	Ranger B Ore (This Study)	Ranger UOC (Keegan et al. 2009)	Δ (from Ranger A Ore) (%)	Δ (from Ranger B Ore) (%)
	<i>Conc. (μg/g U)</i>	<i>Conc. (μg/g U)</i>	<i>Conc (μg/g U)</i>		
Na	77895	753237	834	-9.24E+01	-9.02E+02
Mg	43373418	129878119	434	-9.99E+04	-2.99E+05
Al	38280404	249302980	447	-8.56E+04	-5.58E+05
S	< dl	< dl	1052	-	-
Ca	1732137	5914689	99	-1.75E+04	-5.97E+04
Sc	6289	42116	2	-3.14E+03	-2.11E+04
Ti	1274417.2	9126985.0	2.4	-5.31E+05	-3.80E+06
V	81147	353373	59	-1.37E+03	-5.99E+03
Cr	48591.5	173872.8	1.8	-2.70E+04	-9.66E+04
Mn	400216	486004	135	-2.96E+03	-3.60E+03
Fe	16378274	55844471	537	-3.05E+04	-1.04E+05
Co	16533.33	35783.06	0.41	-4.03E+04	-8.73E+04
Ni	< dl	< dl	0.6	-	-
Cu	1132744	< dl	22	-5.15E+04	-
Zn	55249	108480	5	-1.10E+04	-2.17E+04
As	1092.00	< dl	0.48	-2.27E+03	-
Rb	17432.56	197295.73	0.24	-7.26E+04	-8.22E+05
Sr	< dl	< dl	2.8	-	-
Y	< dl	< dl	8.5	-	-
Zr	< dl	< dl	419	-	-
Mo	< dl	< dl	79	-	-
Sn	< dl	< dl	4.1	-	-
Ba	< dl	< dl	0.94	-	-
La	9737.73	29950.30	0.52	-1.87E+04	-5.76E+04
Ce	< dl	78226.95	0.54	-	-1.45E+05
Pr	< dl	< dl	0.14	-	-
Nd	< dl	< dl	0.66	-	-
Sm	3458.21	8644.33	0.52	-6.65E+03	-1.66E+04
Eu	839.66	1198.95	0.19	-4.42E+03	-6.31E+03

Gd	< dl	< dl	0.65	-	-
Tb	753.80	1464.81	0.25	-3.01E+03	-5.86E+03
Dy	6078.47	9795.64	1.54	-3.95E+03	-6.36E+03
Ho	< dl	< dl	0.31	-	-
Er	< dl	< dl	0.79	-	-
Tm	< dl	< dl	0.12	-	-
Yb	1880.24	5050.01	0.73	-2.57E+03	-6.92E+03
Lu	163.960	812.979	0.095	-1.72E+03	-8.56E+03
Pb	< dl	<dl	2.9	-	-
Th	7850.8	50181.9	6.1	-1.29E+03	-8.23E+03

Table 24 Elemental composition of Olympic Dam Ores A&B and Olympic Dam UOC (Keegan et al. (2008)) and their respective percentage changes (%)

	Olympic Dam A Ore (This Study)	Olympic Dam B Ore (This Study)	Olympic Dam UOC (Keegan et al. 2009)	Δ (from Ranger A Ore) (%)	Δ (from Ranger B Ore) (%)
	Conc. ($\mu\text{g/g U}$)	Conc. ($\mu\text{g/g U}$)	Conc ($\mu\text{g/g U}$)		
Na	2586593	2604273	1069	-2.42E+03	-2.44E+03
Mg	2238536	5143959	22	-1.02E+05	-2.34E+05
Al	74452357	102273741	21	-3.55E+06	-4.87E+06
S	< dl	< dl	2215	-	-
Ca	7490823	46033474	93	-8.05E+04	-4.95E+05
Sc	5898	9564	<1	-	-
Ti	1773372.6	2643041.4	2.92	-6.07E+05	-9.05E+05
V	73001	94063	<5	-	-
Cr	33665	52104	<1	-	-
Mn	115820.06	308972	0.35	-3.31E+05	-8.83E+05
Fe	331838193	1557199360	19	-1.75E+07	-8.20E+07
Co	76183.28	121444.50	0.06	-1.27E+06	-2.02E+06
Ni	< dl	< dl	0.25	-	-
Cu	35380506	3635974	115	-3.08E+05	-3.16E+04
Zn	< dl	< dl	34	-	-
As	106707.00	284470.14	0.20	-5.34E+05	-1.42E+06
Rb	163633.82	277060.76	0.22	-7.44E+05	-1.26E+06
Sr	510745.57	1144234.77	1.14	-	-1.00E+06
Y	< dl	< dl	<0.1	-	-
Zr	< dl	1859096	239	-	-7.78E+03
Mo	< dl	< dl	107	-	-
Sn	< dl	< dl	0.69	-	-
Ba	6921828.14	21531753	1.08	-	-1.99E+07
La	1900937.649	1900937.649	0.41	-4.64E+06	-4.64E+06
Ce	3017954.288	7123447.657	0.27	-1.12E+07	-2.64E+07
Pr	303398.9373	1900937.649	0.02	-1.52E+07	-9.50E+07
Nd	673329.318	1605051.778	0.07	-9.62E+06	-2.29E+07
Sm	63121.93009	1900937.649	0.01	-6.31E+06	-1.90E+08
Eu	24140.7692	1900937.649	0.003	-8.05E+06	-6.34E+08

Gd	< dl	225578.3386	0.44	-	-5.13E+05
Tb	5164.182041	10768.17301	0.001	-5.16E+06	-1.08E+07
Dy	30637.08847	54389.43829	0.004	-7.66E+06	-1.36E+07
Ho	37805.282	36476.90148	0.001	-3.78E+07	-3.65E+07
Er	< dl	< dl	0.005	-	-
Tm	< dl	< dl	<0.001	-	-
Yb	18589.96977	24942.42169	0.007	-2.66E+06	-3.56E+06
Lu	3248.294416	4395.842649	<0.001	-	-
Pb	< dl	< dl	0.4	-	-
Th	65085.10	104227.73	0.35	-1.86E+05	-2.98E+05

With only the uranium ores and a UOC (i.e. the first and last stage in the UOC production process) to investigate compositional changes, the lack of intermediates samples between each of the individual processes used by these three Australian mines, makes the task of ascribing why the composition changes extremely difficult. As mentioned previously, the lack of knowledge concerning the relationship between the uranium ore samples UOC, with respect to where both types of were mined within the deposit(s), when they were mined and whether the original feed material is compositionally identical to the uranium ore samples analysed in this study, further compounds this difficulty.

6.3 Conclusions

Prior to the elemental analysis of the Australian and North American uranium ore samples by k_0 -NAA, the concentration of uranium within the North American samples was analysed using three different analytical techniques. The analytical approaches of both SEM and pXRF were found to be inadequate for the accurate measurement of uranium within the bulk U ore samples, as they both featured high uncertainties due to fundamental issues with how the measurements were performed (Figure 94). The third technique, DNAA, was found to provide the most precise measurement of the uranium concentration of the North American samples, finding the concentration varied between 0.197 – 46.6% (Figure 97). The Ike-Nixon Shaft sample, which featured the highest uranium concentration, was reanalyzed using a corrected DNAA method developed by Anvia (2016), finding the uranium concentration was instead higher at 55.7 % (Figure 98). This information was used to determine the masses of sample analysed by k_0 -NAA irradiations, and exclude the Ike-Nixon Shaft sample from further analysis due to its high uranium concentration.

Short and long k_0 -NAA irradiations were used to measure the REE and trace composition of the Australian and North American uranium ore samples, as well as four uranium ore CRMs from OREAS. In the two uranium ore CRMs (OREAS 106 and 124), which featured the two highest uranium concentrations (1143 and 1794 ppm, respectively), the measurement of the REEs was hampered by uranium with only eight and seven measurable by k_0 -NAA (Figure 102 & Figure 104). The measurement of the REEs in the CRMs (OREAS 100a and 120) with lower concentrations of uranium (135 and 40.8 ppm, respectively) was improved, with thirteen and ten REEs measured, respectively (Figure 101 & Figure 103). Several REEs, particularly holmium (when measurable), were found to feature a positive bias likely due to the generation of fission products from uranium during irradiation. Despite the contribution from fission products, the chondrite-normalised REE patterns of the OREAS CRMs analysed by k_0 -NAA still largely remained similar to the chondrite-normalised REE patterns from the certified REE concentrations of the respective CRMs. However, the major complications for the interpretation of the chondrite-normalised REE pattern from k_0 -NAA were found to be the inconsistency in the detection of REEs and the large positive bias of holmium.

Good agreement was generally found between the measured and literature values for the certified trace elements within the OREAS uranium ore CRMs where measurable by k_0 -NAA, with some exceptions. Copper and vanadium were measured in concentrations greater than 10% of their certified values with OREAS 100a (Table 17), whilst magnesium, chromium, tantalum, cesium and

hafnium were found to deviate considerably from their certified values in the OREAS 120 CRM (Table 19). Hafnium, as well gallium and strontium, were also found to deviate greatly from the certified values in the OREAS 124 CRM (Table 20).

Of the Australian uranium ore samples, the chondrite-normalised REE pattern was typically consistent (where measurable with k_0 -NAA) with patterns obtained from other UOC and/or uranium ore samples originating from the same location within the literature, with the exception of the Ranger A & B samples. The chondrite-normalised REE patterns of the two uranium ore samples from Olympic Dam were found to be consistent with other UOC and ore samples from Olympic Dam [39, 311], with an enriched LREE/depleted HREE pattern (Figure 105). The chondrite-normalised REE pattern of the Beverley uranium ore sample was more difficult to compare with the pattern of the Four Mile uranium ore sample and other uranium ore samples from this location in the literature, due to the limited number of REE that were able to be measured by k_0 -NAA (Figure 106). Both samples could be characterised as having an enriched LREE/ HREE plateau pattern with a negative europium anomaly (Figure 106).

The uranium ore sample from Mary Kathleen featured a similar pattern to a UOC also from Mary Kathleen with an enriched LREE/depleted HREE pattern and negative europium anomaly, however it was also found to feature a significant holmium interference arising from uranium fission (Figure 108). The pattern of the Mary Kathleen uranium ore sample did diverge from the partial pattern of a uraninite sample from Mary Kathleen with respect to the LREEs, however it was found to be consistent with the complete pattern of a whole rock sample and the partial pattern of a allanite sample from Mary Kathleen [314].

The most remarkable Australian chondrite-normalised REE patterns measured by k_0 -NAA came from the two Ranger samples. Despite several REEs being unable to be detected within both samples, one Ranger sample was found to have a different pattern to the other Ranger sample (Figure 107). The Ranger A sample featured a relatively flat profile whilst the Ranger B sample featured an enriched LREE/flat HREE pattern. A comparison with a UOC sample analysed by Keegan *et al.* (2008) found the Ranger A & B uranium ores samples had a different pattern to the UOC sample, with the UOC sample featuring depleted LREE/HREE plateau (Figure 107) [39]. A study of uranium ore samples at Ranger by Fisher *et al.* (2013) found the chondrite-normalised REE pattern varied according to the concentration of uranium in the ore; the pattern of low-grade uranium ore

(0.06%) had a similar pattern to the Ranger B sample, whilst higher-grade ore (0.85%) had a pattern similar to the Ranger UOC sample [313].

The analysis of the REE composition of the North American uranium ore samples by k_0 -NAA was found to be more difficult relative to the Australian uranium ore samples due to the higher concentrations of uranium present, resulting in less REEs being able to be measured. Limited REE data obtained by k_0 -NAA made comparing the partial chondrite-normalised REE patterns of Cardiff (Figure 109) and Ruggles Mine (Figure 110) uranium ore samples to patterns calculated from REE data reported in the literature difficult, whilst for several other samples (Mi Vida, Big Indian Wash District, Calyx No 8, Green Dragon and Midnite Mine) it was difficult to ascertain the pattern themselves due to the limited number of REEs reported (Figure 111 & Figure 115).

For the measurement of REEs within uranium ore samples, the results obtained in this chapter indicate that k_0 -NAA is not currently a viable alternative or successor to ICP-MS, given the fission product interferences of REE arising from the samples' relatively high uranium content. Whilst ICP-MS analysis can be complicated by matrix effect and isobaric interferences, it is well established within the literature and the nuclear forensics discipline as the technique of choice for the measurement of trace elements and REEs within UOCs and uranium ore samples. The results from this study do not, in any way, provide any evidence for a change in status quo with respect to the analytical technique of choice for the measurement of trace elements and REEs for nuclear forensics.

The comparison between the Ranger uranium ore samples from this study, the Ranger UOC sample from Keegan *et al.* (2008) and the Ranger uranium ore samples from Fisher *et al.* (2013), finding the chondrite-normalised REE pattern varied significantly according to uranium concentration of the ore, does highlight an issue concerning the representativeness of samples that may be kept as references for a mine/deposit. Ideally, if uranium ore samples are to be used to help assist in the establishment of provenance for an unknown UOC sample, multiple reference samples should be taken throughout the deposit(s) across the lifetime of the mining activity, in order to reflect changes with the uranium grade and associated mineralogy that may impact the chondrite-normalised REE patterns. Realistically however, this scenario has several flaws, as it would likely result in significant number of uranium ore samples being collected across the lifetime of the deposit, require the cooperation and assistance of several large mining corporations or regulatory agencies to provide these samples and naturally does not work for mines/deposits that have ceased production or closed unless archived samples may be accessed. This approach would be significantly more difficult if applied to UOCs

for similar purposes, due to heightened risks and more stringent regulatory requirements when compared to uranium ore. To the best of my knowledge however, this comparison between the various UOC and uranium ore samples from Ranger is the first example where the chondrite-normalised REE patterns have been found to significantly vary within the same mine site. On the balance of these issues, the most reasonable approach appears to be to maintain the current practice of using multiple signatures in concert for the identification of an unknown UOCs provenance.

6.4 Future Work

6.4.1 Reanalysis of Australian and North American uranium ore samples by ICP-MS

Despite issues of isobaric interferences and matrix effects, as well as difficulties concerning the digestion of samples, ICP-MS still appears to be the most appropriate technique for the analysis of trace and REE within uranium ore samples. As such, the Australian and North American uranium ore samples should be reanalyzed using ICP-MS in order to attain a more complete dataset regarding their trace and REE composition. The more complete REE data for the Australian uranium ore samples in particular, in the form of the chondrite-normalised REE pattern, will allow a better comparison with UOCs from the same mine.

6.4.2 HPLC Separation or Online HPLC-ICP-MS method for the analysis of REEs within UOCs

A potential alternative to extraction chromatography resins for the separation and analysis of REEs within high uranium matrices is the use of ion pairing chromatography in a high performance liquid chromatography (HPLC) system. This approach is of particular interest to studies concerning spent nuclear fuel, where the measurement of key REEs, particularly ^{148}Nd , is critical as they are used as a means to measure the consumption of fissionable material within the fuel [315]. A concern with these measurements by ICP-MS is the impact isobaric interferences may have, which could result in an overestimation of the concentration of the REEs of interest.

These studies commonly involve the coating of a reverse-phase or ion-exchange HPLC column with Di-(2-ethylhexyl) phosphoric acid (HDEHP) and use a mobile phase containing α -hydroxy isobutyric acid (α -HIBA), a complexing agent [315, 316], however other coatings may be used [317]. Some authors have been able to individually elute the REEs [316], as well as couple the HPLC to the ICP-MS for online detection of the individually-eluting REEs [315]. A more complex HPLC-ICP-MS methods had a dual column system, where the first column retained the matrix element uranium, whilst the second column performed the separation and elution of the REE [318].

Image removed due to copyright restriction.

Figure 127 Chromatogram of the elution of individual REEs through the HDEHP/ α -HIBA HPLC system [316]

6.4.3 CRM development

As seen through the use of the OREAS uranium ore CRMs for the evaluation of the performance of k_0 -NAA towards the analysis of the REE and trace elemental composition, there is a need for a CRM with certified values that are independent of the sample preparation procedure (i.e. acid digestion procedure). Furthermore, there is a need for a CRM (or series of CRMs) that better represents the diversity of uranium ores particularly with regards to the uranium concentration, which can vary significantly as seen within this chapter, in order to understand how the uranium concentration may impact the measurement of REE and trace elements by ICP-MS or other elemental analysis techniques.

A survey of sixty-one commercially available CRMs that encompass uranium ores, UOCs, uranium tailings, gold and uranium ores and uranium-thorium ores, found that fifty-seven had certified uranium concentrations less than 1%, whilst there was only one non-UOC CRM that had a concentration greater than one (7.09%) (Figure 128). Not included within this survey are four known UOC CRMs from CETAMA as their certificates of analysis and other details such as their availability have been difficult to acquire. Further examination of the CRMs with certified uranium

concentrations of less than 1% revealed that the majority of this group (n=36) in fact had certified uranium concentrations of less than 0.1% (Figure 129).

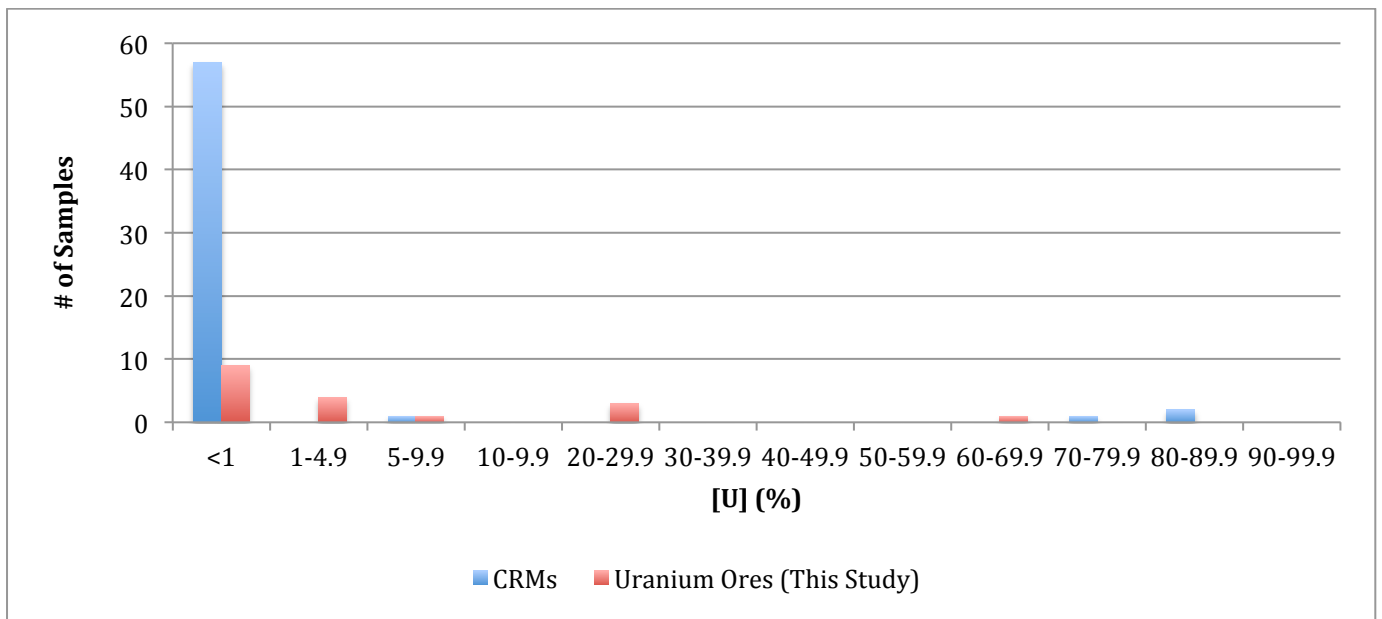


Figure 128 Histogram of CRMs available and uranium ores analysed in this study binned according to their uranium concentration (%)

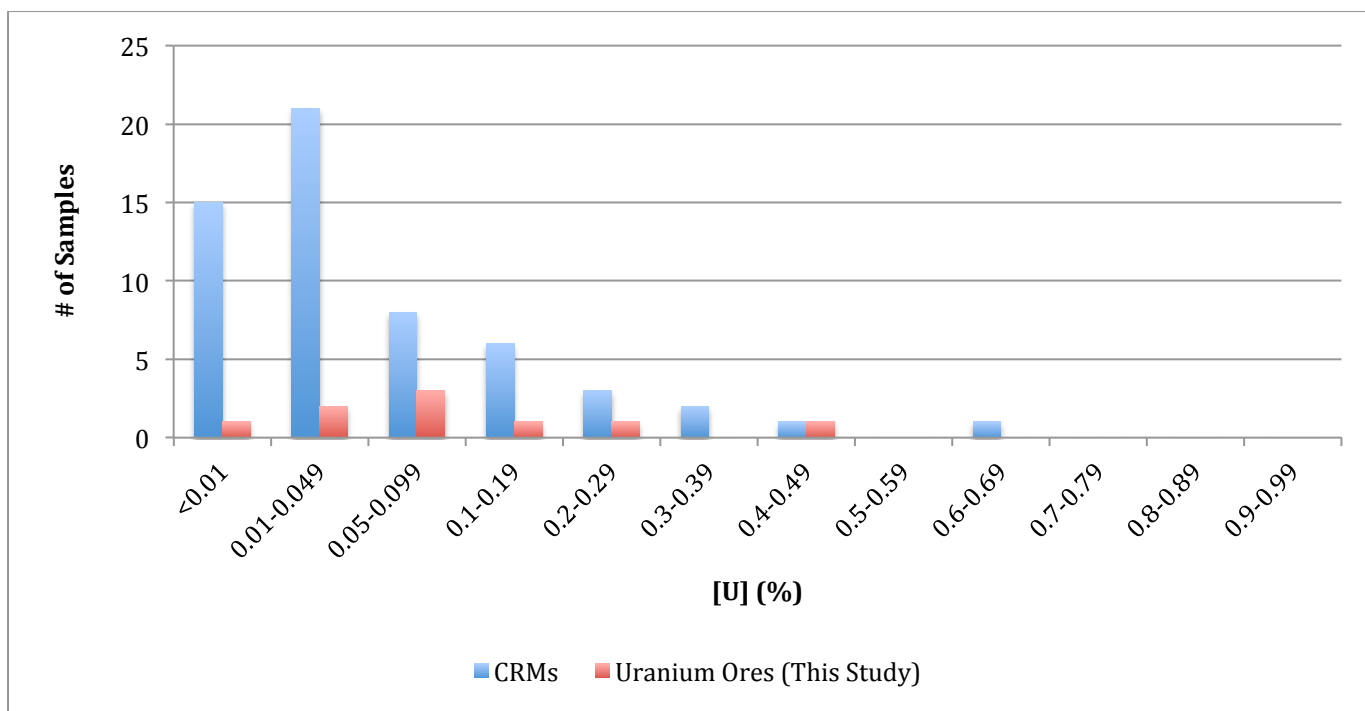


Figure 129 Histogram of CRMs and uranium ores analysed in this study with uranium concentrations less than 1% binned according to their uranium concentration (%)

With regards to the certified REE composition, only seventeen of the CRMs have at least one certified REE, which is often lanthanum and is present at low range of concentrations with limited variations (0.0021 – 0.0861 ppm) (Figure 130). The OREAS suite of CRMs were found to measure all of the REEs, with the exception of one (OREAS 121), whereas the CRMs from African Mineral Standards (AMIS) were more variable (Figure 130).

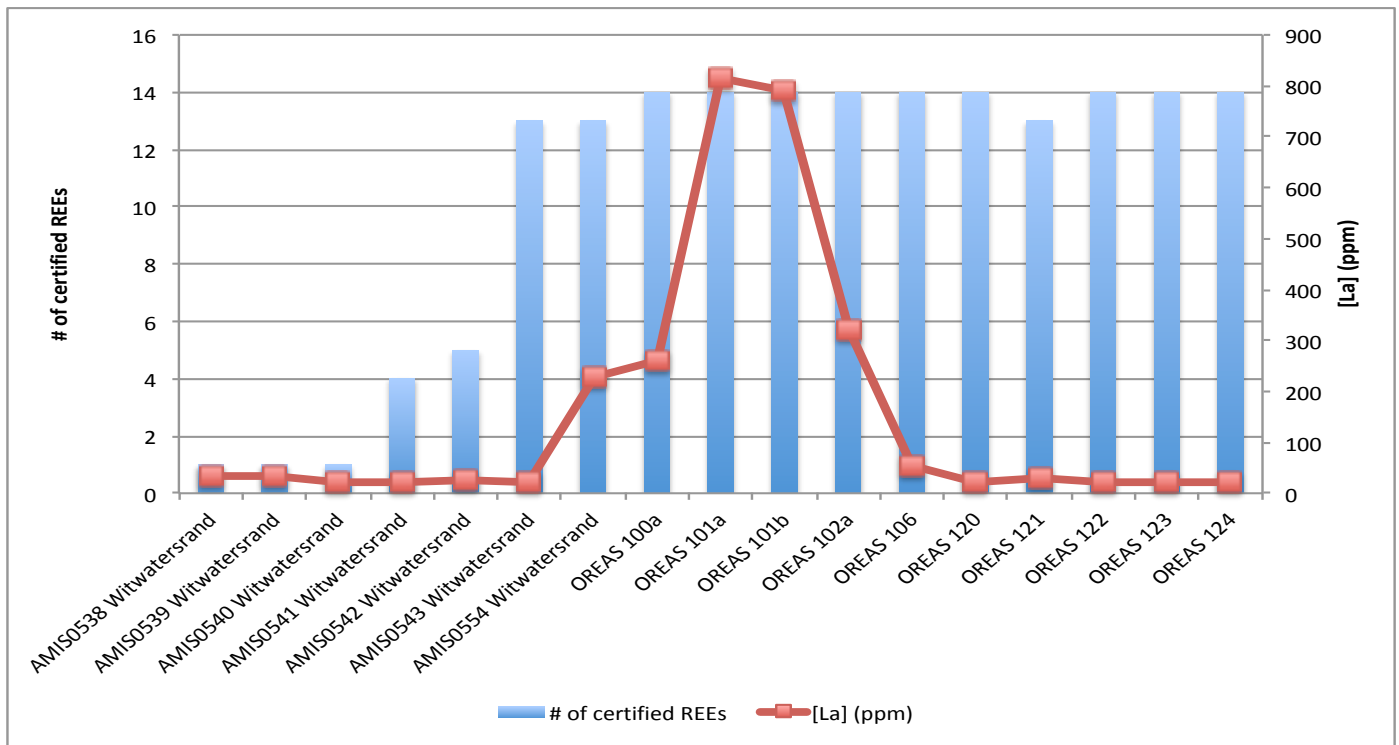


Figure 130 Number of certified REEs and concentration of lanthanum [La] within the seventeen CRMs with at least one certified REE

The commercially available CRMs typically are shown to predominantly feature certified concentrations of lanthanum, which is being used as a proxy to represent the certified concentrations of the other REEs, of less than 50 ppm, (Figure 131). The concentrations of lanthanum within the Australian and North American uranium ore samples, where measurable by k_0 -NAA, are more diverse; particularly as three uranium ore samples (Olympic Dam A, Olympic Dam B and Mary Kathleen) have concentrations greater than 1000 ppm (1422, 1780.5 and 9330.5 ppm, respectively).

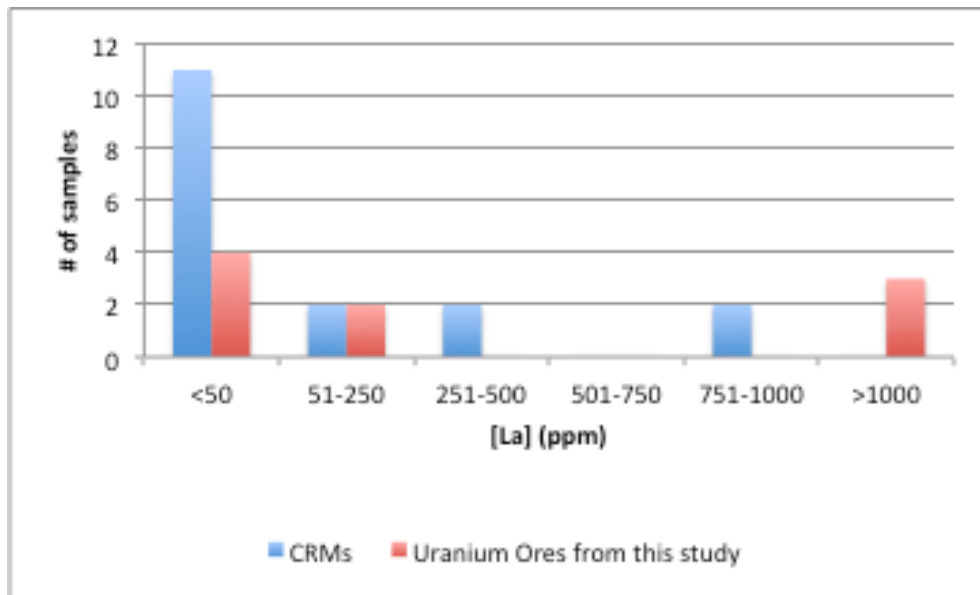


Figure 131 Histogram of lanthanum concentrations (ppm) of commercially available CRMs and uranium ores analysed in this study

With regards to the certified trace element composition, fifty-four of the sixty-one CRMs have more than one certified trace element in an overall pattern not unlike a bimodal distribution (Figure 132). The major mode is centered on the '5-9' certified trace elements bin whereas the minor mode peak is shared between the '25-29' and '30-34' bins.

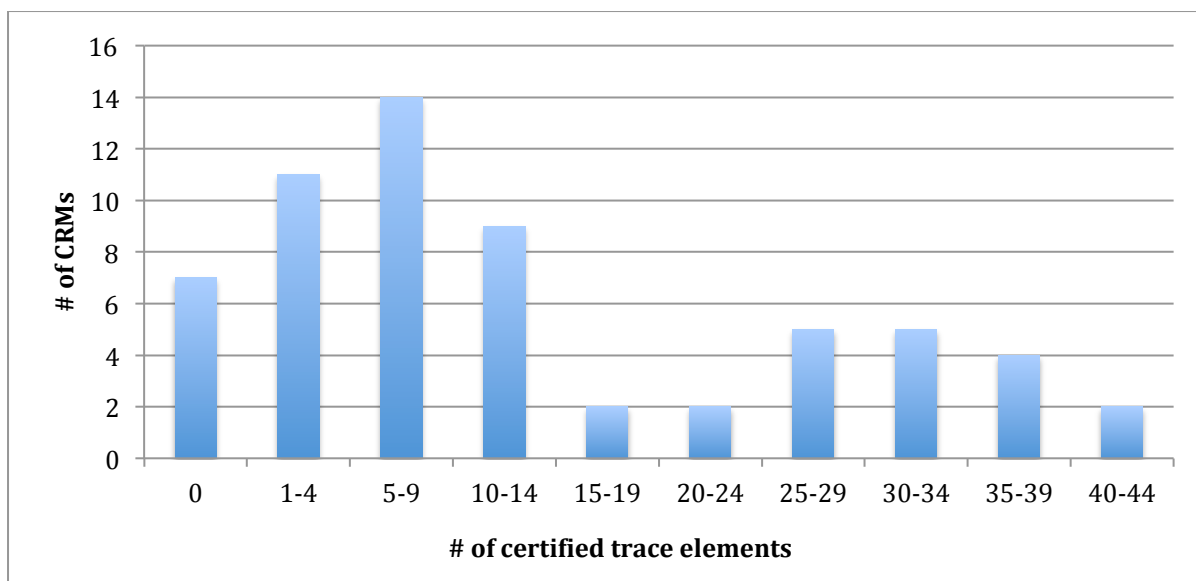


Figure 132 Histogram of the number of certified trace elements amongst the survey of commercially available CRMs

From the previous histograms concerning the concentration of uranium (Figure 128 and Figure 129) and the number of certified REEs and lanthanum concentrations within the commercially available CRMs (Figure 130), it is apparent there is a lack of CRMs that represent the variety of different uranium ore and UOC samples that may be encountered in a nuclear forensics investigation or the focus of a research study into signatures or the development of new analytical strategies or techniques for nuclear forensics. For instance, only one CRM based upon a uranium ore sample (BL-5, CANMET) has a certified uranium concentration greater than 1% (7.09%), however the two accompanying certifications concern the activity of ^{226}Ra and ^{210}Pb [319]. Due to the lack of certified REE and trace elements, it is practically unusable for this application and therefore results in no functional CRM between the 1% and 70% uranium content.

The inverse is also true, with the selection of OREAS standards featuring thirteen to fourteen REEs and sixteen to forty-two trace elements certified, however the concentration of uranium across these CRMs is considerably low (0.00408 – 0.1794 ppm U). Furthermore, the OREAS standards do not have consensus certified values for the REEs and trace elements, but are certified multiple times according to the analytical technique and the preparation procedure used (i.e. 4-acid digestion and sodium peroxide or lithium borate fusion method for ICP-MS/OES or pressed powder pellets and lithium borate fusion for XRF). As illustrated in Section 5.3.3, the lack of a single consensus value for a particular analyte within the OREAS CRMs makes benchmarking of alternative elemental

analysis techniques difficult, particularly when the technique itself is a bulk analysis technique, as in this particular case where k_0 -NAA was trialed.

Ideally, a series of uranium ore CRMs with uranium concentrations interspersed between the 1%-70% concentration range that has all fourteen REEs certified at different concentrations as well as as many trace elements as possible would be valuable to facilitate this type of research, where new analytical methodologies and different instrumental approaches are investigated. This approach, where a series of uranium CRMs have increasing concentrations of certified elements, is observed within the New Brunswick Laboratory (NBL) CRM 123(1-7) U_3O_8 set, where eighteen trace elements have artificially been added to produce seven individual CRMs with increasing concentrations of their certified elements [320]. Depending on whether an appropriate ore source that could be sourced in sufficient quantity to be viable for the certification procedure much less the enough to be sold, the artificial addition of REEs or uranium may be required to obtain a desirable composition for certification.

Chapter 7. Conclusions

In Chapter 4, I reported the first instance within the literature of real-world UOC samples being analysed by TGA for nuclear forensics purposes. Eight UOC samples from three different Australian uranium mines (Beverley, Ranger and Olympic Dam) were analysed by TGA in both air and nitrogen atmospheres. In both atmospheres, the three different mines could be differentiated from one another as the Ranger and Olympic Dam (primarily U_3O_8) decomposed differently to Beverley (primarily $UO_4 \cdot 2H_2O$) but had different initial amounts of moisture that allowed Ranger and Olympic Dam to be differentiated from one another. DSC measurements were also taken simultaneous to the TGA measurements, and despite large intra-mine variability observed across all three mines, a number of peaks and their directions were valuable in identifying the different intermediates and products formed. Three different analytical techniques (NIR, Raman and XRD) were employed to assist in the identification of the starting compositions of the three groups of UOCs, as well as the intermediates and final products formed across the temperature range examined using TGA. NIR was found to be too insensitive for the identification of minor phases within the three different UOCs and was not used further in this study. Raman spectroscopy and XRD were found in most cases to mostly sufficiently measure the major and minor uranium compounds present within the three different groups of UOCs, and the intermediates and final products formed. There were, however, several inconsistencies between the Raman and XRD data and the suggested thermal decomposition pathways reported in the literature, as well as between the two techniques. Further analysis is required to clarify these discrepancies and elucidate the identity of intermediates that formed during heating.

A second direction of this study was to investigate the morphological features of the three different groups of UOCs and how increased temperature impacted them. At both the macro- (500x magnification) and micro-scale ($\geq 30,000x$ magnification), the Beverley, Ranger and Olympic Dam UOCs could be differentiated from one another. At 500x magnification, Olympic Dam UOCs were found to feature smooth spherical agglomerates which varied in size between ~ 5 to $55 \mu m$. The Beverley and Ranger UOC samples were found to be more similar to each other as they predominately featured smaller, irregular agglomerates with some larger structures also observed, albeit at a higher frequency within the Beverley samples. At the micro-scale, the three Beverley UOC samples consisted primarily of thin rectangular plates, however some variation was observed across all three samples. The UOCs from Ranger were found to feature the most diverse morphologies, with four distinct features observed; rod-like structures, large smooth-faced structures,

globular structures and quasi-cuboidal structures. Variation was also observed across the Ranger UOCs, with the globular structures in Ranger 1 appearing to have a more jagged appearance with sharp edges and points, whereas more rounded and smooth globular structures were observed within Ranger 2 and 3 UOCs. Olympic Dam UOCs were found to feature no observable variability between the two samples and consisted of small, globular structures with a number of rod-like structures. All eight UOC samples behaved similarly when subjected to increased temperature, where no change in their respective morphological features was observed until the samples were heated beyond 500 °C; at 1000 °C, mild sintering was found to occur. While this resulted in the fusing of individual particles within each sample, the distinct morphological features of each of the Ranger, Olympic Dam and Beverley UOCs were found to still be identifiable.

In Chapter 5, eight UOCs and four uranium ore samples from Beverley, Ranger, Olympic Dam and Mary Kathleen were analysed by MC-ICP-MS for their $^{235}\text{U}/^{238}\text{U}$ and $^{234}\text{U}/^{238}\text{U}$ isotope ratios. In addition to the UOC and uranium ore samples, four non-certified natural U_3O_8 standards were analysed as a quality control check. When the uncertainty is represented as expanded uncertainty ($k=2$), poor agreement was found between these four standards and the results of similar standards analysed by Brown *et al.* (2014) against the consensus value, as single-factor ANOVA on the samples returned a p-value of 0.0078. Good agreement was however found between the replicate analyses of this study and Brown *et al.* (2014) for the $^{234}\text{U}/^{238}\text{U}$ isotope ratio, with a single-factor ANOVA test reported a p-value of 0.061. Examination of the expanded uncertainty budget for the four non-certified natural U_3O_8 standards however demonstrated the counting of ^{235}U and ^{238}U isotopes for the $^{235}\text{U}/^{238}\text{U}$ contributed 49.18% each (98.36% in total, whereas ^{234}U and ^{238}U contributed 61.11% and 18.20% (89.31% in total), respectively, to the expanded uncertainty of the measured isotope ratios.

On advice from our collaborators from MURR who analysed the samples, the $^{235}\text{U}/^{238}\text{U}$ and $^{234}\text{U}/^{238}\text{U}$ isotopes ratios measured within the Beverley, Ranger, Olympic Dam and Mary Kathleen UOC and uranium ore samples were reexamined, with their respective uncertainties instead represented by standard deviation. It was found that the only sample distinguishable from the others analysed was the uranium ore sample from Mary Kathleen, however the validity of this is questionable given the anomalous isotope ratio values measured within the sample and no ability at that time to reanalyze a second sample. A comparison between the Australian UOC and uranium ore samples with other UOC and uranium ore samples from the corresponding source with respect to their $^{235}\text{U}/^{238}\text{U}$ and $^{234}\text{U}/^{238}\text{U}$ was also performed. For the $^{235}\text{U}/^{238}\text{U}$ isotope ratio, all of the UOCs

and uranium ore samples from Beverley, Ranger and Olympic Dam agreed with values reported from the same sources within the literature, whereas Olympic Dam was the only mine to agree with respect to the $^{234}\text{U}/^{238}\text{U}$ isotope ratio. Two of the four samples from Ranger (Ranger UOC 1 & 3) were found to agree with both comparison values from the literature, whereas the four samples from Beverley were found to have $^{234}\text{U}/^{238}\text{U}$. Due to the considerably questionable $^{235}\text{U}/^{238}\text{U}$ and $^{234}\text{U}/^{238}\text{U}$ isotope ratios measured within the twelve uranium ore samples from Beverley, Ranger, Olympic Dam and Mary Kathleen, reanalysis using a reliable, robust MC-ICP-MS method is required to examine the intra-mine variability of $^{235}\text{U}/^{238}\text{U}$ and $^{234}\text{U}/^{238}\text{U}$ isotope ratios.

In Chapter 6, the efficacy of k_0 -NAA towards the analysis of REE and trace elements within uranium ores for nuclear forensics provenancing was investigated through the analysis of seventeen Australian and North American uranium ore samples and 4 OREAS reference standards. Prior to their analysis by k_0 -NAA, the uranium ore samples were analysed by pXRF, SEM/EDX and DNAA in order to determine their uranium content, which would impact the masses of each sample analysed by k_0 -NAA. While pXRF and SEM/EDX were found to produce poor results with regards to their measurement of the uranium concentrations within the ore samples, DNAA was able to provide a far more accurate measurement. As the concentration of uranium within the Ike-Nixon Shaft was so high, a modified DNAA method developed by Anvia *et al.* (2016) was used to correct for non-linearity during the detection of delayed neutrons.

Analysis of the four OREAS uranium ore standards revealed that the measurement of REEs within samples with relatively low concentrations (40-1794 ppm U) of uranium problematic, due to the production of fission product interferences from the fission of ^{235}U . This resulted in several REEs being unable to be measured, as well as impacting the measurement of the REEs (for example holmium) that were measureable. The impact on the measurement of REEs was proportional to the concentration of uranium within the OREAS standards; i.e. OREAS 100a and 120 with lower uranium concentrations (40 and 135 ppm U) were less affected than OREAS 106 and 124 (1143 and 1794 ppm U). In the measurement of the REEs within the Australian and North American uranium ore samples, the Australian samples typically had more REEs measured, likely due to the lower uranium concentrations relative to the North American samples. Amongst the Australian uranium ore samples, good agreement was found between the uranium ores analysed by k_0 -NAA and chondrite-normalised REE patterns of other uranium ores and UOCs from the same mine from the literature. The only significant departure from this was the Ranger uranium ore sample, which had a different pattern to a Ranger UOC sample (Keegan *et al.* (2008)); however, a second study analysing

several uranium ore samples throughout the Ranger deposits found the chondrite-normalised REE pattern changes according to the uranium concentration (Fisher et al. (2013)). While the mechanism underpinning the variable chondrite-normalised REE pattern is not known, this result does impact the interpretation of chondrite-normalised REE patterns and their use in provenancing unknown UOCs as there is now evidence the pattern can significantly change throughout a deposit(s). The North American uranium ore samples had fewer REEs reported, which made comparisons and interpretations impossible to perform.

From the results of this study, the application of k_0 -NAA for the analysis of REEs within uranium ores for provenancing in nuclear forensics is not recommended, as the technique appears to be inferior to ICP-MS, notwithstanding its own issues concerning interferences and sample preparation. DNAA, however, appears to be highly valuable as an accurate and expedient means of determining the concentration of uranium within uranium-rich matrices, such as uranium ores and UOCs, with next-to-no sample preparation required. A major obvious disadvantage, which will prevent DNAA from being used routinely, is access to a facility capable of performing such measurements.

Of the different areas of research investigated in this thesis, TGA and SEM/EDX analysis of the morphology appear to be the most promising areas to further the materials provenancing capabilities of nuclear forensics. While further research is required to resolve the aforementioned inconsistencies experienced in this thesis with TGA, it may potentially prove to be a valuable technique in the examination of unknown UOCs.

Appendix A Comparison of Uranium Isotope Ratios Measured Within Australian UOCs and Uranium Ores with Literature Ratios

8.1 Analysis of several Australian UOCs and uranium ore samples by MC-ICP-MS

8.1.1 Beverley UOC and uranium ore samples

The three UOCs and single ore samples from Beverley were found to feature consistent $^{235}\text{U}/^{238}\text{U}$ ratios (Figure 133 **Error! Reference source not found.**), however a single-factor ANOVA across all seven samples reported a p-value of 0.36, which is greater than the alpha-value of 0.05, indicating that there is not a significant difference between the means. All of the replicate results from the Beverley UOCs appear to suggest the samples are homogenous, despite no sample homogenisation procedure being implemented, such as milling or grinding, during any of the sample preparation stages. As the chemical processes used to process uranium ore into UOC do not fractionate the $^{235}\text{U}/^{238}\text{U}$ uranium isotope ratio of the ore [231], the measured $^{235}\text{U}/^{238}\text{U}$ isotope ratios of the Beverley UOC samples can be considered representative of the original ore processed. All six E_n scores were found to be < 1 , finding each UOC and ore samples from Beverley in agreement with respect to $^{235}\text{U}/^{238}\text{U}$ and $^{234}\text{U}/^{238}\text{U}$ ratios.

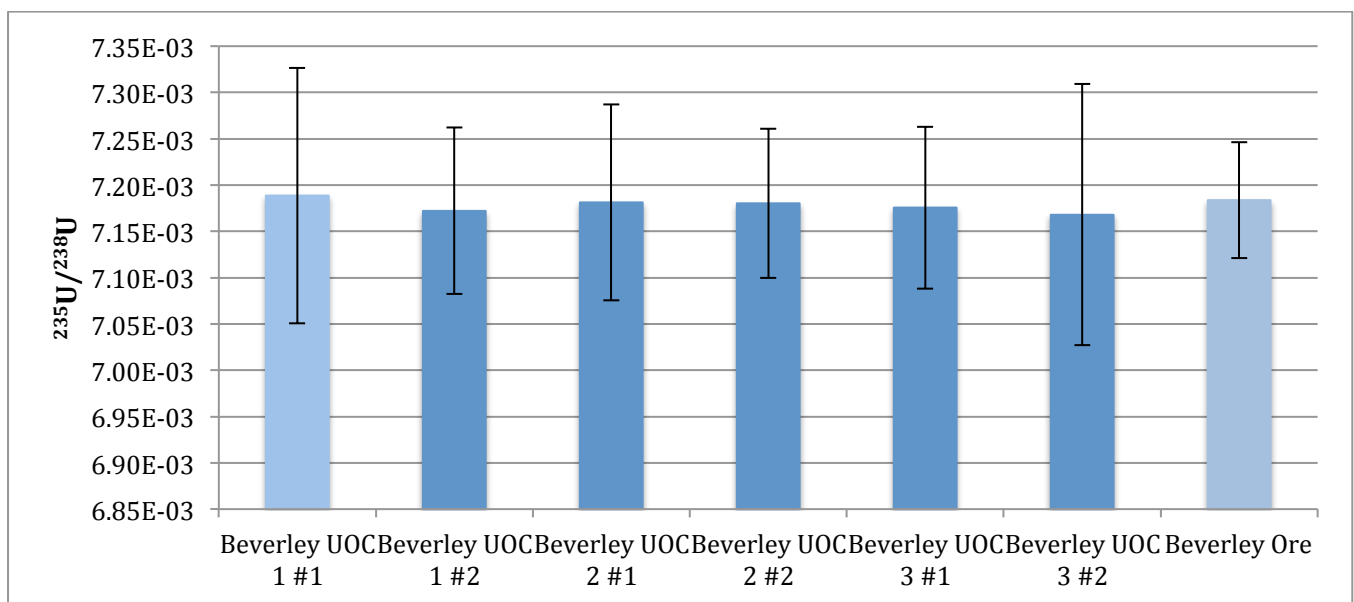


Figure 133 Replicate analyses of the $^{235}\text{U}/^{238}\text{U}$ isotope ratios of Beverley UOCs 1-3 and Beverley Ore analysed by MC-ICP-MS (error bars = expanded uncertainty (k=2))

The $^{234}\text{U}/^{238}\text{U}$ isotope ratios reveal some variability within the Beverley UOC samples, as the mean of both Beverley 1 UOC subsamples have a lower $^{234}\text{U}/^{238}\text{U}$ ratio than the other two Beverley UOC

samples and the Beverley ore (Figure 134 **Error! Reference source not found.**). However, due to their expansive error bars, the difference between Beverley 1 UOC and the other UOC samples from Beverley is likely to not be of any significance.

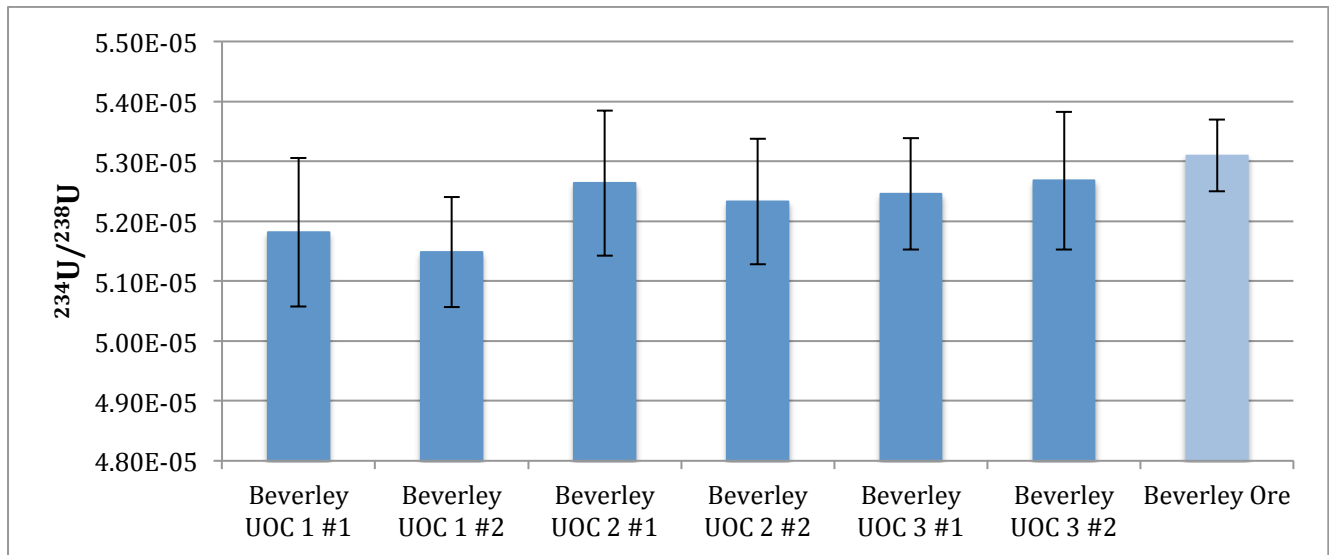


Figure 134 Replicate analyses of the $^{234}\text{U}/^{238}\text{U}$ isotope ratios of Beverley UOCs 1-3 and Beverley Ore analysed by MC-ICP-MS (error bars = expanded uncertainty (k=2))

8.1.2 Ranger UOC and uranium ore samples

The UOC and uranium ore samples from Ranger were found to feature indistinguishable $^{235}\text{U}/^{238}\text{U}$ isotope ratios, with large expanded uncertainties (Figure 135 **Error! Reference source not found.**). With respect to the $^{234}\text{U}/^{238}\text{U}$ ratios, a greater variation was observed in the mean values however; their large associated expanded uncertainties make it difficult to identify any differences amongst the samples from Ranger (Figure 136). All six E_n scores were found to be < 1 , finding the each UOC and ore samples from Ranger in agreement with respect to $^{235}\text{U}/^{238}\text{U}$ and $^{234}\text{U}/^{238}\text{U}$ ratios.

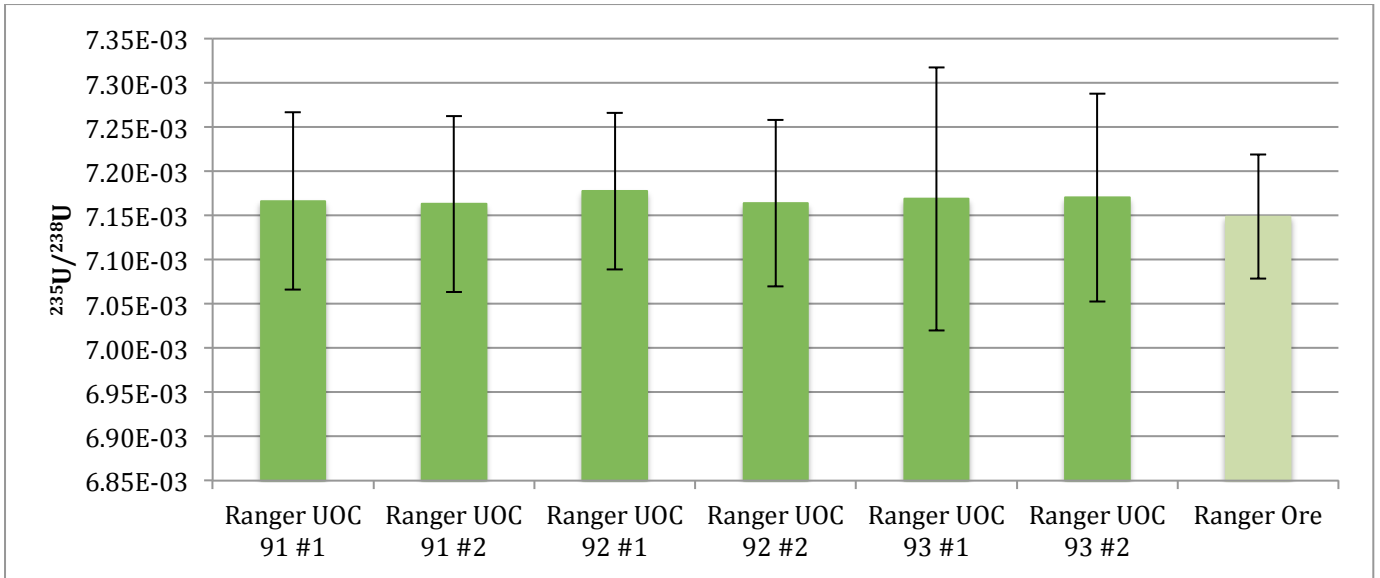


Figure 135 Replicate analyses of the $^{235}\text{U}/^{238}\text{U}$ isotope ratios of Ranger UOC 1-3 and Ranger Ore analysed by MC-ICP-MS (error bars = expanded uncertainty (k=2))

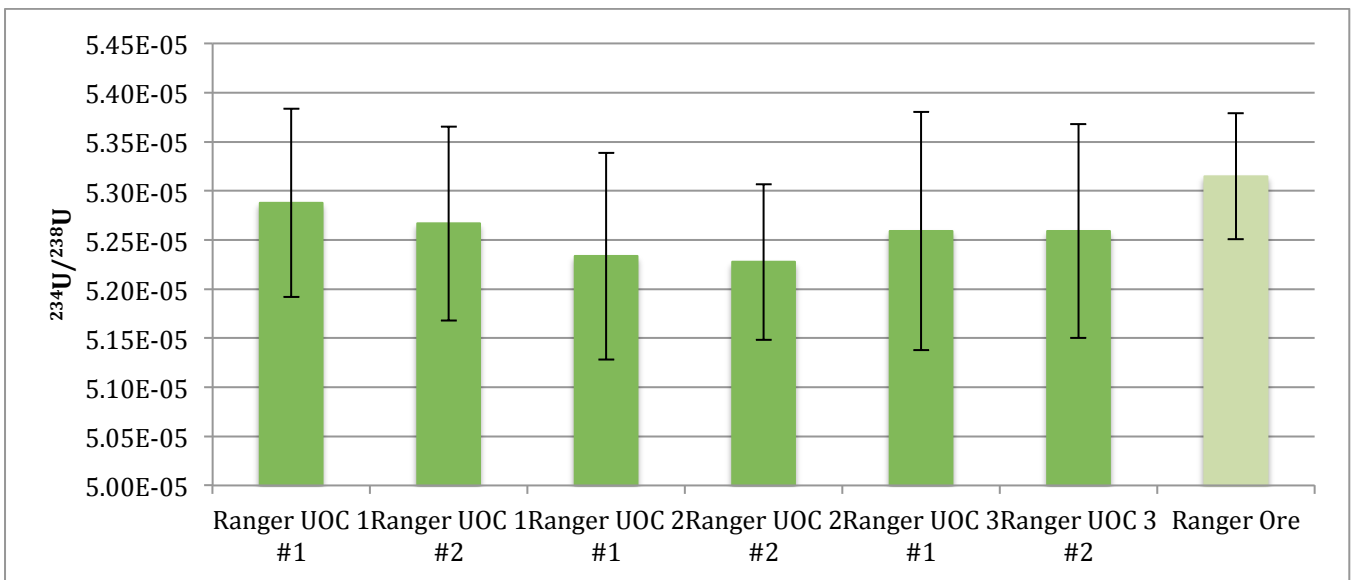


Figure 136 Replicate analyses of the $^{234}\text{U}/^{238}\text{U}$ isotope ratios of Ranger UOCs 1-3 and Ranger Ore analysed by MC-ICP-MS (error bars = expanded uncertainty (k=2))

8.1.3 Olympic Dam UOC and uranium ore samples

Similar to the Beverly and Ranger samples previous, little variation is seen between the UOC and uranium ore samples from Olympic Dam due to their expansive expanded uncertainties in both the $^{235}\text{U}/^{238}\text{U}$ and $^{234}\text{U}/^{238}\text{U}$ ratios (Figure 137 & Figure 138, respectively). All three E_n scores were found to be < 1 , finding each UOC and ore samples from Olympic Dam in agreement with respect to $^{235}\text{U}/^{238}\text{U}$ and $^{234}\text{U}/^{238}\text{U}$ ratios.

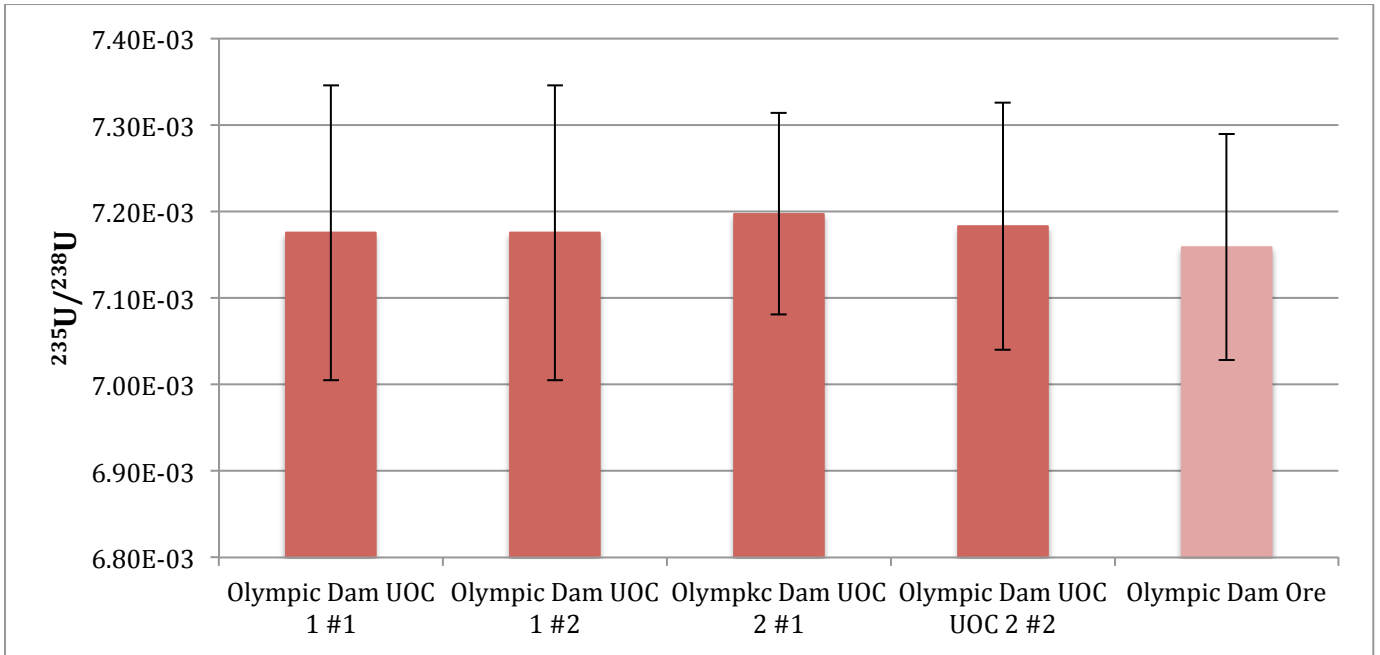


Figure 137 Replicate analyses of the $^{235}\text{U}/^{238}\text{U}$ isotope ratios of Olympic Dam UOCs 1&2 and Olympic Dam Ore analysed by MC-ICP-MS (error bars = expanded uncertainty (k=2))

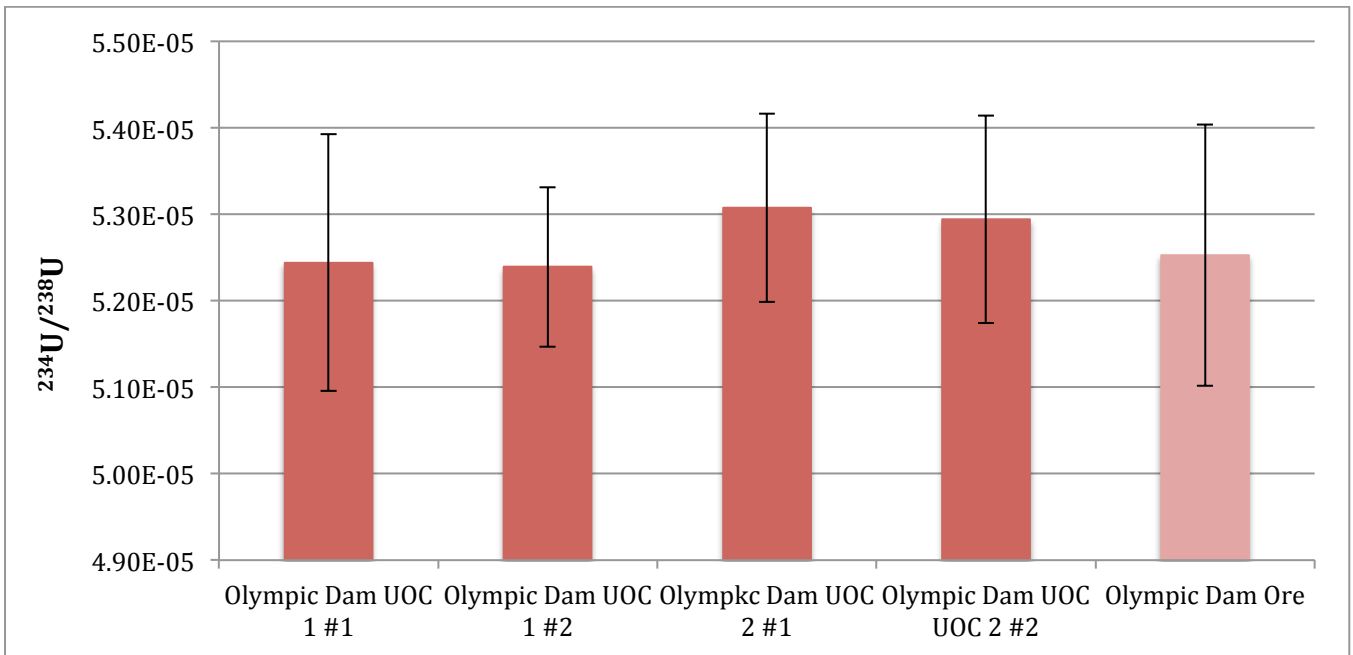


Figure 138 Replicate analyses of the $^{234}\text{U}/^{238}\text{U}$ isotope ratios of Olympic Dam UOCs 1&2 and Olympic Dam Ore analysed by MC-ICP-MS (error bars = expanded uncertainty (k=2))

8.1.4 Mary Kathleen ore sample

The Mary Kathleen ore sample featured the highest $^{235}\text{U}/^{238}\text{U}$ ratio of all of the Australian UOC and uranium ore samples analysed, and far exceeding other $^{235}\text{U}/^{238}\text{U}$ ratios reported from the mine

(Figure 139 **Error! Reference source not found.**) [103]. A previous study found that incomplete leaching with nitric acid has shown not to impact the $^{235}\text{U}/^{238}\text{U}$ isotope ratio of uraninite [233], but the lack of a replicate analysis for this sample in addition to its significant departure from the natural $^{235}\text{U}/^{238}\text{U}$ ratio ($\sim 7.2 \times 10^{-3}$) raises some questions in regards to the result.

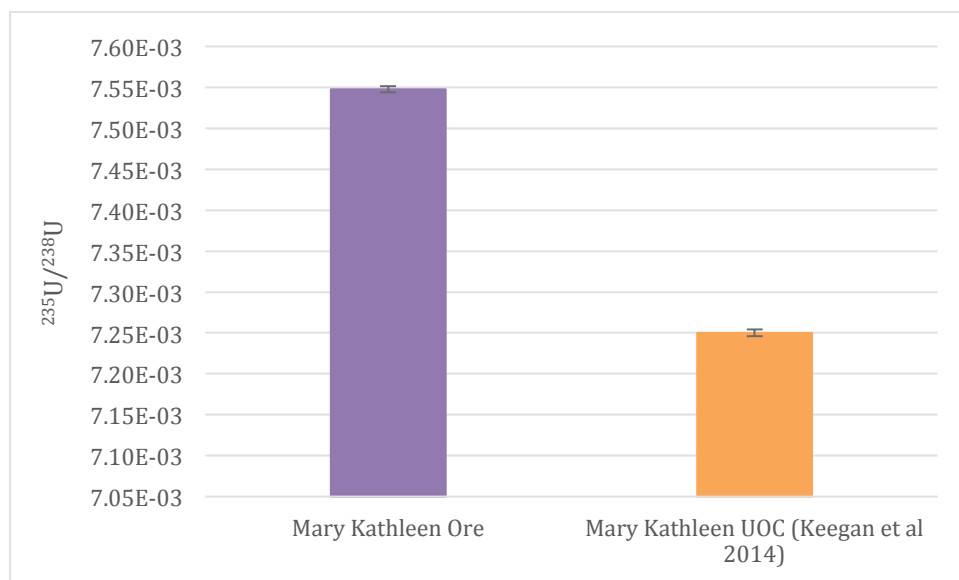


Figure 139 Comparison between the $^{235}\text{U}/^{238}\text{U}$ isotope ratio of a Mary Kathleen uranium ore samples analysed by MC-ICP-MS (error bars = 1σ) and a literature value of a UOC from Mary Kathleen analysed by Keegan *et al.* (2014) [103].

8.1.5 Comparison between all Australian UOC and uranium ore samples

Amongst all of the UOC and uranium ore samples analysed as part of this study, the only sample that could be thought of as distinguishable is the Mary Kathleen uranium ore sample with respect to the $^{235}\text{U}/^{238}\text{U}$ ratio (Figure 140). However, a single-factor ANOVA test determined the p-value to be 1.02×10^{-9} , which is smaller than the alpha value of 0.05, indicating that there is a significant difference between all of the samples analysed based upon their $^{235}\text{U}/^{238}\text{U}$ ratio. Similarly, the p-value from the single-factor ANOVA performed on the $^{234}\text{U}/^{238}\text{U}$ ratios of all of the UOC and uranium ore samples in this study (Figure 141) was determined to be 3.35×10^{-8} , which is also smaller than the alpha value of 0.05, indicating there is a significant difference between the samples. When plotted $^{234}\text{U}/^{238}\text{U}$ vs $^{235}\text{U}/^{238}\text{U}$, the majority of UOC and uranium ore samples are clustered together, with the exception of the Mary Kathleen UOC, with no point of differentiation (Figure 142).

A smaller expanded uncertainty is observed in the uranium ore samples when compared to the UOC samples from the same source; however, this is likely caused by the propagation of uncertainty when averaging the value and the expanded uncertainty from the duplicate measurements of the UOC

samples. Due to issues digesting the uranium ore samples, only one sample for each source was analysed, and therefore didn't have to average values and expanded uncertainties from more than one measurement.

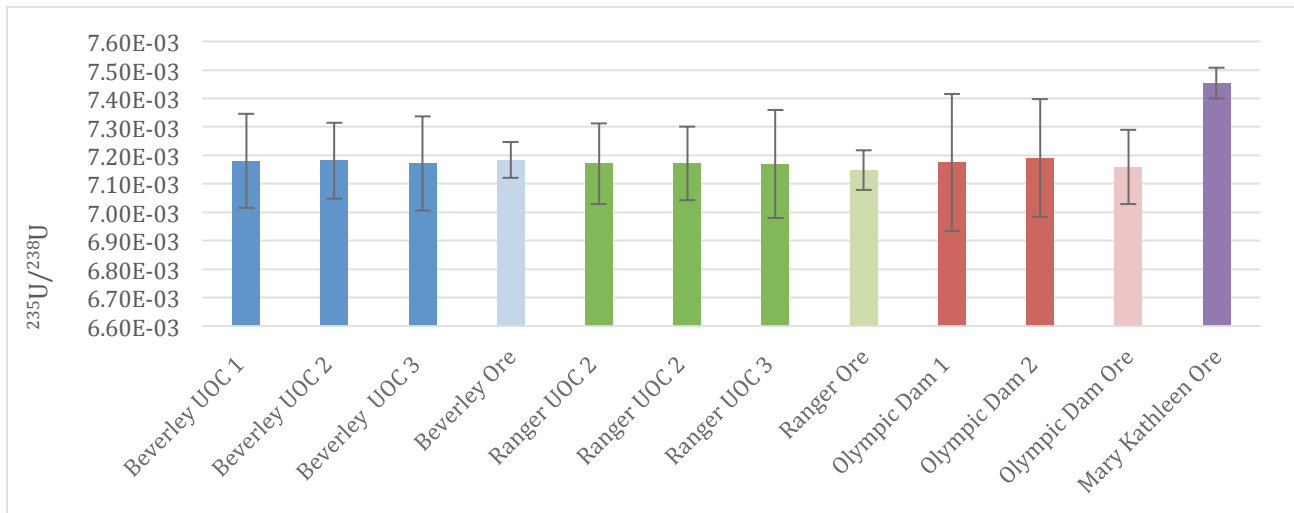


Figure 140 Average $^{235}\text{U}/^{238}\text{U}$ isotope ratios of Beverley, Ranger, Olympic Dam and Mary Kathleen UOC and uranium ore samples analysed by MC-ICP-MS (error bars = expanded uncertainty (k=2)).

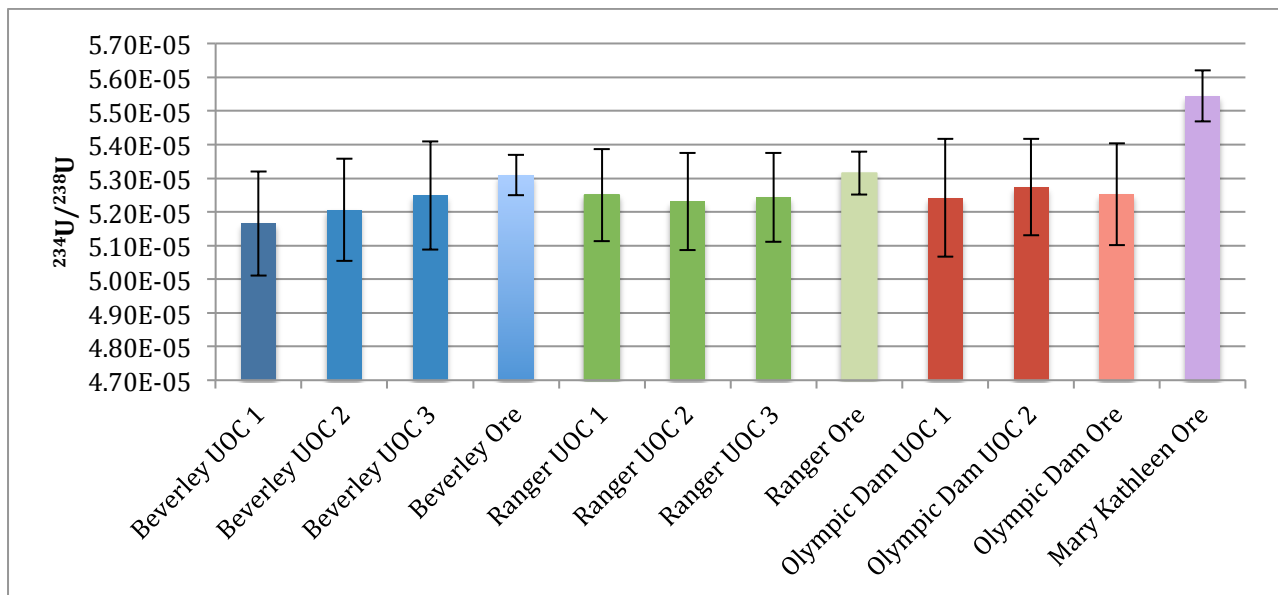


Figure 141 Average $^{234}\text{U}/^{238}\text{U}$ isotope ratios of Beverley, Ranger, Olympic Dam and Mary Kathleen UOC and uranium ore samples analysed by MC-ICP-MS (error bars=expanded uncertainty (k=2)).

The indistinguishable nature of the measured $^{235}\text{U}/^{238}\text{U}$ and $^{234}\text{U}/^{238}\text{U}$ ratios within Australian UOC and uranium ore samples with the exception of the Mary Kathleen uranium ore samples, when plotted two-dimensionally (Figure 142 **Error! Reference source not found.**). The large errors bars,

representing the expanded uncertainty (k=2) make it impossible to identify any clusters or trends within the uranium isotope data.

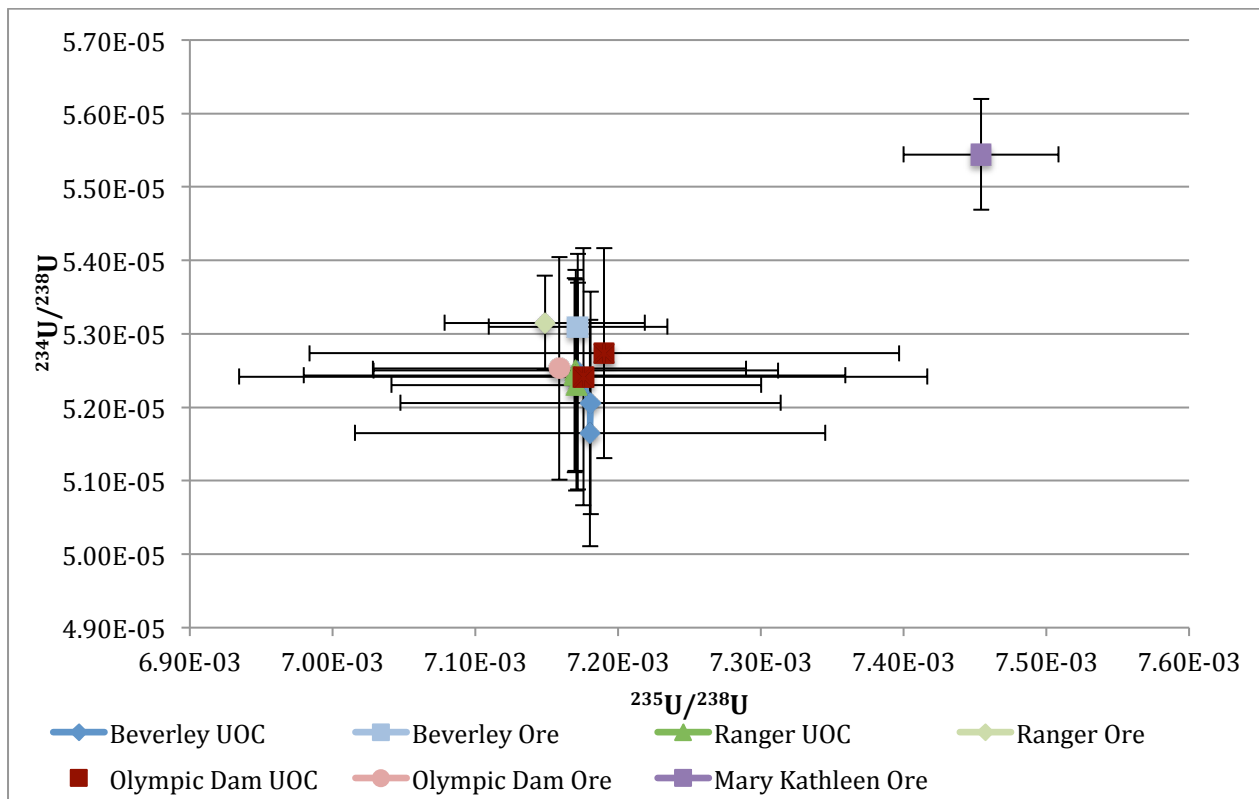


Figure 142 Average $^{234}\text{U}/^{238}\text{U}$ vs $^{235}\text{U}/^{238}\text{U}$ comparison between Beverley, Ranger, Olympic Dam and Mary Kathleen UOC and uranium ore samples (error bars = expanded uncertainty (k=2))

Similar results are observed in the comparison between the Australian UOC and uranium ore samples where the uncertainty in the $^{235}\text{U}/^{238}\text{U}$ isotope ratios is represented as standard deviation, where the most noticeable difference is the Mary Kathleen uranium ore sample as an outlier (Figure 143 **Error! Reference source not found.**). For the remainder of the dataset, the majority of the Australian UOC and uranium ore samples are indistinguishable from one another due to their overlapping error bars, with the exception of the Ranger U ore sample. The within-group variability of typically consistent with the Beverley and Ranger UOC samples featuring similar $^{235}\text{U}/^{238}\text{U}$ isotope ratios, however the Olympic Dam UOC 1 & 2 samples are significantly different from one another. Of the three sources, Beverley was found to have the most consistent $^{235}\text{U}/^{238}\text{U}$ isotope ratios across both the UOC and uranium ore samples; Ranger was found to feature a considerable discrepancy between the $^{235}\text{U}/^{238}\text{U}$ isotope ratios of the UOCs and uranium ore sample, whilst Olympic Dam UOC 1 and Olympic Dam U ore were similar with Olympic Dam UOC 2 being the outlier of the three samples.

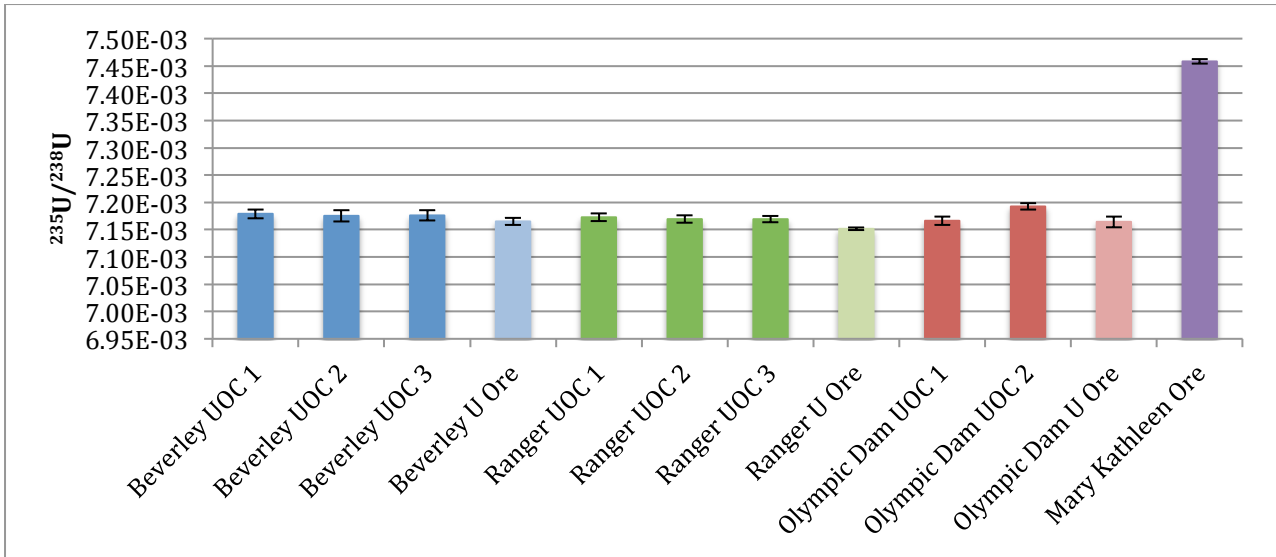


Figure 143 Average $^{235}\text{U}/^{238}\text{U}$ isotope ratios of Beverley, Ranger, and Olympic Dam and Mary Kathleen UOC and uranium ore samples analysed by MC-ICP-MS (error bars = standard deviation).

There appears to be no apparent pattern or trend of significance amongst the $^{234}\text{U}/^{238}\text{U}$ isotope ratios measured in the Australian UOC and uranium ore samples, with the exception again being the much larger $^{234}\text{U}/^{238}\text{U}$ isotope ratio for the Mary Kathleen ore sample (Figure 144 **Error! Reference source not found.**). Of the remaining sources, all Beverley and Ranger exhibit a considerable degree of intra-mine variability with Beverley UOC 1 and Ranger U ore featuring $^{234}\text{U}/^{238}\text{U}$ isotope ratios that are significantly different from the other samples from the same mine.

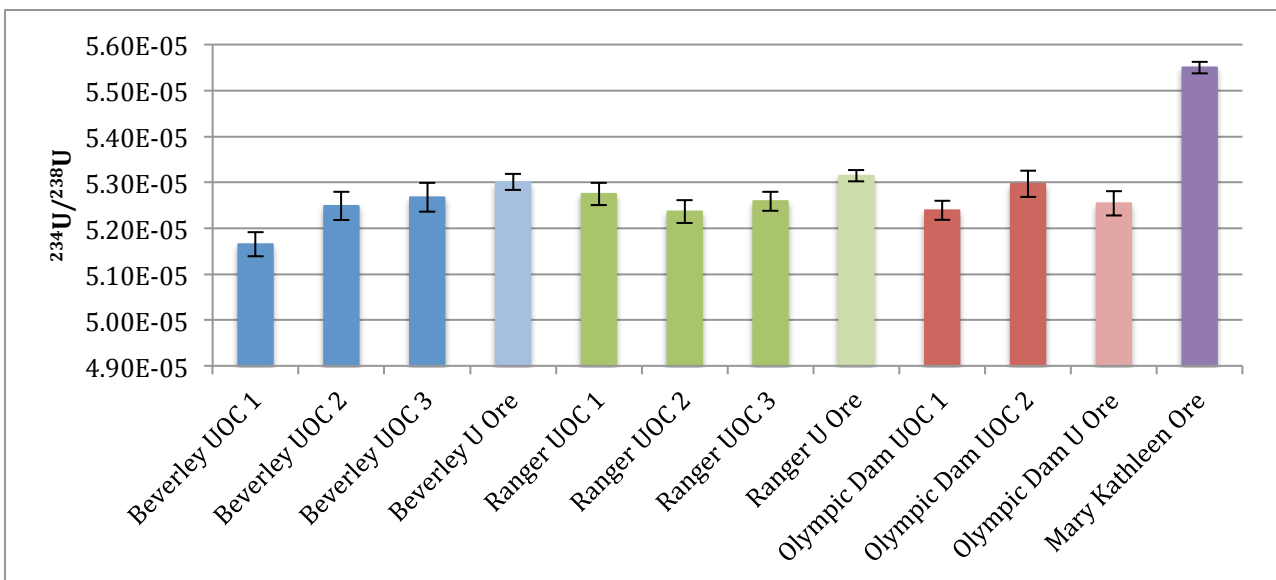


Figure 144 Average $^{234}\text{U}/^{238}\text{U}$ isotope ratios of Beverley, Ranger, and Olympic Dam and Mary Kathleen UOC and uranium ore samples analysed by MC-ICP-MS (error bars = standard deviation).

A large cluster with the majority of samples is observed within a two-dimension $^{234}\text{U}/^{238}\text{U}$ versus $^{235}\text{U}/^{238}\text{U}$ ratios plot, featuring all of the samples with the exception of the Mary Kathleen ore outlier (Figure 145 **Error! Reference source not found.**). The only difference, however, is the presence of 2-3 satellite samples that can be distinguished from the central cluster, but are inconsistent with respect to their source as well as the means they differ from the other samples. The Beverley UOC sample is the satellite sample furthest from the main cluster, and is separated purely on the basis of its low $^{234}\text{U}/^{238}\text{U}$ ratio. The other two satellite samples identified, Ranger Ore and Olympic Dam UOC, vary according to their relatively low and high $^{235}\text{U}/^{238}\text{U}$ isotope ratios.

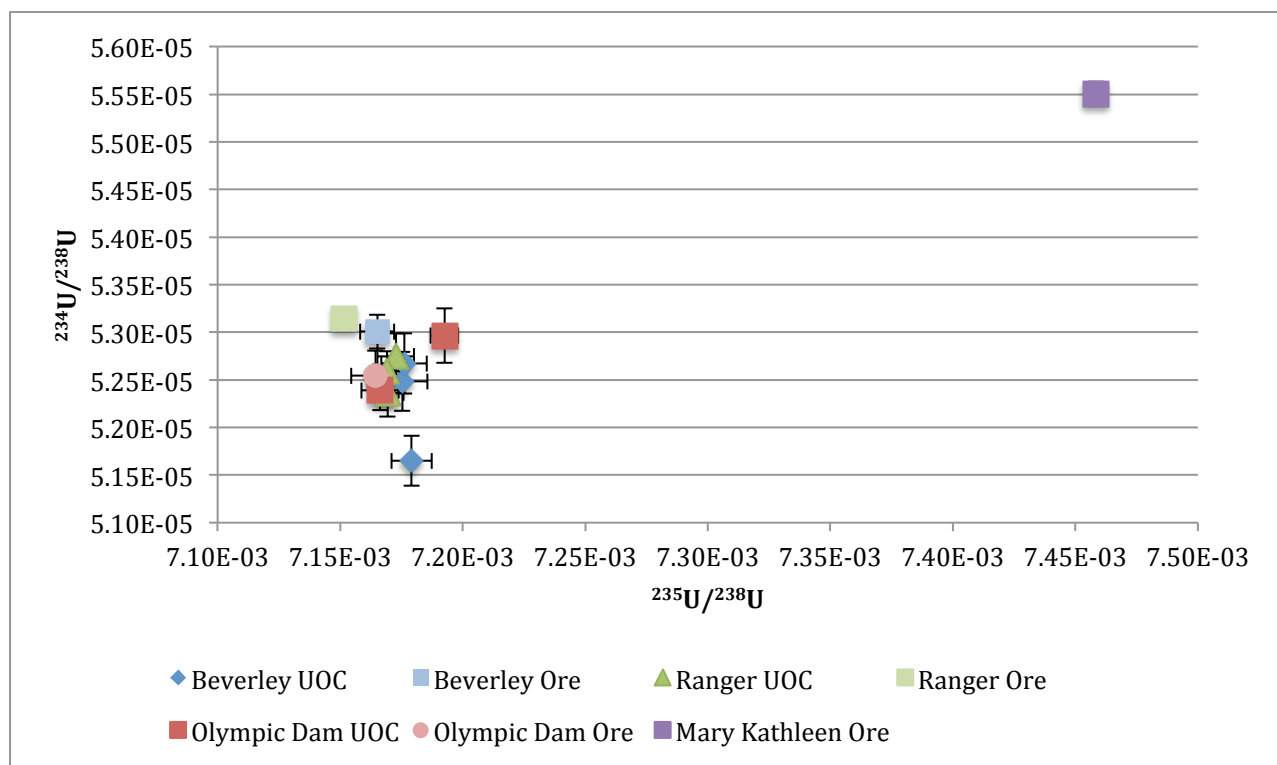


Figure 145 Average $^{234}\text{U}/^{238}\text{U}$ vs $^{235}\text{U}/^{238}\text{U}$ comparison between Beverley, Ranger, Olympic Dam and Mary Kathleen UOC and uranium ore samples (error bars = standard deviation).

8.2 Comparison with other UOC and uranium ore samples reported in the literature

The Beverley UOC samples measured as part of this study was compared to a UOC sample analysed by Keegan *et al.* (2008), which analysed the $^{235}\text{U}/^{238}\text{U}$ and $^{234}\text{U}/^{238}\text{U}$ isotope ratios using a double-spike thermal ionization mass spectrometry (TIMS) method [257]. Again, due to the large overlapping associated expanded uncertainties, the UOC samples from this study were unable to be distinguished from the UOC sample analysed by Keegan *et al.* (2008) on the basis of the $^{235}\text{U}/^{238}\text{U}$ isotope ratio [39], however what is immediate when comparing to two studies is the significant difference in the precision of the TIMS analysis (Figure 146 **Error! Reference source not found.**).

A significantly greater isotope ratio was however observed between the Beverley UOC and uranium samples from this study and the UOC sample from Keegan *et al.* (2008) for the $^{234}\text{U}/^{238}\text{U}$ isotope ratio (Figure 147**Error! Reference source not found.**).

Interestingly, a smaller expanded uncertainty was observed for the uranium ore samples when compared to the UOC samples from the same source. Due to issues digesting the uranium ore samples, only one sample for each source was analysed, rather than two for the UOC samples. Consequently, we didn't have to average the values and expanded uncertainties from more than one measurement. This likely caused the expanded uncertainties from the duplicate UOC sample measurements to be larger as they also contain an evaluation of the sample variability that is not available for the ore samples.

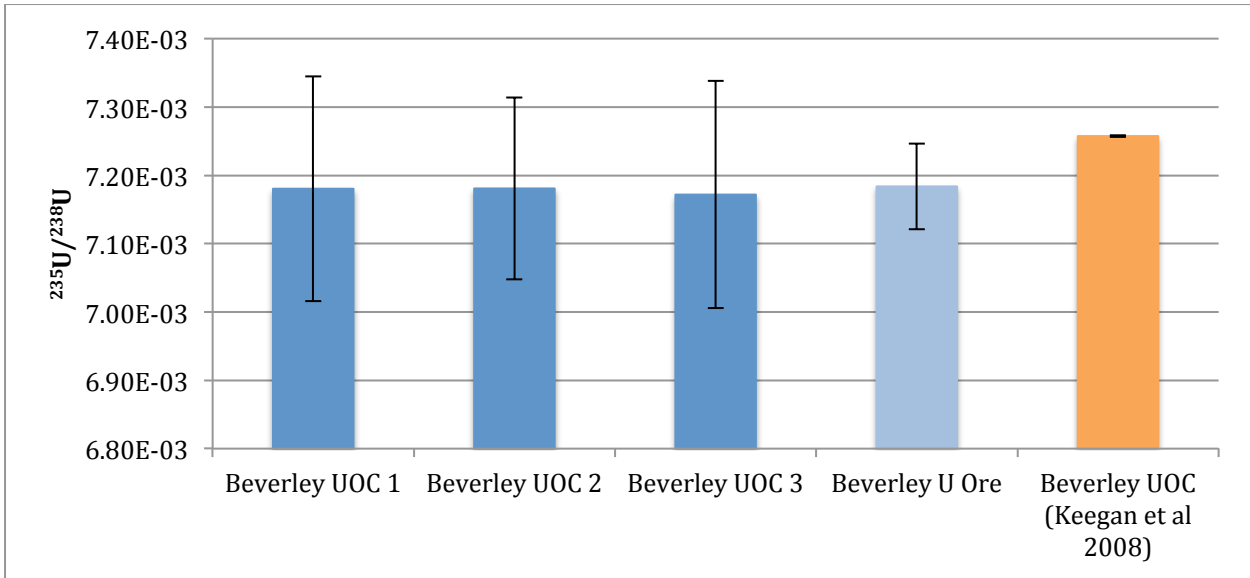


Figure 146 Comparison of measured $^{235}\text{U}/^{238}\text{U}$ isotope ratios from uranium ore and UOCs samples originating from Beverley and a UOC sample from Beverley previously analysed by Keegan *et al.* (2008) [39]. Error bars = Expanded uncertainty (k=2)

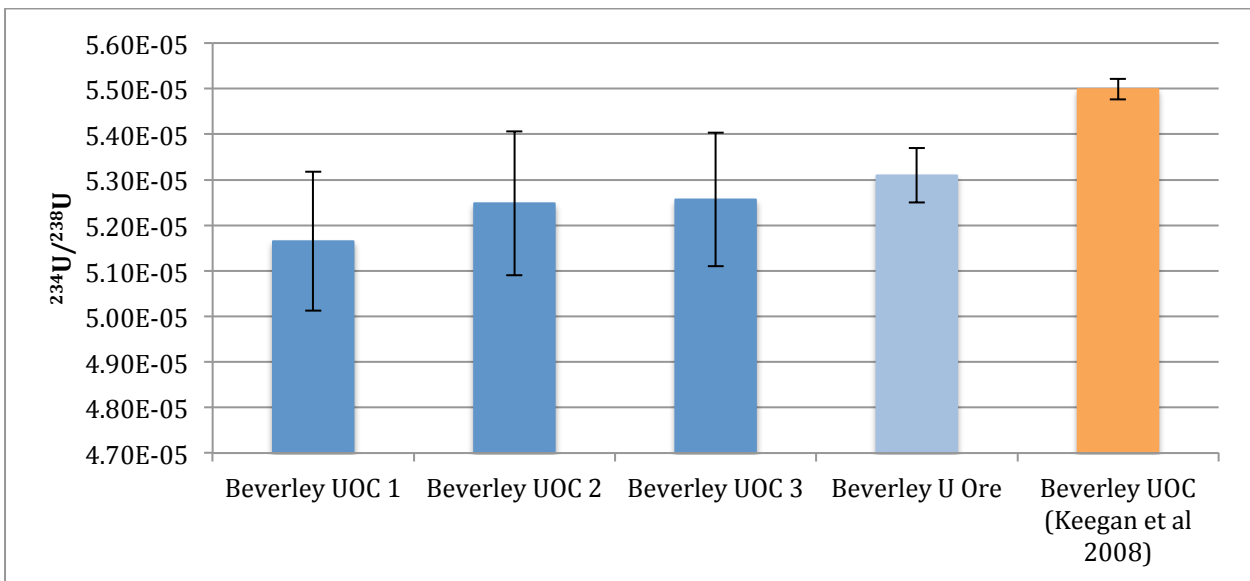


Figure 147 Comparison of measured $^{234}\text{U}/^{238}\text{U}$ isotope ratios from uranium ore and UOCs samples originating from Beverley and a UOC sample from Beverley previously analysed by Keegan *et al.* (2008) [39]. Error bars = Expanded uncertainty (k=2)

The measured $^{235}\text{U}/^{238}\text{U}$ isotope ratios for the UOC and uranium ore samples from Ranger somewhat agree with ratios of Ranger UOC and uranium ore samples reported in the literature ([39, 232]), cognizant of the uncertainty surrounding the accuracy and precision during the analysis of the Ranger samples analysed within this study due to aforementioned calibration issues (Figure 148). There is, however, a considerable difference between the precision achieved in this study and the

precision reported by the other two studies, with the uncertainty associated with the reported $^{235}\text{U}/^{238}\text{U}$ isotope ratios for the Ranger UOC and uranium ore samples from literature are significantly smaller than the uncertainties associated with the Ranger samples analysed in this study.

The $^{234}\text{U}/^{238}\text{U}$ isotope ratio comparison also featured a reasonable agreement between the four Ranger samples analysed in this study and the Ranger UOC sample analysed by Keegan *et al.* (2008) (Figure 149**Error! Reference source not found.**) [39]. The Ranger ore sample analysed by Richter *et al.* (1999) ($5.444 \times 10^{-5} \pm 0.048 \times 10^{-5}$) only agreed with two of the four Ranger samples analysed in this study (Ranger UOC 1 & 3), but importantly disagreed with the UOC sample from Keegan *et al.* (2008) ($5.3687 \times 10^{-5} \pm 0.0023 \times 10^{-5}$) [39, 232]. While these results indicate that some variability existed within the $^{234}\text{U}/^{238}\text{U}$ isotope ratios from UOCs and uranium ores sourced from Ranger, reanalysis of the Ranger samples analysed in this study is needed to better evaluate the magnitude of the variability.

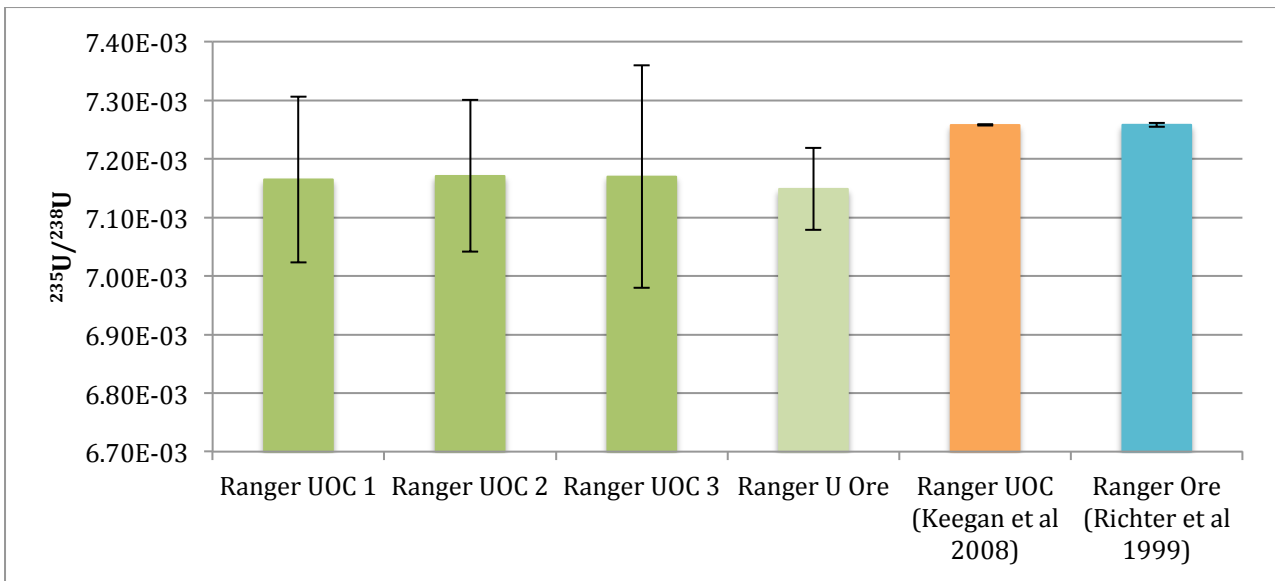


Figure 148 Comparison of measured $^{235}\text{U}/^{238}\text{U}$ isotope ratios from uranium ore and UOCs samples originating from Ranger and a UOC and uranium ore sample from Ranger previously analysed by Keegan *et al.* (2008) and Richter *et al.* (1999), respectively. Error bars = Expanded uncertainty (k=2)

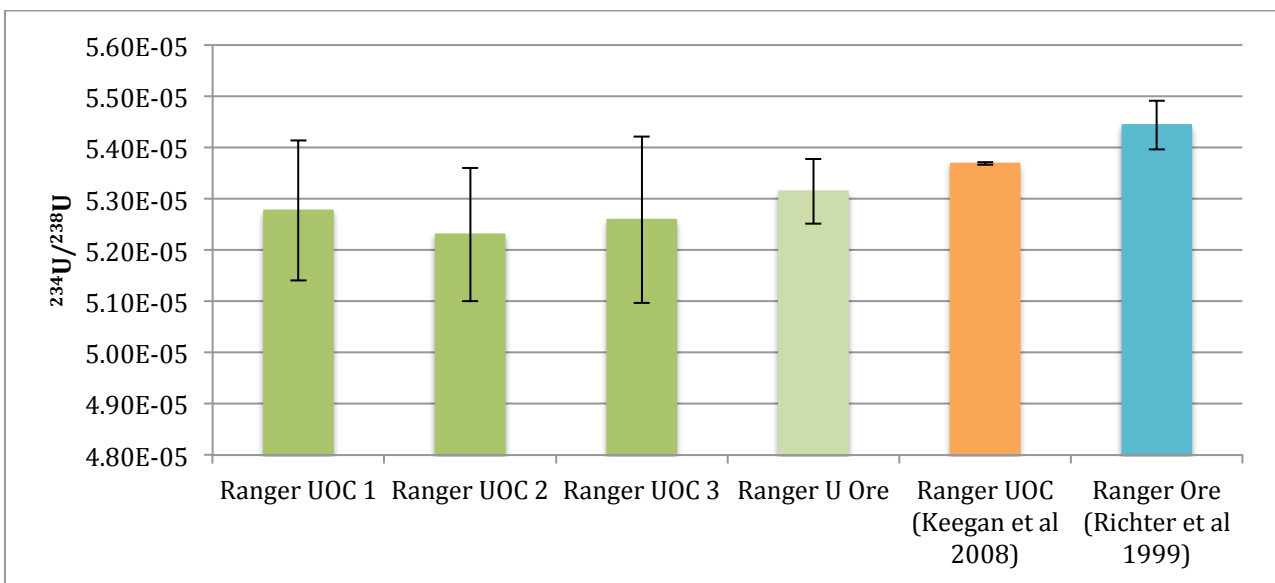


Figure 149 Comparison of measured $^{234}\text{U}/^{238}\text{U}$ isotope ratios from uranium ore and UOCs samples originating from Ranger and a UOC and uranium ore sample from Ranger previously analysed by Keegan *et al.* (2008) and Richter *et al.* (1999), respectively. Error bars = Expanded uncertainty (k=2)

The UOC and uranium ore samples from Olympic Dam analysed in this study agree with the $^{235}\text{U}/^{238}\text{U}$ isotope ratios of other UOC and uranium ore samples previously reported in the literature ([39, 232]) (Figure 150Error! Reference source not found.). The difference between the magnitude of the uncertainty from the samples analysed in this study and the other studies reported

in the literature from Olympic Dam are consistent with the other comparisons previously made, with the results of our study featuring considerably greater uncertainties. Similarly, there appears to be agreement between the Olympic Dam samples of this study and the Olympic Dam UOC and uranium ore samples from literature with respect to the $^{235}\text{U}/^{238}\text{U}$ isotope ratio (Figure 151 **Error! Reference source not found.**).

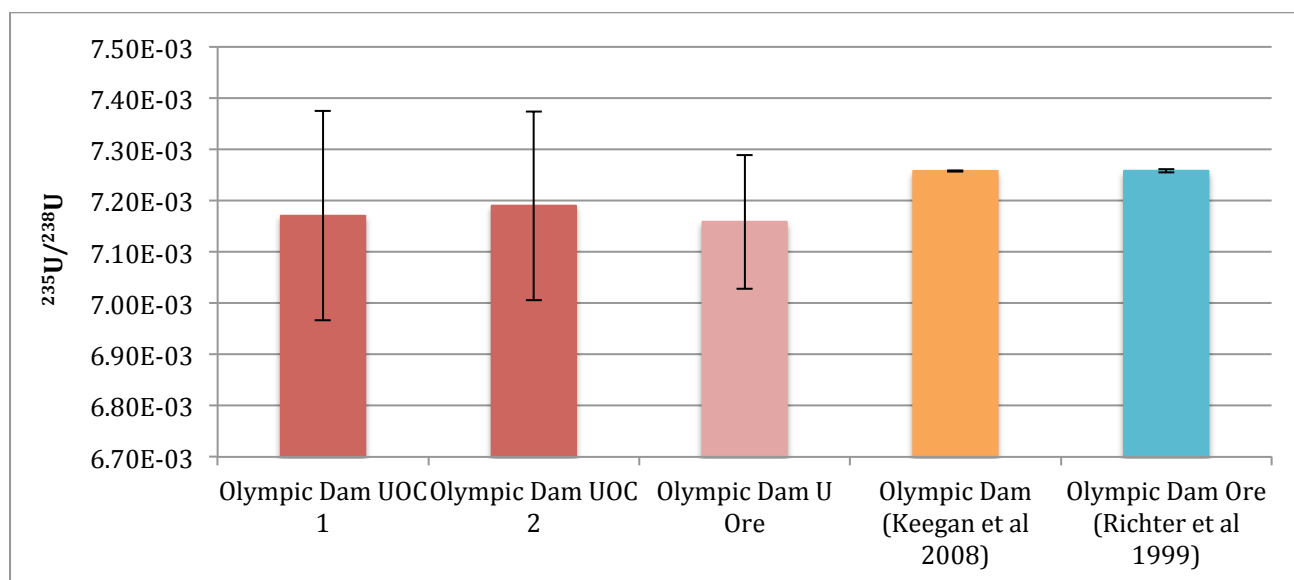


Figure 150 Comparison of measured $^{235}\text{U}/^{238}\text{U}$ isotope ratios from uranium ore and UOCs samples originating from Olympic Dam and a UOC and uranium ore sample from Olympic Dam previously analysed by Keegan *et al.* (2008) and Richter *et al.* (1999), respectively. Error bars = Expanded uncertainty (k=2)

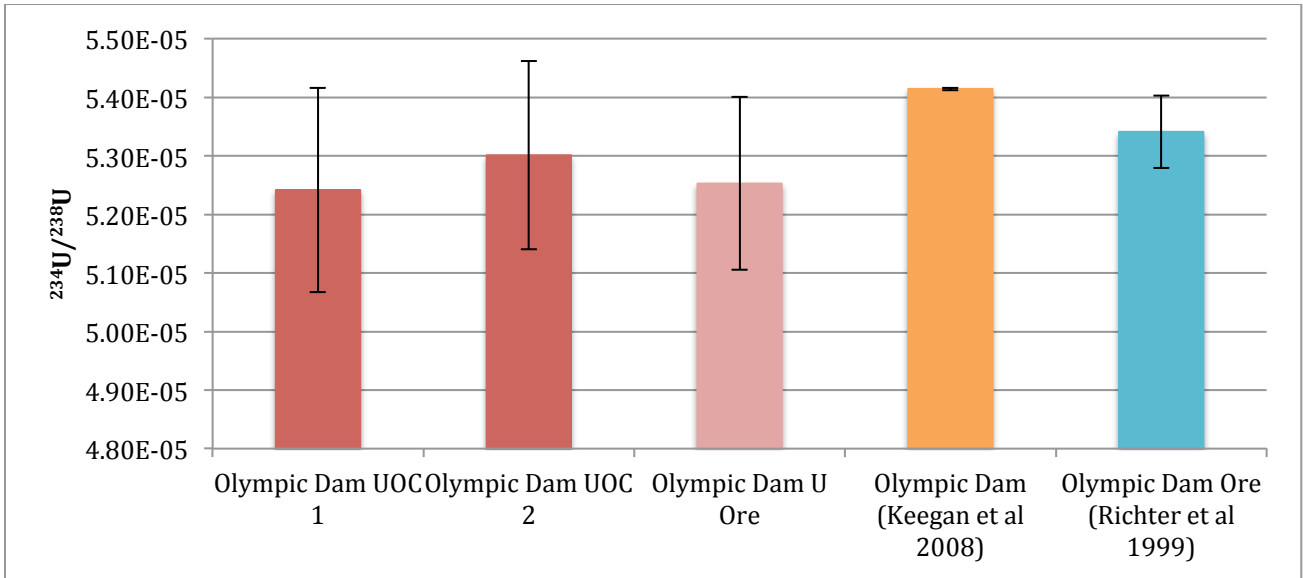


Figure 151 Comparison of measured $^{234}\text{U}/^{238}\text{U}$ isotope ratios from uranium ore and UOCs samples originating from Olympic Dam and a UOC and uranium ore sample from Olympic Dam previously analysed by Keegan *et al.* (2008) and Richter *et al.* (1999), respectively. Error bars = Expanded uncertainty (k=2)

References

References

1. International Atomic Energy Agency, *Incidents of nuclear and other radioactive material out of regulatory control - 2017 Fact Sheet*, 2017, IAEA: Vienna.
2. Varga, Z., Wallenius, M., and Mayer, K., *Origin assessment of uranium ore concentrates based on their rare-earth elemental impurity pattern*. *Radiochimica Acta*, 2010. **98**: p. 771-778.
3. Dann, G.E., *Martin Heinrich Klaproth*1958, Berlin.
4. Cuney, M. and Kyser, T.K., *Recent and Not-So-Recent Developments in Uranium Deposits and Implications for Exploration*. Short Course Series, ed. Mineralogical Association of Canada. Vol. 39. 2009. 257.
5. Nash, J.T. and Granger, H.C., *Geology and Concepts of Genesis of Important Types of Uranium Deposits*. *Economic Geology*, 1981. **75th Anniversary Edition**(1): p. 63-115.
6. Hazen, R.M., Ewing, R.C., and Sverjensky, D.A., *Evolution of uranium and thorium minerals*. *American Mineralogist*, 2009. **94**(1): p. 1293-1311.
7. Brenneka, G.A., et al., *Natural variations in uranium isotope ratios of uranium ore concentrates: Understanding the $^{238}\text{U}/^{235}\text{U}$ fractionation mechanism*. *Earth and Planetary Science Letters*, 2010. **291**(1): p. 228-233.
8. Sylvain, D., Elisabeth, H., and Hervé, N., *Revisiting the thorium-uranium nuclear fuel cycle*. *Europhysics News*, 2007. **38**(2): p. 24-27.
9. Reynolds, C., *Decay Chain of Isotope U-238*, metadata.berkeley.edu/nuclear-forensics/U238.svg, Editor 2012, Nuclear Forensic Search Project: Berkeley, US.
10. Weyer, S., et al., *Natural Fractionation of $^{238}\text{U}/^{235}\text{U}$* . *Geochimica et Cosmochimica Acta*, 2008. **72**(345-359).
11. Katz, J.J. and Seaborg, G.T., *The Chemistry of the Actinide Elements*1957, Bath, Great Britain: Methuen & Co. LTD.
12. Reynolds, C., *Decay Chain of Isotope U-235*, metadata.berkeley.edu/nuclear-forensics/U235.svg, Editor 2012, Nuclear Forensic Search Project: Berkeley, US.
13. Srncik, M., et al., *Investigation of the $^{236}\text{U}/^{238}\text{U}$ isotope abundance ratio in uranium ores and yellow cake samples* *Radiochimica Acta*, 2011. **99**(1): p. 335-339.
14. Hotchkis, M.A.C., et al., *Measurement of ^{236}U in environmental media*. *Nuclear Instruments and Methods in Physics Research Section B: Beam Interactions with Materials and Atoms*, 2000. **172**(1): p. 659-665.
15. Wilcken, K.M., et al., *Nucleogenic ^{36}Cl , ^{236}U and ^{239}Pu in uranium ores*. *Nucl. Instrum. Methods Phys. Res. B*, 2008. **266**(1).
16. Nero, A.V., *A Guidebook to Nuclear Reactors*1979, Berkeley: University of California Press.
17. International Atomic Energy Agency, *Nuclear Power Reactors in the World*2019, Vienna: INTERNATIONAL ATOMIC ENERGY AGENCY.
18. OECD/International Atomic Energy Agency, *Uranium 2011*, ed. OECD/International Atomic Energy Agency: OECD Publishing,.
19. Wikipedians, B., *Chemical Elements*: PediaPress.
20. Reed, B.C., *The Physics of the Manhattan Project*2010: Springer.
21. Kristensen, H.M. *Status of World Nuclear Forces*. Nuclear Information Project 2013 [cited from: 2013 02/08]; Available from: <http://www.fas.org/programs/ssp/nukes/nuclearweapons/nukestatus.html>.

22. Hecker, S.S., Englert, M., and Miller, M.C., *Nuclear non-proliferation*, in *Fundamentals of Materials for Energy and Environmental Sustainability*, D. Ginley and D. Cahen, Editors. 2012, Cambridge University Press.
23. Saleh, T.B., *Radiopharmacy: Basics*, in *Basic Sciences of Nuclear Medicine*, M.M. Khalil, Editor 2011, Springer Berlin Heidelberg: Berlin, Heidelberg. p. 25-39.
24. Le, V.S., *Specific Radioactivity of Neutron Induced Radioisotopes: Assessment Methods and Application for Medically Useful Lu-177 Production as a Case*. *Molecules*, 2011. **16**(1): p. 818-846.
25. Yura, Y. and Fujita, Y., *Boron neutron capture therapy as a novel modality of radiotherapy for oral cancer: Principle and antitumor effect*. *Oral Science International*, 2013. **10**(1): p. 9-14.
26. Schnöller, M., *Neutron Transmutation Doping (NTD) of Silicon*, in *Silicon: Evolution and Future of a Technology*, P. Siffert and E.F. Krimmel, Editors. 2004, Springer Berlin Heidelberg: Berlin, Heidelberg. p. 231-241.
27. Garry, J.M. and Peter, J.H., *Neutron scattering at the OPAL research reactor*. *Journal of Physics: Conference Series*, 2016. **746**(1): p. 012001.
28. Australian Nuclear Science and Technology Organisation. *ECHIDNA - High Resolution Powder Diffractometer*. 2018 [cited 2018; Available from: <http://www.ansto.gov.au/ResearchHub/OurInfrastructure/ACNS/Facilities/Instruments/Echidna/index.htm>].
29. Glascock, M.D., *Activation analysis*, in *Instrumental Multi-Element Chemical Analysis*, Z.B. Alfassi, Editor 1998, Springer Netherlands: Dordrecht. p. 93-150.
30. Hammond, C.R., *The Elements*, in *Handbook of Chemistry and Physics, 81st Edition*, CRC Press, Editor 2000, CRC Press.
31. Bleise, A., Danesi, P.R., and Burkart, W., *Properties, use and health effects of depleted uranium (DU): a general overview*. *Journal of Environmental Radioactivity*, 2003. **64**(1): p. 93-112.
32. Fayek, M., Horita, J., and Ripley, E.M., *The oxygen isotopic composition of uranium minerals: A review*. *Ore Geology Reviews*, 2011. **41**: p. 1-21.
33. Gauthier-Lafaye, F., Holliger, P., and Blanc, P.L., *Natural fission reactors in the Franceville basin, Gabon: A review of the conditions and results of a "critical event" in a geologic system*. *Geochimica et Cosmochimica Acta*, 1996. **60**(23): p. 4831-4852.
34. IAEA, *World Distribution of Uranium Deposits (UDEPO) with Uranium Deposit Classification*, 2009, IAEA: Vienna, Austria.
35. IAEA, *Classification of Uranium Reserves/Resources*, 1998, IAEA: Vienna.
36. Kyser, T.K. and Cuney, M., *Introduction In: Cuney M., Kyser, T.K. (Eds.), 2009, Mineralogical Association of Canada - Short Course Series 39*. p. 1-14.
37. McKay, A.D. and Miezzitis, Y., *Australia's Uranium Resources, Geology and Development of Deposits in Mineral Resources Report 1*, AGSO - Geoscience Australia, Editor 2001.
38. Leroy, J. and George-Aniel, B., *Volcanism and uranium mineralisation: the concept of source rock and concentration mechanisms*. *Journal of Volcanology and Geothermal Research*, 1992. **50**: p. 247-272.
39. Keegan, E., et al., *The provenance of Australian uranium ore concentrates by elemental and isotopic analysis*. *Applied Geochemistry*, 2008. **23**(4): p. 765-777.
40. IAEA, *Methods of exploitation of different types of uranium deposits*, 2000, IAEA: Vienna, Austria.
41. mining-technology.com. *Rössing Uranium Project, Namibia*. 2012 2012 [cited 2013 31/7/2013]; Available from: <http://www.mining-technology.com/projects/rossingsouth-uranium/rossingsouth-uranium1.html>.

42. Edwards, C. and Oliver, A., *Uranium Processing: A Review of Current Methods and Technology*. JOM, 2000. **52**(9): p. 12-20.
43. Map, A. *Beverley uranium mine*. 2012 1/19/2012 [cited 2013 31/7/2013]; Available from: <http://australianmap.net/beverley-uranium-mine/>.
44. ASTM, *D C967-02a Standard Specification for Uranium Ore Concentrate*, ASTM International, Editor 2002.
45. Chapter, I.I.o.M.E.B., *Energy, Environment and Resource Development: Selected Papers Contributed for the National Seminar on Energy, Environment and Resource Development for Mineral Industry (ENRED-95), January 18 and 19, 1995*1995: Allied Publishers.
46. Cordfunke, E., *The Chemistry of Uranium: Including Its Application in Nuclear Technology*1969, Amsterdam: Elsevier Publishing Company.
47. IAEA and OECD, *Environmental Activities in Uranium Mining and Milling*1999, Paris: OECD Publishing.
48. Gupta, C. and Singh, H., *Uranium Resource Processing: Secondary Resources*2003: Springer. 519.
49. IAEA, *Uranium Extraction Technology*, in *Technical Report Series*1993: Vienna.
50. Desson, M., Michel, P., and Rerolle, C., *Research, Development and Industrial Experience in Simo in the precipitation of Ammonium Diuranate*, in *Crystallisation and Precipitation: Proceedings of the International Symposium*, G.L. Strathdee, M.O. Klein, and L.A. Melis, Editors. 1987, Elsevier: Saskatoon, Saskatchewan.
51. Australian Safeguards and Non-Proliferation Office, *2018 Annual Report* Australian Safeguards and Non-Proliferation Office, Editor 2018: Barton, ACT.
52. World Nuclear Association. *Australia's Uranium*. 2018 [cited 2019 31/3/2019]; Available from: <http://www.world-nuclear.org/information-library/country-profiles/countries-a-f/australia.aspx>.
53. Department of Resources Energy and Tourism, *Australia's Uranium Industry*, 2012.
54. IAEA. *IAEA Safeguards Overview: Comprehensive Safeguards Agreements and Additional Protocols*. Factsheets and FAQs 2013 [cited 2013 1/8/2013]; Available from: http://www.iaea.org/Publications/Factsheets/English/sg_overview.html.
55. Hodge, A., *Talks to start on sale of uranium to India*, in *The Australian*2013, News Corp Australia: Surry Hills.
56. Doherty, B., *Australia and India to start uranium sales talks*, in *The Sydney Morning Herald*2013: Sydney.
57. Bennett, J. *Australia quietly makes first uranium shipment to India three years after supply agreement*. [Online News Article] 2017 19/7/2017 [cited 2018 20/11/2018]; Available from: <https://www.abc.net.au/news/2017-07-19/australia-quietly-makes-first-uranium-shipment-to-india/8722108>.
58. International Atomic Energy Agency, *Uranium 2018: Resources, Production and Demand*, International Atomic Energy Agency, Editor 2018: Vienna.
59. Australian Safeguards and Non-Proliferation Office, *Annual Report 2016-2017*, A.S.a.N.-P. Office, Editor 2017: Canberra.
60. Department of Industry Innovation and Science, *Resources and Energy Quarterly June 2018*, Office of the Chief Economist, Editor 2018: Canberra.
61. Johnston, J.P. and Cross, K.C., *U-Pb Geochronological constraints on the genesis of the Olympic Dam Cu-U-Au-Ag deposit, South Australia*. *Economic Geology*, 1995. **90**(1): p. 1046-1063.
62. Enghardt, J., *The Olympic Dam Cu-U-Au-Ag-REE deposit, South Australia*, T. Seifert, Editor, University of Mining and Technology, Freiberg. p. 10.
63. Oreskes, N. and Einadi, M.T., *Origin of Hydrothermal fluids at Olympic Dam: preliminary results from fluid incursions and stable isotopes*. *Economic Geology*, 1992. **87**(1): p. 64-90.

64. Haynes, D.W., et al., *Olympic Dam Ore Genesis: A Fluid-Mixing Model*. *Economic Geology*, 1995. **90**(1): p. 281-307.
65. BHP Billiton, *Annual Report 2012*, B. Billiton, Editor.
66. BHP Billiton, *Annual Report 2018*, 2018: Melbourne, Australia.
67. Reeve, J., et al., *Olympic Dam copper-uranium-gold deposit*, in *Geology of the Mineral Deposits of Australia and Papua New Guinea*, F. Hughes, Editor 1990, The Australasian Institute of Mining and Metallurgy: Melbourne. p. 1009-1035.
68. Jeuken, B., Marten, H., and Phillips, R., *Uranium ISL Operation and Water Management under the Arid Climate Conditions at Beverley, Australia*. *Mine Water and the Environment, Proceedings*, ed. N. Rapantova and Z. Hrkal2008, Ostrava: Vsb-Tech Univ Ostrava. 487-490.
69. Wulser, P.A., et al., *The Sandstone-Hosted Beverley Uranium Deposit, Lake Frome Basin, South Australia: Mineralogy, Geochemistry, and a Time-Constrained Model for Its Genesis*. *Economic Geology*, 2011. **106**(5): p. 835-867.
70. Marten, H., *Environmental management and optimization of in-situ-leaching at Beverley*. *Uranium in the Environment: Mining Impact and Consequences*, ed. B.J. Merkel and A. HascheBerger2006, Berlin: Springer-Verlag Berlin. 537-546.
71. Government of South Australia, *South Australia's Major Operating/Approved Mines Resource Estimates and Production Statistics*, Department for Energy and Mining, Editor 2019: Adelaide.
72. Ludwig, K.R., et al., *Age of Uranium Mineralization at the Jabiluka and Ranger Deposits, Northern-Territory, Australia - New U-PB Isotope Evidence*. *Economic Geology*, 1987. **82**(4): p. 857-874.
73. Hein, K.A.A., *Geology of the Ranger Uranium Mine, Northern Territory, Australia: structural constraints on the timing of uranium emplacement*. *Ore Geology Reviews*, 2002. **20**(3-4): p. 83-108.
74. Energy Resources of Australia Ltd, *2012 Annual Report*, Energy Resources of Australia Ltd, Editor 2013: Darwin.
75. Energy Resources of Australia Ltd. *Stockpile Processing*. 2019 [cited 2019 12/8/2019]; Available from: <https://www.energyres.com.au/operations/stockpile-processing/>.
76. Energy Resources of Australia Ltd, *Uranium Processing at Ranger - Information Sheet*, 2013: Darwin.
77. Australia, G., *Australia's Identified Mineral Resources 2012*, E.a.T. Department of Resources, Editor 2013, Geoscience Australia: Canberra.
78. Southern Cross Resources Australia Pty. Ltd., *Honeymoon Uranium Project - Environmental Impact Statement*, S.C.R.A.P. Ltd., Editor 2000: Toowong.
79. Boss Resources. *Honeymoon Uranium Project*. Projects [cited 2018 24/07/2018]; Available from: <https://bossresources.com.au/honeymoon-uranium-project/>.
80. Ben Creagh, *Honeymoon uranium mine restart takes shape*, Australian Mining, Editor 2018, Prime Creative Media,.
81. Sharma, R.K., Putirka, K.D., and Stone, J.J., *Stream sediment geochemistry of the upper Cheyenne River watershed within the abandoned uranium mining region of the southern Black Hills, South Dakota, USA*. *Environmental Earth Sciences*, 2016. **75**(9): p. 823.
82. Ahmad, M., et al., *Pine Creek SD52-8, Explanatory Notes and Mineral Deposit Data Sheets*, in *1:250 000 Metallogenic Map Series*, Northern Territory Geological Survey, Editor 1993.
83. Alfredson, P.G. *Australian Experience in the production of yellow cake and uranium fluorides*. in *Production of Yellow Cake and Uranium Fluorides*. 1979. Paris: IAEA.
84. Keegan, E., et al., *Attribution of uranium ore concentrates using elemental and anionic data*. *Applied Geochemistry*, 2012. **27**(1): p. 1600-1609.

85. Maas, R., *Nd-Sr isotope constraints on the age and origin of unconformity-type uranium deposits in the Alligator Rivers uranium field, Northern Territory, Australia*. Economic Geology, 1989. **84**(1): p. 64-90.
86. Ewers, G.R., Ferguson, J., and Donnelly, T.H., *The Nabarlek uranium deposits Northern Territory Australia: some petrologic and geochemical constraints on ore genesis*. Economic Geology, 1983. **78**(1): p. 823-837.
87. Lucas, G.C., et al., *Queensland Mines plant trials with Caro's acid*. Australasian Institute of Mining & Metallurgy, 1983. . **287**: p. 27-34.
88. Mernagh, T.P., et al., *Chemistry of low temperature hydrothermal gold, platinum, and palladium (\pm uranium) mineralisation at Coronation Hill, Northern Territory*. Economic Geology, 1998. **89**(1): p. 1053-1073.
89. Needham, R.S., *A Review of Mineralisation in the South Alligator Conservation Zone*, B.o.M. Resources, Editor 1987: Australia.
90. Wyborn, L.A.I., *Au-Pt-Pd-U mineralisation in the Coronation Hill-El Sherana region, NT*. BMR Research Newsletter, 1992. **16**: p. 1-3.
91. Mayer, K., Wallenius, M., and Fanghänel, T., *Nuclear Forensic Science - From cradle to maturity*. Journal of Alloys and Compounds, 2007. **444-445**: p. 50-56.
92. Joint Working Group of the American Physical Society and Science, A.A.f.t.A.o., *Nuclear Forensics: Role, State of the Art, Program Needs*, 2008: USA.
93. Wallenius, M., Mayer, K., and Ray, I., *Nuclear forensic investigations: Two case studies*. Forensic Science International, 2006. **156**: p. 55-62.
94. International Atomic Energy Agency, *IAEA Incident and Trafficking Database - 2019 Fact Sheet*, International Atomic Energy Agency, Editor 2019: Vienna.
95. *Yellowcake theft alleged*, in *The Canberra Times* 1980: Canberra, ACT. p. 8.
96. *Man for trial over uranium*, in *The Canberra Times* 1980: Canberra, ACT. p. 13.
97. *Yellowcake theft*, in *The Canberra Times* 1980: Canberra, ACT. p. 1.
98. *Tighter security planned at Mary Kathleen*, in *The Canberra Times* 1980: Canberra, ACT. p. 9.
99. ABC News *Yellowcake jars found at Olympic Dam village*. 2007.
100. Trounson, A., *Jars of stolen yellowcake found in BHP camp*, in *The Australian*, 2009: Sydney, NSW.
101. Kristo, M.J., et al., *Nuclear forensic analysis of uranium oxide powders interdicted in Victoria, Australia*, in *Radiochimica Acta* 2015. p. 487.
102. Peter Gregory *Uranium found during police raids*. The Sydney Morning Herald, 2009.
103. Keegan, E., et al., *Nuclear forensic analysis of an unknown uranium ore concentrate sample seized in a criminal investigation in Australia*. Forensic Science International, 2014. **240**: p. 111-121.
104. *Nuclear Forensics in Support of Investigations* 2015, Vienna: INTERNATIONAL ATOMIC ENERGY AGENCY.
105. Mayer, K., Wallenius, M., and Varga, Z., *Nuclear Forensic Science: Correlating Measurable Material Parameters to the History of Nuclear Material*. Chemical Reviews, 2013. **113**(1): p. 884-900.
106. Mayer, K., Wallenius, M., and Varga, Z., *Nuclear Forensic Science: Corelating Measurable Material Parameters to the History of Nuclear Material*. Chemical Reviews, 2013. **113**(1): p. 884-900.
107. Stanley, F.E., *A beginner's guide to uranium chronometry in nuclear forensics and safeguards*. Journal of Analytical Atomic Spectrometry, 2012. **27**(11): p. 1821-1830.
108. Manna, S., et al., *Study of calcinations of ammonium diuranate at different temperatures*. Journal of Nuclear Materials, 2012. **426**(1-3): p. 229-232.

109. Wallenius, M., Meyer, K., and Ray, I., *Nuclear forensic investigations: Two case studies*. Forensic Science International, 2006. **156**(1): p. 55-62.
110. Kigoshi, K., *Alpha recoil thorium-234: dissolution into water and uranium-234/uranium-238 disequilibrium in nature*. Science, 1971. **173**(1): p. 47-48.
111. Wilcken, K.M., et al., *AMS of natural ²³⁶U and ²³⁹Pu produced in uranium ores*. Nuclear Instruments and Methods in Physics Research B, 2007. **259**(1): p. 727-732.
112. Badaut, V., Wallenius, M., and Mayer, K., *Anion analysis in uranium ore concentrates by ion chromatography*. Journal of Radioanalytical and Nuclear Chemistry, 2009. **280**(1): p. 57.
113. Varga, Z., et al., *Characterisation and classification of uranium ore concentrates (yellow cakes) using infrared spectrometry*. Radiochimica Acta, 2011. **99**(1): p. 807813.
114. Svedkauskite-LeGore, J., et al., *Investigation of the sample characteristics needed for the determination of the origin of uranium-bearing materials*. Journal of Radioanalytical and Nuclear Chemistry, 2008. **278**(1): p. 201-208.
115. Mercadier, J., et al., *Origin of uranium deposits revealed by their rare earth element signature*. Terra Nova, 2011. **23**(1): p. 264-269.
116. Varga, Z., et al., *Application of Lead and Strontium Isotope Ratio Measurements for the Origin Assessment of Uranium Ore Concentrates*. Anal. Chem., 2009. **81**: p. 8327-8334.
117. Švedkauskite-LeGore, J., et al., *Investigation of the isotopic composition of lead and of trace elements concentrations in natural uranium materials as a signature in nuclear forensics*. Radiochimica Acta, 2007. **95**(1): p. 601-605.
118. Rosman, K. and Taylor, P.D., *The isotopic composition of the elements*. Pure Applied Chemistry, 1998. **70**(1).
119. Baertschi, P., *Absolute O-18 content of standard mean ocean water*. Earth and Planetary Science Letters, 1976. **31**(3): p. 341-344
120. Mashirov, L., Mikhalev, V.A., and Suglobov, D.N., *Stoichiometry of uranyl hydrolysis reaction in acidic aqueous solutions from the evidence of oxygen exchange kinetics* Comptes Rendus Chimie, 2004. **7**(1): p. 1179-1184.
121. Gordon, G. and Taube, H., *The uranium(V)-catalysed exchange reaction between uranyl ion and water in perchloric acid solution*. 1961.
122. Pajo, L., Mayer, K., and Koch, L., *Investigation of the oxygen isotopic composition in oxidic uranium compounds as a new property in nuclear forensic science*. Fresenius Journal of Analytical Chemistry, 2001. **371**(3): p. 348-352.
123. Plaue, J.W., et al., *Near infrared reflectance spectroscopy as a process signature in uranium oxides*. Journal of Radioanalytical and Nuclear Chemistry, 2013. **296**(1): p. 551-555.
124. Klunder, G.L., et al., *Application of Visible/Near-Infrared Reflectance Spectroscopy to Uranium Ore Concentrates for Nuclear Forensic Analysis and Attribution*. Applied Spectroscopy, 2013. **67**(9): p. 1049-1056.
125. Linge, K.L. and Jarvis, K.E., *Quadrupole ICP-MS: Introduction to Instrumentation, Measurement Techniques and Analytical Capabilities*. Geostandards and Geoanalytical Research, 2009. **33**(4): p. 445-467.
126. Jakubowski, N., Moens, L., and Vanhaecke, F., *Sector field mass spectrometers in ICP-MS*. Spectrochimica Acta Part B, 1998. **53**: p. 1739-1763.
127. Varga, Z., et al., *Determination of rare-earth elements in uranium-bearing materials by inductively coupled plasma mass spectrometry*. Talanta, 2010. **80**(1): p. 1744-1749.
128. Quemet, A., et al., *Analysis of twenty five impurities in uranium matrix by ICP-MS with iron measurement optimized using reaction collision cell, cold plasma and medium resolution*. Talanta, 2012. **99**: p. 207-212.
129. Labexchange.com. *VG Plasmaquad PQ2*. 20/08/2013]; Available from: <http://www.labexchange.com/en/buy-devices/d/?sn=15413>.

130. Thomas, R., *Practical Guide to ICP-MS: A Tutorial for Beginners, Third Edition* 2013: Taylor & Francis.
131. Durrant, S.F., *Laser ablation inductively coupled plasma mass spectrometry: achievements, problems, prospects*. *Journal of Analytical Atomic Spectrometry*, 1999. **14**(9): p. 1385-1403.
132. Vandecasteele, C. and Block, C.B., *Modern Methods for Trace Element Determination* 1997, Chichester: John Wiley & Sons.
133. Garcia, C.C., et al., *Elemental fractionation and stoichiometric sampling in femtosecond laser ablation*. *Journal of Analytical Atomic Spectrometry*, 2008. **23**(4): p. 470-478.
134. March, R.E., *An introduction to quadrupole ion trap mass spectrometry*. *Journal of Mass Spectrometry*, 1997. **32**(4): p. 351-369.
135. Micek, C. *Mass Spectrometer: Detector - Electron Multiplier*. Huygens Probe Gas Chromatograph Mass Spectrometer 14/08/2013]; Available from: http://huygensgcms.gsfc.nasa.gov/MS_Detector_1.htm.
136. Ketterer, M.E. and Szechenyi, S.C., *Determination of plutonium and other transuranic elements by inductively coupled plasma mass spectrometry: A historical perspective and new frontiers in the environmental sciences*. *Spectrochimica Acta Part B-Atomic Spectroscopy*, 2008. **63**(7): p. 719-737.
137. Vanhaecke, F. and Degryse, P., *Isotopic Analysis: Fundamentals and Applications Using ICP-MS* 2012: Wiley.
138. Barshick, C., Duckworth, D., and Smith, D., *Inorganic Mass Spectrometry: Fundamentals and Applications* 2000: Taylor & Francis.
139. Potts, P.J., *Nuclear techniques for the determination of uranium and thorium and their decay products*, in *A Handbook of Silicate Rock Analysis*, P.J. Potts, Editor 1992, Springer US: Boston, MA. p. 440-471.
140. *Neutron Activation Analysis*, in *Atomic and Nuclear Analytical Methods: XRF, Mössbauer, XPS, NAA and B63 Ion-Beam Spectroscopic Techniques*, H.R. Verma, Editor 2007, Springer Berlin Heidelberg: Berlin, Heidelberg. p. 243-268.
141. NMI3. *For chemical analysis: Neutron Activation Analysis*. 2012 [cited 2018 01/07/2018]; Available from: <https://nmi3.eu/neutron-research/techniques-for-/chemical-analysis.html>.
142. Jevremovic, T., *Neutron Physics*, in *Nuclear Principles in Engineering*, T. Jevremovic, Editor 2009, Springer US: Boston, MA. p. 281-376.
143. Greenberg, R.R., Bode, P., and De Nadai Fernandes, E.A., *Neutron activation analysis: A primary method of measurement*. *Spectrochimica Acta Part B: Atomic Spectroscopy*, 2011. **66**(3): p. 193-241.
144. Filby, R.H., *Part IX. Neutron Activation Analysis*, in *Isotopic and Nuclear Analytical Techniques in Biological Systems: A Critical Study*, I.U.o.P.a.A. Chemistry, Editor 1995: Great Britain. p. 1929-1941.
145. De Corte, F., et al., *Recent advances in the k_0 -standardization of neutron activation analysis: Extensions, applications, prospects*. *Journal of Radioanalytical and Nuclear Chemistry*, 1993. **169**(1): p. 125-158.
146. Murrie, R.P., Quinton, J.S., and Popelka-Filcoff, R.S., *Determination of the f parameter for k_0 -neutron activation analysis at the Australian 20 MW OPAL research reactor*. *Journal of Radioanalytical and Nuclear Chemistry*, 2013. **298**(1): p. 77-86.
147. De Corte, F., et al., *Accuracy and applicability of the k_0 -standardization method*. *Journal of Radioanalytical and Nuclear Chemistry*, 1987. **113**(1): p. 145-161.
148. Glascock, M.D., et al., *Correcting for uranium fission in instrumental neutron activation analysis of high-uranium rocks*. *Journal of Radioanalytical and Nuclear Chemistry*, 1986. **99**(1): p. 121-131.
149. Landsberger, S., *Update of uranium fission interferences in neutron activation analysis*. *Chemical Geology*, 1989. **77**: p. 65-70.

150. El-Taher, A. and Khater, A.E.M., *Elemental characterization of Hazm El-Jalamid phosphorite by instrumental neutron activation analysis*. Applied Radiation and Isotopes, 2016. **114**: p. 121-127.
151. Sadikov, I.I., et al., *Neutron Activation Analysis of pure uranium: Preconcentration of impurity elements*. Journal of Radioanalytical and Nuclear Chemistry, 2009. **280**(3): p. 489-493.
152. Bottom, R., *Thermogravimetric Analysis*, in *Principles and Applications of Thermal Analysis*, P. Gabbott, Editor 2008.
153. Gabbott, P., *A Practical Introduction to Differential Scanning Calorimetry*, in *Principles and Applications of Thermal Analysis*, P. Gabbott, Editor 2008.
154. Eloirdi, R., et al., *Investigation of ammonium diuranate calcination with high-temperature X-ray diffraction*. Journal of Materials Science, 2014. **49**(24): p. 8436-8443.
155. Yahia, M.E., ElFekey, S.A., and ElRazek, A.M.A., *The impact of ammonium and nitrate impurities on the formation of uranium oxides, in the composition range UO₃-U₃O₈-z, during thermal decomposition of ammonium uranates*. Radiochimica Acta, 1996. **72**(4): p. 205-208.
156. Kim, B.H., et al., *Thermal and X-ray diffraction analysis studies during the decomposition of ammonium uranyl nitrate*. Journal of Radioanalytical and Nuclear Chemistry, 2012. **292**(3): p. 1075-1083.
157. Egerton, R.F., *Physical Principles of Electron Microscopy: An Introduction to TEM, SEM, and AEM* 2006: Springer US.
158. Goldstein, J.I., et al., *Scanning Electron Microscopy and X-ray Microanalysis*. 3rd ed 2007, New York, NY: Springer.
159. Lifshin, E., Ciccarelli, M., and Bolon, R. in *8th International conference of X-ray optics and microanalysis*. 1980. Pendell, Midland.
160. Kramers, H.A., *XCIII. On the theory of X-ray absorption and of the continuous X-ray spectrum*. The London, Edinburgh, and Dublin Philosophical Magazine and Journal of Science, 1923. **46**(275): p. 836-871.
161. Caistaing, R., *Application of electron probes to local chemical and crystallographic analysis*, 1951, University of Paris.
162. Manna, S., et al., *Study of calcinations of ammonium diuranate at different temperatures*. Journal of Nuclear Materials, 2012. **426**(1): p. 229-232.
163. Tamasi, A.L., et al., *Comparison of morphologies of a uranyl peroxide precursor and calcination products*. Journal of Radioanalytical and Nuclear Chemistry, 2016. **309**(2): p. 827-832.
164. Kim, K.-W., et al., *Effects of the different conditions of uranyl and hydrogen peroxide solutions on the behavior of the uranium peroxide precipitation*. Journal of Hazardous Materials, 2011. **193**(Supplement C): p. 52-58.
165. Manna, S., Roy, S.B., and Joshi, J.B., *Study of crystallization and morphology of ammonium diuranate and uranium oxide*. Journal of Nuclear Materials, 2012. **424**(1): p. 94-100.
166. Paik, S., et al., *Effect of ammonium nitrate on precipitation of Ammonium Di-Uranate (ADU) and its characteristics*. Journal of Nuclear Materials, 2013. **440**(1): p. 34-38.
167. Singh, D.K., et al., *Development of a phosphate precipitation method for the recovery of uranium from lean tenor alkaline leach liquor*. Hydrometallurgy, 2017. **171**(Supplement C): p. 228-235.
168. Hanson, A.B., et al., *Quantifying Impurity Effects on the Surface Morphology of α -U₃O₈*. Analytical Chemistry, 2019. **91**(15): p. 10081-10087.
169. Olsen, A.M., et al., *Quantifying Morphological Features of alpha-U₃O₈ with Image Analysis for Nuclear Forensics*. Analytical Chemistry, 2017. **89**(5): p. 3177-3183.

170. Fongaro, L., et al., *Application of the angle measure technique as image texture analysis method for the identification of uranium ore concentrate samples: New perspective in nuclear forensics*. *Talanta*, 2016. **152**(Supplement C): p. 463-474.
171. Olsen, A.M., et al., *A response surface model of morphological changes in UO₂ and U₃O₈ following high temperature aging*, in *Radiochimica Acta* 2019. p. 449.
172. Pointurier, F. and Marie, O., *Use of micro-Raman spectrometry coupled with scanning electron microscopy to determine the chemical form of uranium compounds in micrometer-size particles*. *Journal of Raman Spectroscopy*, 2013. **44**(12): p. 1753-1759.
173. Stefaniak, E.A., et al., *In-SEM Raman microspectrometry coupled with EDX - a case study of uranium reference particles*. *Analyst*, 2014. **139**(3): p. 668-675.
174. Esaka, F., et al., *Particle isolation for analysis of uranium minor isotopes in individual particles by secondary ion mass spectrometry*. *Talanta*, 2007. **71**(3): p. 1011-1015.
175. Jayasooriya, U.A. and Jenkins, R.D., *Introduction to Raman Spectroscopy*, in *An Introduction to Laser Spectroscopy: Second Edition*, D.L. Andrews and A.A. Demidov, Editors. 2002, Springer US: Boston, MA. p. 77-104.
176. Larkin, P., *Infrared and Raman Spectroscopy: Principles and Spectral Interpretation* 2017: Elsevier Science.
177. Langhoff, N., et al., *X-Ray Sources*, in *Handbook of Practical X-Ray Fluorescence Analysis*, B. Beckhoff, et al., Editors. 2006, Springer Berlin Heidelberg: Berlin, Heidelberg. p. 33-83.
178. Reich, G., *Mid and Near Infrared Spectroscopy*, in *Analytical Techniques in the Pharmaceutical Sciences*, A. Müllertz, Y. Perrie, and T. Rades, Editors. 2016, Springer New York: New York, NY. p. 61-138.
179. Metrohm, *NIR Spectroscopy: A guide to near-infrared spectroscopic analysis of industrial manufacturing processes*, Metrohm, Editor 2013: Herisau, Switzerland.
180. Huber, G.C., *Geology of the Lisbon Valley Uranium district, southeastern Utah*, in *32nd Annual Fall Field Conference* 1981, New Mexico Geological Society,: Western Slope, Colorado. p. 177-182.
181. Chenoweth, W., *Lisbon Valley, Utah's Largest Uranium District*. *Mining Districts of Utah*, 2006: p. 534-550.
182. Johnson, J.H.S. and Thordarson, W., *Uranium Deposits of the Moab, Monticello, White Canyon and Monument Valley Districts Utah and Arizona*, U.S. Department of the Interior, Editor 1966, United States Government Printing House,: Washington DC,.
183. Hawley, C.C., Wyant, D.G., and Brooks, D.B., *Geology and Uranium Deposits of the Temple Mountain District Emory County, Utah*, U.S. Department of the Interior, Editor 1965, United States Government Printing Office: Washington DC.
184. U.S. Geological Survey, *Ike-Nixon Shaft*, in *Mineral Resource Data System (MRDS)* 2018, U.S. Geological Survey,: Washington DC,.
185. mindat.org. *Ike-Nixon Shaft*. 2018 [cited 2018 27/08/2018]; Available from: <https://www.mindat.org/loc-181973.html>.
186. Trites Jr, A.F. and Chew, R.T., *Geology of the Happy Jack mine, White Canyon area, San Juan County, Utah*, U.S. Department of the Interior, Editor 1955: Washington DC.
187. Gross, E.B., *Mineralogy and paragenesis of the uranium ore, Mi Vida Mine, San Juan County, Utah*. *Economic Geology*, 1956. **51**(7): p. 632-648.
188. U.S. Geological Survey, *Green Dragon*, in *Mineral Resource Data Systems (MRDS)*, 2018: Washington DC.
189. Fischer, R. and Hilpert, L., *Geology of the Uravan Mineral Belt*, U.S. Atomic Energy Commission, Editor 1952: Washington DC.
190. Shawe, D.R., *Uranium-vanadium deposits of the Slick Rock district, Colorado*, U.S.G. Survey, Editor 2011: Reston, Virginia. p. 80.

191. Chenoweth, W., *The Uranium-Vanadium Deposits of the Uravan Mineral Belt and Adjacent Areas, Colorado and Utah*, in *Fall Field Conference*, R.C. Epis and J.F. Callender, Editors. 1981, New Mexico Geological Society: Western Slope, Colorado. p. 165-170.
192. Butler Jr, A.P. and Fischer, R.P., *Uranium and vanadium resources in the Moab 10 x 2" quadrangle, Utah and Colorado*, U.S. Geological Survey, Editor 1978. p. B1-B21.
193. Nash, J.T., *Geology of the Midnite uranium mine area, Washington: maps, description, and interpretation*, in *Open-File Report* 1977, US Department of the Interior.
194. URS Corporation, *Final Remedial Investigation Report for Midnite Mine Stevens County, Washington*, 2005, URS Corporation, Seattle, Washington,.
195. M Huntting, *Uranium in Washington*, Department of Mines and Geology, Editor 1957: Olympia, Washington.
196. Frondel, C., *Mineral Composition of Gummite*. *American Mineralogist*, 1956. **41**(7-8): p. 539-568.
197. TheDiggings.com. *Ferguson Lode Claim in Pennington, SD, Feldspar Past Producer*. 2003 [cited 2018 27/08/2018]; Available from: <https://thediggings.com/mines/usgs10012470 - deposit-comments>.
198. Norton, J., *Geology and Mineral Deposits of Some Pegmatites in the Southern Black Hills South Dakota*, U.S. Department of the Interior, Editor 1964: Washington DC,.
199. Nriagu, J.O. and Moore, P.H., *Phosphate Minerals* 2012: Springer Berlin Heidelberg.
200. Olson, J.C., *Mica-bearing Pegmatites of New Hampshire: A Preliminary Report*, U.S. Department of the Interior, Editor 1941: Washington DC, p. 363-403.
201. Shaub, B.M., *The occurrence, crystal habit and composition of the uraninite from the Ruggles Mine, near Grafton Center, New Hampshire*. *American Mineralogist*, 1938. **23**(5): p. 334-341.
202. Korzeb, S.L., Foord, E.E., and Lichte, F.E., *The chemical evolution and paragenesis of uranium minerals from the ruggles and palermo granitic pegmatites, New Hampshire*. *Canadian Mineralogist*, 1997. **35**(1): p. 135-144.
203. Satterly, J. and Hewitt, D.F., *Some Radioactive Mineral Occurrences in the Bancroft Area*, Ontario Department of Mines, Editor 1955, Baptist Johnston: Toronto, Canada. p. 1-54.
204. Sabina, A.P., *Rocks and Minerals for the Collector: Bancroft - Parry Sound area and Southern Ontario*, Geological Survey of Canada, Editor 1986, Canadian Government Publishing Centre: Hull, Quebec.
205. Kristo, M.J., et al., *Nuclear Forensic Science: Analysis of Nuclear Material Out of Regulatory Control*. *Annual Review of Earth and Planetary Sciences*, 2016. **44**(1): p. 555-579.
206. Klunder, G., Plaue, J., and Spackman, P., *Application of Visible/Near-Infrared Reflectance Spectroscopy to Uranium Ore Concentrates for Nuclear Forensic Analysis and Attribution*. *Applied Spectroscopy*, 2013. **67**(9): p. 1049-1056.
207. Lin, D.H.M., et al., *Applicability of Raman spectroscopy as a tool in nuclear forensics for analysis of uranium ore concentrates*. *Radiochimica Acta*, 2013. **101**(12): p. 779-784.
208. Allen, G.C., Butler, I.S., and Nguyen Anh, T., *Characterisation of uranium oxides by micro-Raman spectroscopy*. *Journal of Nuclear Materials*, 1987. **144**(1): p. 17-19.
209. Palacios, M.L. and Taylor, S.H., *Characterization of uranium oxides using in situ micro-Raman spectroscopy*. *Applied Spectroscopy*, 2000. **54**(9): p. 1372-1378.
210. Ho, D.M.L., et al., *Raman spectroscopy of uranium compounds and the use of multivariate analysis for visualization and classification*. *Forensic Science International*, 2015. **251**: p. 61-68.
211. Manara, D. and Renker, B., *Raman spectra of stoichiometric and hyperstoichiometric uranium dioxide*. *Journal of Nuclear Materials*, 2003. **321**(2-3): p. 233-237.

212. Stefaniak, E.A., et al., *Combined SEM/EDX and micro-Raman spectroscopy analysis of uranium minerals from a former uranium mine*. Journal of Hazardous Materials, 2009. **168**(1): p. 416-423.
213. Pointurier, F. and Marie, O., *Identification of the chemical forms of uranium compounds in micrometer-size particles by means of micro-Raman spectrometry and scanning electron microscope*. Spectrochimica Acta Part B: Atomic Spectroscopy, 2010. **65**(9): p. 797-804.
214. Raje, N., et al., *Impurity characterization of magnesium diuranate using simultaneous TG-DTA-FTIR measurements*. Journal of Nuclear Materials, 2013. **436**(1): p. 40-46.
215. Mayer, K., Wallenius, M., and Ray, I., *Nuclear forensics-a methodology providing clues on the origin of illicitly trafficked nuclear materials*. Analyst, 2005. **130**(4): p. 433-441.
216. Eloirdi, R., et al., *Investigation of ammonium diuranate calcination with high-temperature X-ray diffraction*. Journal of Materials Science, 2014. **49**(24): p. 8436-8443.
217. Wotherspoon, A., et al., *Investigating macro- and micro-scale materials provenancing signatures in uranium ore concentrates/yellowcake*, in *International Conference on Advances in Nuclear Forensics: Countering the Evolving Threat of Nuclear and Other Radioactive Material out of Regulatory Control 2014*, IAEA: Vienna, Austria.
218. Sato, T., *Thermal-Decomposition of Uranium Peroxide Hydrates*. Journal of Applied Chemistry and Biotechnology, 1976. **26**(4): p. 107-213.
219. Walenta, K., *STUDTITE AND ITS COMPOSITION*. American Mineralogist, 1974. **59**(1-2): p. 166-171.
220. Boggs, J.E. and El-Chehabi, M., *The Thermal Decomposition of Uranium Peroxide, UO₄.2H₂O*. Journal of the American Chemical Society, 1957. **79**(16): p. 4258-4260.
221. Guo, X., et al., *Thermodynamic studies of studtite thermal decomposition pathways via amorphous intermediates UO₃, U₂O₇, and UO₄*. Journal of Nuclear Materials, 2016. **478**: p. 158-163.
222. Guo, X., et al., *Energetics of metastudtite and implications for nuclear waste alteration*. Proceedings of the National Academy of Sciences, 2014. **111**(50): p. 17737-17742.
223. Odoh, S.O., et al., *Structure and Reactivity of X-ray Amorphous Uranyl Peroxide, U₂O₇*. Inorganic Chemistry, 2016. **55**(7): p. 3541-3546.
224. Hoekstra, H.R., Siegel, S., and Gallaghe.Fx, *URANIUM-OXYGEN SYSTEM AT HIGH PRESSURE*. Journal of Inorganic & Nuclear Chemistry, 1970. **32**(10): p. 3237-&.
225. Hoekstra, H.R. and Siegel, S., *The uranium-oxygen system: U₃O₈ □ UO₃*. Journal of Inorganic and Nuclear Chemistry, 1961. **18**: p. 154-165.
226. Enokihara, C., Guttler, R., and Rela, P. *Gamma Irradiation of Quartz from Parana Basin, South America*. in *International Nuclear Atlantic Conference*. 2007. Santos, Brazil.
227. Yamagishi, H., Nakashima, S., and Ito, Y., *High temperature infrared spectra of hydrous microcrystalline quartz*. Physics and Chemistry of Minerals, 1997. **24**(1): p. 66-74.
228. Sweet, L.E., et al., *Investigation of the polymorphs and hydrolysis of uranium trioxide*. Journal of Radioanalytical and Nuclear Chemistry, 2013. **296**(1): p. 105-110.
229. Hoekstra, H.R. and Siegel, S., *CHEMISTRY AND CRYSTALLOGRAPHY OF URANIUM OXIDE SYSTEMS*. Journal of Inorganic & Nuclear Chemistry, 1958. **7**(1-2): p. 174-175.
230. Sato, T., *Preparation of uranium peroxide hydrates*. Journal of Applied Chemistry, 1963. **13**(8): p. 361-365.
231. Wallenius, M., et al., *Propagation of Nuclear Forensics Signatures at the Front-End of the Fuel Cycle*, in *Identification of High Confidence Nuclear Forensics Signatures; Results of a Coordinated Research Project and Related Research*, IAEA, Editor 2017, IAEA: Vienna, Austria. p. 31-38.
232. Richter, S., et al., *Isotopic 'fingerprints' for natural ore samples*. International Journal of Mass Spectrometry, 1999. **193**(1): p. 9-14.

233. Stirling, C.H., et al., *Low-temperature isotopic fractionation of uranium*. Earth and Planetary Science Letters, 2007. **264**(1-2): p. 208-225.
234. DePaolo, D.J., et al., *Sediment transport time measured with U-series isotopes: Results from ODP North Atlantic drift site 984*. Earth and Planetary Science Letters, 2006. **248**(1-2): p. 394-410.
235. Murphy, M.J., et al., *Fractionation of U-238/U-235 by reduction during low temperature uranium mineralisation processes*. Earth and Planetary Science Letters, 2014. **388**: p. 306-317.
236. Dauphas, N. and Schauble, E.A., *Mass Fractionation Laws, Mass-Independent Effects, and Isotopic Anomalies*. Annual Review of Earth and Planetary Sciences, 2016. **44**(1): p. 709-783.
237. Bigeleisen, J., *Nuclear Size and Shape Effects in Chemical Reactions. Isotope Chemistry of the Heavy Elements*. Journal of the American Chemical Society, 1996. **118**(15): p. 3676-3680.
238. Fujii, Y., et al., *An Anomalous Isotope Effect of ^{235}U in U(IV)-U(VI) Chemical Exchange*, in *Zeitschrift für Naturforschung A* 1989. p. 395.
239. Nomura, M., Higuchi, N., and Fujii, Y., *Mass Dependence of Uranium Isotope Effects in the U(IV)-U(VI) Exchange Reaction*. Journal of the American Chemical Society, 1996. **118**(38): p. 9127-9130.
240. Eiler, J.M., et al., *Frontiers of stable isotope geoscience*. Chemical Geology, 2014. **372**: p. 119-143.
241. Abe, M., et al., *An ab initio molecular orbital study of the nuclear volume effects in uranium isotope fractionations*. Journal of Chemical Physics, 2008. **129**(16): p. 7.
242. Abe, M., et al., *An ab initio study based on a finite nucleus model for isotope fractionation in the U(III)-U(IV) exchange reaction system*. Journal of Chemical Physics, 2008. **128**(14): p. 6.
243. Knyazev, D.A. and Myasoedov, N.F., *Specific effects of heavy nuclei in chemical equilibrium*. Separation Science and Technology, 2001. **36**(8-9): p. 1677-1696.
244. Schauble, E.A., *Role of nuclear volume in driving equilibrium stable isotope fractionation of mercury, thallium, and other very heavy elements*. Geochimica Et Cosmochimica Acta, 2007. **71**(9): p. 2170-2189.
245. Bigeleisen, J. and Mayer, M.G., *CALCULATION OF EQUILIBRIUM CONSTANTS FOR ISOTOPIC EXCHANGE REACTIONS*. Journal of Chemical Physics, 1947. **15**(5): p. 261-267.
246. Bigeleisen, J., *Temperature dependence of the isotope chemistry of the heavy elements*. Proceedings of the National Academy of Sciences of the United States of America, 1996. **93**(18): p. 9393-9396.
247. Rademacher, L.K., et al., *Experimentally determined uranium isotope Fractionation during reduction of hexavalent U by bacteria and zero valent iron*. Environmental Science & Technology, 2006. **40**(22): p. 6943-6948.
248. Bopp, C.J., et al., *Variations in U-238/U-235 in uranium ore deposits: Isotopic signatures of the U reduction process?* Geology, 2009. **37**(7): p. 611-614.
249. Fernandes, H.M., et al., *Management of uranium mill tailing: Geochemical processes and radiological risk assessment*. Journal of Environmental Radioactivity, 1996. **30**(1): p. 69-95.
250. Varga, Z., et al., *Identification of uranium signatures relevant for nuclear safeguards and forensics*. Journal of Radioanalytical and Nuclear Chemistry, 2017. **312**(3): p. 639-654.
251. Albarède, F., et al., *Precise and accurate isotopic measurements using multiple-collector ICPMSI*. Geochimica et Cosmochimica Acta, 2004. **68**(12): p. 2725-2744.
252. Williams, R., *Uncertainty in Measurement of Isotope Ratios by Multi-Collector Mass Spectrometry*, in *Safeguards Symposium 2010*: Vienna, Austria.

253. Kragten, J., *A standard scheme for calculating numerically standard deviations and confidence intervals*. Chemometrics and Intelligent Laboratory Systems, 1995. **28**(1): p. 89-97.
254. Horsky, M., Irrgeher, J., and Prohaska, T., *Evaluation strategies and uncertainty calculation of isotope amount ratios measured by MC ICP-MS on the example of Sr*. Analytical and Bioanalytical Chemistry, 2016. **408**(2): p. 351-367.
255. Alonso, J.I.G. and Rodriguez-Gonzalez, P., *Response to "Comments on the uncertainties in isotope patterns of molecules" by J. Meija and Z. Mester (doi: 10.1016/j.aca.2010.09.029)*. Analytica Chimica Acta, 2011. **694**(1-2): p. 177-180.
256. Brown, J.N.W., Robertson, J.D., and Brockman, J.D., *Measurement of U and Pu isotope ratios in hair and nail samples using extraction chromatography and multi-collector inductively coupled plasma mass spectrometry*. Talanta, 2014. **129**: p. 481-485.
257. Richter, S., et al., *The isotopic composition of natural uranium samples - Measurements using the new n(U-233)/n(U-236) double spike IRMM-3636*. International Journal of Mass Spectrometry, 2008. **269**(1-2): p. 145-148.
258. Uvarova, Y.A., et al., *Variations in the uranium isotopic compositions of uranium ores from different types of uranium deposits*. Geochimica Et Cosmochimica Acta, 2014. **146**: p. 1-17.
259. Kirchenbaur, M., et al., *Uranium and Sm isotope studies of the supergiant Olympic Dam Cu-Au-U-Ag deposit, South Australia*. Geochimica Et Cosmochimica Acta, 2016. **180**: p. 15-32.
260. Pollington, A.D., et al., *Polyatomic interferences on high precision uranium isotope ratio measurements by MC-ICP-MS: applications to environmental sampling for nuclear safeguards*. Journal of Radioanalytical and Nuclear Chemistry, 2016. **307**(3): p. 2109-2115.
261. Stirling, C.H., Halliday, A.N., and Porcelli, D., *In search of live ²⁴⁷Cm in the early solar system*. Geochimica et Cosmochimica Acta, 2005. **69**(4): p. 1059-1071.
262. Mitroshkov, A.V., Olsen, K.B., and Thomas, M.L., *Estimation of the formation rates of polyatomic species of heavy metals in plutonium analyses using a multicollector ICP-MS with a desolvating nebulizer*. Journal of Analytical Atomic Spectrometry, 2015. **30**(2): p. 487-493.
263. Boulyga, S.F., et al., *Uranium isotope analysis by MC-ICP-MS in sub-ng sized samples*. Journal of Analytical Atomic Spectrometry, 2016. **31**(11): p. 2272-2284.
264. Mayer, K., Wallenius, M., and Varga, Z., *Interviewing a Silent (Radioactive) Witness through Nuclear Forensic Analysis*. Analytical Chemistry, 2015. **87**(23): p. 11605-11610.
265. Balboni, E., et al., *Chemical and Sr isotopic characterization of North America uranium ores: Nuclear forensic applications*. Applied Geochemistry, 2016. **74**: p. 24-32.
266. Shannon, R.D., *REVISED EFFECTIVE IONIC-RADII AND SYSTEMATIC STUDIES OF INTERATOMIC DISTANCES IN HALIDES AND CHALCOGENIDES*. Acta Crystallographica Section A, 1976. **32**(SEP1): p. 751-767.
267. Fryer, B.J. and Taylor, R.P., *RARE-EARTH ELEMENT DISTRIBUTIONS IN URANINITES - IMPLICATIONS FOR ORE GENESIS*. Chemical Geology, 1987. **63**(1-2): p. 101-108.
268. Spano, T.L., et al., *Trace element and U isotope analysis of uraninite and ore concentrate: Applications for nuclear forensic investigations*. Applied Geochemistry, 2017. **84**: p. 277-285.
269. Frimmel, H.E., Schedel, S., and Bratz, H., *Uraninite chemistry as forensic tool for provenance analysis*. Applied Geochemistry, 2014. **48**: p. 104-121.
270. Bürger, S., et al., *Quantifying multiple trace elements in uranium ore concentrates: an interlaboratory comparison*. Journal of Radioanalytical and Nuclear Chemistry, 2014. **301**(3): p. 711-729.
271. Balboni, E., et al., *Rare-earth element fractionation in uranium ore and its U(VI) alteration minerals*. Applied Geochemistry, 2017. **87**: p. 84-92.

272. Fraser, M.M. and Beauchemin, D., *Effect of concomitant elements on the distribution of ions in inductively coupled plasma-mass spectroscopy. Part 1. Elemental ions*. Spectrochimica Acta Part B: Atomic Spectroscopy, 2000. **55**(11): p. 1705-1731.
273. May, T.W. and Wiedmeyer, R.H., *A table of polyatomic interferences in ICP-MS*. Atomic Spectroscopy, 1998. **19**(5): p. 150-155.
274. Stroh, A., Bea, F., and Montero, P.G., *ULTRATRACE-LEVEL DETERMINATION OF RARE-EARTH ELEMENTS, THORIUM, AND URANIUM IN ULTRAMAFIC ROCKS BY ICP-MS*. Atomic Spectroscopy, 1995. **16**(1): p. 7-11.
275. Jenner, G.A., et al., *ICP-MS — A powerful tool for high-precision trace-element analysis in Earth sciences: Evidence from analysis of selected U.S.G.S. reference samples*. Chemical Geology, 1990. **83**(1): p. 133-148.
276. Beary, E.S., Paulsen, P.J., and Fassett, J.D., *SAMPLE PREPARATION APPROACHES FOR ISOTOPE-DILUTION INDUCTIVELY-COUPLED PLASMA-MASS SPECTROMETRIC CERTIFICATION OF REFERENCE MATERIALS*. Journal of Analytical Atomic Spectrometry, 1994. **9**(12): p. 1363-1369.
277. Zhang, S.Z., et al., *The determination of rare earth elements in soil by inductively coupled plasma mass spectrometry*. Atomic Spectroscopy, 1997. **18**(5): p. 140-144.
278. Varga, Z., et al., *Development and validation of a methodology for uranium radiochronometry reference material preparation*. Analytica Chimica Acta, 2012. **2012**(718): p. 25-31.
279. Premadas, A. and Srivastava, P.K., *Inductively coupled plasma atomic emission spectrometric determination of lanthanides and Y in various uranium hydrometallurgical products*. Journal of Radioanalytical and Nuclear Chemistry, 2002. **251**(2): p. 233-239.
280. Krajko, J., et al., *Development of a versatile sample preparation method and its application for rare-earth pattern and Nd isotope ratio analysis in nuclear forensics*. Journal of Radioanalytical and Nuclear Chemistry, 2015. **304**(1): p. 177-181.
281. Gméling, K., et al., *Comparative PGAA and NAA results of geological samples and standards*. Journal of Radioanalytical and Nuclear Chemistry, 2014. **300**(2): p. 507-516.
282. Wang, Y.Q., et al., *Determination of the contents and distribution characteristics of REE in natural plants by NAA*. Journal of Radioanalytical and Nuclear Chemistry, 1997. **219**(1): p. 99-103.
283. Popelka-Filcoff, R.S., et al., *Evaluation of relative comparator and k₀-NAA for characterization of Aboriginal Australian ochre*. Journal of Radioanalytical and Nuclear Chemistry, 2012. **291**(1): p. 19-24.
284. MacDonald, B.L., et al., *Geochemical characterization of ochre from central coastal British Columbia, Canada*. Journal of Archaeological Science, 2011. **38**(12): p. 3620-3630.
285. Kirishima, A., et al., *Interaction of rare earth elements and components of the Horonobe deep groundwater*. Chemosphere, 2017. **168**: p. 798-806.
286. Kayasth, S. and Gangadharan, S., *A search for rare and other trace elements in different stages of a copper mill by NAA*. Journal of Radioanalytical and Nuclear Chemistry, 1994. **181**(2): p. 425-431.
287. Vieira, B.J., Freitas, M.C., and Wolterbeek, H.T., *Elemental composition of air masses under different altitudes in Azores, central north Atlantic*. Journal of Radioanalytical and Nuclear Chemistry, 2012. **291**(1): p. 63-69.
288. Canion, B., et al., *Trace analysis of Indonesian volcanic ash using thermal and epithermal neutron activation analysis*. Nukleonika, 2012. **57**(4): p. 585-589.
289. El-Taher, A., *INAA and DNAA for uranium determination in geological samples from Egypt*. Applied Radiation and Isotopes, 2010. **68**(6): p. 1189-1192.
290. El-Taher, A., *Rare-earth elements in Egyptian granite by instrumental neutron activation analysis*. Applied Radiation and Isotopes, 2007. **65**(4): p. 458-464.

291. Stanley, F.E., Stalcup, A.M., and Spitz, H.B., *A brief introduction to analytical methods in nuclear forensics*. Journal of Radioanalytical and Nuclear Chemistry, 2013. **295**(1): p. 1385-1393.
292. Asim, M., Wasim, M., and Mohammad, B., *Development of methodologies for the analysis of uranium ores by k(0)-instrumental neutron activation analysis and inductively coupled plasma atomic emission spectrometry*. Journal of Radioanalytical and Nuclear Chemistry, 2017. **311**(3): p. 1963-1969.
293. Ribeiro, I.S., et al., *Samarium determination by neutron activation analysis in uranium-rich samples*. Journal of Radioanalytical and Nuclear Chemistry, 2015. **305**(1): p. 299-303.
294. Ribeiro, I.S., et al., *Determination of uranium fission interference factors for INAA*. Journal of Radioanalytical and Nuclear Chemistry, 2013. **296**(2): p. 759-762.
295. Tshishala, M.D.A., *Instrumental neutron activation analysis in geochemistry: Emphasis on spectral and uranium fission product interferences*. Journal of Radioanalytical and Nuclear Chemistry, 2005. **265**(3): p. 511-514.
296. de Soete, D., Gijbels, R., and Hoste, J., *Neutron Activation Analysis [by] D. de Soete, R. Gijbels [and] J. Hoste*1972: Wiley-Interscience.
297. Strelci, C., et al., *A new total reflection X-ray fluorescence vacuum chamber with sample changer analysis using a silicon drift detector for chemical analysis*. Spectrochimica Acta Part B: Atomic Spectroscopy, 2004. **59**(8): p. 1199-1203.
298. Anvia, M. and Brown, S.A., *Correction methods for uranium analysis by DNAA*. Journal of Radioanalytical and Nuclear Chemistry, 2017. **311**(2): p. 1453-1458.
299. Dyer, F., Emery, J., and Leddicotte, G., *A comprehensive study of the neutron activation analysis of uranium by delayed neutron counting*, Oak Ridge National Laboratory, Editor 1962: Oak Ridge, TN,.
300. Potts, P.J. and West, M., *Portable X-ray Fluorescence Spectrometry: Capabilities for in Situ Analysis*2008: RSC Pub.
301. Eriksson, S.M., et al., *Delayed-neutron activation analysis at NIST*. Journal of Radioanalytical and Nuclear Chemistry, 2013. **298**(3): p. 1819-1822.
302. Wanke, C., et al., *Activity standardization and decay data of ⁶⁴Cu*. Applied Radiation and Isotopes, 2010. **68**(7): p. 1297-1302.
303. Linstedt, K.D. and Kruger, P., *DETERMINATION OF VANADIUM IN NATURAL WATERS BY NEUTRON ACTIVATION ANALYSIS*. Analytical Chemistry, 1970. **42**(1): p. 113-&.
304. Stopic, A., T. Ditcham, Editor 2016.
305. Baedecker, P. and McKown, D., *Instrumental neutron activation analysis of geochemical samples*. Methods of Geochemical Analysis, 1987.
306. Kin, F.D., et al., *Determination of rare earth elements in geological reference materials: A comparative study by INAA and ICP-MS*. Geostandards Newsletter-the Journal of Geostandards and Geoanalysis, 1999. **23**(1): p. 47-58.
307. Glascock, M.D., et al., *CORRECTING FOR URANIUM FISSION IN INSTRUMENTAL NEUTRON-ACTIVATION ANALYSIS OF HIGH-URANIUM ROCKS*. Journal of Radioanalytical and Nuclear Chemistry-Articles, 1986. **99**(1): p. 121-131.
308. Brunfelt, A.O. and Steinnes, E., *DETERMINATION OF LUTETIUM, YTTERBIUM AND TERBIUM IN ROCKS BY NEUTRON ACTIVATION AND MIXED SOLVENT ANION-EXCHANGE CHROMATOGRAPHY*. Analyst, 1969. **94**(1124): p. 979-&.
309. Manna, S., Roy, S.B., and Joshi, J.B., *Study of crystallization and morphology of ammonium diuranate and uranium oxide*. Journal of Nuclear Materials, 2012. **424**(1-3): p. 94-100.
310. Bonhoure, J., et al., *Methodology for rare earth element determinations of uranium oxides by ion microprobe*. Geostandards and Geoanalytical Research, 2007. **31**(3): p. 209-225.

311. Ciobanu, C.L., et al., *Uranium-bearing hematite from the Olympic Dam Cu–U–Au deposit, South Australia: A geochemical tracer and reconnaissance Pb–Pb geochronometer*. Precambrian Research, 2013. **238**: p. 129-147.
312. Oreskes, N. and Einaudi, M.T., *Origin of rare earth element-enriched hematite breccias at the Olympic Dam Cu-U-Au-Ag deposit, Roxby Downs, South Australia*. Economic Geology, 1990. **85**(1): p. 1-28.
313. Fisher, L.A., et al., *3D representation of geochemical data, the corresponding alteration and associated REE mobility at the Ranger uranium deposit, Northern Territory, Australia*. Mineralium Deposita, 2013. **48**(8): p. 947-966.
314. Maas, R., et al., *SM-ND ISOTOPE SYSTEMATICS IN URANIUM RARE EARTH ELEMENT MINERALIZATION AT THE MARY-KATHLEEN-URANIUM-MINE, QUEENSLAND*. Economic Geology, 1987. **82**(7): p. 1805-1826.
315. Van Hoecke, K., et al., *Isolation of lanthanides from spent nuclear fuel by means of high performance ion chromatography (HPIC) prior to mass spectrometric analysis*. Journal of Radioanalytical and Nuclear Chemistry, 2017. **314**(3): p. 1727-1739.
316. Sivaraman, N., et al., *Separation of lanthanides using ion-interaction chromatography with HDEHP coated columns*. Journal of Radioanalytical and Nuclear Chemistry, 2002. **252**(3): p. 491-495.
317. Akhila Maheswari, M., et al., *High performance liquid chromatographic studies on lanthanides, uranium and thorium on amide modified reversed phase supports*. Talanta, 2007. **72**(2): p. 730-740.
318. Datta, A., et al., *Single-Stage Dual-Column HPLC Technique for Separation and Determination of Lanthanides in Uranium Matrix: Application to Burnup Measurement on Nuclear Reactor Fuel*. Nuclear Technology, 2013. **182**(1): p. 84-97.
319. The Canadian Certified Reference Materials Project, *Reference Uranium Ore BL-5 Certificate of Analysis*, Canada Centre for Mineral and Energy Technology, Editor 2017: Ottawa, Ontario.
320. New Brunswick Laboratory, *CRM 123(1-7) Certificate of Analysis*, Department of Energy, Editor 1991: Lemont, Illinois.